



Quantitative relationships between chemical composition, microstructure and mechanical properties for bainitic steels

Victor Bordereau

► To cite this version:

Victor Bordereau. Quantitative relationships between chemical composition, microstructure and mechanical properties for bainitic steels. Materials. Ecole Nationale Supérieure des Mines de Paris, 2015. English. NNT : 2015ENMP0063 . tel-02892101v1

HAL Id: tel-02892101

<https://pastel.hal.science/tel-02892101v1>

Submitted on 7 Jul 2020 (v1), last revised 8 Jul 2020 (v2)

HAL is a multi-disciplinary open access archive for the deposit and dissemination of scientific research documents, whether they are published or not. The documents may come from teaching and research institutions in France or abroad, or from public or private research centers.

L'archive ouverte pluridisciplinaire **HAL**, est destinée au dépôt et à la diffusion de documents scientifiques de niveau recherche, publiés ou non, émanant des établissements d'enseignement et de recherche français ou étrangers, des laboratoires publics ou privés.

École doctorale n° 432 : Sciences des Métiers de l'Ingénieur

Doctorat ParisTech

T H È S E

pour obtenir le grade de docteur délivré par

l'École nationale supérieure des mines de Paris

Spécialité Sciences et Génie des Matériaux

présentée et soutenue publiquement par

Victor BORDEREAU

le 26 mars 2015

Confidentiel jusqu'au 25 mars 2020

Relations quantitatives entre composition chimique, microstructure et propriétés mécaniques d'aciers bainitiques

Quantitative relationships between chemical composition, microstructure and mechanical properties for bainitic steels

Directrice de thèse : **Anne-Françoise GOURGUES-LORENZON**

Co-encadrement de la thèse : **Marie-Thérèse PERROT-SIMONETTA, Kangying ZHU**

Jury

M. Sébastien ALLAIN, Professeur, Institut Jean Lamour, Université de Lorraine
Mme Sabine DENIS, Professeur, Institut Jean Lamour, Université de Lorraine
M. Sybrand VAN DER ZWAAG, Professeur, Aerospace Engineering, TU Delft
M. Damien FABREGUE, Maître de Conférences HDR, MATEIS, INSA Lyon
Mme Marie-Thérèse PERROT-SIMONETTA, Docteur, ArcelorMittal Europe Long Products
Mme Anne-Françoise GOURGUES-LORENZON, Professeur, MINES ParisTech

Président
Rapporteur
Rapporteur
Examinateur
Examinatrice
Examinatrice

**T
H
È
S
E**

AKNOWLEDGEMENT

Je commencerais ces remerciements par mes trois drôles de dames :

- Anne-Françoise Gourgues-Lorenzon, Professeur à Mines ParisTech, pour tous ses conseils judicieux, ses retours d'expérience, ses connaissances et sa disponibilité qui m'ont permis d'avancer tout au long de cette thèse. Elle est pour moi un exemple, car elle mène de front une vie de famille bien chargée, des heures d'enseignement, de la gestion de thèse et de thésards tout en gardant une énergie et une positivité incroyables.
- Marie-Thérèse Perrot-Simonetta, pour m'avoir choisi pour ce projet et m'avoir fait confiance tout au long de la thèse. Elle m'a apporté sa vision globale du sujet, avec ses enjeux et ses perspectives industrielles.
- Kangying Zhu, pour ses connaissances et ses idées. J'ai toujours pu compter sur elle pour m'aider à réaliser les expériences les plus techniques de cette thèse. Aussi, si cette présente thèse n'excède pas les 500 pages, c'est beaucoup grâce à elle. Vous la remercierai aussi quand vous aurez eu le courage de la lire jusqu'au bout.

Je suis très reconnaissant à Sabine Denis, professeur à l'Université de Lorraine, Sybrand Van Der Zwaag, professeur à TU Delft, Sébastien Allain, professeur à l'Université de Lorraine et Damien Fabregue, maître de conférences à l'INSA de Lyon, d'avoir accepté d'être membre du jury de cette thèse.

Un grand merci à :

- Anne Laurent, technicienne du groupe *Matériau et Mécanique* (Centre des Matériaux Mines ParisTech) pour sa gentillesse, sa disponibilité et son écoute (qualité nécessaire pour toute personne travaillant avec des doctorants en dernière année de thèse). J'aime imaginer que beaucoup de thésard comme moi te réserve une place particulière dans leur cœur.
- Jean-Paul Weiler, technicien du service *Forge et Traitement Thermique* (centre R&D ArcelorMittal de Gandrange), avec qui j'ai l'occasion de travailler et d'échanger à plusieurs reprises. J'ai pu notamment compter sur son hospitalité à plusieurs reprises durant cette thèse.
- Bruno Cofino, responsable du service *Forge et Traitement Thermique* (centre R&D ArcelorMittal de Gandrange) qui m'a permis une intégration rapide au sein du laboratoire de Gandrange au début ma thèse. J'ai le plaisir aujourd'hui de commencer ma carrière professionnelle dans son service.
- Marie-Claire Estivalet-Sionneau, responsable du centre R&D ArcelorMittal de Gandrange, pour la confiance qu'elle m'a accordée et son intérêt à me garder dans ses effectifs. J'espère que mes futurs travaux vous conforteront dans ces positions.

NOMENCLATURE

Je remercie :

- Toute l'équipe et les thésards du Centre des Matériaux pour leur sympathie et leur amour de la science. J'ai une grosse pensée pour mes collègues de bureau, Franck, Minghao, Alexandre et Mélanie.
- A toute l'équipe du centre R&D de Gandrange. J'ai énormément apprécié chaque moment passé dans ce centre, grâce à vous tous. La preuve, j'ai tenu à y rester.

Plus personnellement à:

- Mes parents, pour tout.
- Mes frères
- Ma femme, Eugénie Vince
- Mes amis.

CONTENTS

INTRODUCTION.....	1
Context	1
Objectives & Approach	2
Manuscript structure	3
CHAPTER 1 – LITERATURE SURVEY: INFLUENCE OF AUSTENITE STATE & ALLOYING ELEMENTS ON THE BAINITIC TRANSFORMATION.....	7
1.1 Bainite microstructures.....	8
1.1.1 Classifications of the various morphologies of bainite microstructures	8
1.1.2 The different scales of the bainitic microstructures	13
1.2 Effect of major alloying elements on the austenite decomposition into bainite	13
1.2.1 Global view	14
1.2.1.a Effect on equilibrium and non-equilibrium diagrams	14
1.2.1.b The incomplete transformation phenomenon	15
1.2.1.c Precipitation behaviour.....	16
1.2.2 Specific role of manganese as alloying element	16
1.2.2.a Manganese in solid solution	16
1.2.2.b Manganese in precipitates	17
1.2.3 Specific role of silicon as alloying element.....	18
1.2.4 Specific role of chromium as alloying element.....	20
1.2.5 Specific role of nickel as alloying element.....	21
1.3 Effect of micro-alloying elements	23
1.3.1 Role of boron as micro-alloying element.....	23
1.3.1.a Phenomenology	23
1.3.1.b Mechanism of boron-induced hardenability	24
1.3.1.c Avoiding precipitation of boron carbo-nitrides	26
1.3.2 Role of niobium as micro-alloying element.....	28
1.3.2.a Effect of niobium in solid solution	28
1.3.2.b Effect of niobium in precipitates	30
1.3.3 Role of molybdenum as micro-alloying element.....	31
1.3.3.a Effect of molybdenum in solid solution	32
1.3.3.b Effect of molybdenum in precipitates.....	34
1.3.3 Role of titanium as micro-alloying element.....	35

CONTENTS

1.3.3.a Effect of titanium in solid solution	35
1.3.3.b Effect of titanium in precipitates	36
1.4 Influence of the austenite state on its decomposition during cooling	38
1.4.1 Influence of the primary austenite grain size on the austenite decomposition	38
1.4.1a Effect on the ferritic transformation.....	38
1.4.1.b Effect on the bainitic transformation	38
1.4.1.c Effect on the martensitic transformation	41
1.4.2 Influence of prior deformation	41
1.5 Conclusions	42
CHAPTER 2 - MATERIALS	44
2.1 Reference materials.....	45
2.1.1 Chemical composition and metallurgical states	45
2.1.2 Segregations & inclusions	45
2.1.2.a Banded structure.....	45
2.1.2.b Characterization of coarser niobium-titanium carbo-nitrides	49
2.1.3 Determination of the non-recrystallization temperature.....	51
2.2 Laboratory heats	52
2.2.1 Design of chemical compositions.....	52
2.2.2 As-received state and pre-forging operations	54
2.3 Forging	54
2.3.1 On-field measurements	54
2.3.1.a Preparation	54
2.3.1.b On-field Measurements.....	57
2.3.1.c Results.....	57
2.3.2 In bulk temperature calculation	59
2.3.3 Setting of the cooling rates considered for the forged laboratory heats.....	62
2.4 Overview of available microstructures.....	62
2.4.1 Identification of microstructural constituents from SEM observations.....	62
2.4.2 LM quantification of the primary austenite grain size	66
2.4.3 Quantification of microstructural constituent	68
2.4.4 Precipitation.....	72
2.5 Discussion	74
2.6 Conclusions	75
CHAPTER 3 - EFFECT OF ALLOYING ELEMENTS ON CONTINUOUS COOLING TRANSFORMATION DIAGRAM	77

CONTENTS

3.1 Conditioning of the primary austenite state	78
3.1.1 Experimental methods	78
3.1.1.a Materials	78
3.1.1.b Parameters of dilatometric cycles	79
3.1.1.c Processing of dilatometric curves	80
3.1.1.d Microstructural characterization	82
3.1.2 Results	82
3.1.3 Conclusions	84
3.2 Continuous cooling transformation diagrams	84
3.2.1 Experimental methods	84
3.2.1.a Dilatometric cycles	84
3.2.1.b Microstructural characterization	85
3.2.2 Results	86
3.2.2.a Typical dilatometric response	86
3.2.2.b Definition of microstructural domains	88
3.2.2.c Variation of the retained austenite content through the different domains	92
3.2.3 Discussion	95
3.2.3.a Comparison with as-forged microstructures	95
3.2.3.b Influence of the micro-alloying elements	99
3.2.3.c Influence of chromium	103
3.2.3.d Influence of nickel	107
3.2.3.e Influence of silicon and manganese	107
3.2.2.f Empirical calculation of the bainitic start temperature	112
3.3 Final remarks, conclusions & Outlooks	113
CHAPTER 4 – PHYSICAL PHENOMENA AND MICROSTRUCTURAL PARAMETERS THAT CONTROL IMPACT TOUGHNESS	116
4.1 Experimental methods	117
4.2 Results	119
4.2.1 Charpy impact test results	119
4.2.2 Fracture mechanisms	120
4.2.3 Damage development	125
4.2.4 Effective packet size	127
4.2.5 Secondary microstructural constituent and austenite	131
4.3 Discussion	133
4.3.1 Calculation of impact toughness from quantitative data	133
4.3.2 Cleavage fracture path	135

CONTENTS

4.4 Conclusions & Outlooks	136
CHAPTER 5 - MICROSTRUCTURAL PARAMETERS THAT CONTROL STRENGTH	138
5.1 Overall tensile behaviour.....	139
5.1.1 Experimental methods.....	139
5.1.2 Results	140
5.1.3 Relationship between average hardness and strength level	144
5.1.4 Relationship between impact toughness and ductility in uniaxial tension	146
5.1.5 Fracture mechanisms	148
5.1.6 Damage mechanisms	153
5.1.6.a Light microscopy observations	153
5.1.6.b Scanning electron microscopy observation	153
5.2 Rationalization of the links between microstructure and yield strength	157
5.2.1 Solid solution strengthening.....	158
5.2.1.a Principle	158
5.2.1.b Mathematical description.....	159
5.2.1.c Data for calculation.....	159
5.2.1.d Coefficients available from literature	160
5.2.1.e Coefficients for calculation	161
5.2.2 Strengthening from boundaries.....	162
5.2.2.a Principle	162
5.2.2.b Mathematical description.....	162
5.2.2.c Data and coefficients for calculation	163
5.2.3 Dislocation strengthening	165
5.2.3.a Principle	165
5.2.3.b Mathematical description.....	165
5.2.3.c Data and coefficients for calculation	166
5.2.4 Precipitation strengthening	167
5.2.4.a Principle	167
5.2.4.b Mathematical description.....	169
5.2.4.c Data and coefficients for calculation	169
5.2.5 Base strength	171
5.2.6 Contribution of the secondary microstructural constituents	171
5.2.6.a Principle	171
5.2.6.b Data & coefficients for calculation	173
5.2.7 Global calculation	174

CONTENTS

5.2.7.a Coefficients for calculation	174
5.2.7.b Results.....	176
5.2.8 Discussion	176
5.2.8.a Contribution of every strengthening mechanism to the total yield strength ...	176
5.2.8.b Calculation of yield strength for reference steels	181
5.2.8.c Comparison between as-rolled and as-forged reference steel.....	181
5.2.8.d Comparison between as-forged reference steel and as-forged laboratory heats	182
5.2.8.e Ways for simplifications of the calculation	182
5.3 Conclusion & Outlooks.....	184
CONCLUSIONS & OUTLOOKS	189
Achievement of the general objectives of the study	189
Evaluation of the microstructural robustness of this steel family.....	190
Key microstructural parameters controlling mechanical properties.....	190
1. The bainitic ferrite packet size	192
1.1 Control of the PAGS	192
1.2 Control of the austenite decomposition into bainite	192
2. The fraction of hard secondary microstructural constituent	193
3. Retained austenite	194
APPENDIX A - MICROSTRUCTURAL CHARACTERIZATION METHODS.....	195
A.I Quantification of the fraction of microstructural constituents	195
A.I.1 Quantification using light microscopy	195
A.I.1.a Etching tests.....	195
A.I.1.b Pre-processing	198
A.I.1.c Processing.....	200
A.I.1.d Limit of this quantification	202
A.I.1.e Special case of allotriomorphic ferrite	204
A.I.1.f Special case of martensite-rich microstructures.....	205
A.I.2 Quantification using electron backscatter diffraction.....	206
A.I.2.a Sample preparation and EBSD data acquisition	206
A.I.2.b Processing of EBSD data	206
A.I.2.c Results.....	208
A.I.3 Quantification using scanning electron microscopy	208
A.I.3.a Protocol	208
A.I.3.b Processing.....	209

CONTENTS

A.I.3.c Results.....	210
A.I.4 Comparison of the results obtained from different quantification methods	210
A.II Quantification of the austenite content.....	213
A.II.1 Literature survey	213
A.II.2 Quantification using X-ray diffraction	215
A.II.2.a Protocol	215
A.II.2.b Data processing.....	215
A.II.3 Quantification using sigmametry	217
A.II.3.a Commissioning	217
A.II.3.b Protocol	217
A.II.3.c Creation of a reference sample for the project's steel grade	218
A.II.3.d Processing.....	220
A.II.4 Benchmark measurements between sigmametry and X-Ray diffraction	220
A.II.4.a Experimental methods	220
A.II.4.b Results and discussion	221
A.II.4.c Conclusions	222
A.III Measurement of grain and packet size	222
A.III.1 Measurement of the primary austenite grain size	222
A.III.1.a Literature survey	222
A.III.1.b Protocol	225
A.III.1.c Image processing	225
A.III.2 Measurement of the effective bainite packet size	226
A.III.2.a Protocol	226
A.III.2.b Pre-processing	227
A.III.2.c Processing.....	228
A.IV Precipitation characterization	228
A.IV.1 Carbon replica analysis.....	228
A.IV.1.a Protocol.....	228
A.IV.1.b Pre-processing	229
A.IV.1.c Processing	231
APPENDIX B – MACHINING PLAN	232
REFERENCES.....	234

INTRODUCTION

Context

High-strength bainitic steels are increasingly being considered as substitutes to quenched & tempered (Q&T) martensitic steels or precipitation hardened ferritic-pearlitic steels for the realization of automotive forged parts. Figure 1 shows the achievable tensile strength according to transformation temperatures for quenched & tempered martensitic, air-cooled bainitic and ferritic-pearlitic steels.

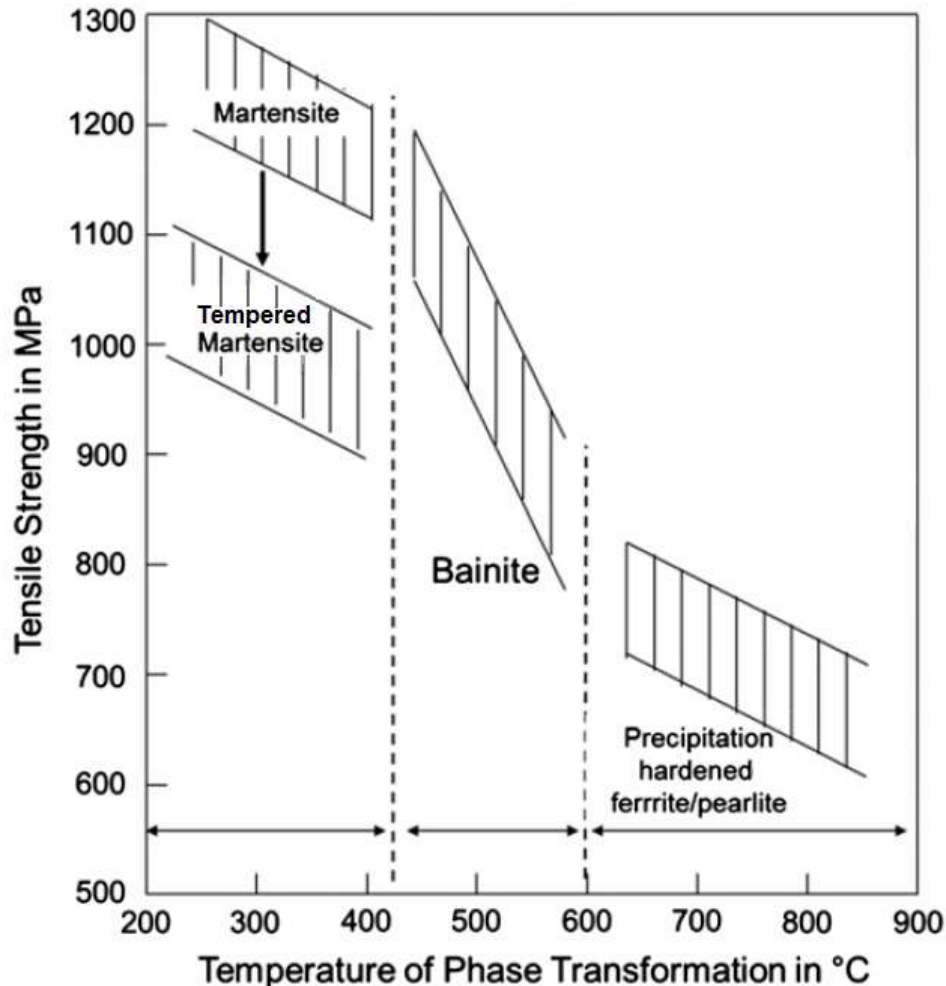


Figure 1: Schematic view of achievable tensile strength levels a function of the austenite decomposition temperature. After [1].

ArcelorMittal has developed since 2007 an air-cooled bainitic steel to compete with Q&T martensitic steels. High mechanical properties (yield strength > 800 MPa, ultimate tensile strength > 1100 MPa, impact toughness > 20 J at room temperature) are provided by a complex chemical composition, leading to a multi-scale and multi-constituent bainitic microstructure after still air-cooling. This steel grade allows significant manufacturing cost and time reductions as the realization of several post-forging thermo-mechanical treatments is avoided, as shown in Figure 2.

In order to stay competitive and to anticipate the market trends and needs, the mechanical properties of this steel grade are continuously being optimized and adapted by adjusting the chemical composition. In this way, a better mastering of the design of such complex chemical

INTRODUCTION

composition (with more than eight major/minor alloying elements), by acquiring deeper understanding of the effect of each alloying element on microstructure and mechanical properties, should allow to significantly decrease response time to new evolving of this steel grade.

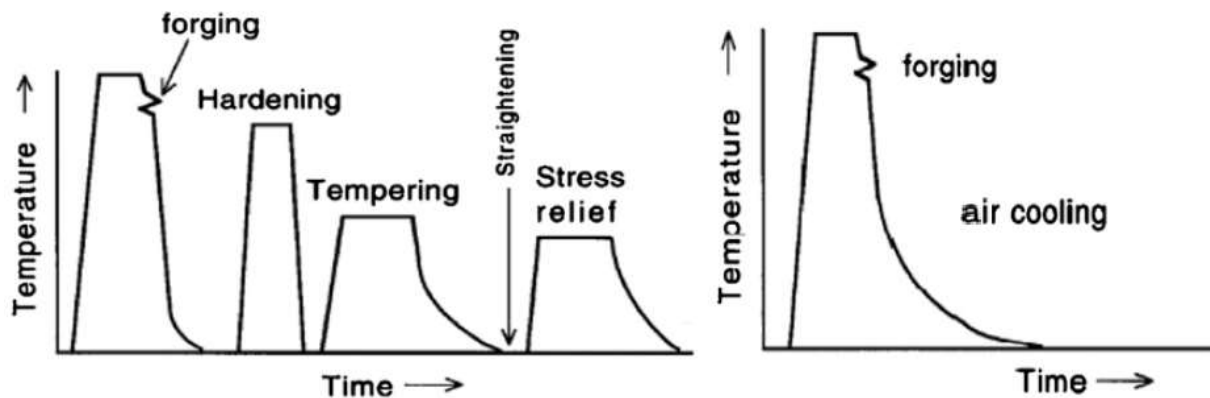


Figure 2: Process routes for forged parts (left: Q&T martensitic steels; right: air-cooled bainitic steels). After [1].

Objectives & Approach

This study is integrated in a project that aims at rationalizing the development of this air-cooled bainitic steel family through:

- Understanding and quantitative physically-based modelling of the relationships between chemical composition, microstructure and mechanical properties of forged parts,
- Modelling of metallurgical transformations during the thermal-mechanical route undergone by the part during processing,
- Optimisation of the chemical composition in order to increase the steel grade performance and/or to reduce production costs.

The present PhD study has been realized to reach the first objective of the project, the other objectives being simultaneously addressed by the project team in ArcelorMittal Long Carbon Europe R&D centre of Gandrange.

The PhD study has three main tasks that are detailed below:

1. Development of new methods or adaptation of existing ones for quantitative microstructural characterization of air-cooled bainite in the targeted range of chemical compositions and mechanical properties. These methods were selected according to equipment and know-how that are available both at the Centre des Matériaux and at ArcelorMittal. These methods are detailed in Appendix A.
2. Using these methods together with dilatometry to get better understanding of microstructural development during the decomposition of austenite under non-equilibrium conditions (i.e. continuous cooling). Specific dilatometric cycles were applied in order to obtain continuous cooling transformations (**CCT**) diagrams adapted to the targeted application.
3. Prediction of mechanical properties of forged parts from their microstructure:

INTRODUCTION

- a. Mechanical tests (uniaxial tension and impact toughness)
- b. Careful observation of tested specimens for the determination of the damage and fracture mechanisms.
- c. From quantitative characterization results, improving the understanding of relationships between microstructure and mechanical properties.

Tasks two and three have been realized using as-forged laboratory heats. These laboratory heats exhibit chemical variations of one or two alloying elements with respect to a reference “base” chemical composition, which is close to the current chemical composition of the reference steel grade. Two different geometries of forged parts have been chosen for each chemical combination. They were fabricated by using a free-forging route. No direct links have been established between chemical composition and mechanical properties as some uncertainties emerge from the chosen forging process. However, direct links between chemical composition and microstructure, as well as between microstructure and targeted mechanical properties (yield strength and impact toughness), have been identified through this PhD project.

The project has been conducted at the Centre des Matériaux (Mines ParisTech) in close partnership with ArcelorMittal Long Carbon Europe R&D centre of Gandrange. Work time of the PhD student in the two different facilities was 60%/40%. In addition, precious results have been obtained at ArcelorMittal Flat Carbon Europe R&D centre of Maizières-lès-Metz.

Manuscript structure

The manuscript is organized as follows:

Chapter 1 is a literature survey on the influence of the austenite state and alloying elements on the bainitic transformation and resulting microstructure. It starts with the different classifications of bainitic microstructures that are commonly used in literature, in order to discuss the microstructures observed in this study with respect to these classifications. The phase transformation mechanism has not been discussed since it is still the subject of a lot of debates in the scientific community and determination of it was judged not necessary to the realization of the PhD objectives.

In the second part of this chapter, the influence of alloying elements on phase transformation is first reviewed in a global approach. Then, the effect of each main alloying element is reviewed in more detail, especially regarding the austenite decomposition into bainite. This information has been used in chapter 2, to design the laboratory heats and in chapter 3, to discuss the influence of alloying elements noticed from CCT diagrams.

Finally, the effects of the austenite state on the bainitic transformation are considered. Focus is made on the austenite grain size. As the targeted process leads to fully recrystallized austenite before final cooling, no effect coming from the austenite deformation is expected. Information from this section has been used to discuss free-forging of laboratory heats (chapter 2) and to design dilatometric cycles (chapter 3).

Chapter 2 is dedicated to the microstructural characterization of the materials used for this study. It starts with the reference material in both as-rolled and as-forged states. Specific microstructure features linked to the process, such as segregation structure and inclusion population, are underlined. Then, chemical compositions of laboratory heats as well as applied forging process are described and discussed. Forging has been monitored by on-field measurements, which allows to gather information about the heat cycles and to point out some uncertainties emerging from the chosen forging process. These uncertainties lead to the segmentation of the link between chemical composition and mechanical properties as

INTRODUCTION

schematically described in Figure 3. Finally, an overview of the available microstructures is presented in terms of primary austenite grain size, fractions of microstructural constituents and precipitation state. These data have been used for Chapters 4 and 5, where links between microstructure and mechanical properties are studied.

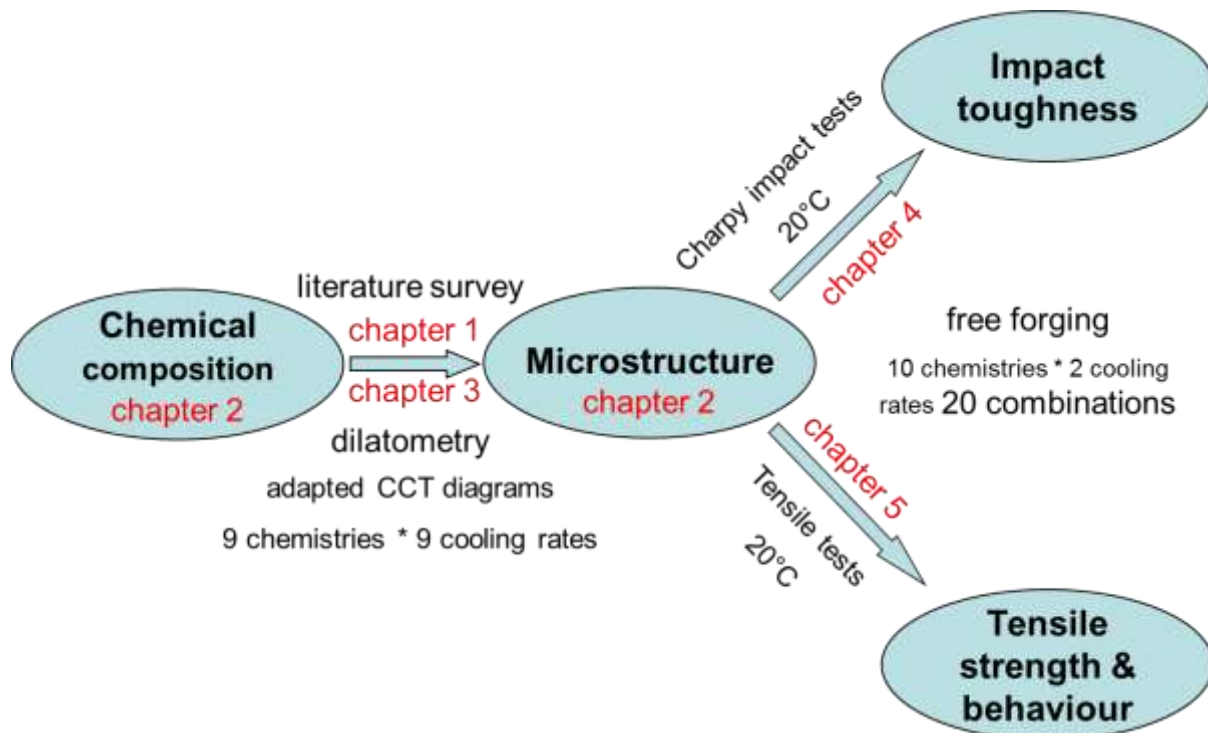


Figure 3: Approach to the link between chemical composition and mechanical properties applied in this PhD study.

The effect of alloying elements on the bainitic transformation during continuous cooling is investigated in **Chapter 3** using dilatometry experiments. Particular attention has been paid to the conditioning of austenite in order to avoid any grain size or decarburization effects on its decomposition. Dilatometric cycles have also been designed to build CCT diagrams relevant to the targeted application. Following these dilatometric cycles, every considered material exhibits some typical dilatometric responses depending on specific range of cooling rates. The resulting microstructures have been classified into different microstructural domains that are defined according to the fraction of microstructural constituents, hardness and transformation temperatures. The variation of austenite content through the different domains has also been investigated. Then, the effects of the various alloying elements are discussed, using the obtained CCT diagrams and the relationships between microstructural domains and cooling rates. The comparison between microstructures obtained after continuous cooling (i.e. CCT diagrams) and after still air-cooling (i.e. free-forging) is also made. It points out a noticeable effect of undercooling on the final microstructure.

Chapter 4 focuses on the physical phenomena and microstructural parameters that control impact toughness. The physical phenomena have been determined thanks to a careful and quantitative analysis of the fracture surface, together with damage investigations of the tested specimens. The microstructural parameters playing the main role in each physical phenomenon have been identified using data from microstructural quantification, together with literature data. All these observations have been then rationalized into a post-mortem relationship that fits with experimental results.

Chapter 5 is dedicated to physical phenomena and microstructural parameters that control strength, and especially the yield strength. It starts with the study of the overall tensile behaviour of every considered material, including tensile curves, fracture mechanisms and

INTRODUCTION

damage development mechanisms. By the way, relationships are established between average hardness and strength level as well as between impact toughness and amount of strain during necking. Then, using a classical additive approach, the contribution of each strengthening mechanism to the yield strength is determined for all as-forged laboratory heats. Such a calculation shows good agreement with the experimental results and underlines microstructural features that govern yield strength.

In chapters 4 & 5, the behaviour of two states of a unique reference steel are compared with that of as-forged laboratory heats.

To finish, a summary of obtained results is made in the **conclusion**, concentrating on the targeted application by making indirect links between chemical composition and microstructure. In the course of this final conclusion, some **outlooks** are also introduced, presenting research subjects that might be investigated further in the future.

INTRODUCTION

CHAPTER 1 – LITERATURE SURVEY: INFLUENCE OF AUSTENITE STATE & ALLOYING ELEMENTS ON THE BAINITIC TRANSFORMATION

Résumé : L'étude bibliographique réalisée dans ce chapitre traite de l'influence de l'état de l'austénite et des éléments d'alliage sur la transformation bainitique. Le mécanisme de transformation bainitique en lui-même n'est pas discuté car il est encore sujet à beaucoup de débats dans la communauté scientifique et sa détermination n'était pas strictement nécessaire à la réalisation de cette thèse.

Cette étude commence par lister les différentes classifications existantes concernant les microstructures bainitiques qui sont fréquemment utilisées dans la littérature. Les classifications proposées par Zajac et al. [6] et Bramfitt et Speer [10], très complètes, seront préférées par la suite pour nommer les microstructures rencontrées au cours de cette thèse.

La seconde partie de cette étude bibliographique est dédiée à l'influence des éléments d'alliage sur la transformation bainitique. Cette influence est premièrement observée dans son ensemble, sans focalisation particulière sur un élément d'alliage. Dans un deuxième temps, l'influence spécifique de chaque élément d'alliage présent dans la composition de l'acier de référence pour cette thèse est discutée séparément. Un tableau récapitulatif des informations retenues à la fin de cette partie est donné en conclusion. Ces informations ont permis d'établir les différentes compositions chimiques des coulées de synthèse réalisées pour cette thèse. Elles permettront ensuite de discuter de l'effet des éléments d'alliage observées sur les différents diagrammes TRC réalisés.

Finalement, l'influence de l'état de l'austénite sur sa décomposition en bainite est abordée. Cette partie traite essentiellement de l'effet de la taille de grains car le procédé de mise en forme utilisé mène à une austénite totalement recristallisée avant le refroidissement final. Cette partie amènera par la suite des éléments de discussion sur le procédé de forgeage libre utilisé pour les coulées de synthèse, ainsi que sur les cycles thermiques réalisés en dilatométrie.

1.1 Bainite microstructures

The bainite transformation is the least clearly understood austenite decomposition reaction. It exhibits both features of diffusive and displacive transformations. Numerous similarities with martensite have led some authors to develop a “displacive approach” for bainite transformation [2;3]. On the opposite, the kinetic similarities with Widmanstätten ferrite have led other authors to develop a “diffusive approach” for bainite transformation [4;5]. It seems also possible that iron passes from the face-centred cubic (fcc) structure of austenite to the bcc structure of the bainitic ferrite by a displacive mechanism but the kinetics of transformation is limited by the diffusion of carbon in austenite. As the deep understanding of the bainitic transformation is not the focus of this PhD project, no experiment has been realized in order to support one or another proposed mechanism.

Bainite has been generally considered as a generic word to name all microstructures coming from continuous cooling or isothermal holding that are observed between ferrite and martensite domains in Fe-C-X alloys. The result is the existence of numerous and varied microstructures called bainite, which has certainly not helped understanding of its transformation mechanism or establishing quantitative links between microstructural parameters and mechanical properties. To overcome this issue, numerous works have emerged in the literature with the aim to classify all microstructures referenced as bainite [3;6-8].

Nowadays, it has become primordial, when talking about bainite, to describe which kind of bainite is under consideration, and to use, if possible, a known and approved classification. It informs that the results of a research work may be relevant to this specific microstructure and not necessarily to other bainitic microstructures. As such, the first work that has been realized in this PhD project is a short review of the different classifications of bainite microstructure and the choice of the most relevant one as a framework for the present study.

1.1.1 Classifications of the various morphologies of bainite microstructures

Bainite microstructure varies with cooling conditions and alloy composition. It is common to make a distinction between “upper” and “lower” bainite as illustrated in Figure 4. Upper bainite is formed at higher temperatures (near but below the bainite start temperature, B_s) than lower bainite, which is formed at lower temperatures (near but above the martensite start temperature, M_s). Upper bainite is constituted of bainitic ferrite laths, separated by iron carbides and/or residual phases which can be untransformed austenite or martensite. Carbides can appear as continuous layers, semi-continuous layers or particle arrays. The precipitation of carbides is a secondary process, not essential to the mechanism of formation of bainitic ferrite. Lower bainite contains an additional fine intra-lath dispersion of plate-like carbides sharing the same crystallographic variant. The slower diffusion associated with the reduced transformation temperature provides an opportunity for some of the carbon to precipitate within the supersaturated bainitic ferrite. Bainitic ferrite in lower bainite can also be plate-like shaped instead of lath-like shaped.

However, in this classification established by Mehl between upper and lower bainite, there is some possibility that degenerated pearlite, in which fine cementite platelets also precipitate with a given morphological orientation, can be misleadingly identified as lower bainite.

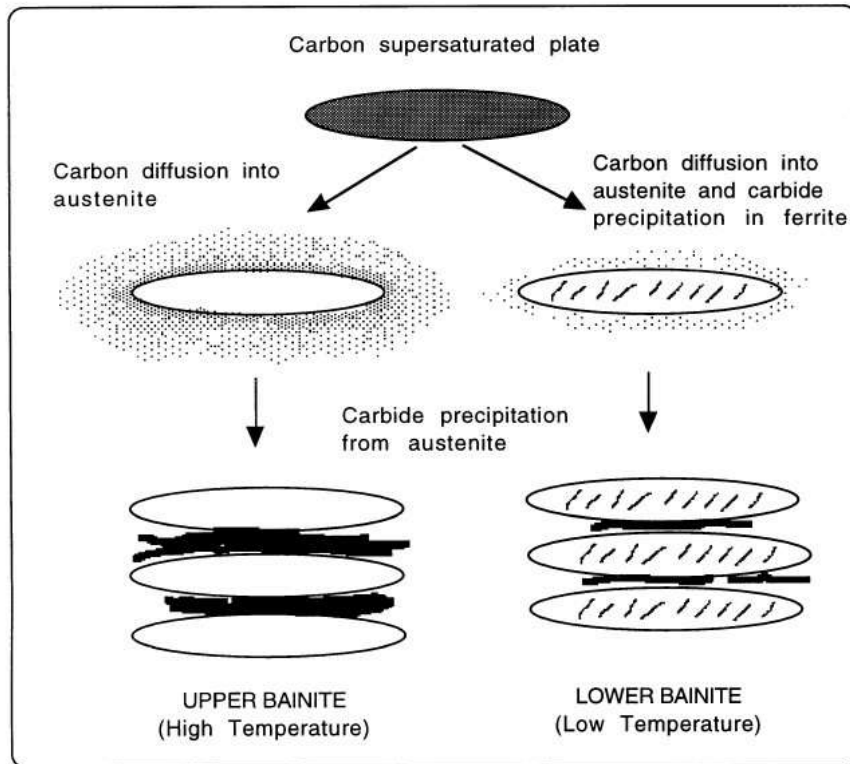


Figure 4: Schematic representation of the transition from upper to lower bainite. After [9].

Ohmori and Maki [3] established a classification by considering the ferrite morphology after isothermal transformation at various temperatures. They defined upper bainite as lath-like ferrite and lower bainite as plate-like ferrite. The morphology of bainite would change from lath-like to plate-like by increasing the average carbon content. In addition, they divided upper bainite into three categories: B-I, B-II and B-III, as follows:

- B-I: bainite formed without any carbide precipitation between bainitic ferrite laths. This kind of structure may be found in low alloy steels and high Si steels. The temperature range of such bainite transformation generally runs from B_s down to 550°C depending on steel chemistry.
- B-II: for temperatures between 550°C and about 450°C , cementite layers mainly form between bainitic ferrite laths. This is the equivalent of the upper bainite structure according to Mehl's definition.
- B-III: between 450°C and 350°C (or M_s for low carbon steels), fine cementite platelets aligned along specific crystallographic planes precipitate within the bainitic ferrite laths.

At the same time, Bramfitt and Speer [6] realized a more comprehensive classification, based on commercial continuously cooled steels, clearly including every acicular-shaped ferrite under the name "bainite": Widmanstätten ferrite, acicular ferrite, upper and lower bainite (Figure 5). Transformation mechanisms of such phases being not clearly understood and due to the difficulties to distinguish them, the authors claimed that this simple classification has been realised for industrial use. In addition to the three main classes of bainite (B_1 , B_2 , and B_3), superscripts are used to define the appropriate micro-constituents associated with each microstructure when such information is available. Lower bainite is classified as B_1^c (or B_1^e), upper bainite (according to Mehl's definition) as B_2^c and most of the existing granular bainites as $B_3^{m,a}$. Granular bainite is thus considered as a lath-like microstructure with the occurrence of discrete islands of secondary phases.

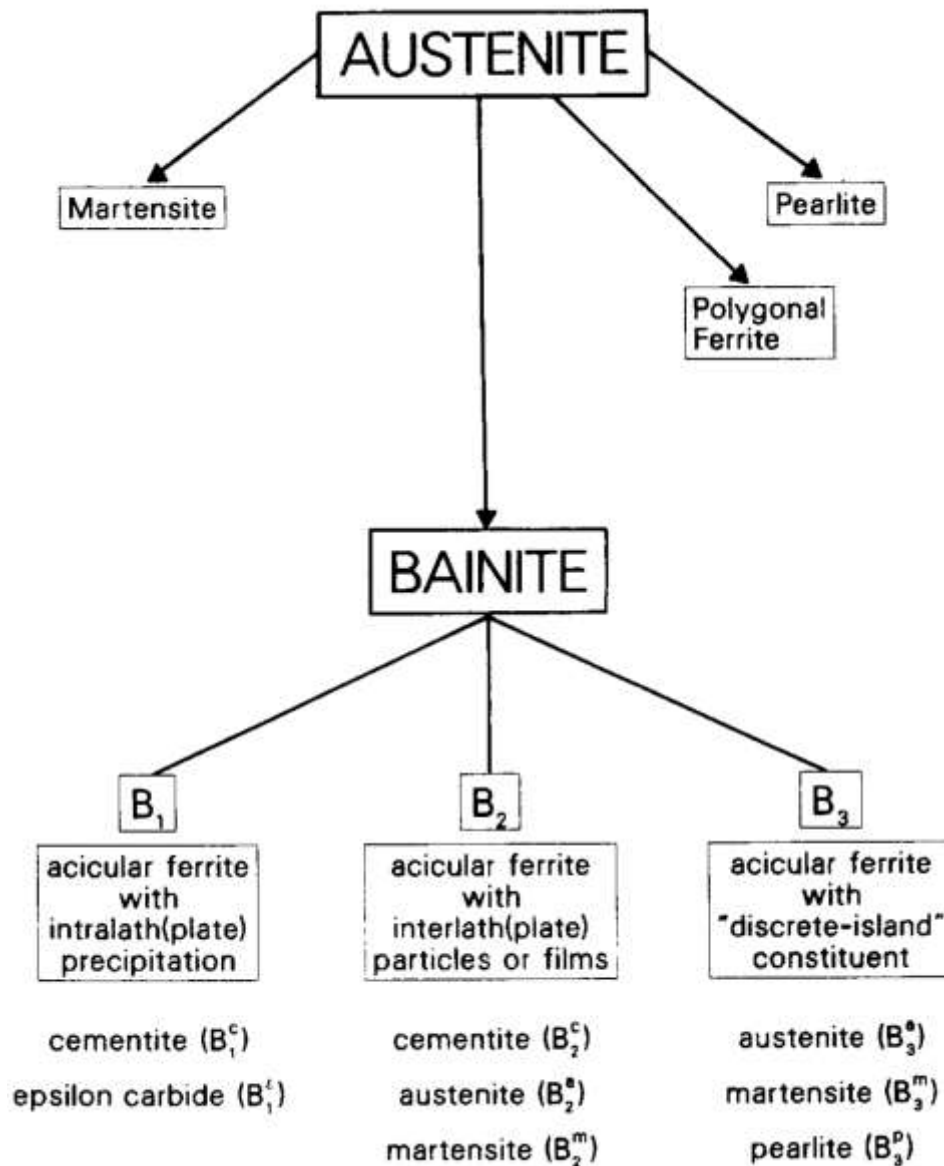


Figure 5: The classification system for bainite proposed by Bramfit and Speer [6].

More recently, Zajac et al. [10] proposed a new classification for bainite, based on the distribution of misorientation angles of the bainitic ferrite grain boundaries and on the nature of residual phases. The name “bainite” refers to lath-like or plate-like bainitic ferrite (here, the distinction between Widmanstätten ferrite, acicular ferrite, upper and lower bainite is made). The authors distinguished five types of bainitic microstructures (Figure 7):

- Granular bainite (Figure 7a, also called quasi-polygonal ferrite) composed of irregular ferrite grains/plates and a mix of degenerated pearlite, cementite, and fine mixture of martensite and austenite (**MA**) islands. No cementite precipitation occurs in such ferrite.
- Upper bainite (Figure 7b), according to Mehl’s definition, i.e. bainitic ferrite laths or plates separated by cementite and residual phases which can be untransformed austenite or martensite.
- Degenerated upper bainite or cementite-free upper bainite (Figure 7c), the same as upper bainite but with MA islands instead of cementite between the bainitic ferrite laths

CHAPTER 1 – LITERATURE SURVEY

or plates. This can be obtained in low-C steels using particular thermo-mechanical processing conditions, or in steels with a sufficient Si content to avoid cementite precipitation.

- Lower bainite (Figure 7d), similar to that defined by Mehl, with cementite particles between and within bainitic ferrite plates or laths. Silicon can avoid the precipitation of cementite between the plates of bainitic ferrite, but is less efficient in retarding the precipitation of cementite from ferrite plates at low temperature [11]. Therefore, the formation of lower bainite cannot be inhibited in low-C high-Si steels.
- Degenerated lower bainite (Figure 7e) containing MA particles within the plates or laths of bainitic ferrite. This very particular microstructure was discovered in complex Mo-Ni-Cu-Cr-B-bearing steels [10].

Moreover, Zajac et al. suggested a crystallographic criterion in order to distinguish granular, upper and lower bainite microstructures from the distribution of misorientation angles of the bainitic ferrite grain boundaries. Indeed, upper bainite presents a high fraction of low angle boundaries ($<15^\circ$) and few high angle boundaries ($>50^\circ$), the opposite case being met for lower bainite as illustrated in Figure 6. For granular bainite, the misorientation angles distribution is wide with a broad maximum around 45° and a minor peak around 20° due to the existence of a substructure.

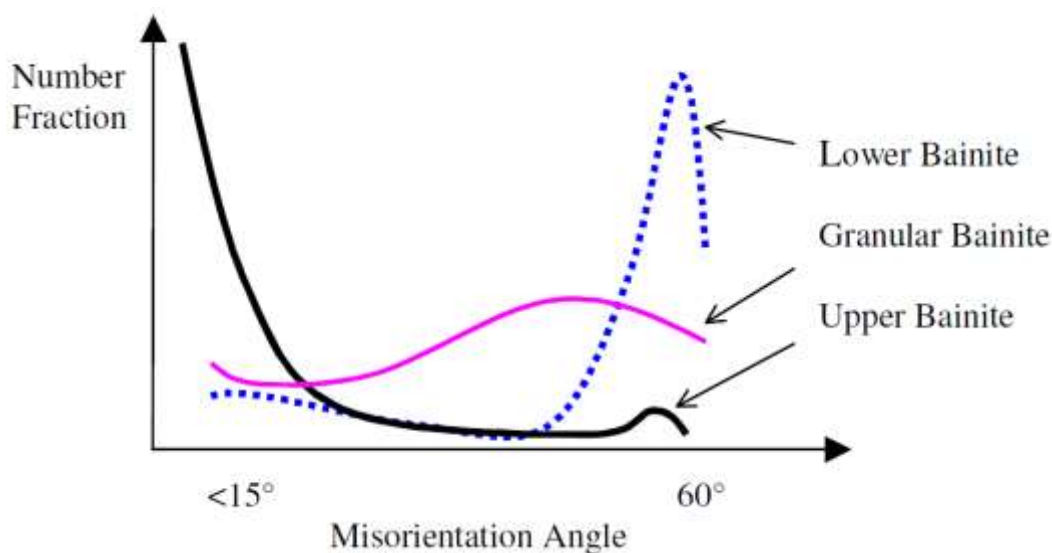


Figure 6: Distribution of misorientation angles for lower, upper and granular bainite. After [10].

Some authors have expressed reticence in the use of “granular bainite” terminology [2;12]. The first report of granular bainite emerged from the early 1950s, in the work of Habraken and coworkers [13;14], and has become popular because many industrial heat-treatments involve continuous cooling rather than isothermal transformation. Granular bainite is supposed to only form in steels which have been cooled continuously and it cannot be produced by isothermal transformation. The extent of transformation of austenite into granular bainite depends on the undercooling below the B_s temperature [13;14].

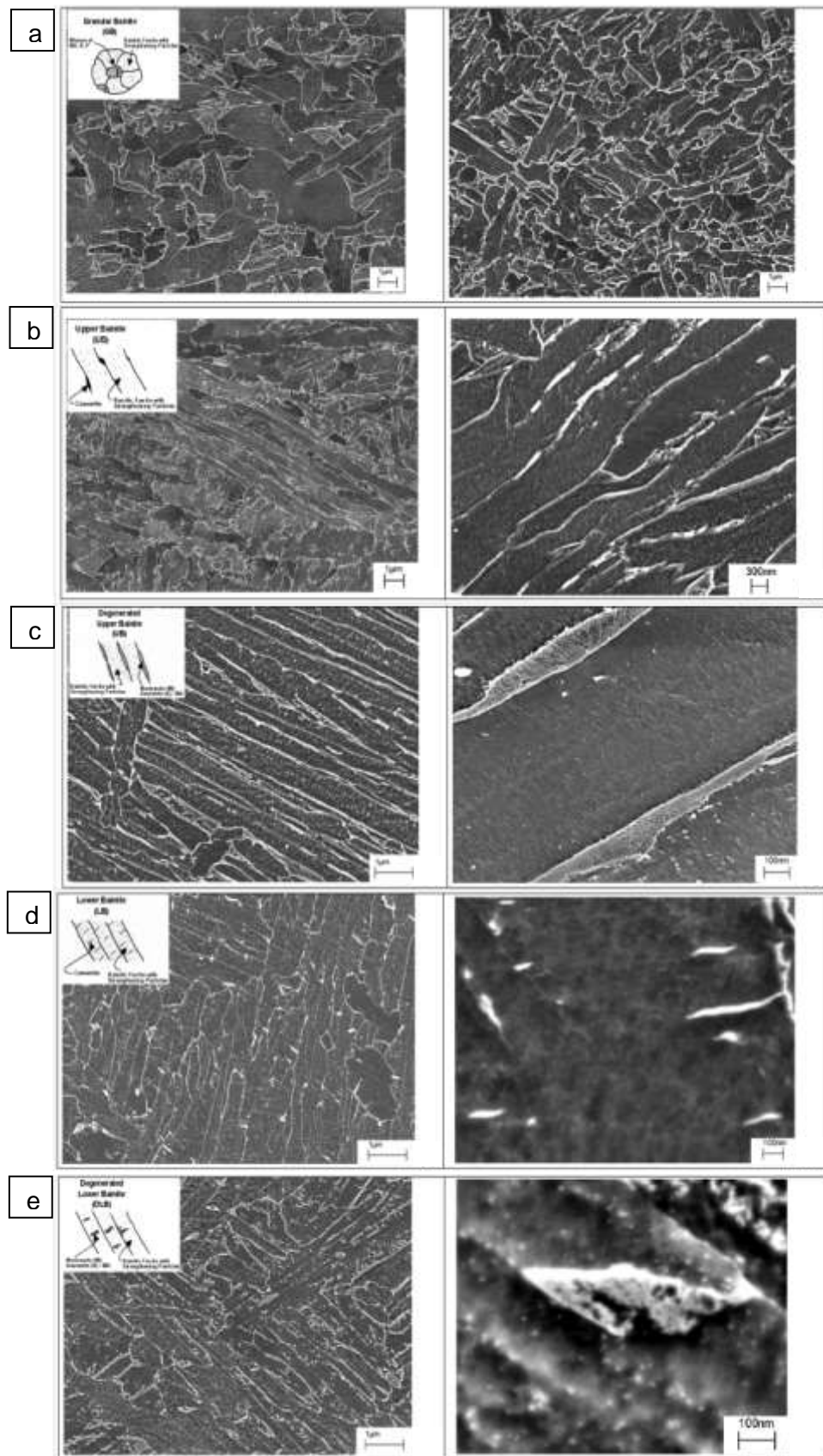


Figure 7: Field electron gun, scanning electron micrographs of (a) granular bainite in a 0.06%C boron-free steel (left) and a 0.045%C boron-bearing steel (right), (b) upper bainite in a boron-free steel, (c) degenerated upper bainite in a boron-bearing steel, (d) lower bainite in a boron-bearing steel, (e) degenerated lower bainite in a boron-bearing steel. After [10].

CHAPTER 1 – LITERATURE SURVEY

These authors [2;12] assume that coarse ferrite plates/grains do not really exist. They are, in fact, packets of bainitic ferrite with very thin regions of austenite between the sub-units because of the low carbon content of the steels involved. Hence, on light microscopy (**LM**) and scanning electron microscopy (**SEM**) scales, they give the appearance of coarse plates. In fact, many of the original conclusions were reached from microstructural observations which were not of sufficient spatial resolution to reveal the sub-structure within the packets of bainite.

1.1.2 The different scales of the bainitic microstructures

The aggregates of plates or laths sharing a common crystallographic orientation are called packets. The plates or laths, also called as sub-units, are not isolated from each other but are connected in three dimensions [6]. Sub-units grow into laths (at higher temperatures) or plates (at lower temperatures). Each lath or plate has its longest dimension along the close-packed direction of the bainitic ferrite, which is closest to a close-packed direction of the parent austenite. Plates or laths are frequently idealized in 3D as rhombus-shaped objects, as reported in Figure 8.

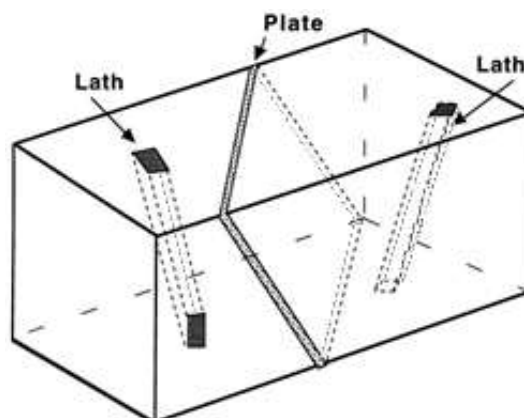


Figure 8: The three-dimensional shapes of a plate and laths. After [2].

The packet is generally thicker near its nucleation site, which is usually located along an austenite grain boundary. A packet, and thus a sub-unit, is known to never cross the austenite grain boundaries. Nevertheless, for particular austenite grain misorientations, bainite packets with close crystal orientations may grow on either side of an austenite grain boundary, making that former boundary sometimes hard to distinguish by metallography. The relative orientations of the bainitic ferrite and its parent austenite are always close to the classical Kurdjumov-Sachs and Nishiyama-Wasserman relationships, so there is a “memory effect” of the parent austenite [6]. A textured austenite can thus lead to a textured bainite. This “memory effect” can allow reconstructing the prior austenite grain from the analysis of the different crystallographic orientation variants exhibited by bainitic ferrite [15-17] (as shown in appendix A-III-1) or the re-emerging of the prior austenite grain during heating from retained austenite between bainitic ferrite [18-20].

1.2 Effect of major alloying elements on the austenite decomposition into bainite

In this part, the effect of alloying elements on phase transformation is described in a global view. Then the effect of each main alloying element is reviewed in more detail, especially regarding the austenite decomposition into bainite, the principal findings being summarized at the end of this Chapter. All chemical compositions are given in wt%.

CHAPTER 1 – LITERATURE SURVEY

1.2.1 Global view

1.2.1.a Effect on equilibrium and non-equilibrium diagrams

Alloying element X in iron can influence binary Fe-X equilibrium diagrams in two ways:

- By expanding the austenite (γ) field, and encouraging the formation of austenite over wider compositional limits. Such elements are called γ -stabilizers.
- By contracting the austenite field, and encouraging the formation of ferrite over wider compositional limits. Such elements are called α -stabilizers.

Four shapes of austenite fields can be obtained in Fe-X equilibrium diagrams [21]:

- Type 1 (Figure 9a): Open austenite field. Such Fe-X equilibrium diagrams can be obtained mainly by the addition of Mn and Ni. These alloying elements enlarge the temperature range for stable austenite by depressing the α - γ transformation temperature and raising the γ - δ transformation temperature. Sufficiently high concentration in these alloying elements can even completely suppress the ferrite occurrence, leading to fully austenitic microstructures at room temperature.
- Type 2 (Figure 9b): Expanded austenite field. C and N are the most important elements in this group. The γ -phase field is expanded, but its range of existence is cut short by ordered precipitation of carbide or nitride, forming particular compounds such as pearlite in the case of the Fe-C equilibrium diagram. It is important to notice that austenite accepts much higher concentration than ferrite in carbon (up to 2.0 wt% in austenite rather than 0.03% in ferrite) and in nitrogen (up to 2.8 wt% in austenite rather than 0.015% in ferrite).
- Type 3 (Figure 9c): Closed austenite field. This kind of Fe-X diagram can be obtained with the addition of Cr, Si, Mo, V, Ti, Al and P. In such binary diagrams, the austenite field forms a loop. δ -ferrite and α -ferrite phase fields can even merge when these alloying elements are added in sufficient quantity.
- Type 4 (Figure 9d): Contracted austenite field. The γ -loop is strongly contracted, but is accompanied by compound formation. B and Nb are the most important elements of this group.

When coming to transformation out of equilibrium conditions, these features stay relevant.

Time Transformation Temperature (**TTT**) and Continuous Cooling Transformation (**CCT**) diagrams of low-alloy steels classically exhibit two transformation noses, corresponding to the ferrite/pearlite and bainite/martensite fields. They may be separated, or not, by a “bay” whose width depends on alloying elements.

Alloying elements that are only partitioned between austenite, ferrite and cementite without any other precipitate, such as Mn and Ni, generally speed up or slow down austenite decomposition (affecting austenite decomposition start temperature A_{r3} , austenite decomposition end temperature A_{r1} , and transformation kinetics) according to their γ -stabilizing or α -stabilizing character, respectively. Silicon is a particular case as it delays cementite precipitation, so it tends to speed up austenite decomposition into ferrite but to slow down the austenite decomposition into bainite and pearlite as discussed later in this chapter. Carbide-forming elements (e.g., Cr, Mo, Nb, V, etc.) can influence the austenite decomposition differently at different temperatures. The addition of such alloying elements can reveal a well-defined bay between the two fields (ferrite/pearlite and bainite/martensite) leading to the occurrence of a temperature range within which the austenite is metastable [22].

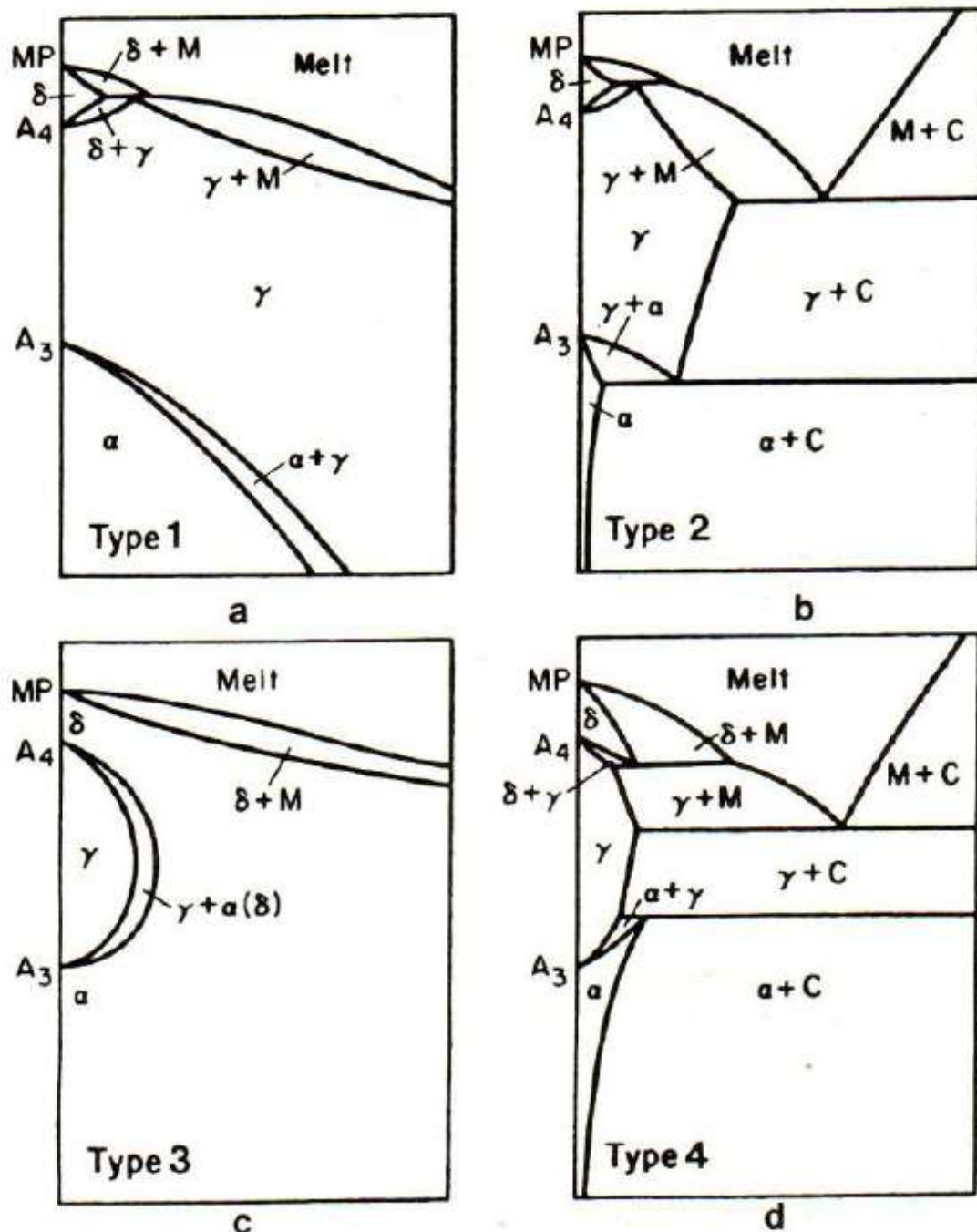


Figure 9: Classification of iron alloy phase diagrams; (a) open, (b) expanded, (c) closed and (d) contracted austenite-field. M: Melt, C: carbide or nitride. After [21].

1.2.1.b The incomplete transformation phenomenon

Focusing now on the bainitic transformation only, alloying elements may increase the so-called incomplete transformation phenomenon. According to Hehemann et al. [23], “the incomplete transformation phenomenon is the cessation of transformation of austenite to ferrite at a fraction transformed significantly less than that allowed by application of the Lever rule of the $\alpha+\gamma$ region or its metastable equilibrium extrapolation to temperatures below that of the eutectoid”. This phenomenon has been explained slightly differently according to the two proposed mechanisms for bainitic transformation.

For the “displacive” theory, Zener [24] explains the occurrence of this phenomenon as follows: bainite can only be formed below the line of equal Gibbs energy (T_0 line), where

CHAPTER 1 – LITERATURE SURVEY

thermodynamics allows ferrite to inherit all the carbon of the parent austenite by partitionless growth. Due to carbon enrichment of austenite, as carbon moves away from bainitic ferrite, the carbon content in austenite reaches a value greater than the one allowed by the T_0 line that automatically stops the transformation. Le Houillier et al. [25] later proposed that the T_0 line should be calculated with an additional term for ferrite due to strain energy. This additional energy was taken into account by Bhadeshia and Edmonds [26] to calculate a new equilibrium line called T_0' .

For the “diffusive” theory, carbon is partitioned between bainitic ferrite and austenite as bainitic ferrite grows. So, bainitic ferrite grows with low carbon content. It is admitted that there is a carbon content for austenite above which acicular ferrite, Widmanstätten ferrite and bainite cannot grow. This limit, first evaluated by Hillert et al. [27], is called **WB_s** and varies with temperature.

The maximum allowed amount of transformation into bainitic ferrite can be increased by adjusting the T_0' or WB_s curves to higher carbon concentration with the use of substitutional solutes and by controlling the mean carbon content.

1.2.1.c Precipitation behaviour

Alloying elements that have higher affinity than iron with oxygen (such as Al, Ti and V) might form oxides in liquid iron (such as Al₂O₃, TiO₂ and V₂O₅). Commonly added at the very end of the steelmaking process, such elements deoxidize the steel by removing oxygen from the melt. However, a part of the resulting oxides might not have enough time to agglomerate or to pass to slag. As a result, they could be retained in the solid steel as non-metal inclusions [28]. Similar situation can be encountered with alloying elements that have higher affinity than iron with nitrogen and sulphur (Ti and Mn, both known to have a strong tendency to form TiN and MnS particles during the steelmaking process). In addition of being potentially detrimental to steel ductility [29-31], such inclusions may have an impact on the austenite decomposition, as they slightly decrease the solid solution content of the inclusion former alloying element, and may act as nucleation sites for ferrite or acicular ferrite [32;33].

Strong carbo-nitride formers such as Ti, Nb, V, Mo and Cr can be found in solid solution or in different kinds of carbo-nitride particles (iron carbides, carbo-nitrides, pure carbides or pure nitrides) according to the carbon content of the steel, presence of other carbide-forming elements, cooling path from high temperature and presence of carbide inhibitors. The cooling path considered in the present study (relatively slow air-cooling) may not suppress precipitation. However, the high amount of both carbide forming and carbide inhibiting elements, combined with low carbon content may lead to noticeable amounts of Ti, Nb, Mo and Cr that remain in solid solution. This is especially true for Mo and Cr that are less stronger carbide forming elements than Ti and Nb.

Moreover, due to the specificity of the bainitic transformation, less carbon is available in ferrite to form precipitates, as it is rejected into austenite during the transformation. Carbides expected to start precipitating at a temperature lower than B_s might be avoided. On the other hand, carbides that precipitate prior to austenite decomposition into bainite might accelerate the transformation kinetics and increase the transformation extent (as global carbon content in austenite decreases).

1.2.2 Specific role of manganese as alloying element

1.2.2.a Manganese in solid solution

An increase in Mn content lowers the Ar₃ temperature [34;35] to such extent that Mn can strongly delay or even suppress the austenite to ferrite transformation [36;37] due to solute drag effect and solute drag like effect caused by segregation at austenite grain boundaries and interphase boundaries [38;39]. The solute drag phenomenon is the retardation of

CHAPTER 1 – LITERATURE SURVEY

boundary motion by a substitutional solute element. The solute drag-like effect is the interaction between substitutional and interstitial elements, which affects both interface concentrations and the near-interface concentration gradient of each element. Thus, in CCT diagrams, the transformation range of bainite can be separated from that of ferrite when the manganese content approaches a certain level (depending on the steel chemical composition).

Usui et al. [40] have experimentally shown the strong influence of Mn content on the critical C content of austenite for 1.5Si steels. The critical carbon content of austenite is the value required to stop the transformation of austenite into bainitic ferrite as explained earlier in this part. Thus, addition of Mn clearly favours the incomplete transformation phenomenon. Later measurements [41] on 0.2C steels containing various Si contents for 1.5Mn and various Mn content for 1.5Si, have shown that the effect of Si on the critical carbon content of austenite is negligible up to 2% compared to the strong effect of Mn (Figure 10).

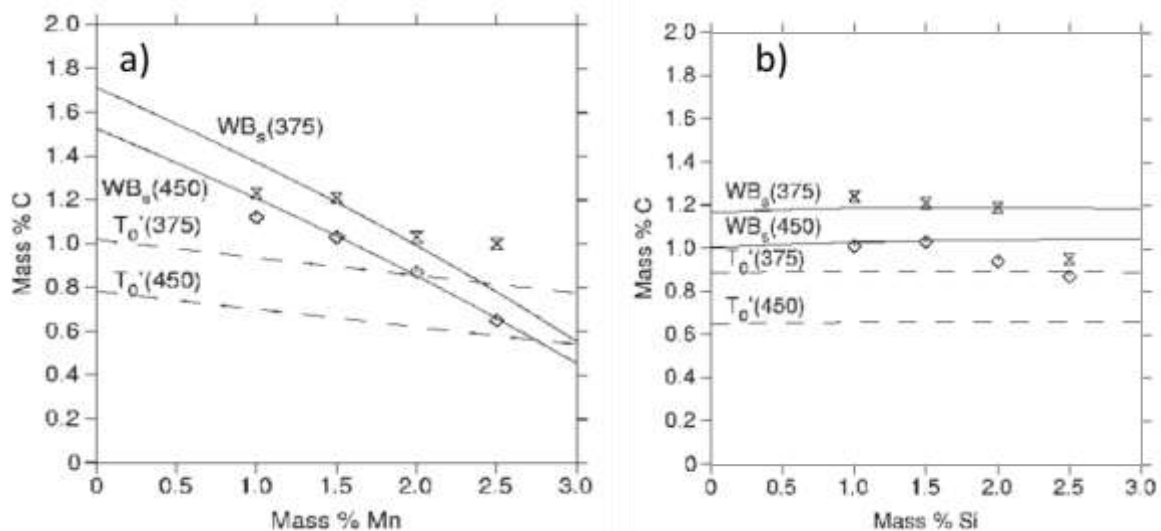


Figure 10: a) Carbon content of retained austenite as a function of the Mn content at 1.5 wt% Si and at two temperatures from Sugimoto et al [41]. Measurements are compared to T_0' and WB_s line for the two temperatures [27]. b) The same as a) but as a function of the Si content for 1.5 wt% Mn. $\times=450^\circ\text{C}$ $\diamond=350^\circ\text{C}$.

The continuous cooling transformation (CCT) behaviour of high strength micro-alloyed steels (0.08C-0.18Mo-0.035Nb-0.014Ti) containing two different levels of Mn+Si additions has been investigated by Manohar and Chandra [42] in undeformed and deformed conditions. For equivalent deformation state of austenite, the Ar_3 temperature and the transformation kinetics are lower in high Mn-Si steel (1.55Mn, 0.41Si) compared to the low Mn-Si steel (1.08Mn, 0.09Si) for all cooling rates. The bainitic structure, in this case granular bainite, becomes dominant in deformed high Mn-Si steel at a cooling rate higher than about 10°C/s whereas it needs at least 30°C/s for low Mn-Si steel. Indeed, polygonal ferrite continues to form at cooling rates as high as 30°C/s in the latter one.

1.2.2.b Manganese in precipitates

Manganese is a strong sulphide former. MnS is the most well-known and widely used compound for machinability improvement in steels [43]. After rolling, MnS precipitates are elongated along the rolling direction and can affect the toughness of the steel.

The aluminium content affects the shape of MnS particles, which in turn has a significant effect on ductility [44]. Manganese sulphides with a globular shape (type I of Figure 11) are characteristic for steel containing relatively high oxygen contents. Addition of small amounts of aluminium, such that the steel is partially deoxidised, gives rise to films or envelopes of manganese sulphides (type II of Figure 11) at the austenite grain boundaries. Films or envelopes decrease the ductility of the cast steel significantly.

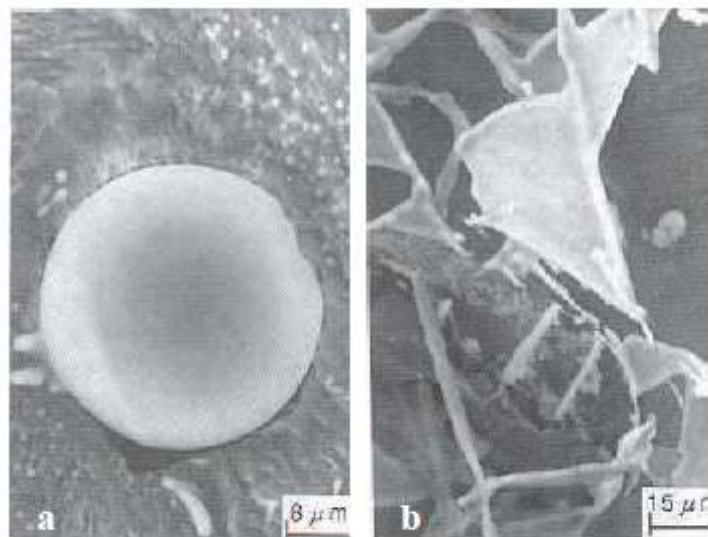


Figure 11: Morphology of manganese sulphides depending on steel composition: (a) globular (type I), (b) enveloped (type II). After [45].

Hilty and Farrell [46] experimentally showed that modification of angular and cluster-type aluminium oxide inclusions into globular, low melting point inclusions was more efficient when calcium was added instead of rare earth elements. This last point is applicable for manganese sulphides, calcium being massively used today to control their shape.

1.2.3 Specific role of silicon as alloying element

It has been shown that an addition of Si raises the activity of carbon in austenite promoting its transformation into pro-eutectoid ferrite [47;48]. The increase in A_{r3} with increasing the Si content is more pronounced in undeformed conditions. Cai et al. [49] proposed two arguments to account for this phenomenon:

- Deformation of austenite enhances its transformation into ferrite due to the increase in density of nucleation sites. This effect on A_{r3} is higher than that of Si.
- Si enhances the segregation of Mn at austenite grain boundaries due to its negative interaction coefficient with carbon, slowing down the transformation kinetics of austenite due to an inverse solute drag effect [38]. The addition of Si makes the solute drag-like effect of Mn more obvious under the deformed condition in contrast to the undeformed condition [42;50;51].

The addition of Si reduces the driving force for cementite nucleation. Indeed, Si hinders precipitation and diffusion-controlled growth of carbides by forming a Si-enriched layer around precipitate nuclei [52]. Therefore austenite gets enriched in carbon which reduces the driving force for sympathetic nucleation during the bainitic transformation. As a consequence, addition of Si slows down the overall bainitic transformation kinetics and enhances the incomplete transformation phenomenon. High Si contents may lead to the occurrence of carbide-free bainite (or degenerated upper bainite/granular bainite) instead of classical upper bainite with cementite films. In such a case, no cementite precipitation is observed between bainitic ferrite laths [38;49;53-57]. The amount of silicon necessary to produce cementite-free bainite might decrease with increasing content of austenite stabilizing elements and/or decreasing carbon content.

Cai et al. [49] have investigated the effect of two different silicon contents in a 0.08C-0.97Mn steel. The segregation of Si and Mn at austenite grain boundaries has been studied by

CHAPTER 1 – LITERATURE SURVEY

transmission electron microscopy (**TEM**) combined with X-ray energy dispersive analysis (**EDX**) in samples deformed (at 850°C with a true strain of 0.4) and then cooled at 40 °C/s for both steels. Their results are summarized in Table 1. As previously stated, the higher the Si content, the higher the segregation level of Mn at grain boundaries.

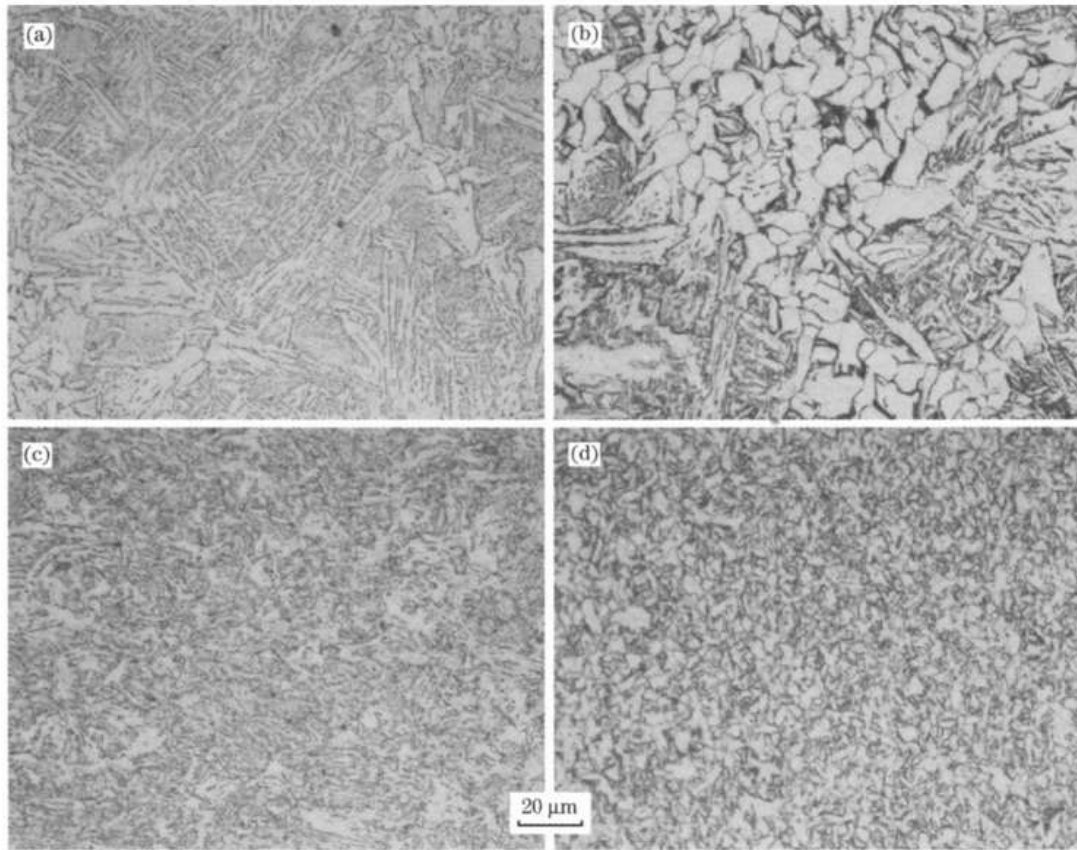


Figure 12: Optical microstructures of samples cooled from 850 °C to room temperature at 40 °C/s; (a) Undeformed low Si steel; (b) Deformed low Si steel; (c) Undeformed high Si steel; (d) Deformed high Si steel. After [49].

Grade	Si	Si _{GB}	Mn	Mn _{GB}
low Si	0.5	0.27	0.97	0.98
High Si	1.35	0.29	0.97	1.25

Table 1: Si and Mn contents (wt%) at the austenite grain boundaries (GB subscripts) compared to the initial bulk content. After [49].

As shown in Figure 12, in the low Si steel (0.5wt%), high cooling rates promote upper bainite as predominant non-ferrite microstructure in undeformed and deformed samples, whereas the high Si steel (1.35wt%) exhibits granular bainite i.e. martensite-austenite islands evenly distributed in a bainitic ferrite matrix.

The overall kinetics of isothermal decomposition of austenite at intermediate temperatures and the obtained microstructures were investigated by Liu and Zhang [38] in 0.12/0.16C-0.11/0.32Ti, 0.14C-0.11Ti-0.62Si, 0.14C-0.10Ti-1.96Mn, and 0.148C-0.10Ti-2.03Mn-0.40Si steels. The rate of austenite decomposition is lower and the precipitation of carbide is inhibited in these Ti-containing steel by addition of Si, Mn, or Si+Mn. In addition to bainite and degenerate ferrite plates, a large amount of granular structure consisting of martensite and retained austenite is observed in these alloys if the isothermal reaction time is not long enough to get complete decomposition of austenite. It is suggested that the inhibiting effect of Si on carbide precipitation, segregation of Mn to α/γ interfaces and enhancement of segregation of these elements by the interaction of Mn with Si lead to such results.

1.2.4 Specific role of chromium as alloying element

Suzuki et al. [58] studied the effects of Si and Cr contents on bainite microstructure of medium carbon steels (0.6C, 0.2 to 2.0Si, 0.75Mn and 0.15 to 0.70Cr) after isothermal transformation in a temperature range from 300°C to 500°C. For the authors, the mechanism of suppressing carbide formation by Cr addition is different from, and less effective than the one by Si. Cementite is stabilised but its growth is retarded by the partitioning effect of Cr between cementite and respectively ferrite or austenite. However, retardation of cementite growth induces a higher carbon concentration in austenite leading to an increase in the incomplete transformation phenomenon. The formation of retained austenite seems to be promoted by the decrease in martensite end transformation temperature (M_F) resulting from the increase in Cr and C contents. The retained austenite fraction decreases as the fraction of pearlite or cementite increases in the later stages of the transformation.

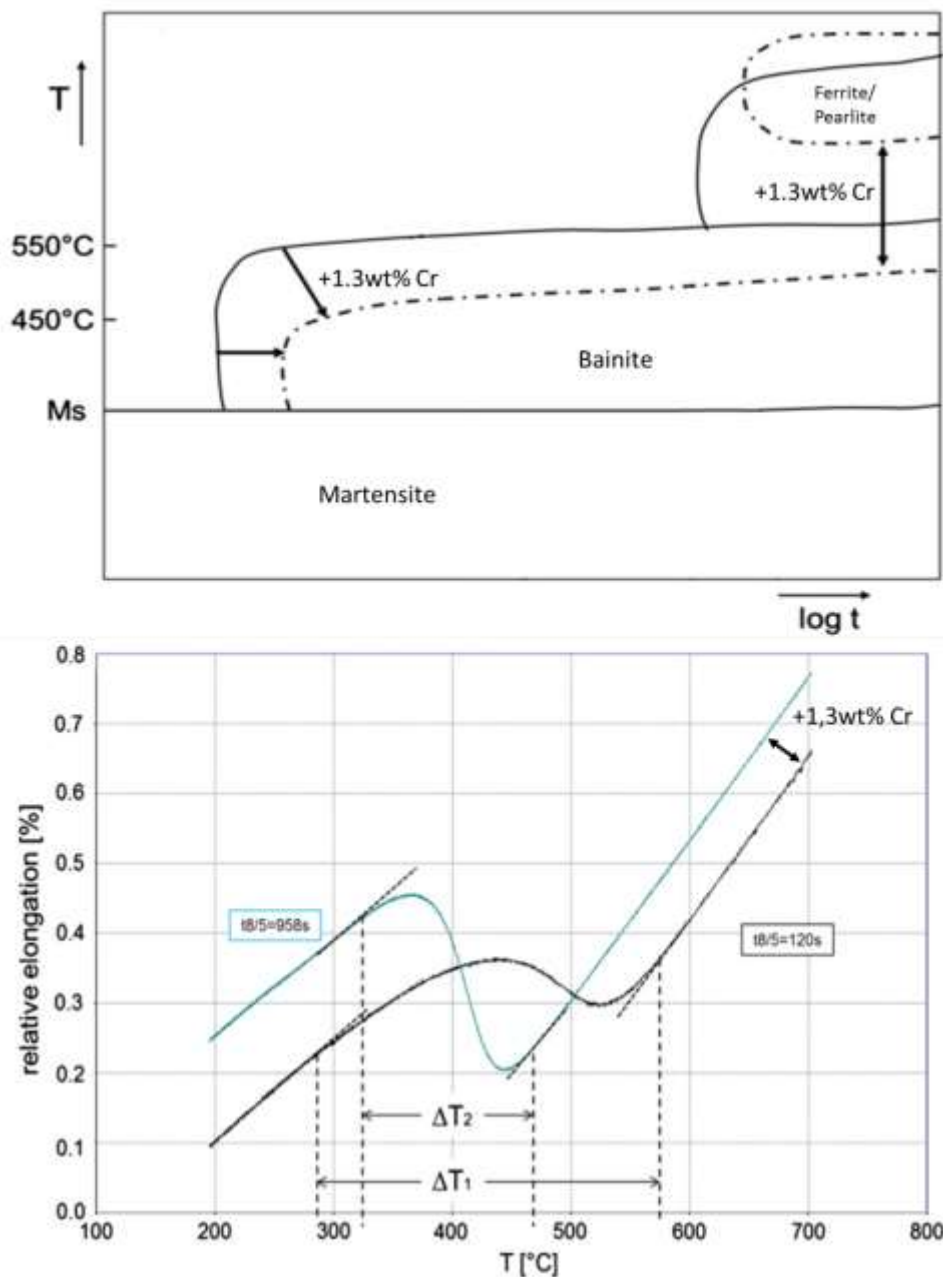


Figure 13: (a) Schematic TTT-diagram for 0Cr and 1.3Cr containing bainitic steels. (b) Comparison of dilatation curves for continuous cooling of 0Cr and 1.3Cr containing bainitic steels. Austenitization parameters and initial prior austenite grain size were not specified. After [1].

CHAPTER 1 – LITERATURE SURVEY

Han et al. [59] investigated the effects of 0.1-0.3Mo, 0.3Cr, and 0.06V additions on low carbon steels (0.08C, 0.24Si and 1.9Mn) after deformation of austenite at high temperatures (above and below the non-recrystallization temperature) and continuous cooling. Chromium was found to promote the formation of a coarse granular bainite structure at the expense of acicular ferrite. The authors supposed that the addition of V enhances initial nucleation of ferrite and effectively prevents the formation of Cr carbo-nitrides in granular bainite. Addition of 0.3Mo in the Cr-containing steel leads to a fine microstructure, as acicular ferrite, promoted by Mo, and granular bainite, promoted by Cr, are homogeneously distributed. This was attributed to a repulsive interaction between Cr and Mo atoms in steels [60].

Keul et al. [1] investigated the effect of 1.3Cr addition on a bainitic steel grade for forging applications, which contained approximately 0.22C, 1.5Si, 1.5Mn, 0.08Mo, 0.003B and 0.01Ti. The Si addition was utilized to suppress carbide formation in order to obtain a carbide-free bainitic microstructure, whereas Mo and B were added to promote the bainite formation. Their main conclusions are as follows:

- Chromium shifts the B_s temperature to lower values and develops a bay where austenite stays metastable in continuous cooling or isothermal transformations as shown in Figure 13a.
- Cr-containing steels show a more homogeneous and finer bainite microstructure after continuous cooling due to a narrower transformation temperature range of bainite as shown in Figure 13b.
- On the other hand, Cr-containing steels tend to develop martensite islands after isothermal transformation due to an increase in the incomplete transformation phenomenon in isothermal conditions. The authors did not mention if an enhancement in the incomplete transformation phenomenon was also observed in continuous cooling.

1.2.5 Specific role of nickel as alloying element

It is well known that Ni has a powerful effect on hardenability, i.e. Ni addition decreases both M_s and the critical cooling rate to get full martensite. Nickel is a very expensive alloying element and the current tendency is to reduce its amount as far as possible in steels that are not used at very low temperatures, and for which its anti-corrosion effect is not necessary. Most of the references found in literature concerning both nickel and bainitic/martensitic microstructures present high nickel content (>1wt%). However, some of them give nickel effects that might be extrapolated to lower contents.

Umemoto et al. [61] investigated the influence of nickel on cementite precipitation (0.48-0.61C, 0.01Si, variable Ni). They found that a high level of Ni (7.64 wt%) prevents the formation of cementite precipitates. Indeed, after austenitisation and continuous cooling, the steel containing a higher amount of Ni shows almost no precipitation whereas the Ni-free steel does. Austenite can thus be stabilised by the addition of Ni leading to a greater extent of incomplete transformation. There are, for the authors, two main reasons for the occurrence of this phenomenon:

- Nickel is hardly partitioned into cementite and must diffuse out during cementite formation. Therefore the nucleation of cementite at grain boundaries may occur more slowly. Furthermore, nickel atoms diffusing out from cementite might concentrate at the austenite/cementite interface and retard the growth of cementite by a solute-drag effect.

CHAPTER 1 – LITERATURE SURVEY

- Ni addition decreases the M_s temperature, leading to a faster formation of martensite in the Ni-free alloyed steel. Since the diffusivity of carbon is much higher and its solubility is much lower in martensite than in austenite, nucleation and growth of cementite may occur considerably faster in martensite with respect to austenite.

In a bainitic structure of a high-Ni low-carbon steel (0.20C, 0.48Mn, 0.33Si, 3.65Ni), Joarder and Sarma [62] found that Ni promotes the occurrence of profuse retained austenite films at the lath boundaries of martensite, this martensite coming itself from the untransformed austenite by quenching of the steel after isothermal treatment. They suggested that Ni has a much stronger effect than Mn on thermal stabilisation of austenite, as such austenite films were not observed in Mn steel.

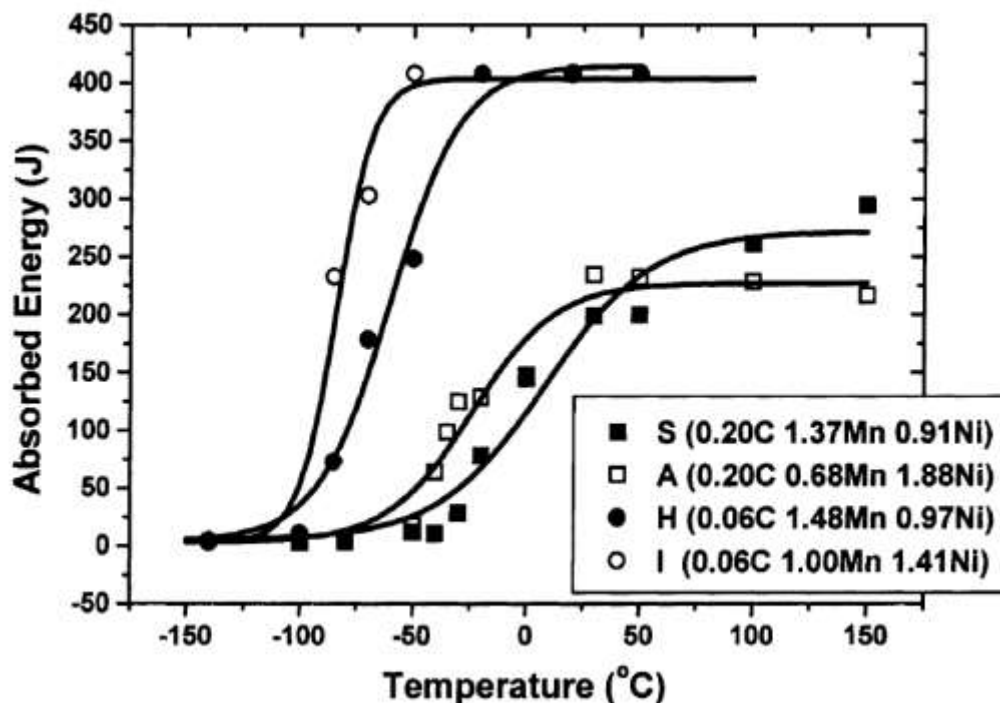


Figure 14: Change in Charpy impact toughness substitution of manganese by nickel. After [63].

Nickel is known to be beneficial to the ductile-to-brittle transition behaviour [64-66]. The effect of substituting Mn by Ni on Charpy impact toughness of tempered upper bainitic Mn-Ni-Mo steels has been investigated by Im et al. [63]. Eleven different laboratory heats were used exhibiting variation in C (0.05-0.20), Mn (0.5-1.50), Ni (0.9-3.5) and Mo (0.5-1.5) for fixed 0.15Cr and 0.20Si contents. These heats were forged into plates, normalized at 1200°C, soaked at 900°C, cooled at 0.3°C/s and tempered at 660°C for 10h. All investigated materials exhibited a prior austenite grain size around 30µm, which excludes any effect of this parameter on mechanical properties. The difference in microstructure after tempering with the substitution of Mn by Ni was not significant, in spite of an obvious difference in impact toughness as shown in Figure 14. Enhanced cross slip of dislocations in higher nickel alloys [66;67] was suggested by the authors to explain this effect.

Sorokin et al. [68] investigated the influence of Cr and Ni on the microstructure over the section of forging parts with diameter from 50 to 800 mm, made of medium carbon steels (0.33C, 0.27Si, 0.71Mn, 1.10 to 2.80 Cr, 0.25Mo, 0.90 to 3.68Ni). The realization of CCT diagrams (no experimental protocol was reported) made it possible to discover some tendencies of the influence of Cr and Ni on the stability of austenite in continuous cooling. Increasing the Cr and Ni contents has practically no effect on the pearlitic transformation start temperature but it somewhat raises the transformation end temperature (P_F). These

CHAPTER 1 – LITERATURE SURVEY

alloying elements also affect the bainitic transformation: B_S and B_F temperatures are lowered while at the same time the temperature range of this transformation becomes narrower. As B_S is decreased and P_F is increased, they have observed in some instances the occurrence of a bay where austenite does not decompose during cooling between the pearlitic and the bainitic fields.

In the same study, Sorokin et al. [68] noticed that an increase in Ni content by 1wt% in steels containing 2wt%Cr leads to an abrupt decrease in the critical cooling rates: from 10 to 0.75°C/s for a full bainitic transformation and from 0.92 to 0.1°C/s to get a fully ferrite-pearlite microstructure. A further increase in Ni content up to 2wt% has no influence on the stability of austenite during continuous cooling either in the pearlitic or in the bainitic regions. In steels with 1wt%Ni, the critical cooling rates are reduced at most when the Cr content is increased from 1 to 2wt%. A further increase in Cr content up to 3wt% does not increase the stability of austenite anymore.

1.3 Effect of micro-alloying elements

1.3.1 Role of boron as micro-alloying element

Boron is usually added in very small quantity since only a few ppm can lead to significant structural changes. With this level of addition, boron has no effect in the bulk because of the very low ratio of boron atom per iron atom (generally <0.00005) and so does not lead to solid solution hardening or precipitation strengthening. In fact, boron strongly segregates to the austenite grain boundaries where, for large grain size, boron atoms can be as numerous as iron atoms. This segregation leads to the retardation of ferrite and pearlite formation that promotes bainitic or martensitic microstructures during cooling and thus increases the strength of such steels after austenite decomposition at moderate cooling rates.

1.3.1.a Phenomenology

As a typical example of the role of boron on austenite decomposition, CCT diagrams in non-deformed and deformed conditions of a low carbon steel (0.05C, 0.25Si, 1.90Mn, 1.1Mo+Ni+Cr, 0.07Ti+Nb, 0.004N) with or without boron addition (15ppm) were determined by Jun et al. [69] and are reported in Figure 15. No indication of the grain size prior to austenite decomposition is given for any of the deformed and un-deformed cases.

Without any deformation of prior austenite, there are only three fields corresponding to the granular bainite for low cooling rates, bainite for medium cooling rates and martensite for high cooling rates. These microstructures are consistent with the high alloying content of this steel (Mn, Ni, Mo and Cr). Deformation, which produces high dislocation density, promotes the formation of quasi-polygonal ferrite, pearlite and acicular ferrite. The critical cooling rate needed to form the martensite microstructure is also increased, leading to a disappearance of the partly martensitic domain in the studied range of cooling rates. Addition of boron prevents the formation of quasi-polygonal ferrite and pearlite from deformed austenite. Every field is pushed to the right side of the CCT diagram that leads to reappearance of the partly martensitic domain. This experimental evidence suggests that boron also segregates on dislocation cell structures of austenite. For both cases (with or without deformation), the B_S temperature is strongly lowered for low cooling rates with the addition of boron, leading to refinement of the microstructure. On the other hand, the M_S temperature (for martensite as secondary phase) does not seem to be affected by the boron content of the steel.

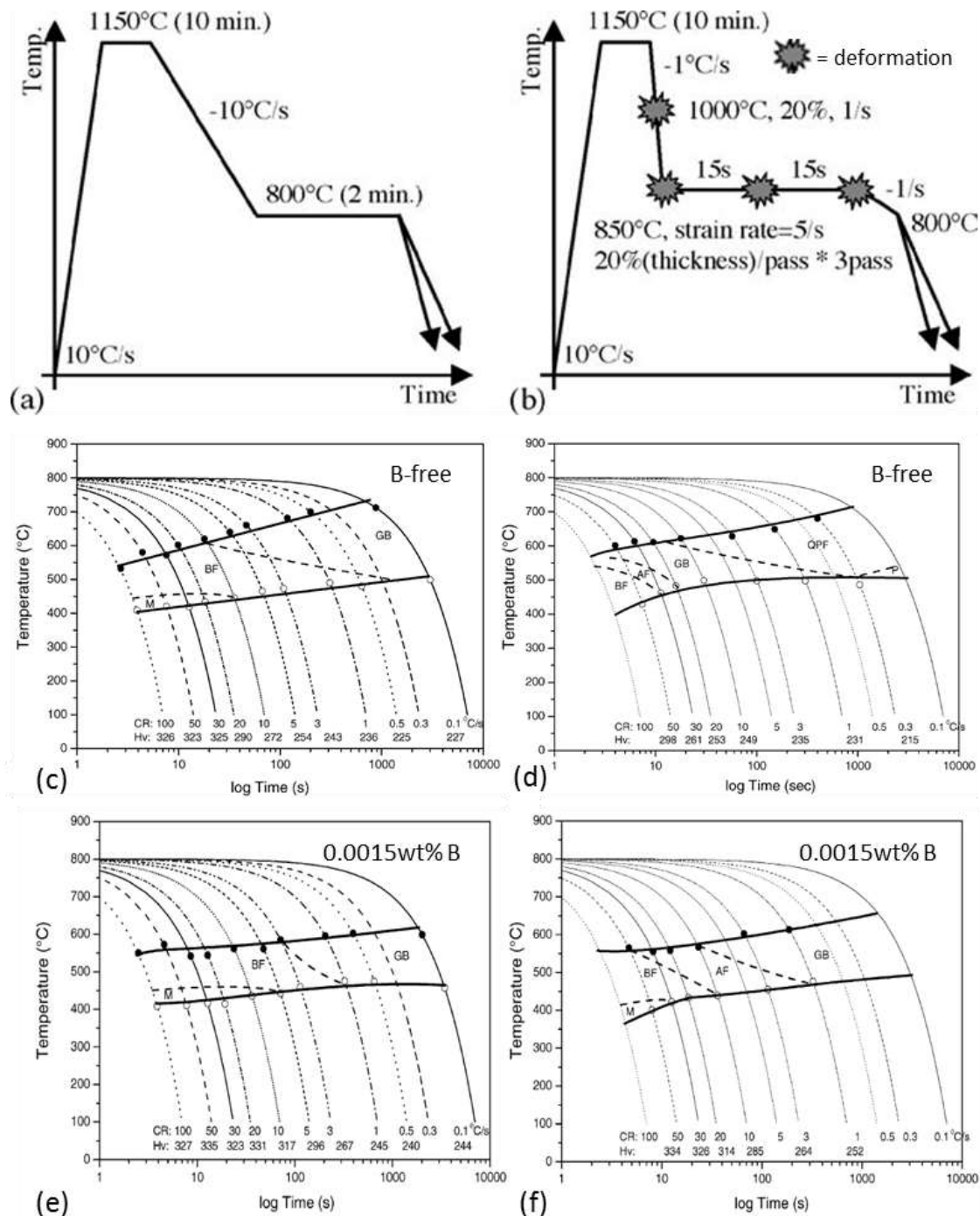


Figure 15: Effect of boron on austenite decomposition in a low carbon micro-alloyed steel. (a) and (b) are the thermo-mechanical cycles used to determine the following CCT diagrams. The continuous cooling start temperature was chosen at 800°C to reflect the industrial end of rolling temperature for such steel ($T_{nr} > 800^\circ\text{C}$). CCT diagrams of (c) non-deformed and (d) deformed steel without boron. CCT diagrams of (e) non-deformed and (f) deformed steel containing boron. No austenite grain size measurements given. P: pearlite, QPF: quasi-polygonal ferrite, AF: acicular ferrite, GB: granular bainite, BF: bainitic ferrite, M: martensite. After [69].

1.3.1.b Mechanism of boron-induced hardenability

In his PhD work, Djahazi [70] realized a comprehensive literature survey from open literature data published before 1989. He reported four proposed mechanisms as follows:

- The reduction in austenite grain boundary energy leading to a more cohesive interface. This reduction in interfacial energy is only by about 1% but can lead, for proper conditions of nucleus shape, to an effective reduction of the nucleation rate.

CHAPTER 1 – LITERATURE SURVEY

- The reduction in diffusivity of iron atoms across the austenite grain boundaries in the presence of boron. The nucleation rate is known, in carbon free alloys, to be proportional to the iron atom jump frequency, boron would thus lead to a decrease in the ferrite nucleation rate.
- The decrease in number density of nucleation sites by a poisoning effect. Boron segregation would increase the atomic density of austenite grain boundaries making them ineffective to act as nucleation sites.
- Precipitation of small boro-carbides $M_{23}(B,C)_6$ ($T < 950^\circ\text{C}$) at austenite grain boundaries.

However, coarse $Fe_{23}(B,C)_6$ are considered as ferrite precursors by some authors [71;72] as they promote ferrite nucleation at their incoherent interfaces when they are sufficiently large [73]. Nowadays, it is well known that the effect of “free” boron is obviously stronger than the one of boron trapped into carbides. So there is a necessity to maintain it “free” in order to obtain bainitic or martensitic microstructures for moderate cooling rates. The best hardenability is obtained when the boron content ranges between 15 and 30wtppm for low carbon (up to 0.20wt%) steel [74-77]. Higher boron content rapidly deteriorates the low temperature toughness of such steels.

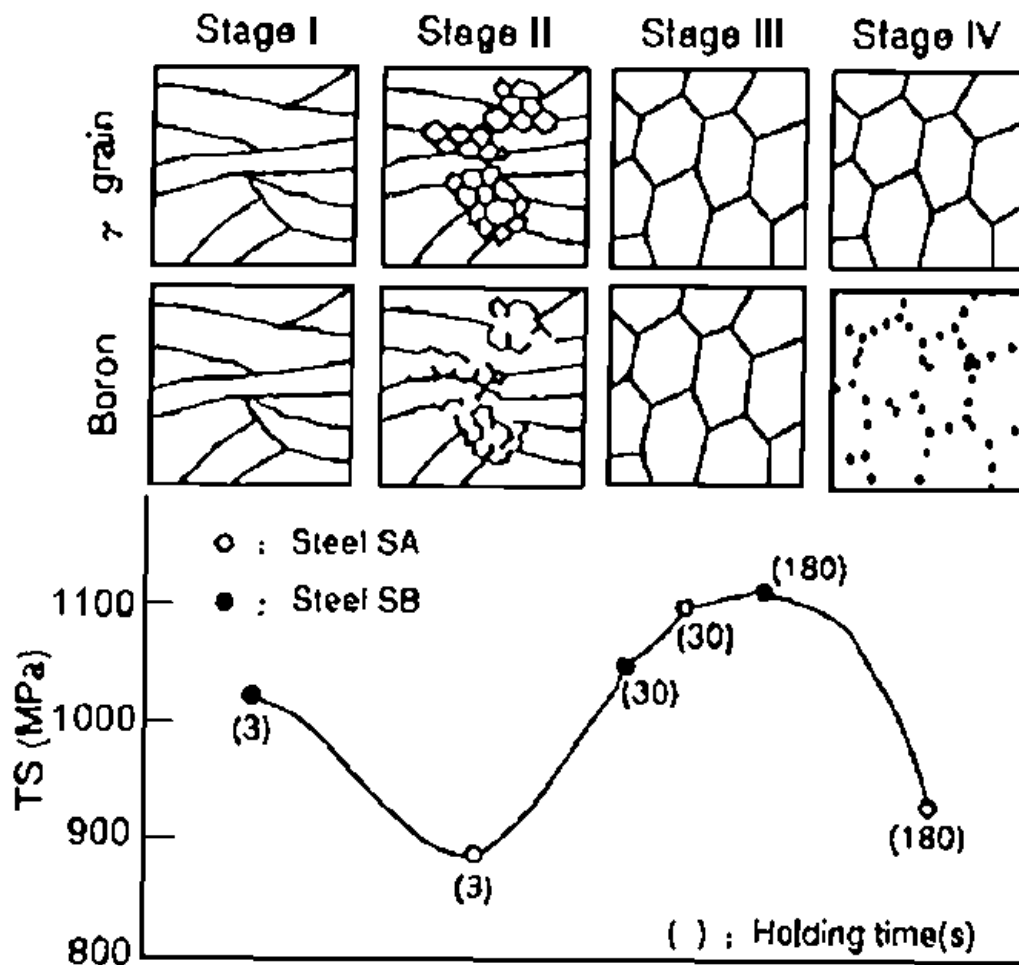


Figure 16: Schematic representation of the hardenability effect of boron according to the holding time between final rolling and quenching. Upper schematics show the shape of austenite grain boundaries and the location of boron at these boundaries. After [75].

CHAPTER 1 – LITERATURE SURVEY

The boron hardenability reaches its maximum value at the end of the austenite recrystallization process [75]. A schematic representation of the hardenability effect of boron according to the holding time between final rolling and quenching is given in Figure 16. In the first stage of recrystallization, grain boundaries move faster than boron and thus their boron concentration decreases, leading to a loss of hardenability (from stage I to stage II in Figure 16). As the grain boundary migration velocity begins to slow down with the achievement of recrystallization, the number of boundaries that display boron segregation increases leading to improved hardenability (from stage II to stage III in Figure 16). The intensity of segregation reaches a maximum when continuous segregation is present around the recrystallized grains. When the holding time is further increased, boron precipitation occurs, leading to a loss of hardenability, i.e. strong increase in the critical cooling rate to form martensite (from stage III to stage IV in Figure 16).

For given boron content, an increase in carbon content leads to a decrease in efficiency of boron regarding hardenability [76]. Two main reasons have been pointed out by Zhu et al. [78]:

1. The equilibrium value of boron concentration in the grain boundary is reduced as carbon atoms fill up the grain boundary sites.
2. Below the solvus temperature, carbon tends to reduce the solubility of boron in steel by reacting with it to form borocarbides.

It is thus necessary to protect boron from carbon (and from nitrogen) to keep it in “free” form to improve hardenability.

1.3.1.c Avoiding precipitation of boron carbo-nitrides

Molybdenum and niobium are used to prevent the formation of boro-carbides because of their strong affinity with carbon [79-82]. Addition of Mo or Nb leads to a fine distribution of Nb carbonitrides or Mo carbonitrides. The carbon diffusivity within the austenite grain is thus reduced and the formation of $\text{Fe}_{23}(\text{B,C})_6$ during cooling (in the bulk and at grain boundaries) is suppressed if the Nb or Mo content is high enough.

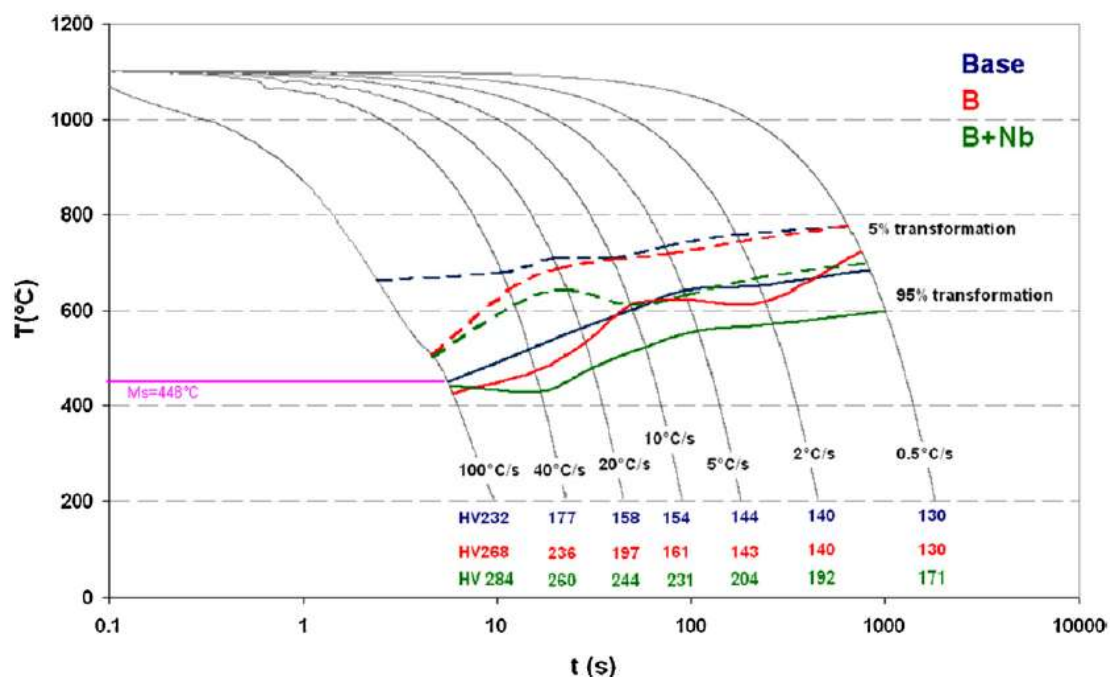


Figure 17: CCT diagrams after soaking at 1100 °C for 5min of the base (blue), the B micro-alloyed steel (red) and the B+Nb micro-alloyed steel (green). After [81].

CHAPTER 1 – LITERATURE SURVEY

In a more recent study, Zhu et al. [81] have analysed the effect of boron (0.003B) and boron plus niobium (0.003B, 0.036Nb) additions in low carbon steels (0.051C, 1.49Mn, 0.305Si, 0.009Al, 0.01Ti, 0.0025N). CCT diagrams were built after a soaking at 1100°C for 5min (prior austenite grain size, **PAGS** = 30µm). Thermodynamic calculations, performed in the case of B+Nb composition, verified that this soaking temperature was sufficient to ascertain the dissolution of the fine niobium-carbides. Results are presented in Figure 17. For cooling rates lower than 10°C/s, the addition of B only slightly delays the phase transformation whereas the combined addition of B+Nb delayed it strongly. For cooling rates higher than 10°C/s, B_s temperature starts to decrease as less and less of coarse $Fe_{23}(B,C)_6$ particles precipitate. At the same time, B_s temperature for B+Nb composition increases, which is perhaps due a decrease in Nb(C,N) precipitation (not enough time to form at this cooling rate) and so, a less effective protection of boron from boro-carbide precipitation. At cooling rates higher than 40°C/s, B and B+Nb share close transformation points, as no precipitation of $Fe_{23}(B,C)_6$ and Nb(C,N) occurs anymore.

Hara et al. [82] investigated hardenability improvement by the combined addition of B+Nb (0.0009B, 0.04Nb) and B+Mo (0.0008B, 0.035Mo) in a low carbon steel (0.014C, 0.20Si, 1.54Mn, 0.015Ti, 0.020Al). The studied steels were hot-rolled between 880 and 800°C (cumulative reduction = 80%), then air cooled to room temperature. The average cooling rate in the mid-thickness between 800 and 500°C was 20°C/s, which is high but the precipitation had already occurred during the hot-rolling step. Addition of Nb leads to the formation of Nb-C clusters and Nb(C,N) or (Ti,Nb)(C,N) precipitates, whereas addition of Mo leads to the formation of Mo-C clusters, Mo(C,N) and (Ti,Mo)(C,N) precipitates. The amount of C-rich precipitates and C-rich clusters that are formed in the Nb–B steel is much higher than that in the Mo–B steel.

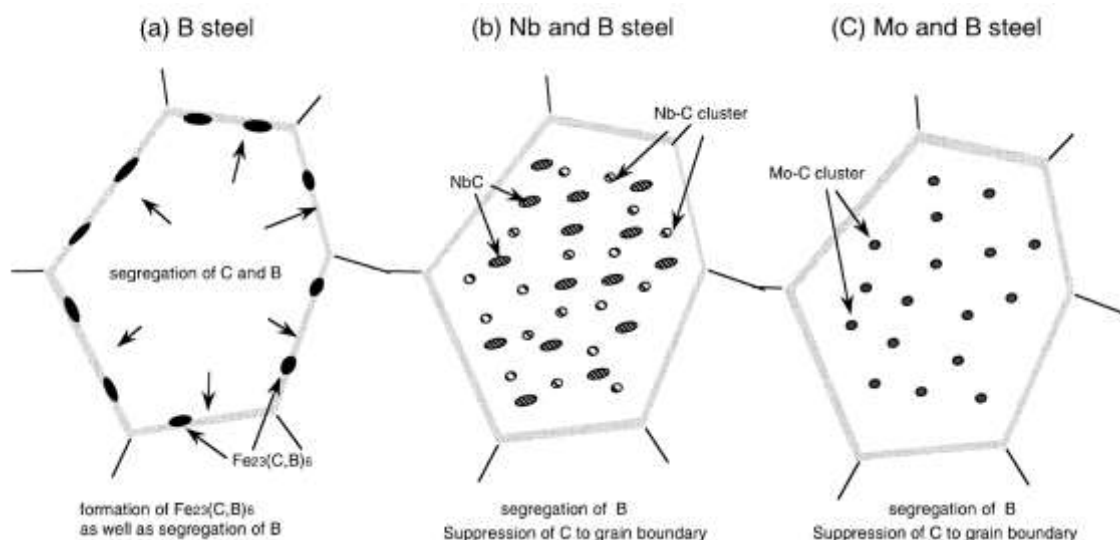


Figure 18: Schematic representation showing mechanism for suppression of formation of $Fe_{23}(BC)_6$ due to combined addition of Nb and B or Mo and B. After [82].

Carbon is not the only element that tends to precipitate with boron. High enough free-nitrogen content can lead to the formation of boron nitride (BN). The formation of boron nitrides may be avoided by the addition of nitride forming elements such as titanium, aluminium and zirconium [83-85]. Aluminium protection is not the best choice because the kinetics of AlN formation is slower than that of BN even if AlN has a better relative stability [83].

It is well known that titanium is the most effective element to pump nitrogen out of solid solution by forming the very stable TiN precipitate [86], whose solubility is the lowest among the carbides and nitrides formed with the micro-alloying elements. TiN precipitates rapidly (it

CHAPTER 1 – LITERATURE SURVEY

can nucleate directly from the melt in secondary steelmaking). It remains stable at high temperature (dissolution temperature above the iron liquidus) and ensures the best protection for boron against precipitation with nitrogen.

1.3.2 Role of niobium as micro-alloying element

Niobium is a micro-alloying element that is added to increase the steel hardenability by delaying diffusive transformation when in solid solution. As seen just previously, it can also been used in synergy with boron. Moreover niobium is known to slow down recrystallization and austenite grain growth kinetics (both in solid solution and in precipitates), which is widely used in thermo-mechanical controlled processing of steels.

1.3.2.a Effect of niobium in solid solution

The work of Feng et al. [87] is used here as a typical example of the niobium influence on microstructure. They used two billets, one with 0.02Nb and the other without niobium (0.08C, 2-2.5Mn, 0.8Si, 1.2Cr, 0.002N). They carried out an austenitisation at 1250°C for 1h followed by hot rolling ($T_{\text{finish}}=850^{\circ}\text{C}$) and final cooling at 0.4°C/s. The obtained microstructure of the Nb-free steel was a nearly equal distribution of large pro-eutectoid ferrite grains and bainite whereas that with Nb was mostly bainite as illustrated in Figure 19.

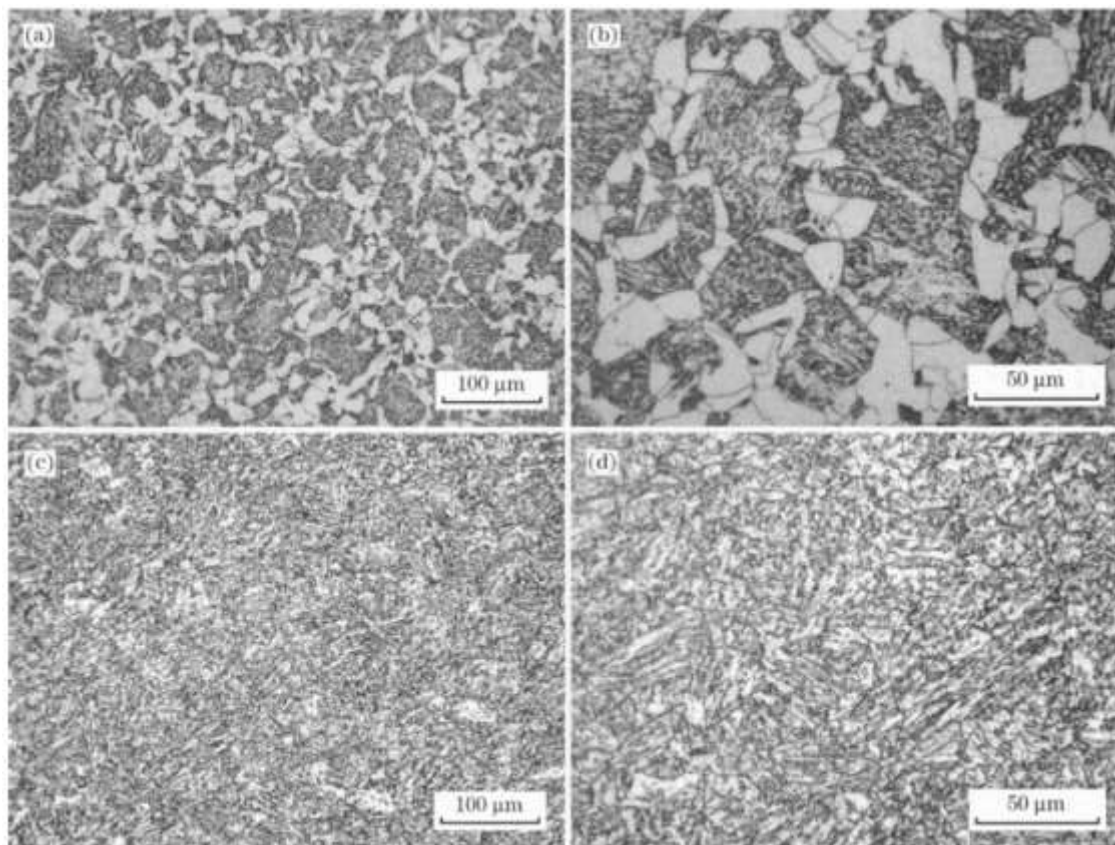


Figure 19: Effect of Nb addition on the microstructure of an air-cooled bainitic steel (LM, Nital4%). (a,b) Nb-free steel. (c,d) Nb-bearing steel. After [87].

One of the first investigations of the niobium effect on Fe-C alloy was realised by Thomas and Michal [88]. They observed that the addition of niobium promoted bainitic ferrite at the expense of allotriomorphic ferrite by segregating at austenite grain boundaries. This segregation induces a solute-drag effect. Thomas and Michal obtained a critical concentration for which the onset of γ/α transformation occurs at higher temperatures. Above this critical concentration, the precipitation of niobium carbides begins, such carbides acting as nucleation sites for ferrite. Similar results have been reported by Yuan et al. (Figure 20)

CHAPTER 1 – LITERATURE SURVEY

on Nb micro-alloyed steels (0.1C, 0.2Si, 1.2Mn, 0.005N, from 0 to 0.4Nb) [89]. In this last study, the primary austenite grain size of the steel with the highest niobium content is much lower than that of other steels (69 μ m against 212-248 μ m). Such a decrease in primary austenite grain size might explain the observed increase in γ/α transformation start temperature.

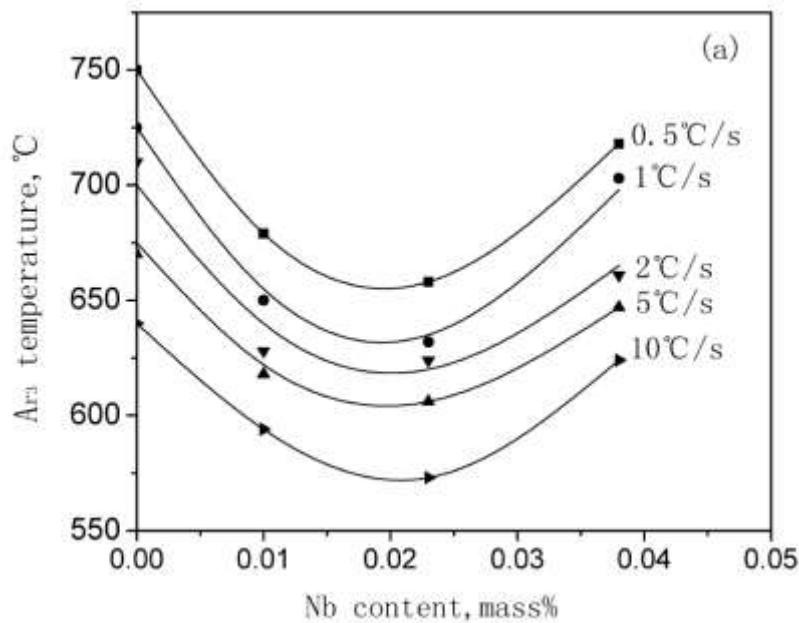


Figure 20: A_{r3} temperature as a function of the Nb content in a low carbon steel for several cooling rates from 900°C. Soaking condition 1200°C, 5min. After [89].

There is a great discrepancy about the value of the shift in A_{r3} and about the range of niobium content that provides this effect in literature [89-92]. Some of these results are presented in Table 2. Cooling rates are given because of their well-known influence on A_{r3} . This discrepancy can be explained by the use of different thermal processing routes, carbon content and primary austenite grain size.

	°C/0.01Nb in wt%	range of wt% Nb	cooling rate °C/s
Hong et al. [91]	7	0-0.052	2
Manohar et al. [92]	10	0.031-0.052	0.3-50
Abe et al. [90]	30	0.006-0.015	1-10
Yuan et al. [89]	26-39	0-0.023	0.5-10

Table 2: Shift in A_{r3} in °C according to the niobium content of low-carbon steels and associated investigated range of Nb content and cooling rates.

Rees et al. [93] have built CCT diagrams containing PAGS measurements, on several steels only differing in their niobium concentration (0.14C, 0.44Si, 1.60Mn, 0.025Ni, 0.016Mo, 0.027Cr, 0.002Ti). The soaking temperature was 1250°C with two different holding times (3s and 10s) to produce various grain sizes. This temperature was judged high enough to dissolve all niobium carbides as austenite grains exhibited a fast growth within a few seconds. Following soaking, fast cooling down to 800°C was performed in order to freeze the austenite grain size. Then, several cooling rates were applied. They found that an increase in Nb content in solid solution retards the bainite transformation and suppresses allotriomorphic ferrite formation without affecting the critical cooling rate to get a full martensite microstructure. Fully and finer bainitic microstructures can thus be obtained over a wider range of cooling rates.

Moreover, Rees et al. [93] found that the samples without niobium had an austenite grain size much larger than the samples containing niobium, but there is no linear relationship between the niobium content of the steel and the austenite grain size. Yuan et al. [89]

CHAPTER 1 – LITERATURE SURVEY

reported the same effect of niobium on the kinetics of austenite grain coarsening (undeformed condition). Moreover, Cuddy [94] reported that Nb in solid solution greatly raises the non-recrystallization temperature of austenite (T_{nr}). Similar conclusions were drawn later by Barbosa et al. [95]. This effect on static recrystallization was found to saturate at 0.06wt% [94]. In addition, several studies reported that Nb in solid solution strongly delayed dynamic recrystallization [96-98].

1.3.2.b Effect of niobium in precipitates

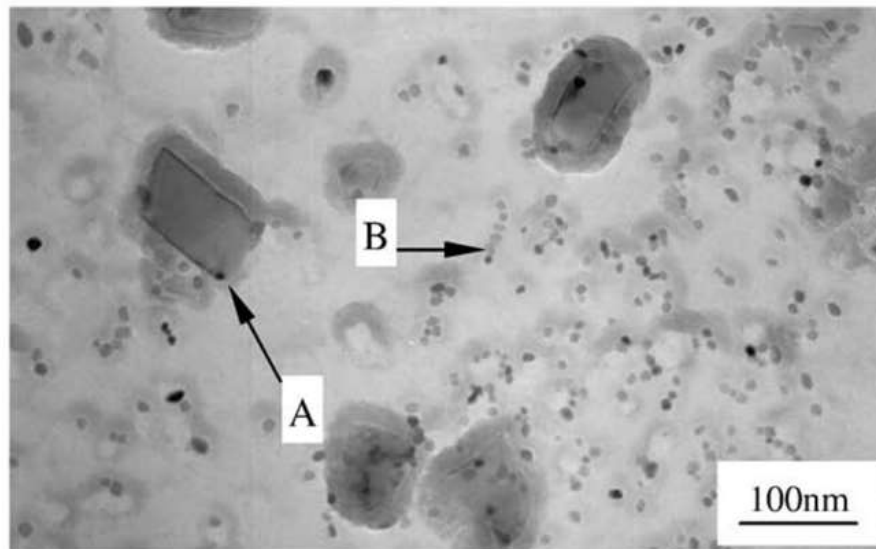
Rees et al. [93] used an industrial steel (0.15C, 0.47Si, 1.55Mn, 0.03Ni, 0.02Cr, 0.003Ti, 0.035Nb) to investigate the effect of niobium precipitation on the bainite transformation kinetics. After a first austenitisation at 1250°C, the samples were held at various temperatures for various amounts of time for a second austenitisation in order to precipitate niobium carbides before cooling down to room temperature at various rates. They observed a strong acceleration of bainite transformation kinetics following the second austenitisation stage that induced carbide precipitation. This effect was stronger than the acceleration expected by the removal of niobium from solid solution. This result is similar to those obtained earlier by Thomas and Michal [88] and Jung et al. [80] for the ferrite transformation. Particles that are responsible for this acceleration are not numerous in the microstructure. Electron diffraction patterns revealed that these carbides have face-centred cubic structure with an approximate lattice parameter of 4,38Å (versus 4,41Å for stoichiometric NbC). EDX analysis showing that carbides contain a majority of Nb as a metallic element, indicating that NbC or Nb(C,N) are responsible for this kinetic effect.

More recently, Guo et al. [99] analysed the structure of ultrahigh strength (900MPa) steel micro-alloyed with niobium (0.01-0.06C, 0.20-0.40Si, 1.50-2.10Mn, 0.20-0.70(Ni+Mo), 0.060-0.100Nb, 0.030-0.060V, 0.010-0.020Ti). They observed small rod-like carbides inside granular bainite. From TEM and X-ray diffraction (XRD) analysis, they classified the precipitates into three different groups as reported in Table 3. Ti leads to the occurrence of (Ti,Nb)(C,N) at austenite grain boundaries, which remain stable even at high temperature. The retarding effect on the austenite grain growth (increase in the Zener pinning force) in Nb-Ti steels is more effective than that in Nb or Ti bearing steels because of the (Ti,Nb)(C,N) precipitates. Similar groups of precipitates, containing in addition a small quantity of boron, have been observed by Djahazi [70]. Djahazi also reported that the number density of Nb(C,N) precipitates is higher and the precipitates seem smaller when the steel contains boron. It has been shown that to be effective the particles should be less than 0.1µm in diameter [100]. Some of the particles mentioned in Table 3 are thus too large to pin austenite grain boundaries effectively.

size (nm)	<50	40-150	70-180
type	(Nb _{rich} ,Ti)(C,N)	(Nb,Ti)(C,N)	(Ti _{rich} ,Nb)(C,N)

Table 3: Size and nature of precipitates observed by Guo et al. [99].

Yuan and Liang [101] worked on the dissolution behaviour of secondary phase particles in a low carbon Nb–Ti micro-alloyed steel (no chemical composition given) during isothermal holding at 1300°C. They notice two kinds of particles, large (Ti,Nb)(C,N) precipitates originated from solidification, and finer (Nb,Ti)(C,N) particles that were attributed to solid state strain induced precipitation. Large precipitates containing Nb and Ti still remain even if held for 48 h at 1300°C pointing out, according to these authors, that the assumption that TiN inherited from high temperature would become nucleation sites for NbC is false. Indeed, if NbC had formed around TiN, due to its poor thermo-stability compared to TiN, it would dissolve away quickly at 1300°C and only TiN cores should remain, which was not the case here.



	A	B
size (nm)	> 50	< 10
type	(Ti _{rich} ,Nb)(C,N)	(Nb _{rich} ,Ti)(C,N)
ratio Nb:Ti	14:86	90:10

Figure 21: TEM image of the two types of precipitates in as-rolled Nb-Ti micro-alloyed steel. After [101].

Cao et al. [102] investigated precipitation in 0.08Nb–0.14Mo and 0.06Nb–0.02Ti steels (0.04C, 1.1Mn, 0.3Si), both exhibiting polygonal and acicular ferrite microstructure with similar grain size of around 4.5 μ m. In all (Nb,X)C particles, the mass% of the (Nb,X)C particles lower than 10 nm in size obtained in Nb–Mo and Nb–Ti steels were 58% and 30% respectively. The observed presence of molybdenum in the precipitates increases coherency strains of the particle with the matrix due to a decrease in lattice parameter compared to pure NbC. This results in higher precipitation strengthening by (Nb,Mo)C than by NbC, at given average size, spatial distribution and volume fraction of precipitates.

As does Nb in solid solution, Nb(C,N) precipitation in austenite reduces the static recrystallization rate by pinning dislocations [103;104]. Nb(C,N) precipitates are effective to prevent static recrystallization as long as the progress of precipitation does not bring the solute content below the critical amount needed to prevent the boundary from breaking away from its solute atmosphere [105;106].

Akben et al. [107;108] investigated the effects of multiple micro-alloying additions on the dynamic recovery and recrystallization behavior of austenite in a series of 0.05C–1.25Mn steels. Increasing Mo, V and Mn contents of Nb microalloyed steels significantly delays the precipitation of NbC, by decreasing the diffusivity of Nb in austenite (solute-drag like effect). Thus, it becomes possible to play with one or several of these contents in order to delay precipitation and maximize the effect of Nb in solid solution. However, if Nb is used to protect B from boron carbide precipitation, the Mn content must be controlled in order to keep B free. Si can be added to countercharge the effect of Mn. Indeed, Kurokawa et al. [109] found that an addition of 0.6Si balances an addition of 1.5Mn on the solubility of NbC.

1.3.3 Role of molybdenum as micro-alloying element

Molybdenum does not affect austenite at high temperature as much as niobium does [110]. However, in addition to the efficient boron protection from boron-carbide precipitation, molybdenum carbides are often used to increase the yield strength thanks to a fine Mo₂C precipitation [63]. Mo also has an obvious effect on steel hardenability [111]. By reducing

carbon diffusivity and exerting a strong drag force on moving inter-phase boundaries, solute Mo substantially delays ferrite formation [112].

1.3.3.a Effect of molybdenum in solid solution

Garcia de Andrés et al. [113] investigated the effect of Mo (0.025 and 0.16) on continuous cooling transformations and on austenite grain growth for two medium carbon forging steels (0.40C, 1.4Mn, 0.6Si, 0.05Cr, 0.1V, 0.015Ti, 0.012-0.016N). Mo was found to promote austenite grain growth as shown in Figure 22. No indications are given on the state of molybdenum but it should be in solid solution at least for temperatures higher than 1000°C. Two CCT diagrams were built for each chemical composition, testing the influence of two primary austenite grain sizes (11µm and 66µm). From these diagrams, at a given primary austenite grain size, an increase in Mo content only slightly affects A_{r3} but strongly delays the austenite-to-pearlite transformation. No bainite but acicular ferrite was observed with this chemical composition, which was attributed to the ferrite layer present along primary austenite grain boundaries. Thus, the range of cooling rates at which acicular ferrite forms extends over lower cooling rates when the Mo content increases. Mo does not seem to have a large effect on the M_s temperature for high cooling rates (>30°C/s, pure martensite microstructure have only been achieved with PAGS=66µm). However, Mo enhances the appearance of martensite in the final microstructure. Indeed, for the highest Mo content, martensite can be detected for cooling rates as low as 0.6°C/s. Otherwise, it needs at least 3°C/s to be readily observable.

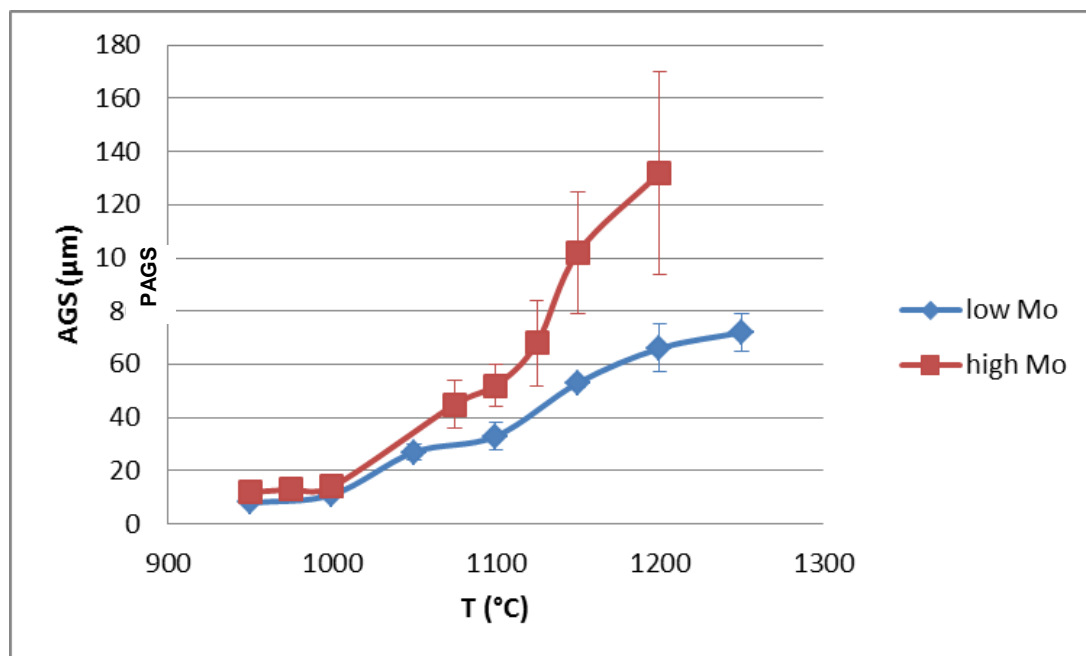


Figure 22: Primary austenite grain size at the end of the heating process (5°C/s) according to the temperature reached for two different Mo contents. After [113].

Masimov and Kwiaton [114] also studied the effect of molybdenum on hardenability. They used different levels of Mo (0, 0.25 and 0.5wt%) to a constant low carbon Mn-Cr base alloy (0.05C-1.5Mn-0.1Cr). The samples were heated to a temperature of 50°C above their A_{c3} temperature and held for 10 minutes. Then, they were cooled at various rates. As reported by Garcia de Andrés et al. [113], Mo tends to delay or even suppress the pearlite formation and lowers the transformation temperature, leading to a wider bainite field toward lower cooling rates. At cooling rates above 30°C/s, a fully bainitic microstructure is obtained in the steel with the highest Mo content. At a given cooling rate, the bainitic packet size decreases with increasing Mo content whereas the misorientation angle between bainite laths as well as the dislocation density increases. These effects are mainly due to the decrease in transformation temperature with Mo addition.

CHAPTER 1 – LITERATURE SURVEY

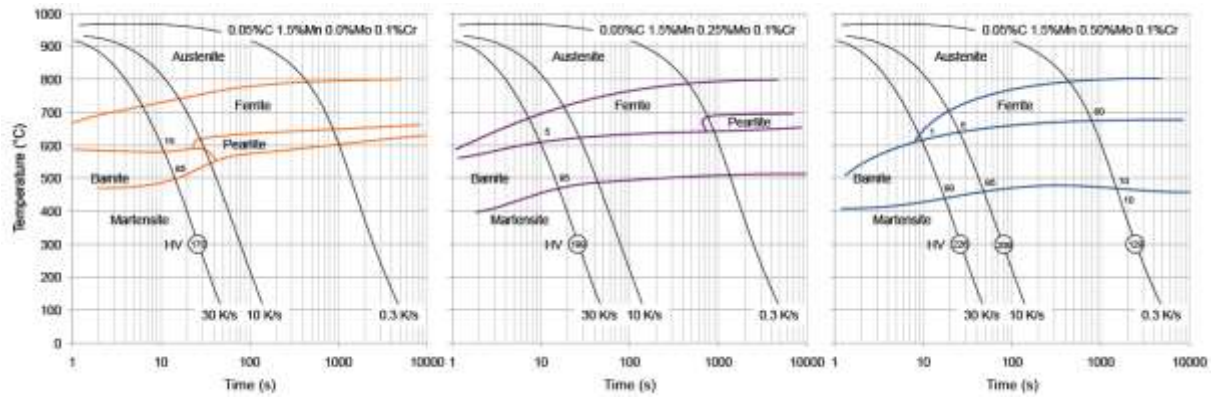


Figure 23: Effect of Mo alloying on the transformation behavior of a low-carbon steel. After [114].

Tang and Stumpf [115] investigated the roles of molybdenum addition and prior deformation on austenite decomposition in Nb–Ti micro-alloyed low-carbon line pipe steels (0.5–0.6C, 1.2–1.6Mn, 0.001–0.22Mo, 0.04–0.06Nb, 0.02Ti, 0.004–0.07Al, 0.3Si) with various Mo additions. Microstructure consisted mostly of acicular ferrite plus polygonal ferrite after hot rolling and rapid cooling but no clear relationship between the acicular ferrite fraction and Mo content was obtained. Continuous cooling transformation diagrams of two alloys, one Mo-free and the other containing 0.22wt% Mo, were determined for cooling rates from 0.1 to 40 °C/s without and with prior deformation of austenite below its non-recrystallisation temperature. Molybdenum additions slightly enhanced the acicular ferrite and bainite formation in the strain-free austenite. As shown in Figure 24, both microstructures were reachable at lower cooling rates but polygonal ferrite was still present up to a cooling rate of 2°C/s whatever the chemical composition. Prior deformation (and subsequent primary austenite grain size reduction) had a much more significant effect, strongly promoting polygonal ferrite and acicular ferrite formation at the expense of bainite in both alloys.

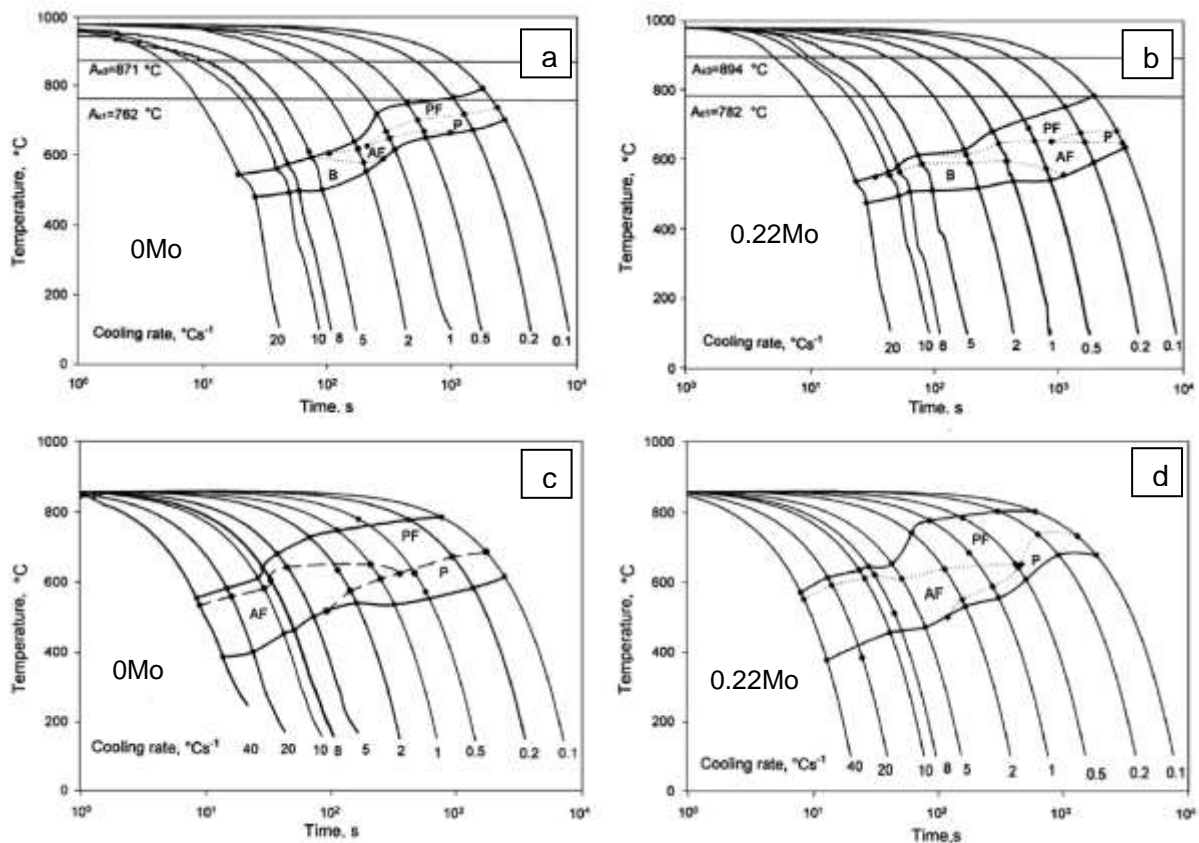


Figure 24: Strain-free CCT diagrams of (a) Mo-free and (b) 0.22Mo alloys. Strain affected CCT diagrams of (c) Mo-free and (d) 0.22Mo alloys after a single compression of austenite by 0.6 at 860 °C with a strain rate of 0.5 s⁻¹. PF: polygonal ferrite, P: pearlite, AF: acicular ferrite and B: bainite. After [115].

Increasing the Mo content from 0.1% to 0.6% leads to a significant retardation of the static recrystallization by solute-drag. Adding 0.3% Mo to a 0.04%C-0.09%Nb steel raises T_{nr} by 40°C (from 900°C to 940°C) [116]. Since the static recrystallization delaying effect of Nb saturates above 0.06%Nb [94], addition of Mo can effectively help to further increase T_{nr} despite the solute drag-like effect of Mo on Nb in austenite. Akben et al. [3] revealed that the solute drag effect of Mo alone on retarding dynamic recrystallization is intermediate between that of Nb, which has the greatest effect and that of V, which has the lowest effect on an equal atom fraction basis.

1.3.3.b Effect of molybdenum in precipitates

The effects of 0.2Mo and 0.04Nb additions on the precipitation strengthening in a low-alloy steel (0.1C, 0.1Si, 1.5Mn, 0.2Ti, 0.004N) have been investigated by Chen et al. [117]. Focus was made on carbide precipitation by soaking at 1200°C for 3min, cooling at 20°C/s down to 800°C then cooling between 0.5°C/s and 0.1°C/s. Such conditions were used in order to increase the degree of carbon supersaturation in ferrite compared to classical continuous cooling. In each case, the ferrite matrix contains very fine, banded dispersions of carbides, typical of interphase precipitation. As shown in Figure 25, titanium molybdenum complex carbide, (Ti,Mo)C, has a tendency to maintain nanometer-scaled sizes as the final cooling rate decreases whereas TiC and (Ti,Nb)C do not.

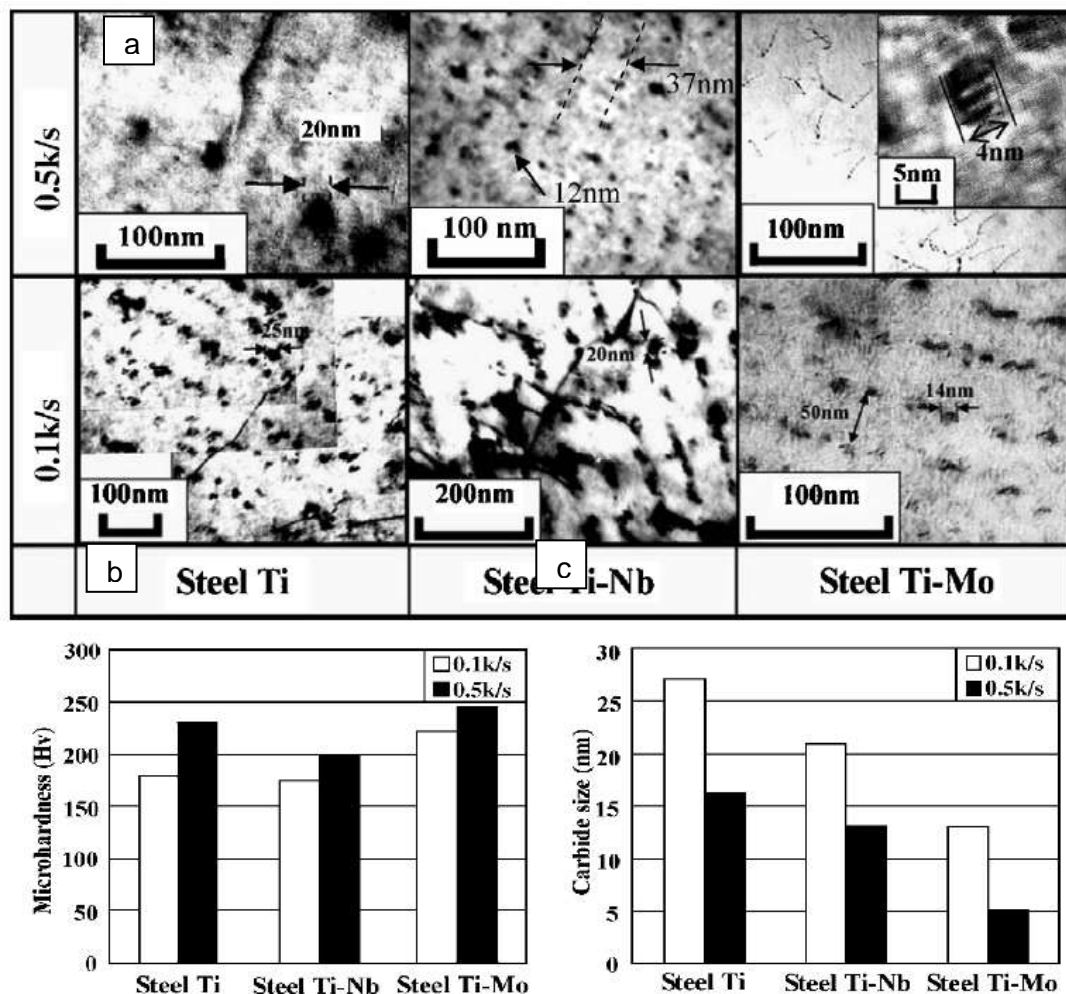


Figure 25: (a) TEM images, (b) microhardness and (c) average carbide particle size for three microalloyed steels after interrupted cooling at 800°C and then cooling at 0.5 and 0.1 °C/s, respectively, to room temperature. After [117].

Such precipitation features were also observed by Funakawa et al. [118] in 0.04C–1.5Mn steels exhibiting Ti and Mo variations from 0 to 0.19wt% and from 0 to 0.37wt%, respectively.

CHAPTER 1 – LITERATURE SURVEY

Hot rolling was simulated using dilatometry, by performing three iso-thermal deformation stages (the last one at 950°C) through cooling at 10°C/s from 1250°C. The characteristic arrangement of the nanometer-sized (around 3nm) Mo-Ti carbides indicates that the carbides were formed at austenite–ferrite interfaces during transformation. The calculated amount of precipitation strengthening by the carbides was approximately 300MPa. This is two or three times higher than that brought by TiC particles in Ti-Nb steel.

Jang et al. [119] studied interphase precipitation of carbides in Ti-Nb and Ti-Nb-Mo micro-alloyed steels (0.07C, 1.8Mn, 0.01Ti, 0.03Nb, 0.03Al, 0 or 0.2Mo). After a complex thermo-mechanical treatment simulating hot deformation, an isothermal step at 700°C during 40min (for transformation and interphase precipitation) was performed to obtain precipitates of (Ti,Nb)C and (Ti,Nb,Mo)C, respectively. Both steels exhibited a banded dual phase microstructure, composed of allotriomorphic ferrite (formed at 700°C) and martensite (formed during cooling to room temperature) of equivalent grain size. Molybdenum significantly reduced the size of carbide precipitates (4.1 to 2.8nm in average) as well as the spacing between the rows of precipitates (from 40-45nm to 22nm), which was related to the stepwise translation of the ferrite/austenite interface. As already reported in an earlier study [120], Mo also strongly retards the coarsening of (Ti,Nb,Mo)C during prolonged aging treatments that were additionally applied. These authors assumed that molybdenum was not thermodynamically favoured as a solute within TiC but nevertheless reduced the lattice misfit between carbide and ferrite (in agreement with Cao et al. [102]), thus making the nucleation process easier. The role of molybdenum was therefore to accelerate nucleation and hence to refine length scales during interphase precipitation. In the context of growth and coarsening, molybdenum retards both growth and coarsening of carbide by partitioning into the matrix.

1.3.3 Role of titanium as micro-alloying element

1.3.3.a Effect of titanium in solid solution

Garcia de Andrés et al. [121;122] compared the kinetics of austenite decomposition in 0.31C-1.22Mn-0.25Si-0.14Cr and 0.36C-1.56Mn-0.33Si-0.24Cr-0.026Ti steels (Figure 26). Titanium enhances the allotriomorphic ferrite transformation during the isothermal decomposition of austenite, i.e the transformation begins earlier and is faster in C-Mn-Ti steel despite the slight increase in manganese and carbon content compared to the Ti-free steel. This effect might be due to the lower solubility of Ti in austenite rather than in ferrite.

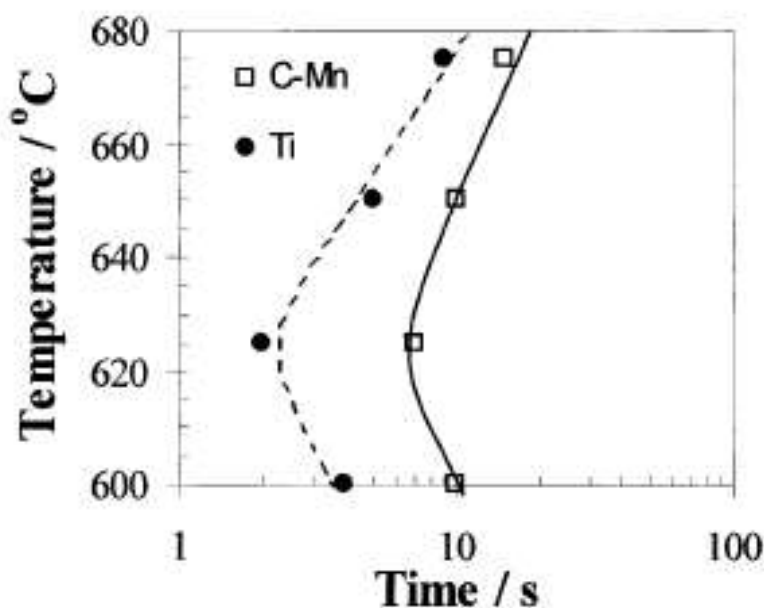


Figure 26: Experimental start transformation curves for allotriomorphic ferrite isothermally transformed at temperatures ranging from 675 to 600 °C for various holding times and subsequently quenched to room temperature. Austenitisation parameters were selected to achieve an austenite grain size of 70µm. After [122].

CHAPTER 1 – LITERATURE SURVEY

On the contrary, in a earlier study, Liu and Zhang [116] noticed a decrease in austenite decomposition rate with the increase in Ti content. This effect is shown in Figure 27, on TTT curves of three different Ti containing steels. Indeed, Ti is a strong carbide-former. Ti decreases the carbon activity in austenite, thus producing a solute drag-like effect by segregating to ferrite/austenite interfaces and retarding carbon diffusivity through these interfaces.

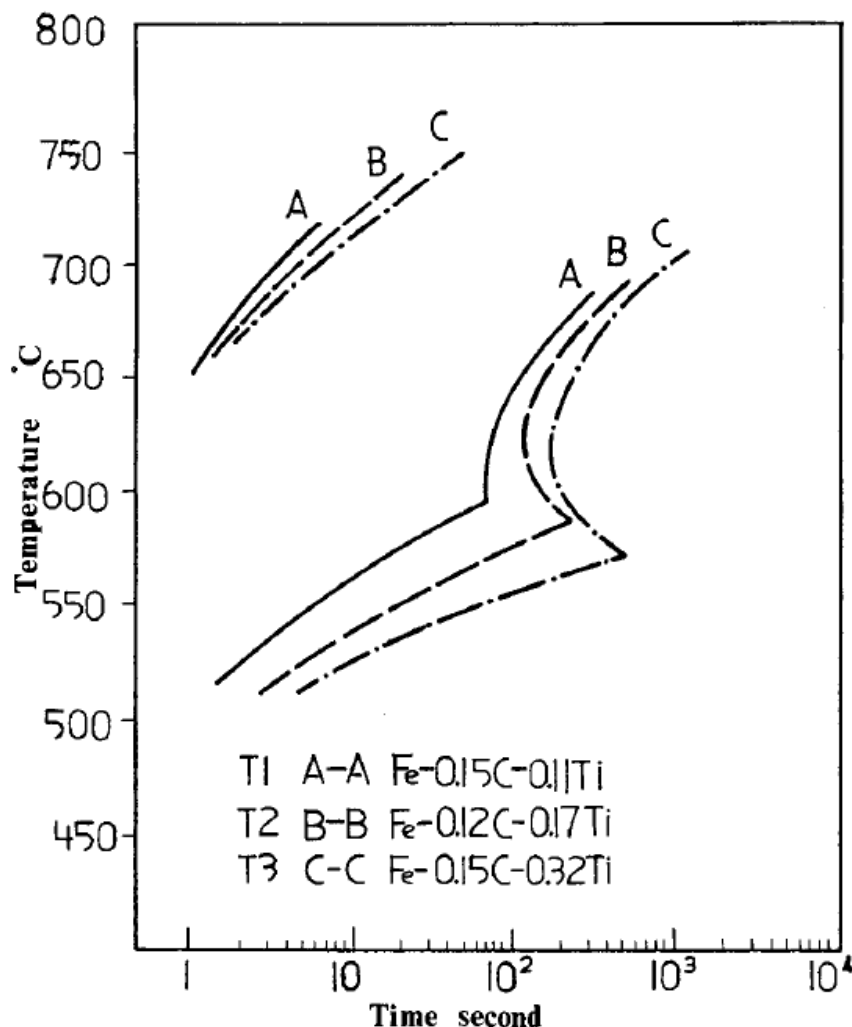


Figure 27: Initial and finish curves of TTT diagram of three different Ti containing steels. No indication of primary austenite grain sizes was given. After [38].

These previous studies lack of comprehensive study of Ti precipitation to evaluate the Ti solid solution content in their steels. These opposite effects on ferrite transformation may be linked to the dominant environment of Ti (in solid solution or in precipitate) in these steels, or to differences in amounts of other alloying elements.

1.3.3.b Effect of titanium in precipitates

Ti nitrides are well known for their efficiency in limiting austenite grain growth even at high temperatures. In most cases the TiN particle distribution is not altered at temperatures below 1250°C. An efficient use of TiN is realised when the Ti content lies between 0.010-0.015wt% together with a Ti/N ratio <3.42 [123]. Using an over-stoichiometric nitrogen content leads to an increase in the TiN dissolution temperature (TiN are more stable) but also to an increase in the size of these particles, which is not only less efficient to pin the austenite grain boundaries but also increases the probability for TiN particles to act as fracture initiation sites.

CHAPTER 1 – LITERATURE SURVEY

Wang [124] has evaluated the influence of titanium content (from 0.006 to 0.042 wt%) in three steels presenting various nitrogen contents (0.1C, 1.3Mn, 0.2Si, 0.02Al, 0.0027-0.0048-0.0062N) on the coarsening behaviour of austenite grains during soaking. Grain size and TiN particle size were measured after austenitization at various temperatures ranging from 950 to 1260°C for 1.5h followed by quenching in iced brine. As shown in Figure 28, the critical temperature for significant grain coarsening (i.e., boundary between Regions I and II) is obviously increased by the presence of titanium. Moreover, for a given nitrogen content, the highest grain coarsening temperature occurs around the Ti/N stoichiometric ratio, i.e. 3.42 (in wt%) and an increase in grain coarsening temperatures with increasing nitrogen content also occurs at Ti/N around 3.42. Higher titanium content, beyond the stoichiometric ratio decreases the grain coarsening temperature as a result of TiN particle growth.

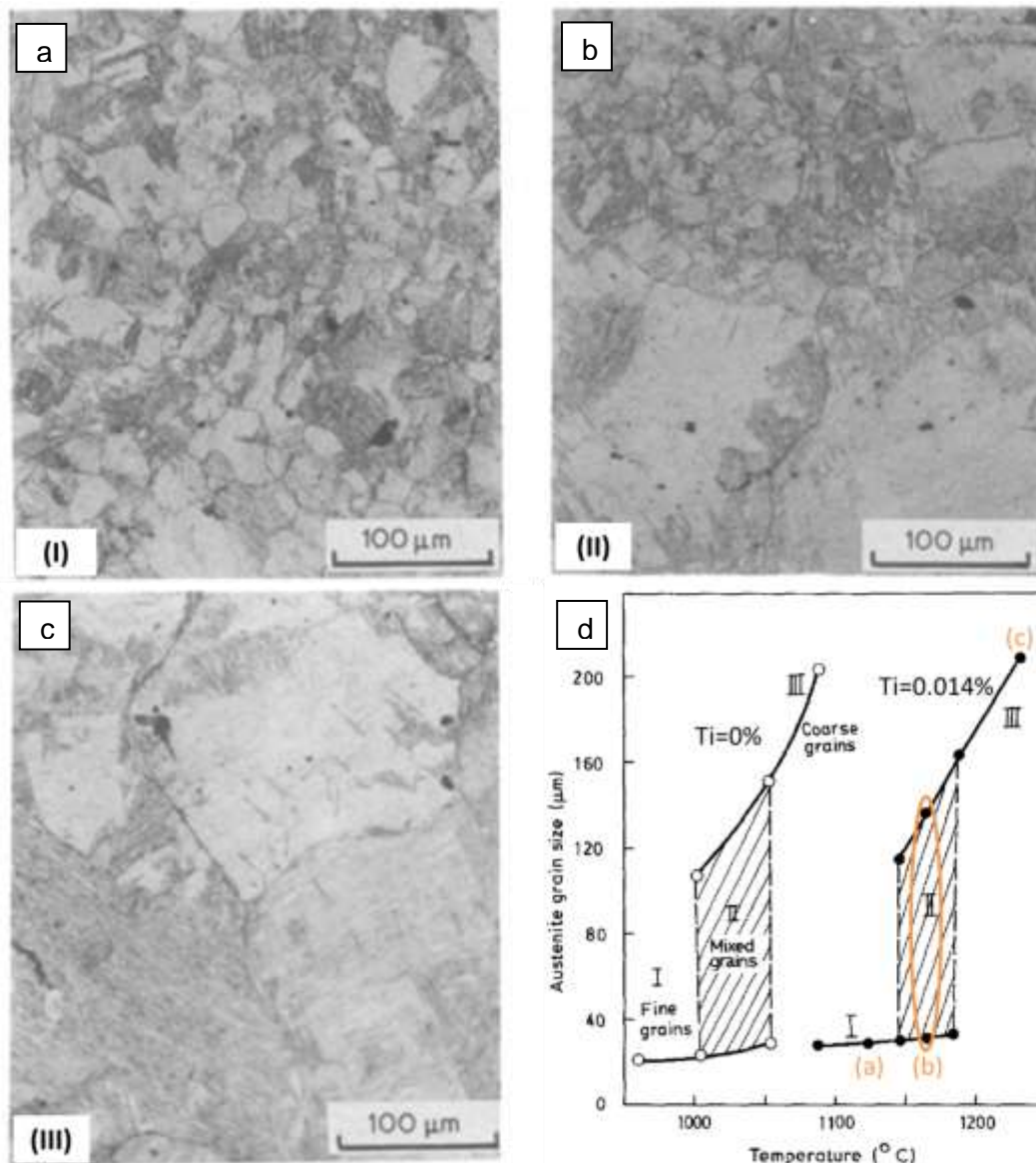


Figure 28: Microstructure of 0.1C, 1.3Mn, 0.2Si, 0.02Al, 0.0027N and 0.014Ti steel austenitized and quenched from (a), 1123°C (b) 1165°C and (c) 1232°C. (d) Variation of austenite grain size with the austenitization temperature of 0.1C, 1.3Mn, 0.2Si, 0.02Al, 0.0027N steel with 0 and 0.014 Ti content (in wt%). After [124].

Adrian and Pickering [125] investigated the evolution of austenite grain size in 0.4C-0.4Si-1.6Mn aluminium-killed steels containing various amounts of V, Ti and Nb. They performed a quantitative metallographic analysis of carbo-nitrides particles. The largest volume fraction of (Ti-rich,Nb)(C,N) was found in the steel which contained the highest Ti content (0.037wt%) and an average Nb content (0.07wt%). The smallest amount of coarse primary carbo-

CHAPTER 1 – LITERATURE SURVEY

nitrides, which precipitated during solidification (see the section about the effect of Nb), was observed in the steel which, although containing a fairly high Ti content (0.034wt%), had the largest Nb content (0.13wt%). It seems that Nb may inhibit the formation of (Ti-rich,Nb)(C,N) during solidification. The underlying mechanism (by which Nb prevents Ti-rich carbo-nitride formation during solidification) is not fully understood, but it may be a result of Nb entering into solution into the Ti-rich carbonitride and lowering its melting point so that a much lower amount of such precipitates forms above the solidus temperature of the steel.

1.4 Influence of the austenite state on its decomposition during cooling

The mechanical properties of forged components made of micro-alloyed steels are obtained by proper determination of forging process conditions, such as austenitisation temperature, forging temperature, dwell time and time intervals between consecutive operations, and final cooling conditions. The austenitisation temperature must provide good forgeability as to obtain the desired geometry at minimum number of forging passes and, on the other hand, must keep some of the carbo-nitrides undissolved to prevent austenite grain growth.

1.4.1 Influence of the primary austenite grain size on the austenite decomposition

1.4.1a Effect on the ferritic transformation

It is well known that Ar_3 depends on the primary austenite grain size (**PAGS**), on the chemical composition of the steel and on the cooling rate [89;126]. For a given steel chemistry and cooling rate, Ar_3 increases as the austenite grain size decreases. In fact, the density of austenite grain boundaries is higher if the PAGS is smaller. Since austenite grain boundaries act as ferrite nucleation sites, all diffusive transformations are enhanced in fine-grained austenite microstructures.

However, good hardenability for small austenite grain size can still be observed in certain conditions. Garbarz and Pickering suggested [127] that pinning austenite grain boundaries by undissolved carbonitride particles creates the possibility for segregation of dissolved alloying element atoms, such as boron, at immobile grain boundaries. The resulting decrease in grain boundary energy reduces their potential for the nucleation of non-martensitic products.

The PAGS also has an impact on the segregation intensity of elements such as boron, niobium, phosphorus at austenite grain boundaries. When the PAGS is large, segregating atoms need more time to reach the grain boundaries, the time needed to reach equilibrium is thus longer. Moreover, the area density of grain boundaries is lower, and thus, their segregation level at equilibrium is higher.

1.4.1.b Effect on the bainitic transformation

The effect of the PAGS on the continuous cooling transformation rates of upper and lower bainite in a low-alloy steel (Fe–0.39C–0.65Mn–0.24Si–1.60Ni–0.67Cr–0.15Mo) has been investigated by Lee et al. [128] based on dilatometric analysis. Samples were heated up to a selected temperature in the range 950–1150°C, held for 10min and quenched down to 550°C, which is the B_s temperature, by blowing nitrogen gas and then cooled to room temperature at 1.6°C/min. This heat treatment was scheduled to obtain a fully bainitic structure.

On the dilatometric curves, an inflection point was observed which corresponds to the transition temperature between upper and lower bainite (B_t^{cont}) as illustrated in Figure 29. This inflection was attributed to the differences in transformation mechanism and kinetics between upper and lower bainite.

The average PAGS was measured by the linear intercept method based on optical micrographs and was found between 24 and 162 μ m as the austenitization temperature increased from 950 to 1150°C. B_t^{cont} was independent of the PAGS, while both B_s and B_f

CHAPTER 1 – LITERATURE SURVEY

(bainite finish transformation temperature) decreased with decreasing PAGS. The fraction of bainite formed at any temperature was estimated from the dilatometric curve by using a lever rule:

$$V(T) = \frac{S(T) - S_A(T)}{S_B(T) - S_A(T)} \quad \text{eq. 1.1}$$

where $V(T)$ is the volume fraction of bainite formed at temperature T . Authors found that the overall bainitic transformation rate ($\Delta V/\Delta t$) is accelerated by decreasing the PAGS for both upper and lower bainite. The higher the density of austenite grain boundaries, the higher the number density of nucleation sites that are available for bainitic ferrite. The instantaneous transformation rate of lower bainite had no strong dependence on the PAGS, probably due to the pre-existing upper bainite already formed close to the grain boundaries during continuous cooling.

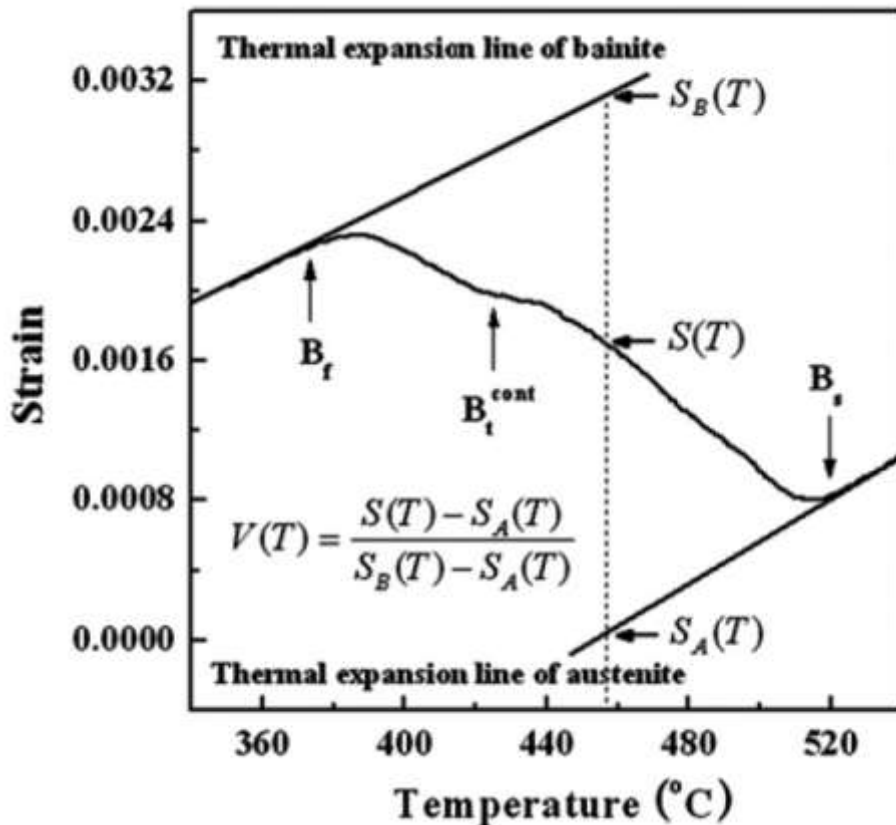


Figure 29: Example of a dilatometric curve showing an inflection point presumed to be a transition temperature between upper and lower bainite. After [128].

These results are in contradiction with the earlier results of Yamamoto et al., who reported that PAGS has no appreciable effect on B_S , B_F and overall austenite to bainite transformation kinetics under continuous cooling conditions [129]. They determined CCT diagrams for three different steels (chemical compositions shown in Table 1) using deformation below or above the non-recrystallization temperature to obtain the desired grain size and shape.

Steel	C	Si	Mn	P	S	Mo	Nb	Ti	Al	B	N
1	0.040	0.20	2.94	0.001	0.0004	-	0.028	0.023	0.017	0.0002	0.0018
2	0.040	0.20	2.95	0.001	0.0004	-	-	0.002	0.017	0.0003	0.0019
3	0.178	0.21	1.72	0.008	0.0020	0.25	0.039	0.011	0.024	0.0003	0.0052

Table 1: Chemical composition in wt% of steels investigated in [129].

The austenitisation temperatures in Nb-bearing steels and Nb-free steel were set to 1200 and 1160°C, respectively (no indication of holding time). Three different types of prior

CHAPTER 1 – LITERATURE SURVEY

austenite, namely equiaxed austenite grains with average diameters of $200\mu\text{m}$ and $20\mu\text{m}$ and elongated austenite grains with the same grain boundary area per unit volume as that of $20\mu\text{m}$ equiaxed austenite grains, were prepared by varying the reheating and hot deformation conditions. The cooling rate between the temperature of the last deformation and 800°C was set to 10°C/s to avoid any microstructural change in austenite.

The bainitic domains in CCT diagrams were the same for prior equiaxed austenite grains of $200\mu\text{m}$ and $20\mu\text{m}$, only the ferritic C-curve was modified. Despite the increase in potential nucleation site density, the volume fraction of bainite was not dependent on the primary austenite grain size, but only depended on cooling rate. On the contrary, elongated and unrecrystallized primary austenite grains raised B_S and B_F temperatures as compared with the equiaxed structure having the same grain boundary area per unit volume. Moreover, intragranular nucleation of bainitic ferrite was also observed in this case.

In fact, many investigations have been realised on this subject defending either of these assumptions [61;130-135]. All these works have demonstrated that different steels (in chemical composition) can show opposite effects of PAGS. Matsuzaki and Bhadeshia [136], addressing isothermal transformation, assumed these two different behaviours were linked to the bainite morphology at the early stages of transformation. If the growth rate of the bainite sheaves is relatively high compared with the rate of nucleation at austenite grain boundaries (Figure 30, Steel A, 0.12C, 2.03Si, 2.96Mn), the reaction rate increases with increasing austenite grain size. Once nucleation is completed the sheaves penetrate the parent grain rapidly until impingement occurs. If the growth rate is not as high compared with the nucleation rate at austenite grain boundaries (Figure 30, Steel B, 0.96C, 0.21Si, 0.38Mn, 1.26Cr), the boundaries become almost completely decorated well before impingement occurs, the reaction rate thus decreases with increasing austenite grain size.

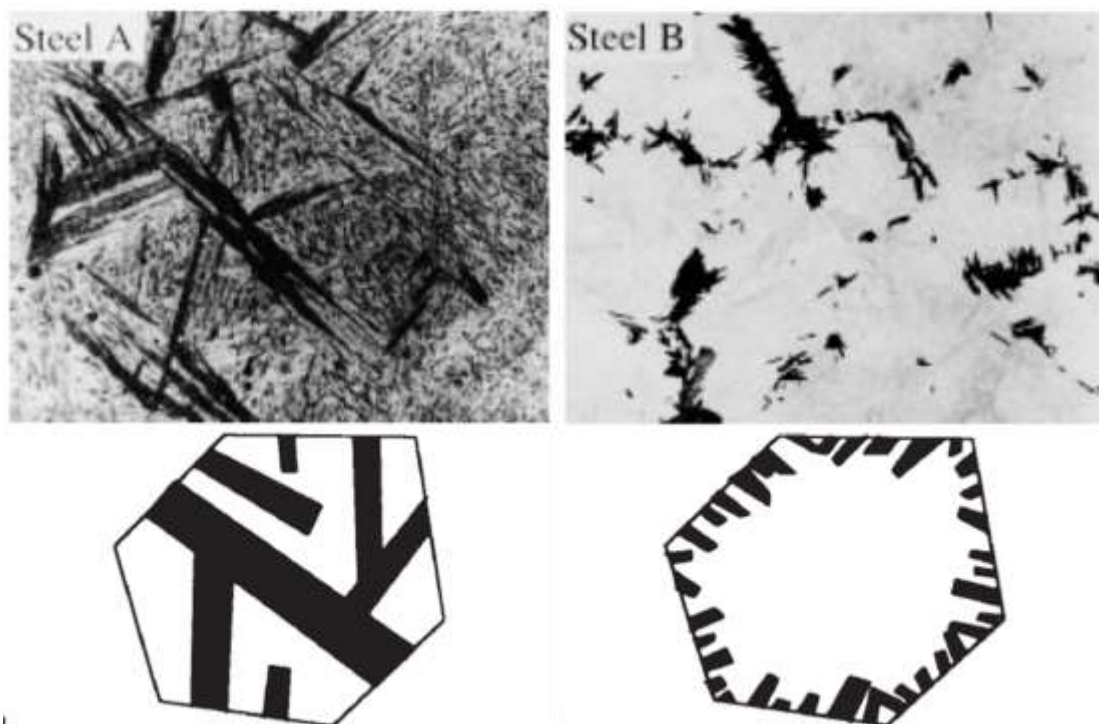


Figure 30: Observed (optical, $\times 100$) and schematic morphology of bainite sheaves at early stages of isothermal transformation. After [136].

In this case (Figure 30), these two different bainite morphologies at the early stages of transformation might be linked to cementite precipitation. Indeed, steel B, with relatively high C and low Si contents, might exhibit extensive cementite precipitation whereas steel A, with relatively low C and high Si contents, might be cementite-free. PAGS itself might also influence bainite morphologies at the early stages of transformation, so the influence of

CHAPTER 1 – LITERATURE SURVEY

PAGS on the bainitic transformation might not be linear, especially in boron steel, as PAGS controls the boron concentration along primary austenite boundaries.

Zarei-Hansaki et al. [55] investigated the effect of the prior austenite grain size on the retained austenite characteristics and the corresponding mechanical properties in a 0.22C-1.55Si-1.55Mn TRIP steel (in wt%). Measurement of the retained austenite volume fraction was performed by XRD. Final microstructures obtained after various thermo-mechanical processes were a mix of allotriomorphic ferrite, cementite-free upper bainite and lower bainite. The smaller the prior austenite grain size, the smaller the bainite packet size. A decrease in austenite grain size in the Nb-bearing steel, from 230 to 70 μm , led to a reduction in the volume of retained austenite from 12.1 to 9.5%. The largest grain size in the Nb steel not only resulted in the highest amount of retained austenite, but also led to the largest total elongation. In the Nb-free steel, however, the opposite tendency was observed, an increase in austenite grain size from 45 to 350 μm leading to a decrease in volume of retained austenite from 7.1 to 5.1%. Following the authors, such difference occurs for the following reasons:

1. The larger bainite packets with higher volume fraction of bainitic ferrite platelets per packet reduces the volume fraction of interpacket and interlayer untransformed austenite at the end of isothermal bainite holding (i.e., less remaining austenite to be retained).
2. The coarser remaining austenite particles trapped in between bainite packets more likely transform into lower bainite and/or into martensite during subsequent cooling to room temperature (the finer the austenite particle size, the lower the M_s and therefore the higher the stability of parent austenite).
3. The higher the level of Nb in solid solution, the higher the stability of parent austenite, thereby increasing the volume fraction of retained austenite at the end of the process. This is true for coarser austenite grain sizes rather than for finer grain sizes. On the other hand, fine parent austenite grains were generated by deformation, which also promoted the kinetics of Nb(C,N) precipitation during subsequent treatment, removing Nb from solid solution.

1.4.1.c Effect on the martensitic transformation

It has been reported in several studies that the M_s temperature is also influenced by the PAGS. For a given steel, M_s is higher when the PAGS is larger due to the decrease in number density of nucleation sites. Yang and Bhadeshia [137] (in a publication dedicated on the calculation of M_s according to the PAGS) give a comprehensive list of experimental evidence supporting this assumption that will be not developed here.

1.4.2 Influence of prior deformation

As-forged microstructure is dependent of strain distribution and temperature gradients in the volume. The nature of the forging process itself involves additional variables, which contribute to possible non-uniformity of obtained microstructure after forging. For complex-shaped parts, some sections significantly differ in thickness, causing both non-uniform distribution of strain and local variation in strain rate, and as a result, a significant amount of deformation-induced heat. Complex geometry produces a metal flow pattern resulting in heterogeneous contact times of deformed metal with tool surface. The temperature gradient decreases during subsequent stages before cooling. Nevertheless, as a consequence of the temperature and strain gradients, local differences in microstructure are still expected at the end of the process.

CHAPTER 1 – LITERATURE SURVEY

It is necessary to have some prior idea of the non-recrystallization Temperature (T_{nr}) to design efficient thermo-mechanical forging schedules. Deformations above T_{nr} induce static and dynamic recrystallization resulting in a fine austenite grain size when properly controlled. The effects of this kind of deformation are thus linked to the austenite grain size. Deformation at temperatures below T_{nr} produces a deformed austenite grain structure that can have a strong influence on phase transformation. Deformation below the T_{nr} might:

- Accelerate the onset of the γ/α transformation (by raising the A_{r3} temperature) and increase the transformation time (i.e slow down the progress of transformation) as reported by many studies [42;69;92;138;139]. The increased diffusion rate in the plastically deformed austenite and the significantly increased density of sites for heterogeneous nucleation feature the decisive factors causing A_{r3} raising.
- Promote the formation of acicular ferrite instead of bainite [138;140;141]. Even if the field of acicular ferrite is enlarged after deformation, decomposition of austenite into allotriomorphic ferrite is always more significantly enhanced by deformation than that into acicular ferrite [142]. If we consider that acicular ferrite is intragranular bainite (that can be supported by the fact that these two microstructures share the same C-curve in a CCT diagram), B_s was found to increase with the increase in strain in prior austenite because of the increase in density of nucleation sites [129;138;143-146]. Deformation in austenite below the T_{nr} reduces the length of bainitic ferrite laths remarkably [143]. The overall extent of transformation might also be reduced, this effect being known as austenite mechanical stabilisation [147]. In continuous cooling conditions, it leads to an increase in the MA constituent fraction [148].

In our study, it is expected that the targeted forging process ends well over the T_{nr} . As a consequence, the above mentioned effects might not be observed. To ensure it, the T_{nr} has to be evaluated using hot torsion tests before the design of thermo-mechanical processing cycles.

1.5 Conclusions

Based on this literature review, Table 2 summarizes the effects of alloying elements on austenite decomposition into bainite, austenite state prior its decomposition and precipitation. These effects are evaluated according to the respective content of each alloying element in the chemical composition of the targeted air-cooling bainitic steel.

Alloying element	Bainitic transformation temperature	Incomplete transformation phenomenon	particle	primary austenite state	other effects
Major					
Mn	▼▼▼	▲▲▲	primary: MnS		strong austenite stabilizer ▼▼▼ M_s and the critical cooling rate to get full martensite microstructure might delay Nb-rich carbide precipitation
Si	▼▼	▲▲	none	~	delay/inhibit cementite precipitation enhance the segregation of Mn at austenite grain boundaries
Cr	▼▼	▲▲	secondary: Cr_7C_3 , but not very probable according Ti, Nb and Mo content	~	might delay cementite precipitation can reveal a well-defined bay between the ferrite/pearlite and bainite/martensite fields in continuous cooling
Ni	▼▼	▲▲	none	~	strong austenite stabilizer ▼▼ M_s and the critical cooling rate to get full martensite microstructure
Minor					
B	▼	~	secondary: $Fe_{23}(B,C)_6$ or BN in case of ineffective boron protection by Nb/Mo or Ti respectively	decrease phosphorus segregation level along primary austenite grain boundaries	suppress austenite decomposition into ferrite without ▼ the critical cooling rate to get full martensite microstructure resulting in a wide bainitic field
Nb	▼	~	secondary: (Nb,Ti)(C,N) and/or (Nb,Mo)C and/or NbC	▼ grain coarsening kinetics strongly retard static and dynamic recrystallization ▲▲ T _{tr}	protect boron from carbon complementary action between Nb-free (if >0.06%wt) and Nb-precipitate on the primary austenite state
Mo	▼	~	secondary: Mo_2C cluster	▲ grain coarsening kinetics retard static and dynamic recrystallization ▲ T _{tr}	protect boron from carbon strongly delays the austenite-to-pearlite transformation ▼ average size of titanium-rich and niobium-rich carbides
Ti	~	~	primary: TiN secondary: (Ti,X)(N,C) and (Ti,X)(C,N) with X=Nb and/or Mo	Ti particles are expected to pin the primary austenite grain boundaries	might not remain in solid solution protect boron from nitrogen ▲ stability and average size of niobium-rich carbide

Table 2: Expected effects of alloying elements on the bainitic transformation, primary austenite and precipitation in the targeted bainitic steel. ▲ : increase, ▼ : decrease. The number of symbol reflects the expected strong of the effect. ~ no effect expected.

CHAPTER 2 - MATERIALS

Résumé : Ce chapitre présente les matériaux utilisés lors de cette thèse. Il commence par le matériau de référence dans son état brut de laminage et son état brut de forgeage. Des particularités microstructurales, liées au procédé, telles que la structure de ségrégation et la population inclusionnaire avec la présence de certains types d'inclusions, sont mises en avant.

Les compositions chimiques des dix coulées de synthèse réalisées pour cette thèse sont décrites et discutées. La mise en forme de ces coulées de synthèse, par forgeage libre, a été suivie par différents équipements de mesure de température. Ces mesures soulignent les variations pouvant exister sur le cycle thermo-mécanique d'une coulée de synthèse à l'autre. Ces variations ont mené à la segmentation du lien réalisable entre la composition chimique et les propriétés mécaniques en deux liens distincts :

- l'un entre la composition chimique et la microstructure, qui sera obtenu par dilatométrie, c'est-à-dire par des traitements thermiques contrôlés sur des échantillons de laboratoire, les propriétés mécaniques étant uniquement évaluées par des essais de dureté ;
- l'autre entre la microstructure et les propriétés mécaniques, qui sera obtenue grâce aux caractérisations microstructurales et mécaniques des coulées de synthèse forgées.

Les résultats concernant ces caractérisations microstructurales (taille de grains de l'austénite primaire, quantification des différents constituants microstructuraux, précipitation) sont présentés dès ce chapitre et montrent la grande variété de microstructures dites de bainite supérieure/granulaire obtenue grâce aux coulées de synthèse. Cette variété permettra justement d'établir le lien entre microstructure et propriétés mécaniques à partir d'une large base expérimentale.

CHAPTER 2 – MATERIALS

The very first objective of this chapter is to introduce the materials that have been used along the PhD project, together with their processing route and microstructure. The choice of their chemical composition, as well as their specific hot-forming process are also discussed when necessary. It has been made by taking into consideration findings from literature, existing design methodology in Gandrange R&D centre, the limited knowledge on the chosen forging process that we have and the targeted application. The similarities and differences between reference and laboratory materials concerning their microstructure are also pointed out here. This chapter also highlights the noticeable range of bainitic microstructures obtained with these materials, with only slight changes in chemical composition.

The second objective was to identify any issues that could affect the building of significant links between chemical composition, microstructure and mechanical properties, for the actual approach adopted in this study. The point was then how to overcome or avoid these issues to achieve the project objectives by adapting the experimental methodology.

2.1 Reference materials

2.1.1 Chemical composition and metallurgical states

Two different states of a unique heat of a reference steel grade were selected as reference materials:

- As-rolled state, hot-rolled into a bar (80mm in diameter, section area=5026mm²).
- As-forged state, closed-die forged after rolling. Due to its geometry, this forged part exhibit a heterogeneous section along its longitudinal direction. The analysed section was the biggest available on this forged part, where the cooling rate was expected to be the lowest (analyzed section area ~5440mm²).

These two different states were selected to provide two different microstructures from the same chemical composition, exhibiting inclusion populations and segregation intensity that are typical of any industrial process. The chemical composition of this reference steel grade (**IS**) is indicated in Table 3 (detailed chemical composition is given in Appendix C [ArcelorMittal version only]).

C	Mn+Si	Cr+Ni	P+S	Mo+Nb+Ti+B
0.18-0.20	2.50-2.70	1.30-1.60	0.02-0.03	0.15-0.18

Table 3: Chemical composition of reference reference steel grade (wt%).

This is a low-carbon steel, strongly alloyed (4.15-4.71wt%) compared to the other bainitic steels, mainly for automotive or pipe application, that have been encountered along the first chapter (with the exception of one Fe-Ni bainitic steel). The variety of alloying elements, that are able to form precipitates in austenite leads to a significant decrease in the average carbon content in the steel matrix before the bainitic transformation. With such a protection, boron successfully segregates along primary austenite grain boundaries and avoids any austenite decomposition into allotriomorphic ferrite. This pre-bainite precipitation, in addition to relatively high contents of silicon and of austenite stabilizing elements, supresses most of the cementite precipitation from retained austenite during the bainitic transformation, leading to so-called “carbide-free” bainite. As a consequence, a high fraction of secondary phases is present in the final microstructures. The obtained bainitic microstructure is presented in more details at the end of this chapter, where it is compared with the bainitic microstructures obtained from as-forged laboratory heats.

2.1.2 Segregations & inclusions

2.1.2.a Banded structure

Light microscopy observations have been realized in a plane containing the rolling direction for both states, at mid-radius (or mid-section) of the part. Samples have been mirror polished

CHAPTER 2 – MATERIALS

and then etched using LePera reagent. As shown in Figure 31, both as-forged and as-rolled states present a banded structure. In both cases, the steel matrix exhibits coarser primary austenite grains (up to $100\mu\text{m}$) than do segregation bands, with apparently larger bainite packets and wider ferritic bainite laths. Segregation bands exhibit a much finer microstructure with localised occurrence of martensite blocks and large groups of inclusions. At mid-radius of the as-rolled state, the average distance between segregations bands in the transverse direction is about $500\mu\text{m}$, the apparent width of segregation bands going from 20 up to $100\mu\text{m}$. This banded structure is less marked at mid-section of the as-forged state. A banded structure is still observable, but there is no observable thick ($>50\mu\text{m}$) segregation band. No typical distance between segregation bands has thus been measured in this region. The PAGS out of segregation bands seems coarser in the as-forged state than in the as-rolled state. This last parameter is measured for both states later in this chapter.

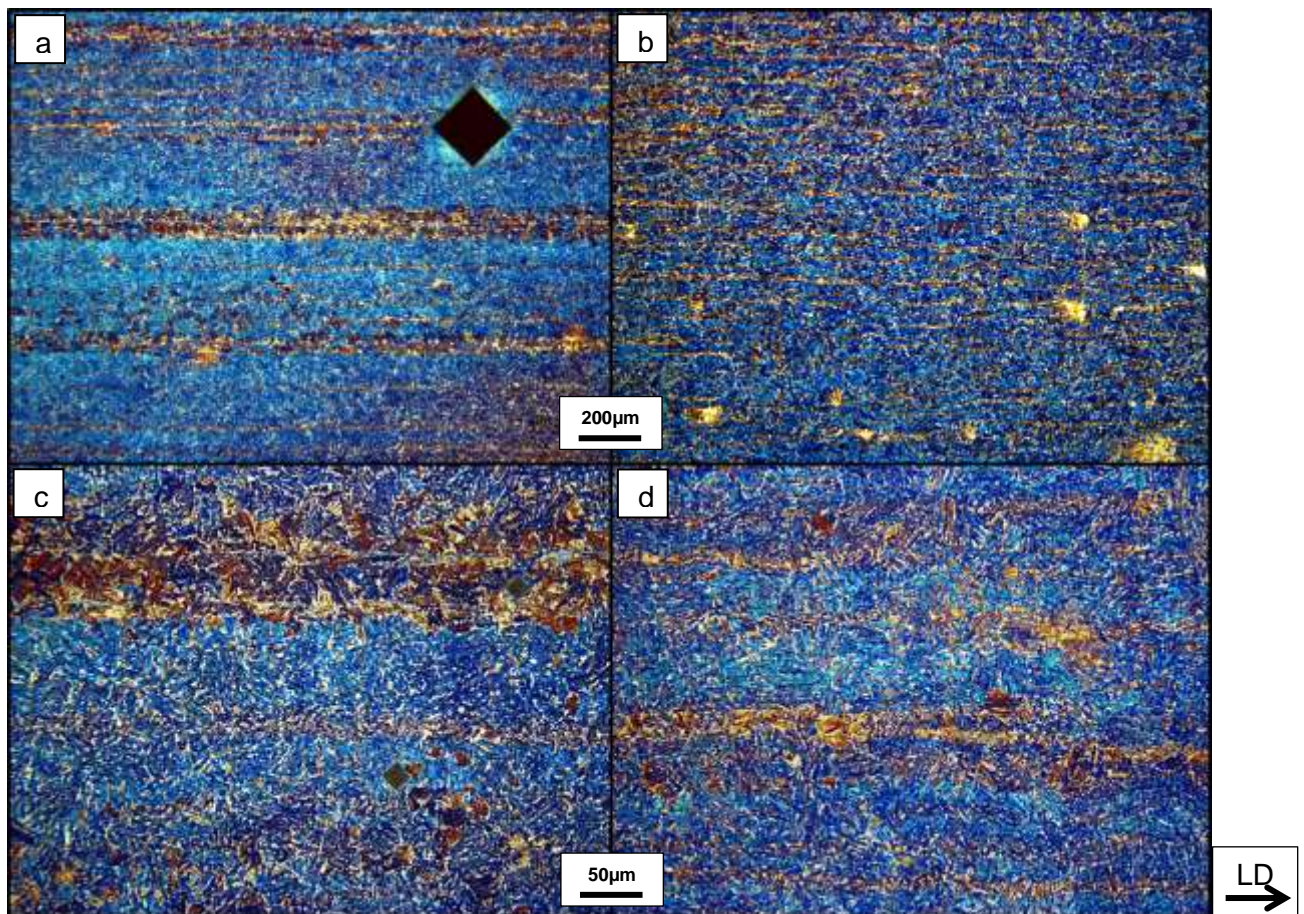


Figure 31: LM, LePera etching, (a)(c) mid-radius of as-rolled reference steel, (b)(d) mid-section of the as forged part. White=MA constituent, yellow/beige=Martensite, blue/brown=bainite.

The banded structure is due to local variations in chemical composition which lead to local differences in resulting microstructure after thermo-mechanical processing. This inhomogeneity stems from segregations that occur during the solidification and hot-rolling processes. Alloying elements that have a greater partitioning coefficient with the liquid are entrapped in regions where solidification occurs last. The segregation is more and more important as [149]:

- The range between liquidus and solidus temperatures is wide.
- The dendrites are coarser.
- The solidification temperature is lower.

The hot-rolling process then deforms these segregated regions, forming a banded microstructure. In addition, chemical segregations may also occur during the hot-rolling process. Indeed, slabs deformed in cycles revealed that if the interval between the

CHAPTER 2 – MATERIALS

consecutive deformations is smaller than the total austenite recrystallization time, superposition of consecutive shearing bands develop into austenite. These bands will present higher alloying elements concentration [150].

A micro-hardness profile ($HV_{0.025}$, dwell time of 10s) has been measured across the steel matrix and segregation bands of the as-forged reference steel. The matrix has an average hardness of $379HV_{0.025}$ (range: $364-410 HV_{0.025}$), whereas segregation bands have an average hardness of $481HV_{0.025}$ (range: $404-524 HV_{0.025}$). Martensite regions have a hardness higher than $520 HV_{0.025}$. The maximum inhomogeneity in hardness that was found in this microstructure is thus around $160 HV_{0.025}$.

Influence of the banded structure on the bainitic transformation

The austenite decomposition behaviour in banded microstructures has been studied in detail by Khan and Bhadeshia [151] on a 0.44C-1.74Si-0.67Mn-1.85Ni-0.83Cr-0.39Mo-0.09V steel (in wt%). As for the reference steel of the present project, the steel matrix, which is predominantly bainitic, exhibits segregation bands of predominantly martensitic microstructure. Homogenization was realised on some samples by holding them at 1300°C for 3 days, with the samples sealed in quartz tubes containing argon.

During isothermal transformation at high undercooling (more than 20°C below the B_S temperature determined for the average chemistry), the maximum amount of bainitic ferrite obtained experimentally is found to be larger for homogenized samples, because bainite is able to nucleate uniformly throughout the samples. In the heterogeneous samples, bainite nucleates mainly in regions depleted in austenite forming elements, i.e. outside segregation bands. Furthermore, the regions enriched in such elements become more and more stable as they trap excess carbon during the growth of bainitic ferrite, leading to low transformation rates and to high levels of retained austenite at the end of the reaction in the heterogeneous samples.

At low undercooling (less than 20°C below the B_S determined for the average chemistry), the extent of isothermal transformation is larger in the heterogeneous samples, since, at such undercooling, the authors believed that the transformation is nucleation dominated. Thus, some regions of the heterogeneous samples are able to transform even at temperatures above the B_S temperature of the homogenized alloy (i.e. there are higher local B_S temperatures according to the local chemistry).

Continuous cooling experiments were carried out at cooling rates between 0.001°C/s and 0.060°C/s on both heterogeneous and homogenized samples. The results from the slowest cooling rate show that in the heterogeneous sample, the bainitic transformation occurs up to a greater extent than in the homogenized sample. Indeed, with this cooling rate, opportunity is provided for carbon to homogenize in untransformed austenite during transformation. As the cooling rate increases, the possibility of long-range carbon diffusion diminishes, so the degree of transformation is higher in the homogenized samples. Cooling rates at the beginning of the bainitic transformation for both states of the reference steel of this present project are believed to be higher than 0.060°C/s , so in our case, the observed segregation might lead to lower extent of the bainitic transformation compared to an hypothetical case of non-banded microstructure.

Determination of the segregation level in both states of the reference steels

The chemical composition of the steel matrix and of a segregation band has been investigated using electron probe microanalysis in as-forged and as-rolled reference steels. The following elements have been taken into account: manganese, silicon, chromium, nickel, molybdenum, niobium and titanium. Carbon and boron were not quantitatively accessible with the present operating conditions. Only 5 measurements have been taken per analysed

CHAPTER 2 – MATERIALS

region, as no noticeable variation occurred in alloying element content from point to point (with the exception of Ti content). These points have been taken in the apparent middle of the segregation band and of a neighbouring steel matrix region, all along the longitudinal direction. Table 4 shows the average variation according to the nominal composition of each investigated chemical element.

		Si	Ti	Cr	Mn	Ni	Nb	Mo
As-rolled state	Steel Matrix	86%	35%	95%	91%	82%	30%	90%
	Segregation Band	161%	7%	156%	149%	134%	85%	198%
As-forged state	Steel Matrix	95%	44%	98%	98%	90%	25%	87%
	Segregation Band	125%	54%	121%	128%	115%	87%	162%

Table 4: Relative variation according to the nominal composition of each investigated chemical element in a steel matrix band and a segregation band for as-rolled and as-forged reference steels.

As expected, in both states of the reference steel, each chemical element is in a higher amount in the segregation band than in remaining steel matrix. The as-rolled state seems to exhibit a higher level of segregation than the as-forged state. This might indicate that the thermo-mechanical treatment undergone during forging tends to homogenize the chemistry (the autenization temperature is believed to be around 1250°C but the time spent at this temperature is unknown). However, such effect can also come from the region chosen for the microprobe analysis, several other measurements would have been necessary to improve statistical significance of these results.

The only noticeable exceptions in the segregation band concern titanium and niobium. Niobium and titanium exhibit obvious decreases in content according to the nominal composition in both steel matrix and segregation bands. Reason pointed out for such decreases is the strong tendency of these alloying elements to precipitate in relatively coarse niobium-titanium carbo-nitrides (length along the rolling direction: 1-20µm, width <5µm), lowering their content in solid solution. These so-called “coarser” carbo-nitrides are commonly found in the segregation bands, but mainly near the interface with the steel matrix i.e., in a region that was not analyzed by our experiments. Considering their size and their location, they might have formed during steel solidification. As the molten metal starts to solidify, the liquid gets richer in alloying elements than the solid. Precipitation of precursors such as oxide or nitride might start to occur into the liquid. As solidification comes to the end, there might be precipitation and growth of these niobium-titanium carbo-nitrides (and, additionnally, of manganese sulphides) into the liquid that still remains in the inter-dendritic regions, the initial presence of carbide/nitride precursors making this precipitation possible at such high temperature.

As coarser niobium-titanium carbo-nitrides have often been seen together with manganese sulphides as shown in Figure 32a, there are probably interactions between each other. Niobium-titanium carbo-nitrides are oriented along the rolling direction and mainly found as clusters. Some metallographs as in Figure 32b seems to indicate that these clusters could come from larger inclusions that have been fractured during the hot forming process.

Whatever the origin of these niobium-titanium carbo-nitrides, the loss in niobium and titanium in the steel matrix due to such segregation-induced coarser particles probably might lead to the decrease of finer (<200nm) secondary niobium-titanium carbo-nitrides precipitates within the steel matrix. As only finer particles are effective pin austenite grain boundaries during austenitization [100], the reference steel might be sensitive to grain coarsening at high temperature.

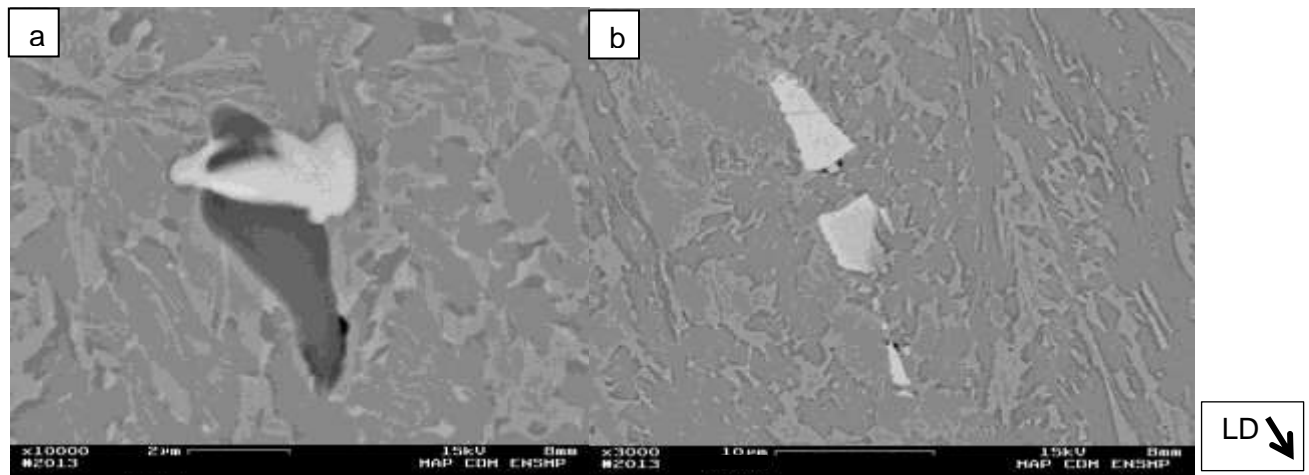


Figure 32: As-forged reference steel, x10000, FEG-SEM, BSE, Nital2% (6s). Precipitate in white is a niobium(rich)-titanium-carbon(rich)-nitride, particle in dark grey is a manganese sulphide. LD: long direction of the forged part

2.1.2.b Characterization of coarser niobium-titanium carbo-nitrides

As shown in Figure 33, even if these coarser particles do not exhibit significant shape variation, noticeable changes in colour have been observed in light microscopy. Indeed, some of them are light pink whereas others are light orange. From Castaing electron microprobe analysis of the same particles, this change in colour comes from a change in the Ti/Nb ratio. Niobium-rich particles are light pink (bright in BSE mode, due to a relatively high average atomic number) whereas titanium-rich ones are light orange (dark in BSE mode, due to a relatively low average atomic number).

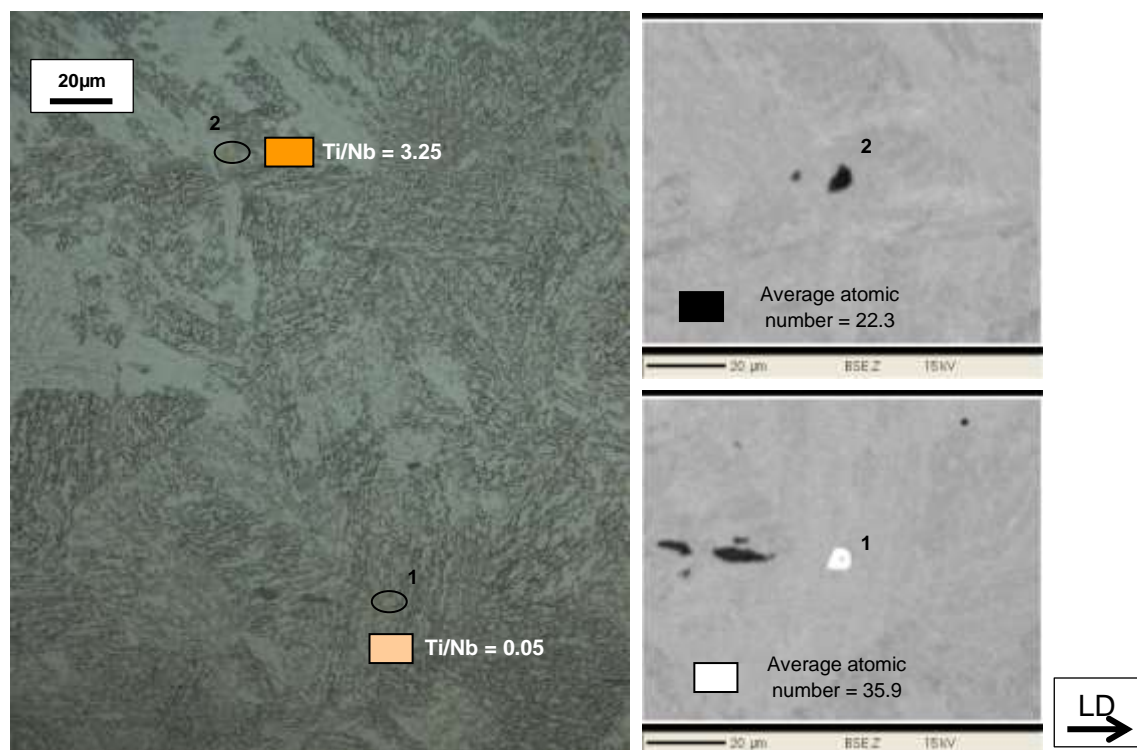


Figure 33: As-forged reference steel. Left: LM, Nital 2%, x500. Right: Castaing electron microprobe analyser, BSE (chemical contrast) image of the particles that are labelled in the left picture. Average atomic numbers are obtained using Castaing electron microprobe analysis.

Additional SEM observations in BSE mode seem to indicate the existence of a noticeable variety of these particles in Ti/Nb weight ratio. It even seems that they might exhibit an internal gradient in Ti/Nb weight ratio as shown in Figure 34. This observation was confirmed by EDX analysis. Moreover, as the Ti/Nb weight ratio increases, the N/C weight ratio also

CHAPTER 2 – MATERIALS

increases (Figure 35). This observation is of course only qualitative, as 15kV is not the most suitable high voltage to measure C or N contents. Notice that preliminary observations using a lower voltage (5kV) with a longer acquisition time have been realized to ensure that the N/C weight ratio decreases as the particle appears brighter (these observation parameters being judged more suitable for the analysis of light chemical elements). In both observation conditions, the carbon contamination effect on EDX spectra has been removed using a reference spectrum obtained from the steel matrix.

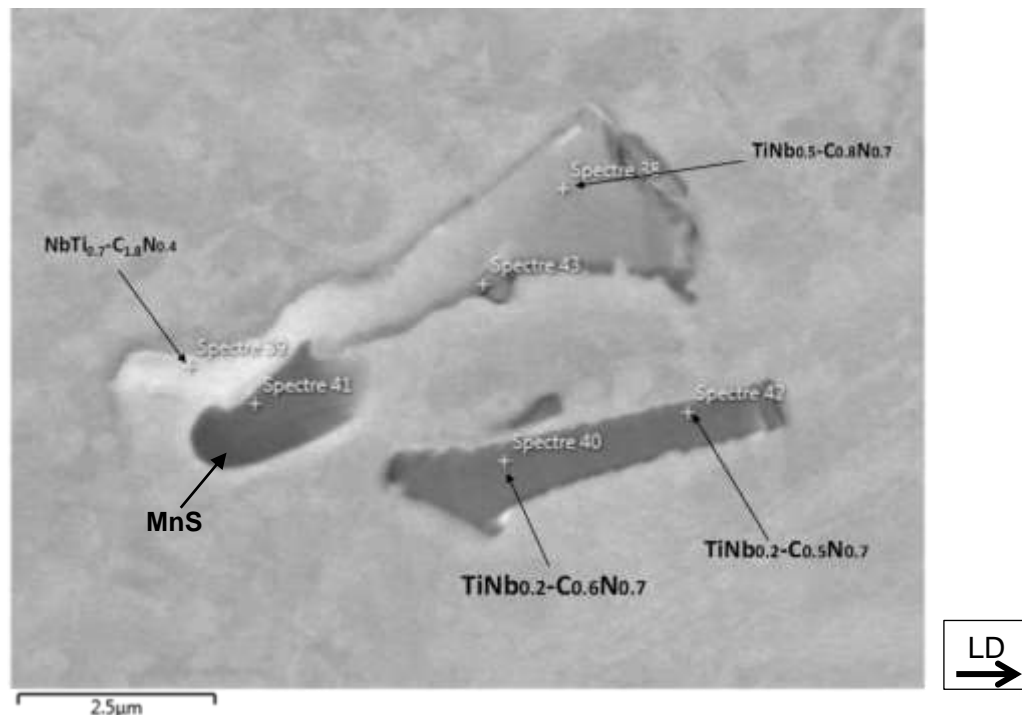


Figure 34: As-forged reference steel, x10000, SEM, BSE. Chemical formulas are normalised to one atom of the main metallic element. They have been calculated using results of EDX analyses at 15kV.

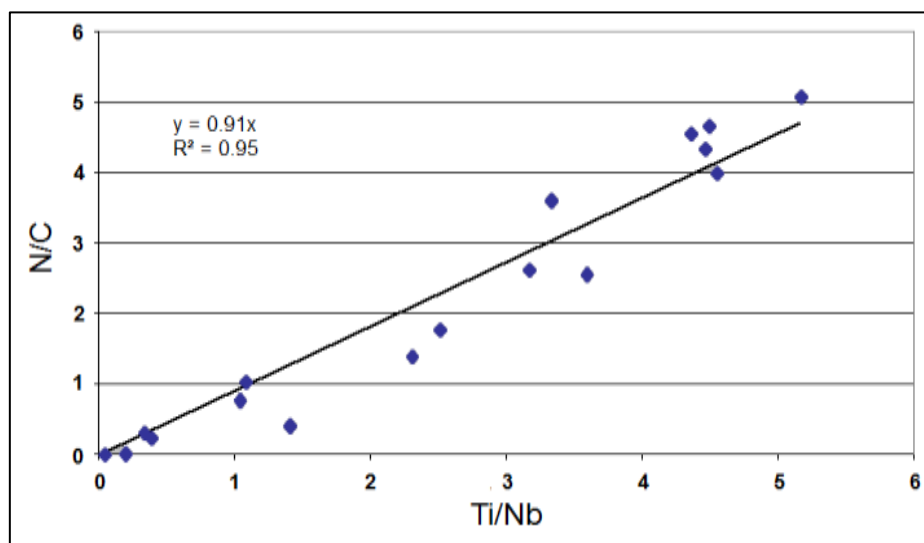


Figure 35: Evolution of the nitrogen to carbon weight ratio according to the titanium to niobium weight ratio. Ratios have been calculated from EDX analyses at 15kV.

This last result tends to confirm the work of Yuan and Liang [101], that niobium carbide does not precipitate on titanium nitride, but form a mixed compound (solid solution) at high temperature, during solidification. These particles can thus be differentiated from small secondary carbo-nitrides (<200 nm) that are expected to precipitate at lower temperature in

austenite. The chemical composition of these coarser particles might change according to their temperature of formation. They might be less and less rich in titanium and nitrogen as the temperature decreases continuously during solidification, which might explain the chemical gradient observed for such particles.

2.1.3 Determination of the non-recrystallization temperature

The non-recrystallization temperature (T_{nr}) is a key parameter for proper setting of rolling and forging thermo-mechanical processes, especially when grain size reduction or dislocation hardening is targeted. The T_{nr} value is classically determined using a hot torsion bench by the so-called “Jonas test”. This test is based on the evolution of the stress needed to prescribe a given value of strain at different temperatures, measured repeatedly during cooling from high temperature.

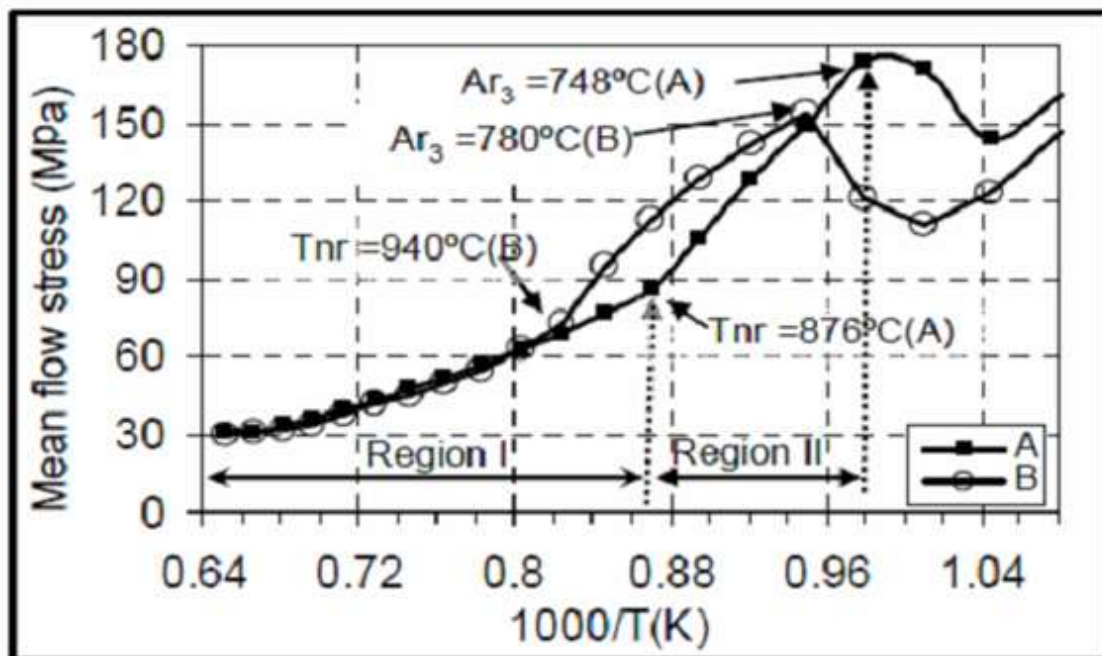


Figure 36: Typical mean flow stress vs. temperature curve found for C-Mn steels after Jonas-type experiments. After [152].

In Figure 36, at high temperature (region I), the stress needed to deform the specimen smoothly increases as the temperature decreases. Once T_{nr} is reached (region II), this stress increases much faster as the specimen becomes stronger. In this range of temperature, a noticeable increase in dislocation density happens in the material after each deformation stage, as recrystallization phenomena do not occur any longer. The boundary between region I and region II is considered to be the T_{nr} . Then, as the temperature continues decreasing, the material softens following the austenite decomposition (into ferrite in this example).

To determine T_{nr} for the chemical composition under interest, the following thermo-mechanical cycle has been realized on three hot torsion specimens cut from the as-rolled reference steel:

- Heating from 20°C to 1200°C at 10°C/s
- Soaking at 1200°C for 5min
- Cooling from 1200°C to 800°C at 1°C/s
- Final still air-cooling from 800°C down to room temperature

During cooling, a single hit is realized every 15°C ($\dot{\epsilon}=3.6s^{-1}$ and $\epsilon=0.26$) from 1100°C to 800°C.

CHAPTER 2 – MATERIALS

Measurement uncertainties are estimated around 15°C ($\pm 7.5^\circ\text{C}$), which corresponds to the temperature gap between two hits. Figure 37 shows the evolution of the maximum reached torque (believed to be proportional to the mean flow stress) according to the hit temperature, obtained during the second test. The change in slope is easily observable. The value of T_{nr} is determined at the intersection of the linear regression of the two slopes. T_{nr} temperatures that have been found to be 917°C, 931°C and 931°C for the three tested specimen, which gives an average of 926°C.

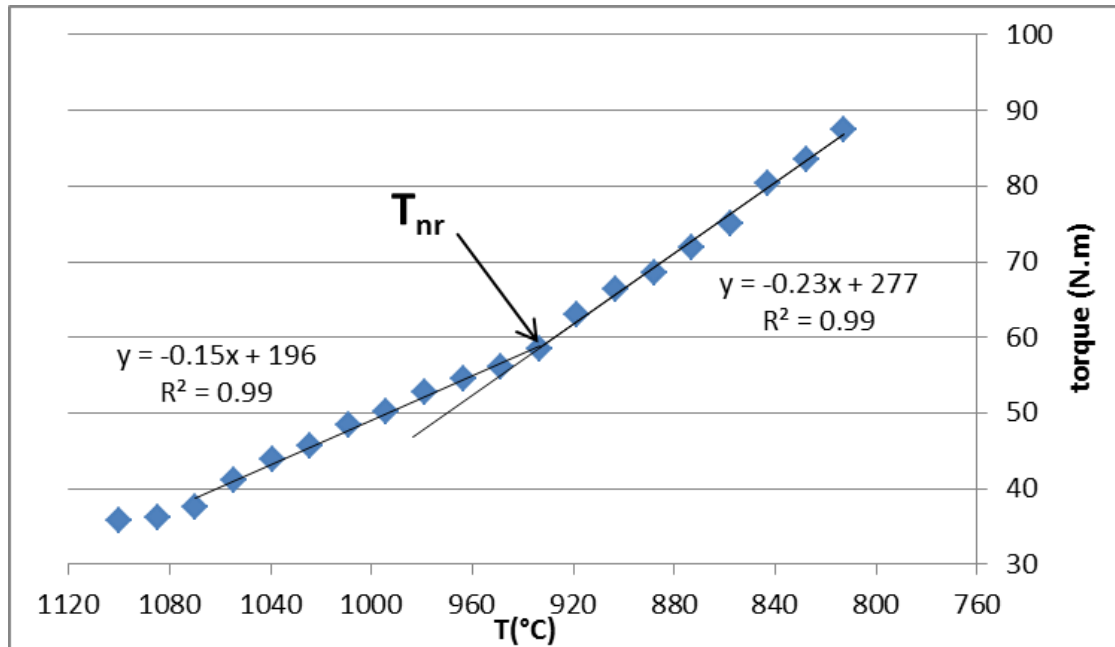


Figure 37: Evolution of the maximum reached torque according to the hit temperature.

2.2 Laboratory heats

The main part of this project has focused on laboratory heats of various chemical compositions. The objective was to produce a comprehensive panel of air-cooled microstructures, presenting enough variations on several microstructural parameters to be able to assess the effects of these parameters on the mechanical properties while keeping realistic thermo-mechanical processing conditions with respect to the targeted application. These variations have been centred on the microstructural parameters of the reference as-forged steel to stay relevant in regard to the final aim of this project, i.e., rationalization of the steel grade development. Thermo-mechanical process is an efficient lever to improve mechanical properties by affecting microstructure. However, this lever is partly used by the customers in the present case. So, it has not been considered as a free variable for this PhD project. The only lever that has been thus used was the chemical composition of the steel.

2.2.1 Design of chemical compositions

Table 5 shows the different laboratory heats (30kg each) that have been designed for this PhD project. They have been cast by batch of two chemistries and forged in two different campaigns. Each laboratory heat exhibits a variation of one or two alloying elements according to a reference laboratory heat, which is called “base” in the following. With the exception of Ni content (-100%), the base chemistry has the same chemical composition as the reference steel described in the previous section. After casting, actual chemistries of laboratory heats have been found by chemical analysis in good agreement with the expected ones.

CHAPTER 2 – MATERIALS

tag	chemical variation according to base	casting + forging
0Ti	-100% Ti	campaign 1
base	reference	
0Nb	-100% Nb	
+Ni	+50% Ni*	
-Si	-25% Si	
-Si+Mn	-25% Si +12% Mn	campaign 2
0Mo	-100% Mo	
+Mn	+12% Mn	
-Cr	-26% Cr	
+Cr	+28% Cr	

Table 5: List of laboratory heats designed for this PhD project. Colours indicate the pair of laboratory heats cast in the same batch. Chemical variations are relative to the base composition.*half way between base and reference reference steel.

According to literature data reported in the previous chapter, these laboratory heats aim at:

- Optimizing boron protection with playing on Nb, Mo and Ti contents. Each of these last alloying elements is added to prevent precipitation of iron boron carbides or boron nitrides in austenite that would suppress the strong influence of boron on diffusive phase transformations. The main objective of boron addition is to avoid austenite decomposition into ferrite, leading to a very wide bainitic domain on CCT diagrams. However, we do not know whether all of these micro-alloying elements are actually necessary in such a complex chemical composition. This is particularly true for Nb and Mo, as both might compete/interact concerning carbide precipitation.
- Assessing the effects of Mn and Si contents on the amount of retained austenite after forging and subsequent cooling. Both tend to stabilize austenite using different mechanisms (Mn by solute drag and solute drag-like effects, Si by increasing the average carbon content in austenite as cementite precipitation is delayed). Moreover, it seems that Si might have an influence of the Mn segregation at transformation interfaces, improving its effectiveness to delay/slow down austenite decomposition.
- Controlling microstructure, especially residual MA constituent and martensite contents by playing with Cr and Ni contents. The literature review does not allow determining very specific and reproducible effects of these two alloying elements, with the exception that they both increase significantly the steel hardenability.
- Assessing links between chemical composition, microstructure and mechanical properties.

Laboratory heats have not been used in the as-cast state. Two different parts were forged from each lab heat, one with a 74x74mm² section, the other with a 35x35mm² section that work as envelope values for the targeted application. Notice that the 74x74mm² area (5476mm²) is very close to the area of the section investigated in the as-forged reference steel (5440mm²). This choice is expected to allow us to assess the effect of the two extreme cooling kinetics, so the two extreme microstructures and resulting mechanical properties for each chemistry.

The following **nomenclature** is to be used all along this manuscript. Each chemical composition is named following its attributed tag in Table 5. Numbers 35 and 74 can be added in the following of the tag to indicate the dimensions of the forged part combined with the chemical composition. 0Nb 74 thus indicates the forged part of 74x74mm² in section realized from (-100% Nb) chemical composition.

CHAPTER 2 – MATERIALS

2.2.2 As-received state and pre-forging operations

After the removal of the dead head of the heat, the ingot was cut at 140mm from the bottom resulting into two parts, one of 125x125x140mm³ and the other from 125x125xLmm³ (L depending of the length of the removed dead end). The shortest part exhibits a massive central shrinkage at its surface just behind the dead head (30-40mm). A track of this central shrinkage can be seen even in the longest part (which means that the central shrinkage goes at least 80mm deep into the lab heat, without even considering the dead head). Photographs of this central shrinkage are shown in Figure 38 (a) and (b).

Ultrasonic non-destructive evaluation has been performed after cutting on one laboratory heat (-Si) that has the lowest density (so the greatest expected amount of porosity) to evaluate the internal quality of the heats. The ultrasonic image of this laboratory heat is given in Figure 38(c). The width of the central shrinkage decreases from 30-40mm to 25-15mm over the first 25mm in depth into the laboratory heat and then, remains constant over 30mm (55mm of total depth). Afterward, the central shrinkage goes 10 to 30 mm deeper, but its width there is lower than 10mm.

2.3 Forging

The shortest parts (125x125xLmm³) have been forged into a square section of 35x35mm² in order to close at maximum the central shrinkage and especially, the micro-porosities. However, oxide will still be present in the central region of the forged part as shown later in this manuscript. The longest parts that were believed to exhibit less porosity have been forged into square sections of 74x74mm². A schematic drawing of the shape evolution of the laboratory heat due to forging is shown in Figure 39.

The forging procedure is as follows: heating at 1190±10°C for 80min, then forging between 1190°C and 950°C (>T_{nr}~926°C) and finally still air-cooling on sand. One or two reintroductions into the furnace for 20min can be necessary to realize the forging of the shortest square section to ensure the requested forging temperatures. The minimum soaking time to guarantee the homogeneity in temperature across the entire part has been calculated using Forge®. According to these calculations, a re-heating of 20min is enough to get from 900°C to 1190°C in the bulk of the material.

Parts that have been forged in one time to their final geometry (74x74mm²) are expected to exhibit a homogeneous distribution of primary austenite grain size within the entire volume whereas parts that were forged in two steps, one end and then, the other end (as for 35x35mm²), might not. The end forged first could exhibit significant grain growth due to the last reheating stage without subsequent forging. This phenomenon has been taken into account in this study.

2.3.1 On-field measurements

On-field measurements have been taken during the second forging campaign in order to improve the knowledge of the thermo-mechanical history of the forged parts, especially, the forging temperatures and the cooling rate during the bainitic transformation. These data are thought to be useful in the understanding of the obtained microstructure.

2.3.1.a Preparation

The emissivity calibration of the measurement equipment (hand pyrometer and infrared (IR) camera) had been previously realized on a part of as-rolled reference steel instrumented with 2 thermocouples. The calibration operates during air cooling after a simple austenitisation (900°C during 2h). The part was put on two wedges of refractory material, with limited contact between the part and the wedge, in order to ensure as homogeneous air cooling as possible.

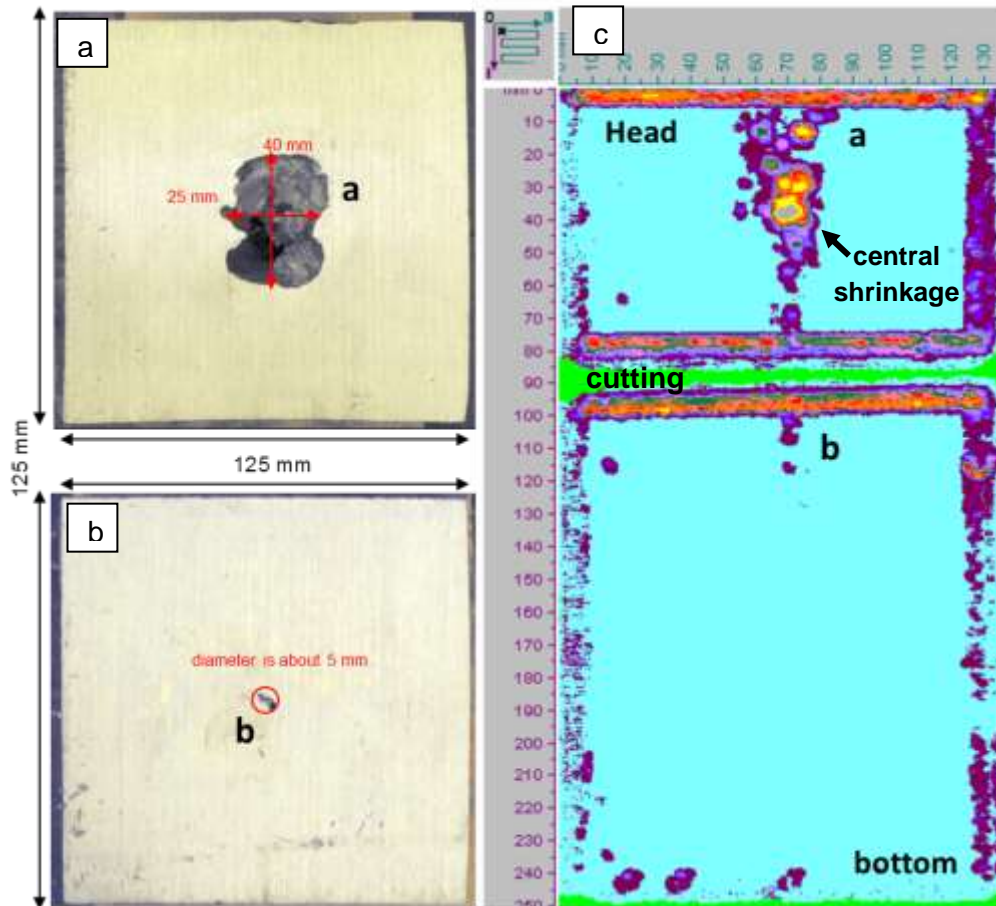


Figure 38: Top views of the central shrinkage (a) just behind the removed dead head and (b) 8mm deep into the -Si laboratory heat. (c) Ultrasonic image of -Si laboratory heat.

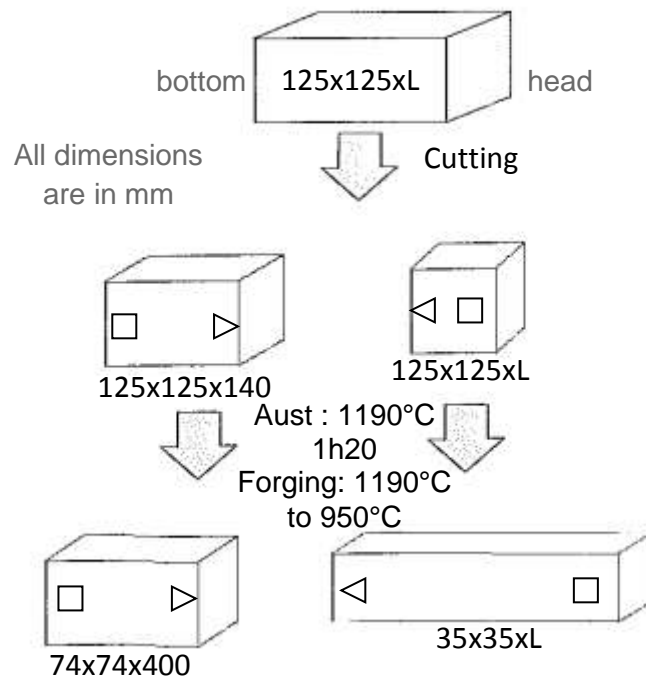


Figure 39: Typical schematic representation of the shape evolution from the laboratory heat to the forged part. Labels that correspond to reference of the cast, the bottom (or the region near the dead head) and the middle of the lab heat have been realized on every part. "L" means a variable length (not the same for the three steps).

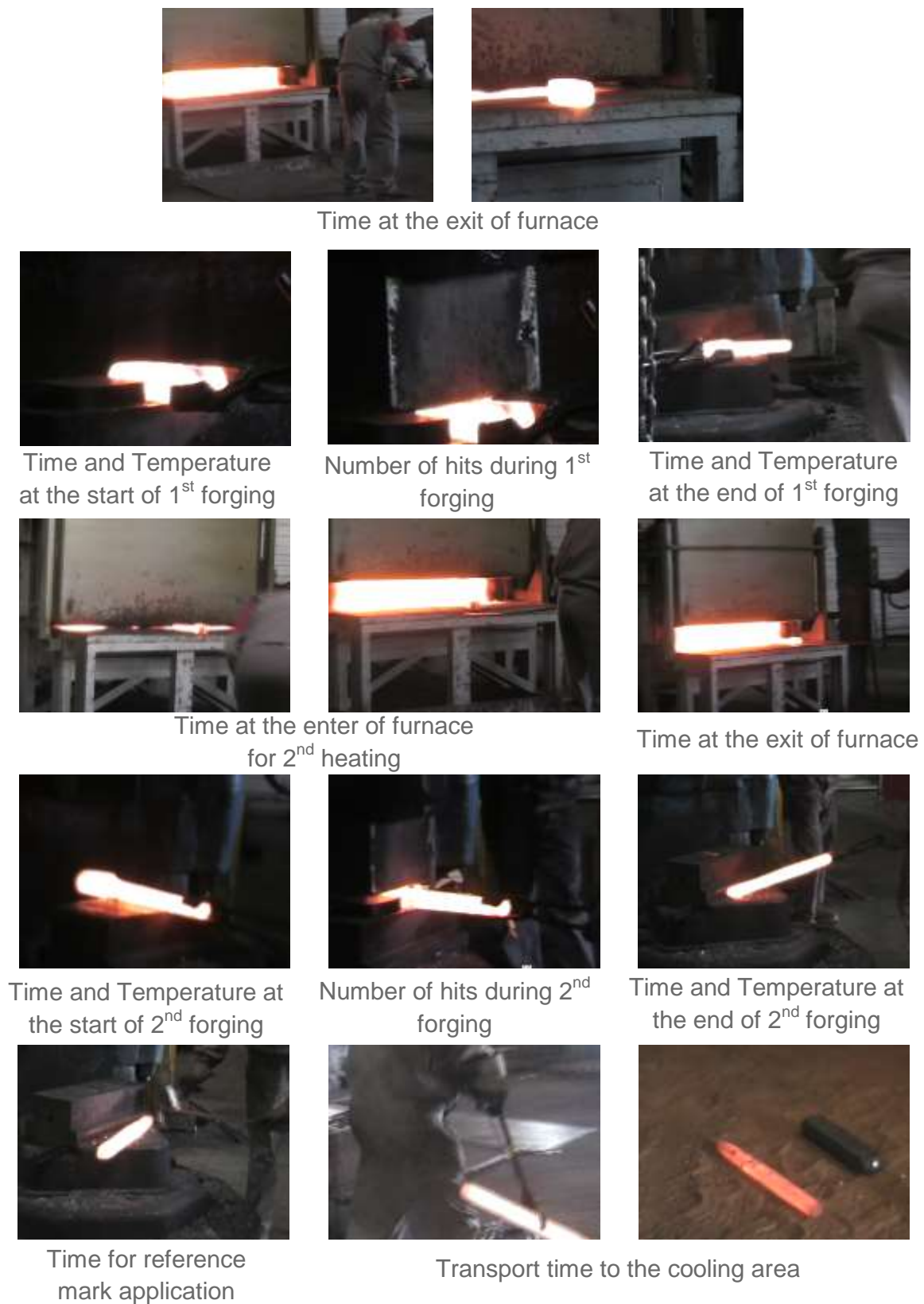


Figure 40: Screenshots from the video taken during the forging. Recorded data is noticed under every screenshot (or pair of screenshots).

CHAPTER 2 – MATERIALS

2.3.1.b On-field Measurements

A video recording has been realized all among the forging procedure and has been used as time reference for thermal measurements made by hand pyrometer during forging. In addition, the video allows noticing the number of hits and the time spent under the forging tool. Figure 40 shows an example of all data that have been collected per forged part.

From on-field observations, 35x35mm² forged parts necessitate two final forging steps, and thus one reheating step between the two steps, whereas 74x74mm² bars only require one final forging. A previous forging operation has probably been realized on the ingots that we had sent to the forging plant, as we noticed an obvious change of dimension from 125x125xLmm³ to 90x90x270mm³ and to 125x125x50mm³ to 60x60x200mm³ before final forging

The IR camera was placed on the cooling area which was a sand box. As forged parts were realized, they were put directly on the sand, with some spacing between them (Figure 41a). The IR camera allowed monitoring the surface temperature during cooling of the two –Cr forged parts at the same time, on two side faces per part. Figure 41a shows the IR camera location with respect to the forged parts. Figure 41b shows a screenshot of the recorded video. The crosses that can be seen on the forged parts are the points chosen for plotting of the evolution of temperature with cooling time (9 points per forged part).

2.3.1.c Results

Forging has occurred between 1000°C and 900°C. If all 74x74mm² forged parts of this campaign (0Mo 74, +Mn 74, -Cr74, +Cr 74) were finish forged slightly over the T_{nr} measured on the reference steel (around 926°C), it was not the case for two 35x35mm² forged parts (893°C and 906°C for 0Mo 35 and –Cr 35 respectively). Notice that these temperatures are surface temperatures. Bulk temperature at the end of forging might be higher and has been estimated in the next part (2.3.2) using numerical simulation, to ensure that this temperature was actually higher than the T_{nr} . Nevertheless, this feature would only concern a limited region of the forged part, as shown in Figure 40.

According to data collected with the hand-pyrometer and the video, the average cooling rate between the exit of the furnace and the cooling area was around 1.6°C/s and 3.5°C/s for 74x74mm² and 35x35mm² forged parts respectively.

The evolution of the surface temperature vs. time spent in the cooling area for –Cr 35 and –Cr 74 combinations is shown in Figure 41c. No great discrepancies are observable between the nine monitoring points on each forged part below 800°C. Cooling rates seem relatively constant from 800°C down to 550°C and from 500°C down to 300°C (which is the calibration limit of the IR camera). From this figure, the bainitic transformation starts around 550°C for the 74x74mm² forged part and between 500 and 520°C for the 35x35mm² forged part. As soon as the transformation occurs, the cooling rate decreases due to the latent heat released by the phase transformation.

Table 6 reports the cooling rates between 800 and 550°C and between 500 and 300°C respectively, measured on each monitoring point of –Cr 35 and –Cr 74 parts (Figure 41b). Before the bainitic transformation, the cooling rate is close to 0.75°C/s (0.65-0.88°C/s) and 0.37°C/s (0.33-0.38°C/s) for the 35x35mm² and 74x74mm² forged parts, respectively. It is divided approximately by four once the bainitic transformation has started, giving 0.18°C/s (0.16-0.20°C/s) and 0.09°C/s (variations below 0.005°C/s) for the 35x35mm² and 74x74mm² forged parts, respectively.

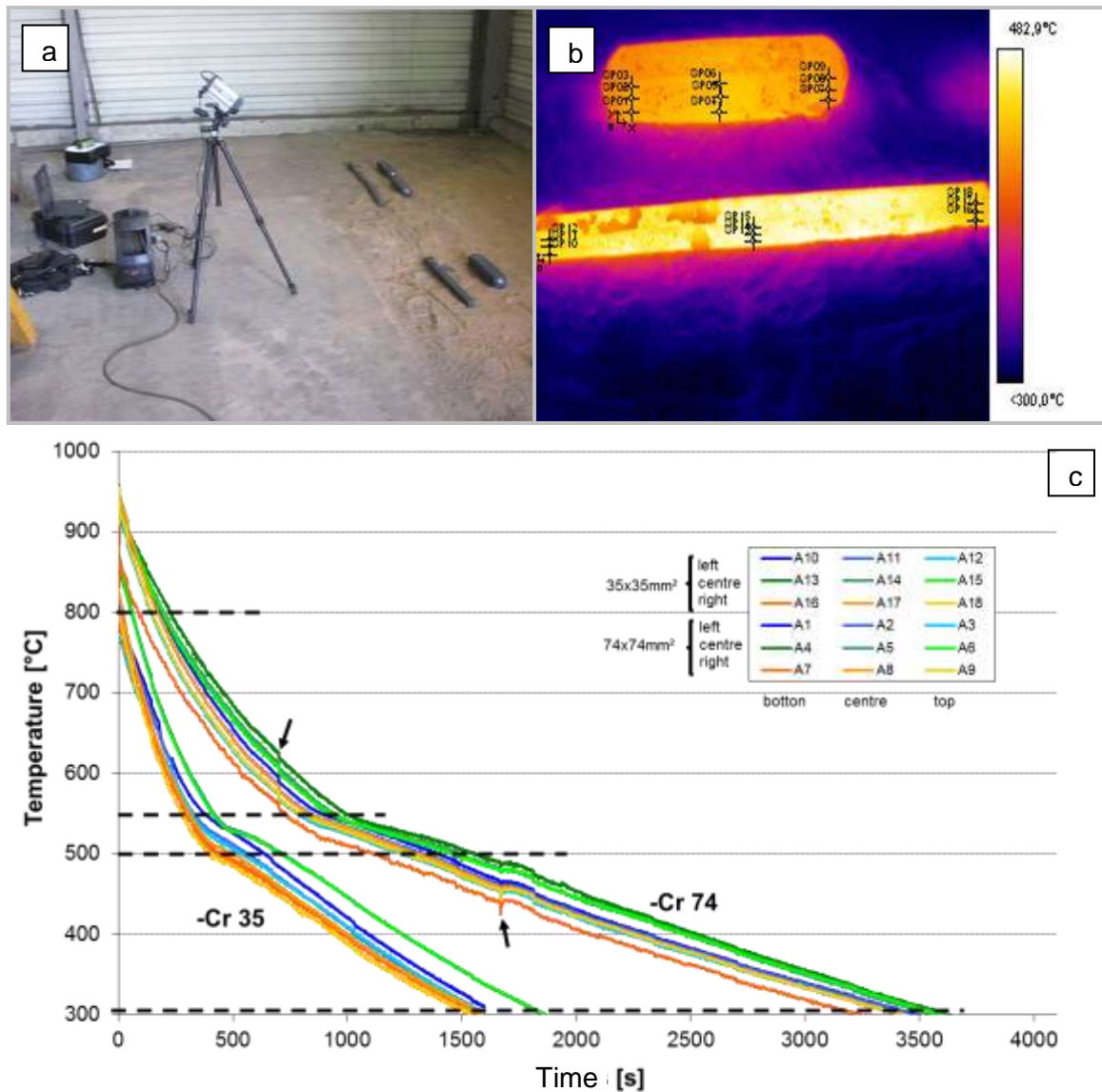


Figure 41: (a) IR camera placement, (b) IR camera view, (c) plot from measurements of the IR camera. Black arrows pointed out measurement artefacts.

As a consequence, the 74x74mm² forged part cools down twice slower in average than does the 35x35mm² forged part, regardless temperature. The ratio between surface area available for heat exchange and the volume of the forged part is 0.06m⁻¹ and 0.12m⁻¹ for 74x74mm² and 35x35mm² forged parts respectively, which can explain the two-fold ratio between average cooling rates if driven by surface thermal exchanges.

At temperatures higher than 550°C, the part of the surface near the floor always cooled down slower than the rest of the surface. After reaching 500°C, the cooling rate is homogeneous along the height of the vertical face of the parts. Both edges of the forged parts have a tendency to cool down initially faster than the mid-length of the part. Once again, below 500°C, cooling is homogeneous along the forging direction at the surface (and thus over the entire surface).

35x35mm				
cooling rate 800-550°C				
location	left	centre	right	average
top	0.68	0.71	0.88	0.76
centre	0.79	0.70	0.87	0.79
bottom	0.65	0.70	0.80	0.72
average	0.71	0.70	0.85	0.75
cooling rate 500-300°C				
location	left	centre	right	average
top	0.16	0.17	0.18	0.17
centre	0.19	0.17	0.18	0.18
bottom	0.20	0.17	0.18	0.18
average	0.18	0.17	0.18	0.18

74x74mm				
cooling rate 800-550°C				
location	left	centre	right	average
top	0.39	0.34	0.38	0.37
centre	0.38	0.34	0.38	0.37
bottom	0.36	0.33	0.39	0.36
average	0.38	0.34	0.38	0.37
cooling rate 500-300°C				
location	left	centre	right	average
top	0.09	0.09	0.09	0.09
centre	0.09	0.09	0.09	0.09
bottom	0.09	0.09	0.09	0.09
average	0.09	0.09	0.09	0.09

Table 6: Cooling rates between 800 and 550°C and between 500 and 300°C respectively, measured on –Cr 35 and –Cr 74.

2.3.2 In bulk temperature calculation

Calculations of the temperature evolution in the bulk of the forged parts during cooling have been realized using the Forge© software in Gandrange R&D centre by the numerical simulation service. This calculation has been realized to ensure, in a simple manner, that there is no significant cooling rate gradient from skin to the bulk, which could potentially lead to noticeable heterogeneities in the final microstructure. Parameters and boundary conditions used for these calculations are shown in Figure 43. No phase transformation or forging-induced heat variation have been taken into account in the calculation due to the absence of suitable database on phase transformation for this grade (full TTT diagram) and on the forging tools.

As shown in Figure 42, the simulation results were first compared to the experiment in order to attest their validity. Table 7 exhibits the surface cooling rate found by calculation and measurements at the centre of a side surface, for both forged part geometries. Due to a limitation of the calculation to the first 2000s, the cooling rate is only evaluated from 500-400°C for the second part of the cooling. The maximum difference is 0.06°C/s in the case of 35x35mm² forged part in the 800°C-550°C temperature range, which is considered as acceptable. Of course, due to the noticeable heat release by the bainitic transformation between 550°C and 500°C, the experimental and the calculated cooling rate exhibit high difference in cooling rate in this temperature range.

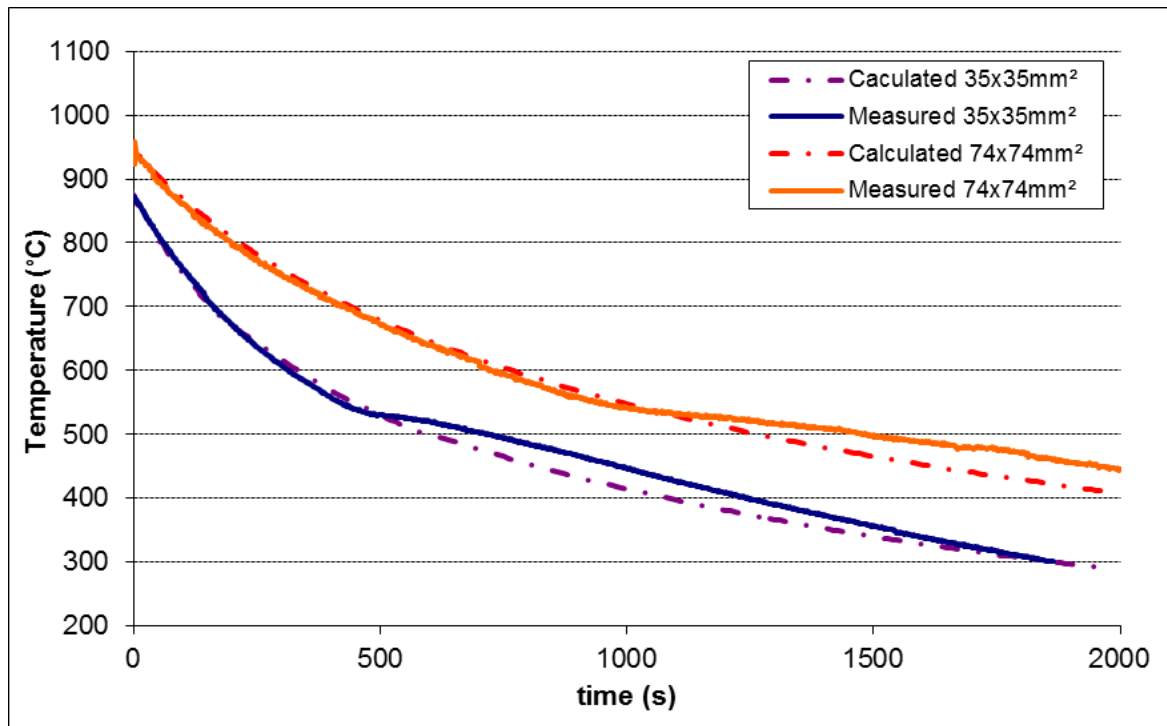


Figure 42: Surface temperature evolution according to the time found by calculation and measurements at the centre of a lateral surface for both forged part geometries.

surface	T range (°C)	Calculated cooling rate (°C/s)	Measured cooling rate (°C/s)
35x35mm ²	800-550°C	0.64	0.70
	500-400°C	0.21	0.19
74x74mm ²	800-550°C	0.32	0.34
	500-400°C	0.13	0.10

Table 7: Difference between calculated and measured surface cooling rates at the centre of a side surface for both forged part geometries.

So, the in bulk-temperature evolution obtained by calculation could be estimated with good confidence. Table 8 shows the average cooling rates calculated for the volume centre of the forged part, of its projection on one of the lateral surface, and of a point at the far extremity of the forged part (one corner), for all geometries of forged parts and temperature ranges. These three points are indicated in red in the two forged parts schematic shown in Table 8.

calculated cooling rate 35x35mm ² (°C/s)			
T range (°C)	extremity	volume centre	surface centre
800-550°C	0.73	0.64	0.64
500-400°C	0.21	0.21	0.21

calculated cooling rate 74x74mm ² (°C/s)			
T range (°C)	extremity	volume centre	surface centre
800-550°C	0.38	0.32	0.32
500-400°C	0.13	0.13	0.13

Table 8: Difference between calculated cooling rate of the centre, of its projection on a lateral surface, and of a corner of the forged parts.

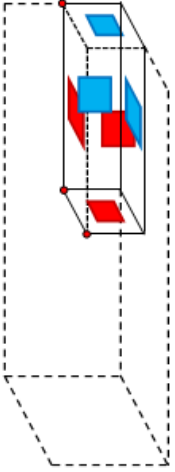
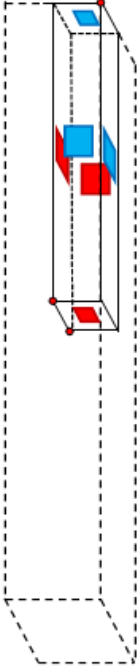
Bar	74×74×400	35×35×600
Boundary conditions	 <ul style="list-style-type: none"> Considered points for cooling rate calculation Thermal extraction through natural convection and radiation Symmetry, thermal diffusion in the bulk 	 <ul style="list-style-type: none"> Considered points for cooling rate calculation Thermal extraction through natural convection and radiation Symmetry, thermal diffusion in the bulk
Mesh size	6x6x6mm ³	3x3x3mm ³
Boundary condition : Convection	h coefficient set from measurements of IR camera : $h = 1,5 \text{ W.m}^{-2}.\text{K}^{-1}$ → This parameter has been set constant during the cooling	
Boundary condition : Radiation	Emissivity ϵ obtained from specific experimental tests : $\epsilon = 0,85$ → This parameter has been set constant during the cooling	
Materials Data (from data base)	Thermal conductivity $\lambda = 35,5 \text{ W.m}^{-1}.\text{K}^{-1}$ Density $\rho = 7850 \text{ kg.m}^{-3}$ Specific heat capacity $cp = 778 \text{ J.kg}^{-1}.\text{K}^{-1}$ → These parameters have been set constant during the cooling	

Figure 43: Parameters used for temperature evolution in the bulk of both forged parts.

CHAPTER 2 – MATERIALS

There is no noticeable gradient in cooling rate across the section of the material, as no difference in cooling rate has been found between the centre of the volume and its projection on the lateral surface for both temperature range and materials. Even between the volume centre and the extreme corner of the materials, the cooling rate gradient does not reach 0.1°C/s in the 750°C - 550°C temperature range. Once the bainite transformation has occurred, the cooling rate seems homogeneous through the entire volume.

The maximum difference in temperature that occurs between these two points (the volume center and a corner) is 70°C and 140°C for $35\times 35\text{mm}^2$ and $74\times 74\text{mm}^2$ forged parts respectively, and is reached before 800°C . These temperature gradients decrease slowly during the rest of the cooling, being lower than 23°C and 35°C at 400°C for $35\times 35\text{mm}^2$ and $74\times 74\text{mm}^2$ forged parts, respectively.

At 900°C , the difference in temperature between the volume centre and its projection is around 20°C for the $35\times 35\text{mm}^2$ forged part, which gives some margin in concern of the two $35\times 35\text{mm}^2$ forged parts that exhibits a surface temperature at the end of forging around 900°C (lower than the $T_{nr}\sim 926^{\circ}\text{C}$). However, forging has not been taken into consideration in such calculation. So, there is no certitude that these two forged parts have not suffered some deformation slightly below the T_{nr} . It can also have been the case for some materials of the first series of forging. This risk is discussed later on in this chapter (section 2.5.2), before the description of set of experiments on these materials.

2.3.3 Setting of the cooling rates considered for the forged laboratory heats

The numerical calculation allows concluding that there is no significant cooling rate gradient across the section of the material in the considered range of temperature. Cooling rates that have been calculated from on-field measurements of surface temperature are thus representative of the entire volume. Cooling rates used in this manuscript are considered as equal to the average values over the nine monitoring points for both temperature ranges and materials. They are thus equal to:

- 0.8°C/s and 0.4°C/s before the onset of the bainitic transformation for $35\times 35\text{mm}^2$ and $74\times 74\text{mm}^2$ parts, respectively.
- 0.2°C/s and 0.1°C/s after the onset of the bainitic transformation for $35\times 35\text{mm}^2$ and $74\times 74\text{mm}^2$ parts, respectively.

2.4 Overview of available microstructures

An overview of the microstructure of all available materials (as-forged laboratory heats and both states of the reference steel) is given here to appreciate, at this point, the range of available microstructures for this study. This overview consists of:

- An identification of the main microstructural constituents;
- The measurement of the PAGS;
- A phase quantification using LM and Le Pera etching;
- XRD to evaluate the amount of retained austenite.

2.4.1 Identification of microstructural constituents from SEM observations

Most observations have been made using Nital2% or Picral4% etching after mirror polishing of the samples. They have been made on a sample dedicated for microstructural investigation, extracted from a region just between ($35\times 35\text{mm}^2$ forged parts) or close to

CHAPTER 2 – MATERIALS

(74x74mm² forged parts) the regions where tensile test and impact test specimens have been extracted from.

All investigated materials (including the reference steel) exhibit the same typical microstructural constituents. Figure 44 shows typical SEM pictures taken from base 35 and base 74. The two different magnifications allow appreciating the relatively coarse scale of the microstructure more easily. The matrix is mainly composed of coarse so-called degenerated upper bainite and of granular bainite according to the classification of Zajac et al [10] (or $B_2^{m,a}$ and $B_3^{m,a}$ according to the classification of Bramfitt and Speer [6]). This bainite is cementite-free, even if very isolated and cementite precipitation has been scarcely observed.

Martensite-austenite constituent is the main secondary constituent. It presents various shapes:

1. Coarse films (>200nm in width) were found between the bainitic ferrite laths of upper bainite. Some of these films are indicated with red arrows in Figure 44. Notice that these ones are often seen as islands, according to the packet orientation with respect to the observation plane. In this case, the spatial distribution of these islands still remains more or less ordered, which is a sign of a textured matrix morphology (i.e. lath-like structure).
2. Islands in granular bainite, between bainitic ferrite elements of sub-structure. Some of these islands are indicated with white arrows in Figure 44. These islands appear isolated in the bainitic ferrite, with no apparent ordered spatial distribution at all.
3. In blocks between bainitic packets. Some of these blocks are indicated with blue arrows in Figure 44.

The word “block” is used here when the MA island is large enough to exhibit another secondary microstructural constituent in its centre. The smallest blocks observed on the different microstructures have an area around 5µm² but a noticeable part of these blocks exceed 20µm² in area and some of them can be larger than 100µm².

There is a gradient in carbon concentration inside the block. The edges are much richer in carbon than the center. At higher temperature, these blocks were entirely composed of austenite, which was trapped between misoriented bainitic ferrite packets as the bainitic transformation went to an end (incomplete transformation phenomenon, see Chapter 1). According to the thickness of the block, cooling rate and temperature, austenite might transform into different products as the temperature continued to fall down. The central part could thus transform into martensite, auto-tempered martensite or lower bainite. These secondary microstructural constituents exhibit cementite precipitation that makes them easy to identify with SEM after etching. Between the centre and the border of the block, austenite decomposes into MA constituent (fine mixture of retained austenite and martensite). The borders of the block always stay untransformed. All these features can be well appreciated in Figure 45, which shows four examples of coarse blocks.

Thin austenite films can also be observed between bainitic ferrite sub-structures and laths. Together with the austenite trapped in MA constituent, there is still a noticeable amount of austenite in the microstructure but with noticeable variations in shape, chemical composition and (possibly) amount of residual stresses or strains (due to phase transformation of the neighbouring material into bainite or martensite).

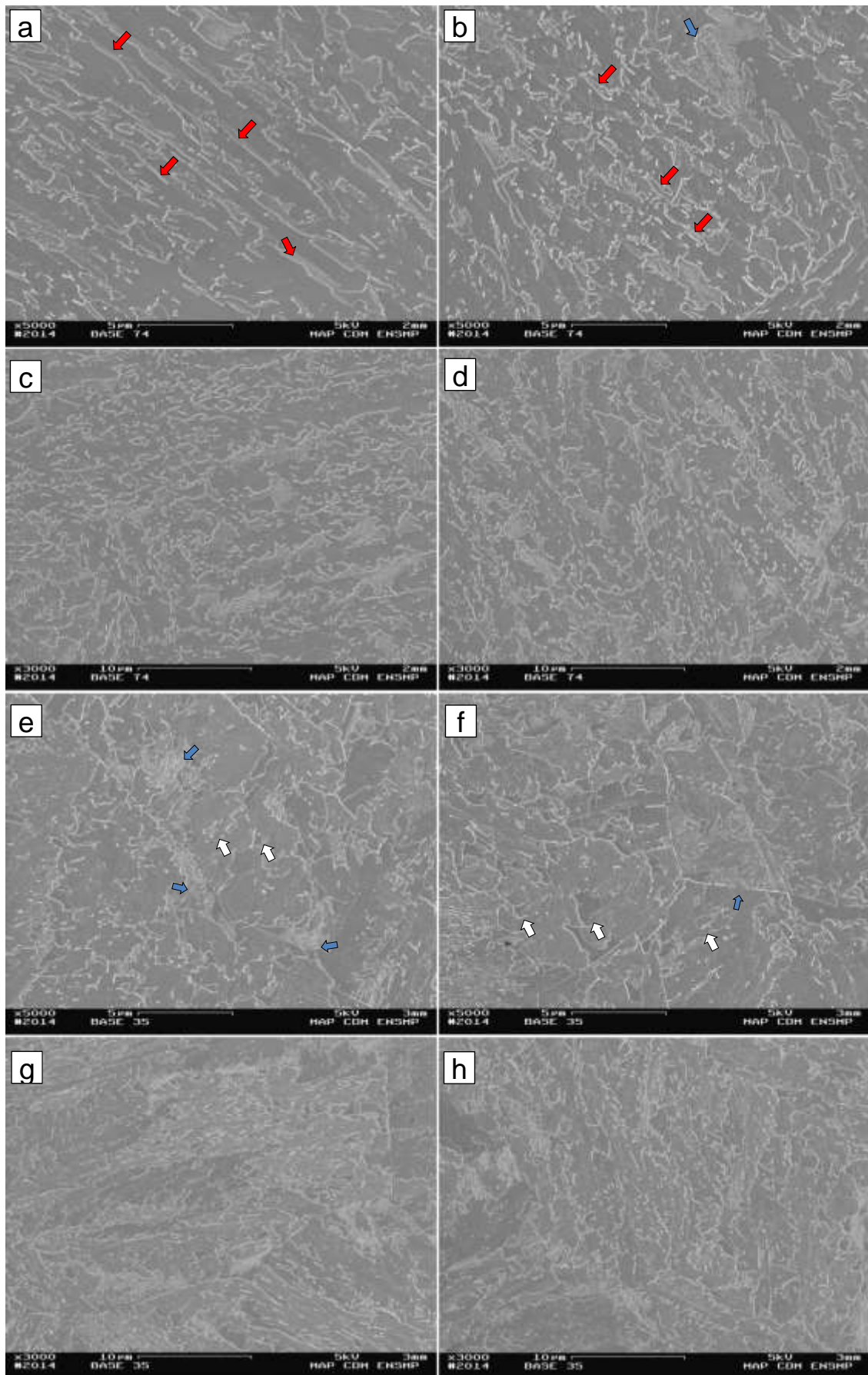


Figure 44: Examples of typical microstructure exhibiting its relatively coarse scale and the different shape of the secondary microstructural constituent. SEM, Nital 2%, SE in-lens, (a)->(d) base 74, (e)->(h) base 35. Red arrows: coarse films between the bainitic ferrite laths of upper bainite. White arrows: islands in granular bainite. Blue arrows: blocks between bainitic packets

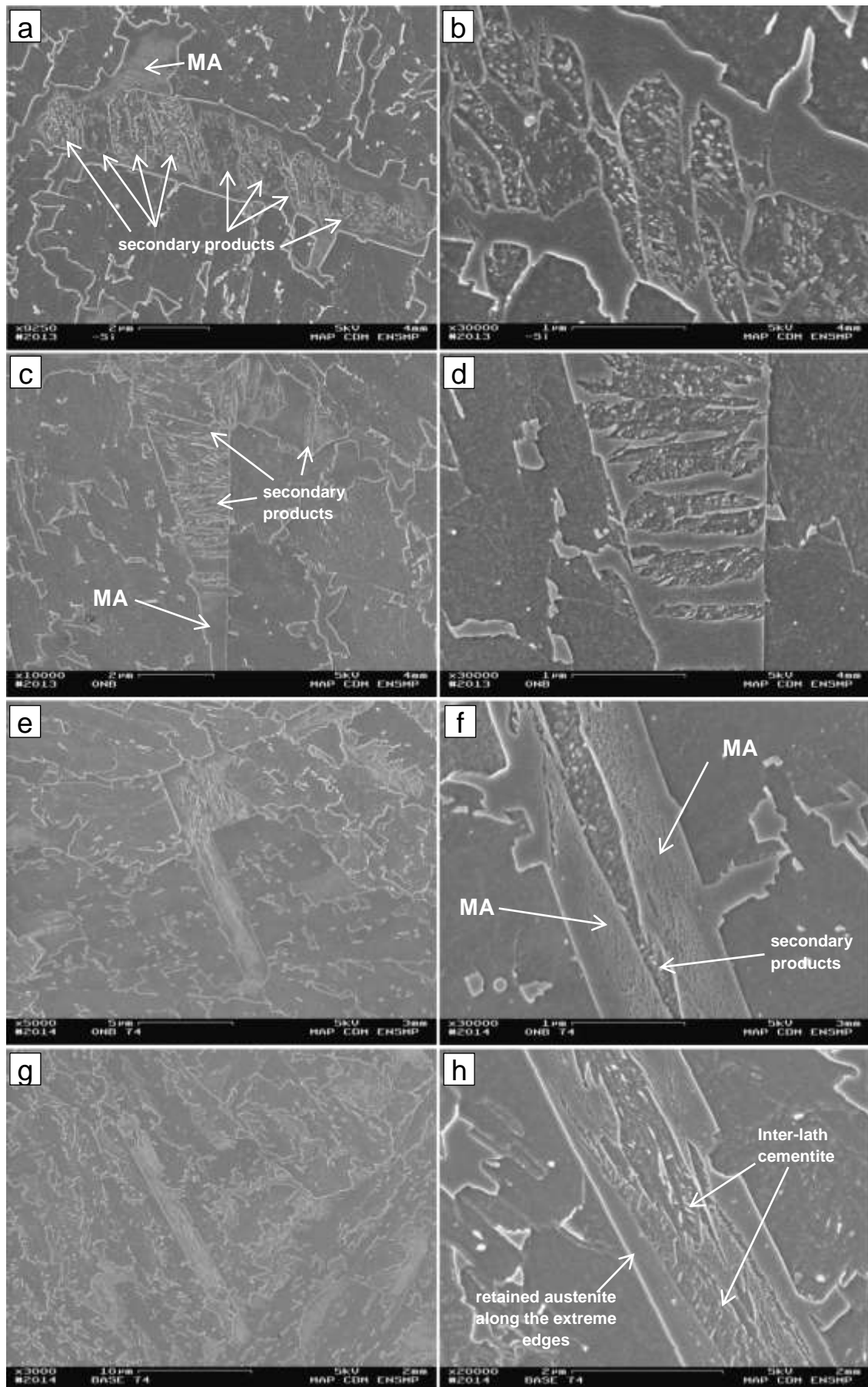


Figure 45: Blocks of secondary microstructural constituent. SEM, Nital 2%, SE in-lens, (a)(b) –Si 35, (c)(d) 0Nb 35, (e)(f) 0Nb 74 and (g)(h) base 74. Right pictures are closer views of the block of secondary phases in the middle of the left picture.

2.4.2 LM quantification of the primary austenite grain size

0Ti 35 presents regions (over about 1/3 of the surface area) with very large primary austenite grains ($>400\mu\text{m}$ versus $40\text{--}50\mu\text{m}$ for all other combinations). This is even observable in light macroscopy as shown in Figure 46a. The difference with other combinations is obvious (as for example, base 35 in Figure 46c). Such large austenite grains might come from abnormal growth of austenite grains during the soaking stage and, as 0Ti 74 does not exhibit such grains, more precisely during the last reheating stage of the forging. This side of 0Ti 35 might have been little (or even not) strained in the last forging operation. The apparent bainite packet size in regions of abnormal austenite growth is also much larger than in other regions. As shown in Figure 46b, the lath-like structure is more appreciable as bainitic ferrite laths are very elongated in these regions (large PAGS significantly decrease B_s , which may result in a less granular microstructure).

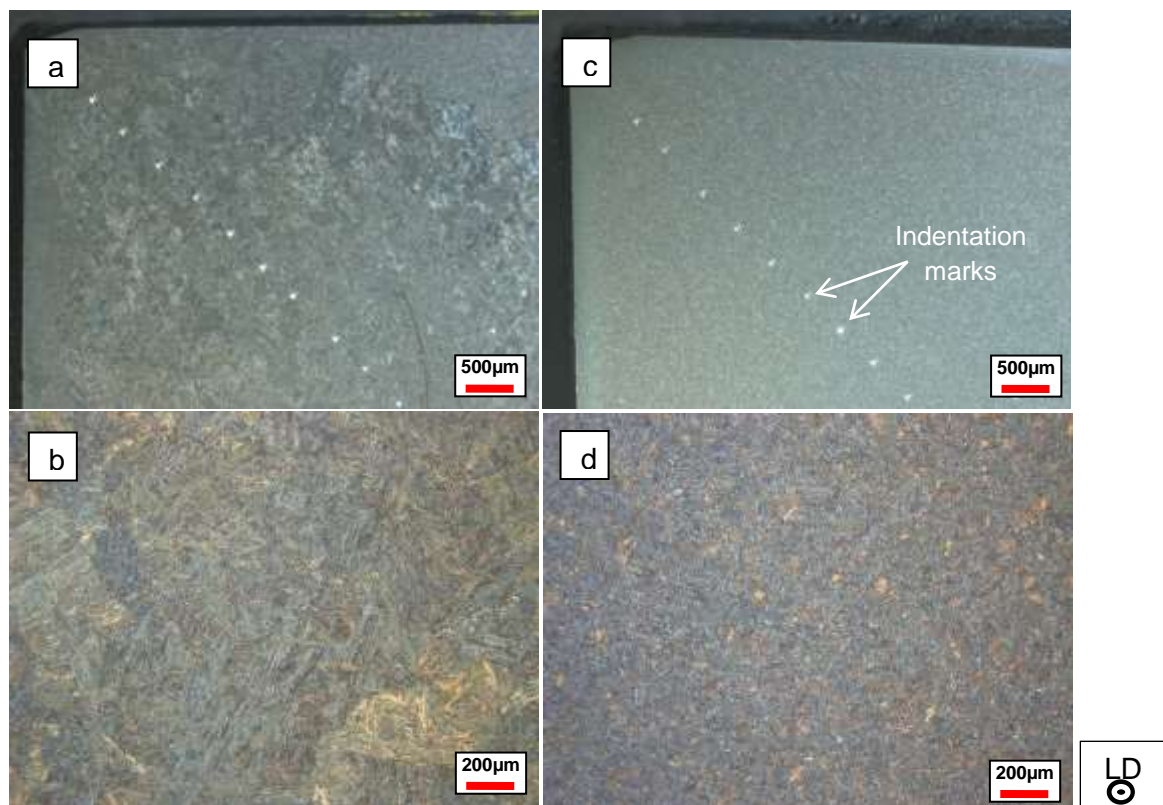


Figure 46: 0Ti 35, on corner of transverse section, Nital 4% (a) light macroscopy and (b) light microscopy. Base 35, transverse section, Nital 4% (c) light macroscopy and (d) light microscopy.

The primary austenite grain size was measured parallel to the fracture surface of impact specimens, more precisely, at few mm under their fracture surface. The bainitic packet size has been measured as reported later in chapter 4, from the same region. The method used to realize these measurements, based on Béchet & Beaujard etching and image analysis of LM pictures, is given in appendix A.III.1.

Table 7 shows the obtained results. After several trials, no proper contrast could be obtained on –Si 35 so no PAGS measurement has been realized on this combination. Some other combinations exhibited only few regions where primary austenite grain boundaries were sufficiently distinguishable from the rest of the microstructure, so the average equivalent diameter has only been calculated from a low amount of primary austenite grains. This pointed out that chemical etching is not necessarily the best suited method to measure PAGS as discussed in appendix A.III.1.

CHAPTER 2 – MATERIALS

tag	number of analysed grains	equivalent circle diameter (μm)			
		average	st. dev.	max	min
OTi 35	326	75*	42	230	19
OMo 74	53	53	25	108	14
as-forged	50	52	25	119	16
-Cr 74	60	51	20	107	13
-Cr 35	64	51	20	92	16
-Si 74	243	50	21	126	19
ONb 35	255	49	19	123	19
OTi 74	134	47	19	108	20
+Cr 74	70	47	22	114	12
+Ni 35	420	46	17	125	19
ONb 74	28	45	20	95	14
base 74	67	45	19	92	13
-Si+Mn 35	234	44	16	99	19
-Si+Mn 74	288	42	15	119	19
base 35	431	42	15	94	19
+Mn 74	119	39	18	92	13
+Ni 74	428	38	13	95	19
OMo 35	140	38	16	84	12
+Cr 35	135	38	16	84	13
+Mn 35	132	37	16	84	13
as-rolled	207	31	15	82	4

Table 9: Results of PAGS measurements by decreasing values of average PAGS. *bimodal distribution. "As-forged" and "as-rolled" are for the reference steel

For OTi 35, only the regions presenting no abnormal grain growth have been quantified. Despite this, OTi 35 still presents the highest average equivalent diameter, due to an inhomogeneous grain size distribution. Two peaks are present on its number distribution of equivalent diameter, the first one being centred on an equivalent diameter of $50\mu\text{m}$, and the second one on $120\mu\text{m}$. This bimodal distribution is shown in Figure 47. All other materials presented a number distribution of equivalent diameter with one peak, centred on the average equivalent diameter, highlighted by lower values of standard deviation.

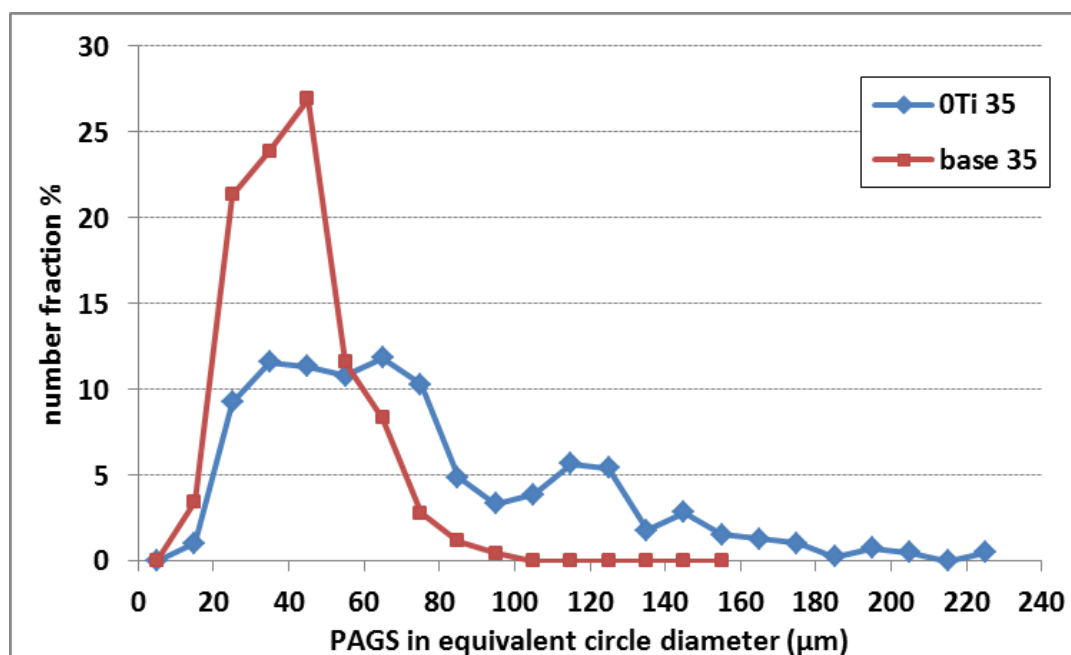


Figure 47: Examples of number distribution of PAGS in equivalent circle diameter.

CHAPTER 2 – MATERIALS

There are only few other noticeable differences in PAGS, as all other combinations exhibit a PAGS between 37 and 53 μm . Nevertheless, –Cr chemical composition tends to exhibit slightly larger grain size than other chemical compositions as both forged parts exhibit PAGS higher than 50 μm . All materials exhibit equiaxed grains. No indication of a possible deformation lower than the T_{nr} has been observed (even in the case of –Cr 35 and 0Mo 35 that were finish forged at lowest temperatures).

It is important to notice that both states of the reference steel stay in or near the range of PAGS exhibited by as-forged laboratory heats. As-rolled reference steel has the lowest measured PAGS. Difference with the as-forged reference steel may come from rolling temperature lower than the forging, forging of the reference part being realized at temperatures higher than 1100°C, and/or from austenite grain growth during the soaking step of the forging operation.

2.4.3 Quantification of microstructural constituent

The quantification methodology has been built on the reference steel grade. It has been first validated by comparing results from LM observations with those from two other quantification methods (electron backscatter diffraction (**EBSD**) and SEM imaging associated to manual counting). All these quantification methods are explained in detail in appendix A.I. The LM quantification has then been applied on every combination of chemical composition and thermo-mechanical treatment considered in the present study, as well on every CCT diagram samples.

Only the EBSD quantification can allow separating a part of the austenite from the rest. However, as shown in section A.I.2.b, the total austenite level is underestimated using EBSD. So whatever the method used, due to the very fine distribution of austenite, it is not possible to separate all phases to realize proper *phase* quantification. However, it is still possible to find a way to compare the different microstructures obtained in this study with a recurrent and known error. If we consider that pure austenite films do not exceed 650nm in width (which is highly probable as no austenite films exceeding 270nm have been detected during scanning transmission electron microscopy (**STEM**) observations), we have built a quantification of *microstructural constituents* as follows:

- The microstructural constituent named ferrite corresponds to allotriomorphic ferrite.
- The microstructural constituent named bainite corresponds to bainitic ferrite (granular, upper or lower bainite), including microstructural elements with a dimension lower than 650nm, i.e. all retained austenite films plus a certain amount of MA constituent, which is the recurrent error.
- The microstructural constituent named martensite corresponds to the isolated spans of secondary phases such as martensite, auto-tempered martensite and lower bainite (as they cannot be differentiated with this method) that are present in the middle of secondary blocks in mixed upper/granular bainite microstructures. It also refers to purely martensitic regions that can be encountered with high cooling rates (see CCT diagrams in Chapter 3).
- The microstructural constituent named MA excludes the purely austenitic films and corresponds to MA islands (very fine mixture of austenite and martensite). In other words, all microstructural constituents that are not bainite or martensite or ferrite.

Following these rules, all quantification methods have been compared in appendix A.I.4. Light microscopy with Le Pera etching seems to be the best suited method to realize this quantification, with respect to the addressed microstructural scale and to the number of microstructures that have to be investigated quantitatively. In the conditions used in this study, LM quantification ensures the highest statistical significance of results due to an area

CHAPTER 2 – MATERIALS

of quantification that is 21 times and 37 times larger than for the quantification methods using SEM imaging and EBSD, respectively. Moreover, numerical processing is fully automated and fast, and obtained results are reproducible (very low scatter is obtained between different images coming from a given sample). In counterpart, it is still necessary to use XRD to realize proper measurement of the total austenite content (see appendix A.II.2 for the complete methodology). Moreover, LM quantification over-evaluates the amount of bainite in the microstructure due to its spatial resolution limit, which is 9 times greater than the one of EBSD and **FEG-SEM** (scanning electron microscopy with field electron gun) quantifications for the experimental conditions used in this study.

Light optical micrographs used for this quantification have been taken in the same region as for SEM observation (extracted from a region just between, or close to the regions where the mechanical test specimens have been extracted from). As for bainite packet size determination, XRD measurements were directly realized on impact toughness specimens, in a plane parallel to the fracture surface analysed in chapter 4, using θ -2 θ X-ray diffraction, with a Co source, an analysed area of 20 mm² and 1s per 0.032° of acquisition step (see appendix A.II.2 for the complete methodology).

Table 10 shows the results of this quantification for every material available for mechanical characterization. The amounts of bainite and of MA constituent exhibit noticeable variations and point out the wide variety of mixed upper/granular bainite microstructures that are available for this study. Figure 48 shows some microstructures obtained from high to low bainite content. Variations in martensite and austenite contents are not as strong (especially for martensite content: between 1 and 3%, with only a few exceptions). However, they might lead to observable effects on mechanical properties. We believe that more significant variation of these constituents would have been difficult to reach without changing the nature of the microstructure considerably (departing from a mix between upper and granular bainite). Only one material exhibits allotriomorphic ferrite, in addition, in only a low amount. The influence of allotriomorphic ferrite on mechanical properties is thus not expected to be necessarily very strong.

Here follows a list of noticeable variants of microstructure. The effect of the chemical composition on the microstructure will be discussed in the next chapter, in view of links between chemical composition and microstructure established in better controlled thermal conditions.

The highest amount of bainite among all forged parts is found for –Si+Mn 74. –Si 74 and +Cr 74 also exhibit high bainite content. In a general case, 74x74mm² forged parts have a tendency to exhibit slightly more upper bainite than do 35x35mm² forged parts.

0Ti 74 exhibits the highest amount of MA constituents among all combinations, closely followed by base 35. This increase is mainly due to an increase in number and size of the residual blocks that are composed mainly of MA constituents, with respect to other combinations. Other combinations that present high amounts of MA constituents (18% and more) are –Si 35 and base 74.

–Si+Mn 35 exhibits the highest martensite contents among all combinations, and shares the highest content of secondary microstructural constituent with base 35. The number as well as the size of blocks containing martensite is clearly higher with respect to other combinations. Other combinations that present high martensite content (5% or more) are +Mn 35, +Ni 35, base 35 and +Ni 74. These are mainly 35x35 forged parts with the most hardenable chemical compositions.

		LM + Le Pera (area%)				XRD
combination		bainite	MA	Martensite	ferrite	austenite
35x35 mm ²	0Ti	82 ± 1	16 ± 1	2 ± 1	0 ± 0	15.7 ± 0.6
	base	75 ± 2	20 ± 4	5 ± 1	0 ± 0	13.4 ± 0.4
	+Ni	83 ± 2	12 ± 2	5 ± 1	0 ± 0	11.7 ± 0.8
	ONb	82 ± 2	16 ± 2	2 ± 0	0 ± 0	10.0 ± 0.0
	-Si	78 ± 1	19 ± 2	3 ± 0	0 ± 0	7.3 ± 1.9
	-Si+Mn	75 ± 3	18 ± 1	7 ± 1	0 ± 0	10.2 ± 0.3
	+Mn	82 ± 1	13 ± 1	5 ± 1	0 ± 0	8.9 ± 1.1
	OMo	80 ± 1	17 ± 0	3 ± 1	0 ± 0	11.4 ± 0.2
	-Cr	83 ± 1	14 ± 1	3 ± 1	0 ± 0	7.4 ± 0.2
	+Cr	87 ± 1	11 ± 1	2 ± 0	0 ± 0	10.8 ± 0.6
	average	81 ± 1	15 ± 2	4 ± 1	0 ± 0	10.7 ± 0.6

		LM + Le Pera (area%)				XRD
combination		bainite	MA	Martensite	ferrite	austenite
74x74 mm ²	0Ti	76 ± 1	21 ± 2	3 ± 1	0 ± 0	12.7 ± 0.1
	base	80 ± 1	18 ± 1	2 ± 2	0 ± 0	11.0 ± 1.8
	+Ni	79 ± 1	16 ± 1	5 ± 2	0 ± 0	12.4 ± 0.4
	ONb	84 ± 0	13 ± 0	1 ± 1	2 ± 1	10.7 ± 0.4
	-Si	89 ± 1	10 ± 1	1 ± 1	0 ± 0	12.3 ± 0.2
	-Si+Mn	92 ± 1	7 ± 1	1 ± 1	0 ± 0	15.5 ± 0.1
	+Mn	82 ± 1	15 ± 2	3 ± 1	0 ± 0	14.1 ± 1.2
	OMo	86 ± 1	13 ± 1	1 ± 1	0 ± 0	10.0 ± 0.8
	-Cr	81 ± 1	16 ± 1	3 ± 1	0 ± 0	8.3 ± 0.3
	+Cr	90 ± 0	9 ± 0	1 ± 1	0 ± 0	13.9 ± 1.7
	average	84 ± 1	14 ± 1	2 ± 1	0 ± 0	12.1 ± 0.7

		LM + Le Pera (area%)				XRD
reference steel		bainite	MA	Martensite	ferrite	austenite
As-forged		74 ± 1	24 ± 1	2 ± 1	0 ± 0	12.9 ± 0.2
As-rolled		72 ± 3	25 ± 2	3 ± 1	0 ± 0	9.0 ± 0.2

		LM + Le Pera (area%)				XRD
all materials		bainite	MA	Martensite	ferrite	austenite
minimum		72 ± 3	7 ± 1	1 ± 1	0 ± 0	7.3 ± 1.9
maximum		92 ± 1	25 ± 2	7 ± 1	2 ± 1	15.7 ± 0.6
difference		20 ± 4	18 ± 3	6 ± 2	2 ± 1	8.4 ± 2.5

Table 10: Results of microstructural constituent quantification. Austenite (in volume fraction) is shared by the different microstructural constituents (except of martensite and ferrite). Intervals mentioned in this table for LM+LePera are standard deviations between results from the set of pictures used for each material. For XRD measurements, this is the absolute difference between two methods of calculations from peak areas (see A.II.2 for further details).

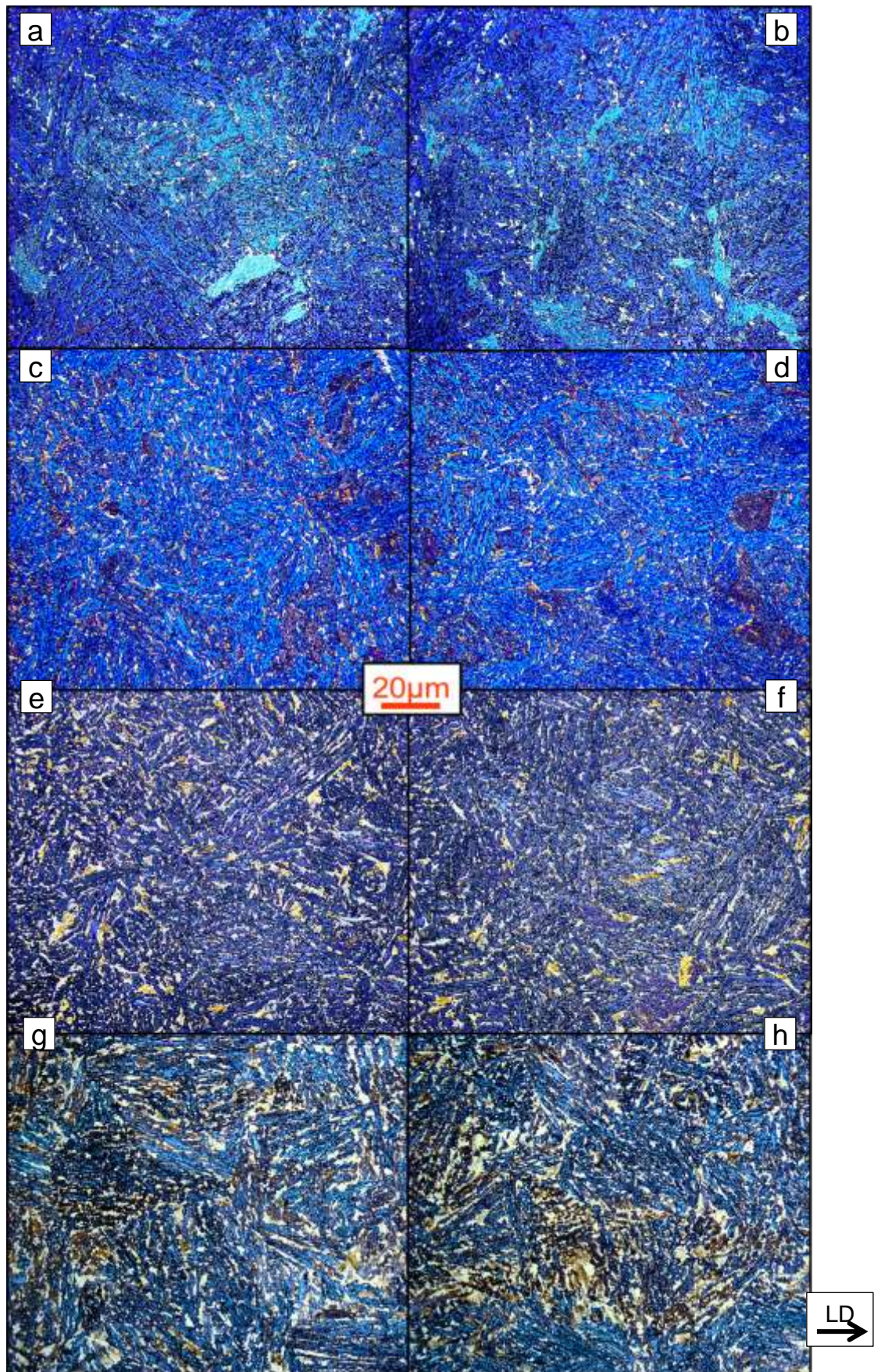


Figure 48: LM + LePera etching, (a)(b) -Si 74, (c)(d) +Mn 74, (e)(f) base 35, (g)(h) as-forged reference steel. To facilitate the comparison between microstructures, these pictures have been processed (using HSB) in order to put all equivalent microstructural constituents on the same colour range. White=MA constituent, yellow/beige=martensite, blue/brown=bainite.

CHAPTER 2 – MATERIALS

These observations point out the high amount of secondary microstructural constituents in 0Ti 74, base 74 and +Ni 74. Their microstructures are different from those of other 74x74mm² forged parts and, as shown later in this manuscript, their mechanical properties too (relatively good impact toughness and strength). So perhaps they might have encountered some difference in forging process for unknown reasons, such as fastest cooling rates. In fact, they have been forged in the first campaign, for which no on-field measurements are available.

In Table 10, only the result obtained in regions out of abnormal primary austenite grains have been considered for 0Ti 35. In the 0Ti 35 material, the bainitic microstructure obviously changes when the primary austenite grain size increases from 75µm up to more than several hundreds of micrometres. In these coarse grained regions, microstructure exhibit 90% of bainite and only 10% of MA constituent with no martensite as no blocks of residual phase are present. The bainite lath-like structure becomes also more appreciable. The apparent bainitic packet size is very coarse, some bainitic packet going from one side to the other of the primary austenite grain. The amount of film-like austenite is also higher in these regions, which explains the highest austenite content measured for this combination.

The microstructures of both states of the reference steel have the highest amount of MA constituent among all materials. Differences in thermo-mechanical processing, the higher level of segregation and the slightly different chemical composition (high nickel content, which is twice that of +Ni heat) have apparently led to the strongest incomplete transformation phenomenon obtained in this study.

2.4.4 Precipitation

Carbon extractive replicas have been taken from on 0Nb 74, 0Ti 74, 0Mo 74 and base 74 combinations in order to investigate the micro-alloying precipitation behaviour. These replicas have been taken in a plane normal to the forging direction according to the procedure explained in appendix A.IV.1. The nature of precipitates has been determined using EDX analysis. As illustrated in Figure 49, identified precipitates were Ti(C,N), (Ti,Nb)(C,N) and NbC. Two sizes of precipitates have been observed, smaller ones, between 40 and 80nm, and medium ones, between 200 and 240nm. No molybdenum carbo-nitride or chromium carbide has been detected in these combinations.

Selective dissolution has been realized in order to quantify the amount of niobium, titanium and molybdenum trapped in precipitates. It has been realized on the same combinations as for carbon replicas, from samples extracted from the specimen dedicated to microstructural characterization. This experiment has been totally carried out in Maizières R&D center, using a proprietary procedure well mastered for such kind of precipitates. Obtained residues were analysed by mass-spectrometry. Table 11 exhibits the results of such analysis.

tag	Nb		Ti		Mo	
	in precipitates	in solid solution	in precipitates	in solid solution	in precipitates	in solid solution
0Ti 74	70%	30%	X	X	6%	94%
0Nb 74	X	X	97%	3%	6%	94%
0Mo 74	78%	22%	96%	4%	X	X
base 74	81%	19%	97%	3%	6%	94%

Table 11: Result of mass-spectrometry analysis of selective dissolution residues.

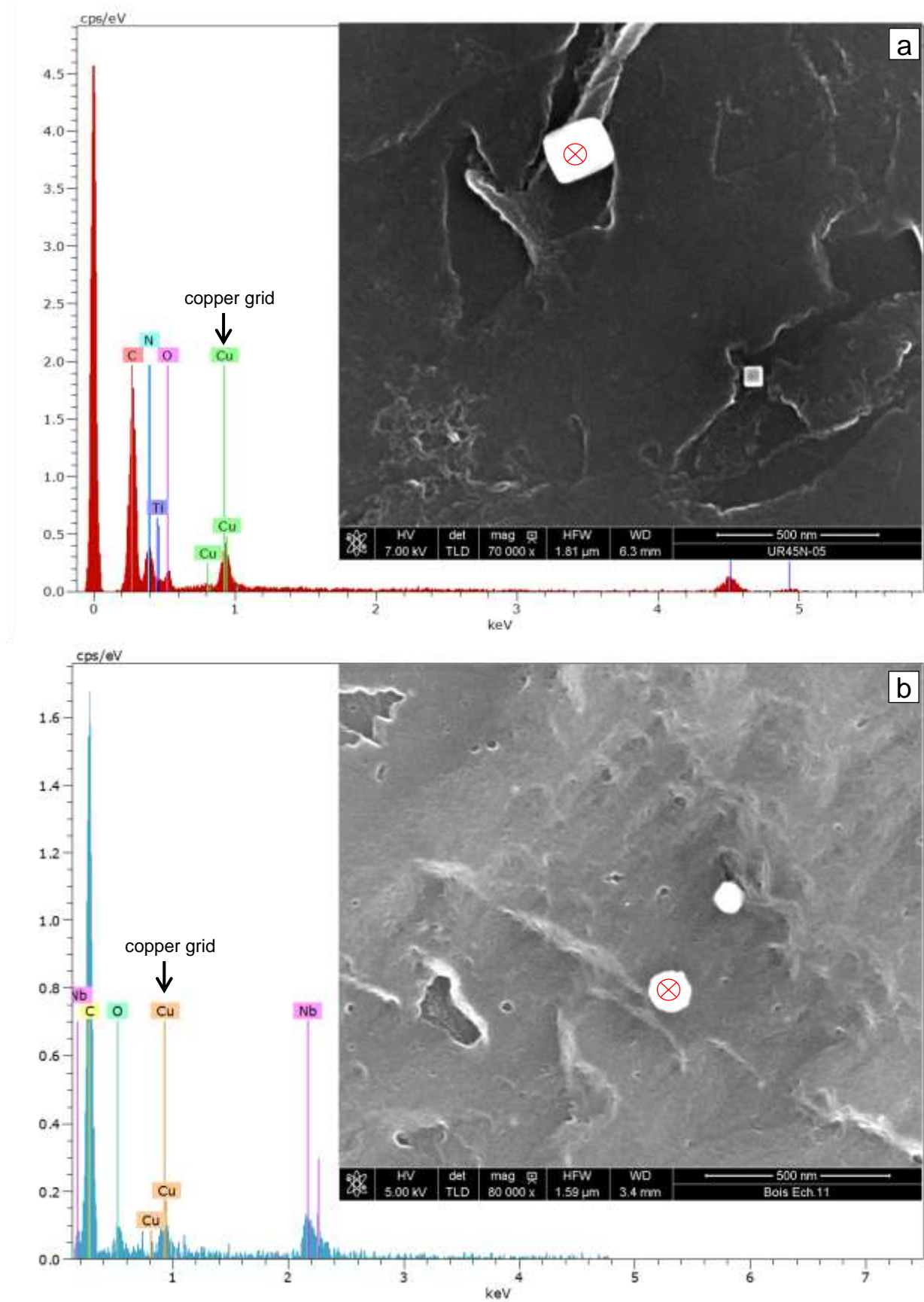


Figure 49: EDX spectra and associated SEM pictures of (a) Ti(C,N) particles observed in 0Nb 74 (K-ray of Ti visible at around 4.5 keV) and (b) NbC particles observed in 0Ti.

CHAPTER 2 – MATERIALS

As seen in the previous chapter, niobium and molybdenum are added together with the objective to prevent the formation of coarse boro-carbides whereas the role of titanium is to prevent precipitation of boron nitrides. Around 81% of niobium atoms have been found to precipitate but only 6% of molybdenum atoms do and this, whatever niobium being in the chemical composition or not. As both niobium and molybdenum are added to the same extent, niobium precipitation seems more effective than molybdenum one to protect boron in the present condition.

No molybdenum particle has been detected in carbon replicas. By the way, such particles would have been very difficult to identify, as molybdenum precipitation is believed to be in clusters of very thin nanometric precipitates (see previous chapter) that are nearly impossible to analyse in these observation conditions. No molybdenum has been detected in niobium carbide. The removal of molybdenum does not obviously affect the amount of niobium or titanium trapped in precipitates.

The fraction of niobium trapped in precipitates is higher when titanium is also present in the chemical composition. The reverse is not true as the fraction of precipitated titanium is not affected by the presence of niobium in solid solution. We do not know, for such fine precipitates (which are much finer than coarser particles mentioned at the beginning of this chapter), whether niobium and titanium form a solid solution or if niobium carbide precipitates at the interface between $Ti(C,N)$ and the matrix.

As only 0Ti 35 exhibited abnormal growth of primary austenite grains during the re-heating operation after forging, $Ti(C,N)$ and $(Ti,Nb)(C,N)$ are the particles that act efficiently in pinning the primary austenite grain boundaries at high temperature. Fine NbC precipitates might have dissolved at such high temperature (1190°C).

2.5 Discussion

Some issues that could affect building significant links between chemical composition, microstructure and mechanical properties have been identified:

1. Microstructural features linked to the solidification process.

Heterogeneities are easily observable on the reference steels, especially in the as-rolled state (banded structure), and in the 0Ti 35 combination (abnormal grain growth). Thermo-mechanical treatments that could reduce such heterogeneities are clearly outside the scope of the present study.

To limit the impact of the deep central shrinkage, and of the surrounding oxide layer observed on laboratory heats, the free forging process has been adapted by applying a higher reduction ratio on the part of laboratory heat that exhibit these features. The hole has been closed but it still lets its mark and an important concentration of oxides in the middle of the forged part. This mark cannot be removed by any subsequent heat treatment from the material.

These problems are more easily addressed by adjusting the casting process, which was not the aim of the present study. So, we just have to live with these two issues, being very cautious on analysis of results obtained from mechanical tests and microstructural characterization according to the regions and the materials of interest. Samples extraction has been realized in order to avoid the regions that were most susceptible to present such defects or heterogeneities. In addition, preliminary microstructural observation and hardness profiles have been used recurrently (even if not always indicated) to reveal any detrimental heterogeneity.

CHAPTER 2 – MATERIALS

2. Uncertainties introduced by the free-forging process

Re-heating operation between forging sequences is on the line here, as 35x35mm² forged parts might present an as-forged side and an as-reheated side (cooled down from 1190°C without any deformation). As forging was intended to be carried out over the non-recrystallization temperature, the impact of this re-heating on final microstructure might be limited if no grain coarsening occurs during reheating. Microstructural characterization has been realized as close as possible to the specimens used for mechanical tests; they will thus come from the same side of the forged part.

Moreover, as forging of the parts made from laboratory heats is manually operated, there might also be some differences in the forging temperature (temperature is not recorded, and controlled only through furnace index). From on-field measurements, at least two forged parts might have undergone a finish forging temperature slightly lower (in the bulk) than the non-recrystallization temperature. Hopefully, the amount of strain below this temperature might be very low. Nevertheless, this feature would only concern a limited region of the forged part.

Final cooling can also be slightly different between the different forged parts, as it might be sensitive to several parameters such as time to transport to cooling area, location in that cooling area and environment in the factory (temperature and wind).

Due to all these uncertainties in free forging conditions, it was not considered appropriate to make any direct link between the chemical composition of the laboratory heats and the mechanical properties after forging. However, it was still possible to make links between the microstructure and the mechanical properties, because the microstructural characterization has been realized near/on the region of the forged part that has been mechanically tested. Relevant links can thus be only reached if analysed materials presents significant microstructural variations. This is the case here, in the view of the wide range of microstructures exhibited by the studied materials.

Before coming to mechanical properties (chapters 4 and 5), links between chemical composition and microstructure have been investigated, from dilatometry, using dedicated thermal cycles with accurate control of the metallurgical state of austenite before cooling. This is reported in next chapter.

2.6 Conclusions

An as-forged and an as-rolled state of the same cast of a reference steel grade (denoted as “IS” hereafter) were selected as reference materials. Both exhibit a banded structure, with noticeable inhomogeneity in chemical composition, microstructure and hardness. They also exhibit coarser (Ti,Nb)(C,N) particles that decrease the niobium and titanium content in both steel matrix and segregation bands.

Ten different laboratory heats have been designed and cast for this PhD project. Each of them exhibits a variation of one or two alloying elements according to a reference laboratory heat, which is called “base” in the following. These laboratory heats aim at:

- Optimizing boron protection with playing on niobium, molybdenum and titanium contents.
- Assessing the effects of manganese and silicon contents on the amount of retained austenite after forging and subsequent cooling.
- Controlling microstructure, especially residual MA constituent and martensite contents with playing on chromium and nickel contents.

CHAPTER 2 – MATERIALS

- Assessing links between chemical composition, microstructure and mechanical properties.

Laboratory heats have been forged in two different parts, one with a 74x74mm² section, the other with a 35x35mm² section. This is expected to allow us to assess the effect of the two extreme cooling kinetics for the targeted application, and thus “extreme” microstructures and resulting mechanical properties for each chemistry.

Due to the uncertainties introduced by free-forging process (re-heating stage, some deformation near T_{nr}) no direct link can be made between the chemical composition of the laboratory heats and the mechanical properties after forging. The project has thus been conducted as follows.

Firstly, the link between chemical composition and microstructure has been made by the study of the austenite decomposition in the range of cooling rates relevant for forging. This link is addressed in the next chapter (chapter 3).

Secondly, it is still possible to make links between the microstructure and the mechanical properties because the microstructural characterization has been carried out near/in the region of the forged parts that have been mechanically tested. The mechanical properties that have been studied are the impact toughness, in chapter 4, and the tensile properties in chapter 5.

Thanks to the apparently wide range of mixed upper and granular bainite microstructures, relevant links between the microstructure and the mechanical properties are expected to be established on a rich microstructural database. Indeed, from quantification results of microstructural constituents, bainite and MA constituent contents exhibit noticeable variations (from 72 to 92% and from 7 to 25% of the microstructure for bainite and MA constituent, respectively). Variations in martensite and austenite contents are not as high. However, they might lead to observable effects on mechanical properties. Only one material exhibits allotriomorphic ferrite, in addition, in only a low amount. Prior austenite grain size and precipitation states have also been characterized.

The microstructures of both states of the reference steel have the highest amount of MA constituent among all materials but are still comparable to those of the laboratory heats.

CHAPTER 3 - EFFECT OF ALLOYING ELEMENTS ON CONTINUOUS COOLING TRANSFORMATION DIAGRAM

Résumé : Le lien entre la composition chimique et la microstructure bainitique obtenue en refroidissement continu a été construit ici grâce à la réalisation de diagrammes TRC spécifiques. Une attention particulière a été portée au conditionnement de l'austénite afin d'éviter tout effet de la taille de grain et de la décarburation sur la décomposition de l'austénite au cours du refroidissement. De cette manière, seules la composition chimique et la vitesse de refroidissement ont pu impacter la transformation bainitique.

Le domaine bainitique obtenu sur les diagrammes TRC a été scindé en plusieurs sous-domaines bainitiques définis en fonction de l'évolution des fractions des différents constituants microstructuraux, du taux d'austénite résiduelle, de la dureté et des températures de transformation.

L'impact des différents éléments d'alliage sur l'étendue de ces différents domaines a ensuite été discuté. La nuance étudiée est très robuste, vis-à-vis d'écarts à la composition chimique de référence, en ce qui concerne son comportement métallurgique en refroidissement continu, dans la gamme étudiée. Aucune variation significative n'a été observée d'une coulée de synthèse à l'autre. On peut cependant dire que :

- Sans molybdène, et plus particulièrement sans niobium, le domaine ferritique tend à s'étendre vers des vitesses de refroidissement plus rapides. Ceci a été relié à la multiplication d'un certain type de précipités le long des anciens joints de grains de l'austénite (suspectés être des $\text{Fe}_{23}(\text{B,C})_6$).
- Par rapport à la composition de base, une diminution de la teneur en chrome entraîne une augmentation significative des températures de transformation bainitique et mène à une microstructure bainitique très grossière possédant une faible dureté. A l'inverse, une augmentation de la teneur en chrome par rapport à la composition de base n'entraîne pas de diminution des températures de transformation.
- Une augmentation de la teneur en manganèse et nickel entraîne une croissance plus rapide de la fraction de martensite en fonction de la vitesse de refroidissement. Cependant, l'effet du nickel n'est perçu que pour des vitesses de refroidissement supérieures à 0.8°C/s .
- Une baisse de la teneur en silicium mène à une augmentation significative de la fraction de bainite maximale atteignable. Cependant, la dureté de cette bainite est grandement affectée.

Une comparaison entre les microstructures obtenues par forgeage libre et celle obtenues en dilatométrie à même vitesse de refroidissement au cours de la transformation bainitique a aussi été réalisée. Les pièces brutes de forgeage de petite section possèdent systématiquement une microstructure plus riche en constituants martensite-austénite, ce qui est attribué à la modification du cycle thermique (refroidissement temporairement ralenti) du fait de la chaleur latente libérée lors de la transformation bainitique. Cette chaleur est en effet moins bien évacuée des pièces de forgeage par rapport aux échantillons de dilatométrie.

The purpose of this chapter is to overview the influence of alloying elements on the bainitic microstructure along the range of cooling rates encountered in still air-cooling after high temperature forging ($> 1100^{\circ}\text{C}$). As the temperature at the end of forging is still very high with respect to the non-recrystallization temperature for this steel family (around 926°C , see chapter 1), recrystallization of austenite is believed to be fully achieved when the first transformation occurs (below 750°C). The same goes for precipitation due to deformation and slow cooling rates at high temperature (between 1.6°C/s and 3.5°C/s). In this case, the CCT diagram is believed to be the best suited tool to achieve our objective, with the conditions that:

1. Primary austenite grain size (**PAGS**) is controlled in order to reflect the one that is found in forged product (after deformation and full recrystallization).
2. Full precipitation can occur as in targeted industrial cooling conditions.

3.1 Conditioning of the primary austenite state

Preliminary dilatometric cycles have been realized to set the austenitization parameters in order to obtain PAGS with the same range of size as on the forged parts, but also, to find the best suited cooling rate between 1200°C and 800°C . Indeed, the cooling between 1200°C and 20°C has been separated in two segments. Keeping the same cooling rate between 1200°C and 800°C allows proper comparison between different cooling rates applied in the second segment, between 800°C and 20°C . Effect on austenite decomposition is then only due to the cooling rate close to the austenite decomposition temperature (i.e. driving force) but not to a difference in austenite state (decarburization, grain size, precipitation state) induced by the cooling rate itself.

The more rapid cooling at the first segment allows avoiding excessive austenite grain growth and decarburization that can occur at high temperature for low cooling rates. The decarburization that occurs during this additional time at high temperature could lead to the occurrence of ferrite transformation in carbon-depleted regions. In the same way, grain coarsening affects the transformation kinetics as reported in chapter 1. Precipitation in austenite has not been investigated, the major part of it being expected to occur at temperatures higher than 800°C , thus during cooling between 1200°C and 800°C . As a consequence, the precipitation state has been considered equivalent for each sample of a given chemical composition.

3.1.1 Experimental methods

3.1.1.a Materials

36 dilatometric samples have been extracted from the XD 74 section of each $74\times 74\text{mm}^2$ forged part (see the extraction map in Appendix B). Dilatometric samples, used in the dilatometer BAHR 805A TAinstruments at Gandrange R&D center, have a diameter of 4mm and a length of 10mm. They were cut along the longitudinal direction, from one-third of the XD 74 section. No sample has been extracted from the central region of the section, the closest dilatometric sample being at least 20mm away from the central point in order to avoid any macro-segregation or shrinkage-induced effects. In addition, samples were at least 4mm away from the surfaces of the forged part.

The 0Nb, 0Ti and the base chemical compositions have been selected for this preliminary study. As shown in chapter 1, niobium and titanium can have an obvious effect on the primary austenite grain size so 0Nb and 0Ti chemical compositions were considered worth being investigated. The base chemical composition, which contains both Ti and Nb, served as reference for all other considered chemistries.

3.1.1.b Parameters of dilatometric cycles

The heating rate was set to 100°C/s. This value is believed to still lead to the memory effect or structural inheritance phenomenon [18-20]. In this case, it is assumed that the austenite grain directly grows from the previous retained austenite that is present in the initial bainitic microstructure. The austenite grows into an acicular morphology until the original austenite grain structure is recovered without request for nucleation of new austenite grains. Acicular austenitic grains within a given prior austenite grain have a common orientation owing to growth from retained austenite, and they coalesce on impingement, leading to a reconstitution of the original prior austenite grain structure. This memory effect can be enhanced by the presence of carbides in the microstructure if these ones can sufficiently stabilize the lath boundaries so that acicular austenite growth occurs before the recovery and recrystallization of laths. As a consequence, the texture can be expected to be close to that produce by forging.

Wang et al. [18] have studied the effect of three different heating rates on the austenite morphology (steel chemistry: 0.044C, 0.520Si, 1.070Mn, 0.016P, 0.005S, 1.050Cu, 0.540Cr, 0.720Ni, 0.240Mo, 0.001B in wt%). Their initial microstructure was composed of bainitic ferrite plates, which were separated by retained austenite films with no cementite precipitation. The initial PAGS was 16.5µm. The experimental procedure consisted to heat the sample at 2°C/s, 100°C/s or 1000°C/s up to 1250°C, and then quenching the sample at 400°C/s by injecting iced water.

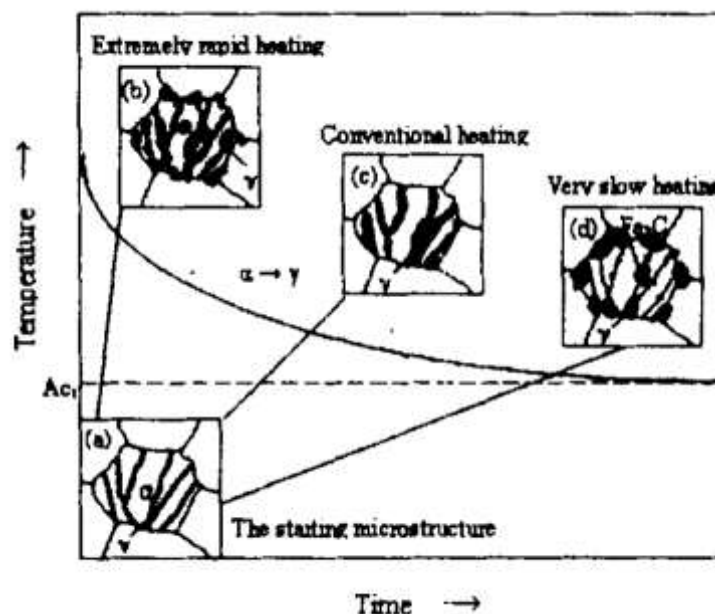


Figure 50: Formation of austenite during heating from a bainitic ferrite with retained austenite microstructure. (a) starting microstructure is a mix between ferritic bainite (in white) and retained austenite film (in black). According to the heating rate, the obtained austenite comes from: (b) a competition between acicular and granular austenite, (c) the growth of acicular austenite emerging from retained austenite, (d) nucleation and growth of granular austenite [18].

They found that after heating at 2°C/s and 100°C/s, the obtained austenite grain was similar to the one that was prior to the bainitic microstructure, with an increase or a slight decrease in size according to the heating rate (a fast heating rate tends to decrease the austenite grain size). The authors did not indicate obtained grain sizes precisely. High heating rate, like 1000°C/s, significantly increased both the driving force for austenite nucleation and the atom diffusivity due to overheating. New austenite grains were able to nucleate at all possible sites, including prior austenite grain boundaries, adjacent ferrite plate interfaces and even from inside the plates. In addition, retained austenite films thickened simultaneously. The austenite then developed into an equiaxed and ultrafine-grained morphology. On the opposite, very low heating rates can lead to the decomposition of retained austenite into carbide (most likely cementite) and ferrite in the early stages of heating. As no austenite remains in the microstructure, new austenite nucleates at prior austenite grain boundaries,

leading to a complete change in the final austenite morphology [19]. A schematic view of these mechanisms is shown in Figure 50.

In our experiments, the austenitization stage was set to 1200°C for 5 minutes. Under these conditions, the austenitization lasts for enough time for the thermal expansion to stabilize without noticeable grain coarsening thanks to (Ti,Nb)(C,N) or Ti(C,N) precipitates. Indeed, in view of our chemical compositions, these precipitates are expected to remain stable at this temperature according to literature data (see chapter 1) and the dissolution temperatures that have been additionally calculated using equations found in [153-155].

Cooling rates of 1.5 and 3.5°C/s between 1200°C and 800°C have been measured during the forging of laboratory heats for the 74x74mm² and 35x35mm² forged parts respectively (see previous chapter). The influence of these two cooling rates at high temperature on the transformation temperatures has been tested for a cooling rate of 0.8°C/s between 800°C and 20°C, which is the measured cooling rate before the bainitic transformation for the thinnest forged part. A cooling rate between 1200°C and 800°C of 0.8°C/s has additionally been tested to investigate the case of a constant continuous cooling from 1200°C down to 20°C, as for more conventional CCT diagrams.

In order to facilitate measurement of the austenite grain size, a helium gas quench has been carried out at 100°C/s from 1200°C, directly after the austenitization stage on one specimen per chemical composition. Another interrupted cycle has been done but this time, the helium gas quench has been realized after a cooling at 0.8°C/s between 1200°C and 800°C. The PAGS measurements have been realized following the metallographic procedure and data processing reported in A.III.2.

To summarize, a schematic view of all preliminary dilatometric cycles that have been realized per chemical composition are shown in Figure 51.

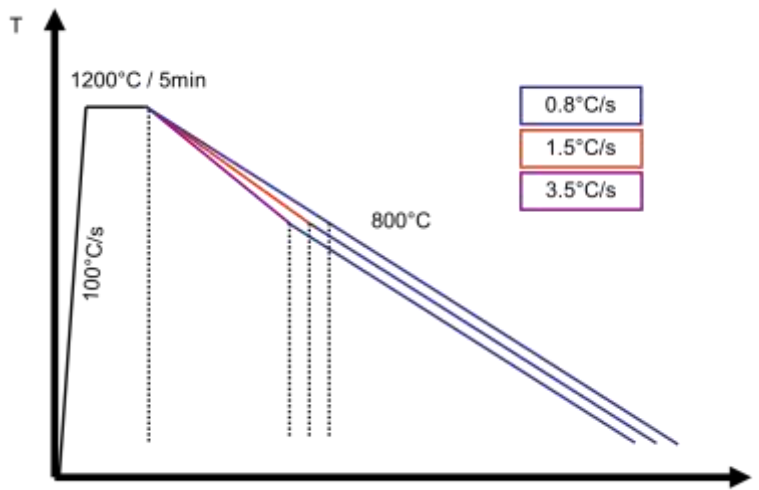


Figure 51: Schematic of all dilatometric cycles realized for the preliminary study. Dotted lines are used to represent helium gas-quench at 100°C/s.

3.1.1.c Processing of dilatometric curves

In order to determine the transformation temperatures, processing of the obtained dilatometric curves has been realized under Excel 2003 software. Transformation temperatures have been directly determined on dilatation versus temperature curves ($\Delta l(T)$) using linear regressions according to the following method:

- According to the temperature gap between two transformations, a temperature range (between 30°C and 50°C) is set at least 15°C upper, in the case of a start

temperature, or 15°C below, in the case of a finish temperature, the apparent transformation temperature.

- A linear regression is calculated from this previously established temperature range. The coefficient of determination (R^2) must be very close to 1 (>0.995), showing that the temperature range exhibits no transformation but only nearly-linear thermal expansion.
- A linear curve ($\Delta l'(T)$), which is parallel to the linear regression, is plotted 0.5 μm upper, in the case of a starting temperature, or lower, in the case of a finish temperature, than the linear regression curve.
- The transformation temperature is considered to be reached when the difference between $\Delta l(T)$ and $\Delta l'(T)$ becomes positive. In fact, due to the occurrence of a residual noise on the $\Delta l(T)$ curve, the transformation temperature is considered to be reached as soon as:

$$\sum_{T-1^\circ C}^{T+1^\circ C} (\Delta l(T) - \Delta l'(T)) \geq 0 \quad eq. 3.1$$

- If there is less than 15°C between the obtained transformation temperature and the previously defined temperature range for the linear regression, this procedure is repeated now considering the obtained transformation temperature as the starting point.

Figure 52 shows an example of this method on one curve of 0Nb chemical composition with a cooling rate of 0.1°C/s between 800°C and 20°C. The uncertainty on the transformation temperature depends on the dilatation kinetics (i.e. on the transformation kinetics). This may be estimated based on the half of the temperature gap between the following two conditions:

$$\sum_{T-1^\circ C}^{T+1^\circ C} (\Delta l(T) - \Delta l'(T)) \geq -1\mu m \text{ and } \sum_{T-1^\circ C}^{T+1^\circ C} (\Delta l(T) - \Delta l'(T)) \geq 1\mu m \quad eq. 3.2$$

This correspond to an average of 3°C for B_s , 4°C for B_F and 5°C for ferrite start transformation temperature (F_s) and for ferrite end transformation temperature (F_F).

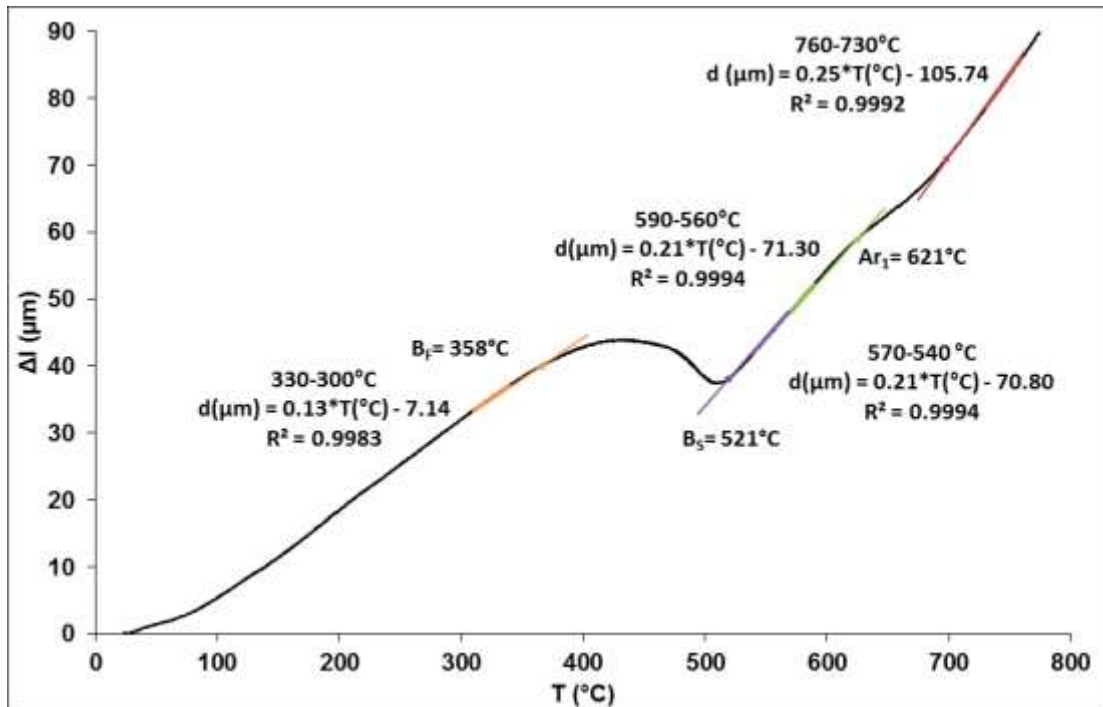


Figure 52: Dilatation versus temperature curve for the 0Nb chemical composition with a cooling rate of 0.1°C/s between 800°C and 20°C.

The ferrite transformation is only observed in some chemical compositions, for very slow cooling rates. The amount of ferrite transformed from austenite is generally low, leading to only a slight variation on the $\Delta l(T)$ curve. The previously described method for determining the transformation point was found ineffective when the ferrite represents less than 5% of the final microstructure. In this case, the transformation temperature F_S and F_F were determined manually, using the classical tangential method. When the ferrite is less than 1% of the final microstructure, no observable transformation points were found on the $\Delta l(T)$ curve.

3.1.1.d Microstructural characterization

For this preliminary study, focus has been made on transformation temperatures and not on microstructure. Microstructural observations have been realized only on samples with a same chemical composition but having obvious changes in hardness and austenite content.

For each sample, the austenite content has been measured directly after the end of the dilatometric cycle by a magnetic method using a sigmometer B3513A from Aimants Ugimac and following the procedure described in A.II.2. Indeed, round robin measurements using both XRD and sigmometry have been realized using samples from all 74x74mm² forged parts and some dilatometric samples coming from the realization of the CCT diagrams (as shown later in this chapter). Details are given in A.II.3. A linear relationship was found between the volume fraction of austenite (f_y) and the specific magnetization at saturation (σ_s). This relationship is considered valid for the entire CCT diagram with the exception of samples presenting some allotriomorphic ferrite. In this last case, the linear relationship tends to over-evaluate the austenite content.

In order to facilitate the realization of PAGS or hardness measurements, samples have been regrouped together according to, firstly, their chemical composition and secondly, whether they had been quenched or not. They have been mounted together using cold resin. The mounting has been then ground using coarse-grained abrasive papers (P160) until the width of each sample in the mounting comes close to 4mm.

One HV0.5 profile has been realized along the longitudinal direction in the centre of each dilatometric sample, from 3mm to 7mm (sample length is 10mm), with a step of 200 μ m (20 points in total). Profiles have been made using a Buehler MicroMet 5124 after conventional mirror polishing down to 1 μ m diamond paste. Errors associated to these hardness measurements are the standard deviation.

PAGS measurements have been realized according to the procedure reported in A.III.1.

3.1.2 Results

Table 12 shows the measurement results for conditions with different cooling rates between 1200°C and 800°C. The studied parameters do not exhibit recurrent variation that may indicate a strong influence of the cooling rate at high temperature on the following transformation at 0.8°C/s.

The maximum difference in B_S that was found among samples with a same chemical composition is only 9°C. In the case of B_F , the maximum difference is slightly higher, being equal to 16°C. The end of the bainitic transformation was found very sluggish in every case. The last 20% of the transformation necessitates almost a temperature decrease by 50°C at 0.8°C/s, so we assumed that 16°C is not a significant change in B_F .

CHAPTER 3 - EFFECT OF ALLOYING ELEMENTS ON CCT DIAGRAM

ONb	0.8°C/s (1200-800°C) + 0.8°C/s (800-20°C)	1.5°C/s (1200-800°C) + 0.8°C/s (800-20°C)	3.5°C/s(1200-800°C) + 0.8°C/s (800-20°C)
B _S (°C)	525 ± 3	528 ± 3	522 ± 4
B _F (°C)	381 ± 4	378 ± 5	390 ± 4
B _S -B _F (°C)	144 ± 7	150 ± 8	132 ± 8
HV0.5	337 ± 15	339 ± 15	336 ± 12
σ (G.cm ³ /g)	178.3 ± 0.2	177.4 ± 0.1	176.1 ± 0.1
f _γ	0.15 ± 0.015	0.16 ± 0.015	0.16 ± 0.015

OTi	0.8°C/s (1200-800°C) + 0.8°C/s (800-20°C)	1.5°C/s (1200-800°C) + 0.8°C/s (800-20°C)	3.5°C/s(1200-800°C) + 0.8°C/s (800-20°C)
B _S (°C)	518 ± 6	517 ± 4	516 ± 5
B _F (°C)	368 ± 3	364 ± 4	372 ± 4
B _S -B _F (°C)	150 ± 9	153 ± 8	144 ± 9
HV0.5	343 ± 9	347 ± 25	345 ± 15
σ (G.cm ³ /g)	181.2 ± 0.1	181.5 ± 0.1	178.3 ± 0.1
f _γ	0.13 ± 0.015	0.13 ± 0.015	0.15 ± 0.015

base	0.8°C/s (1200-800°C) + 0.8°C/s (800-20°C)	1.5°C/s (1200-800°C) + 0.8°C/s (800-20°C)	3.5°C/s(1200-800°C) + 0.8°C/s (800-20°C)
B _S (°C)	524 ± 4	519 ± 4	515 ± 2
B _F (°C)	368 ± 3	354 ± 3	370 ± 3
B _S -B _F (°C)	156 ± 7	165 ± 7	145 ± 5
HV0.5	352 ± 17	357 ± 23	359 ± 17
σ (G.cm ³ /g)	182.6 ± 0.2	183.9 ± 0.1	181.3 ± 0.1
f _γ	0.12 ± 0.015	0.12 ± 0.015	0.13 ± 0.015

Table 12: Results of the different measurements realized for the different cooling rates between 1200°C and 800°C before final cooling at 0.8°C/s down to 20°C.

Average hardness values follow the same trend, each chemical composition exhibits a slightly different hardness level but no significant differences are found between the average hardness values for a given chemistry. The difference between the minimum and the maximum hardness value found on every profile is about 60 but most of the values were closer to the average one as indicated by the standard deviation. Remind that the indentation mark is in the same order of size as a bainitic packet (20-30μm) so it may be very sensitive to a local variation of fraction of microstructural constituent (such as a block of residual phase). In concern of austenite content, cooling at 3.5°C/s leads to the highest austenite content in every case but the variation, less than 0.02 can be considered as not significant.

Table 13 shows the results of the PAGES measurement realized on interrupted dilatometric cycles. All inspected microstructures were fully martensitic. No satisfactory pictures for the realization of this measurement were obtained for ONb chemical composition with the lower cooling rate. No other trials were attempted in view of the other results.

Tag	PAGES (μm)		
	0.8°C/s (1200-800°C) + 100°C/s (800-20°C)	100°C/s (1200-800°C) + 100°C/s (800-20°C)	35x35mm ²
ONb	X	49 ± 18 [178]	49 ± 19 [255]
OTi	85 ± 38 [47]	80 ± 36 [88]	75 ± 424 [326]
base	48 ± 17 [68]	48 ± 18 [220]	42 ± 15 [431]

Table 13: Results of the PAGES measurement realized after interrupted dilatometric cycles and on associated 35x35mm² forged parts. Numbers in square brackets are the number of analysed austenite grains. Targeted average grain size ranged between 37 and 53μm to stay relevant with as-forged state.

As expected, the heating rate and austenitization parameters allow to stay close to the post-forging primary austenite grain size (between 37 and 53 μm). A slight additional increase in grain size has been noted when the quench is realized at 800°C after a cooling rate of 0.8°C/s without titanium, pointing out that the grain size increases during slow cooling from 1200°C if no Ti(C,N) particles are present in the microstructure to pin austenite grain boundaries.

As for the forged parts, the distribution in size of the PAGS of 0Ti chemical composition is different from that of both base and 0Nb chemical compositions. In the last two cases, the PAGS at the maximum number fraction is barely equal to the average PAGS, suggesting a centred distribution around the maximum number fraction. In the case of 0Ti laboratory heats, PAGS at maximum number fraction is the same as for base or 0Nb chemical composition (40-45 μm) but the maximum number fraction is 0.10 lower. The distribution is broad and asymmetric, spreading toward higher grain size.

3.1.3 Conclusions

No significant differences have been found in transformation temperatures, PAGS, austenite content and hardness for the different cooling rates used between 1200°C and 800°C. The austenite grain size just after the austenitization stage was found in the same order of size as PAGS measured on forged parts (37-53 μm). In order to maximize the chances to keep a narrow range of PAGS, comparable with as-forged state, and to reduce decarburization extent, the cooling rate between 1200°C and 800°C has been set to 3.5°C/s for the following experiments.

3.2 Continuous cooling transformation diagrams

3.2.1 Experimental methods

3.2.1.a Dilatometric cycles

The same equipment and sample geometry as in the preliminary study have been used. CCT diagrams have been built following the parameters set in the preliminary study: heating rate of 100°C/s, austenitization at 1200°C for 5 minutes, then cooling at 3.5 °C/s down to 800°C. At this point, the cooling rate down to 20°C was set following one of these values: 2°C/s, 1.5°C/s, 1°C/s, 0.8°C/s, 0.6°C/s, 0.4°C/s, 0.2°C/s, 0.1°C/s and 0.08°C/s. One sample has been heat treated for each of these cooling rates. In order to facilitate reading of the present chapter, the following nomenclature has been used: “+Cr 0.8°C/s” for the chemical composition with an increase in chromium content, after a cooling rate between 800°C and 20°C of 0.8°C/s. A schematic of all dilatometric cycles realized per chemical composition for the construction of one CCT diagram is shown in Figure 53.

High cooling rates have generally not been tested, firstly to save time as these CCT diagrams have been realized for 9 different chemical compositions and secondly, because they are much too far from still air-cooling cooling rates which are generally lower than 1°C/s for the targeted bar geometry (at least 35x35mm² in section). The exception concerns 0Nb, base, +Ni and –Si+Mn, for which an additional cooling rate of 100°C/s between 800°C and 20°C has been applied.

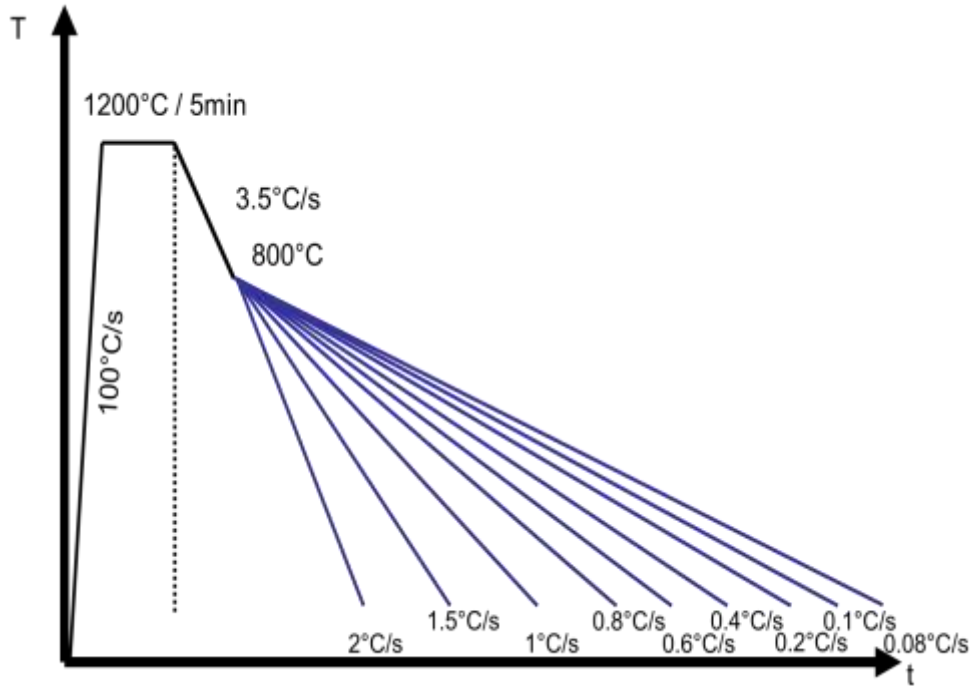


Figure 53: Schematic of all the dilatometric cycles realized per chemistry for the establishment of CCT diagram. Dotted lines represents helium gas-quench at 100°C/s. Gas-quench has only been realized for 0Nb, base, +Ni and -Si+Mn chemical compositions.

A specific thermo-mechanical treatment would have been necessary to reduce and homogenize the grain size of the 0Ti chemical composition in order to be comparable with the other chemical compositions. Time has been missed to investigate proper heating process or to realize some trials with dilatometric equipment equipped with a deformation module. We have decided thus not to realize CCT diagram for 0Ti chemical composition. At first sight, one may think that no significant change are awaited between CCT diagrams of base and 0Ti chemical composition at a same PAGS, but, as it is shown later in chapter 5, the boron protection from nitrogen is less effective in the absence of titanium, which may have led to a greater extent of the ferritic domain.

In addition to the determination of transformation temperatures following the same data processing as for the preliminary study, transformation kinetics have been determined by calculating the extent of the transformation at any temperature between B_S and B_F (or M_F as it is shown later in this chapter, as bainite and martensite transformation are not always well separated on dilatometric curves) using a classical lever rule:

$$F(T) = \frac{(\Delta l(T) - \Delta l_2(T))}{(\Delta l_2(T) - \Delta l_1(T))} \cdot (x_{BA} + x_M) \quad eq. 3.3$$

where $F(T)$ is the extent of the transformation at temperature T , x_{BA} and x_M are the fraction of bainite and martensite respectively, $\Delta l(T)$ is the dilatation in μm at temperature T , $\Delta l_1(T)$ and $\Delta l_2(T)$ are the dilatation in μm calculated at a temperature T from linear regressions established below B_F and beyond B_S (or M_F) respectively.

3.2.1.b Microstructural characterization

Samples have been hot mounted (180°C, 350bar, 5min) in phenolic red resin (Multifast) using a CitoPress-1 from Struers. In order to reduce the preparation time of metallographic samples, samples have been regrouped nine by nine according to their cooling rate between 800°C and 20°C as shown in Figure 54. If they had been regrouped according to their chemical composition, the high hardness difference resulting from very low cooling rates

(>0.2°C/s) and relatively high ones (>1°C/s) would have generated some scratching issues during polishing.

In fact, even by grouping samples according to their cooling rate between 800°C and 20°C, there are still some noticeable hardness differences for the relatively high cooling rates, as for -Cr and +Mn chemistries ($\Delta HV_{30} > 70$). However, this arrangement ensures that the same kind of microstructures are polished and etched the same way, facilitating further image analysis.

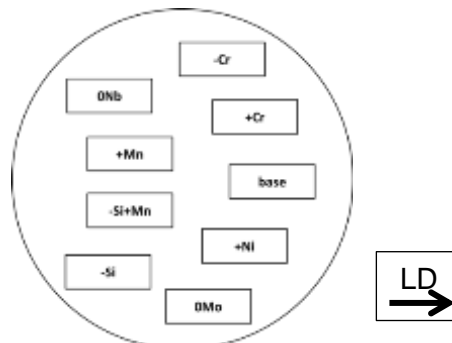


Figure 54: Schematic of a mounting ($\varnothing=40\text{mm}$). Order of each chemical composition stays the same whatever the cooling rate between 800°C and 20°C. They are located in order to observe the longitudinal plane.

Mounted samples have been ground using coarse abrasive paper (P160) until the width of each sample on the mounting comes close to 4mm. Then, a typical mirror polishing has been operated. Once polished with the 1 μm diamond paste, three HV30 points have been realized in the central region of each dilatometric sample using a Dia Testor 2RcS from Testwell. The middle hardness point is located close to the exact centre of the sample, the other two points being made 2.5mm away on either side of the middle one along the longitudinal direction. No harmful segregation (texture effect or numerous obvious changes in hardness) had been observed previously on laboratory heats or on dilatometric samples of the preliminary study, so no HV0.5 profiles have been realized as we expected that this situation stays unchanged in this part of the study.

The fraction of each microstructural constituent has been quantified using the method described in A.I.1. The 12 LM pictures for the image analysis have been taken from the central region of the dilatometric sample. Observations have been realized with a magnification of x500 on a Zeiss Axiovert 405M equipped with ProgRes CF scan camera from Jenoptik.

To finish, field electron gun FEG-SEM observations have been realized on some selected samples following a 3s Nital2% etching. Observations have been performed on a Zeiss DSM 982 Gemini. Samples have been mirror polished, the last two steps being a 0.25 μm diamond paste polish and a 60s polish with colloidal silica.

3.2.2 Results

3.2.2.a Typical dilatometric response

In the following part, transformation rates are compared relatively to the overall transformation kinetics that is observed on $\Delta I(T)$ curves for a given cooling rate. As example, 0.19 s⁻¹ is a relatively high transformation rate at 0.08°C/s but is very weak compared to those at higher cooling rates. Table 14 shows average bainite transformation rates for all chemical compositions at different cooling rates.

CHAPTER 3 - EFFECT OF ALLOYING ELEMENTS ON CCT DIAGRAM

F_{yd}	F(T)/s								
	2°C/s	1.5°C/s	1°C/s	0.8°C/s	0.6°C/s	0.4°C/s	0.2°C/s	0.1°C/s	0.08°C/s
0->0.1	0.53 ± 0.09	0.44 ± 0.05	0.37 ± 0.06	0.29 ± 0.05	0.21 ± 0.03	0.16 ± 0.03	0.09 ± 0.01	0.05 ± 0.01	0.04 ± 0.01
0.1->0.2	1.32 ± 0.16	1.12 ± 0.14	0.88 ± 0.08	0.73 ± 0.08	0.55 ± 0.11	0.40 ± 0.07	0.22 ± 0.02	0.12 ± 0.03	0.08 ± 0.01
0.2->0.3	2.06 ± 0.16	1.55 ± 0.15	1.25 ± 0.13	1.08 ± 0.15	0.85 ± 0.11	0.60 ± 0.08	0.33 ± 0.04	0.15 ± 0.03	0.11 ± 0.02
0.3->0.4	2.57 ± 0.64	1.91 ± 0.17	1.39 ± 0.17	1.27 ± 0.13	1.00 ± 0.19	0.72 ± 0.12	0.36 ± 0.08	0.17 ± 0.04	0.12 ± 0.05
0.4->0.5	2.38 ± 0.68	1.89 ± 0.30	1.41 ± 0.17	1.28 ± 0.22	1.05 ± 0.22	0.71 ± 0.22	0.38 ± 0.12	0.14 ± 0.04	0.10 ± 0.03
0.5->0.6	2.41 ± 0.96	1.70 ± 0.20	1.38 ± 0.14	1.18 ± 0.08	0.93 ± 0.14	0.63 ± 0.11	0.34 ± 0.11	0.11 ± 0.03	0.08 ± 0.03
0.6->0.7	1.82 ± 0.31	1.55 ± 0.30	1.21 ± 0.20	1.06 ± 0.09	0.85 ± 0.14	0.53 ± 0.08	0.23 ± 0.04	0.07 ± 0.03	0.05 ± 0.02
0.7->0.8	1.55 ± 0.43	1.14 ± 0.24	0.91 ± 0.12	0.81 ± 0.10	0.59 ± 0.05	0.36 ± 0.05	0.15 ± 0.03	0.05 ± 0.01	0.03 ± 0.00
0.8->0.9	0.86 ± 0.17	0.70 ± 0.20	0.60 ± 0.11	0.49 ± 0.08	0.36 ± 0.04	0.20 ± 0.03	0.07 ± 0.02	0.03 ± 0.00	0.02 ± 0.00
0.9->1	0.32 ± 0.06	0.27 ± 0.09	0.24 ± 0.04	0.19 ± 0.03	0.13 ± 0.02	0.07 ± 0.01	0.03 ± 0.00	0.02 ± 0.00	0.01 ± 0.00

Table 14: Average bainite transformation rate for all chemical compositions at different cooling rates F(T) and different relative amounts of decomposed austenite (F_{yd}). Values highlighted in blue are over 75% of the highest transformation rate found for the corresponding cooling rate. Errors are standard deviations between chemical compositions.

Figure 55 shows some typical $\Delta I(T)$ curves obtained for different cooling rates. Figure 55a and Figure 55b exhibit two different responses in the case of a low cooling rate ($c_r < 0.2^\circ\text{C/s}$, whatever the chemical composition) depending on the occurrence of a noticeable decomposition of austenite into allotriomorphic ferrite (final fraction of ferrite > 0.05). The bainitic transformation has a relatively fast start in both cases. A relative high transformation rate is reached once 10% of the transformation has occurred. This rate stays stable until 50% (~40-50°C) of the bainitic transformation has been realized (this stage is highlighted in blue in Table 14).

As shown in Table 15, this constant stage is reached faster with the occurrence of allotriomorphic ferrite, but with a lower average transformation rate. Moreover, with the occurrence of allotriomorphic ferrite, the transformation rate shows a more regular decrease after 50% of the bainitic transformation. Without allotriomorphic ferrite, this decrease may exhibit a second constant stage at lower transformation rate for at last 40°C.

F_{yd}	F(T)/s			
	no ferrite		with ferrite	
	0.1°C/s	0.08°C/s	0.1°C/s	0.08°C/s
0->0.1	0.05 ± 0.01	0.04 ± 0.01	0.06 ± 0.00	0.05 ± 0.00
0.1->0.2	0.12 ± 0.02	0.09 ± 0.01	0.14 ± 0.06	0.08 ± 0.02
0.2->0.3	0.17 ± 0.01	0.12 ± 0.01	0.12 ± 0.04	0.09 ± 0.03
0.3->0.4	0.18 ± 0.03	0.14 ± 0.05	0.13 ± 0.03	0.09 ± 0.02
0.4->0.5	0.16 ± 0.03	0.11 ± 0.02	0.11 ± 0.03	0.08 ± 0.02
0.5->0.6	0.13 ± 0.02	0.10 ± 0.02	0.08 ± 0.01	0.05 ± 0.00
0.6->0.7	0.08 ± 0.03	0.06 ± 0.01	0.05 ± 0.00	0.04 ± 0.01
0.7->0.8	0.05 ± 0.01	0.03 ± 0.00	0.04 ± 0.00	0.03 ± 0.00
0.8->0.9	0.03 ± 0.00	0.02 ± 0.00	0.03 ± 0.00	0.02 ± 0.00
0.9->1	0.02 ± 0.00	0.01 ± 0.00	0.01 ± 0.00	0.01 ± 0.00

Table 15: Distinction between average transformation rates found at low cooling rates, depending on the occurrence of allotriomorphic ferrite.

For cooling rates between 0.2°C/s and 1°C/s, the bainitic transformation rate stays relatively high and constant up to 80% of the bainitic transformation as it can be seen in Figure 55c and in Table 14. In addition, an inflection point has been found regularly on $\Delta I(T)$ curves whatever the chemical composition. This inflection point may be the finish transformation temperature that is linked to the end of the austenite decomposition into martensite. This is consistent with the amount of martensite found with medium cooling rates (below 5%).

B_F was found relatively constant (only a small decrease by about 20-30°C) through the cooling rates between 0.2°C/s and 1°C/s, and then drops suddenly to the inflection point level for higher cooling rates (decrease by around 100°C). This fall in finish transformation temperature happens while the martensite fraction strongly increases and martensite

becomes the main microstructural constituent. As a consequence, all finish transformation temperatures that have been noticed at the same level as the inflection point are in fact M_F and not B_F . The bainitic transformation may be finished at a time when the martensitic one is at a high transformation rate, leading to an indiscernible B_F on $\Delta l(T)$ curves. The decrease of the extent of the transformation realized at relatively high and stable transformation rate could be linked to the end of the bainitic transformation.

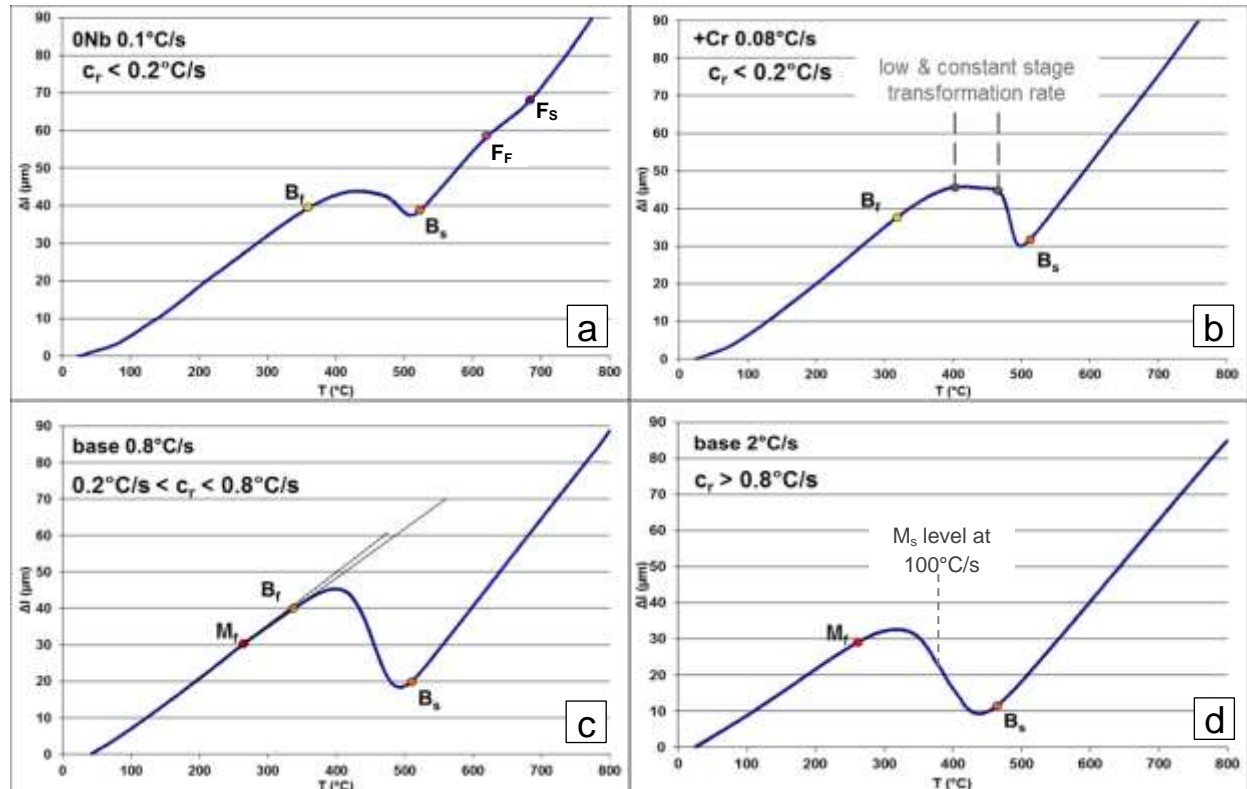


Figure 55: Typical dilatation curves for different ranges of cooling rates. $\Delta l(T)$ of (a) 0Nb 0.1°C/s, (b) +Cr 0.08°C/s, (c) base 0.8°C/s and (d) base 2°C/s.

The decrease in B_s in the same range of cooling rates (higher than 1°C/s) is less abrupt. Even if martensite has become the main microstructural constituent, as long as the austenite decomposes first into bainite, B_s does not drop heavily. As shown in Figure 55d, the $\Delta l(T)$ curve can exhibit one inflection point at 20-30°C higher than the noticed B_s . We assumed that the austenite decomposition into a little amount of upper bainite is responsible for the occurrence of such inflection point. Such little amount of upper bainite is betrayed by the presence of isolated regions with a significant amount of MA islands in the microstructure. The bainite transformation is only detected once lower bainite transformation occurs. Indeed, for these cooling rates, lower bainite is by far the main bainitic microstructure.

M_s , which value is between 350 and 400°C at 100°C/s according to the chemical composition, is never detected for the investigated cooling rates for two main reasons:

1. The final martensite fraction is too low
2. If the final martensite fraction is high enough, because of the significant amount of bainite presents prior to the first martensite occurrence, there is a wide range of carbon content in austenite, leading to a wide range of local M_s rather than a global M_s . Moreover, the first occurrence of martensite may start as the austenite decomposition into bainite is not yet finished.

3.2.2.b Definition of microstructural domains

Six different microstructural domains have been established in order to extract the effect of alloying elements on the bainitic transformation in a synthetic manner. They have been built using a transversal analysis of nearly all the obtained quantitative results (transformation

temperatures, hardness, and fractions of microstructural constituent) and some SEM qualitative observations. Figure 56 and Figure 57 exhibit the explicit limit of these domains according to the quantitative results. Figure 58 and Figure 59 exhibit LM and SEM illustrations from base chemistry in domains A, B C and D. Each domain is presented in more details in the following paragraphs. Particular cases or specific variations of a domain linked to specific chemical compositions are discussed later in section 2.2.3.

Domains 0 and A are twin domains, exhibiting a microstructure that is a mixture between coarse cementite-free upper bainite and granular bainite (both can be described as $B_3^{m,a}$ according to the Bramfitt and Speer classification), with maybe some regions of auto-tempered bainite. Domain 0 exhibits in addition a significant amount of allotriomorphic ferrite plus some rare regions of pearlite. The occurrence of allotriomorphic ferrite significantly increases the amount of MA constituent in the microstructure due to rejection of alloying elements into the surrounding austenite. B_S and B_F are lowered in these domains for the same reason.

Domain 0 extends from 0.08°C/s up to 0.2°C/s and is only seen in 0Nb, 0Mo and –Cr. As the cooling rate increases, the amounts of ferrite and MA constituent decrease fast to the benefit of bainite. Hardness also increases fast, for example, going from 299 to 328 HV30 through the domain for 0Nb (mainly due to the decrease in ferrite content).

The increase in hardness is slower across **domain A**. This domain goes from 0.08°C/s up to 0.6°C/s (case of –Cr) but generally stops near 0.2°C/s. The principal characteristic of this domain is its relatively high amount of MA constituent; higher than 10% of the microstructure. As expected, chemical compositions having higher contents in austenite stabilizers like Ni and Mn show the highest fraction of MA constituent in the absence of ferrite. On the other hand, an addition of ferrite stabilizer like Cr decreases the average fraction of MA constituent found across the microstructural domain.

In most cases, B_S is relatively stable in domain A, but B_F continues to increase with the increase in cooling rate. With the exception of –Si+Mn chemical composition, the extent of the bainitic transformation significantly increases through the domain due to an increase in driving force (i.e. cooling rate). For the same reason, the sluggishness of the transformation happens later and later (until a maximum around 80% of total transformation of the prior austenite), leading to the observed increase in B_F .

The following domain, **domain B**, goes from the end of domain A up to a cooling rate between 0.5°C/s and 1°C/s, with the exception of –Cr for which this domain goes up to approximately 1.2°C/s. Domain B exhibits both regions of coarse upper bainite microstructure and refined one according to the regions that transform first or last ($B_2^a + B_3^{m,a}$ according to the Bramfitt and Speer classification). The observed refinement is obvious and can be well appreciated using only LM (Figure 58).

The fraction of MA constituent continues to decrease, and is now less than 10% of the microstructure in every case (in fact, this is the first condition for the setting of the lower limit of domain B). No significant variations in HV30 are observed through the domain (here is the second condition) despite the decrease in MA constituent fraction, which has been found later in chapter 5, as a source of hardening. It seems that the refinement of the microstructure compensates the decrease in MA constituent fraction.

B_S and B_F decrease only slightly across **domain B**. This can be explained by two phenomena:

- The extent of the bainitic transformation has nearly reached its maximum.
- The transformation rate always begins to sluggish around 80% of the austenite decomposition.

CHAPTER 3 - EFFECT OF ALLOYING ELEMENTS ON CCT DIAGRAM

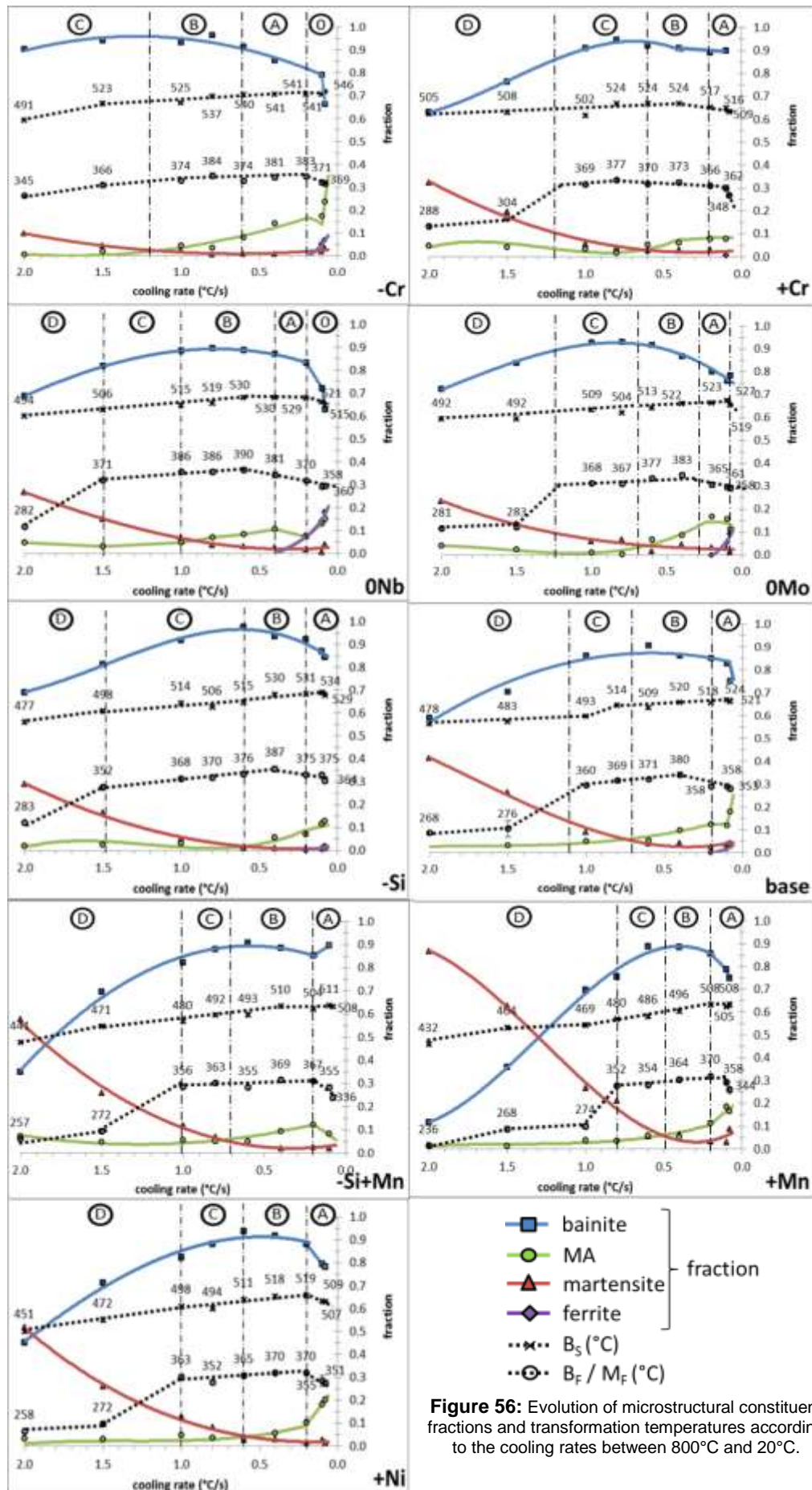


Figure 56: Evolution of microstructural constituent fractions and transformation temperatures according to the cooling rates between 800°C and 20°C.

CHAPTER 3 - EFFECT OF ALLOYING ELEMENTS ON CCT DIAGRAM

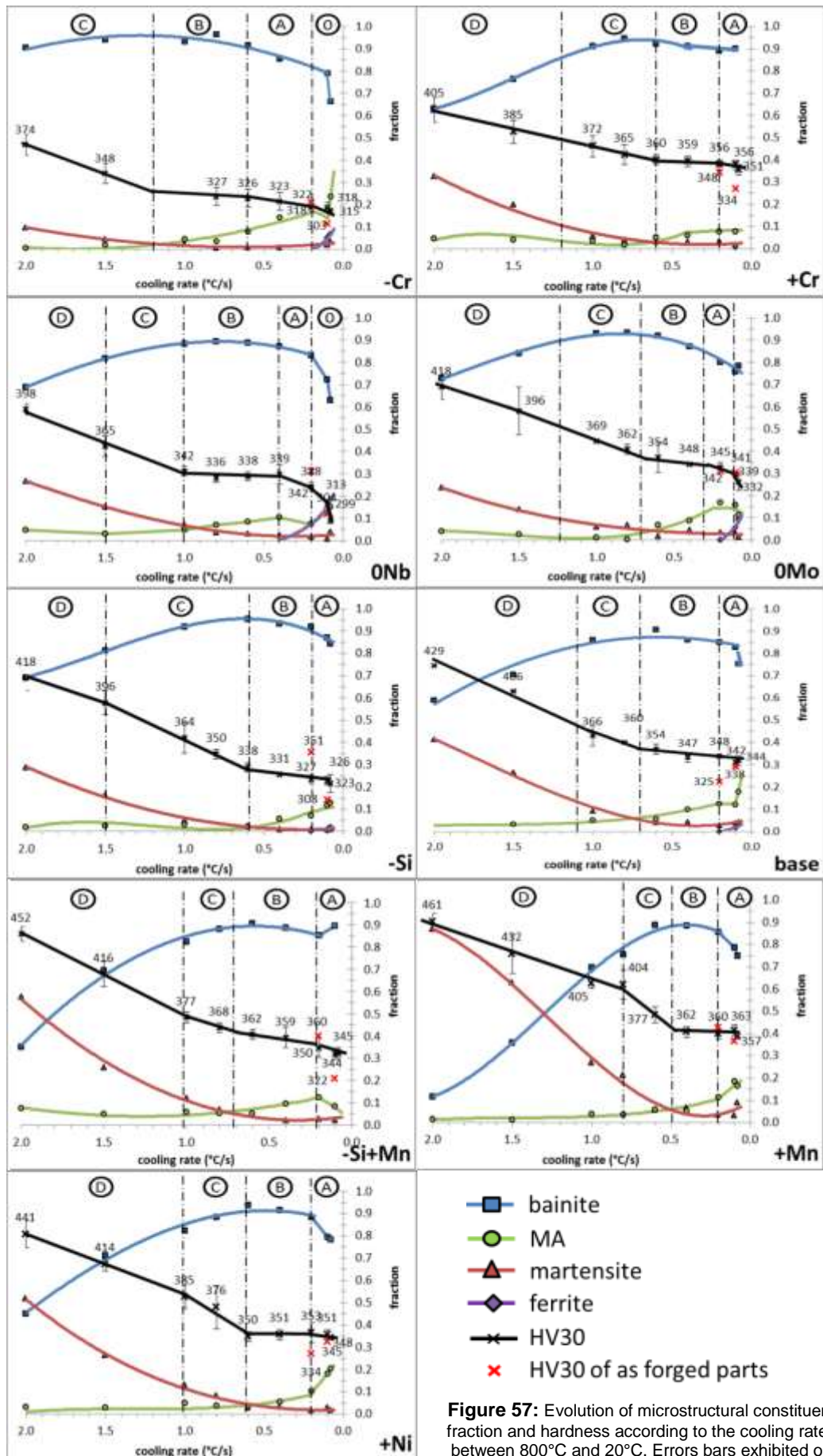


Figure 57: Evolution of microstructural constituent fraction and hardness according to the cooling rates between 800°C and 20°C. Errors bars exhibited on average hardness are the experimental scatter.

Up to this point, the martensite fraction in the different examined microstructures has been relatively stable and below 0.05. As the cooling rate is further increased, the fraction of MA constituent continues to fall down and reaches the martensite fraction level. The maximum of bainite fraction is globally reached at the same time. Here ends domain B and begins domain C.

The cooling rate limits of **domain C** are various and there is no general rule. This domain exhibits a very fine upper bainite microstructure (B_2^a). Regions, which exhibit bainitic packets obviously finer than those of previous domains (0, A and B) and without any coarse MA islands, start to be more and more frequently observed as the cooling rate rises up. Intra-lath cementite precipitation is observed using SEM, confirming the occurrence of lower bainite in such region (B_1^c according to the Bramfitt and Speer classification). In addition, these regions exhibit blocks of martensite between the packets of upper bainite. As a consequence, the fraction of martensite starts to increase whilst more and more regions of lower bainite are observed across this domain. A fast increase in HV30 is measured through the domain. Such an increase is linked to the increase in the ratio between lower bainite and upper bainite as well as the increase in martensite fraction.

B_S and B_F keep on decreasing slowly inside **domain C** for similar reasons to those in domain B. This time, the bainite fraction has passed its maximum value and starts to decrease. The sudden drop of finish transformation temperature close to the M_F level sets the end of domain C. Bainite is still the first microstructural constituent transformed from austenite so B_S does not exhibit such a violent drop of temperature and continues to decrease.

Domain D is the last domain that has been defined before the 100% martensitic domain (**domain E**) so it is the transition domain between the bainitic microstructure and the fully martensitic one. The martensite fraction increases fast at the expense of the bainite through the domain and martensite becomes the main microstructural constituent even under 2°C/s for chemical compositions such as +Ni, -Si+Mn and +Mn. Caution has to be taken on the microstructural fraction obtained in this domain as measurement errors are high (see appendix A.I.1.e). An overview of **domain E** obtained for chemical compositions that have been tested with a cooling rate of 100°C/s between 800°C and 20°C is also given on CCT diagrams.

3.2.2.c Variation of the retained austenite content through the different domains

As shown in Figure 60, all chemical compositions share the same typical evolution of the austenite fraction as a function of the cooling rate. This evolution slides toward higher cooling rates, for lower-hardenability chemistries, and inversely, slides toward lower cooling rates, for higher-hardenability chemistries.

The highest austenite content is reached every time in domain B but can be located at the beginning (+Ni, +Mn, -Cr), the middle (-Si+Mn, base) or the end (-Si, 0Mo, 0Nb and +Cr) of this domain. There are no high discrepancies between the maximum fractions reached for the different chemical compositions (0.13 to 0.15). More surprisingly, chemical compositions which promote the austenite stability (such as +Ni) do not necessarily exhibit the highest value of retained austenite.

The maximum fraction is not reached in domain A where the fraction of MA constituent is observed at its highest level, which points out that MA constituent of this domain are martensite-rich. In domain B, MA constituents are smaller, which involve higher average carbon content of them, so higher austenite content. Moreover, the refinement of the microstructure due to higher cooling rate leads to an increase in the amount of austenite films. This can also explain why chemical compositions containing more austenite stabilizer elements do not have necessarily the highest austenite content. These chemical compositions reach their maximum austenite content at the beginning of domain B, when the amount of MA constituent is still relatively high, and on the contrary, the amount of austenite films is relatively low.

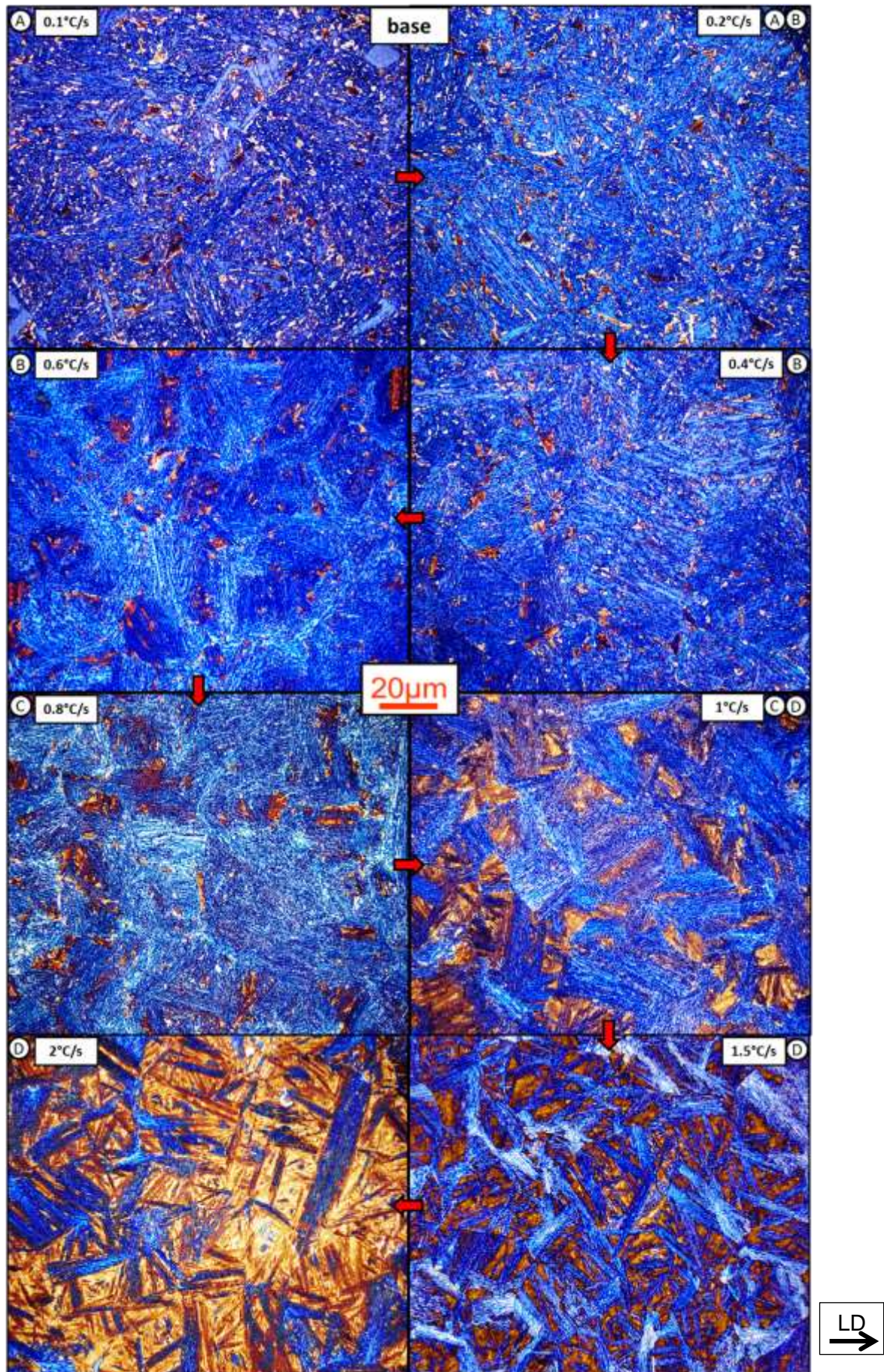


Figure 58: LM, LePera, base chemical composition for different cooling rates and microstructural domains.

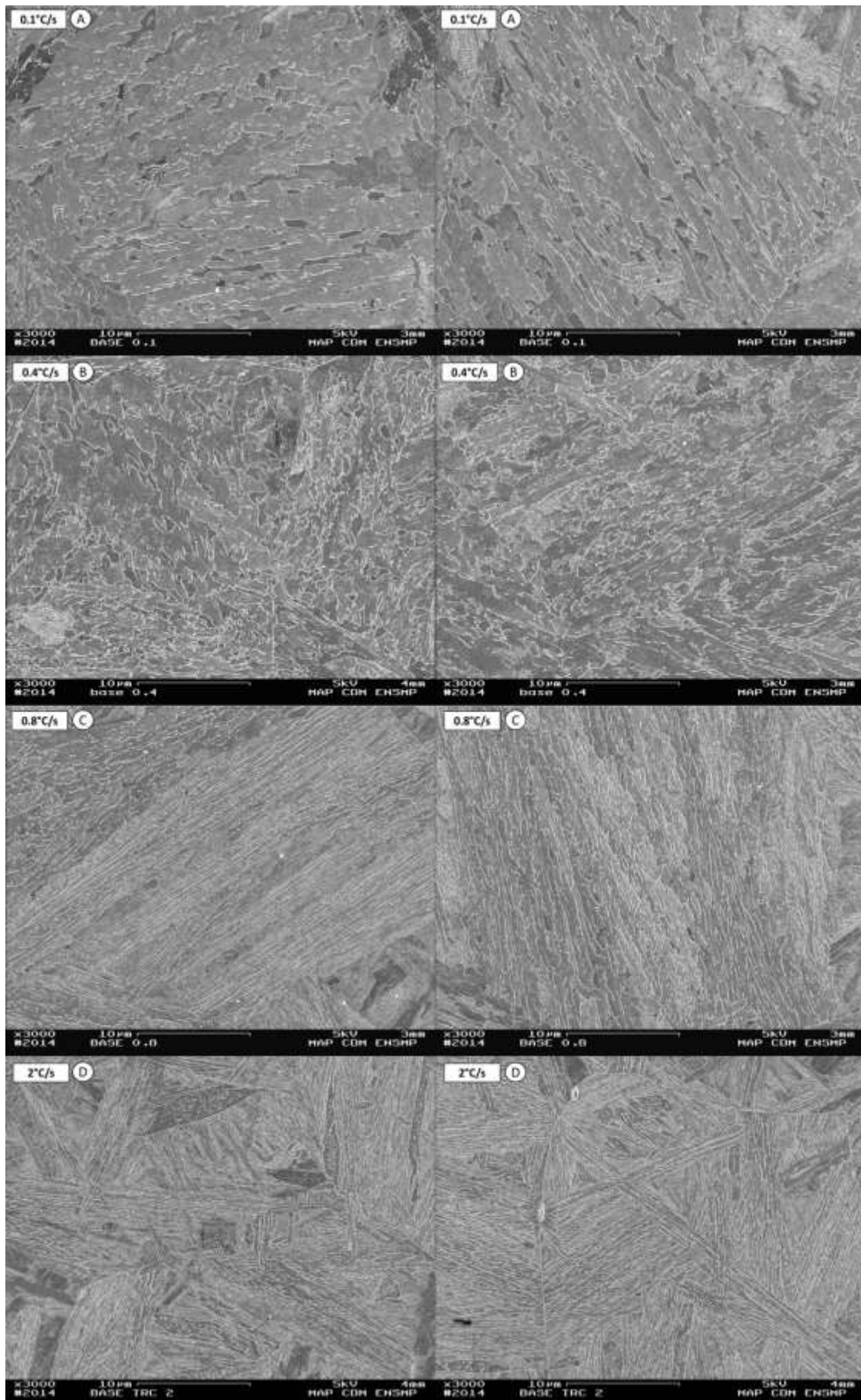


Figure 59: FEG-SEM, Nitral2%, base chemical composition for different cooling rates and microstructural domains.

3.2.3 Discussion

3.2.3.a Comparison with as-forged microstructures

As seen in Chapter 2, cooling rates of forged parts during the bainitic transformation are around 0.2°C/s and 0.1°C/s for the 35x35mm² and the 74x74mm² sections, respectively. There may be some differences in microstructure, hardness or austenite content between as forged parts and samples from CCT diagram cooled down using comparable cooling rates. Figure 61 is the compilation of graphs exhibiting the evolution of microstructural constituent fractions of every chemical composition according to the cooling rate realized for the CCT diagram. Microstructural constituent fractions of forged parts have also been plotted with red markers in this figure.

Two main differences are noticed. In 74x74mm² forged parts, a considerable amount of ferrite that can be found on dilatometric samples cooled down at 0.1°C/s is replaced by bainite (in two cases out of nine). On the other hand, 35x35mm² forged parts often exhibit a lower amount of bainite (to the benefit of martensite and, especially, of MA constituent) than dilatometric samples cooled down at 0.2°C/s (in five cases out of nine).

The cooling rate before the occurrence of bainitic transformation is 0.8°C/s and 0.4°C/s for the 35x35mm² and 74x74mm² forged parts respectively. With the exception of 0Nb 74, these cooling rates avoid the decomposition of austenite into allotriomorphic ferrite. There might be some isolated small ferritic grains (fraction much lower than 0.01) on some other forged parts with chemical compositions that are sensitive to formation of ferrite such as -Si 74, -Cr 74 or 0Mo 74, but nothing being comparable to the amount of ferrite found for -Si 0.1°C/s, -Cr 0.1°C/s or 0Mo 0.1°C/s (ferrite fractions are 0.003, 0.049, 0.055 respectively). The same goes for 0Nb 74 and 0Nb 0.1°C/s, the only change is that both present more ferrite than the other three ferrite-sensitive chemical compositions (0.020 and 0.141). Indeed 0Nb74 has the wider ferrite domain among all CCT diagrams, a domain that goes at least up to 0.4°C/s. Reasons of the occurrence of this ferritic domain will be discussed later.

A higher cooling rate can avoid the ferritic domain and leads to an increase in the extent of the bainitic transformation. In forged parts, this extent is equal to the ferrite fraction that would have been normally found if the cooling rate had been kept constant at 0.1°C/s from 800°C down to 20°C. We believe that there is no noticeable change in the temperature range of transformation. The difference between B_s at 0.4°C/s and at 0.1°C/s is no more than 9°C for every chemical composition. The difference may occur on the level of the transformation kinetics. The absence of ferrite in the case of forged parts will lead to a higher overall bainitic transformation kinetics, as it has been noticed earlier for this steel grade (Table 15).

The difference between B_s at 0.8°C/s and at 0.2°C/s, however, is noticeable and can reach 28°C for +Mn chemical composition. These differences, called “undercooling” hereafter, are shown in Table 16 and are influenced by the hardenability of each chemical composition in the investigated conditions. This effect is more appreciable when B_s values at 0.8°C/s and 0.2°C/s are corrected according to the tendency of B_s through the two neighbouring cooling rates:

$$B_s[0.2^\circ\text{C/s}]_{\text{corrected}} = \frac{B_s[0.4^\circ\text{C/s}] + B_s[0.2^\circ\text{C/s}] + B_s[0.1^\circ\text{C/s}]}{3} \quad \text{eq. 3.4}$$

$$B_s[0.8^\circ\text{C/s}]_{\text{corrected}} = \frac{B_s[1^\circ\text{C/s}] + B_s[0.8^\circ\text{C/s}] + B_s[0.6^\circ\text{C/s}]}{3} \quad \text{eq. 3.5}$$

CHAPTER 3 - EFFECT OF ALLOYING ELEMENTS ON CCT DIAGRAM

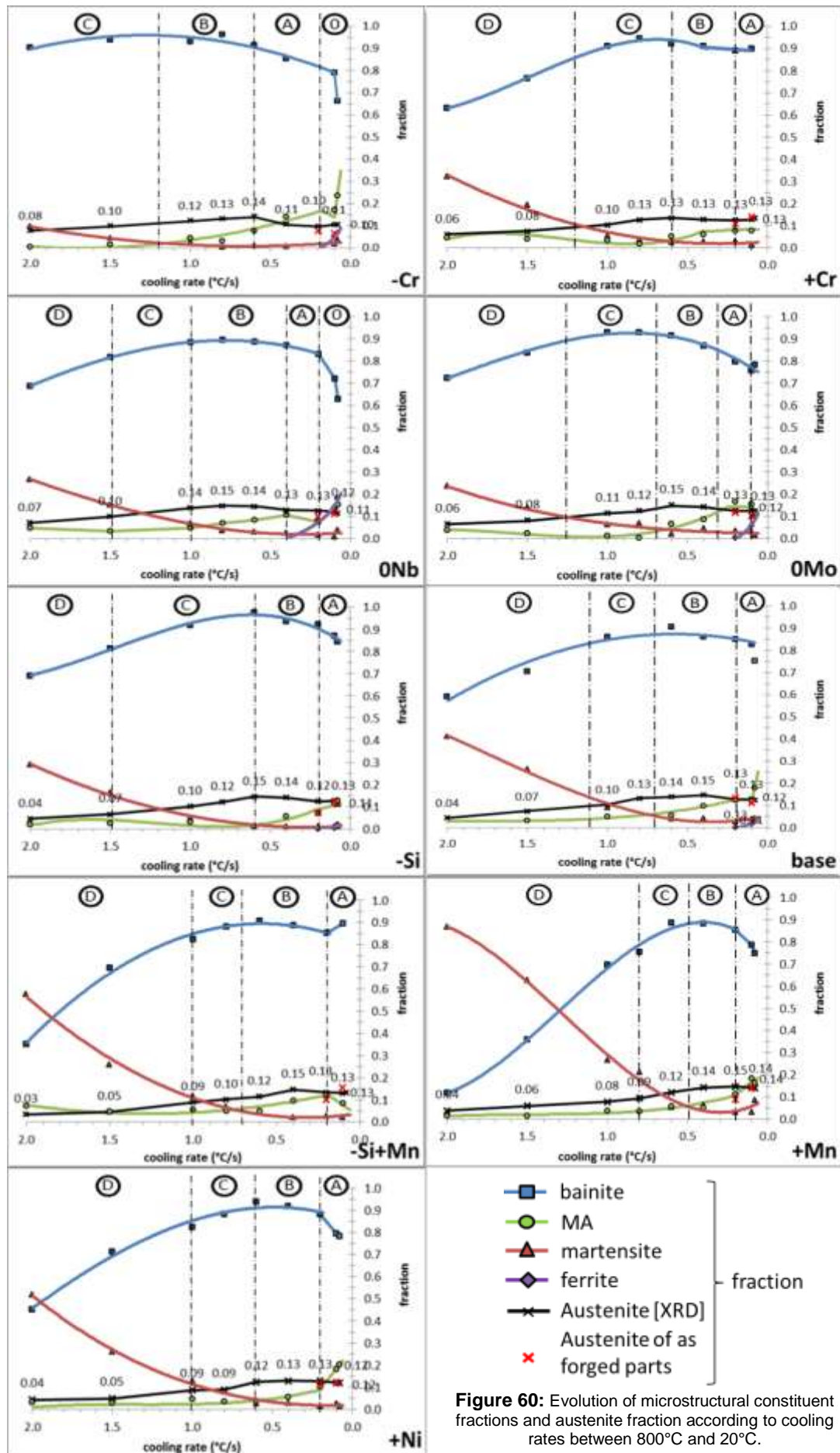


Figure 60: Evolution of microstructural constituent fractions and austenite fraction according to cooling rates between 800°C and 20°C.

CHAPTER 3 - EFFECT OF ALLOYING ELEMENTS ON CCT DIAGRAM

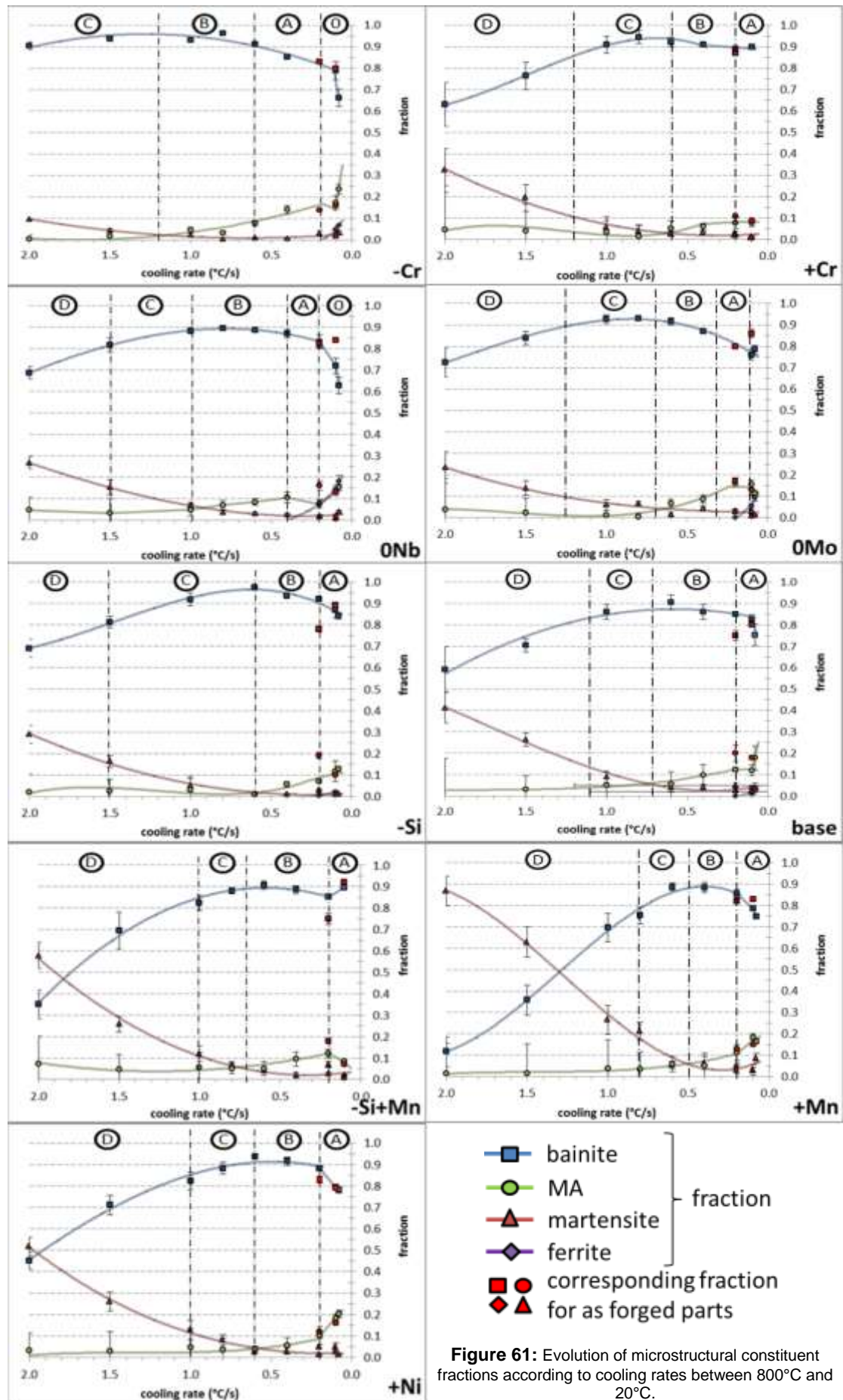


Figure 61: Evolution of microstructural constituent fractions according to cooling rates between 800°C and 20°C.

	Experimental $B_S[0.2^\circ\text{C/s}] - B_S[0.8^\circ\text{C/s}]$ in $^\circ\text{C}$	$B_S[0.2^\circ\text{C/s}] - B_S[0.8^\circ\text{C/s}]$ corrected according the tendency of B_S through the neighbouring cooling rates in $^\circ\text{C}$	Bainite fraction [CCT] – Bainite fraction [as-forged]
+Mn	28 \pm 5	26 \pm 6	0.04 \pm 0.03
+Ni	25 \pm 7	14 \pm 6	0.05 \pm 0.03
-Si	25 \pm 4	20 \pm 5	0.14 \pm 0.02
0Mo	19 \pm 5	15 \pm 5	<0.01 \pm 0.02
-Si+Mn	12 \pm 4	20 \pm 5	0.10 \pm 0.04
0Nb	10 \pm 5	6 \pm 4	0.01 \pm 0.05
Base	4 \pm 5	15 \pm 4	0.10 \pm 0.03
-Cr	4 \pm 6	7 \pm 6	X \pm X
+Cr	-7 \pm 5	3 \pm 6	0.02 \pm 0.03

Table 16: Difference in B_S at 0.8°C/s and 0.2°C/s . X quantification data are still missing for $-\text{Cr } 0.2^\circ\text{C/s}$.

The decrease in the bainitic transformation extent is believed to be due to the decrease in the temperature range of transformation. Forged parts might exhibit a higher transformation rate at the very beginning of the bainitic transformation than CCT diagram samples (due to a lower value of B_S) but nothing that can effectively overcome the decrease in the temperature range of transformation.

However, the assumptions proposed previously in concern of the difference in microstructural constituent fractions cannot explain ones that are apparently encountered in hardness. Average difference in hardness between a $74 \times 74 \text{ mm}^2$ forged part and the corresponding 0.1°C/s CCT samples is 12 HV30, but can reach 22 HV30 in the case of +Cr and $-\text{Si}+\text{Mn}$. Measurement errors on hardness value are in average ± 7 and ± 6 HV30 for forged parts and CCT samples respectively, so most of the differences that have been found can be considered in fact as negligible.

With the exception of 0Mo 74, average hardness values of $74 \times 74 \text{ mm}^2$ forged parts are always lower than the ones of corresponding CCT samples. This is especially surprising in the case of 0Nb where hardness was expected to exhibit a significant increase, as 12% of allotriomorphic ferrite is replaced by upper bainite. This might indicate a slightly extended auto-tempering in the case of forged parts, perhaps due to a noticeable difference between controlled cooling (by both induction and gas flow) of a small dilatometric sample and natural cooling of a massive forging bar (with an obvious effect of latent heat release during the austenite-to-bainite transformation).

In the case of $35 \times 35 \text{ mm}^2$ forged parts, the average difference in hardness with corresponding 0.2°C/s CCT samples is again 12 HV30. This time, these differences can be positive as well as negative. No systematic increase in hardness has been noticed for forged parts that exhibit higher MA constituent fraction than corresponding dilatometric sample. As will be shown in Chapter 5, base 35 exhibits an abnormally low hardness value (325 HV30), which is 23 HV30 lower than base 0.2°C/s . No reasons have been found for these non-reproducible differences.

The last studied parameter is the austenite content. Austenite fractions of forged parts are reported in Figure 60 with the ones of CCT samples. Only slight differences are found, the average difference is 0.02, which correspond to the standard errors linked to the sigmometer in these characterization conditions (see appendix A.II.4). Only two combinations have a difference larger than 0.03, these ones are $-\text{Si } 35$ and $+\text{Mn } 35$ (-0.05 and -0.06 respectively), which are also two combinations that exhibit relatively high error measurement as reported in Chapter 2 (Section 2.4.3, Table 10). In a general way, austenite fractions of $35 \times 35 \text{ mm}^2$ forged parts have been found lower than those of 0.2°C/s CCT samples. This is consistent with a higher amount of coarse MA constituent islands, linked to undercooling.

3.2.3.b Influence of the micro-alloying elements

As shown in Figure 62, the ferritic domain is wider for the two chemical compositions without molybdenum or niobium. No ferrite can be seen at cooling rates higher than 0.1°C/s for the base chemical composition whereas small and isolated ferrite grains can still be observed for cooling rates higher than 0.2°C/s and 0.4°C/s in chemical compositions without molybdenum and niobium respectively. As expected, F_s is increased by 20 to 30°C by the removal of niobium. Indeed, the amount of niobium that remains in solid solution, around 19% of the nominal composition following the results of selective dissolution (section 2.4.4), is believed to easily lead to such a decrease (according to Figure 20 after [89], section 1.3.2.a). The removal of molybdenum, on the other hand, has no noticeable effect on this temperature. There is no significant change in Ar_1 between the different chemical compositions at 0.08°C/s. However, as the cooling rate increases, Ar_1 increases more or less rapidly according to the different chemical compositions.

Using light microscopy and SEM observation, recurrent precipitation of relatively thin (less than 200nm) but long (up to 5µm) particles have been observed in the middle of the ferrite grain. As shown in Figure 63, these particles are elongated along the prior austenite grain boundaries. This indicates that they were present before the austenite decomposition into ferrite. We believe that these particles are carbides. The carbide precipitation has created a local depletion in carbon content in the surrounding matrix, leading to the nucleation of ferrite along the prior austenite grain boundary. This precipitation, and thus, the presence of ferrite, is more frequently observed in 0Mo and especially 0Nb, i.e. in absence of two strong carbide formers, which points out that carbon tends to precipitate with alloying elements other than Mo and Nb. The perfect candidate seems to be boron.

As seen in chapter 1, grain boundary segregation of boron atoms has a strong capacity to delay or avoid the ferrite transformation by several mechanisms. This effect decreases as soon as the boron precipitates. Furthermore, coarse boron carbides have been noticed to be allotriomorphic ferrite precursors. No experimental evidences, which proved that the observed carbides are indeed boron carbides, are available yet. However, these particles are very similar to those described by Taylor [77] in his study on the segregation and precipitation behaviour of boron in 0.2C-0.6Mn-0.5Mo (in wt%) steel containing 50ppm of boron. For such steel, iron borocarbide particles ($Fe_{23}(B,C)_6$) start to precipitate during air-cooling from 1260°C down to 860°C (8°C/s), but obtain this specific morphology only after 5000s of holding at 860°C (because of the Mo content, which is more than twice the total amount of Mo, Nb and Ti in our steels).

We can assume that the occurrence of the ferrite transformation is due to this $Fe_{23}(B,C)_6$ precipitation. For our steel family, from the analysis of selective dissolution residues (see in chapter 2), around 81% of the niobium precipitates but only 6% of molybdenum does and thus, whatever niobium being present in the chemical composition or not. So, a removal of niobium from chemical composition leads to more $Fe_{23}(B,C)_6$ precipitation than the removal of molybdenum. So, as both niobium and molybdenum are added in the same amount (in wt%), niobium seems more effective than the molybdenum to protect boron. The molybdenum effect on decreasing the $Fe_{23}(B,C)_6$ precipitation might more be due to its capacity to decrease carbon diffusivity in austenite [112] rather than to its capacity to decrease the average carbon content in austenite by the precipitation of Mo_2C clusters in austenite.

The amount of transformed ferrite may both be linked to the number density of this kind of particle as well as to the sample chemical composition (which affects nucleation and transformation kinetics). The size of the particle may be also a factor as the particle may act directly as ferrite nucleation site (incoherent interface). Bigger particles means larger depleted regions. However, we cannot conclude whether this precipitation enhances the ferritic transformation more than does the removal of boron from the chemical composition.

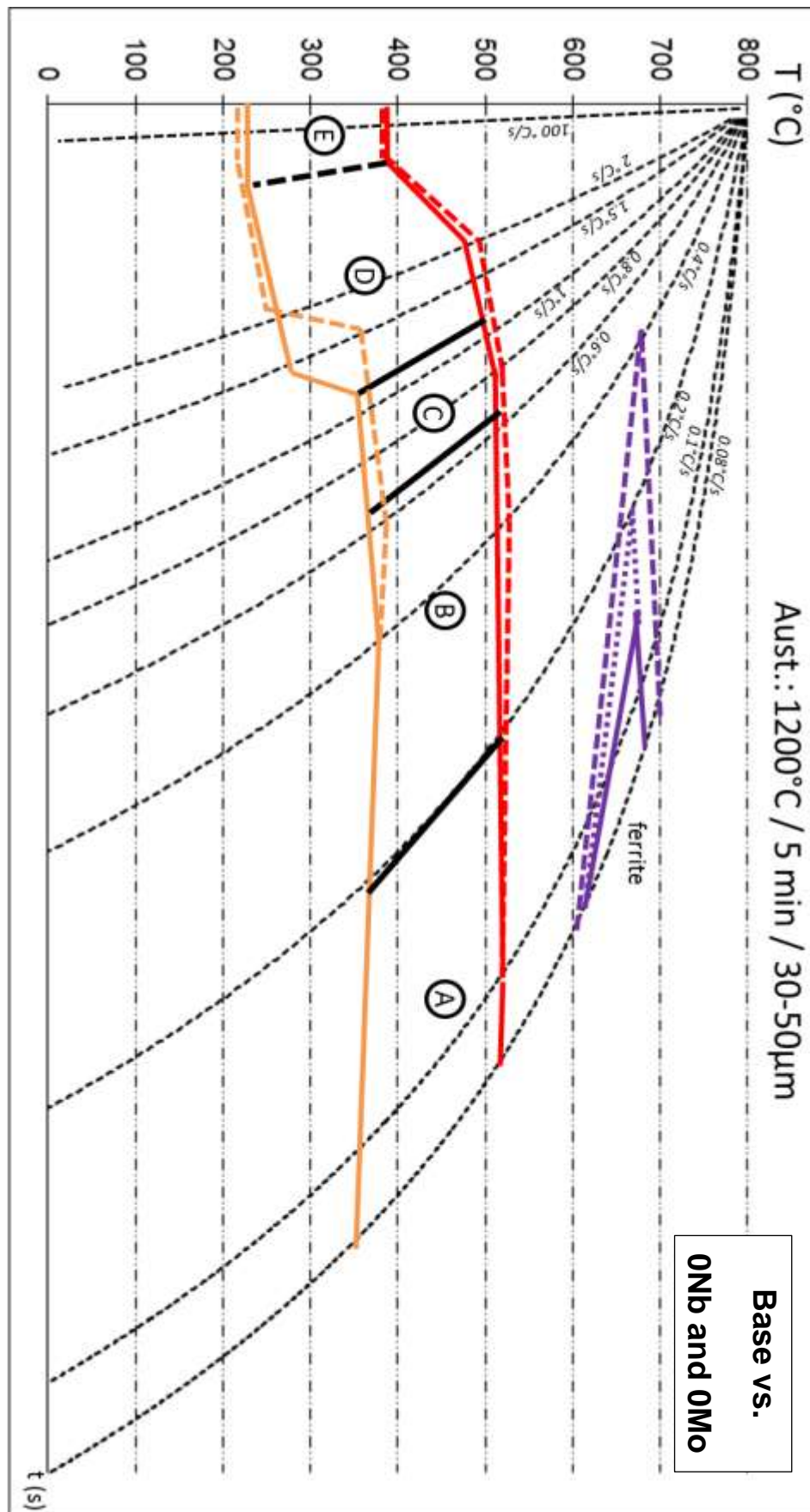


Figure 62: Schematic CCT diagrams of base (continuous line), 0Mo (dotted lines), and 0Nb (dashed lines). The only noticeable difference between base and 0Mo is the ferrite domain. Microstructural domain limits of base are shown in black.

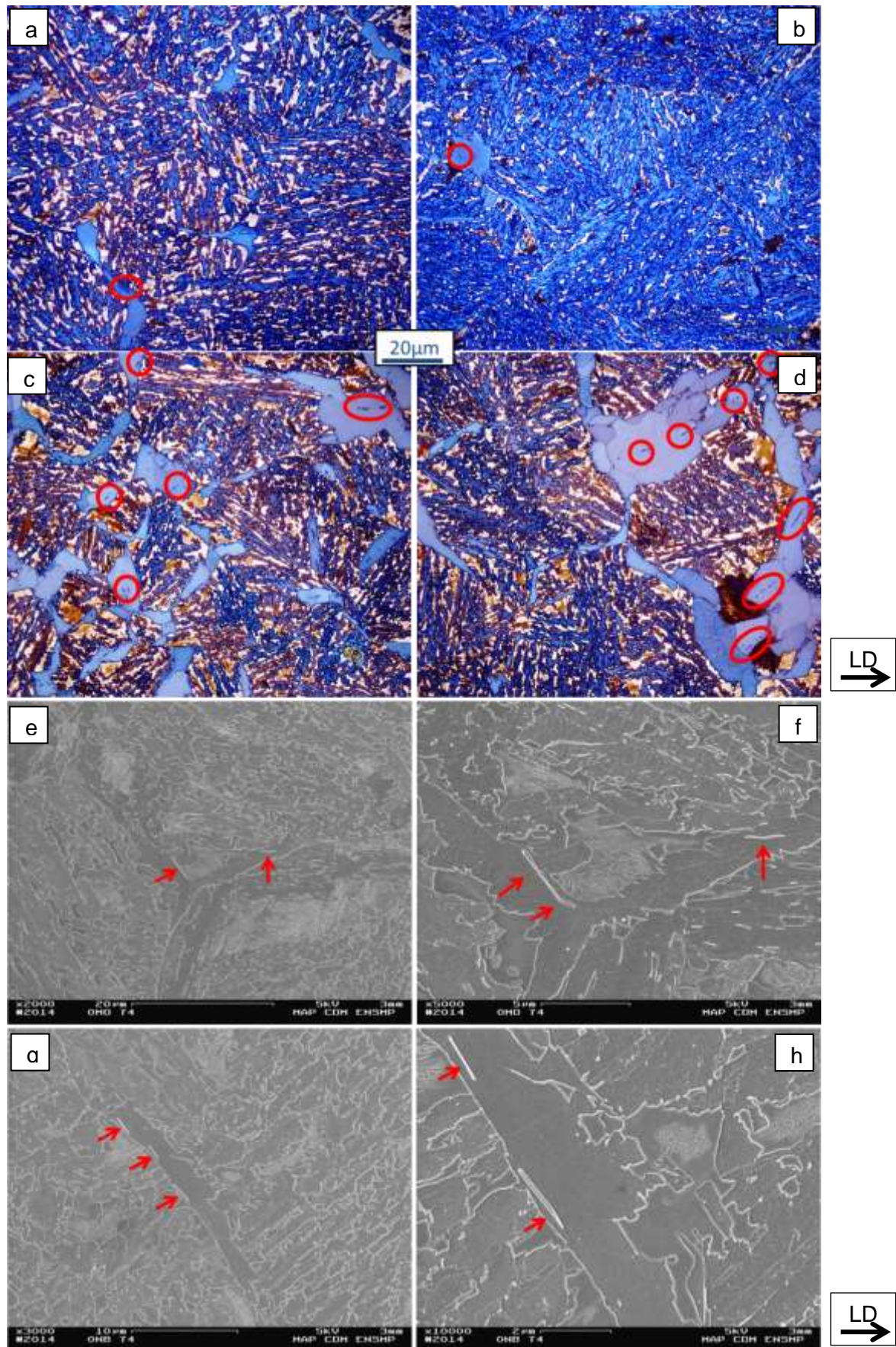


Figure 63: Precipitation in allotriomorphic ferrite. LM, x500, LePera etching, CCT diagram sample, 0.08°C/s, (a) -Cr, (b) -Si, (c) and (d) 0Nb. Precipitates are encircled in red. SEM, Nital 2%, various magnifications, (e) to (h) 0Nb 74 forged part. Red arrows are showing the precipitates.

CHAPTER 3 - EFFECT OF ALLOYING ELEMENTS ON CCT DIAGRAM

This boron precipitation may happen only because of exceeding boron segregation at austenite grain boundary with regards to the initial Mo and Nb content, as boron precipitation even occurs with the presence of both alloying elements in nominal composition. In other regions, “free” boron may always play its role of delaying the ferrite transformation, as the ferrite layer is far from covering all primary austenite grain boundaries even in the least favourable case (0Nb 0.08°C/s).

Such precipitation, and thus ferrite, has not been observed for cooling rates higher than 0.4°C/s. Of course, it would have been less evident to be seen in a bainitic matrix than in a ferritic matrix using SEM and LM. However, a noticeable precipitation should have been seen, if any, owing to the number of microstructural observations that has been realized. So it seems that this precipitation is avoided with cooling rates higher than 0.6°C/s between 950°C and 550°C. So every observation that will be realized for cooling rates higher than 0.4°C/s may only concern the effect of molybdenum and niobium in solid solution (and not an indirect effect of boron precipitation).

For cooling rates below 0.2°C/s, there is no noticeable difference on B_S or B_F due to the ferrite transformation. However, beyond 0.2°C/s (0.4°C/s and more), when no more ferrite is seen, B_S and B_F are between 10 and 20°C higher without niobium. The abrupt drop of B_F also happens at higher cooling rates. As for the ferrite transformation, the increase in transformation temperature is due to the removal of the solute-drag effect induced by niobium in solid solution. On the other hand, no recurrent noticeable difference in B_S or B_F (>10°C) are seen between 0Mo and base whatever the cooling rate.

All microstructural domains are moved to higher cooling rates in the case of 0Nb. High fraction of bainite (0.8) with relatively high pure austenite content (>0.10) are reachable between 0.4°C/s and 1.5°C/s (domains B+C). Hardness is more constant but slightly lower (due to higher transformation temperature) than for the base and 0Mo across domain B (336-342 against 348-354 and 345-354 HV30 for base and 0Mo respectively). However, this hardness level is not expected to provide 1100MPa in tensile strength (see eq. 5.1 in chapter 5). In addition, hardness drops rapidly for cooling rates lower than 0.4°C/s, as soon as the ferrite transformation occurs. Niobium can be thus removed from chemical composition only if the cooling rate between the end of forging and the bainitic transformation is higher than 0.4°C in the bulk of the biggest section of the targeted forged part.

The extent of the bainitic transformation in domains B and C has always been found higher in 0Mo and 0Nb chemical compositions than in base one. As shown in Table 17, this is due to higher transformation kinetics.

tag	F(T)/s			
	1°C/s	0.8°C/s	0.6°C/s	0.4°C/s
base	1.27	1.05*	0.82	0.63
0Mo	1.37	1.25	1.03	0.76
0Nb	1.46	1.19	1.05	0.70

Table 17: Average transformation rate during relatively high and constant stage of the bainitic transformation.* For this calculation, bainite and martensite fraction have been evaluated according to their tendency through the two neighbouring cooling rates as proper quantification at 0.8°C/s for base chemistry was missing.

Despite the increase in the bainite fraction compared to the base chemistry, no significant change is found in austenite content or in hardness. More profuse austenite films might be present in the 0Mo microstructure than in the base microstructure, leading to similar austenite content despite a lower MA constituent fraction. In concern of hardness, it might be linked to the average carbon content of MA constituent, which decreases together with their hardness with increasing their average size.

Lower martensite fractions are found for 0Nb and 0Mo than for base at relatively high cooling rate. In the view of transformation temperatures and hardness, martensite fractions may have been under-evaluated in the case of 0Mo (real martensite fractions may have been closer to the ones of base). M_S and M_F do not seem to be affected by the niobium content. M_S and M_F are 7°C and 11°C lower than for the base chemistry respectively. This temperature gap can be considered as negligible in view of the error measurements ($\pm 5^\circ\text{C}$). Indeed, gas-quench (100°C/s) generates noticeable noise and artefacts on dilatometric curves.

3.2.3.c Influence of chromium

Figure 64 shows CCT diagrams of base, -Cr and +Cr chemistries. Addition of chromium suppressed any noticeable occurrence of allotriomorphic ferrite. Nevertheless some small and isolated ferrite grains can always be encountered down to 0.1°C/s due to the occurrence of some iron boro-carbide particles (but the ferrite fraction is still much lower than 0.01). On the other hand, the removal of some chromium from solid solution promotes the occurrence of ferrite, which was expected. No noticeable influence on both F_S and F_F has been seen at 0.08°C/s but the fraction of ferrite is higher (0.067 against 0.027) with less chromium in the steel chemical composition. Ferrite grains can be seen down to 0.4°C/s in -Cr. Once again, the difference in ferrite fraction may also be linked (in addition of the intrinsic effect of Cr) with the amount of boron precipitation. Chromium, as niobium and molybdenum, is a strong carbide forming element. So it is probable that a decrease in chromium content leads to additional precipitation of $\text{Fe}_{23}(\text{B,C})_6$ and thus higher ferrite content. However, no Cr-containing precipitation has been noticed in carbon replicas (see chapter 2) so Cr does not seem to precipitate in our case. Cr addition has also been found to be able to delay iron carbide precipitation as cementite [58] but no such effect on $\text{Fe}_{23}(\text{B,C})_6$ precipitation has been reported in literature. We do not know the impact of chromium on niobium or molybdenum precipitation either.

The decrease in chromium content has an obvious effect on B_S and B_F . The value of B_S is at least 20°C higher through the bainitic domain and exhibits a very stable value for cooling rates lower than 0.8°C/s (around 540°C). The difference in B_F varies by up to 20°C according to the cooling rate (before the B_F drop). All the microstructural domains are shifted toward higher cooling rates. Domain D is not even reached for the investigated cooling rates. Domain A, which exhibits a coarse upper bainite microstructure with regions of granular (and maybe some auto-tempered) bainite, lasts up to 0.6°C/s. The difference with the base chemistry, which at this cooling rate is at the end of domain B (a mix of fine and coarse upper bainite microstructure), is obvious and it can be well observed in Figure 65a to Figure 65d. Some coarse upper bainite packets are highlighted in red. These packets are formed at the very beginning of the bainite transformation. An apparent lath width of several micro-meters can be observed. As shown in Figure 65e to Figure 65f, some packets only exhibit few secondary phases and hardly observable lath-like structure. This very coarse microstructure provides low hardness level (between 330 and 320 HV30).

The extent of the bainitic transformation is very high in domains B and C (average of 0.93 for cooling rates between 0.6°C/s and 2°C/s), which was expected, as chromium is known to decrease the extent of the bainitic transformation [58]. However, despite the highest B_S and the reduced chromium content, the transformation rate during the steady-state stage of transformation shows no increase for cooling rates between 0.6°C/s and 1°C/s. The higher extent of bainitic transformation is only due to the higher difference in B_S and B_F . As all other chemical compositions exhibit a drop of B_F for cooling rates higher than 1°C/s, this time, transformation rates of -Cr are found to be the highest.

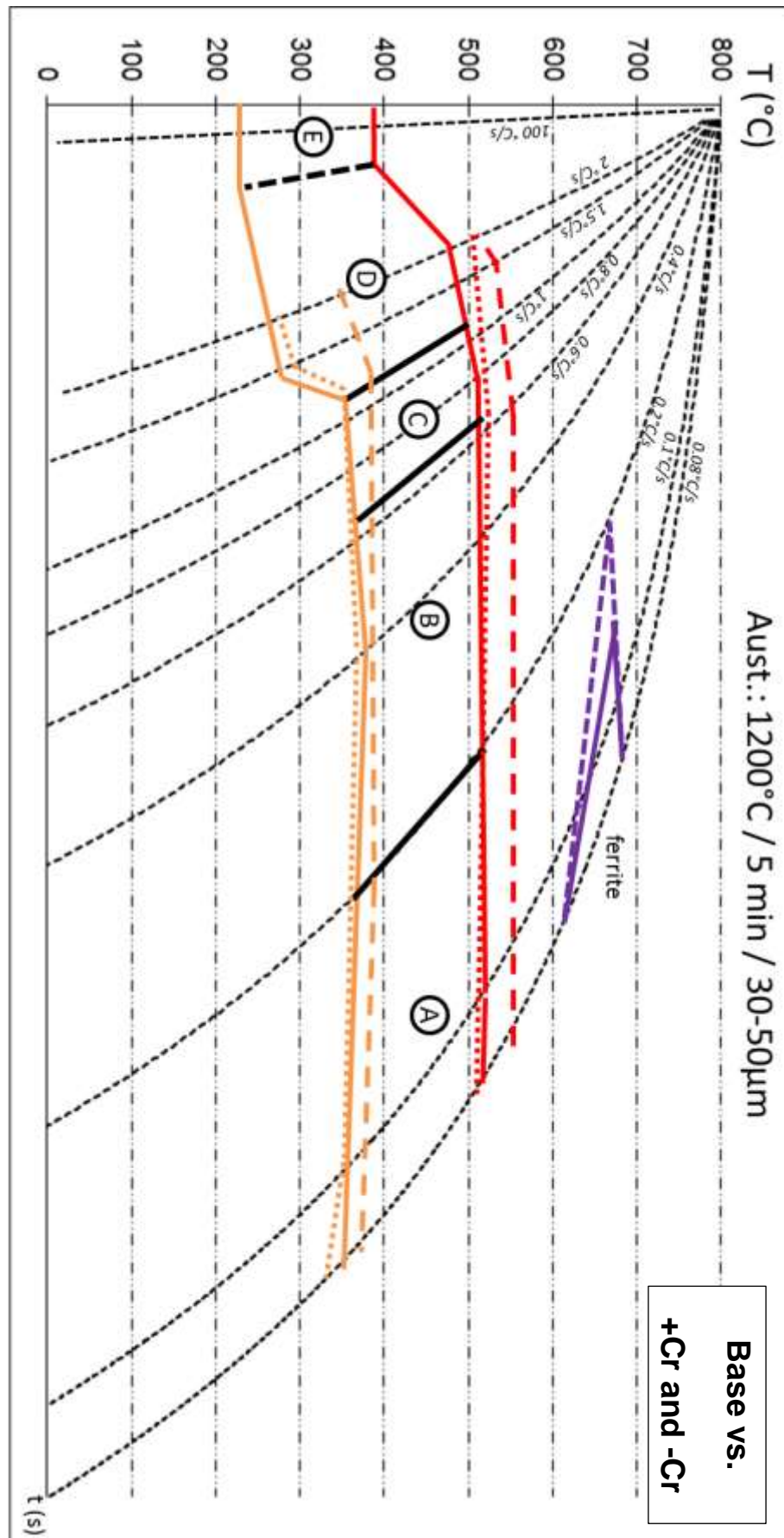


Figure 64: Schematic CCT diagrams of base (continuous line), +Cr (dotted lines), and -Cr (dashed line). No ferrite domain for +Cr. Microstructural domain limits of base are shown in black.

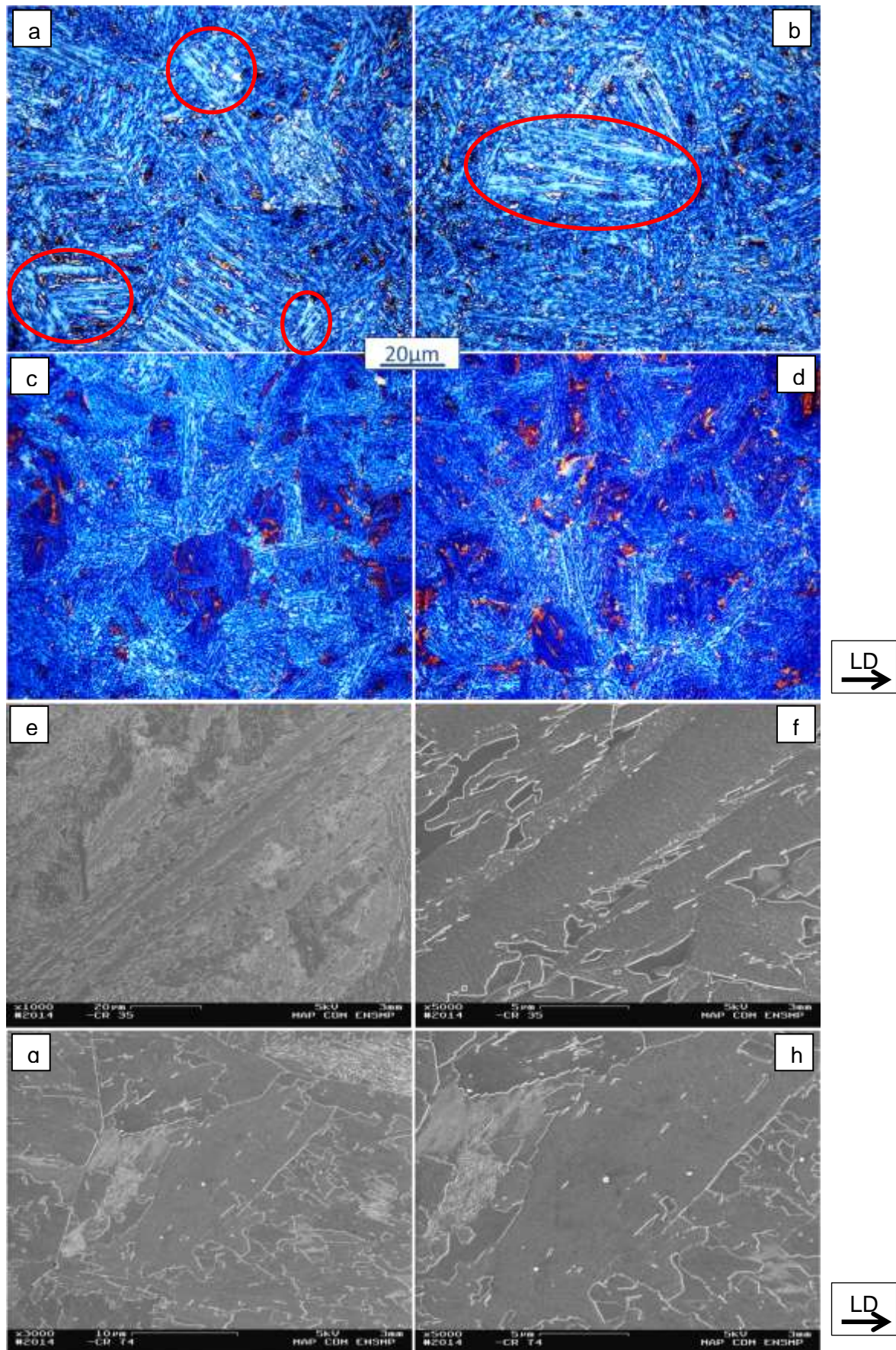


Figure 65: Coarse upper bainite microstructure of -Cr compared to base. LM, x500, LePera etching, CCT diagram samples, 0.6°C/s, (a) and (b) -Cr, (c) and (d) base. Some coarse upper bainite packets are highlighted in red. SEM, Nital 2%, various magnifications, forged parts (e) to (f) -Cr 35, (g) to (h) -Cr 74.

CHAPTER 3 - EFFECT OF ALLOYING ELEMENTS ON CCT DIAGRAM

An increase in chromium content does not lead to any further decrease in B_S or B_F as compared to the base chemistry. On the contrary, B_S tends to be stable even for relatively high cooling rates. B_F shows its usual drop due to the increase in martensite content for cooling rates higher than 1°C/s . Both combined lead to very surprising microstructures in domain D. Unlike for the other chemical compositions, there is still a noticeable amount of upper bainite that is present in this domain D with the increase in chromium content. In fact, this higher amount of upper bainite leads to the detection of B_S at the level of the inflection point described earlier in Figure 55d.

This is highlighted when considering transformation rates that have been calculated through the first 20% of the transformation. As shown in Table 18, these ones are much lower for +Cr than for all other chemical compositions. This upper bainite is easily observable using LM because of the presence of MA islands. Some examples are shown in Figure 66. This microstructure may exhibit high local variation of hardness as upper bainite, lower bainite, auto-tempered martensite and martensite coexist.

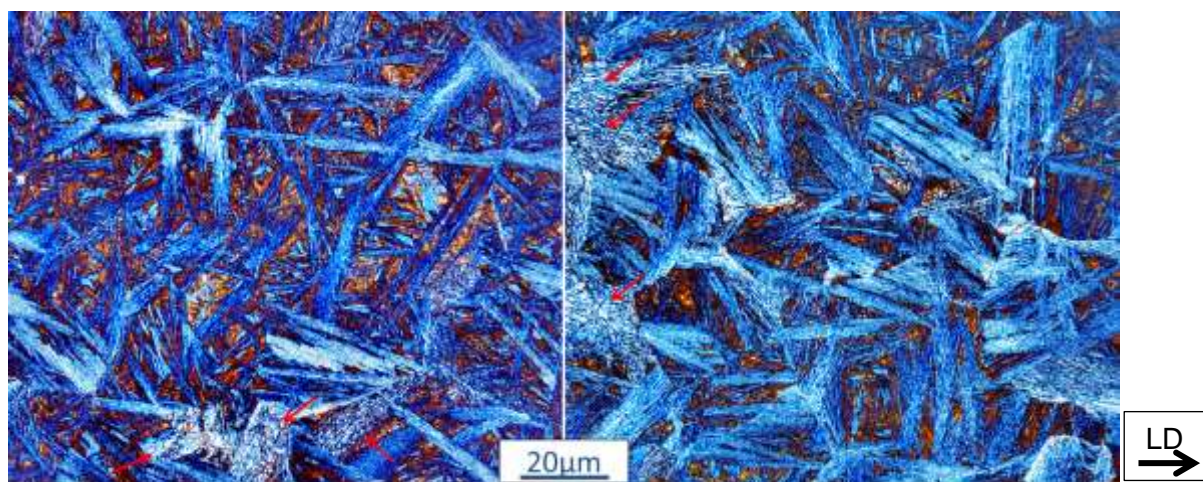


Figure 66: LM, LePera etching, +Cr 2°C/s . Red arrows shows upper bainite.

tag	F(T)/s	
	2°C/s	1.5°C/s
+Cr	0.75	0.64
base	0.84	0.78
average*	0.90	0.76

Table 18: Transformation rate through the first twenty percents of the transformation. Average values have been calculated over all chemical compositions that are in domain D for these cooling rates with the exception of +Cr.

In the same way as Han et al. [59] found that addition of chromium leads to the increase in coarse granular bainite fraction in acicular ferrite/granular bainite microstructure, we found here that chromium addition increases the occurrence of upper bainite in lower bainite/martensite microstructure. However, we did not notice any increase in coarse upper bainite or granular one in all other microstructural domains, as B_S does not increase at lower cooling rates. Due to absence of the ferritic transformation, the fraction of bainite stays relatively stable between 0.08°C/s and 1°C/s (between 0.89 and 0.91 with the exception of 0.95 found at 0.8°C/s).

The hardness follows the same trend. The difference in hardness is only of 21HV30 between 0.08°C/s and 1°C/s , going from 351 to 372 HV30. As bainite fractions are barely the same, this is mainly due to microstructural refinement. In addition, the austenite fraction stays constant at 0.13 in this range of cooling rates. So an increase in chromium content may allow

the realization of forged components exhibiting noticeable changes in section without creating extensive gradients in mechanical properties (at least, as the cooling rate does not exceed 1°C/s during bainite transformation). Nevertheless, even for higher cooling rates, hardness does not exhibit the same increase as for other chemical compositions due to the presence of a noticeable amount of upper bainite. As an example, the difference in hardness between 2°C/s and 0.08°C/s for +Cr is only 49 HV30 whereas it reaches 87 HV30 for the base chemistry.

3.2.3.d Influence of nickel

As shown in Figure 67, the addition of nickel suppresses the ferrite domain. Base and +Ni share very close values of B_S and B_F through the bainitic domain. The only difference between both chemical compositions is in the limits of microstructural domains C and D. These ones are shifted slightly toward lower cooling rates for the +Ni chemistry. Indeed, the martensite fraction starts to increase at lower cooling rates with addition of nickel. The decrease in B_S as a function of cooling rate is higher in domain D for this one. M_S values are 386°C and 360°C for base and +Ni respectively.

The average bainite fractions in domains B and C are slightly higher for +Ni than for the base chemistry (0.90 vs. 0.88) but are reached at lower cooling rates (0.2°C/s to 0.8°C/s instead of 0.4°C/s to 1°C). So, the bainite transformation does not seem to be further limited by the addition of nickel in this cooling range. No particular and recurrent effect on transformation kinetics has been noticed neither. However, at lower cooling rates (0.1°C/s and 0.08°C/s), MA constituent fraction reaches nearly 0.2, which is one of the highest levels measured at these cooling rates, and this, without any ferrite occurrence that would stabilize further austenite by alloying element enrichment before the bainitic transformation. The hardness level is only slightly higher in domains A and B with the addition of nickel. As the martensite fraction rises in domain C, the difference in hardness increases between both chemical compositions.

3.2.3.e Influence of silicon and manganese

As shown in Figure 68, a decrease in silicon content leads to a reduction of the ferritic domain with a slight decrease in F_S . This experimental observation is in agreement with literature [47;49]. It can be only due to the effect of silicon in solid solution but several other interactions can occur at this level. It has been seen earlier in chapter 1 that silicon has also the tendency to promote Nb precipitation by increasing the niobium diffusivity in austenite [109]. Thus, we expect that a decrease in silicon content leads to a slight additional amount of $\text{Fe}_{23}(\text{B,C})_6$ and thus, of ferrite. In addition, manganese segregation at grain boundaries is known to be enhanced with silicon [49]. A decrease in silicon can thus lead to an increase in F_S due to a lowered effectiveness of manganese to delay austenite decomposition into ferrite. Both of these hypotheses would go against the observed tendency. On the contrary, silicon may also play a role directly on boron precipitation by delaying the precipitation and/or slowing down the growth kinetics of such iron-rich carbide (as it can do for cementite). More coarse and incoherent $\text{Fe}_{23}(\text{B,C})_6$ would be present in the microstructure by decreasing the silicon content. Less effective boron segregation along primary austenite grain boundaries would slightly increase F_S . However we do not have any experimental evidences to attest the occurrence of these phenomena.

The values of B_S and B_F are slightly over the ones of base chemistry from 0.08°C/s to 0.4°C/s (average of $+10^{\circ}\text{C}$). The effect of silicon goes this time in the other direction compared to the austenite to ferrite transformation. Perhaps, due to lower transformation temperature (and/or a different transformation mechanism), some previously enounced interactions might become more dominant, as the Mn segregation at boundaries enhancement by silicon for instance.

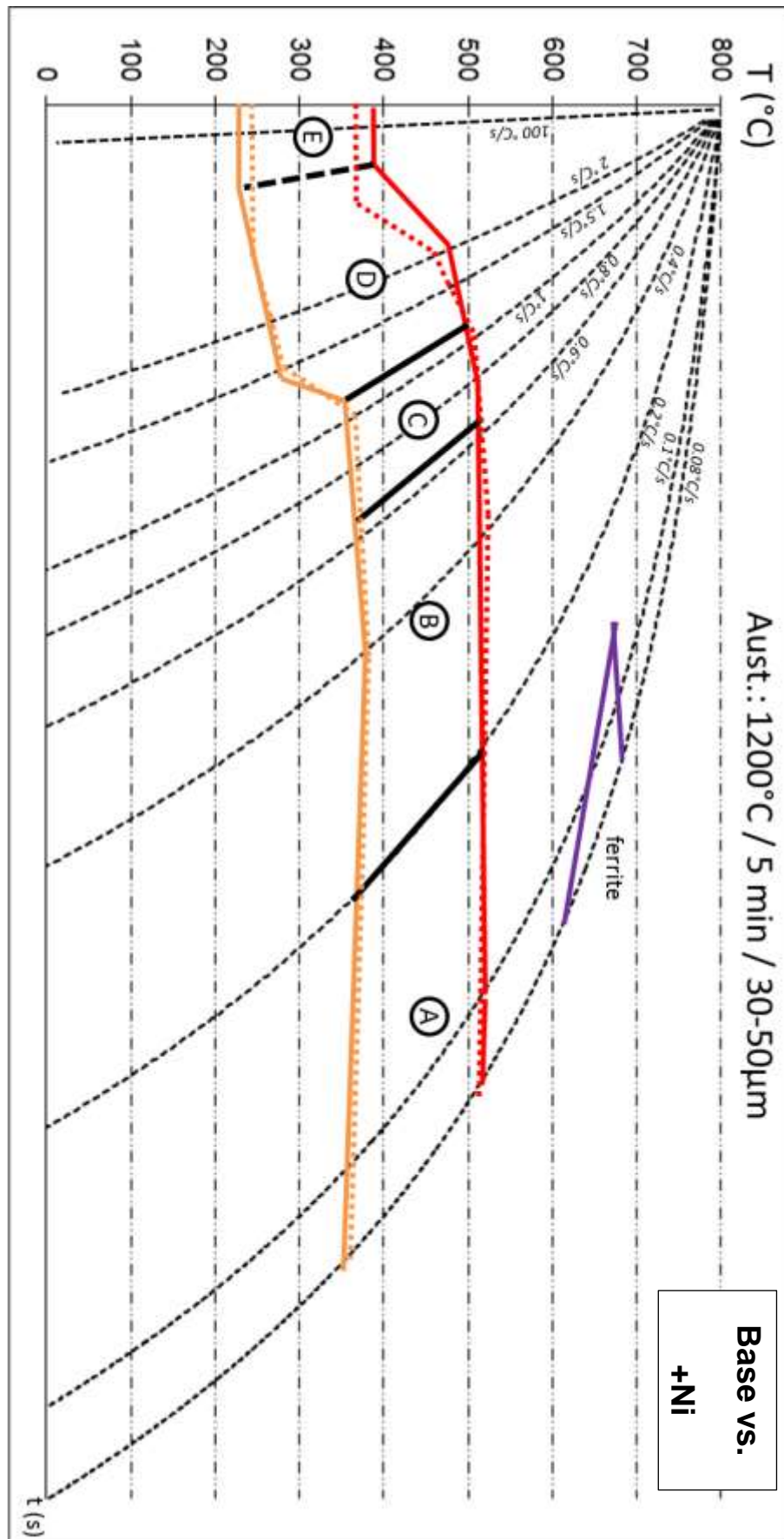


Figure 67: Schematic CCT diagrams of base (continuous line) and +Ni (dotted line). No ferritic domain in the case of +Ni. Microstructural domain limits of base are shown in black.

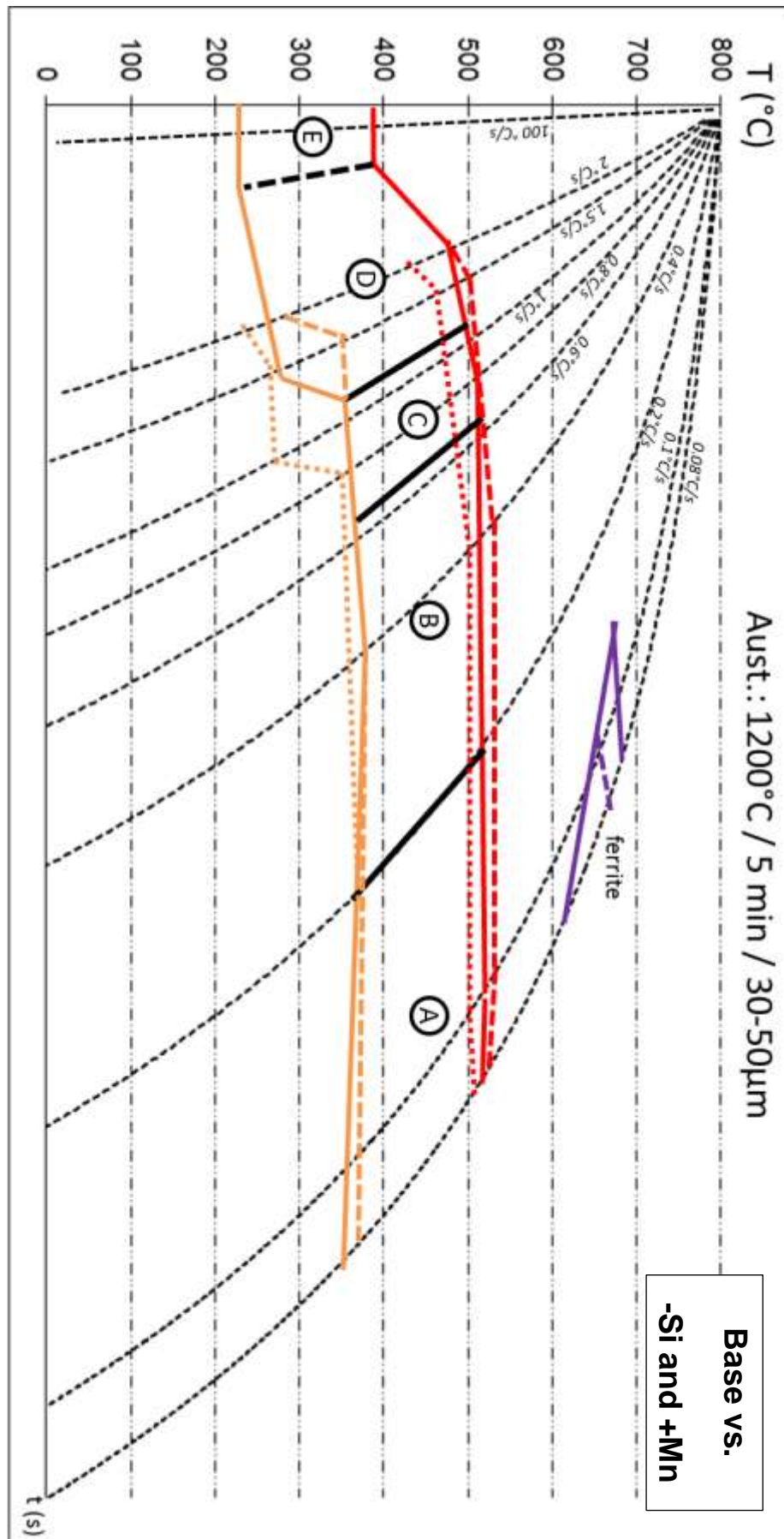


Figure 68: Schematic CCT diagrams of base (continuous line), +Mn (dotted line), and -Si (dashed line). No ferrite domain for +Mn. Microstructural domain limits of base are shown in black.

Once 0.4°C/s has been reached, the difference between transformation temperatures of both steels decreases. B_F is nearly similar for both chemical compositions. However, B_F exhibits a drop at higher cooling rates with less silicon (around 1.5°C/s versus 1.1°C/s). Thus $-\text{Si}$ chemical composition stays in domain C for a wider range of cooling rates (even wider than $+\text{Cr}$) as the increase in martensite content is sluggish before 1°C/s ($-\text{Si}$ still has a martensite fraction below 0.05 at this cooling rate).

$-\text{Si}$ exhibits the highest average bainite fraction between 0.4°C/s and 1°C/s (domains B and C) among all chemical compositions. The average bainite fraction is 0.94 in $-\text{Si}$ against 0.88 for base in this range of cooling rate. This is provided by higher transformation kinetics and a slightly wider temperature range of transformation. The higher extent of bainite transformation may come from some additional but limited cementite precipitation at interface between bainitic ferrite and austenite in upper bainite, leading to a local decrease in carbon content and thus to further austenite decomposition into bainitic ferrite. It might be possible that less martensite blocks are present in regions that exhibit lower bainite. Indeed, the lower bainite transformation extent and kinetics might be caused by the increase in cementite nucleation driving force due to the decrease in silicon content [52]. In addition, such feature is in agreement with the sluggish increase in martensite fraction that has been observed.

The hardness level is around 330 HV30 in domain B which is 20 HV30 lower than the base chemistry in the same domain. A part of this gap is reduced in domain C, and only 10 HV30 separate $-\text{Si}$ from base at 2°C/s (variation by 65 HV30 per $^{\circ}\text{C/s}$).

As expected, an increase in manganese suppresses all ferrite occurrences. B_S is already relatively low, around 500°C until 0.4°C/s , which is 10°C - 20°C lower than that of the base chemistry for these cooling rates. No noticeable change in B_F is observable in this range of cooling rates. B_S starts to decrease already beyond 0.4°C/s . All microstructural domains are strongly shifted toward lower cooling rates. $+\text{Mn}$ exits domain C at a cooling rate (0.8°C/s) where most of chemical compositions tested here are just entering in this domain.

So, domain D starts at 0.8°C/s and the martensite fraction reaches 0.87 at 2°C/s . The maximum level of bainite fraction is the same as that for base chemistry (around 0.88) but is reached, as for $+\text{Ni}$, at lower cooling rates (between 0.2°C/s and 0.6°C/s). Below 0.2°C/s , the MA constituent fraction increases relatively fast to reach 0.2.

The increase in manganese raises the hardness by 10 HV30 in domain B. Hardness values exhibit a huge increase as soon as the martensite fraction starts to increase. 40 HV30 are gained between 0.4°C/s to 0.8°C/s . This is remarkable as both addition of manganese and nickel create such increase in hardness in domain C. Indeed the hardness increases by 88 HV30 per $^{\circ}\text{C/s}$ whereas an average of 37 HV30 per $^{\circ}\text{C/s}$ is found for other chemical compositions with the exception of $-\text{Si}$ (65 HV30 per $^{\circ}\text{C/s}$). In domain C, both the martensite content as well as the ratio between lower and upper bainite increase. Considering the slight errors that exist in domain C limits, there is no noticeable difference in the martensite fractions at these limits (around 0.05 at the beginning, near 0.10 at the end). So, such difference in hardening with cooling rate for $+\text{Mn}$, $+\text{Ni}$ (and $-\text{Si}$) can be due to a faster increase in the ratio between lower and upper bainite and/or harder martensite.

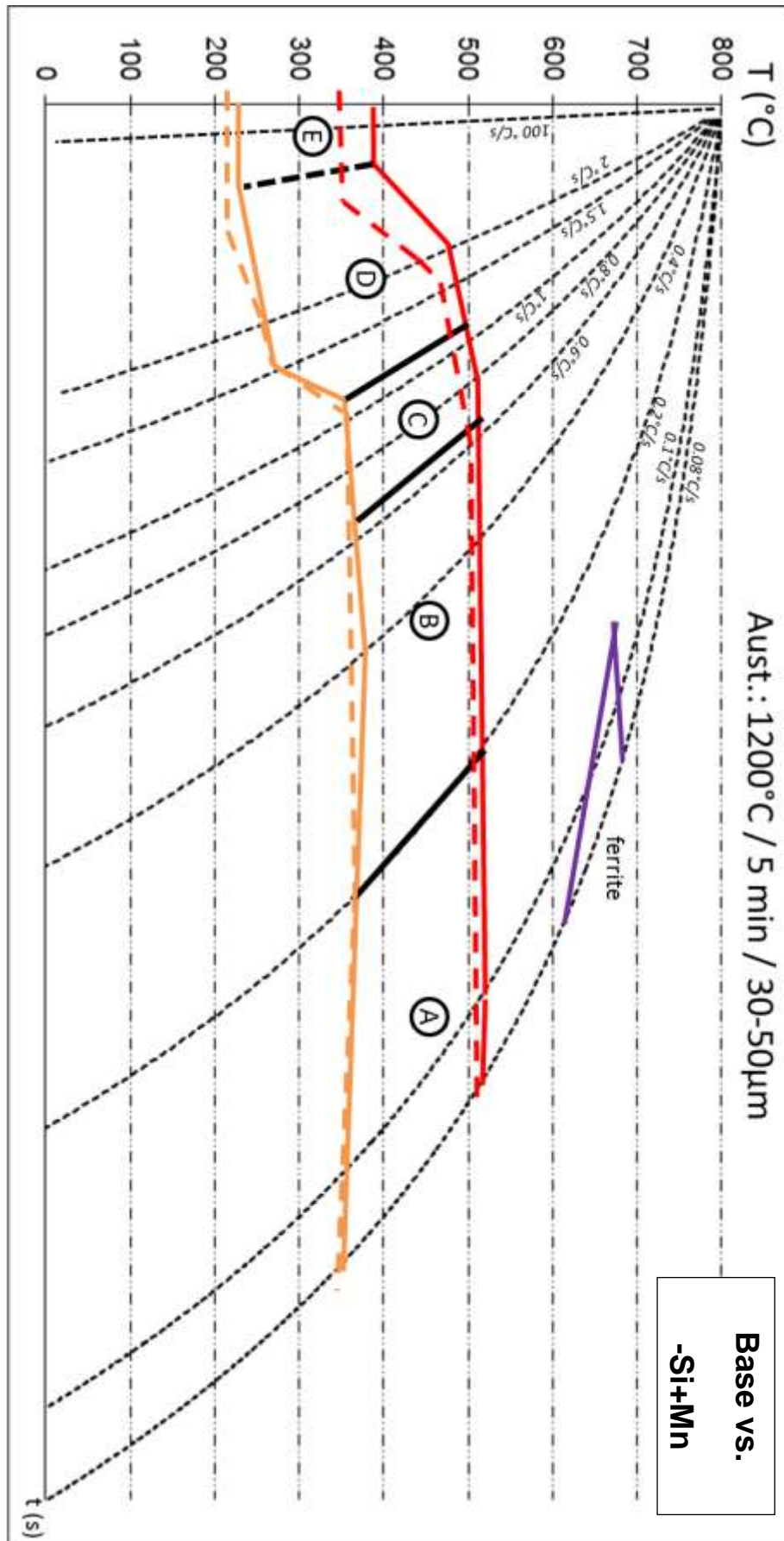


Figure 69: Schematic CCT diagrams of base (continous line), -Si+Mn (dotted line). No ferrite domain for -Si+Mn. Microstructural domain limits of base are shown in black.

For cooling rates lower than 0.6°C/s, a simultaneous increase in manganese and decrease in silicon leads to a slight decrease in B_S by 10°C compared to the base chemistry. The decrease in B_S is larger for –Si+Mn than for base chemistry after 0.6°C/s. So, as the cooling rate increases, B_S has a tendency to stay closer to +Mn B_S temperatures than to those of the base chemistry. From the beginning, the decrease in silicon is not high enough to compensate the increase in manganese. Moreover, the influence of Mn on B_S increases with the cooling rate in –Si+Mn. On other hand, Si+Mn shares very close values of B_F to those of base chemistry for all applied cooling rates (with the exception of 0.4°C/s). B_F falls once a cooling rate of 1°C/s has been reached for both –Si+Mn and base chemistry. Here, the decrease in silicon seems to compensate the increase in manganese more effectively.

Bainite fractions in domains B and C are not of the same extent as for –Si (0.89 in average). In addition, the increase in martensite content is no more sluggish so domain C also shrinks. In fact, all effects of Si on microstructure have been lost and only effects related with manganese stay, but weakened. Moreover, the raise in hardness in domain C is quite low, only 45 HV30 per °C/s, whereas both –Si and +Mn were showing high hardening rates.

3.2.2.f Empirical calculation of the bainitic start temperature

The calculation of the B_S temperature has been rationalized with respect to steel chemistry in the investigated range. This information can be useful to derive some mechanical properties.

Twelve formulas for B_S calculation have been tested on our chemical compositions. For each chemical composition, B_S has been defined as the highest bainite start temperature that has been measured in domain B (which is generally the highest over the entire CCT diagram, and generally found at 0.4°C/s). Domain B exhibits in most cases rather constant B_S and high fraction of bainite. The different formulas have been found in “steel forming and heat treating handbook” realized by Gorni in 2013 [156]. Several formulas have been built from TTT diagrams. Ranges of validity did not match in several cases our chemical composition range. None of these formulas does take niobium and boron into account. However, one of them yielded rather good results after only a slight change in the formula. This one comes from the work of Steven and Haynes [157]. The formula is the following:

$$B_S(^{\circ}C) = 830 - 270C - 90Mn - 37Ni - 70Cr - 83Mo \quad eq. 3.6$$

Where C , Mn , Ni , Cr and Mo are the respective alloying element content in wt%. Reliable chemical composition range is 0.10-0.55C, 0.2-1.7Mn, 0.0-1.0Mo, 0.0-3.5Cr, 0.0-5.0Ni (all in wt%). If 830 is replaced by 816, this formula can predict B_S with an average error of 6°C for our chemical compositions. The main error is due to Cr. It seems that we have reached the concentration limit from which B_S decreases with further Cr addition. In addition of B and Nb, Si is not taken into consideration. As a result, the formula has been further improved to use all information made available by the CCT diagrams of this chapter.

Two new formulas have thus been built in order to increase the calculation accuracy and to be better suited to our chemical compositions. B_S has been calculated both at 0.4°C/s and 0.8°C/s which are the extreme cooling rates encountered at the start of the bainitic transformation for targeted forged parts. These formulas are the following:

$$B_S(^{\circ}C)[0.4^{\circ}C.s^{-1}] = 962 - 288C - 84Mn - 81Si - 6Ni - 95Mo - 153Nb + 108Cr^2 - 269Cr \quad eq. 3.7$$

$$B_S(^{\circ}C)[0.8^{\circ}C.s^{-1}] = 1155 - 248C - 69Mn - 52Si - 28Ni - 85Mo - 291Nb + 333Cr^2 - 752Cr \quad eq. 3.8$$

Chromium contribution is now polynomial to reflect that for Cr contents over a certain value, further increase in Cr leads to a decrease in B_S . This critical content has been calculated to be 1.250wt% and 1.125wt% at 0.4°C/s and 0.8°C/s, respectively. The contribution of nickel increases as the cooling rate increases. Comparison between experimental and calculated

CHAPTER 3 - EFFECT OF ALLOYING ELEMENTS ON CCT DIAGRAM

values of B_s is given in Table 19 and shows good agreement. B_s temperature of base chemistry found at 0.8°C/s has been modified according by taking the values of B_s through the neighbouring cooling rates into account. B_s at 0.8°C/s is 514°C but previous and next ones (0.6°C/s and 1°C/s) were 509°C and 493°C, respectively.

The B_s temperature is believed to have a direct influence on the strength of the steel, as it defines the undercooling at which transformation occurs during isothermal holding or continuous cooling. Refinement of the microstructure as well as the dislocation density of the final product is affected by the B_s temperature. In the review realized by Mohrbaker [110], the strength of very low-C (0.03wt%) Mo-Nb-B steels increases by approximately 17 MPa for every 10°C reduction of the B_s temperature. This change was found similar in magnitude for yield and tensile strength. Close values of 15 MPa per 10°C reduction of the B_s temperature were found by Wang et al. [112] on other ultra-low C steels.

tag	0.4°C/s			0.8°C/s		
	BS exp (°C)	BS calc (°C)	ΔB_s (°C)	BS exp (°C)	BS calc (°C)	ΔB_s (°C)
-Cr	540 ± 4	540	0	537 ± 3	538	+1
-Si	529 ± 2	530	-1	506 ± 2	507	+1
0Nb	530 ± 2	530	0	519 ± 3	520	+1
+Cr	524 ± 2	524	0	524 ± 3	524	0
0Mo	522 ± 3	522	0	504 ± 3	504	0
Base	520 ± 2	520	0	505*	502	+3
+Ni	518 ± 3	518	0	494 ± 4	494	0
-Si+Mn	510 ± 2	511	+1	492 ± 2	492	0
+Mn	496 ± 3	496	0	480 ± 2	483	+3
		av. error	0		av. error	± 1

Table 19: Experimental B_s versus calculated ones. * modified value of B_s .

3.3 Final remarks, conclusions & Outlooks

CCT diagrams established in this chapter allowed making qualitative and quantitative links between chemistry and microstructures, in a range of well controlled transformation conditions. Microstructural domains have been defined, by making use of quantitative analysis of a number of microstructures. The main results are summarized below, as well as some open questions concerning in particular the comparison with forged parts having the same chemistry.

From CCT diagrams, there are some noticeable and reproducible differences between forged parts and CCT samples cooled at the corresponding transformation cooling rates (0.2°C/s and 0.1°C/s). These differences are due to the higher cooling rate experienced by the forged parts before the onset of the bainitic transformation (0.8°C/s and 0.4°C/s for 35x35mm² and 74x74mm² forged parts). By this way, noticeable ferrite occurrence is avoided for ferrite sensitive chemical compositions (0Nb, 0Ti, base, -Si, -Cr), leading to an increase in bainite content in the final microstructure. However, for an unknown reason, the hardness was found slightly lower in the case of forged parts despite this substitution of ferrite by bainite. Moreover, in the case of the 35x35mm² forged parts, the bainitic transformation may start 14°C to 39°C lower than if they were cooled down originally at 0.2°C/s from 800°C. This loss in temperature range of transformation would explain the higher MA constituent fraction that has been observed on the chemical compositions that are supposed to exhibit a difference in B_s by 14°C or more (+Mn, -Si+Mn, -Si, +Ni, base). Nevertheless, no systematic increase in hardness has been noticed for forged parts that exhibit higher MA constituent fraction than corresponding dilatometric samples.

It would have been difficult to use other dilatometric cycles in order to reproduce conditions even more similar to forging. It would have been necessary to change the cooling rate as soon as the transformation begins which is technically very difficult to realize experimentally. Moreover we only knew the ratio between cooling rates before and during the transformation in two situations. It would have been necessary to realize calculations or experimental tests to acquire the rest of them. Nevertheless, the realized CCT diagrams allow making reliable comparisons between chemistries in tightly controlled conditions. Numerous individual or synergy effects have been noticed through this experimental campaign, even if some of them stay poorly-understood.

The first main conclusion is that this steel grade exhibits a noticeable microstructural robustness. No great disruption on CCT diagrams has been observed for every chemical composition, most especially on the top of the bainitic domain. The bainitic transformation temperatures B_S and B_F shown only few differences at cooling rates lower than 0.8°C/s . Maximum difference observed is 40°C , but only in the case of an important drop in chromium content (-30%). The same microstructural domains (defined from the variations of microstructural constituent as well as from hardness and austenite content evolution) were encountered in all chemical compositions but for different cooling rates.

CCT diagrams exhibit noticeable growth of the ferritic domains relative to the occurrence of a given type of precipitate along the primary austenite grain boundaries. This precipitation is believed to be $\text{Fe}_{23}(\text{B,C})_6$ but no experimental evidence is available yet on the concerned samples. This precipitation was found here to occur even with the presence of niobium and molybdenum in the chemical composition and increases as soon as one of these two alloying elements is removed (especially niobium).

It seems that for this amount of niobium and molybdenum, the content of boron is somewhat excessive, as boron precipitation in coarse $\text{Fe}_{23}(\text{B,C})_6$ occurs. So a way of improvement for this steel family could be to further optimize the boron content.

Only a slight amount of molybdenum seems to precipitate (6% of the nominal composition) even if niobium is not present in the chemical composition. Instead of increasing the molybdenum content in order to enhance its precipitation, a trial could be realized to replace all the molybdenum by additional niobium (but not to the same extent). One main reason for this: in our composition, niobium precipitates more heavily than molybdenum (80% instead of 6% of the nominal content for a same initial content). A slight addition of niobium will certainly create more precipitation than the current content of molybdenum. One could think about a second reason, molybdenum is known to decrease the precipitation kinetics of niobium [107;108], so less molybdenum will lead to more niobium precipitation even without any additional increase in niobium content. This phenomenon has not been observed in our steels, as the amount of niobium that precipitates stays relatively the same with (22% of the niobium nominal composition) or without molybdenum (19% of the niobium nominal composition).

In the view of microstructure and hardness, nickel addition to this extent can be lowered without noticeable influence for the targeted range of cooling rates ($>0.8^\circ\text{C/s}$). For higher cooling rates, the influence of nickel is obvious. Nickel can probably be efficiently replaced with a chromium addition to fulfil strength requirements in regard to the hardness level in upper bainite domain (domain A and especially domain B) for +Cr chemical composition. Moreover, such chemical composition can be used for slightly higher range of cooling rates without creating harmful microstructural gradients in the microstructure (at least for cooling rates lower or equal to 1°C/s). A substitution of nickel by a slight addition of manganese can also be considered. This time, such chemical composition ensures high strength with probably relatively good level of ductility (and impact toughness, see chapter 4) as the

austenite fraction at very low cooling rates seems to indicate. However, care will have to be taken to avoid too much difference in cooling rate before and during the bainitic transformation. Indeed, B_s decreases fast as the cooling rate increases, which can lead to a strong decrease in the transformation temperature range. This may lead to more martensitic-rich microstructures (both with the increase in martensite fraction but also more martensitic-rich MA constituent) and a decrease in the amount of thin austenite films.

A decrease in silicon leads to a noticeable increase in bainite fraction in the upper bainite domain with good level of austenite content. However the hardness level exhibited by such microstructure seems too low to ensure strength requirements. An increase in manganese has an obvious effect on the bainitic domain, this one being strongly shifted toward lower cooling rates. Indeed the transition domain between bainitic-rich and martensitic-rich microstructures starts at 0.8°C/s. Finally, silicon interaction with manganese is not well understood. Other chemical compositions, exhibiting an increase in silicon content for the first one and a decrease in manganese for the second one, could be cast and forged. More different Mn contents with the same amount of silicon as well as different silicon contents for the same amount of manganese could be thus available to realize further investigations in the future.

CHAPTER 4 – PHYSICAL PHENOMENA AND MICROSTRUCTURAL PARAMETERS THAT CONTROL IMPACT TOUGHNESS

Résumé : Ce chapitre est dédié à la détermination des phénomènes physiques et des paramètres microstructuraux qui contrôlent la résilience à la température ambiante. Ceux-ci ont été déterminés grâce à une analyse minutieuse et quantitative de la surface de rupture et de l'endommagement interne sur éprouvette de résilience Charpy, mais aussi grâce aux données microstructurales précédemment acquises dans le chapitre 2.

Pour des microstructures mixtes de type bainite supérieure/granulaire, la résilience à 20°C est contrôlée, par ordre décroissant d'importance, par :

1. La quantité d'inclusions de grande taille servant de site d'amorçage de fissure pour le clivage.
2. La capacité du matériau à absorber de l'énergie lors de la rupture ductile. Cette capacité est principalement contrôlée par le taux d'austénite résiduelle.
3. La capacité du matériau à absorber de l'énergie lors de la rupture fragile, qui est principalement contrôlée par la taille de paquet bainitique.

Toutes ces observations ont été rationalisées sous la forme d'une formulation mathématique, qui permet de décrire la résilience à 3J près. Du fait de la distribution aléatoire des inclusions, la mesure de l'avancée ductile reste un paramètre d'entrée de cette équation.

The objective of this chapter is to identify and to quantify dominant fracture mechanisms and microstructural parameters controlling impact toughness. It is well known that as-quenched, strong materials may provide low ductility. Indeed, microstructural parameters that control strengthening mechanisms can also act as damage precursors (precipitation, hard secondary phases) or decrease the absorbed energy during crack propagation (dislocations, interstitial and substitutional solute elements). The only change in microstructural parameter that can be beneficial for both mechanical properties is the increase in high-angle boundary density (i.e. a decrease in effective grain size) [2;7;158].

The effective grain size might be defined differently according to the targeted mechanical properties. Boundaries between crystallographic structures with low misorientation angles from 2° to 15° are commonly believed to participate to strengthening whereas only highly misoriented adjacent crystallographic structures are able to deviate high speed cleavage cracks. Regarding lath-like bainitic microstructures, effective lath size (d_l) or effective packet size (d_p) terminology, according to the chosen cut-off angle and the referred microstructural unit, are more relevant than the effective grain size (d).

Hard secondary microstructural constituents, which are believed to be an important source of strengthening in this material, are suspected to act as cleavage nucleation sites in several studies [12;159;160]. Microstructural counterparts, such as low effective packet size, is hardly reachable in view of the PAGS and of the transformation temperatures (both linked with the process) in the present study. The same goes for retained austenite, which can reduce the stress concentration field in the material by transformation under mechanical loading (the so-called TRIP effect), retarding void initiation and thus damage development and cracking. With the undergone cooling rates, only coarse upper/granular bainite is produced, a great amount of retained austenite is present in form of relatively large microstructural element (island), which is less effective than films to provide such TRIP effect (chemical composition of the retained austenite is also in concern, but is hardly dissociable from its shape) [161-164].

Moreover, MnS inclusions are voluntarily added to the microstructure to facilitate machining. These ones, together with coarser particles such as titanium nitrides and aluminium-rich oxides, significantly increase the density of coarse defects that can be found in the microstructure and could affect the probability of cleavage initiation [29-31].

Despite all of these apparent negative effects on ductility, the reference steel cast has always been able to fulfil the requirement expected in terms of impact toughness (>20J at room temperature) as well as high strength ($TS > 1100\text{MPa}$, $YS > 800\text{MPa}$), which is a performance considering the simple application process (still air-cooling). Deeper understanding and better quantification of underlying phenomena is thus required.

4.1 Experimental methods

At least three so-called DVM U-notched impact specimens were cut at mid-radius, along the axis of each material (as-forged and as-rolled reference steels and as-forged laboratory heats) and tested at 20°C. Dimensions of the DVM U-notched impact specimens are given in Figure 71. For this grade and this kind of microstructure, we expected that all impact specimens would exhibit fracture surfaces typical of the ductile-to-brittle transition. DVM U-notched impact specimens were chosen because the ductile-to-brittle transition extends over a larger range of energy than for so-called KCV V-notched impact specimens. At equal geometry of impact test specimen and notch radius, V-notches generate higher stress concentration compared to U-notches so the occurrence of brittle fracture by cleavage is enhanced [165]. The flow stress is more sensitive to temperature than the critical cleavage

stress [2]. Any effect that changes the flow stress (such as stress concentration field due to the notch shape) without influencing the initiation or propagation mechanisms of cleavage cracks might lead to a change in ductile-to-brittle transition temperature (**DBTT**) [2] as illustrated in Figure 70. The DBTT is therefore shifted toward higher temperatures for V-notched Charpy impact test specimens compared to U-notched ones.

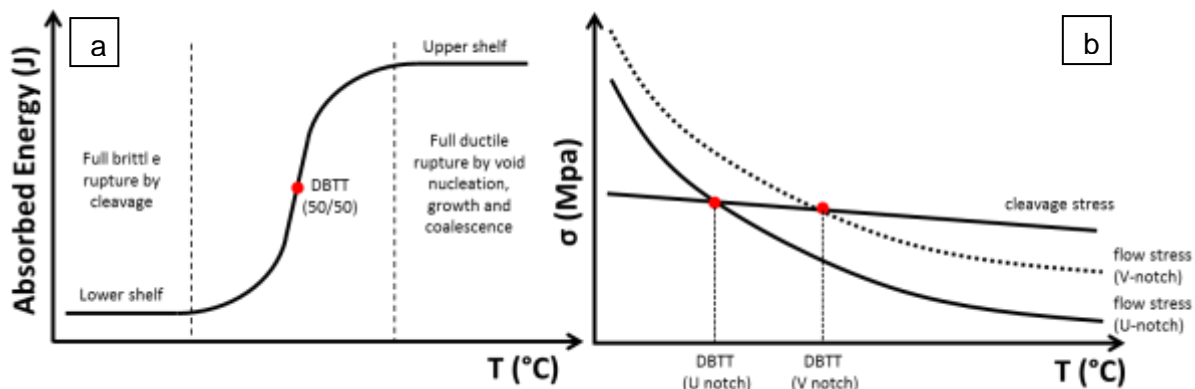


Figure 70: Schematic illustration of impact transition curve (a) and of the cause of the ductile/brittle transition temperature (b) evolution of the DBTT according to the notch shape of the impact test specimen (at equivalent specimen geometry and notch radius).

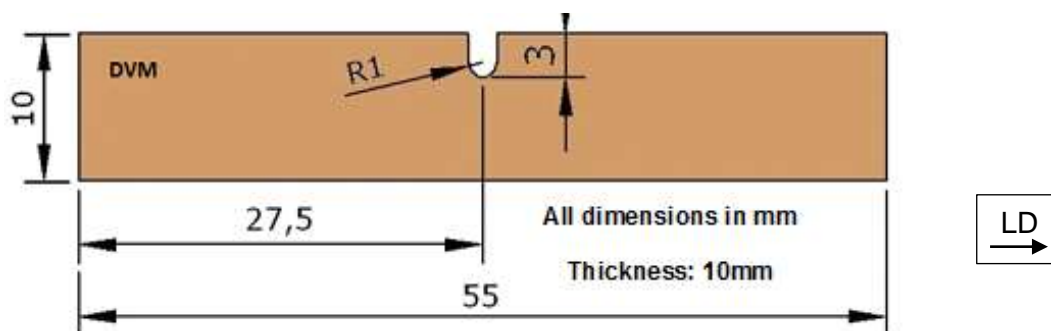


Figure 71: DVM Charpy impact test specimen geometry.

Identification of cleavage fracture initiation sites, qualitative determination of cleavage facet size and quantitative ductile crack extension measurements were realized by SEM fractography of every tested impact specimen. The ductile crack extension area was manually reported with a numerical stack in GIMP software, from a map of the entire fracture surface at low magnification (x20). This stack was used in ImageJ software for area measurement. Figure 27 shows an example of the area that is taken into consideration for the measurement. Area values given in this chapter are the average of the ductile crack extension areas that have been measured on the two sides of each broken Charpy impact specimen. The average relative measurement uncertainty on the ductile crack extension is 13% and it increases as the area decreases (errors go from 1% to 38%). The measurement uncertainties have been determined by comparing area measurement on the two sides of the broken Charpy impact test specimen. Additional observations have been realized after Picral 2% etching on four specimens (+Ni 74 specimen 2, -Si+Mn 74 specimen 3, 0Mo 35 specimen 3, -Cr 35 specimen 1) chosen among some specimens for which the region of crack initiation was known but with no distinctively apparent critical defect from SEM observation of the non-etched fracture surface.

Damage was examined in cross-section, from the mid-thickness of some impact specimens, to observe brittle micro-cracks arrested in the bulk. Specimens that were chosen for this damage study were taken from 0Ti 35 (specimen 1, 60.3J), +Ni 35 (specimen 1, 60.4J), 0Nb 35 (specimen 3, 23.1J) and -Si 35 (specimen 3, 15.5J) as they present noticeable variations in impact toughness and in microstructure. In addition, an EBSD map along an arrested crack of the +Ni 35 specimen has been acquired using an acquisition step of 400nm.

The bainitic packet size was measured by EBSD over 0.5mm^2 (~600 packets) with $1\text{ }\mu\text{m}$ step size for every tested specimen (see appendix A.III.2 for complete characterization methodology). As for XRD measurements reported in chapter 2, EBSD maps were realized parallel to the fracture surface, directly on impact specimens, a few mm under the fracture surface.

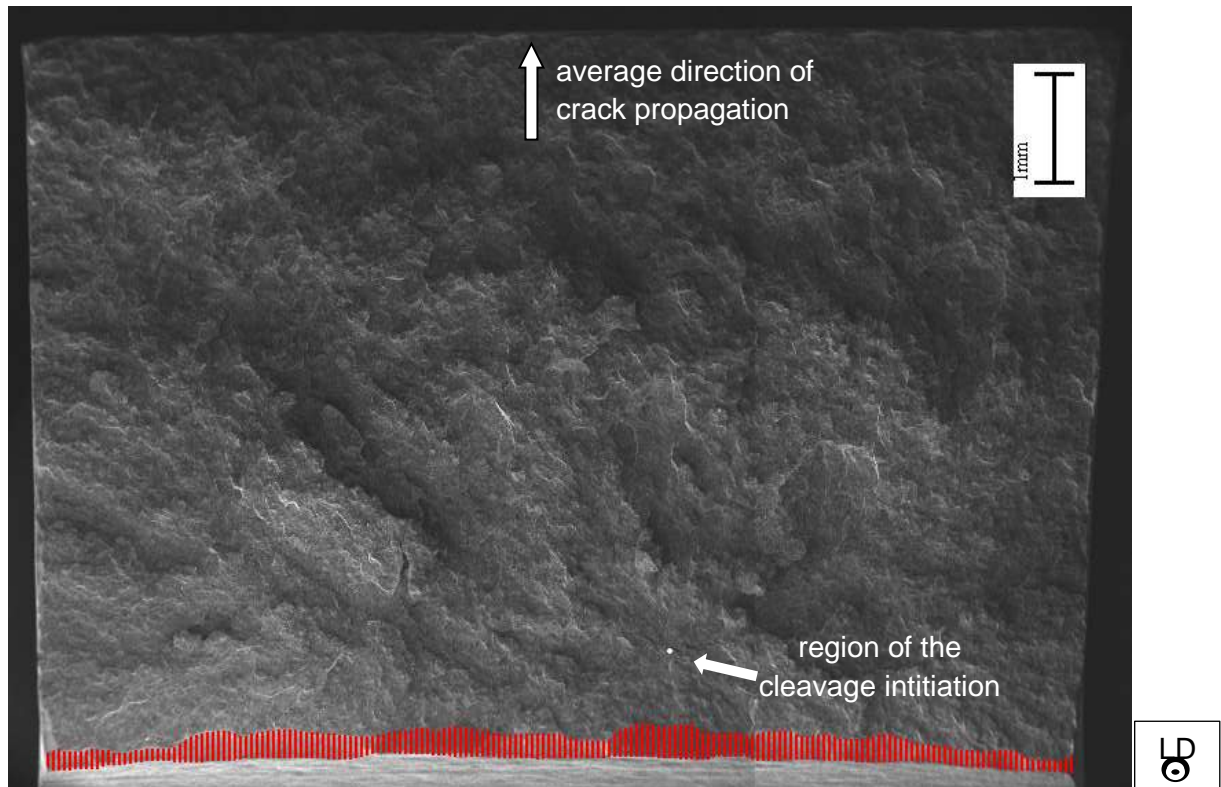


Figure 72: Fracture surface of 0Ti 35, specimen 1. The region highlighted in red is the ductile crack extension.

4.2 Results

4.2.1 Charpy impact test results

Table 20 exhibits the range of impact toughness and the associated average value that have been obtained over three or four tests at 20°C for every considered material.

At first sight, with respect to the base chemistry:

- A decrease in Mo, Si or Cr content seems to be detrimental to impact toughness.
- An increase in Cr or Mn content provides no better impact toughness results but an increase in Mn content could compensate a decrease in Si content regarding impact toughness.
- A decrease in Ti content or an increase in Ni content seems to have no obvious influence on impact toughness.
- Impact toughness values fall as the forged part section increases for all chemical compositions, with the exception of the 0Nb chemistry.

Both reference steels exhibit better impact toughness than $74\times 74\text{mm}^2$ forged parts whereas cooling rates are expected to be barely similar, at least for the as-forged reference steel. The as-rolled reference steel exhibits the best impact toughness among all investigated materials. This might indicate that impact toughness values of laboratory heats are in fact very conservative with respect to those that can be expected from more realistic processing conditions.

CHAPTER 4 - MICROSTRUCTURAL PARAMETERS THAT CONTROL IMPACT TOUGHNESS

DVM 20°C	tag	Impact Toughness (J)	
		range	average
35x35 mm ²	0Ti	29-60	44
	base	35-56	43
	+Ni	25-60	41
	0Nb	17-34	26
	-Si	15-17	16
	-Si+Mn	23-43	31
	+Mn	31-38	34
	0Mo	14-17	16
	-Cr	11-13	12
	+Cr	25-28	27

DVM 20°C	tag	Impact Toughness (J)	
		range	average
74x74 mm ²	0Ti	19-22	20
	base	17-20	19
	+Ni	16-18	17
	0Nb	27-35	31
	-Si	9-13	11
	-Si+Mn	15-16	15
	+Mn	11-18	15
	0Mo	9-16	12
	-Cr	12-12	12
	+Cr	12-14	13

DVM 20°C	tag	Impact Toughness (J)	
		range	average
Ref. steel	as-rolled	43-49	47
	as-forged	22-31	27

Table 20: Average impact toughness of investigated materials. Ref. Steel: reference steel.

However, forging parameters have an obvious effect on microstructure and thus, on final mechanical properties for a given geometry. Due to the uncertainty about thermo-mechanical cycles of the free-forging, as already discussed in Chapter 2, it is impossible to establish well reliable quantitative links between the chemical composition of the steel and the mechanical properties after forging. Nevertheless, it is still possible to establish the links between microstructural parameters and impact toughness, which is the objective of this chapter thanks to:

1. The wide variety of mixed upper/granular bainite microstructures and thus, significant variations in microstructural parameters;
2. The continuum in the values of impact toughness (from 9J to 60J), even if a great part of these ones are below 20J, and not only groups around some specific values.

4.2.2 Fracture mechanisms

All impact specimens exhibited a typical ductile-to-brittle transition fracture surface, which is consistent with measured impact toughness values. In every case, the ductile crack extends over less than 450 μm . The remaining of the fracture surface is composed of large cleavage facets with traces of ductility, such as veins (linear rivers inside the cleavage facets) or bridges (large rivers between two cleavage facets), but also more isolated dimples and cavities.

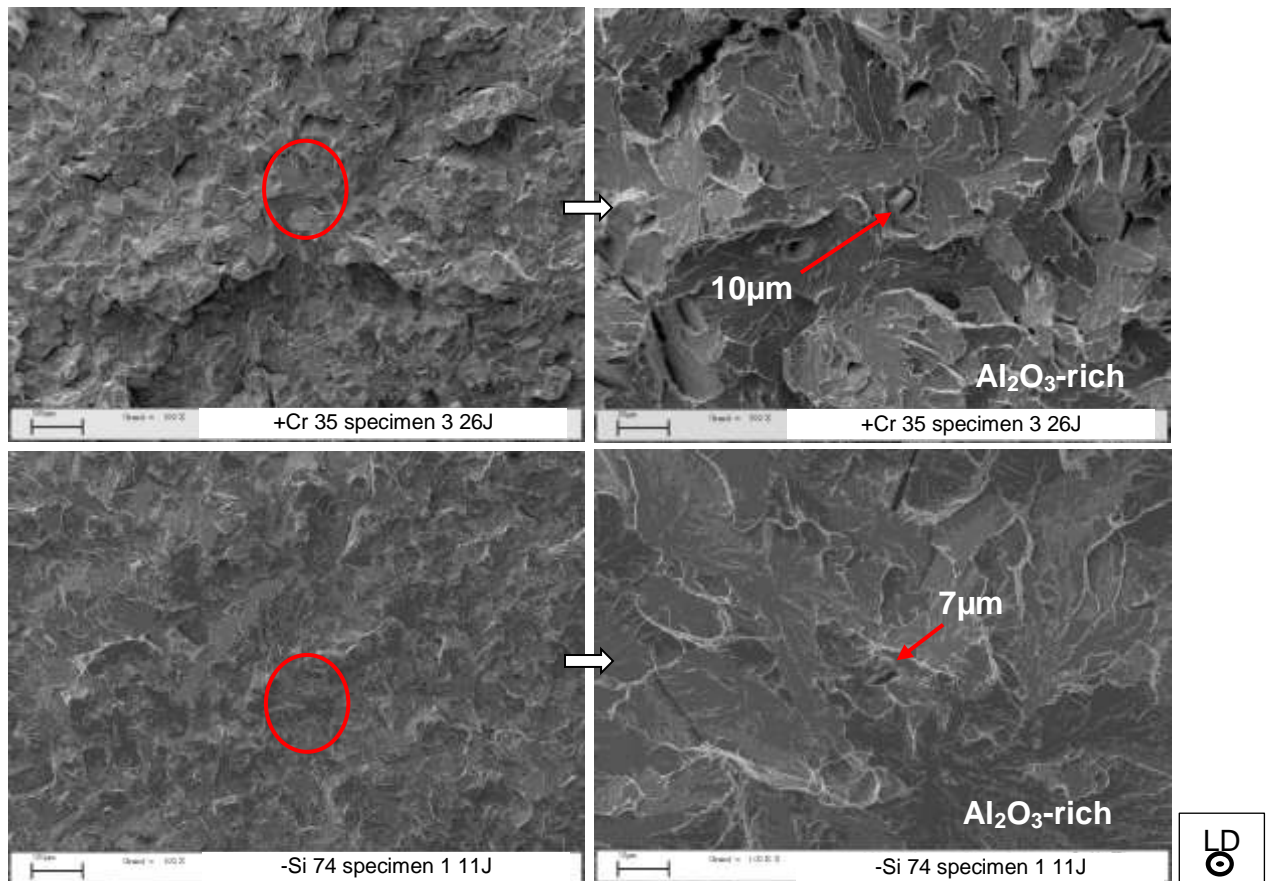


Figure 73: SEM, SE imaging, observations of the fracture surface. Initiation site = Al_2O_3 -rich inclusion(s). (left column) general view, (right column) closer view of the cleavage initiation region encircled in red in the left pictures.

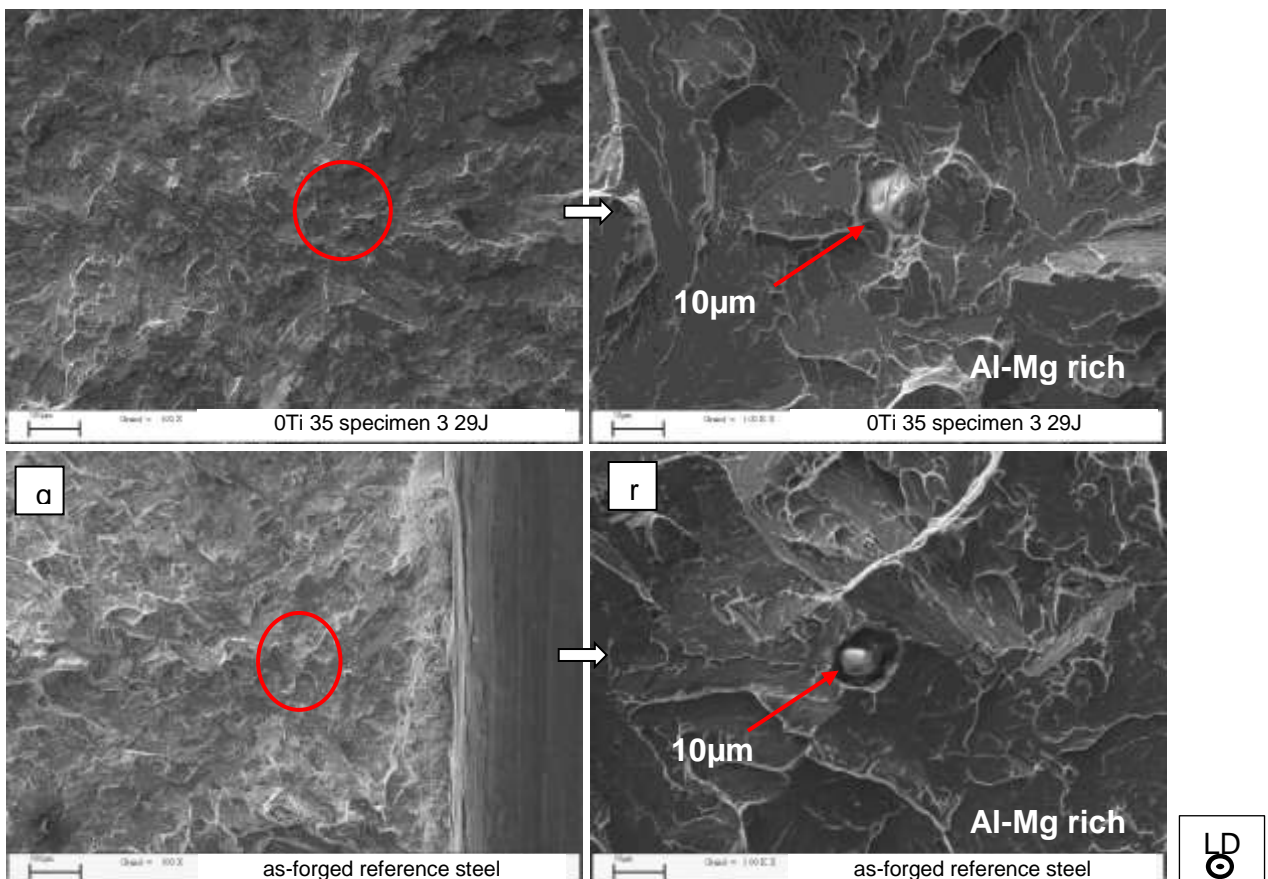


Figure 74: SEM SE, observations of the fracture surface. Initiation site = Al-Mg rich inclusion(s). (left column) general view, (right column) closer view of the cleavage initiation region encircled in red in the left pictures.

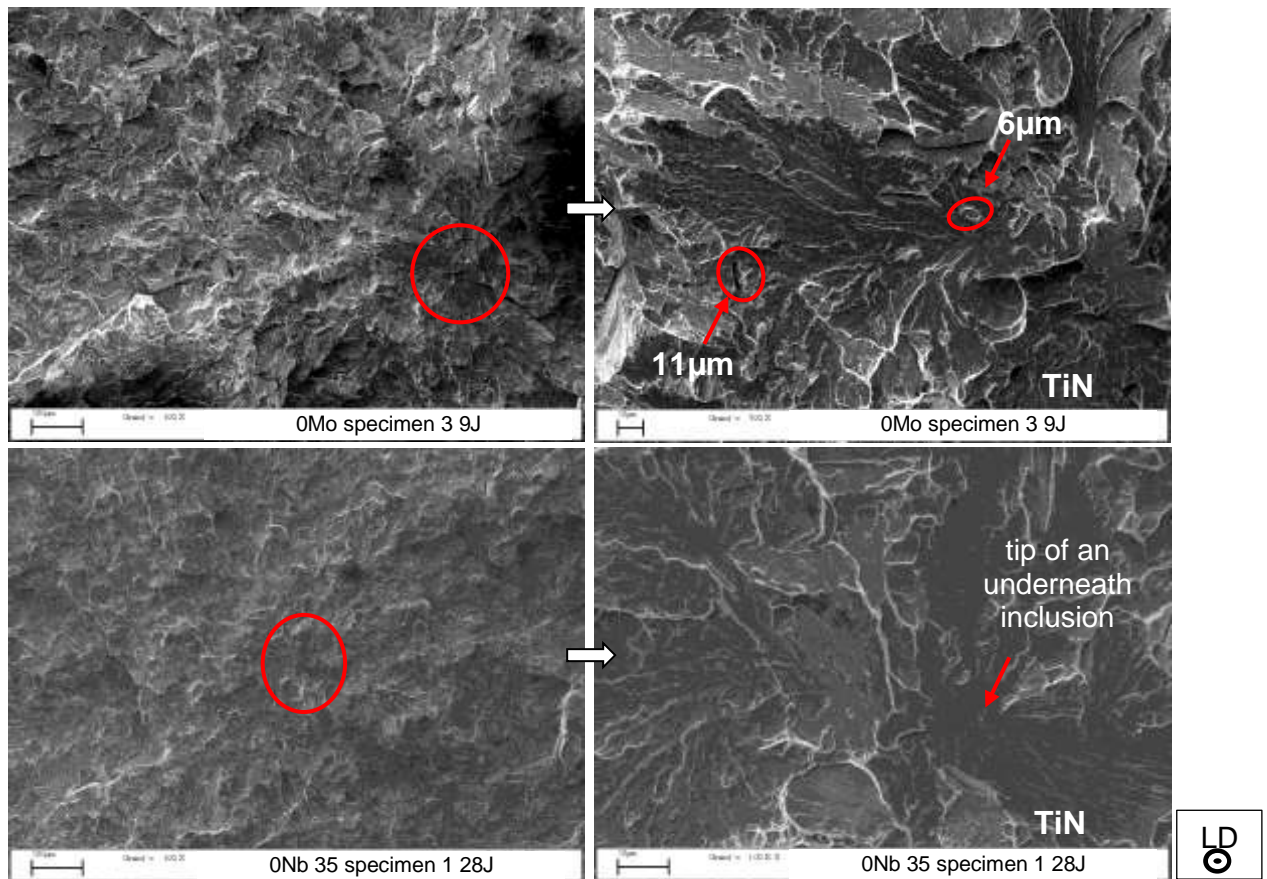


Figure 75: SEM, SE imaging, observations of the fracture surface. Initiation site = TiN inclusion(s). (left column) general view, (right column) closer view of the cleavage initiation region encircled in red in the left pictures.

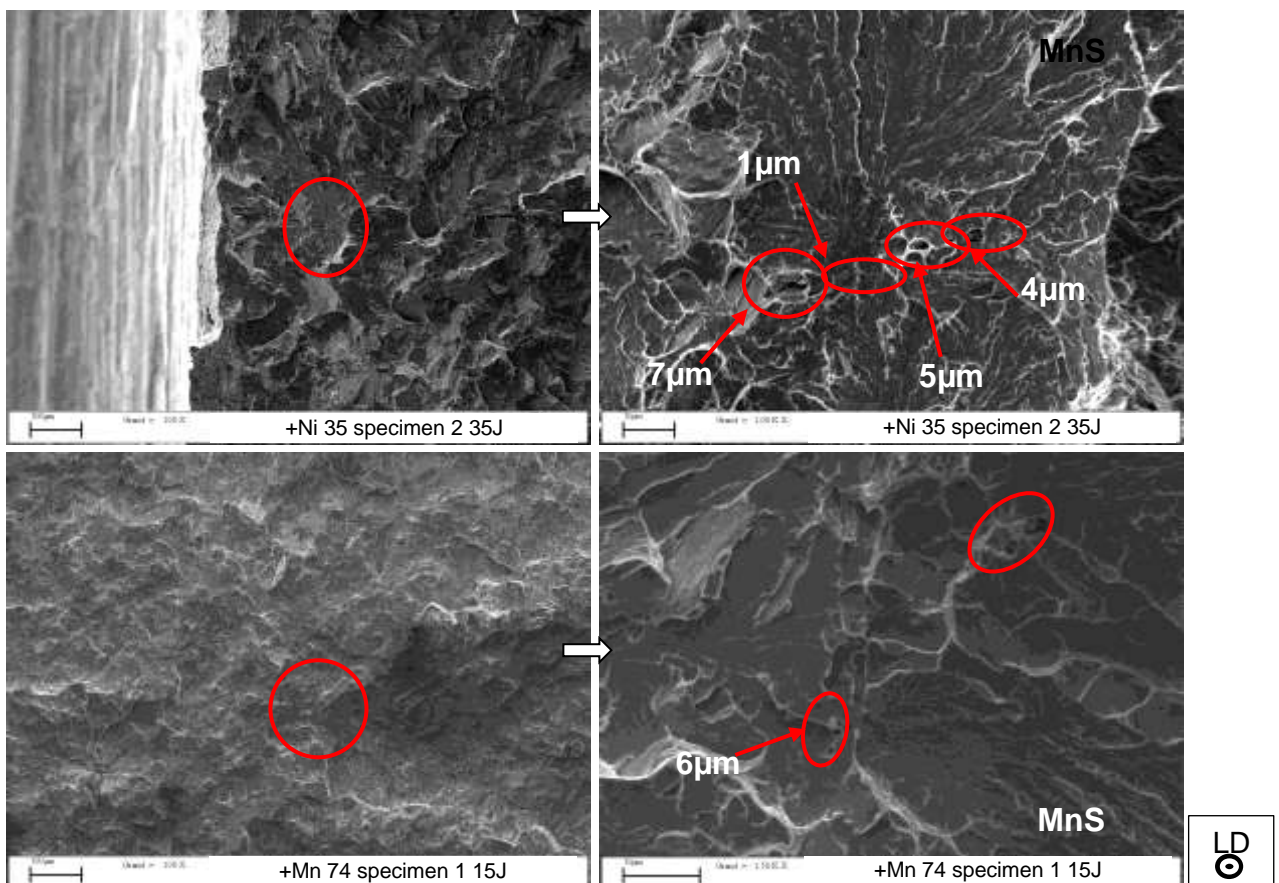


Figure 76: SEM SE, observations of the fracture surface. Initiation site = cluster of MnS inclusion(s). (left column) general view, (right column) closer view of the cleavage initiation region encircled in red in the left pictures.

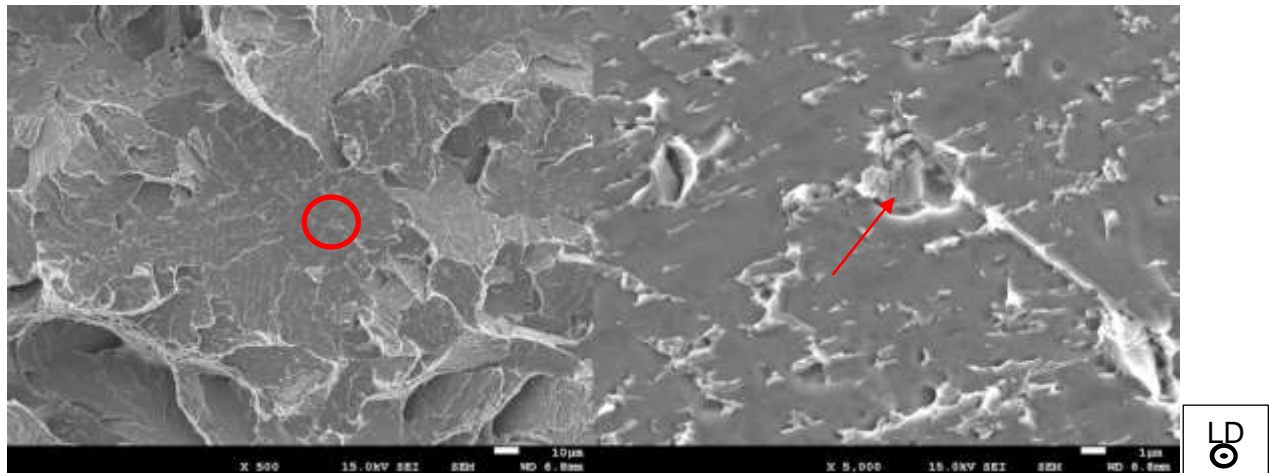


Figure 77: SEM, observations of the fracture surface.—Cr 35, specimen 3, 12J. (left picture) general view, (right picture) closer view of the cleavage initiation region encircled in red in the left pictures. The red arrows points out an un-identified inclusion (2μm).

In most cases, one single initiation site for cleavage leads to final fracture. This site was found between 600μm and 1300μm (950μm in average) beyond the notch tip. In only one case (out of 69 tests) the initiation site was found very close to the front of the ductile crack (+Ni 35, specimen 1, 65J). In any other case, the cleavage initiation site is distant from the ductile crack front by several hundreds of μm. Once the crack has initiated, failure of other features in the vicinity of the cleavage crack may facilitate its propagation into the bulk.

SEM fractographs showing various inclusions active in cleavage crack initiation are shown from Figure 74 to Figure 76. For most specimens the initiation site is a single coarse inclusion from 6 to 10 μm in size, such as Al₂O₃ rich (Figure 73), Al-Mg rich (Figure 74) or TiN (Figure 75), or a cluster of middle-sized MnS inclusions from 3-8 μm in size (Figure 76). It happens that no inclusion or precipitate can be found in the initiation region, but after a slight Picral2% etching, particles located slightly underneath can be revealed as shown in Figure 77. In other cases, brittle fracture seems to have occurred from dimples created in front of ductile crack extension and nucleated along interfaces between harder (e.g. M-A constituent) and softer phases (e.g. bainitic ferrite) or from the possible cleavage cracking of MA constituents depending on their brittleness (whether they are more or less enriched in carbon). The starting point of brittle fracture is not necessarily from the critical feature itself, but from the close vicinity of it, at a distance up to the apparent size of the critical defect, which may correspond to the location of the maximum stress concentration induced by that particle.

It seems probable that the size of the particle triggering brittle fracture decreases with increasing ductile crack extension but no quantitative measurements are available to sustain this assumption. Indeed, it is very difficult to realize proper particle size measurement for two reasons. Firstly, only two dimensions of the particle are apparent and they would not necessarily exhibit the maximum length reached by the particle in three dimensions. Secondly, it would have been necessary to define a measurement criterion in the case of inclusion clusters. Anyway, the distance between the initiation point and the ductile crack front might be related to the probability to find a feature with sufficient size to initiate cleavage.

With the exception of 0Ti 35 combination, cleavage facets have been observed going from 10μm up to around 100μm in size. 0Ti 35 combination can exhibit even larger cleavage facets. The largest one, shown in Figure 78, has a length of nearly 200μm and was observed far from the cleavage initiation region.

As shown in Figure 79, there is a linear relationship between the area of ductile crack extension, denoted as $S_{ductile}$, and impact toughness, denoted as U . U was found to increase with $S_{ductile}$ whatever the considered material. The lower the probability of meeting a critical

feature with a sufficient size to initiate cleavage fracture, the higher the value of $S_{ductile}$ and thus, the value of U . The scatter around the linear relationship increases with the value of impact toughness and of the ductile crack extension area.

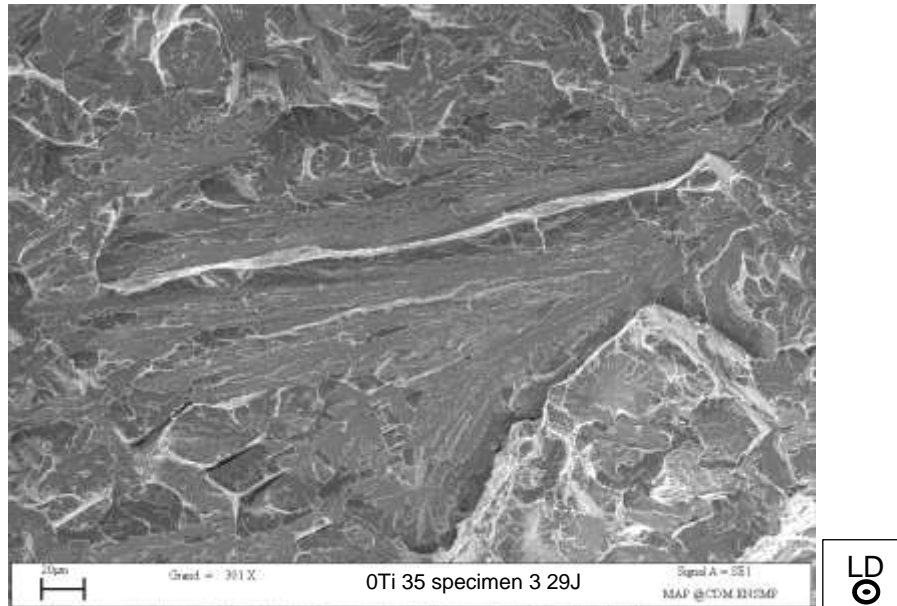


Figure 78: SEM, observation of the fracture surface. Largest cleavage facet observed among all specimens.

By extrapolating the linear relationship down to no ductile crack advance, only about 6J are considered to be absorbed by pure brittle fracture. In average, ductile fracture absorbs 10.5 J/mm² while brittle fracture only absorbs 0.09 J/mm². As a consequence, the impact toughness is nearly governed by the ductile crack extension before final brittle fracture. As cleavage crack initiation controls the end of the ductile fracture and the value of $S_{ductile}$, it is thus the first-order phenomenon controlling impact toughness. With the exception of 0Nb, for a given chemical composition, 35x35mm² forged parts always exhibit higher $S_{ductile}$ value than their 74x74mm² forged counterparts. It seems that the probability to initiate cleavage after only a small amount of ductile crack advance is higher in the largest section, which might imply that the number density of coarse features (such as inclusions) able to initiate cleavage is higher or that the cleavage stress is lower due to other microstructural parameters.

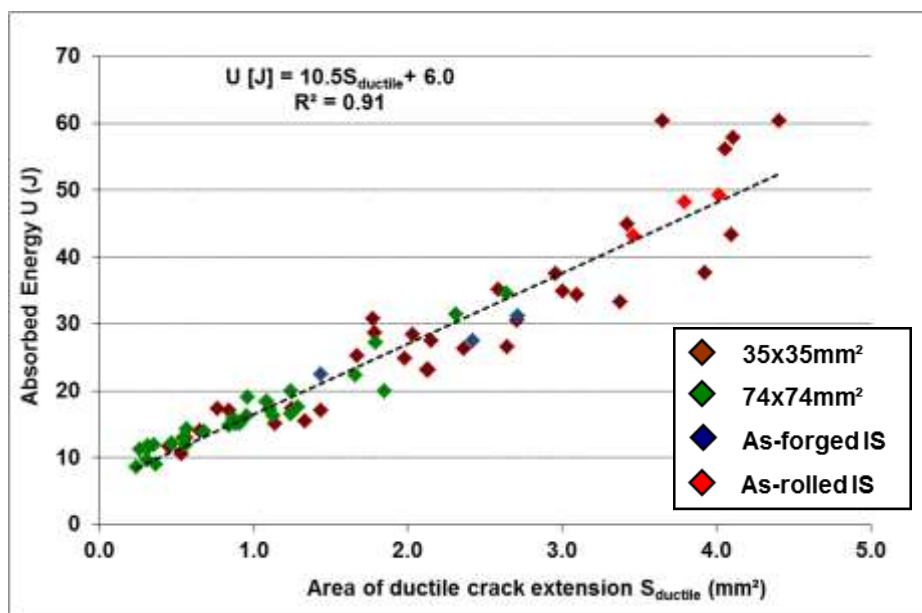


Figure 79: Absorbed energy according to the area of ductile crack extension. One point per Charpy impact test specimen. IS: reference steel.

However, 74x74mm² forged parts were not expected to exhibit a higher probability of meeting a critical feature than their 35x35mm² counterparts. Indeed 74x74mm² forged parts have been realized from the bottom of the ingots whereas 35x35mm² forged parts were made from the top of them, where a massive central shrinkage is present before forging. This central shrinkage was closed but still visible after forging. As mechanical testing specimens have been extracted far from the central shrinkage, such effect on impact toughness is only possible if there is a high concentration of inclusions in the whole volume (due to the laboratory casting process), and due to the higher reduction ratio of 35x35mm² forged parts, the average size of these features could have been reduced during forging, decreasing at the same time the probability of meeting a coarse critical feature to initiate cleavage cracking.

4.2.3 Damage development

An EBSD map has been acquired along one secondary crack that propagated into the bulk (observed in cross section). Several regions of the crack have been analysed with greater interest. They are highlighted in white in Figure 80a. The objective was to measure the deviation of the crack when it goes from one bainitic packet to another one. Every time the micro-crack was deviated by crossing a packet boundary, the misorientation angle between the neighbouring packets was determined. It appears that the minimum angle found to deviate the micro-crack is 17°, and the maximum angle for which the micro-crack is not deviated is 13°. Nevertheless, from the amount of identified packet boundaries with a misorientation angle higher than 3° that have been crossed by the micro-cracks (around 30 in the 4 analysed regions), no one was found between 13° and 16°. This is in agreement with several studies reported in literature [166;167].

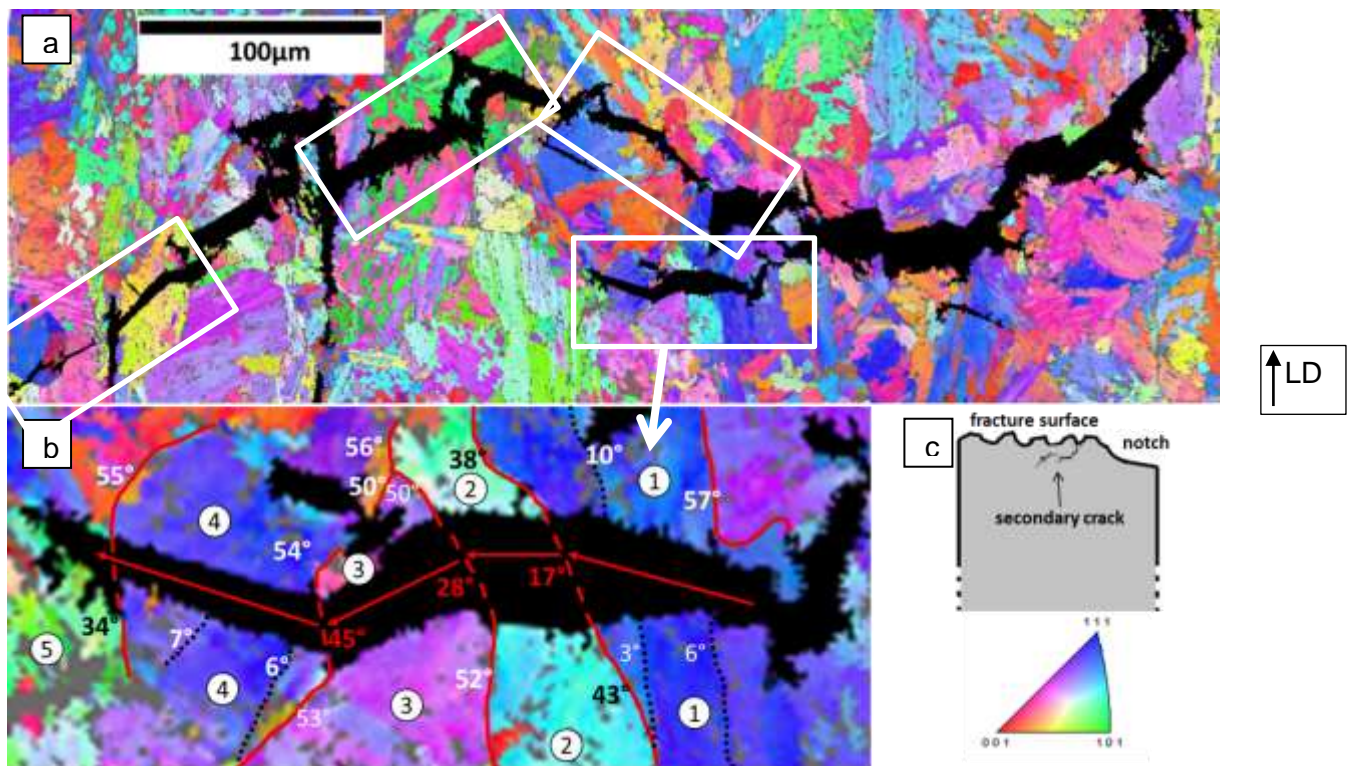


Figure 80: (a) EBSD Inverse Pole Figure map along a secondary crack of the +Ni 35 specimen 4 (45J). In black, the crack and in grey, the secondary microstructural constituent (CI<30) (b) Enlarged view of one specific region of (a). Red boundaries separate packets with more than 16° of misorientation angle. Black-dotted boundaries separate packets with less than 13° of misorientation. White and black figures specify the misorientation angle of neighbouring boundary. Encircled numbers specify the arbitrary effective packet number. Red arrows are average apparent local directions of the crack (in the observed plane), red figures are the apparent local deviation of the crack. (c) Schematic view of the location of the secondary crack and inverse pole figure colour key (reference direction = sample normal).

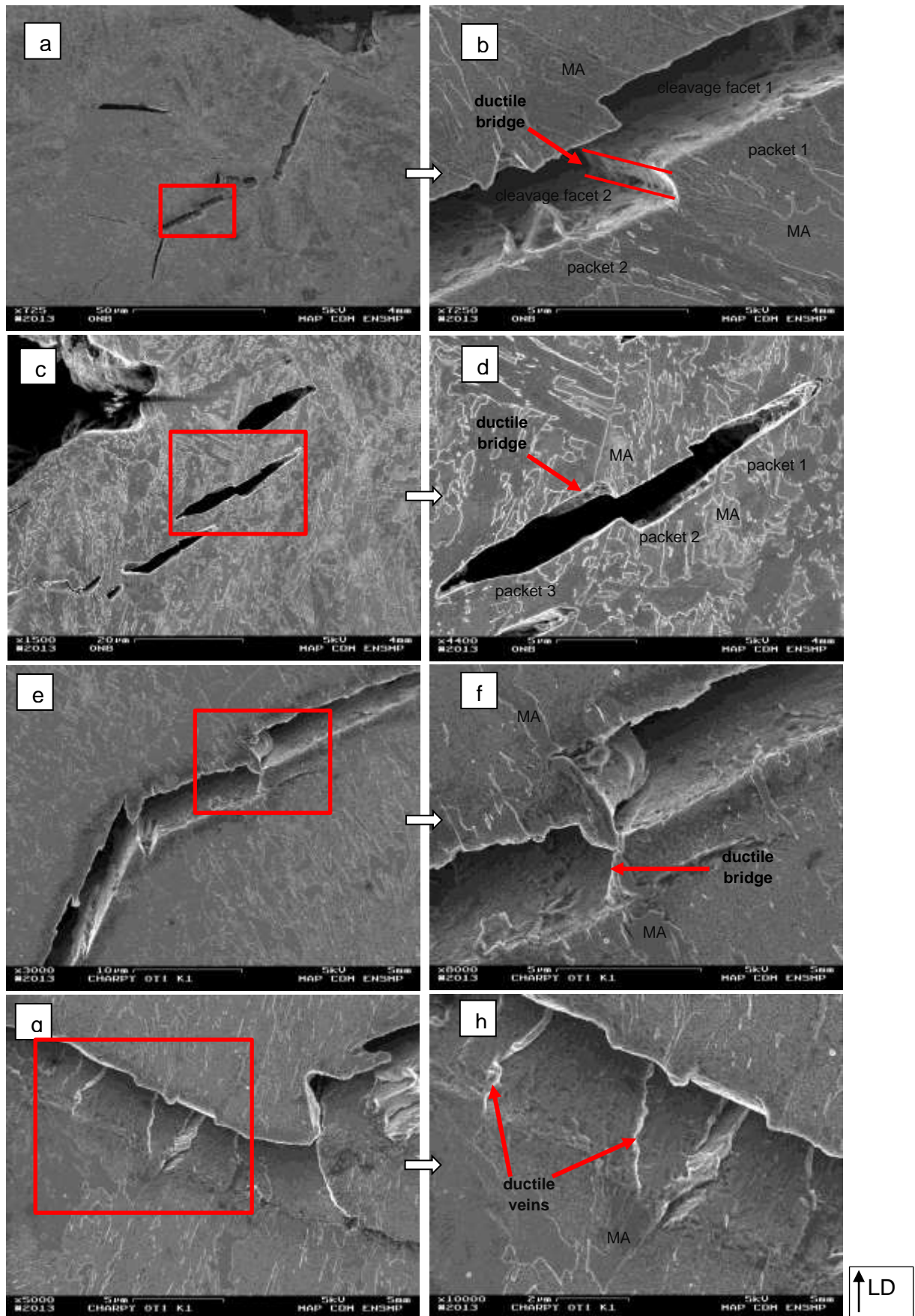


Figure 81: SEM, Nital2%, cross-section, from the middle of impact specimen, SE in-lens. Interactions between secondary microstructural constituents and secondary cleavage cracks. (a) to (d) ONb 35 (specimen 3, 23.1J), (e) to (h) OTi 35 (specimen 1, 60.3J).

The average unit crack path, considered in the cross-section plane, is thus proportional to the bainitic ferrite packet size with a threshold angle of 13° . The lower the effective packet size, the higher the absorbed energy during cleavage propagation, as cleavage cracks statistically encounter more deviation during their propagation.

The energy absorbed by brittle cracking was further investigated using damage observations. As shown in Figure 81a to Figure 81f, blocks of secondary phases, trapped between highly misoriented bainitic ferrite packets create large ductile bridges when encountered by cleavage microcracks. The size of the bridges is equivalent to the width of the blocks of secondary phases, here mostly MA constituent.

As shown in Figure 81g and Figure 81h, films, islands or even small blocks of secondary phases (austenite or MA constituent), located at bainitic packet boundaries with low misorientation angle, create thin ductile veins when crossed by the cleavage crack. All this ductility might contribute to the amount of absorbed energy during cleavage propagation.

4.2.4 Effective packet size

Table 21 shows the average and the maximum values of bainitic packet shape and size indicators (equivalent diameter, major axis, minor axis and aspect ratio) obtained from EBSD data processing for all investigated materials. For each indicator, materials have been ranked from the highest values to the lowest one. The number of investigated bainitic packets goes from 293 to 1401 according to their average size and the amount of secondary microstructural constituents that have been removed using a size criterion of $<12\mu\text{m}$ (see appendix A.III.2 for complete characterization methodology).

There are no great variations between all materials regarding effective packet size, as the average equivalent diameter ranges between 21 and $30\mu\text{m}$. Even if the size distributions obviously do not obey a Gaussian equation, standard deviations have been used as indicators of scatter. The standard deviation values are high due to the broadness and asymmetry of the size distribution as shown in Figure 82. For all investigated materials, the maximum number fraction in the size distribution of effective packet size is nearby 14 - $16\mu\text{m}$. Thus, the difference in average size comes only from decrease in number fraction for the larger packets. In addition of the blocks of secondary microstructural constituent, the relatively high size criterion that has been used might eliminate some bainitic ferrite. As a consequence, the average bainitic packet size might be slightly over-evaluated. However, considering the number of packets that have been analysed, these average values are relevant. Differences in average packet size revealed by such data processing can be well appreciated by direct observation of inverse pole figure (IPF) and grain maps. For this purpose, Figure 83 shows EBSD maps of two extreme cases in terms of effective packet size, -Cr 74 ($30\mu\text{m}$) and -Si+Mn 35 ($22\mu\text{m}$).

Both -Cr combinations exhibit the highest average equivalent diameter (28 - $30\mu\text{m}$), average major axis ($25\mu\text{m}$) and average minor axis (8.8 - $9.6\mu\text{m}$). The reasons for this might be their highest bainitic transformation temperatures among all investigated chemical compositions, combined with relatively high PAGS ($51\mu\text{m}$). So, 0Ti 35 was not found with the highest average effective packet size ($25\mu\text{m}$) despite the highest measured PAGS ($71\mu\text{m}$) and the very large cleavage facets that have been observed on its specimens. The investigated area was lower for the determination of the effective packet size than for the PAGS, which can introduce errors especially for a very heterogeneous PAGS as encountered for 0Ti 35 (the effective packet size becomes very dependent of the EBSD map location).

The as-rolled reference steel exhibits the lowest average effective packet size ($21\mu\text{m}$) and average minor or major axis length ($6.4\mu\text{m}$ and $18\mu\text{m}$, respectively) which is not surprising if considering that this steel has the lowest PAGS ($31\mu\text{m}$) among all investigated materials. In a general way, chemical compositions that tend to stabilize austenite ($-\text{Si}+\text{Mn}$, $+\text{Ni}$, $+\text{Mn}$) have lower packet sizes than the other chemical compositions. This effect is essentially provided by narrower packets (lower minor axis length). The only exception is $+\text{Mn}$ 74.

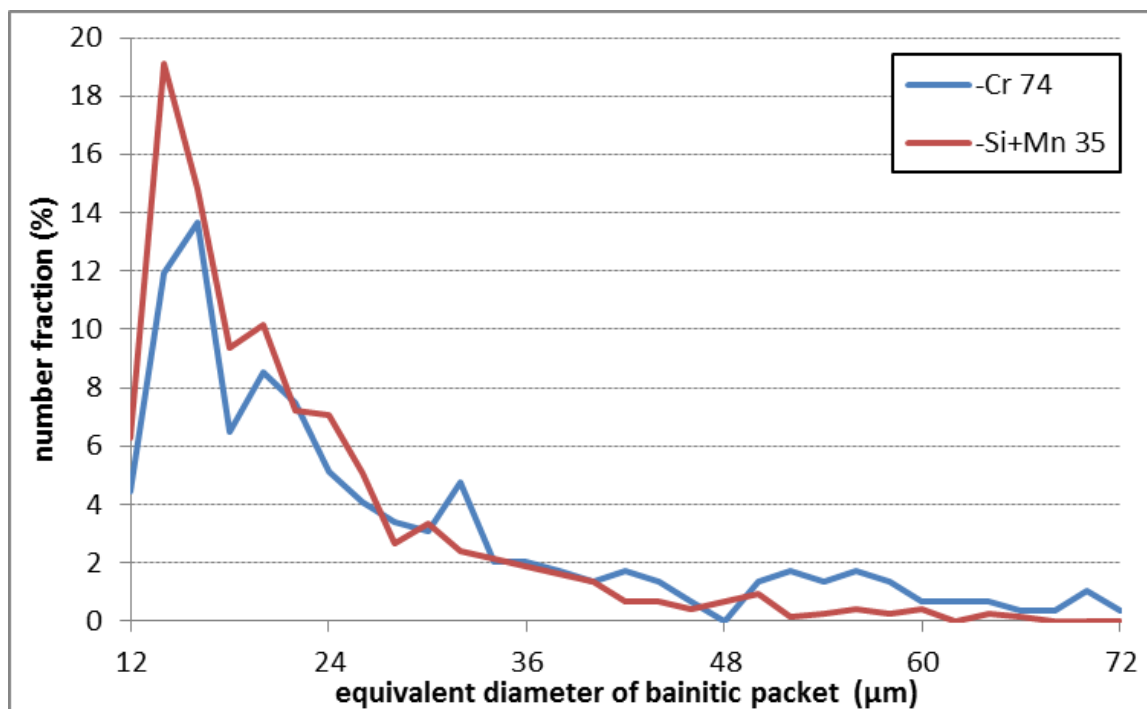


Figure 82: Number distribution of effective packet size (in equivalent diameter) for the two extreme average value of bainitic packet size found on as-forged laboratory heats ($22\mu\text{m}$ and $30\mu\text{m}$ for $-\text{Si}+\text{Mn}$ 35 and $-\text{Cr}$ 74 respectively).

Some chemical compositions seem to provide more granular effective grain shape than the others. This is the case for 0Nb , base, and to a lower extent, for 0Mo , which have over average aspect ratio for both forged part geometries. The contrary goes for $+\text{Ni}$ chemical composition. Even if the $-\text{Cr}$ chemical composition exhibits the highest effective packet sizes, the packet shapes do not become more granular, packets are only bigger.

These observations highlight that the effective packet size might effectively affect the minimum stress to initiate cleavage in the matrix, but that it has less influence on toughness than the number density of coarse inclusions. This is why, despite the highly probable occurrence of huge bainitic packets in its microstructure (in view of its PAGS and of the cleavage facet size noticed on fracture surfaces), 0Ti 35 has the best average impact toughness among all $35\times 35\text{mm}^2$ forged parts ($44\pm 17\text{J}$). Cleavage cracks have a tendency to initiate very late in this chemistry due to the absence of coarse titanium nitride in the microstructure. Surprisingly, even without any TiN inclusions, 0Ti 74 does not exhibit such a high impact toughness. This is certainly because, like all other $74\times 74\text{mm}^2$ forged parts, it might exhibit a higher density of other coarse features such as aluminium oxide. However, 0Ti 74 shows the best impact toughness among all $74\times 74\text{mm}^2$ forged parts ($20\pm 2\text{J}$) if 0Nb 74 is not taken into consideration. This last combination, in fact, exhibits some allotriomorphic ferrite grains that might change the overall impact toughness behaviour.

CHAPTER 4 - MICROSTRUCTURAL PARAMETERS THAT CONTROL IMPACT TOUGHNESS

tag	eq. diameter (μm)		
	average	st. dev.	max
-Cr 74	30	20	127
-Cr 35	28	21	179
OMo 74	27	18	118
-Si 74	27	17	143
+Cr 74	26	16	130
OTi 35	25	15	127
OTi 74	25	16	124
OMo 35	25	14	102
+Mn 74	24	13	106
base 74	24	13	90
+Cr 35	24	11	82
as-forged	24	13	172
ONb 74	24	12	88
base 35	23	12	99
-Si+Mn 74	23	13	111
ONb 35	23	12	106
-Si 35	23	12	100
+Ni 74	22	11	88
+Mn 35	22	10	70
+Ni 35	22	11	93
-Si+Mn 35	22	10	79
as-rolled	21	9	85

tag	major axis (μm)		
	average	st. dev.	max
-Cr 35	25	22	174
-Cr 74	25	17	106
-Si 74	24	17	137
OMo 74	24	17	114
+Cr 74	23	15	122
OTi 35	23	17	161
as-forged	23	14	197
OTi 74	22	15	111
OMo 35	21	12	105
base 74	21	12	105
-Si+Mn 74	21	13	101
+Mn 74	20	12	96
-Si+Mn 35	20	11	116
ONb 74	20	11	74
+Ni 74	20	11	93
base 35	20	11	87
+Ni 35	20	11	110
-Si 35	19	11	95
+Mn 35	19	10	71
+Cr 35	19	10	85
ONb 35	19	11	106
as-rolled	18	8	73

tag	minor axis (μm)		
	average	st. dev.	max
-Cr 74	9.6	6.8	45.3
OMo 74	8.8	5.7	39.3
-Cr 35	8.8	6.7	57.5
+Cr 74	8.3	5.2	42.2
-Si 74	8.2	5.2	45.9
+Cr 35	8.0	3.6	25.2
+Mn 74	8.0	4.1	36.7
OMo 35	8.0	4.6	35.4
OTi 74	7.8	5.3	52.3
base 74	7.8	4.0	29.3
ONb 74	7.8	4.1	31.1
ONb 35	7.6	3.9	33.8
base 35	7.6	4.0	32.0
OTi 35	7.5	4.8	49.0
-Si 35	7.3	3.9	30.8
-Si+Mn 74	7.3	4.1	37.2
as-forged	7.2	4.1	48.2
+Mn 35	7.1	3.2	22.0
+Ni 74	7.1	3.6	28.0
+Ni 35	7.0	3.6	29.2
-Si+Mn 35	6.8	3.2	24.7
as-rolled	6.4	3.0	29.1

tag	aspect ratio		
	average	st. dev.	max
+Cr 35	0.45	0.11	0.75
+Mn 74	0.43	0.12	0.89
ONb 35	0.42	0.11	0.89
ONb 74	0.41	0.11	0.84
base 35	0.41	0.11	0.76
base 74	0.40	0.11	0.77
-Si 35	0.40	0.11	0.74
OMo 74	0.40	0.12	0.71
+Mn 35	0.40	0.11	0.75
OMo 35	0.39	0.11	0.69
-Cr 74	0.39	0.12	0.70
+Cr 74	0.38	0.12	0.72
-Cr 35	0.38	0.12	0.77
-Si+Mn 74	0.38	0.11	0.84
OTi 74	0.38	0.11	0.73
+Ni 74	0.38	0.10	0.65
+Ni 35	0.37	0.11	0.72
-Si 74	0.37	0.11	0.72
-Si+Mn 35	0.37	0.11	0.70
as-rolled	0.37	0.11	0.70
OTi 35	0.36	0.12	0.72
as-forged	0.34	0.11	0.67

Table 21: Apparent effective bainitic packet size and shape measured using EBSD for all investigated materials. As rolled and as-forged are for the reference steel.

Figure 84 exhibits the evolution of the impact toughness according to the effective packet size. With the exception of OTi 35, no combination with an effective packet size larger than $24\mu\text{m}$ (or maximum observed packet size of $106\mu\text{m}$) can reach an impact toughness over 25J. However, an effective packet size lower than $24\mu\text{m}$ does not necessarily guarantee impact toughness higher or equal to 25J either. On the contrary, as represented in Figure 84 with a black-dotted line, any material with an average area of ductile crack extension larger than 2mm^2 can reach an impact toughness higher than 25J whatever its effective bainitic packet size.

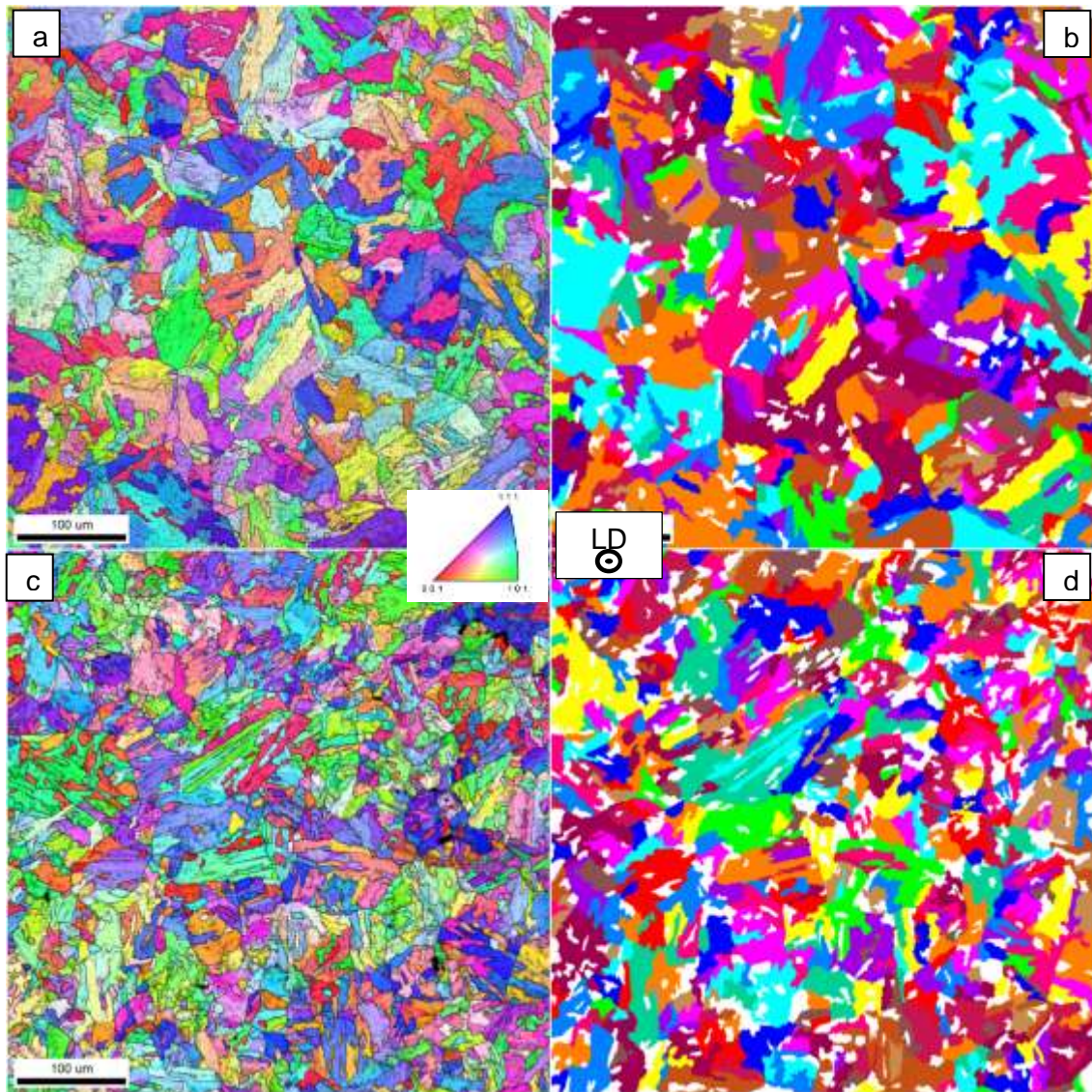


Figure 83: IPF map of –Cr 74 (a) and –Si+Mn 35 (c). Grain map (arbitrary colours) of –Cr 74 (b) and –Si+Mn 35 (d). Cut-off angle of 15°. Average equivalent grain sizes are 30 μ m and 22 μ m for –Cr 74 and –Si+Mn 35, respectively. In white: secondary microstructural constituent ignored for calculation.

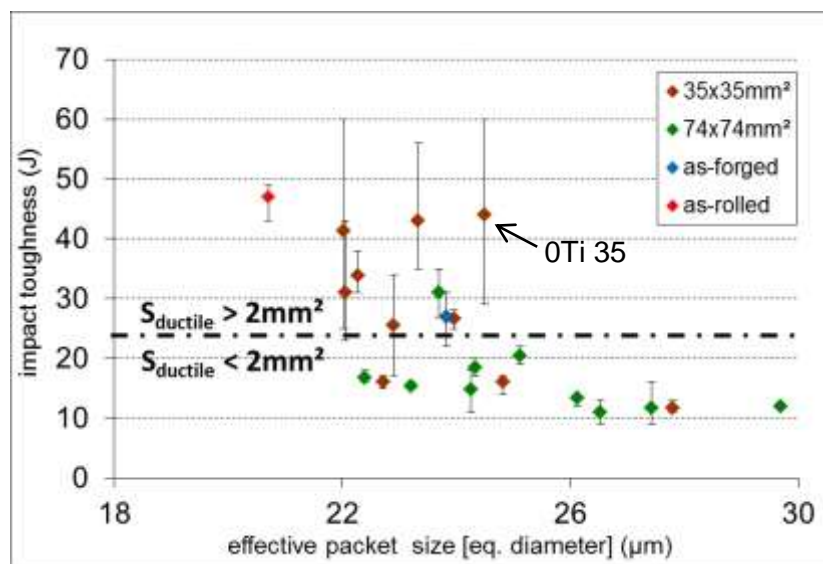


Figure 84: Average impact toughness as a function of the average effective packet size (equivalent diameter). Packet size was determined using a cut-off angle of 15° in EBSD maps. The range of impact toughness is represented by uncertainty bars.

4.2.5 Secondary microstructural constituent and austenite

Figure 85a shows the evolution of the impact toughness as a function of the austenite fraction (f_γ) measured using XRD. Whatever the amount of retained austenite, there is no guarantee to exhibit a higher impact toughness than 25J.

However, a more intrinsic ductile cracking resistance $U_{ductile}/S_{ductile}$ can be calculated for every tested specimen by removing the average amount of energy absorbed by pure brittle cracking, found earlier in Figure 79 (here estimated to 6J whatever the microstructure), from the total absorbed energy U . Two simplifications allow realizing this calculation:

1. The energy absorbed by pure brittle cracking is the same for all the materials, and thus, for all considered microstructures.
2. The energy absorbed by brittle cracking in ductile-to-brittle fracture is equal to the energy absorbed by pure brittle cracking, whatever the extent of the ductile crack extension.

Thus, an average value of $U_{ductile}/S_{ductile}$ can be calculated for every combination considering all their specimens. Specimens with $S_{ductile} < 2\text{mm}^2$ were not taken into account for the calculation of average, so there is no average $U_{ductile}/S_{ductile}$ value for combinations with all specimens below this limit. Indeed, below $S_{ductile} < 2\text{mm}^2$, the different points from each combination are too close to each other and relative measurement uncertainties on $S_{ductile}$ are too high to allow proper calculation (relative measurement uncertainties increase as $S_{ductile}$ decreases, around 8% for $S_{ductile} > 2\text{mm}^2$, higher than 12% for $S_{ductile} < 2\text{mm}^2$). As shown in Figure 86a, $U_{ductile}/S_{ductile}$ value has a strong tendency to increase with the retained austenite content, at least for forged parts made of laboratory heats, showing an impact of the retained austenite on the ductile crack propagation resistance. Ignoring both reference steels, this tendency can be described according to the following relationship:

$$\frac{U_{ductile}}{S_{ductile}} (\text{J/mm}^2) = b f_\gamma \quad \text{eq. 4.1}$$

Where b is equal to 88J/mm². Reasons why the reference steel is out of this tendency are not well-understood at this point. Perhaps the stability of austenite or the ratio between TRIP-available austenite and total austenite content of as-forged and as-rolled reference steel are very different from that of the as-forged laboratory heats due to different thermo-mechanical processing and higher nickel content. According Figure 86a, the retained austenite in as-rolled reference steel is twice more efficient to absorb energy than in the as-forged reference steel. Another possibility could be a difference in particles that trigger void nucleation in ductile fracture.

The retained austenite is believed to reduce the stress concentration field in the material by phase transformation under mechanical loading, absorbing some energy and retarding void initiation and growth, and thus ductile damage development. This is the so-called TRIP effect. The retained austenite that is TRIP-available is believed to be the film-like austenite between bainitic laths, but its stability under mechanical solicitation also depends on its chemical composition [161-164]. For example, 0Ti 35, which exhibits large groups of very long but well-defined bainitic laths in its coarse PAGS regions, has the highest austenite content and the highest $U_{ductile}/S_{ductile}$ ratio, which is believed to be due to more film-like morphology and more profuse spatial distribution of retained austenite linked to the refinement of the sub-structure (but not the refinement of the packet size that is believed to be higher in these regions).

CHAPTER 4 - MICROSTRUCTURAL PARAMETERS THAT CONTROL IMPACT TOUGHNESS

Unfortunately, it is not possible to determine the absolute amount of film-like austenite from XRD measurements. Indeed, the total retained austenite content determined by XRD is shared between MA constituents, martensite and bainite. Nevertheless, there might be a relationship between the total austenite content and the TRIP-available film-like austenite, which would explain the evolution of $U_{ductile}/S_{ductile}$ as a function of the total austenite content (this relationship might be different for both states of reference steel).

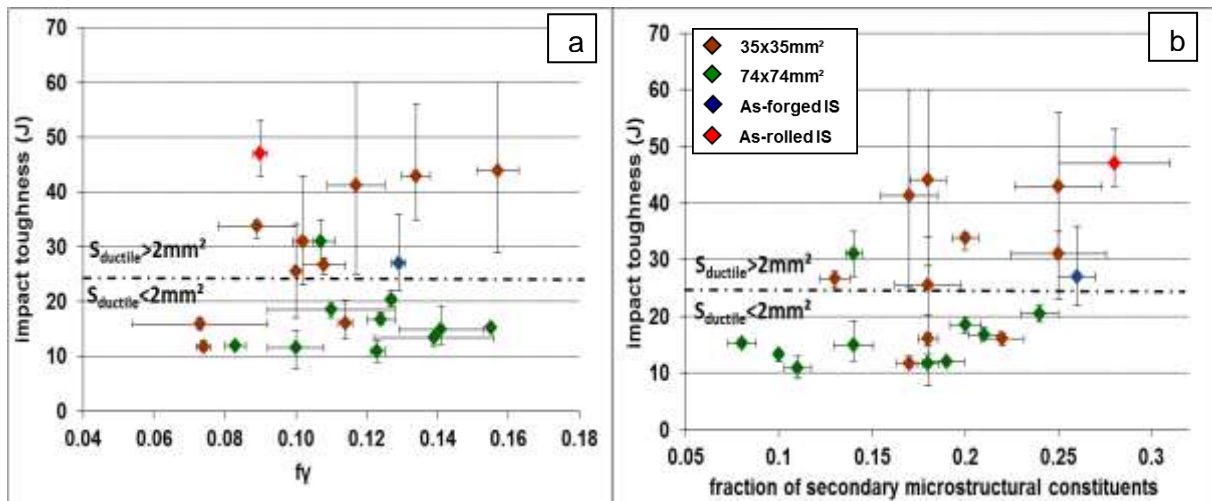


Figure 85: Evolution of impact toughness as a function of (a) the austenite fraction measured with XRD and (b) the fraction of hard secondary microstructural constituent measured using LM and LePera etching quantification. The range of impact toughness values is represented by uncertainty bars. IS: reference steel.

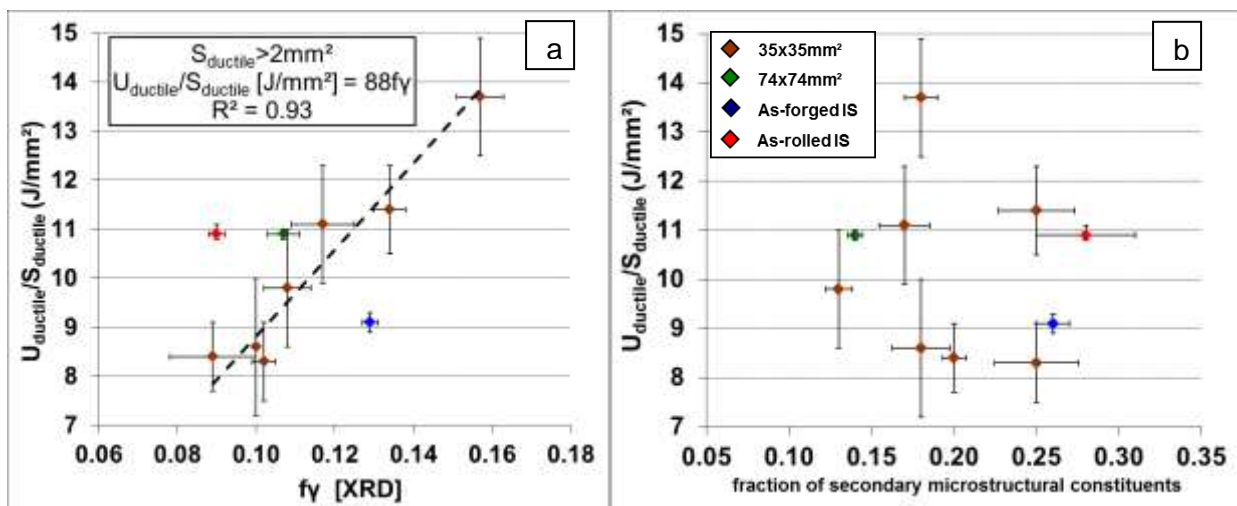


Figure 86: Evolution of the average ductile cracking resistance with (a) the austenite fraction measured with XRD and (b) the fraction of hard secondary microstructural constituent measured using LM and LePera etching quantification. The range of impact toughness and $U_{ductile}/S_{ductile}$ values is represented by uncertainty bars.

Figure 85b shows the evolution of the impact toughness as a function of the fraction of hard secondary microstructural constituents (MA + martensite) quantified using LM and LePera etching. Combinations with a relatively high fraction of secondary microstructural constituent tend to exhibit higher impact toughness than combinations with a relatively low fraction of secondary microstructural constituent. MA constituents are formed from carbon-enriched austenite that is left untransformed following the growth of bainite. The main part of the carbon content is trapped into these MA constituents. For a given chemical composition, as the MA constituent fraction increases, the average carbon concentration in these MA constituents decreases; assuming that brittle behaviour is associated with high carbon content, MA constituent may be less harmful to toughness at sufficiently large fractions [168].

Granular bainite and a more or less coarse upper bainite are present at the same time in the microstructure, but with different extents according to the forged part geometry and chemical composition. Thus, it is also impossible to determine the film-like austenite content from the bainite fraction. So it is not surprising to find no relationship between $U_{ductile}/S_{ductile}$ and hard secondary microstructural constituent (or inversely, bainite fraction) in Figure 86b.

4.3 Discussion

4.3.1 Calculation of impact toughness from quantitative data

From the damage study (Figure 80), the effective packet size has an influence on the amount of energy absorbed during cleavage crack propagation. So, by applying a simple phenomenological approach, absorbed energy during pure brittle fracture, $U_{brittle}^0$, might be approximated using a power law:

$$U_{brittle}^0(J) = ad_p^{-n} \quad eq. 4.2$$

Where d_p is the effective packet size in mm, n is a dimensionless numerical coefficient and a is a numerical coefficient in $J.mm^n$. In order to obtain an average value of $U_{brittle}^0$ equal to 6.0J, a must be equal to $33.1J.mm^{0.5}$ or $182.1J.mm$ for $n=0.5$ and $n=1$ respectively. As the studied materials are in the ductile-to-brittle transition temperature range (i.e. not purely brittle), this value has to be corrected by the brittle area fraction of the fracture surface, $f_{brittle}$, deduced from $f_{ductile}$, which is calculated from the equation below:

$$f_{ductile} = \frac{S_{ductile}}{S_{fracture}} \quad eq. 4.3$$

Where $S_{fracture}$ is the total fracture surface. Considering that the fracture surface is flat and normal to the loading axis, at least for very brittle fracture investigated here, $S_{fracture}$ is equal to $70mm^2$, which gives the following correction of eq.4.1 for ductile-to-brittle fracture:

$$U_{brittle}(J) = a(1 - f_{ductile})d_p^{-n} \quad eq. 4.4$$

Where $U_{brittle}$ is the absorbed energy by the brittle crack propagation during the ductile-to-brittle fracture.

It has been shown in Figure 86a that the ductile cracking resistance, i.e. the energy absorbed during the ductile crack propagation, is proportional to the fraction retained austenite. So, the energy absorbed for a pure ductile failure, $U_{ductile}^0$, might be approximated as follows:

$$U_{ductile}^0(J) = b'f_\gamma \quad eq. 4.5$$

With:

$$b' = bS_{ductile} \quad eq. 4.6$$

Where b' is a numerical coefficient in J. For purely ductile rupture, as $S_{ductile} = S_{fracture}$, b' is equal to 6160J ($b=88J/mm^2$, eq.4.1). Once again, a correction is realized using the ductile area fraction of the fracture surface to obtain the energy absorbed by ductile crack extension before cleavage initiation, $U_{ductile}$, which gives:

$$U_{ductile}(J) = f_{ductile}b'f_\gamma \quad q. 4.7$$

The absorbed energy during the Charpy impact test, U , can be thus estimated by the addition of $U_{brittle}$ (eq.4.4) and $U_{ductile}$ (eq.4.7), which gives:

$$U(J) = a(1 - f_{ductile})d_p^{-n} + f_{ductile}b'f_y \quad eq. 4.8$$

Only a slight difference in the average difference between experimental and calculated impact toughness is found using $n=0.5$, $a=33.1\text{J.mm}^{0.5}$ and $b'=6160\text{J}$ or $n=1$, $a=182.1\text{J.mm}$ and $b'=6160\text{J}$. Indeed, the average difference is equal to 2.8J in the former case and to 2.9J in the latter case. It can be noticed that the toughness of the as-rolled reference steel is badly estimated in both cases, especially in the former one (difference $>11\text{J}$ for all specimens). If the as-rolled reference steel is ignored, the average difference between experimental and calculated impact toughness becomes 2.5J for $n=0.5$ and 2.6J for $n=1$.

By mathematical fitting of a and b , the best agreement between experimental and calculated impact toughness was reached when $n=0.5$, $a=42.\text{J.mm}^{0.5}$, $b'=5942\text{J}$. Figure 87 shows this agreement, in which the average difference between experimental and calculated values is only 2.7J (2.3J without considering the as-rolled reference steel).

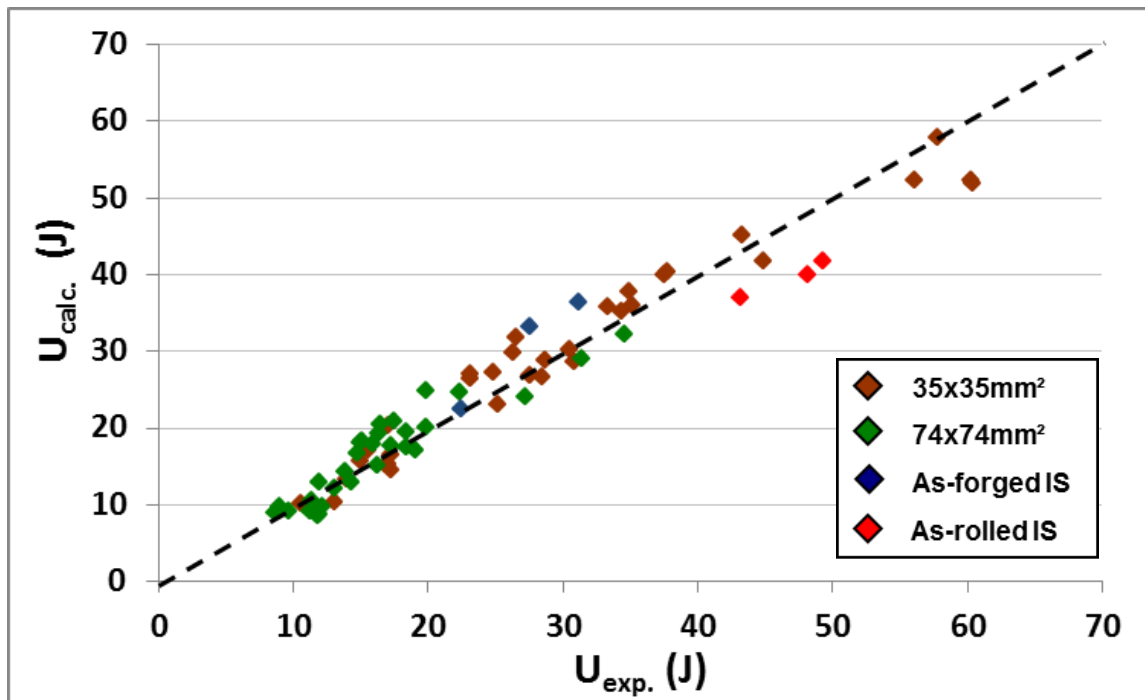


Figure 87: Calculated versus experimental values of impact toughness.

In this last case, the energy absorbed by cleavage cracking goes from 6.4J (-Cr 74) to 8.1J (as-rolled reference steel), representing 10.6% (0Ti 35 specimen 1) to 72.6% (-Si 74 specimen 1) of the total impact toughness despite occupying 93.7% (+Ni 35 specimen 1) to 99.7% (-Si 74 specimen 2) of the fracture surface. With a set to $42.\text{J.mm}^{0.5}$, $U_{brittle}^0$ is equal to 7.6J, which is higher than the initial value of 6.0J found from Figure 79. This increase is attributed to the de-correlation between $U_{brittle}$ and $U_{ductile}$. The linear relationship between the ductile cracking resistance and the fraction of retained austenite (eq.4.1) is also affected by this de-correlation, b going from 88 to 85J/mm².

When $b=85\text{J/mm}^2$, the ductile crack resistance might vary from 6.2 to 13.3J/mm² according to the fraction of retained austenite. This range appears very high once these values are reported on a fully ductile fracture (i.e. $S_{ductile} = S_{fracture}$), as total absorbed energy values obtained would be between 434 and 934 J at 20°C. Shear lips, which dissipate only a very low amount of energy, can represent between 25% and 50% of the fracture surface, reducing

the value of U by almost the same extent. However, the range of U values obtained stays high even considering the most favourable case (between 217 and 472J). The assumption realized here to explain such a high value of ductile crack resistance, is that ductile crack resistance may evolve dynamically according to the amount of strain absorbed by the materials, the very first mm² (or mm³) of ductile cracking dissipating much more energy than the following cracking (as cracking velocity increases and/or loading mod changes, ...).

Such calculation is accurate but not predictive, as f_{ductile} is measured on specimens that have been already tested. Moreover, its validity only stands for low f_{ductile} values, as long as the fracture surface can be considered as flat (i.e. the area of fracture surface is close to the transverse section area at the level of the notch, 70mm²). f_{ductile} is believed to be dependent on the density of critical features that can initiate cleavage cracking (i.e., probability to meet a critical feature) and on the minimum critical stress to initiate and propagate cleavage, two parameters which can be dependent on each other (in the case of initiation-controlled cleavage crack) and extremely difficult to approach by calculation, especially with the presence of a dynamic ductile crack.

Indeed, the critical size of a feature necessary to initiate cleavage decreases as the ductile crack extends, due to the simultaneous increase in stress intensity factor in the vicinity of the ductile crack front. However, in the present case, as the extent of ductile crack is limited, variation of the stress intensity factor might stay limited. The density of such features initially present in the microstructure that can be active to initiate cleavage might thus not change greatly with the extension of the ductile crack. Moreover, only a few in-bulk voids were observed under the ductile crack in cross-section observation, which means that only limited ductile damage occurs in the vicinity of the ductile crack. So, no significant additional defects are introduced in the microstructure during the ductile crack extension. Considering these observations, proper inclusion quantification of each combination might be sufficient to estimate the probability to meet a critical feature according to the minimum critical stress. However, such inclusion quantification has not been realized on any studied materials because it might not be representative of a more realistic processing route for the targeted application.

4.3.2 Cleavage fracture path

Several studies on fully bainitic steels (low-alloy, low-carbon) have demonstrated that the cleavage cracks propagate un-deviated across bainitic packets [169-171], so that the cleavage fracture path is equal to the packet size determined with high misorientation-angle (>15°). This assumption is consistent with the cleavage crack path that has been observed along a micro-crack in cross-section (section 4.2.3).

Some other studies found that the cleavage fracture path might be slightly higher than the bainitic packet size, 1.3 and 1.5 times larger in the case of cementite-free upper bainite [172] and lower bainite, respectively [173]. The larger size of the crack path is believed to come from the high probability in existing fairly parallel cleavage planes between adjacent packets within one prior austenite grain (these packets being different crystallographic variants of one austenite-bainitic ferrite orientation relationship) [172].

The amount of secondary microstructural constituents in our steels is rather high (from 8% of 28% of the microstructure). According to their chemical composition, shape and size, a certain part of them may bring ductility during the cleavage crack propagation. This is translated on brittle fracture surfaces by the occurrence of numerous ductile bridges of several μm in width between packets, and ductile veins of some tens of nm between two laths sharing close orientations. In the case of the main part of secondary microstructural constituent would bring ductility during cleavage crack propagation, the average cleavage fracture path might be near the measured average effective packet size as this last one has

been determined without taking the secondary microstructural constituents into consideration.

However, if the main part of secondary microstructural constituents has a strong tendency to split by cleavage, the average cleavage fracture path might become much lower than the effective bainitic packet size, due to the emergence of numerous small cleavage facets. In this case, it would have been more relevant to measure an effective grain size by taking into consideration every microstructural constituent (primary and secondary). Notice that in this case, even if the average cleavage fracture path decreases, the energy absorbed during the cleavage crack propagation is lowered, as less energy is consumed by crossing of the high-angle misorientation boundaries.

A quantitative measurement of the cleavage facet size on fracture surface would have given keys to know if secondary microstructural constituents mainly follow the first or the second behaviour. Perhaps different behaviours would have been found between the as-forged laboratory heats, as-forged and as-rolled reference steels. It might explain the different $U_{ductile}/S_{ductile}$ ratio found for both states of reference steel, as $U_{ductile}$ was deduced from U by subtraction of the average amount of energy absorbed by brittle cracking on all materials. However, such measurements have not been realized in the time allowed for this thesis project.

4.4 Conclusions & Outlooks

The investigated material family is near the lower shelf of the ductile-to-brittle transition curve at 20°C. Impact toughness is set by, by order of influence:

The first order phenomenon is the initiation stage of brittle cracking from the ductile crack: the later the brittle fracture occurs, the better the impact toughness. There is a need to reduce as much as possible the amount and size of harmful inclusions and clusters of large precipitates. Coarse oxides or nitrides are very detrimental to impact toughness as they act as cleavage initiation sites. These inclusions are Al_2O_3 , TiN and clusters of MnS in the case of as-forged laboratory heats. For the reference steel, they are spinelle, (Ti,Nb)(N,C) inclusions and clusters of MnS and/or (Nb,Ti)(C,N) inclusions.

Cleavage initiation seems to appear later for materials exhibiting lower effective packet size, pointing out that this parameter may play a role on the critical stress to initiate unstable cleavage propagation. This limit may change as the inclusion population changes. Indeed, 0Ti chemical composition tends to exhibit the best impact toughness in both forged-part dimensions due to the decrease in density of features that are critical to cleavage (absence of coarse TiN inclusions), despite a relatively coarse effective grain size.

MA constituents have not been found obviously detrimental. On the contrary, the higher their fraction, the less harmful they tend to be as their average carbon content decreases. They have not been directly identified as initiation sites for cleavage, but might participate to cleavage propagation for the brittlest ones.

The second order phenomenon is the capacity of the microstructure to dissipate energy in ductile fracture (between 2 and 55J), which is mainly controlled by the amount of retained austenite, especially the film-like one. For an equivalent ductile crack extension, the absorbed energy before final cleavage fracture tends to be higher when the austenite fraction is higher.

The third order phenomenon is the capacity of brittle fracture to absorb energy (between 6 and 8J). The more frequently the crack is deflected by high-misorientation boundaries, the more the material absorbs energy. The average unit crack path seems to be proportional to

CHAPTER 4 - MICROSTRUCTURAL PARAMETERS THAT CONTROL IMPACT TOUGHNESS

the bainitic ferrite packet size (misorientation $>15^\circ$). Some secondary microstructural constituents also absorb energy by creating local crack deviation compensated by ductile failure, such as ductile bridges between packets and ductile veins between two laths sharing close crystal orientations.

An empirical equation has been built in order to rationalize these observations. Using this equation, the average accuracy on calculation of impact toughness is $\pm 3J$. However, this calculation is not predictive, as the measurement of the ductile crack extension is a necessary step, and its validity only stands as long as the fracture surface can be considered as flat, without considerable amount of ductility. The extent of the ductile crack extension is believed to be dependent on the density of critical features (with respect to cleavage cracking) and on the minimum critical stress to initiate and propagate cleavage. The next step of this study would be to find a way to predict these two parameters, starting from proper inclusion quantifications.

CHAPTER 5 - MICROSTRUCTURAL PARAMETERS THAT CONTROL STRENGTH

Résumé : Ce chapitre est dédié à la détermination des phénomènes physiques et des paramètres microstructuraux qui contrôlent la résistance mécanique, plus particulièrement la limite d'élasticité. Ce chapitre commence par une étude du comportement général en traction de la nuance d'acier étudiée (acier de référence et coulées de synthèse). Ceci inclut une discussion autour des résultats en traction uniaxiale, des courbes de traction, des faciès de rupture et de l'endommagement. Au passage, des relations sont établies entre la dureté et la résistance et entre la résilience à 20°C et la réduction d'aire à rupture en traction.

Ensuite, la limite d'élasticité est modélisée en combinant une loi des mélanges, tenant compte des différents constituants microstructuraux, et une loi additive, tenant compte des différents mécanismes de durcissement. Ce modèle permet de retrouver avec une bonne précision la limite d'élasticité expérimentale. L'écart moyen aux résultats expérimentaux est de 7 MPa si on tient compte des incertitudes expérimentales, sur une gamme allant de 700 à 900 MPa.

Le modèle a permis d'identifier quantitativement les mécanismes de durcissement prépondérants pour cette nuance, qui sont, par ordre décroissant de contribution à la limite d'élasticité :

- Durcissement fourni par la solution solide
 - Durcissement apporté par les constituants microstructuraux secondaires (principalement les MA).
 - Durcissement fourni par les joints de grains
 - Durcissement fourni par les dislocations.
-

The main requirement of the targeted application is to reach good strength properties (tensile strength, **TS**=1100MPa, yield strength, **YS**=800MPa), especially high yield strength, impact toughness requirement being more a safeguard than property to be optimized. Such mixed microstructure between upper and granular bainite has not been well-studied in literature. Even if strengthening mechanisms are well known, as they are similar to those of other complex high strength steels, this is not at all the case for their respective contribution to the total strength. The purpose of this chapter is to establish these contribution on a quantitative basis. Focus has been made on the yield strength. This would allow identifying the main levers to improve it. At the same time, plenty of other precious information can be extracted from the tensile tests realized at room temperature to measure this yield strength, and especially the ductile-to-brittle transition fracture surface that is not-common for un-notched steel tensile specimens. Such fracture surface reminds that this high strength is provided by a coarse matrix microstructure, that contains hard but brittle secondary microstructural constituents and of other features that can trigger cleavage crack initiation.

5.1 Overall tensile behaviour

5.1.1 Experimental methods

Before machining any tensile specimen, hardness profiles and microstructural observations have been realized near the sections dedicated to the fabrication of tensile specimens to point out any detrimental segregation. In addition, these profiles might allow establishing links between hardness and strength that can be very useful in regard to CCT diagrams. HV30 and HV0.5 hardness profiles have been measured on longitudinal and transverse sections for each forged part. Hardness marks near the central shrinkage (closer than 250µm) and within 2mm from the free surface have been ignored for the calculation of the average hardness value. We used a step of 500µm and of 2mm for HV0.5 and HV30 hardness profiles respectively. HV0.5 profiles were realized using a Buehler MicroMet 5124 and HV30 ones using a Testwell DiaTestor 2RcS apparatus.

As average values of HV0.5 and HV30 profiles exhibit very similar results, as well as average values over profiles from transversal and longitudinal planes, only average values over the HV30 profile from the transverse plane have been reported in the following results. Indeed, each combination exhibits less than 10HV of difference between the different realized profiles without taking into consideration the uncertainties (which are slightly higher for HV0.5 profiles). No noticeable difference in hardness between the extreme surface and the bulk material as well as no harmful segregation has been noticed in every case. Of course, segregation might be present in these steels, but probably with a low intensity and a fine spatial distribution that do not impact microstructure or hardness properties.

At least three so-called TR02 tensile specimens were machined at mid-radius from X T1 35 and X PM 74 sections (see Appendix B) of 35x35mm² and 74x74mm² forged parts, respectively. Figure 88 shows the geometry of such tensile specimens. They were cut along the axis of each forged part. TR02 tensile specimens were also machined from as-rolled and as-forged reference steels with similar location and orientation. All specimens were tested at 20°C following NF EN ISO 6892-1 standard using a CADIS 250 kN tensile machine. The prescribed displacement rate used in these tests was 10mm/min.

Some experimental artefacts, such as serrations that were present along the tensile curves have been removed from the tensile curves. As no extensometer measurement was available, engineering stress-strain curves were derived from load versus load line displacement curves by taking the contribution of load line and specimen ends to measured displacement into account.

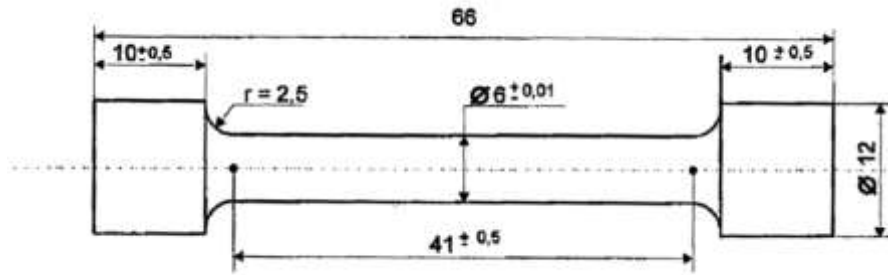


Figure 88: TR02 tensile specimen geometry (dimensions in mm).

In order to determine fracture mechanisms, fracture surfaces of all tensile specimens were observed using a conventional LEO 1450 VP SEM. Damage was also investigated on two tensile specimens of as-rolled and as-forged reference steel, respectively. The tensile specimens were cut along the longitudinal direction in order to observe the median plane. A first observation has been realized using light microscopy after several cycles of fine diamond polishing (down to $0.25\mu\text{m}$) and OPS (colloidal silica slurry) polishing to clearly identify cracks and porosities. A second observation, still with light microscopy, was then realized using LePera etching to locate damage in the bainitic microstructure. These two observations were realized on a Zeiss Axiovert 405M light optical microscope equipped with ProgRes CF scan camera from Jenoptik. Finally, these samples have been observed using a Zeiss DSM 982 Gemini FEG-SEM after an additional polishing and a Nital2% etching.

5.1.2 Results

Table 22 exhibits average values of 0.2% proof stress ($YS_{0.2}$), ultimate tensile strength (UTS), HV30, $YS_{0.2}$ over UTS ratio, total elongation ($E\%$), uniform elongation ($UE\%$), elongation after the onset of necking ($E_n\%$) and reduction of area at fracture or necking ratio ($Z\%$) according to the chemistry and the geometry of the forged part. The average impact toughness is recalled in order to be compared to other ductility indicators such as $E_n\%$ and $Z\%$. Figure 89 shows the typical shape of the plastic region of stress versus strain curves obtained for all materials. It can be seen there are some differences in strain-hardening properties between the different materials.

The first feature that appears by looking at the results in Table 22 is the abnormally low UTS (1034 MPa) of the base 35 in contrast to other $35 \times 35 \text{ mm}^2$ forged parts (1140 MPa in average), resulting in a relatively higher $YS_{0.2}$ over UTS ratio of 0.81. Such feature is easily seen in Figure 89a and comes from the very beginning of the plastic strain. Indeed, a much lower amount of additional stress than any other $35 \times 35 \text{ mm}^2$ forged parts is needed to keep on straining the material once $YS_{0.2}$ has been reached. The average hardness value is also slightly below the one that is found for other $35 \times 35 \text{ mm}^2$ forged parts (325HV30 versus 343HV30). However, the microstructure of base 35 does not present any significant difference (with respect to the other forged parts) that can explain this low value of UTS.

20°C	YS _{0.2} (MPa)	UTS (MPa)	HV30	YS _{0.2} /UTS	E (%)	UE (%)	E _n (%)	Z (%)	IT (J)
35x35mm²									
OTI	872 ± 16	1123 ± 3	325 ± 6	0.78 ± 0.01	12.1 ± 0.2	4.8 ± 0.3	6.6 ± 0.1	56 ± 1	44 ± 17
base	843 ± 18	1034 ± 5	325 ± 5	0.81 ± 0.02	12.5 ± 0.4	4.8 ± 0.1	7.1 ± 0.3	61 ± 1	43 ± 11
+Ni	870 ± 22	1124 ± 2	334 ± 6	0.77 ± 0.02	13.2 ± 0.4	5.3 ± 0.3	7.2 ± 0.5	56 ± 1	41 ± 10
ONb	856 ± 14	1174 ± 6	342 ± 6	0.73 ± 0.01	12.4 ± 0.4	6.4 ± 0.3	5.4 ± 0.5	46 ± 1	26 ± 7
-Si	836 ± 10	1148 ± 11	351 ± 6	0.73 ± 0.01	10.3 ± 0.7	5.0 ± 0.4	4.7 ± 0.5	42 ± 3	16 ± 1
-Si+Mn	860 ± 10	1188 ± 3	360 ± 5	0.74 ± 0.01	11.6 ± 0.4	5.2 ± 0.2	5.7 ± 0.5	46 ± 2	31 ± 11
+Mn	856 ± 4	1173 ± 7	365 ± 4	0.73 ± 0.01	11.9 ± 0.2	5.6 ± 0.3	5.7 ± 0.4	45 ± 1	34 ± 4
OMo	818 ± 3	1129 ± 3	342 ± 7	0.72 ± 0.01	11.3 ± 0.2	5.4 ± 0.2	5.3 ± 0.2	43 ± 4	16 ± 2
-Cr	746 ± 7	1058 ± 2	322 ± 5	0.71 ± 0.01	12.1 ± 0.3	6.2 ± 0.3	5.4 ± 0.1	41 ± 1	12 ± 1
+Cr	843 ± 11	1147 ± 2	348 ± 4	0.73 ± 0.01	11.4 ± 0.9	5.5 ± 0.1	5.3 ± 0.8	46 ± 5	27 ± 2
average	842 ± 38	1140 ± 39	343 ± 14	0.75 ± 0.03	11.9 ± 0.8	5.4 ± 0.5	5.8 ± 0.8	48 ± 7	29 ± 12
74x74mm²									
OTI	820 ± 29	1116 ± 12	336 ± 11	0.73 ± 0.02	11.1 ± 0.3	5.3 ± 0.1	5.1 ± 0.2	42 ± 2	20 ± 2
base	822 ± 14	1134 ± 3	338 ± 11	0.72 ± 0.01	11.0 ± 0.3	5.7 ± 0.4	4.7 ± 0.4	42 ± 3	19 ± 1
+Ni	842 ± 12	1144 ± 9	345 ± 12	0.74 ± 0.02	10.2 ± 0.9	5.0 ± 0.5	4.6 ± 0.4	44 ± 1	17 ± 1
ONb	766 ± 8	983 ± 15	304 ± 10	0.78 ± 0.01	13.1 ± 0.9	6.6 ± 0.4	5.9 ± 0.5	52 ± 1	31 ± 4
-Si	757 ± 13	963 ± 8	308 ± 14	0.79 ± 0.01	12.5 ± 0.9	5.5 ± 0.2	6.4 ± 0.7	53 ± 1	11 ± 2
-Si+Mn	777 ± 9	1003 ± 9	322 ± 9	0.78 ± 0.01	11.8 ± 0.8	5.5 ± 0.3	5.7 ± 0.5	50 ± 1	15 ± 0
+Mn	823 ± 10	1128 ± 2	353 ± 5	0.73 ± 0.01	11.0 ± 0.2	5.7 ± 0.2	4.7 ± 0.3	41 ± 1	15 ± 4
OMo	794 ± 12	1091 ± 8	341 ± 4	0.73 ± 0.01	11.0 ± 1.2	5.8 ± 0.8	4.6 ± 0.6	39 ± 2	12 ± 4
-Cr	697 ± 8	981 ± 6	303 ± 5	0.71 ± 0.01	11.9 ± 0.5	5.9 ± 0.1	5.4 ± 0.5	41 ± 1	12 ± 0
+Cr	800 ± 6	1097 ± 3	334 ± 4	0.73 ± 0.01	11.3 ± 0.6	5.5 ± 0.3	5.2 ± 0.4	42 ± 1	13 ± 1
average	790 ± 43	1064 ± 72	328 ± 18	0.74 ± 0.03	11.5 ± 0.8	5.7 ± 0.4	5.2 ± 0.6	45 ± 5	16 ± 6
As-forged reference steel	823 ± 5	1133 ± 11	354 ± 8	0.73 ± 0.01	11.7 ± 0.7	5.9 ± 0.5	5.2 ± 0.2	46 ± 3	27 ± 4
As-rolled reference steel	908 ± 20	1184 ± 7	354 ± 10	0.77 ± 0.01	11.5 ± 0.5	5.2 ± 0.2	5.6 ± 0.7	48 ± 2	47 ± 3

Table 22: Average values of 0.2% proof stress (YS_{0.2}), ultimate tensile strength (UTS), HV30, YS_{0.2} over UTS ratio, total elongation (E%), uniform elongation (UE%), elongation after the onset of necking (E_n%) and reduction of area at fracture or necking ratio (Z%) according to the chemical composition and the geometry of the forged part. Unexpected values are highlighted in red.

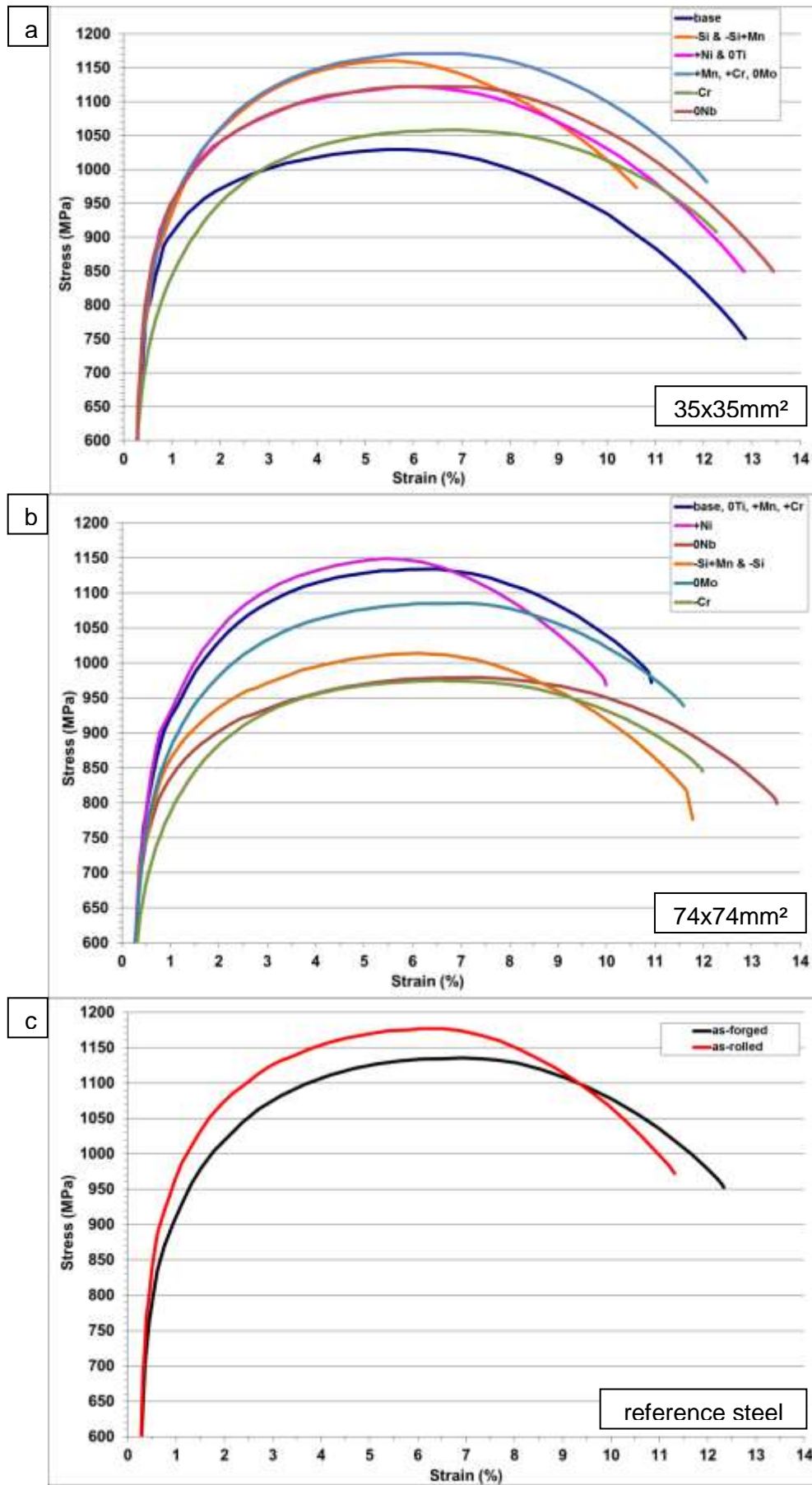


Figure 89: Typical stress vs strain curves of (a) 35x35mm² forged parts, (b) the 74x74mm² forged parts and (d) both state of reference steel.

From the hardness values exhibited in CCT diagrams, no laboratory heats forged with a section of 74x74mm² are expected to have a higher or equivalent strength level than +Mn 74 and +Cr 74 (hardness around 360 and 356 in microstructural domain A for +Mn and +Cr, respectively). From this point of view, 0Ti 74, base 74 and +Ni 74 have unexpected strength values. They also present no obvious change in microstructure and in strength level according to their respective 35x35mm² counterparts. This is not the case for impact toughness, $E_n\%$ and $Z\%$ due to the increase in detrimental defects concentration for 74x74mm² forged parts (as shown in chapter 4).

We first suspected a forging issue to be responsible of such good strength properties, a faster cooling rate for instance, close to the one normally encountered on 35x35mm² forged parts. In fact, these heats were forged during the first campaign and no on-field measurement is available for them. However, base 74 and +Ni 74 average hardness and fractions of microstructural constituents are also well in agreement with a cooling rate of 0.1°C/s during bainite transformation, as for other 74x74mm² forged parts (this is not known for 0Ti 74 for which no CCT diagram is available).

In concern of tensile curves (Figure 89b), 0Ti 74 and base 74 curves exhibit the same shapes as those of +Mn 74 and +Cr 74. The +Ni 74 curve is different. +Ni 74 exhibits the lowest UE_l among 74x74mm² forged parts and a very fast decrease in needed stress to strain once damage localization and necking occurs (but no significant decrease in E_n). This last trend is also observed for the as-rolled reference steel, and for both forged parts of –Si and –Si+Mn chemical compositions.

According to CCT diagrams, every combination is expected to be in microstructural domain A (mixed microstructure between coarse cementite-free upper bainite and granular bainite) or at its extreme limit with domain B (so the amount of cementite-free bainite increasing at the expense of granular bainite). The undercooling encountered by forged parts has been noticed to increase the amount of hard secondary phase in the microstructure for some 35x35mm² forged parts (–Si, –Si+Mn, +Ni, base and +Mn). Combined with microstructural refinement that is observed when the cooling rate increases, these features qualitatively explain the significant difference in strength level between 35x35mm² and 74x74mm² forged parts (difference by 52MPa and 76MPa in average $YS_{0.2}$ and UTS respectively). As observed in chapter 3 (section 3.2.3.a), –Si and –Si+Mn are very sensitive to undercooling (leading to an obvious increase in MA constituent fraction in final microstructure) and thus to the change in forged part dimension as shown in Figure 90. Indeed, their value of $YS_{0.2}$ increases by 79 MPa and 103MPa between 74x74mm² and 35x35mm² forged parts for –Si and –Si+Mn chemical compositions, respectively. The other chemical composition that exhibits huge difference in strength level is 0Nb but this time, this can be explained by the presence of allotriomorphic ferrite in 0Nb 74 but not in 0Nb 35.

–Cr 35 and –Cr 74 forged parts exhibit the weakest values of $YS_{0.2}$ and UTS among parts of the same geometry. Such features may be linked with the occurrence of regions of lath-like ferrite with barely any secondary phases in addition of a very coarse upper/granular bainitic microstructure with the highest effective packet size (as shown in Table 21 in chapter 4) that comes from their highest transformation temperatures (as seen in chapter 3).

As shown in Table 22, Figure 89a and Figure 89b, the best UE_l and $E\%$ for both forged part geometries belongs to 0Nb laboratory heats. This might be due to a slight increase in the bainitic transformation temperature, the occurrence of allotriomorphic ferrite in the case of 0Nb 74 and the absence of NbC or (Nb,Ti)(C,N) precipitation. Austenite content determined for both 0Nb 35 and 0Nb 74 using XRD does not exhibit noticeable variation compared to other combinations that can justify such an increase in UE_l .

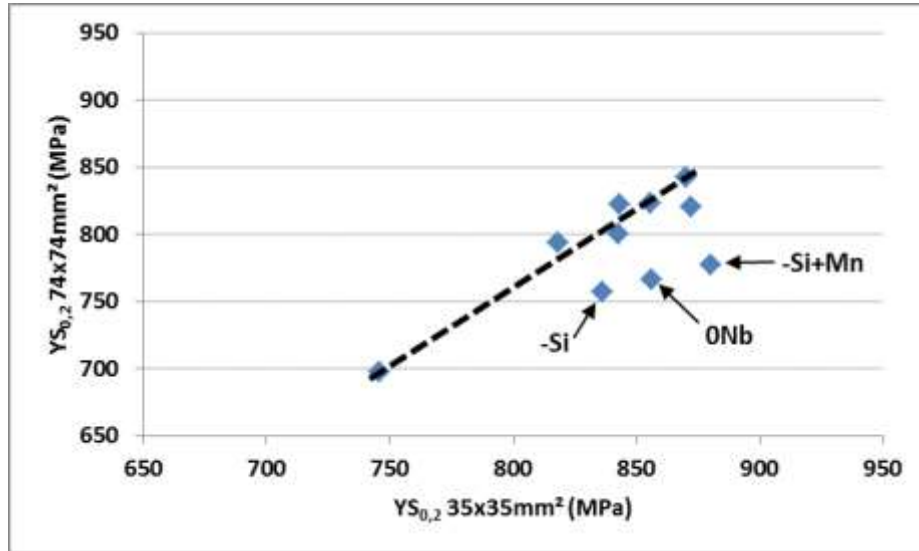


Figure 90: $YS_{0.2}$ of 74x74mm² forged part vs. $YS_{0.2}$ of 35x35mm². Each point corresponds to a chemical composition.

The as-forged reference steel has better strength properties than most of the 74x74mm² forged parts (in fact, than all of them except for 0Ti 74, base 74 and +Ni 74 for which unexpected strength value have been noticed). This is not surprising as cooling rates are believed to be equivalent between these two products (due to similar section area in the vicinity of the tensile specimens); the Ni content in the reference steel is twice of that in +Ni steel grade. On the other hand, the as-forged reference steel shows an important decrease in $YS_{0.2}$ and TS compared to the as-rolled one, by 85MPa and 51MPa respectively. These decreases lead to a lower $YS_{0.2}$ over TS ratio for the as-forged product. Reasons of such change in mechanical properties will be discussed later in this chapter.

5.1.3 Relationship between average hardness and strength level

Figure 91a and Figure 91b show the relationships between Vickers hardness (HV30), UTS and $YS_{0.2}$. Linear relationships have been determined with taking the uncertainties on both strength and hardness values into account. The linear relationship found between HV30 and UTS is between the usual relationship (as described by Parker et al. [174]) and the relationship found by Zajac et al. [7]:

$$UTS[MPa] = 3.64(HV30) - 123 \quad eq.5.1 \text{ (this study)}$$

$$UTS[MPa]_{usual} = 3.3(HV30) \quad eq.5.2$$

$$UTS[MPa]_{Zajac} = 4(HV30) - 258 \quad eq.5.3$$

$$YS_{0.2}[MPa] = 2.32(HV30) + 37 \quad eq.5.4 \text{ (this study)}$$

Even with taking the uncertainties into account, two combinations exhibit experimental values of UTS noticeably higher than the calculations from their average level of HV30 (Figure 91a). These combinations are 0Ti 35 and 0Nb 35. The difference for the first one can be due to abnormal austenite grain growth. Hardness measurements have been realized on a sample that exhibits mostly abnormally grown austenite grains whereas tensile specimens present both regions of abnormally and normally grown primary austenite grains. The reduction of average primary austenite grain size is thus believed to increase the resulting bainite strength due to the refinement of the microstructure (despite the loss in hardenability). In the case of 0Nb 35, no reason for such a difference can be advanced at this stage.

In concern of the relationship between HV30 and $YS_{0.2}$, according to their hardness, two combinations have lower value of $YS_{0.2}$ than expected (Figure 91b). These ones are -Cr 35 and -Cr74. It seems that the presence of a bainite microstructure with a higher transformation temperature has an effect on decreasing $YS_{0.2}$ rather than on UTS. This effect

is perhaps due to its softer bainitic ferrite obtained at higher transformation temperature, as compared to other steel grades (as seen on CCT diagrams in chapter 3). So, more work hardening is possible between $YS_{0.2}$ and TS during a tensile test, which is shown in Figure 89a and Figure 89b.

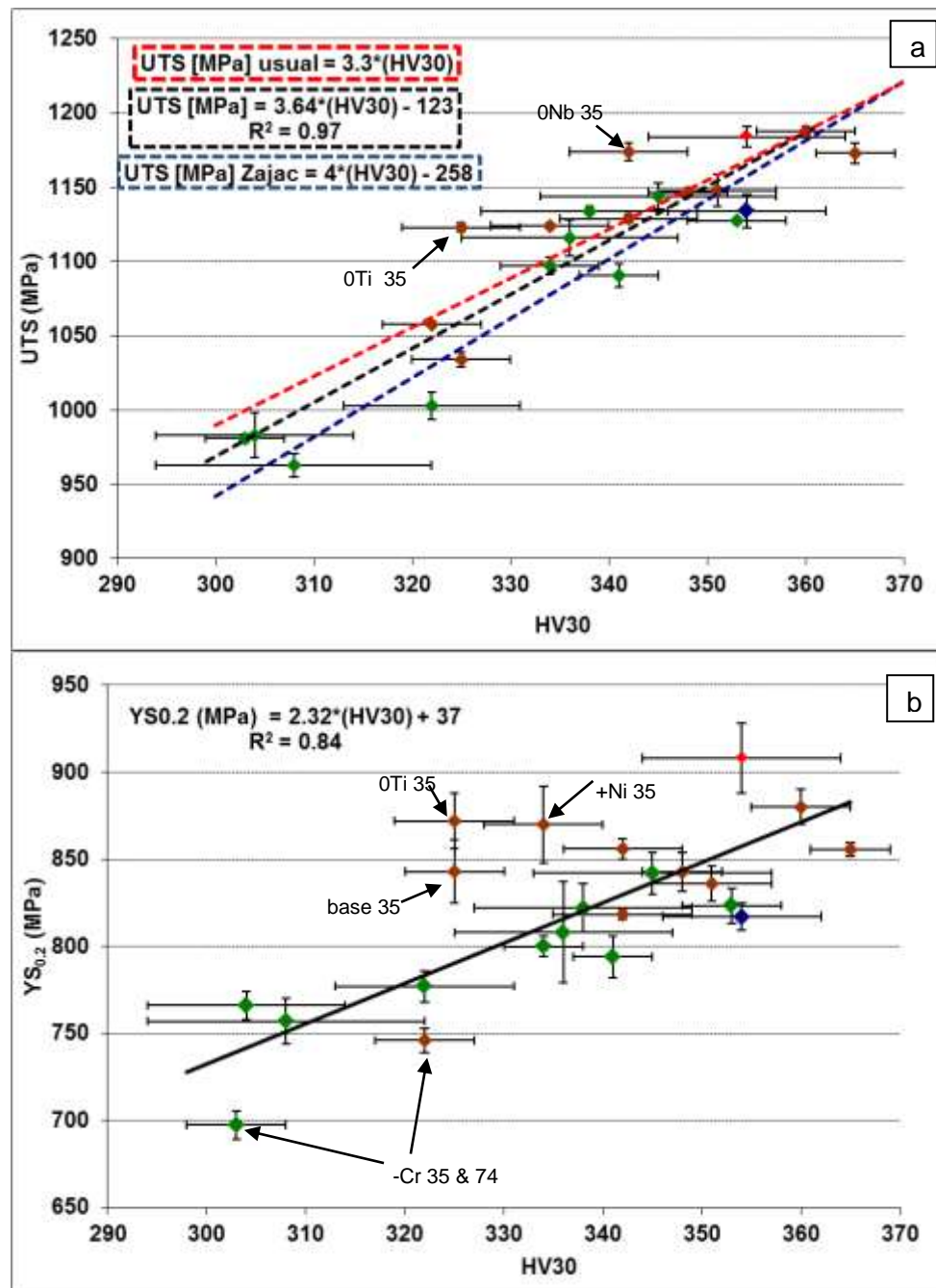


Figure 91: Correlation between hardness and strength under uniaxial tension. One point per combination. (a) Average UTS and (b) average $YS_{0.2}$ versus average Vickers hardness (load 30kg).

On the other hand, three combinations, 0Ti 35, base 35, and +Ni 35, have values of $YS_{0.2}$ higher than expected according to their value of HV30. These combinations have also been found to have a relatively low UE₁% (with the exception of +Ni). Their 74x74mm² counterparts have been forged at the same time and also have relatively low values of UE₁% (compared to the other 74x74mm² forged parts) and unexpected high strength (as noticed earlier). One might believe that these combinations might have experienced a lower forging finish temperature or higher cooling rates, leading to an increase in dislocation density and so a decrease in work hardening properties. It is interesting to mention that 0Ti 35, base 35, and

+Ni 35, also have very good impact toughness properties which may be in contradiction with the last statement. However this is not the work hardening ability of bainitic ferrite that controls impact toughness but the density of harmful particles and the TRIP-available austenite content as indicated in chapter 4.

The value of $YS_{0.2}$ of the as-rolled reference steel is also over-evaluated but this steel presents some noticeable microstructure heterogeneities due to its banded microstructure (as seen in chapter 2). These heterogeneities may affect differently hardness (surface) and yield strength (volume) measurements leading to such a difference.

5.1.4 Relationship between impact toughness and ductility in uniaxial tension

Figure 92a shows the reduction of area at fracture, $Z\%$, as a function of the local elongation that happens after the onset of necking, $E_n\%$. With the exception of –Cr 35 and –Cr 74, all combinations seem to respect the same ratio between $Z\%$ and $E_n\%$. For an equivalent value of $Z\%$, forged parts from –Cr laboratory heats present slightly higher $E_n\%$ compared to other combinations. It has been noticed earlier that interfaces between secondary phases and bainitic ferrite may act as void initiation sites during uniaxial tension. Damage localization seems to occur slightly later in both –Cr combinations, which may be due to a lower number density of void initiation sites in these microstructures, and thus to lower density of hard secondary phases. This last assumption is in agreement with the occurrence of regions that present bainitic packets with only few secondary phases and hardly observable lath-like structure.

As both tensile and Charpy impact specimens exhibit ductile-to-brittle transition fracture surfaces, the impact toughness has been tentatively compared to the reduction of area at fracture (both are correlated to the resistance of the material to localized damage). Indeed, combinations 0Ti 35, base 35 and +Ni 35, which have the best impact toughness, have the best values of $E_n\%$ and $Z\%$. Inversely, combinations with low impact toughness have low value of $E_n\%$ and $Z\%$, such as both forged parts from –Cr laboratory heat. This seems to indicate some similarities in rupture mechanisms in impact and tensile tests. These similarities are highlighted by a linear relationship between the two series of data, as shown in Figure 92b, with few exceptions.

The first exceptions are –Si+Mn 74 and –Si 74. The study of microstructural parameters that control impact toughness shows that 74x74mm² forged parts generally have a higher concentration of inclusions than 35x35mm² (chapter 4). The increase in concentration of isolated middle sized and coarse Al_2O_3 particles may be the cause of such ratio between $Z\%$ and impact toughness. Cleavage cracking initiates more easily, i.e., for a lower strain in the vicinity of the central ductile crack due to this increase in concentration of Al_2O_3 particles. However, the microstructure is still able to stop these cracks because of the relatively slow strain rate during the tensile test. In the case of Charpy impact tests, this increase in Al_2O_3 number density only means that the probability to initiate cleavage increases, and as only one initiation site is necessary to trigger final rupture, this would lead to a lower amount of absorbed energy in impact toughness tests.

The second family of exceptions are +Mn 35 and –Si+Mn 35. The particularity of these two microstructures is to present the smallest bainitic packet size that can be found among any combinations (22.1µm and 22.3µm respectively against an average of 24.5µm). They also have relatively high martensite fraction (0.051 and 0.069 against an average of 0.030 over all combinations). So, it seems that the damage property is more sensitive to the bainitic ferrite packet size at high strain rate as the role played by the brittle fracture is more important (the ratio between brittle fracture surface area and ductile fracture surface area is much higher in impact toughness than in uniaxial tension for the investigated steels).

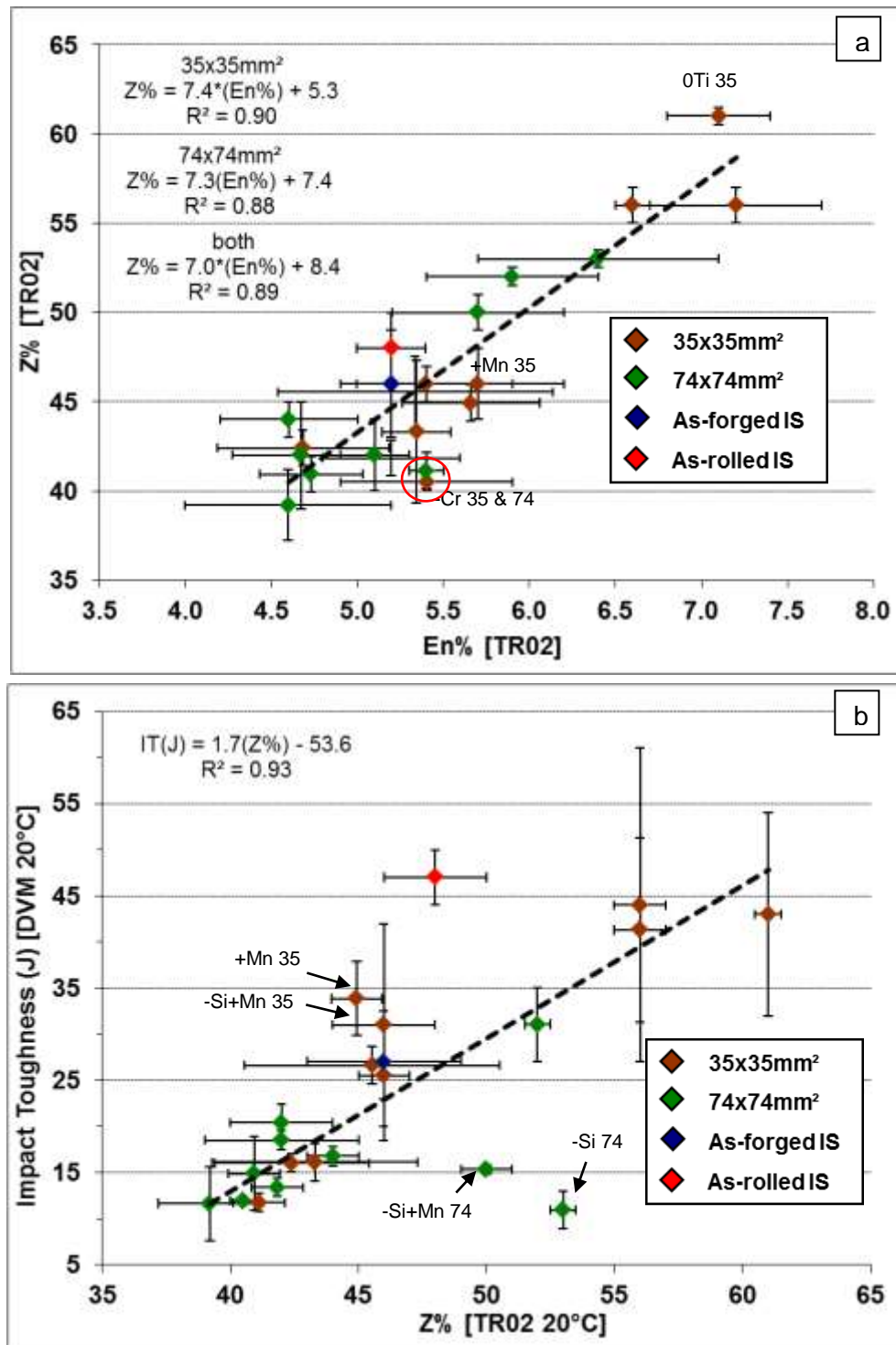


Figure 92: (a) Necking coefficient vs. necking elongation. (b) Impact toughness vs. necking coefficient. IS: reference steel.

The last exception is the as-rolled reference steel. The banded structure and especially, inclusions along the segregation bands, generates a higher density of ductile damage during the tensile test. Once again, this is linked to a lower strain rate in tensile tests than in Charpy impact tests, allowing more ductile damage before the occurrence of brittle fracture. The relative orientation between these bands and the mechanical loading is the same in the two cases and leads to the most favourable experimental testing condition in regard of both mechanical properties (i.e. other relative orientation between segregation bands and the mechanical loading may decrease the obtained mechanical properties). The effect of the bainitic packet size could also contribute to such a difference between as-rolled reference steel and other materials.

5.1.5 Fracture mechanisms

Figure 93 shows a typical fracture surface obtained after a tensile test. The fracture surface can be divided into four regions. The central region of the fracture surface (region 1) is covered by dimples with some larger cavities as shown in Figure 94c. This region exhibits pronounced surface relief. Rare and isolated cleavage facets are seen in the vicinity of this region. Cleavage facets are seen more and more often as we move away from this central region and in turn, dimples become rare and isolated. An example of this transition region (region 2) can be seen in Figure 94b. Then, the fracture surface is mostly composed of cleavage facets with the occurrence of secondary brittle cracks which penetrate into the bulk, as shown in Figure 94. Contrary to the central region, this region (region 3) is very flat. Finally, region 3 is entirely surrounded by shear lips (region 4).

Some isolated damaged regions on fracture surface can be observed, generally near large variations in surface relief (Figure 93). These regions may have been damaged from the elastic release in energy by the load-line after fracture which takes place when the tensile specimen breaks (the two broken parts of the specimen suddenly come into contact).

In the same way as for Charpy impact test specimens, tensile test specimens exhibit a ductile-to-brittle transition fracture surface at 20°C. The main difference between the two kinds of tests is that the strain rate is very low for tensile tests compared to impact toughness tests, which allows the microstructure to have a higher resistance to cleavage propagation (so final rupture is not triggered as soon as the first cleavage crack has initiated).

Ductile damage starts from the centre of the necking region. As the ductile crack propagates under the external applied load, by nucleation, growth and coalescence of cavities, some cleavage microcracking initiates in the vicinity of the ductile crack but quickly stops. The ductile crack continues to propagate and more and more cleavage microcracks initiate and stop until conditions become favourable for brittle cracking propagation. Then, brittle rupture occurs all around the central crack.

The main inclusions, observed for the different laboratory heats that are active for ductile fracture, have been classified from SEM observations of dimples that are present in the central region (Region 1) of the fracture surface. The results can be seen in Table 23 and some examples of these inclusions are shown in Figure 95. The nature of inclusions has been determined using EDX analysis. Most of the laboratory heats exhibit the same kind of inclusions in ductile dimples. No difference in the nature of inclusion population has been noticed between the two forged parts of a same chemical composition. Possible difference in the number of inclusion population has not been established as no quantitative data have been acquired (reminds that from chapter 4, 74x74mm² forged parts are suspected to contain more inclusions than 35x35mm² ones).

Of course, the 0Ti laboratory heat exhibits no titanium nitride. However, a non-negligible precipitation of boron carbo-nitride (nitrogen rich) has been observed. These precipitates are lower than 1µm in size but appear very bright using SEM and are easily found on the fracture surface. This points out that without titanium, the boron protection from nitrogen is less/no effective. Nevertheless, the 0Ti laboratory heat exhibits mechanical properties and microstructure (outside regions of abnormal grain growth) very similar to those of base chemistry whatever the dimension of the forged part. Two hypotheses can thus be made:

1. Boron does not play the expected role (promoting the bainitic transformation at the expense of the ferritic transformation) and is not necessary in this steel chemistry. In most cases, the content of other alloying elements is sufficient to avoid any ferritic transformation.

CHAPTER 5 – MICROSTRUCTURAL PARAMETERS THAT CONTROL STRENGTH

- The average boron content is so high that there is still enough free boron segregated at primary austenite grain boundaries to avoid ferrite occurrence even with the occurrence of some nitride precipitation along primary austenite grain boundaries through air-cooling after forging.

	Mg-Al ₂ O ₄	coarse Al ₂ O ₃ (>10µm)	Al ₂ O ₃	fine Al ₂ O ₃ (<2µm)	(Ti,Nb)(N,C) (>2µm)	TiN (>2µm)	MnS (>1µm)	(Nb,Ti)(C,N) (>1µm)	B(N,C) (<1µm)
base			X	X	X		X		
0Ti			X	X			X		X
+Ni			X	X	X		X		
0Nb			X	X		X	X		
-Si		X	X		X		X		
-Si+Mn		X	X		X		X		
0Mo			X	X	X		X		
+Mn			X	X	X		X		
-Cr			X	X	X		X		
+Cr			X	X	X		X		
reference steel*	X		X		X		X	X	

Table 23: Main kinds of inclusions or precipitates found in the dimples from the central region of tensile specimens for different steels. For carbonitrides, dominating elements are in boldface characters. * Inclusions seen in as-forged and in as-rolled states.

As discussed in chapter 3 in the case of $\text{Fe}_{23}(\text{B,C})_6$, the second assumption is the most reasonable one. No ferrite has been observed in such steel microstructures. It seems that the depletion in boron content with respect to the average chemical composition does not lead to ferrite nucleation along primary austenite grain boundaries. Boron nitride precipitation may occur in regions that exhibit abnormal grain growth as boron concentration may be higher along these primary austenite grain boundaries. In such regions, F_s is decreased due to the very large grain size. Moreover, boron nitrides are not known to enhance ferrite nucleation.

Whatever the geometry of forged bars, -Si+Mn and -Si laboratory heats exhibit clusters of coarse aluminium-rich oxides which are not observed in the other chemistries. These two laboratory heats have been cast from the same batch, so the first possibility that comes in mind is that these coarse aluminium oxides come from a punctual problem during casting. Perhaps an improvement in the steelmaking process has to be made to overcome this problem, in the addition order of alloying element (Al being introduced in the liquid iron after any other alloying element, and thus after Si) or in the process allowing more time for coarser Al_2O_3 oxides to be removed from the liquid metal.

These coarse clusters of aluminium-rich oxides slightly change damage development in tensile specimens. Figure 96 shows an example of corresponding fracture surface. In addition to the mechanism described previously in this section, cleavage occurs very soon around the clusters that are present in the bulk, probably before any other damage development. Cleavage cracks generally stop after having propagated over less than 50µm all around the cluster. The freshly created cracks then blunt as the strain continues to increase. When ductile damage starts (after the onset of necking), it concentrates in the middle of the necking region (which will contain the final fracture plane), but also around the defects created by the clusters of oxides and the surrounding cleavage facets. If some of these defects are in the necking region, the coalescence of the cavities between the central region of the final fracture plane and those around the oxides eventually form wells or hills (according to whether the oxides are located upper or lower with respect to the average fracture plane). Then the remaining fracture mechanism is the same as for all other specimens.

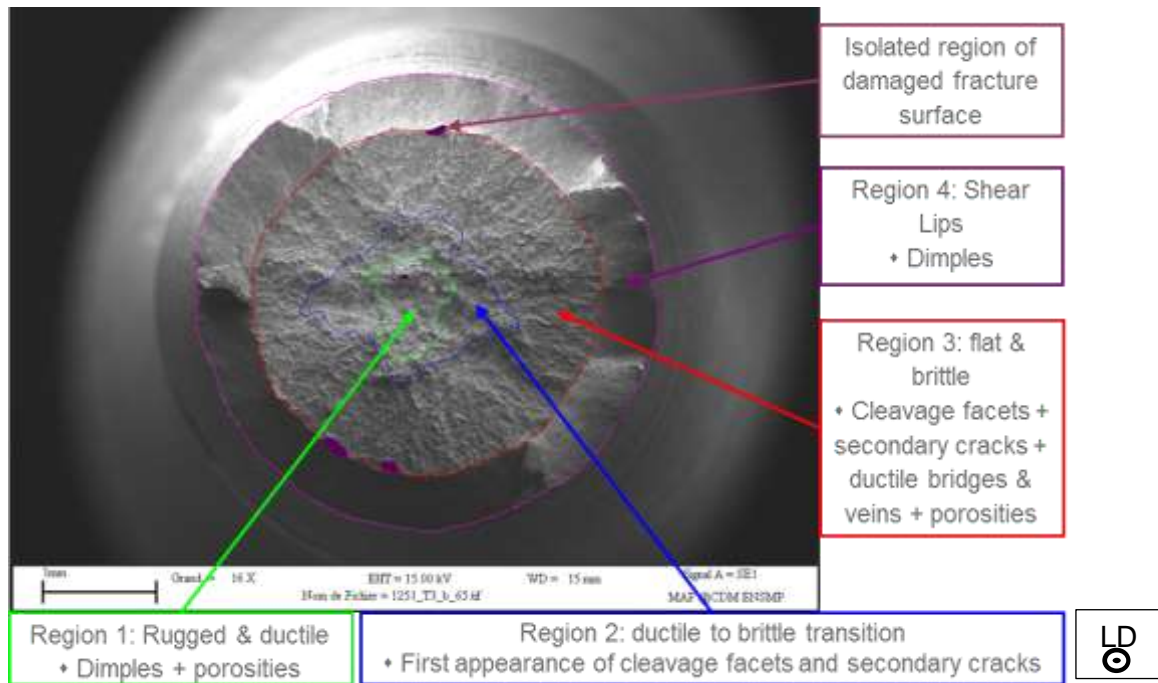


Figure 93: Typical fracture surface. SEM, SE. 0Ti 35 specimen 3.

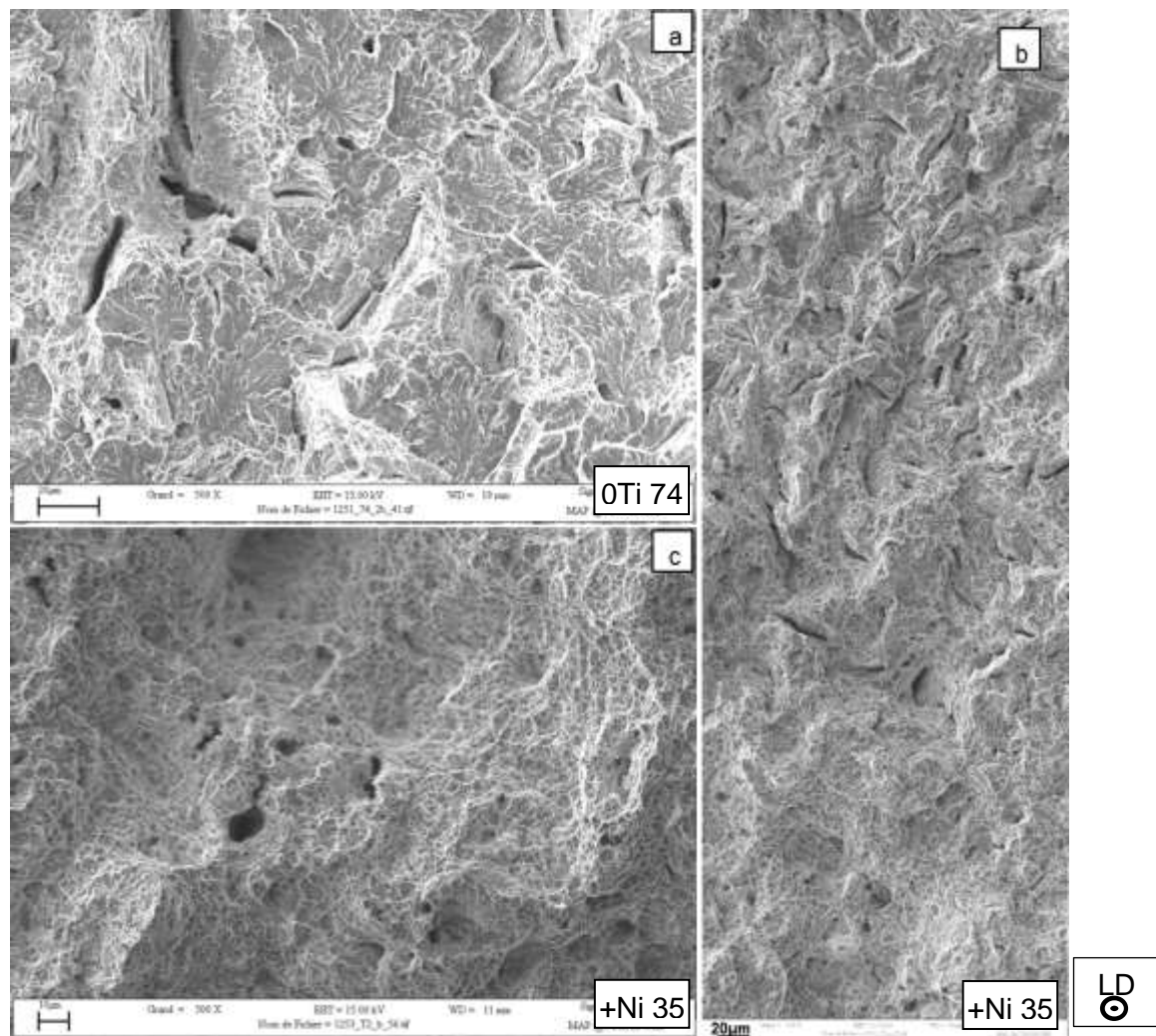


Figure 94: SEM, SE. (a) region 3 of Figure 93, brittle cleavage fracture. (b) region 2 of Figure 93, transition from ductile to brittle fracture. (c) region 1 of Figure 93, ductile fracture.

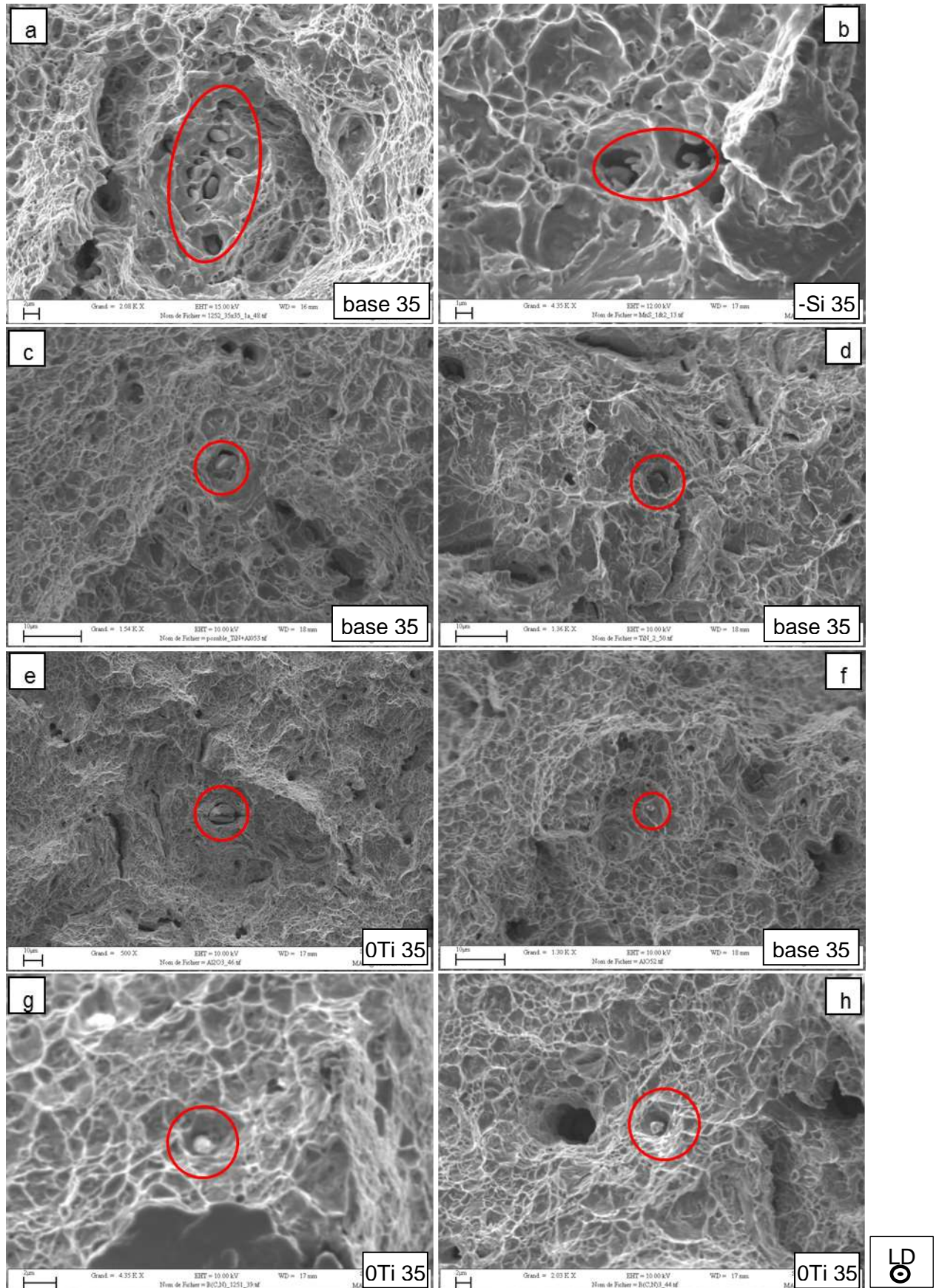


Figure 95: SEM, SE. (a) & (b) cluster of MnS inclusions (<7 μ m). (c) single (Ti,Nb)-(N,C) inclusion (6-10 μ m) or (d) with Al₂O₃ inclusion. (e) Al₂O₃ inclusion (6-16 μ m). (f) fine Al₂O₃ inclusion (<2 μ m). (g) & (h) B(N,C) (<2 μ m).

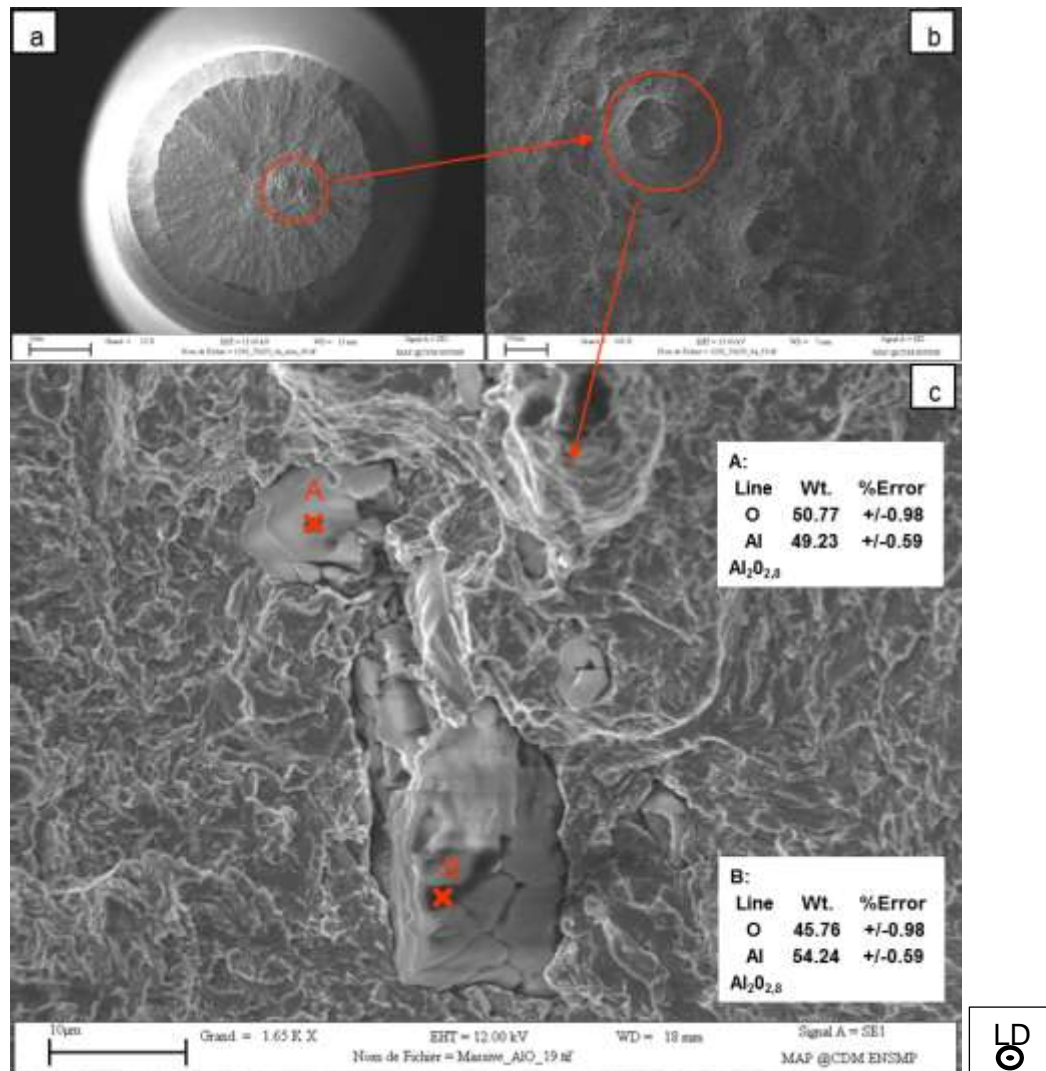


Figure 96: SEM fractography, -Si+Mn 35, specimen 4. (a) General view of the fracture surface, the location of two inclusion defects is encircled in red (b) Closer view of the two inclusion defects. A plateau of cleavage facets is found around each inclusion, these cleavage plateaus are on the top of ductile hills. (c) Closer view of one inclusion defect: cluster of several particles, the coarsest ones being aluminium oxides.

These clusters of coarse oxide-rich inclusions have not been seen on the fracture surface of impact toughness specimens. In fact, the volume submitted to plastic strain is much larger in tensile tests than in Charpy impact tests, and so, fracture occurs more likely around this kind of clusters during tensile tests than during Charpy tests. But as cleavage cracks initiate and stops very soon around these clusters of oxide-rich inclusions in tensile tests, the resulting cracks are blunt and do not have a huge impact on final tensile properties. Should one cluster of oxide-rich inclusions have been present on the volume of material just behind the notch of a Charpy impact specimen, the absorbed energy would have been near 6J (as reported in chapter 4, section 4.2.2, when no ductile cracking occurs at all).

No $Fe_{23}(B,C)_6$, $Ti(C,N)$ or NbC have been identified in dimples of the fracture surfaces of any combinations. All these carbides are small, with at least one dimension lower than 250nm which does not allow reliable EDX analysis in such observation conditions.

The main difference between the reference steel and the laboratory heats is that oxides are rarely found in the former one. These oxides are mainly isolated Spinelles (only a low amount of Al_2O_3 has been found, no CaO at all). The most common inclusion in the investigated reference steels is MnS which is often found together with coarse $(Nb,Ti)(C,N)$

and/or (Ti,Nb)(N,C) inclusions. These last combinations of particles were not found in laboratory heats (due to the difference in steelmaking process).

5.1.6 Damage mechanisms

5.1.6.a Light microscopy observations

Using LM, two kinds of cracks have been observed in cross-section of fractured reference steels:

1. Cracks along inclusions inside segregation bands;
2. Cracks without visible inclusion and developed outside segregation bands.

In every case, the cracks have been found to propagate by growth and coalescence of cavities, denoting a ductile fracture mechanism.

Several groups of cracks along inclusions inside segregation bands are surrounded in light grey in Figure 97a. As shown in Figure 97b, these cracks are mainly the consequences of the cracking and de-cohesion from steel matrix of MnS, (Nb,Ti)(C,N) or (Ti,Nb) (N,C) inclusions under deformation. Interfaces between harder and softer phases inside segregation bands can also be an issue as these bands exhibit a high area fraction of martensite.

Cracks beside segregation bands and without any visible inclusion are also visible. A group of these cracks has been encircled in dark grey in Figure 97a. As shown in Figure 97c and Figure 97d, there are a lot of small cracks inside a primary austenite grain at the interfaces between harder and softer phases such as MA constituents and bainitic ferrite, respectively. The longest cracks seem to follow the primary austenite grain boundary. No question here of inter-granular fracture, these big cracks most probably come from the high density of hard residual blocks along the primary austenite grain boundaries after the bainitic transformation.

The same kind of cracks as in as-rolled reference steel has been found for the as-forged one. In addition, some cracks, surrounded in white in Figure 97f, have been observed emerging at specimen surfaces, parallel to the fracture surface. One of these cracks is shown at higher magnification in Figure 97e. Green lines highlight localized strain, which is a clue that this crack initiated from inside the specimen during the tensile test. The crack did not follow a specific path (along grain boundaries, inclusion or residual blocks). In this case, the crack crossed several bainitic ferrite packets without significant deviation. Except a higher sensitivity for some local strain coming from machining, no specific reasons have been found for the occurrence of this no-detrimental kind of defect along the side surfaces of the tensile specimens.

5.1.6.b Scanning electron microscopy observation

Figure 98a to Figure 98f show that voids initiate at interfaces between harder and softer phases such as MA constituents and bainitic ferrite respectively for both as-rolled and as-forged reference steel. More specifically, voids initiate in regions with multiple MA/bainitic-ferrite/MA interfaces, especially when these interfaces are close to each other along the loading direction. Bainitic ferrite, which is trapped inside large residual islands of secondary phases, is one of these regions sensitive to damage initiation. Once ductile cracking starts, voids grow and coalesce. The resulting fracture surface is composed of small dimples ($\varnothing < 3\mu\text{m}$) with MA constituent in their centres as shown in Figure 98g and Figure 98h.

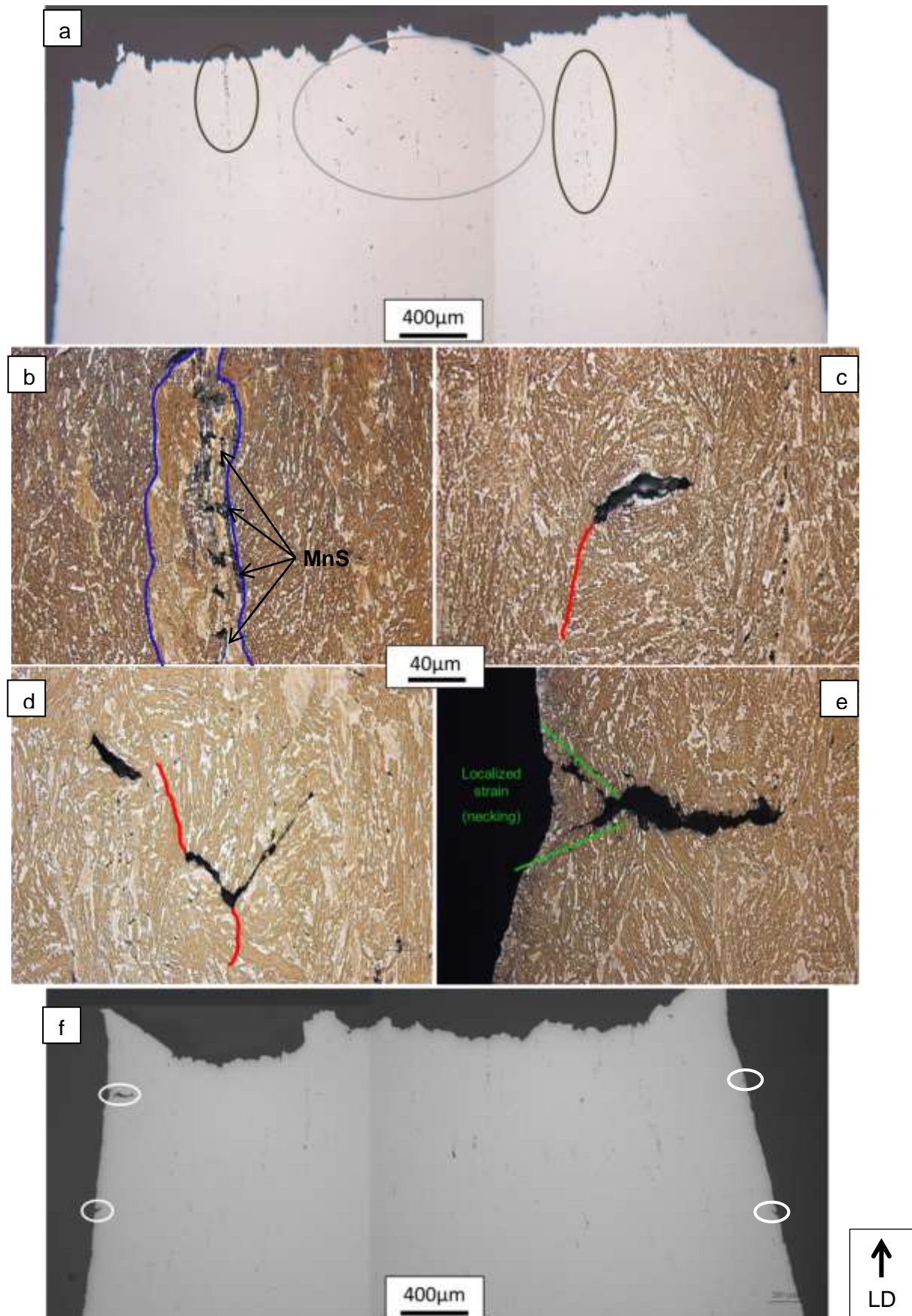


Figure 97: LM with and without LePera etching (colour pictures). (a) to (d) as-rolled reference steel, (e) and (f) as-forged reference steel. Limits of the segregation band are highlighted in blue, some prior austenite grain boundaries are highlighted in red. Secondary cracks at or near the side surface of the specimen are encircled in white.

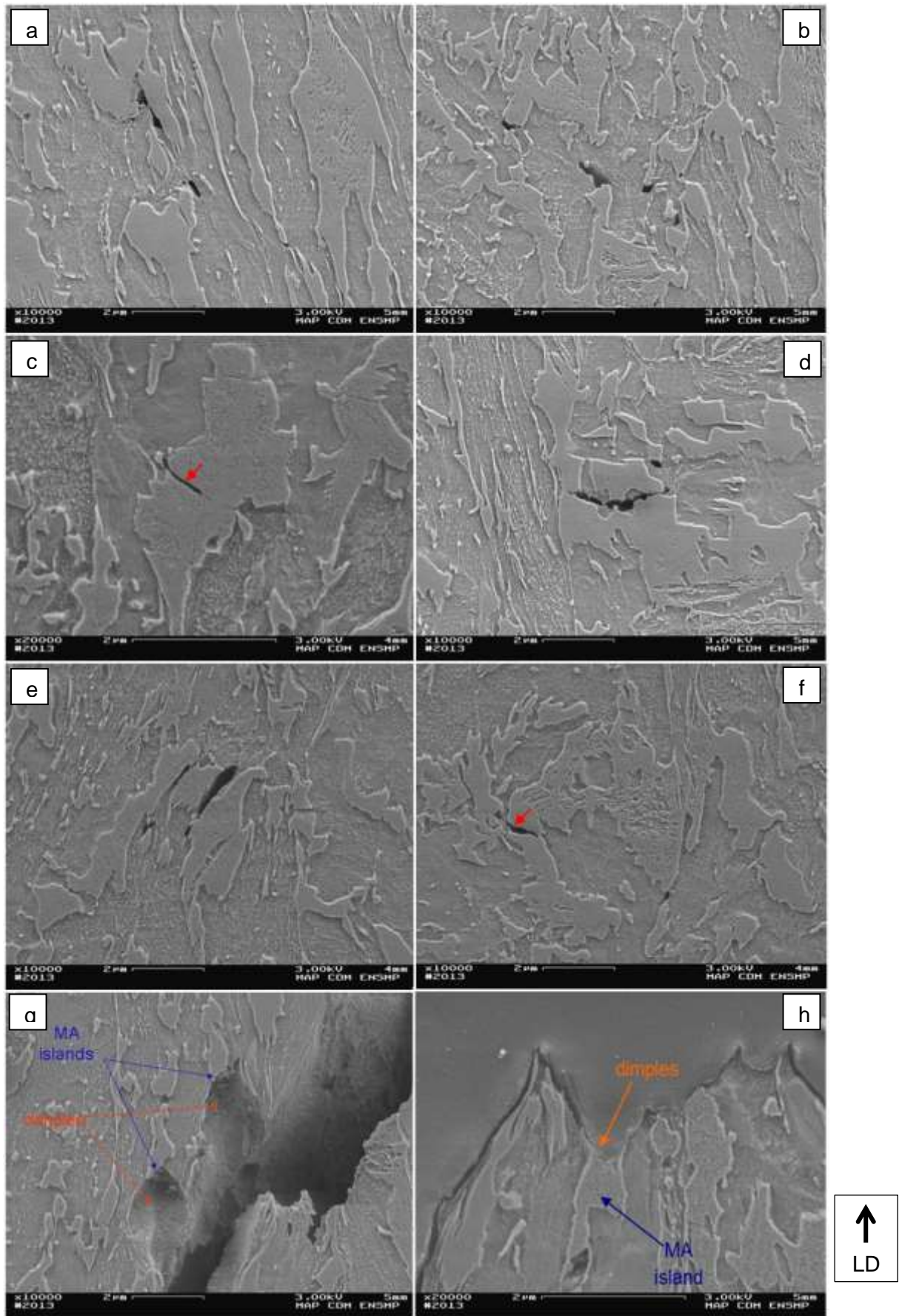


Figure 98: SEM, Nital2% etching. (a)(b)(d)(g)(h) as-rolled reference steel, (c)(e)(f) as-forged reference steel. Short, red arrows point out preferential crack growth into MA constituent.

It seems that some voids, which initiate at the bainitic ferrite/MA constituent interface, may grow preferentially into the MA constituent (red arrows in Figure 98). This phenomenon has only been seen in the as-forged reference steel. This last observation points out that MA constituents in the as-forged steel may be more brittle than in the as-rolled one. It is similar to the lower capacity of austenite to absorb energy during ductile crack advance that has been noticed in Chapter 4 (section 4.2.5, Figure 86a) in the as-forged reference steel than in the as-rolled one. The reason of such difference might come from the difference in their respective thermo-mechanical processing conditions.

In the case of the preferential damage development from the MA constituent, it seems probable that these microstructural features could initiate a brittle crack that would extend into the adjacent bainitic ferrite packets. Such cleavage might also initiate from features such as inclusions that are present in both as-forged and as-rolled reference steel. Then, the crack could meet high misorientation ($>15^\circ$) packet boundaries. At this stage, two events can happen, the micro-crack might be stopped by this obstacle, or continue to propagate into another packet after being deviated. As ductile rupture occurs at the same time in the bulk, the brittle crack can catch up the ductile one and would lead to the transition region observed in the fracture surface in the former case (region 2), and to the flat and brittle region in the latter case (region 3).

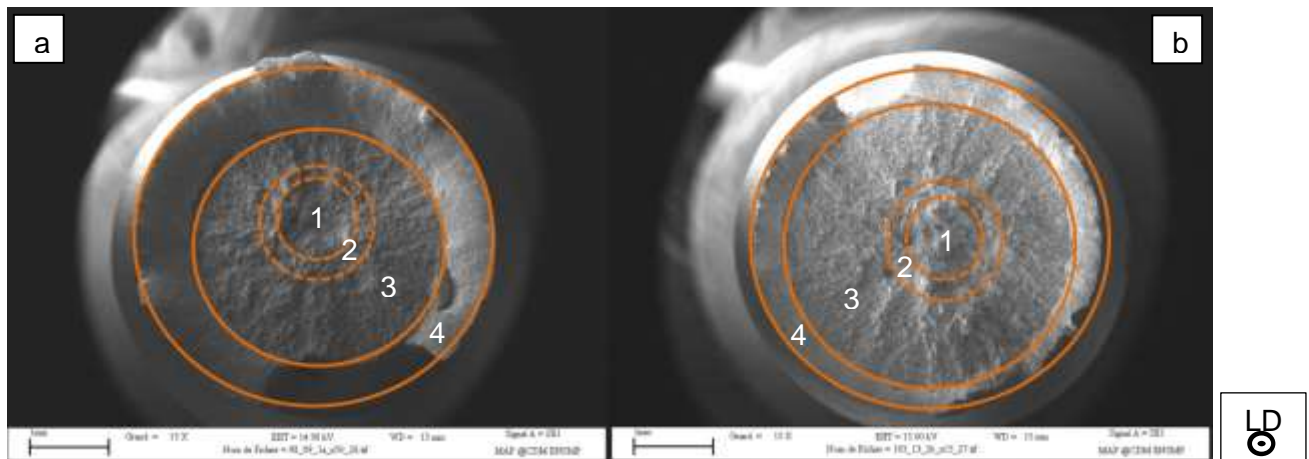


Figure 99: SEM, SE imaging. (a) As-rolled reference steel, (b) as-forged reference steel. Dashed lines represent loosely determined limits that exist between ductile, ductile-to-brittle and brittle regions (1-3) of the fracture surface.

Both regions (regions 2 and 3) may appear after very short ductile crack propagation in the as-forged reference steel, due to the higher density of brittle microstructural constituents, which, as shown in Figure 99, has been observed qualitatively on the fracture surface. Indeed, region 1 seems to be slightly smaller in the as-forged steel. In addition, scarce and isolated cleavage facets can be observed even in this region of the as-forged reference steel whereas none have been observed in region 1 of the as-rolled one. No measurement of area fraction of the different regions present on the fracture surface has been realized due to the difficulty in delimiting every region. The only area that has been measured and compared between both steels with well reproducible results is the shear lips area (region 4), which has been found much higher for the as-rolled steel, with an average value of $6.4 \pm 0.9 \text{ mm}^2$ instead of $4.2 \pm 0.5 \text{ mm}^2$ for barely the same total area of fracture surface ($14.6 \pm 0.5 \text{ mm}^2$ and $15.1 \pm 0.6 \text{ mm}^2$ for as-rolled and as-forged reference steel respectively). So, cleavage fracture seems to appear later and to stop earlier in the as-rolled material. It is important to notice that even if they exhibit noticeable differences in fracture surface, both states share close values of $Z\%$ and similar values of $E_n\%$. However, as shown in Figure 89c, once damage localisation or necking occurs, the stress decreases faster with strain in the case of the as-rolled reference steel.

Figure 100 shows examples of inclusions between 5 and 20µm in size that can induce damage into the microstructure under mechanical stress. These inclusions may deform in the loading direction together with the matrix until they crack according to their own strength and ductility (which are dependent on the nature, the shape, the size and the orientation of the inclusion with respect to the loading axis). At room temperature, most inclusions such as nitrides crack without any elongation (Figure 100a). At this stage, the main crack propagates into the inclusion perpendicularly to the loading axis and stops at the matrix /inclusion interface. Then, the crack opens along the loading direction into avoid, as the matrix continues to elongate under external stress.

As the same time, there may be de-cohesions of the inclusion from the steel matrix. The more the inclusion would resist strain without cracking, the more the de-cohesion is complete as observed around aluminium oxides. De-cohesion happens all around the inclusion, so an inclusion can be totally separated from the steel matrix. For a given inclusion, cracking and de-cohesion can happen several times (Figure 100b) depending on the level of strain imposed to the matrix. When ductile rupture occurs, this kind of feature appears as porosities ($8 < \phi < 20\mu\text{m}$) on the fracture surface, with in some cases, inclusion still being present inside the porosity.

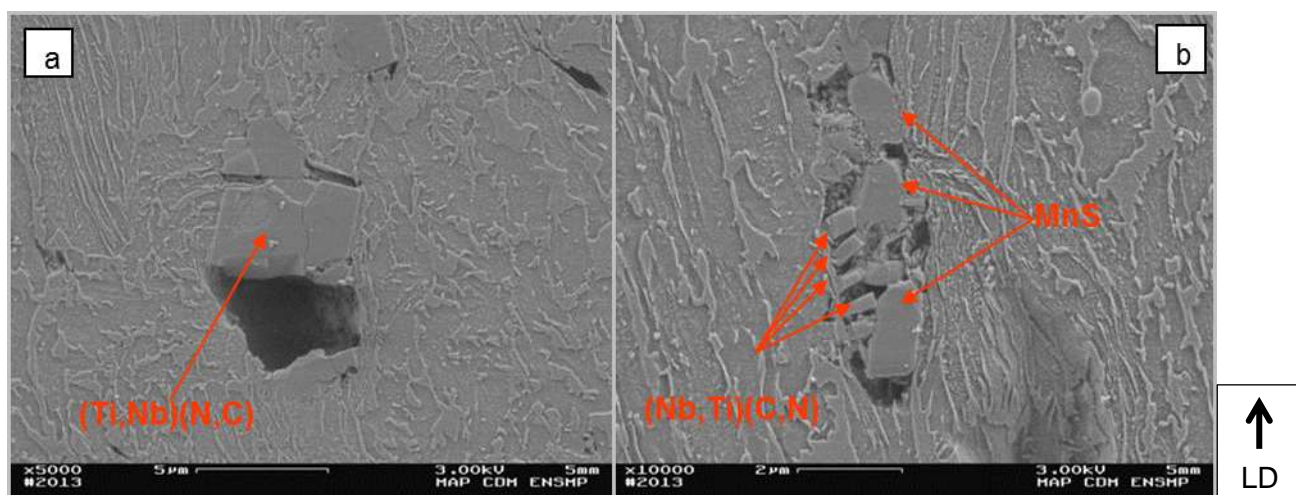


Figure 100: SEM, SE, Nital2% etching, damage development in the as-rolled reference steel.

Smallest inclusions and precipitates, from 1µm to 5µm in size lead to the nucleation of voids at interfaces between these particles and the matrix; these voids then grow and coalesce. This kind of features leads to large dimples ($3 < \phi < 8\mu\text{m}$) on the fracture surface.

5.2 Rationalization of the links between microstructure and yield strength

In this section, quantitative links between microstructure and yield strength have been established in a simple, but physically-based manner.

According to several studies [2;7;174-178], extending of existing relationships between microstructure and yield strength from ferrite-pearlite to bainitic steels is possible. The strength income of upper bainite can be thus divided into 5 components:

$$\sigma_{BA} [\text{MPa}] = \sigma_0 + \sigma_{ss} + \sigma_p + \sigma_b + \sigma_d \quad \text{eq.5.5}$$

In eq.5.5, σ_0 is the base strength, which is mostly the intrinsic strength of bcc iron, σ_{ss} is the contribution of alloying elements to solid solution strengthening, σ_p is the strength contribution of precipitation, σ_b is the contribution of boundaries and σ_d is the contribution of dislocations.

Eq.5.5 does not take the variation in fraction of secondary microstructural constituent into account. However, bainitic steels of this study present 8-28% secondary phases with a size larger than 650nm in their microstructure according to the chemical composition and the thermo-mechanical history. For such kind of multi-microstructural constituent steels, the yield strength can be described using a rule of mixtures, as follows [179]:

$$\sigma_y [\text{MPa}] = \sum_i (\sigma_i x_i) \quad \text{eq.5.6}$$

with x_i being the fraction of microstructural constituent i and σ_i being the strength income (in MPa) of microstructural constituent i . If each identified secondary microstructural constituent is now introduced, eq.5.6 becomes:

$$\sigma_y [\text{MPa}] = \sigma_{BA} x_{BA} + \sigma_{MA} x_{MA} + \sigma_M x_M + \sigma_F x_F \quad \text{eq.5.7}$$

with BA being the bainite, MA being islands of MA constituent, M being martensite and F being allotriomorphic ferrite. With the exception of the strength coefficient of bainite, if each microstructural constituent i is considered to have the same strength coefficient σ_i whatever the combination of chemical composition and forged part geometry, the yield strength can be described as:

$$\sigma_y [\text{MPa}] = (\sigma_0 + \sigma_{SS} + \sigma_p + \sigma_b + \sigma_d) x_{BA} + \sigma_{MA} x_{MA} + \sigma_M x_M + \sigma_F x_F \quad \text{eq.5.8}$$

This last assumption is a very quick shortcut, as the strength income of every microstructural constituent is dependent on the chemical composition of the steel and the cooling rate. However, this model is expected to yield good results without needing input data which would be more difficult to acquire (e.g. on MA constituents) than for the bainitic ferrite matrix.

In the following equations, data and optimized coefficients that have been used for each strength contribution are detailed separately. A short reminder of the principle of each strengthening mechanism is also made. Optimization of the different coefficients has been realized according to the following method:

1. Taking each contribution individually, coefficients have been adjusted mathematically or by using values from literature, in order to find the lowest sum of absolute difference between the calculated and the experimental yield strength for every combinations of laboratory heat chemical composition and forged part geometry (with the exception of OTi, so 18 combinations). The yield strength is calculated using:

$$\sigma_y [\text{MPa}] = \sigma_0^n + \sigma_n \quad \text{eq.5.9}$$

where σ_n is the contribution of the considered strengthening mechanism n , that is dependent of the combination, and σ_0^n is a constant taking other strengthening mechanisms into account for all combinations (both terms are in MPa).

2. Putting all the contributions together, using eq.5.8, and starting from values set in the first step, coefficients have then mathematically tuned to find the lowest sum of absolute differences between the calculated and the experimental yield strength.

“Best result” in the following means the best mathematical results with physically meaningful coefficients in regard of the previous step of optimization.

5.2.1 Solid solution strengthening

5.2.1.a Principle

Atoms of alloying elements interact with steel matrix lattice composed of iron atoms to form a solid solution. There are two kinds of solid solution in steels according to the location of solute atoms in the bcc crystal structure of the iron matrix:

- Substitutional solid solution where solute atoms punctually replace solvent atoms in lattice sites. Solute atoms have to be in the same order of size as solvent atoms. Mn, Si, Cr, Ni, Mo, Nb and Ti are chemical elements that can enter such solid solution in iron.
- Interstitial solid solution where solute atoms occupy interstitial position in the solvent lattice. Solute atoms have to be much smaller than the solvent atoms. C and N enter this kind of solid solution.

A solute atom generates a strain field in the crystal structure according to various kinds of interactions with solvent atoms. These strains create attraction forces between alloying element atoms and dislocations (size effect). In addition, solute atoms locally change the shear modulus of the matrix, which creates interaction forces between the dislocation and the matrix (modulus effect). Both increases the stress required to move dislocations (i.e. it increases the flow stress) and thus the strength.

5.2.1.b Mathematical description

In case of a multiple alloying element addition, Gladman et al. [100] have defined this strengthening effect as an additive contribution of each substitutional and interstitial chemical element:

$$\sigma_{SS} [MPa] = \sum (ss_i \cdot c_i) \quad eq. 5.10$$

Where ss_i is the strengthening in MPa resulting from a 1%wt addition of alloying element i and c_i is the solid solution concentration of alloying element i . This is the formula that has been used in this study, which implies that no interactions between solute atoms in concern of solid solution strengthening have been considered.

5.2.1.c Data for calculation

The solid solution concentrations of every chemical element in the various nominal chemical compositions of the present study have to be established first. The following calculations from the nominal chemical composition have been realized:

- Interstitial elements such as C and N, which are expected to be near their respective solubility limit in ferrite for every microstructure investigated, are incorporated into σ_0 (all remaining C and N atoms are expected to be trapped in residual phases and in precipitates).
- It can be deduced from S concentration that a low amount of Mn is trapped in MnS inclusions (supposed to be stoichiometric). The following approximation has been used:

$$c_{Mn} = Mn - S \frac{M_{[Mn]}}{M_{[S]}} \quad eq. 5.11$$

Where Mn and S are the nominal concentrations in manganese and sulphur, respectively. $M_{[Mn]}$ and $M_{[S]}$ are their respective atomic weight.

- Cr, Ni and Si solid solution concentrations are taken un-changed from nominal composition, i.e. all Cr, Ni and Si are supposed to be in solid solution and have not partitioned during the formation of bainite.
- From the results of selective dissolution presented in chapter 2 (section 2.4.4, Table 11), the following approximations are used to estimate solid solution concentrations of Ti, Nb and Mo:

$$c_{Ti} = 0.03Ti \quad eq. 5.12$$

$$c_{Nb} = 0.19Nb \quad eq. 5.13$$

$$c_{Mo} = 0.94Mo \quad eq. 5.14$$

With the exception of 0Ti combination for which:

$$c_{Nb} = 0.30Nb \quad eq. 5.15$$

Where Ti , Nb and Mo are the nominal amounts of titanium, niobium and molybdenum, respectively.

- Al is not considered in solid solution at first sight. It is believed that most part of the Al is consumed in Al_2O_3 inclusions during the deoxidation process. The rest of Al atoms have been considered implicitly in constant σ_0 later in this chapter.
- No boron is considered in solid solution as it is expected to segregate along primary austenite grain boundaries.
- Cu is taken un-changed from the nominal composition even if there is some doubt on its real involvement in solid solution strengthening. Indeed, Cu is known to fully precipitate in nano ϵ -particles in ferrite [180] or to form CuS layer around MnS particles [33;181], but none of them were investigated in the present work.
- P has a tendency to segregate along the primary austenite grain boundaries [182;183]. However, boron is also known to limit phosphorus segregation. Indeed boron segregates faster than phosphorus due to its highest diffusivity in austenite, linked with its smaller atom size in comparison with phosphorus [184]. A first assumption is made that all the phosphorus remains in solid solution even if it is highly probable that it tends to segregate along the multiple features that are present in a bainitic microstructure (dislocations, boundaries and interphase interfaces).

5.2.1.d Coefficients available from literature

Table 24 shows literature values of ss_i that have been used in two studies for the calculation of σ_{ss} for high strength steels. These studies have been chosen because they also considered the other strengthening mechanisms, so that coefficients in the following table tend to only reflect the effect in solid solution of the different chemical elements.

Authors	ss_{Mn}	ss_{Si}	ss_{Cr}	ss_{Ni}	ss_{Mo}	ss_{Nb}	ss_{Cu}	ss_C	ss_N	ss_P
Zajac et al. [7]	37	83	X	X	11	X	X	X	2920	X
Iza-Mendia & Gutierrez [177]	32	83	-31	X	11	X	39	(5000)	(5000)	678

Table 24: Values of ss_i in MPa per wt% of alloying element found in literature. X means that no contribution from this alloying element has been considered in solid solution strengthening.

The work from Zajac et al. [7] is centred on bainitic microstructures. Among all the steels investigated in their study, they selected 13 combinations of chemical compositions (0.6-1.0C, 0.22-0.45Si, 0.29-1.80Mn, 0.01-1.39Cr, 0.01-0.208Ni, 0.01-0.5Mo, 0.006-0.01N) and transformation conditions (isothermal or continuous cooling) for which they realized tensile tests and YS determination. They have not given ss_i , however, for several chemical elements:

- For chromium and nickel. Their contents were not negligible in their different combinations. They did not give any explanations on this point.
- For copper, niobium and phosphorus. Their amounts were not given in chemical compositions either. Perhaps these ones were negligible.
- For carbon. They assumed that carbon concentration in solid solution was negligible due to cementite precipitation (low silicon content <0.5wt%) and to the presence of

strong carbide formers. In addition, their intrinsic strength of bcc iron had been already evaluated for low carbon ferritic steel so that most of the solid solution strengthening provided by carbon was implicitly taken into account.

- For boron. No solid solution contribution from boron would be expected, despite its small atomic size, since it tends to occupy sites at prior austenite grain boundaries rather than interstitial sites within the grains.

Izias-Mendia and Gutierrez [177] worked on only one chemical composition (0.15C, 0.30Si, 1.42Mn, 0.012P, 0.007N, 0.003Mo, 0.03Nb, 0.012Cu, 0.02Cr and 0.03Ni in wt%) with several thermo-mechanical treatments with final coiling between 650°C and 300°C. Their study focused not only on bainitic microstructures but also on ferrite-pearlite and auto-tempered martensite microstructures. After coiling, they assumed that C and N concentrations in solid solution were very low (near their respective solubility limit in ferrite), leading to a small and almost constant strengthening contribution whatever the thermo-mechanical treatment. The nickel content was negligible so they did not set any coefficient on it. Niobium was believed to be trapped in precipitates for the most part so it was considered in solid solution strengthening.

5.2.1.e Coefficients for calculation

Eq.5.9 in the case of solid solution strengthening gives:

$$\sigma_y [MPa] = \sigma_0^{SS} + \sigma_{ss} \quad eq. 5.16$$

Taking eq.5.10 into consideration, eq.5.16 gives:

$$\sigma_y [MPa] = \sigma_0^{SS} + \sum(ss_i \cdot c_i) \quad eq. 5.17$$

The “best fit” result using eq.5.17 allows to obtain only a poorly accurate prediction of yield strength (± 30 MPa in average difference) with a maximum difference of 86MPa found in the case of –Si+Mn 35 combination. To realize this calculation, ss_i coefficients have been kept as much as possible equal to those found in literature with the exceptions of ss_{Cr} , ss_{Ni} and ss_{Nb} , which gives in eq.5.17:

$$\sigma_y [MPa] = 473 + 185(c_{Cr} + c_{Ni}) + 83c_{Si} + 32c_{Mn} + 11(c_{Mo} + c_{Nb}) + 678c_P + 39c_{Cu} \quad eq. 5.18$$

Chromium was not found to have a negative effect on strength. On the contrary, it has been found to have the strongest strengthening effect in solid solution after mathematical fitting ahead with nickel. These results are consistent with the hardness level noticed for low cooling rates in CCT diagrams (in domains 0, A and B) comparing the base chemistry with –Cr, +Cr and +Ni chemical compositions.

It is interesting to notice that chromium does not have the same saturation effect on the solid solution strengthening as on B_s as viewed in chapter 3. Beyond a critical concentration, the excess chromium content may start to precipitate in austenite at temperatures higher than B_s , which would decrease B_s by trapping Cr, C and/or N nitrogen atoms. The resulting precipitation would strengthen the matrix despite the decrease in chromium concentration in solid solution. In such a situation, the high strengthening coefficient found here for chromium would also integrate a part of precipitation strengthening. Unfortunately, no investigation of the precipitation state has been realized on the +Cr combination to conclude on this point.

The strengthening coefficient of niobium has been set artificially at the level of molybdenum as Nb is believed to have the same effect as Mo in solid solution (due to close atomic sizes).

Nevertheless, some simplifications can be realized on eq.5.14. Nb, Cu and P-related coefficients can be set to 0 without being detrimental to the calculation agreement with experimental results. Indeed, the maximum decrease in calculated yield strength thus generated would be 8MPa. The accuracy on yield strength calculation is not affected in this case by increasing σ_0^{SS} from 473 to 478MPa.

5.2.2 Strengthening from boundaries

5.2.2.a Principle

In the case of microstructures exhibiting equiaxed grains, as a first dislocation is stopped by a grain boundary, another dislocation in the originated structure may arrive and pile up behind the first one. A material with larger grain size is able to get longer dislocations pile-ups, leading to a higher stress concentration in the vicinity of the grain boundaries. This stress concentration may activate sources of new dislocations in adjacent grains. Thus, less force has to be applied to create additional dislocations (and thus plasticity) in a material with larger grains than in a material with smaller grains.

5.2.2.b Mathematical description

The contribution to strengthening from boundaries is classically defined as a power-law equation:

$$\sigma_b [MPa] = k_y d^{-n} \quad \text{eq. 5.19}$$

with k_y being a constant in MPa.mmⁿ, n a dimensionless constant and d the effective grain size (in mm). The main question here is how to define an effective grain size for a coarse upper/granular bainite microstructure in concern of YS_{0.2}. Indeed, in bainite microstructures, more or less important changes in orientation, and thus boundaries, are found between laths in a same packet, between different packets and between different primary austenite grains. If $n=0.5$, eq.5.19 becomes the Hall-Petch equation, which is commonly used for equiaxed grain microstructures such as allotriomorphic ferrite. Allotriomorphic ferrite contains mainly high-angle boundaries (cut-off angle >15°), with no recurrent sub-structures such as packets and laths that increase significantly the amount of medium and low-angle boundaries. Using $n=1$, eq.5.19 becomes the Langford–Cohen equation which is believed to be more relevant to medium and low-angle boundaries.

Table 25 shows some values that have been found in literature for n , k_y and cut-off angle in the case of bainite microstructures. Zhu et al. [185] have considered that the yield strength of bainite is proportional to the inverse effective lath size (d_l) defined with low boundary misorientation between 2 and 7°. Zajac et al. [7] calculated their boundary contributions, by subtracting from the value of their experimental yield strength the total of all other contributions. They noticed that in order to find these boundary contributions, one has to use, in EBSD, a cut-off angle of 8° and 15° for upper bainite and lower bainite respectively.

authors	cut-off angle [°]	k_y coefficient [MPa.mm ⁿ]	n coefficient	effective grain size d [μm]	range of σ_b [MPa]
Zhu et al. [185]	2	0.387	1	X	X
	5	0.564		1.2-4.0 (5°)	170-510 (5°)
	7	0.646		X	X
Zajac et al. [7]	8 (UB) 15 (LB)	15.1	0.5	0.8-8.8	161-532

Table 25: Two sets of n , k_y and cut-off angle with respective ranges of effective grain size and resulting ranges of strengthening from boundary that have been found in literature. UB: upper bainite. LB: lower bainite.

5.2.2.c Data and coefficients for calculation

Data have been extracted from the EBSD maps that have been shown in chapter 4. In that chapter, the objective was to measure the effective packet size so an acquisition step of $1\mu\text{m}$ has been used in order to have better statistical significance. This acquisition step was found very satisfactory for a cut-off angle of 15° where the effective packet size is larger than $20\mu\text{m}$ but may appear less appropriate to determine the effective lath size with cut-off angles lower than 8° , as it is believed to be close to the step size of EBSD maps.

However, the realization of EBSD analysis with a finer acquisition step might not be necessary. Indeed, as shown in Figure 101, the contribution of boundary strengthening to experimental $YS_{0.2}$ can be well-estimated by a calculation using the square root of the effective bainitic packet area ($A_{>15^\circ}$). The relationship that has been used in this calculation starts from eq.5.9 in the case of strengthening from boundaries, which gives:

$$\sigma_y [\text{MPa}] = \sigma_0^b + \sigma_b \quad \text{eq. 5.20}$$

Considering eq.5.19, eq.5.20 becomes:

$$\sigma_y [\text{MPa}] = \sigma_0^b + k_y(\sqrt{A_{>15^\circ}})^{-n} \quad \text{eq. 5.21}$$

“Best fit” agreement between experimental and calculated yield strength is reached for $\sigma_0^b=455\text{MPa}$, $n=1$ and $k_y=8.9\text{MPa.mm}$ (Figure 101). The average difference is then $\pm 18\text{MPa}$ but with a noticeable maximum difference of 69MPa . This one is due to 0Nb 74 and can be partially explained by the presence of allotriomorphic ferrite which reduces $YS_{0.2}$ (thus, σ_0^b may be lower for 0Nb 74 compared to other combinations). Other exceptions such as -Cr74 and -Si+Mn74 cannot be explained with certitude yet, but may also come from noticeable change in σ_0^b compared to other combinations.

As packet areas of 0Ti 35, 0Ti 74, as-forged and as-rolled reference steels have been measured under the same condition of data acquisition, their YS have been calculated using eq.5.21 with the same coefficients as for every other combination. These materials are also presented in Figure 101. With the exception of 0Ti 35, their calculated YS are well in agreement with the experimental one. 0Ti 35 is out of reach due to the occurrence of regions with abnormal growth of primary austenite grains, and thus, heterogeneous bainitic ferrite packet size (as seen in chapter 2 and in chapter 4).

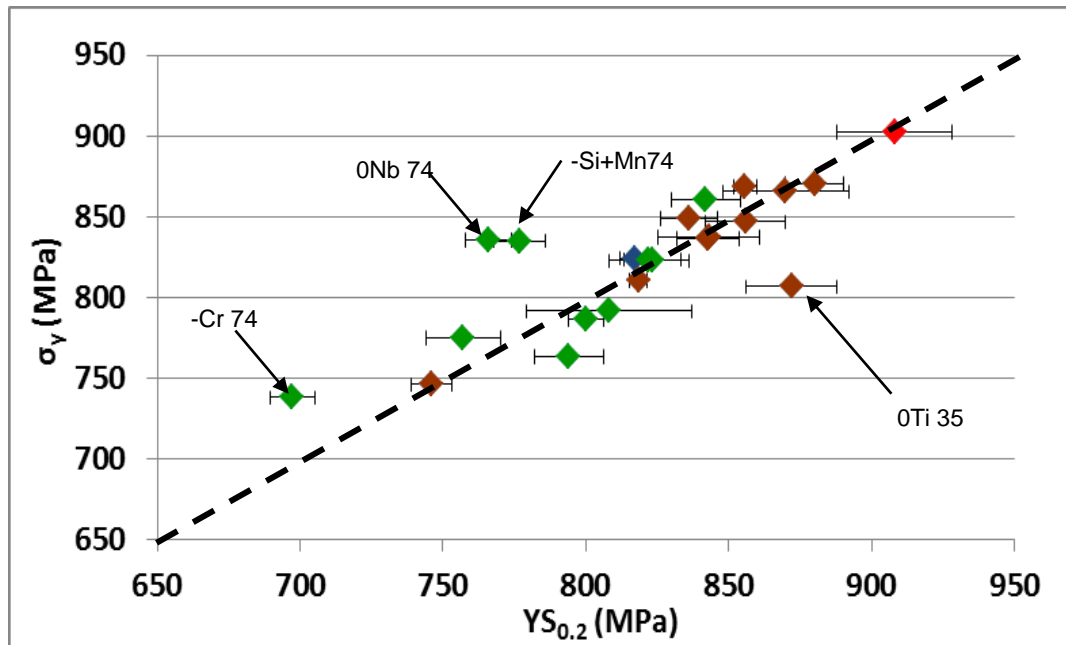


Figure 101: Calculated yield strength using eq.5.17 versus experimental $YS_{0.2}$.

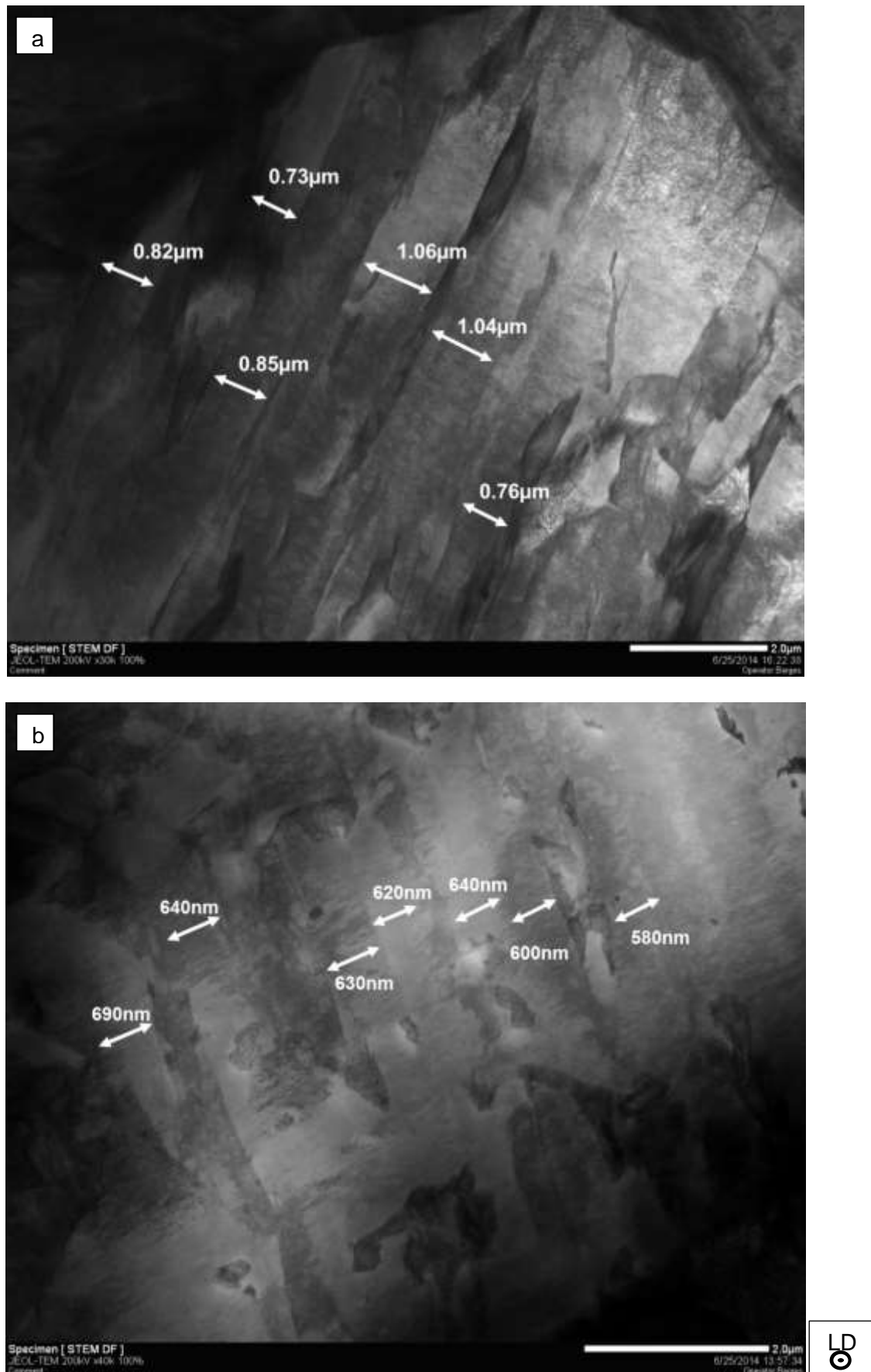


Figure 102: STEM pictures of a thin foil extracted from a Charpy impact specimen of (a) –Cr 35 and (b) 0Mo 35 combinations, observation plane = transversal plane. Observations were realized by P. Barges at Maizières R&D centre.

The same average difference between experimental and calculated yield strength can be reached in eq.5.21 using $\sigma^b_{\sigma}=124\text{MPa}$, $n=0.5$ and $k_y=108.8\text{ MPa}\cdot\text{mm}^{0.5}$. Such value of n coefficient is more consistent with the use of an effective bainitic packet size rather than with the use of an effective lath size. However, strengthening coming from other contributions (σ^b_0) must be very weak in this case and well-lowered compared to the expected one. As a consequence, this set of values for n and k_y coefficients has not been used in the global calculation using eq.5.8.

The fact that eq.5.21 gives better agreement using $n=1$ rather than $n=0.5$ may be completely fortuitous or can occur in the case here the effective lath size is totally dependent of the bainitic packet size (in length, but also in width). Qualitative STEM observations of the apparent lath width have been realized on some forged parts presenting very different packet sizes and/or transformation temperatures. The results of these investigations are the following:

- -Cr 35, $d_p(\sqrt{A_{>15^\circ}})=31\mu\text{m}$ / $B_s(0.8^\circ\text{C/s})=537^\circ\text{C}$ \Rightarrow lath width: 700-1150 nm
- 0Mo 35, $d_p(\sqrt{A_{>15^\circ}})=25\mu\text{m}$ / $B_s(0.8^\circ\text{C/s})=504^\circ\text{C}$ \Rightarrow lath width: 470-700 nm
- +Mn 35, $d_p(\sqrt{A_{>15^\circ}})=22\mu\text{m}$ / $B_s(0.8^\circ\text{C/s})=480^\circ\text{C}$ \Rightarrow lath width: 440-650 nm

Measurements have been realized only where the lath structure was clearly discernible. So only few pictures (less than five) like the ones shown in Figure 102 were available for each combination. Combinations with close values of $\sqrt{A_{>15^\circ}}$ exhibit close ranges of apparent lath width despite noticeable changes in transformation temperature but not enough data are available to conclude definitively on an existing relationship between lath size and packet size. No further investigation has been realized as they would have necessitated a huge amount of work to obtain statistically significant data in such materials (heterogeneous microstructure coming from continuous cooling, very small analysed areas).

5.2.3 Dislocation strengthening

5.2.3.a Principle

Dislocations are both an elastic and a crystallographic defect [186]:

- They generate stress fields in the material that can impede their own motion (by repulsive or attractive interactions). These elastic interactions are relatively long-range. Dislocations with the same sign in the same plane repel one another. If they have opposite signs, they attract and annihilate. If dislocations of opposite signs approach one another on adjacent planes they form a dipole pair.
- When two dislocations that lay on different planes meet, there is the formation of a jog by the entanglement of the dislocation lines which opposes further dislocation motion (jogs act as pinning points). If they pass through one another, each leaves a jog on the other equal to its own Burgers vector. The jog will ordinarily exert a drag on the dislocation, making the dislocation more difficult to continue gliding.

As both of these processes are more likely to occur when more dislocations are present, there is a correlation between dislocation density and yield strength.

5.2.3.b Mathematical description

Strengthening from dislocations is defined using Orowan's equation:

$$\sigma_d [\text{MPa}] = \alpha \mu b \rho^{0.5} \quad \text{eq. 5.22}$$

with μ being the shear modulus (81GPa for iron at room temperature), b the Burgers vector (2.5×10^{-10} m) and α a dimensionless coefficient for which values between 0.15 and 0.6 have been quoted in the literature [9;187]. ρ is the dislocation density (m^{-2}) which can be estimated using the following empirical relationship established on martensitic and bainitic steels [9]:

$$\log_{10}(\rho) = 9.3 + \left(\frac{6880}{T}\right) - \left(\frac{1780360}{T^2}\right) \quad \text{eq. 5.23}$$

With T being the so-called reaction temperature in K. α can be calculated using the following equation of Gladman et al. [175] (eq.5.24) together with equation 5.22:

$$\sigma_d [\text{MPa}] = 1.3(600 - T) \quad \text{eq. 5.24}$$

With T being now the isothermal transformation temperature in °C.

5.2.3.c Data and coefficients for calculation

Transformation temperatures of as-forged parts are not exactly known. However, they can be deduced from CCT diagrams presented earlier in chapter 3. B_s temperatures for 35x35mm² and 74x74mm² forged parts correspond to the B_s temperatures at 0.8°C/s and 0.4°C/s, respectively. B_F temperatures for 35x35mm² and 74x74mm² forged parts correspond to the B_F Temperatures at 0.2°C/s and 0.1°C/s, respectively.

Equation 5.19 and 5.20 are built to fit with an isothermal transformation. In order to use these equations in this study, the transformation temperature that is the most representative of the whole transformation in continuous cooling has to be established for each combination. We assumed that this representative transformation temperature is B_{50} , the temperature for which 50% of the bainitic transformation is completed. This one can be approximated using one of the two following assumptions:

1. The undercooling observed on forged parts has no or slight effect on the transformation kinetics and transformation extent, thus B_{50} for forged parts can be expressed as following:

$$[B_{50}]_{35 \times 35 \text{mm}^2} = [B_s]_{0.8^\circ\text{C/s}} - ([B_s]_{0.2^\circ\text{C/s}} - [B_{50}]_{0.2^\circ\text{C/s}}) \quad \text{eq. 5.25}$$

$$[B_{50}]_{74 \times 74 \text{mm}^2} = [B_s]_{0.4^\circ\text{C/s}} - ([B_s]_{0.1^\circ\text{C/s}} - [B_{50}]_{0.1^\circ\text{C/s}}) \quad \text{eq. 5.26}$$

2. The undercooling observed on forged parts has an effect on the transformation kinetics but not on the transformation extent. The transformation kinetics is accelerated at the beginning of the transformation and the gap with constant cooling rate conditions is quickly fully recovered. Thus, B_{50} for 35x35mm² and 74x74mm² forged parts are equal to B_{50} at 0.2°C/s and 0.1°C/s respectively.

Both aforementioned hypotheses supposed that the transformation extent did not change, which does not seem to be true in view of the comparison of obtained microstructural fractions between as-forged and dilatometric samples. However, this is the only way to approximate the B_{50} temperature from available experimental data. The true value of B_{50} might be between these two hypotheses; the gap due to undercooling might never be fully recovered despite an acceleration in the transformation kinetics at the beginning of the bainitic transformation. As B_F might be only slightly affected by undercooling, the extent of the transformation is actually reduced.

As shown in Table 26, noticeable difference between the values calculated using either of the two hypotheses appears for the 35x35mm² forged parts, where the first hypothesis yields values in average 16°C lower than those estimated using the second one. This is due to the differences between $B_s(0.8^\circ\text{C/s})$ and $B_s(0.2^\circ\text{C/s})$ for chemical compositions with good

hardenability, when using the first hypothesis. For the 74x74mm² forged parts, the difference is negligible, in average $\pm 5^{\circ}\text{C}$, as both cooling rates (0.4°C/s and 0.1°C/s) lead to close values of B_s temperatures.

	35x35mm ²			74x74mm ²		
	hyp. 1	hyp. 2	absolute difference	hyp. 1	hyp. 2	absolute difference
Base	473	477	4	480	484	4
+Ni	446	471	25	480	471	9
ONb	477	487	10	486	477	9
-Si	462	487	25	492	496	4
-Si+Mn	451	463	12	472	473	1
OMo	466	485	19	482	487	5
+Mn	426	454	28	453	462	9
-Cr	491	495	4	504	504	0
+Cr	487	480	7	480	472	8

Table 26: Calculation results of B_{s0} ($^{\circ}\text{C}$) according to the two hypotheses, for every combination.

In the case of strengthening from dislocations, eq.5.9 is written as follows:

$$\sigma_y [\text{MPa}] = \sigma_0^d + \sigma_d \quad \text{eq. 5.27}$$

Inserting eq.5.22 (Orowan) or eq.5.24 (Gladman) into eq.5.27 respectively gives:

$$\sigma_y [\text{MPa}] = \sigma_0^d + \alpha \mu b \rho^{0.5} \quad \text{eq. 5.28}$$

$$\sigma_y [\text{MPa}] = \sigma_0^{d'} + 1.3(600 - T) \quad \text{eq. 5.29}$$

Under the first hypothesis, the lowest average difference reached between calculated and experimental yield strength can be obtained with both equations using $\sigma_0^d = 666\text{MPa}$, $\sigma_0^{d'} = 680\text{MPa}$ and $\alpha=0.17$ (with which Gladman and Orowan equations match the most). This lowest difference is $\pm 32\text{MPa}$. This difference decreases to $\pm 25\text{MPa}$ and $\pm 26\text{MPa}$ with eq.5.28 and eq.5.29 respectively, when combinations from –Cr chemical composition are not taken into account. Indeed, –Cr 35 and –Cr 74 must have much lower values of σ_0^d and $\sigma_0^{d'}$ than the other combinations due to their large bainitic packet size and their lower Cr content. Under the second hypothesis, no lower or equal average difference between calculated and experimental yield strength can be reached.

It should be mentioned that such results are reached using temperatures calculated from CCT diagrams but not from direct measurements. Moreover, as discussed in chapter 2, we cannot certify that all forged parts have been realized with a strictly reproducible forging scheme. Some tensile properties, such as un-expected high yield strength and low uniform elongation, may indicate that 0Ti, base and +Ni forged parts (35x35mm² and 74x74mm²) have undergone some difference in forging process (such as higher cooling rates) that may have changed transformation temperatures and kinetics, and thus, dislocation density. However, even if the yield strengths of these three chemical compositions are underestimated using eq.5.28 or eq.5.29, differences between calculation and experiment are near the average difference.

5.2.4 Precipitation strengthening

5.2.4.a Principle

According to their crystal structure, crystal orientation, hardness, size, shape, volume fraction and spatial distribution (interparticle spacing), particles act in two distinct ways to hinder the motion of dislocations: particles may be sheared by dislocations or particles may be by-

passed by dislocations bowing out around them. Both ways increase the strength of the material.

Particles are classically divided into three categories:

- Incoherent particles: crystallographic structure and crystallographic orientation of the matrix and the particle are not compatible with each other. Thus the interface between the particle and the matrix is completely incoherent and is similar to a grain boundary between two highly misoriented grains.
- Coherent particle: crystal structure and orientation of the matrix and the particle do correspond to each other. Only the nature of the atoms and the lattice spacing are different.
- Semi-coherent particle: the crystallographic structure of the particle shares some common crystallographic plane with the matrix. Interfaces between these planes and the matrix are coherent. All the other planes exhibit incoherent interfaces.

Particles act as pinning points for dislocations. Dislocation may pass a coherent particle using two different ways that are schematized in Figure 103. As strain or stress increases, the dislocation starts to wind around the particle. The stress necessary to bow the dislocation is inversely proportional to the distance λ between two particles in the gliding plane. The maximum stress is reached when the dislocation has realized a half-circle with a radius of curvature equal to $\lambda/2$. If the particle is not able to sustain until this stress level is reached, the dislocation shears the particle (Figure 103a). The strengthening effect of such mechanism only depends on the particle strength for equivalent particle size and spacing. On the contrary, if the particle is able to sustain the maximum stress value, the dislocation will continue to bow until the half-circle arcs merge behind the particle (Figure 103b). The particle is then decorated by a dislocation loop. The actual strength of the particle under this circumstance becomes irrelevant and only the particle size and spacing are taken into account.

For a given spacing and strength of particle, the critical particle size, for which bowing is preferred to shearing, increases according to the coherency of the particle with the matrix (coherency which is also dependent on the particle). As a result, any incoherent particle has a critical size of a few nanometres only, so that incoherent particles are never sheared.

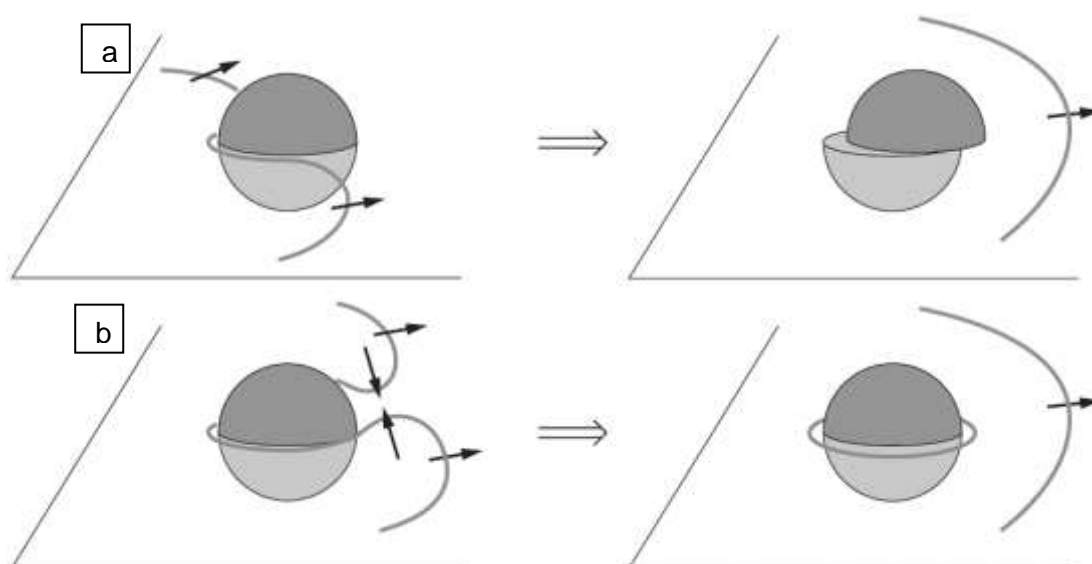


Figure 103: Mechanism of particle crossing by a dislocation. (a) shearing. (b) bowing. After [179].

5.2.4.b Mathematical description

There are different equations according to the mechanism of particle crossing by a dislocation. For this study, particles expected to play a role in the precipitation strengthening are titanium and niobium carbides. Such particles, according to their size (>40nm) and crystal structure (NaCl), are believed to be incoherent particles and thus passed by bowing. In this case, the precipitation strengthening can be described by the Ashby-Orowan equation as:

$$\sigma_p \text{ [MPa]} = \frac{\beta \mu b f^{0.5}}{r} \ln\left(\frac{r}{b}\right) \quad \text{eq. 5.30}$$

with f being the volume fraction of particles, r their average radius (m), μ the shear modulus (81GPa for iron), b the Burgers vector (2.5×10^{-10} m) and β a dimensionless fitting coefficient.

The study by Zajac et al. [7] on quantitative structure-property relationships for complex bainite microstructures used the following Ashby equation, with specific coefficients for bainitic steels:

$$\sigma_p \text{ [MPa]} = \frac{5.9 f^{0.5}}{\emptyset} \ln(2000\emptyset) \quad \text{eq. 5.31}$$

Where \emptyset is the average particle diameter in μm . This last equation, by comparison with eq.5.30, has allowed setting the value of coefficient β .

5.2.4.c Data and coefficients for calculation

Data for calculation are extracted from FEG-SEM pictures that have been taken on carbon replicas normal to the forging direction. Carbon replicas have been realized only on samples suspected to exhibit noticeable variation in carbide precipitation: base 74, 0Ti 74, 0Nb 74 (not on 0Mo 74 in view of the results obtained in selective dissolution that have been presented in chapter 2). It is assumed that $35 \times 35 \text{ mm}^2$ forged parts exhibit the same particle population as $74 \times 74 \text{ mm}^2$ parts, despite the former being cooled down twice faster at high temperature (for $74 \times 74 \text{ mm}^2$ forged parts, cooling rate exhibits an average of 1.6°C/s between 1200°C and 800°C , then an average of 0.4°C from 800°C down to B_s , see chapter 2). It is also assumed that all chemical compositions have the same particle population as the base chemical composition with the exception of 0Ti and 0Nb. The experimental procedure to realize carbon replicas is described in appendix A.

Good quality of carbon replicas was difficult to obtain. Indeed, it seems that a noticeable amount of particles have been snatched from the carbon replica during the preparation. As shown in Figure 104, traces (small holes), with the same morphology and size as observed particles, are present on the replica surface. In view of the relief exhibited by replicas, a too strong etching might also cause the formation of small holes. However, as time has been missed to realize another set of replicas, image analysis has still been made on the pictures realized in this condition.

Image analysis is made using ImageJ software on 16 pictures per combination, with a magnification $\times 10000$. Two sets of results have been obtained from two data processing methods: the first one by ignoring the holes and the second one by considering holes as particles. They are explained in detail in Appendix A. Two parameters are obtained from image analysis: the area of each particle and the area fraction of particles. Two simplifications are then made to use these data in eq. 5.26 or in eq. 5.27. The first one is that all particles are considered as spheres. Thus, areas can be transformed into radius (r) or diameter (\emptyset) and then an average size can be calculated. The second simplification is that the area fraction is equal to the volume fraction.

Table 27 shows the obtained precipitate volume fraction, average diameter and number of particles per μm^2 for both hypotheses. The largest average size is found when both Ti and Nb are present in the chemical composition, with the formation of $(\text{Nb,Ti})(\text{C,N})$. The volume fraction of precipitates exhibits an obvious increase in this case, both due to an increase in size and in number density of particles. The precipitate fraction in Ti and Nb added steel (0.0021) is slightly higher than the sum of precipitate fractions in steels with individual addition of Ti and Nb ($0.0008+0.0011=0.0019$). This was expected, as results of selective dissolution point out that the amount of precipitated Nb is higher when Ti is also present in the chemical composition (as shown in Chapter 2).

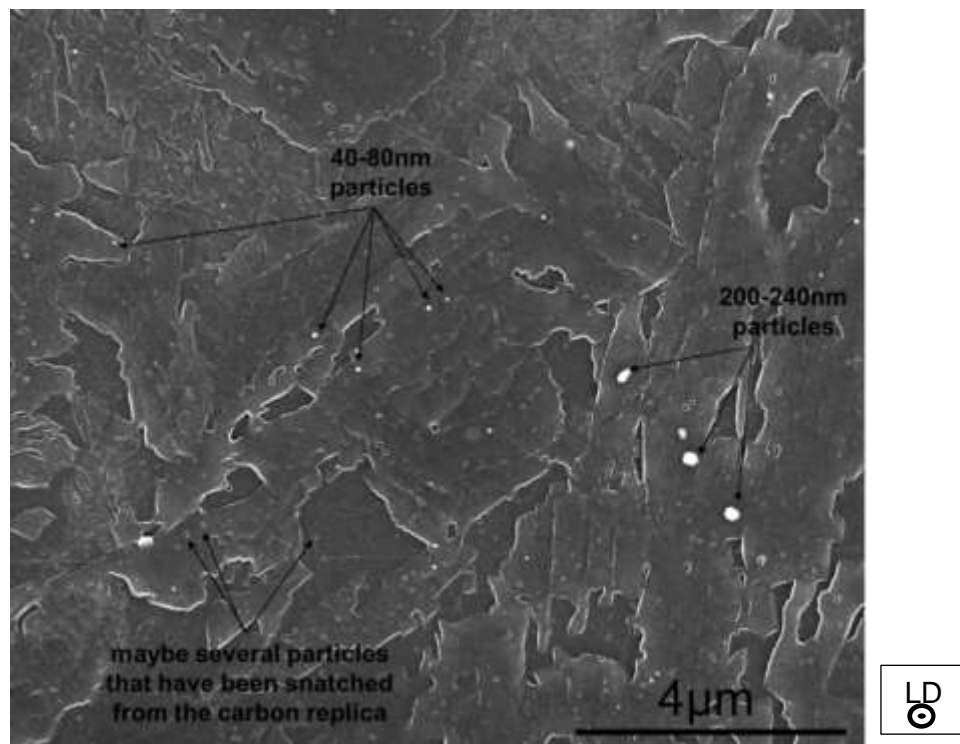


Figure 104: Typical picture obtained from a carbon replica.

If the first hypothesis is true, up to two thirds of precipitates have been snatched from the replica surface. Only small holes of 40-80nm are observed, so snatched particles seems to be only the finer ones and not those of 200-240nm in size, leading to an artificial increase in the average size of particles if only measuring those actually found in the replicas.

tag	particle	small holes = particles			small holes \neq particles		
		f	$\varnothing=2r$ (nm)	particle/ μm^2	f	$\varnothing=2r$ (nm)	particle/ μm^2
0Nb	Ti(C,N)	0.0008	53	0.30	0.0004	57	0.13
0Ti	NbC	0.0011	53	0.43	0.0004	59	0.12
base (all)	NbC – $(\text{Nb,Ti})(\text{C,N})$ – Ti(C,N)	0.0021	59	0.69	0.0007	60	0.21

Table 27: Results of the image analysis realized on carbon replicas.

Eq.5.30 and eq.5.31 gives similar results, whatever the chosen hypothesis, when the value of β coefficient is set to 72000. According to these equations, precipitation strengthening brings between 12 and 18MPa to the total yield strength in the better case (small porosities observed on carbon replica being taken into account), and between 8 and 11MPa in the least favourable one. Using an equation of the type of eq.5.9 in the case of precipitation strengthening would have not lead to any meaningful calculation. The noticeable uncertainties generated by the low quality of carbon replica on the precipitation strengthening

are not very detrimental. Indeed, whatever the hypothesis chosen, the range of precipitation strengthening is so narrow, and low compared to all other strengthening effects, that this one can be replaced by a constant term equal to 17MPa. This value is the average of precipitation strengthening contribution over all the investigated materials. Such a replacement does not have any impact on the calculation accuracy using eq.5.8, when all strengthening coefficient are taken into account.

5.2.5 Base strength

Base strength regroups all contributions to strength that have not been taken into consideration explicitly. Base strength is mainly the contribution of the intrinsic strength of bcc iron and interstitial carbon and nitrogen near their solubility limit in bainitic ferrite. Values of Intrinsic strength of bcc iron of 54 and 88 MPa have been respectively used by Iza-Mendia and Gutierrez [177] and Zajac et al. [7] (the latter one included, in addition, the effect of interstitial carbon in this value). In the present study, the base strength is expected to be slightly higher than both of these values as interstitial nitrogen is also considered in this contribution.

5.2.6 Contribution of the secondary microstructural constituents

5.2.6.a Principle

Microstructures with a mix of two (e.g. dual-phase steels) or several microstructural constituents are commonly used in the automotive industry to combine the conflicting requirements of high strength and good ductility. A hard microstructural constituent can successfully strengthen a softer one according to specific combinations of several parameters like volume fraction (with possible occurrence of a threshold [188-189]), the spatial distribution [190] (banded structure, patchwork of hard grains and soft grains, profuse distribution of hard grains in soft grains), the morphology [191] (size and aspect ratio) and hardness difference between the harder and softer phases (ferrite-bainite, ferrite-martensite). The underlying strengthening mechanisms are [192]:

1. The load transfer between the two microstructural constituents
2. The formation of accommodation dislocations resulting from the strain gradient between the microstructural constituents with different deformation behaviours.
3. Plastic strain from martensite or martensite-rich MA constituent resulting from displacive transformation of austenite into martensite.

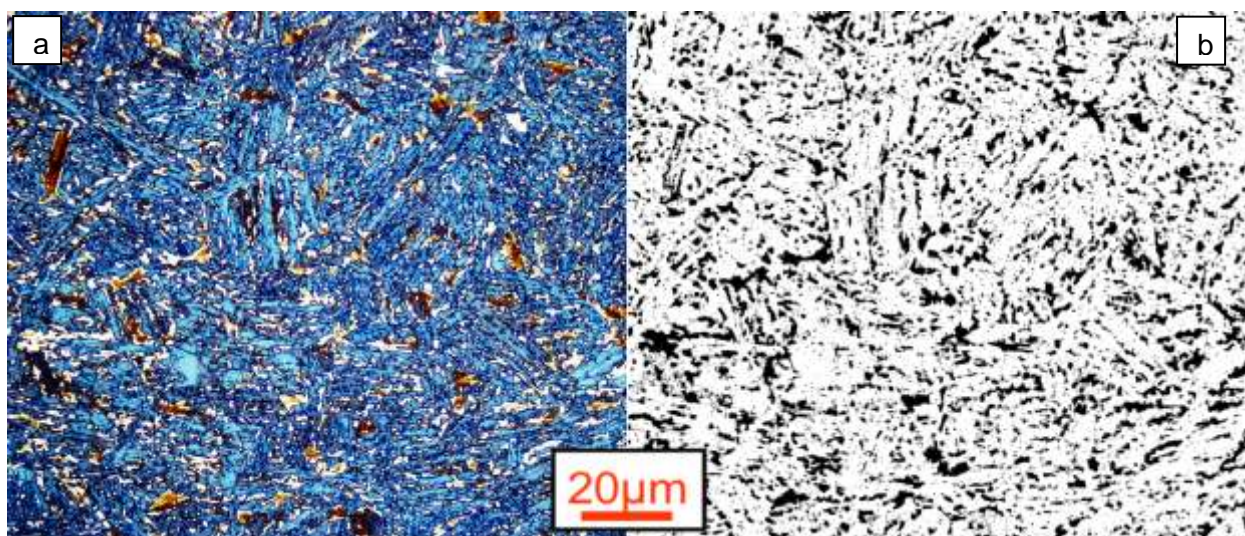


Figure 105: (a) –Si+Mn 35, LePera etching, LM. From light blue to dark brown, the bainite matrix, in white, the MA constituent and in light brown and yellow the martensite. (b) the same picture with secondary hard microstructural constituents in black (21.7 area%) and the bainitic ferrite matrix in white.

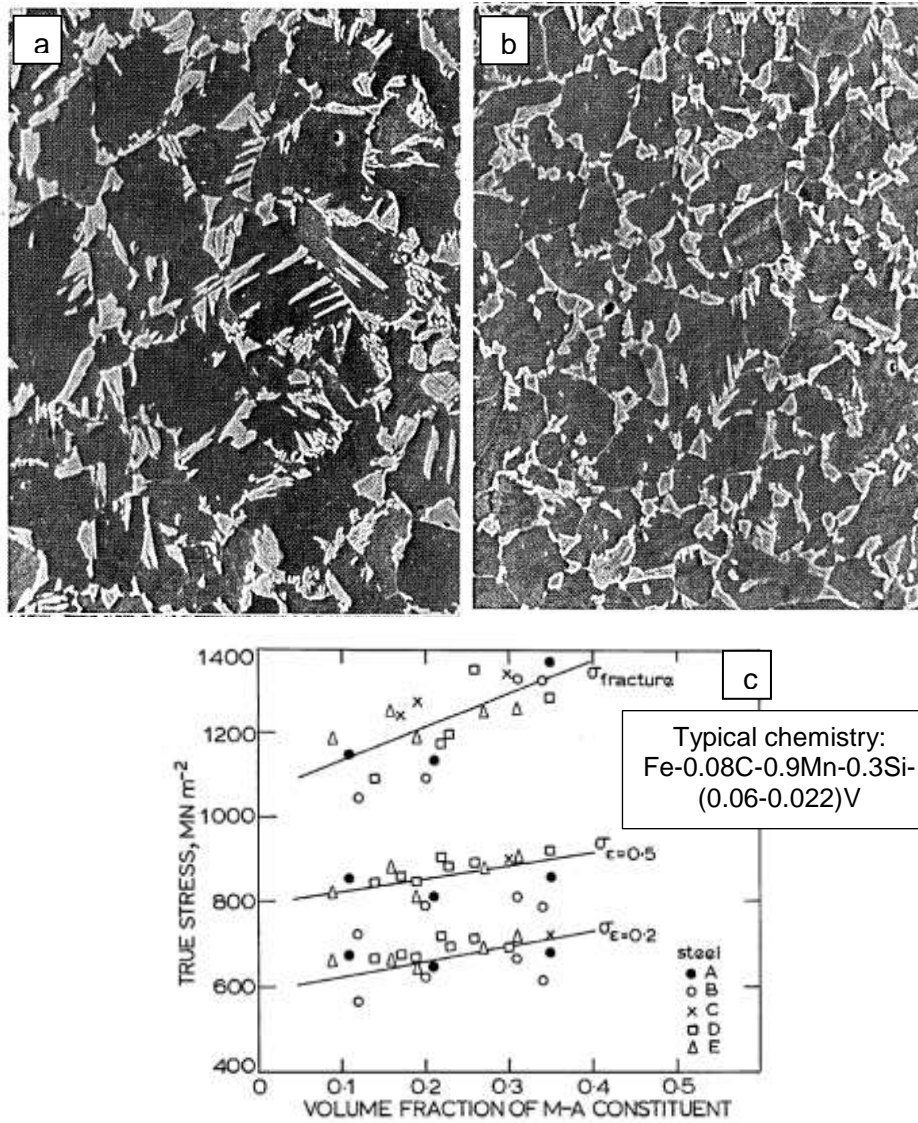


Figure 106: LM picture of dual-phase (a) steel B, (b) steel D after annealing at 845°C. Bright grey islands = MA constituent, dark grey matrix = ferrite. No scale is given. (c) Effect of volume fraction of MA constituent on flow and fracture stresses of dual-phase steels. After [191].

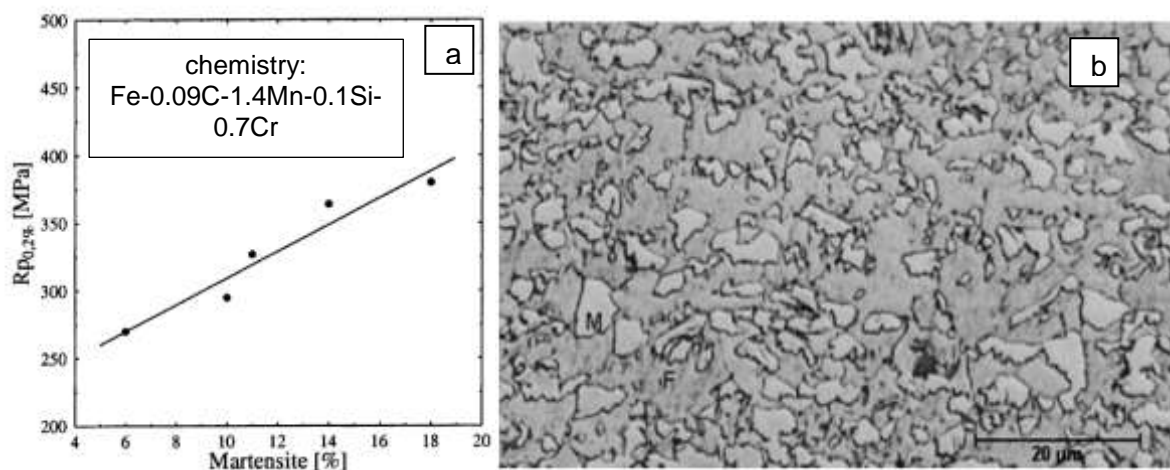


Figure 107: (a) 0.2% yield strength ($R_{p0.2}$) versus the martensite volume content in the ferritic matrix. (b) Metallographic section of a dual-phase steel consisting of ferrite (dark grey) and 11% of profuse martensite islands (bright grey). After [193].

The bainitic microstructure of our forged parts is a mix of granular and coarse cementite-free upper bainite. As seen in chapter 2, such microstructure can be viewed as a bainitic ferrite matrix with a profuse distribution of secondary microstructural constituent of mainly austenite films and MA constituent islands/blocks (martensite being trapped in the middle of the biggest MA islands, called “blocks” in the present study). This is illustrated in Figure 105. MA islands/blocks are located within or between the bainite packets, inter-packet blocks ($5\mu\text{m}^2 < \text{blocks} < 120\mu\text{m}^2$, $21\mu\text{m}^2$ in average for reference as-forged steel) being much larger than intra-packets islands ($< 5\mu\text{m}^2$).

As shown in Figure 106 and Figure 107, profuse island distribution of a hard microstructural constituent in a soft matrix, apparently similar to the one observed in the present study, can lead to a strengthening effect even for low volume fractions of hard microstructural constituent [95;98]. Of course, there are two noticeable differences between the microstructures of these studies and those of the present one. Firstly, ferrite does not exhibit lath sub-structure as bainite does. Secondly, the gap in strength is lower from bainite to MA constituent than from ferrite to MA constituent. However, we assumed that the spatial distribution and the morphology of the hard microstructural constituent are first order parameters in concern of this strengthening mechanism, whereas the strength gap is considered as second order parameter. So, the range of MA constituent and martensite fraction present in our microstructure is believed to induce significant strengthening.

5.2.6.b Data & coefficients for calculation

Yield strength has been calculated using eq.5.7:

$$\sigma_y [\text{MPa}] = \sigma_{BA}X_{BA} + \sigma_{MA}X_{MA} + \sigma_{MXM} + \sigma_{FXF}$$

Data that have been used for the calculation are the surface fractions of microstructural constituents found with LM quantification and presented in Chapter 2. Strengthening coefficients of each microstructural constituent have been determined mathematically by obeying the following two rules:

$$1. \quad \sigma_F < \sigma_{BA} < \sigma_M < \sigma_{MA}$$

The MA constituent has the highest carbon concentration among all microstructural constituents. Moreover this constituent is the last formed from austenite decomposition during cooling. Transformation temperatures of MA constituent are thus the lowest among all microstructural constituents and leads to a very fine mixture of martensite and austenite. For all these reasons, MA constituent might have the highest strength income in such kind of microstructure.

Strength income from martensite might be between the one of MA constituent and the one of bainitic ferrite as the range of transformation temperature of martensite is somewhere between the ranges of transformation temperatures of bainitic ferrite and MA constituent respectively. In addition, the range of carbon contents in martensite is lower than that of MA constituent but much higher than in bainitic ferrite whose carbon is believed to be near its solubility limit in ferrite.

Strength income from allotriomorphic ferrite might be the lowest one as this one comes from the decomposition of austenite at the highest temperature (between 700 and 600°C according CCT diagrams).

$$2. \quad \sigma_{BA} \sim 751\text{MPa from Figure 108}$$

Figure 108 shows the evolution of the 0.2% proof stress as a function of the amount of hard secondary microstructural constituent (MA constituent and martensite) measured using light microscopy and LePera etching. With the exception of some combinations, $YS_{0.2}$ has a tendency to increase with the amount of secondary phases. The two combinations obviously

out of this tendency are –Cr 35 and –Cr 74. These two combinations exhibit by far the lowest matrix yield strength due to a coarse effective bainitic packet size and reduced solute chromium content. Thus, at equivalent amount of harder secondary phase, the two -Cr combinations cannot expect to reach the same level of strength as other combinations.

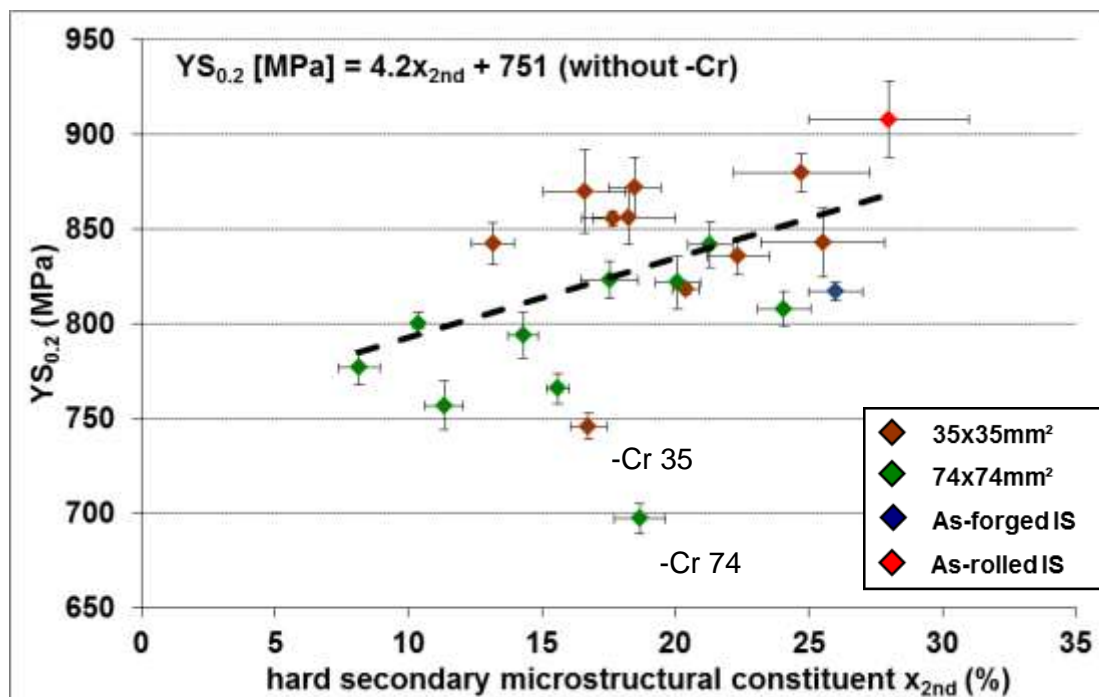


Figure 108: Experimental 0.2% proof stress ($YS_{0.2}$) versus hard secondary microstructural constituent content (MA constituent and martensite). 0Ti forged parts are included in the dataset.

Respecting these two rules, quite accurate prediction of yield strength can be obtained without considering –Cr chemical composition. The lowest average difference between the experimental and calculated values is ± 21 MPa (± 29 MPa with –Cr). In this case, eq.5.7 gives:

$$\sigma_y [\text{MPa}] = 743x_{BA} + 1165x_{MA} + 1165x_M + 300x_F \quad \text{eq.5.32}$$

Strength income from allotriomorphic ferrite has been set artificially. In fact, a lower average difference between calculated and experimental yield strength can be reached when strength incomes of allotriomorphic ferrite is negative, which has no physical meaning yet. As only one forged part exhibits allotriomorphic ferrite with, in addition, a low fraction (0.02), this arbitrary choice has no noticeable impact on the calculated yield strength.

The lowest average difference between calculated and experimental yield strength is reachable when the martensite has a higher strengthening coefficient than MA constituent. Martensite is only present in the centre of coarse blocks of MA constituent, occurs very punctually and is not at all as profusely distributed in the microstructure as MA constituent. For these reasons, martensite might not contribute directly to the strengthening of the bainitic matrix. In addition, martensite surface fraction (between 0.01 and 0.07) is also well below the one of MA constituent (between 0.07 and 0.21) and thus exhibits high relative uncertainties on measurement. So in view of the mathematical fitting and of the previous observations, it is possible to use only one coefficient for MA constituent and martensite.

5.2.7 Global calculation

5.2.7.a Coefficients for calculation

Table 28 shows the different coefficients that have been set mathematically or according to the literature to obtain the “best fit result” using eq.5.8. In this table, they are compared with the ones that have been determined earlier in this chapter, when only one strengthening

CHAPTER 5 – MICROSTRUCTURAL PARAMETERS THAT CONTROL STRENGTH

mechanism is considered at a time, to vary for each combination. This table also recalls hypotheses that have been made to obtain the fitting parameters.

Taken all together rather than individually, the solid solution strengthening, the strengthening from boundaries and the contribution of the secondary microstructural constituents have the tendency to decrease. It points out that strengthening mechanisms might be over-evaluated when viewed individually, as they are not independent of each other.

For example, in the case of nickel addition: viewed individually, using eq.5.13, Ni seems to have an obvious effect on solid solution strengthening. Indeed, its strengthening coefficient is the highest, like that of Cr (185MPa per wt%). When all strengthening mechanisms are considered at the same time, solid solution strengthening of Ni is divided by 3. The high solid solution strengthening coefficient found initially takes into account the tendency of Ni to decrease the average bainitic ferrite packet size (as shown in Chapter4) as well as to increase the fraction of hard secondary microstructural constituent in the case of the 74x74mm² forged part (as shown in Chapter 2) and to decrease significantly B_{50} in the case of the 35x35mm² forged part (as shown earlier in this chapter).

It is shown in Table 28 that only 8 calculation parameters (coefficients and hypothesis with green background) have been fitted in order to obtain the lowest difference between calculated and experimental yield strength. Other parameters have not been considered for the fitting as consistent values for them have been found in the literature, such as in the case of some solid solution strengthening coefficients. α and β have been fixed by crossing existing empirical equations found in the literature.

substitutional solid solution strengthening	σ_0^{SS} [MPa]	SS_{Mn} [MPa]	SS_{Si} [MPa]	SS_{Cr} [MPa]	SS_{Ni} [MPa]	SS_{Mo} [MPa]	SS_{Nb} [MPa]	SS_{Cu} [MPa]	SS_P [MPa]
Individually (eq.5.18)	473	32	83	185	185	11	11	39	678
all together (eq.5.8)	X	32	83	144	53	11	11	39	678

strengthening from boundaries	σ_0^b [MPa]	n	k_y [MPa.mm]
individually (eq.5.21)	455	1	8.9
all together (eq.5.8)	X	1	5.0

dislocation strengthening	hypothesis	σ_0^d [MPa]	α
individually (eq.5.28)	$n^{\circ}1$	666	0.17
all together (eq.5.8)	$n^{\circ}1$	X	0.17

precipitation strengthening	hypothesis	β
individually (not defined)	traces=particles	72000
all together (eq.5.8)	traces=particles	72000

base strength	σ_0 [MPa]
individually (not defined)	X
all together (eq.5.8)	104

contribution of the secondary microstructural constituents	σ_{BA} [MPa]	σ_{MA} [MPa]	σ_M [MPa]	σ_F [MPa]
individually (eq.5.32)	743	1165	1165	300
all together (eq.5.8)	X	1044	1044	300

Table 28: Coefficients for YS calculation. Individually: one strengthening mechanism is considered as variable each time for each combination. All together: all strengthening mechanisms are considered in the same time. The used equation is recalled in bracket. Changes in coefficient between the two ways of calculation are highlighted in bold. X: not present in the calculation. Green background exhibits adjustable mathematical coefficient or hypothesis for the global calculation. Red background shows coefficient or mechanism that can be ignored in the global calculation, most by reporting them in the base strength as constant.

Some coefficients and one strengthening mechanism (with red background) can be ignored in the global calculation, by setting them as a constant in the base strength. When they are all introduced in the base strength, this one goes from 104MPa to 129MPa without affecting the lowest reachable difference between experimental and calculated yield strength.

5.2.7.b Results

Figure 109 shows the calculated yield strength, σ_y , using eq.5.4 versus experimental 0.2% proof stress. This calculation has been done for every combination of forged parts with the exception of 0Ti chemical composition (so 18 points). The lowest average difference between both values with meaningful fitting coefficients is ± 14 MPa (minimum error of 0, maximum error of +37MPa corresponding to –Cr 74). If experimental measurement uncertainties are taken into account, this average difference decreases down to ± 7 MPa (maximum error +29MPa, still corresponding to –Cr 74). The two states of the reference steel are also presented in Figure 109 but have not been taken into consideration for the calculation of the average difference between experimental $YS_{0.2}$ and calculated σ_y . Assessing their value of σ_y has necessitated additional hypotheses that are discussed later in this chapter.

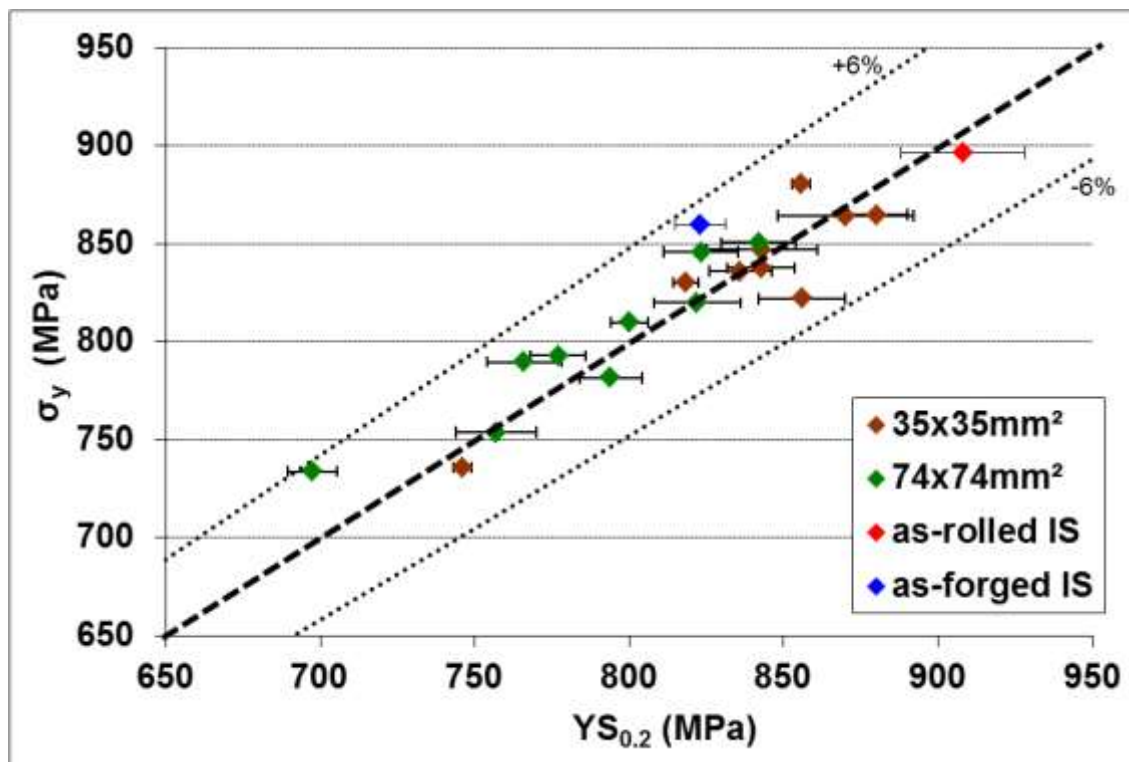


Figure 109: Calculated yield strength versus experimental 0.2% proof stress using eq.5.4. IS: reference steel.

5.2.8 Discussion

5.2.8.a Contribution of every strengthening mechanism to the total yield strength

Figure 110 and Figure 111 show the contribution of each strengthening mechanism to the total yield strength for the different groups of forged parts. There is a slight decrease by 4% in the role played by secondary microstructural constituents between 35x35mm² and 74x74mm² forged parts (contribution the most impacted by the cooling rate). This is due to the decrease in MA constituent fraction and martensite fraction in the final microstructure of the 74x74mm² forged parts. Indeed, MA constituent fraction decreases as undercooling becomes negligible leading to more complete bainitic transformation. This decrease happens

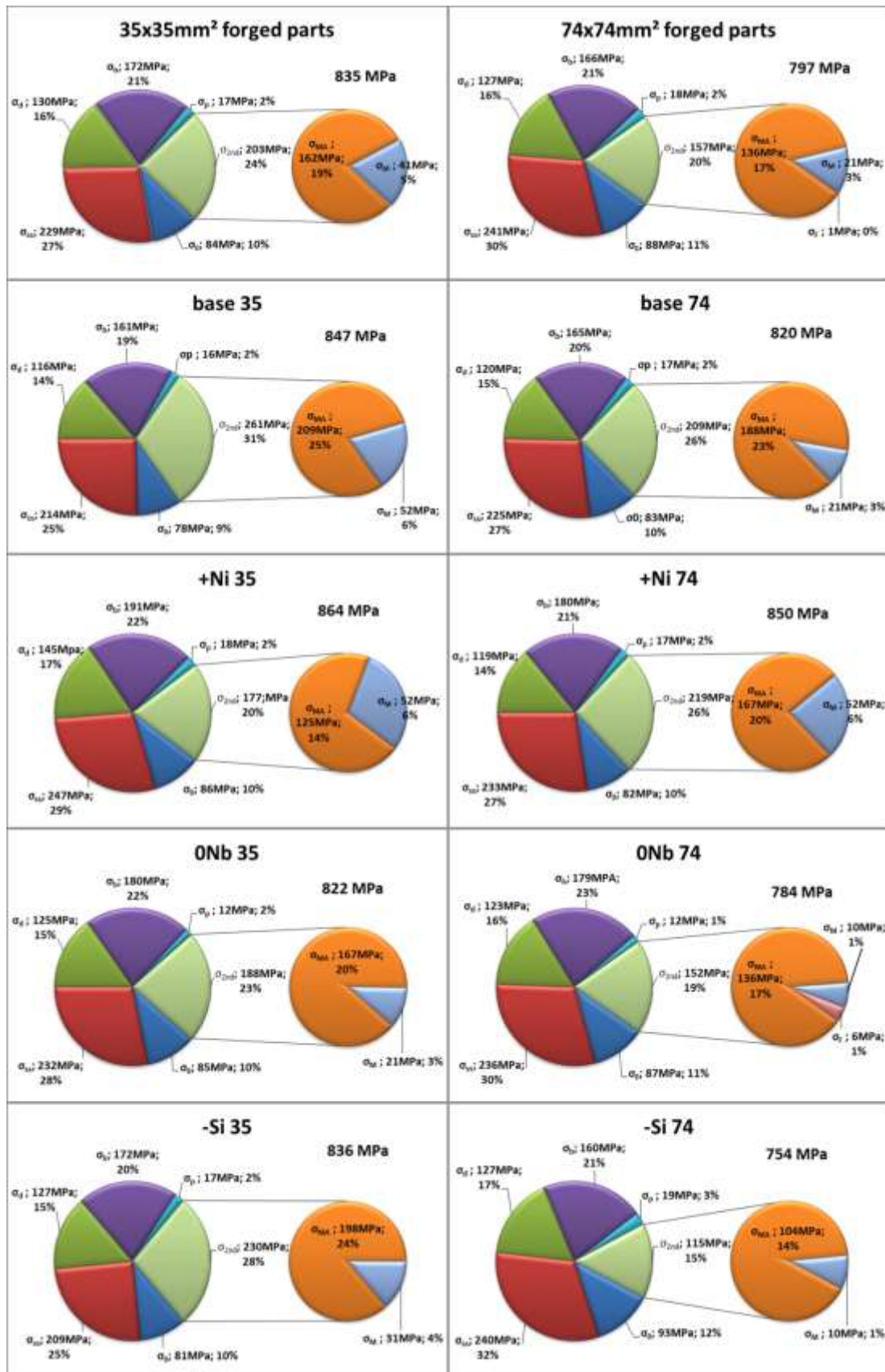


Figure 110: Diagrams showing the part of each strengthening effect in the total yield strength. σ_b : base strength and interstitial solid solution strengthening, σ_{ss} : substitutional solid solution strengthening, σ_p : precipitation strengthening, σ_b : strengthening from boundaries, σ_d : dislocation hardening, σ_{2nd} : strength income of secondary microstructural constituent, σ_{MA} : strength income of MA constituent, σ_M : strength income of martensite, σ_F : strength income of ferrite.

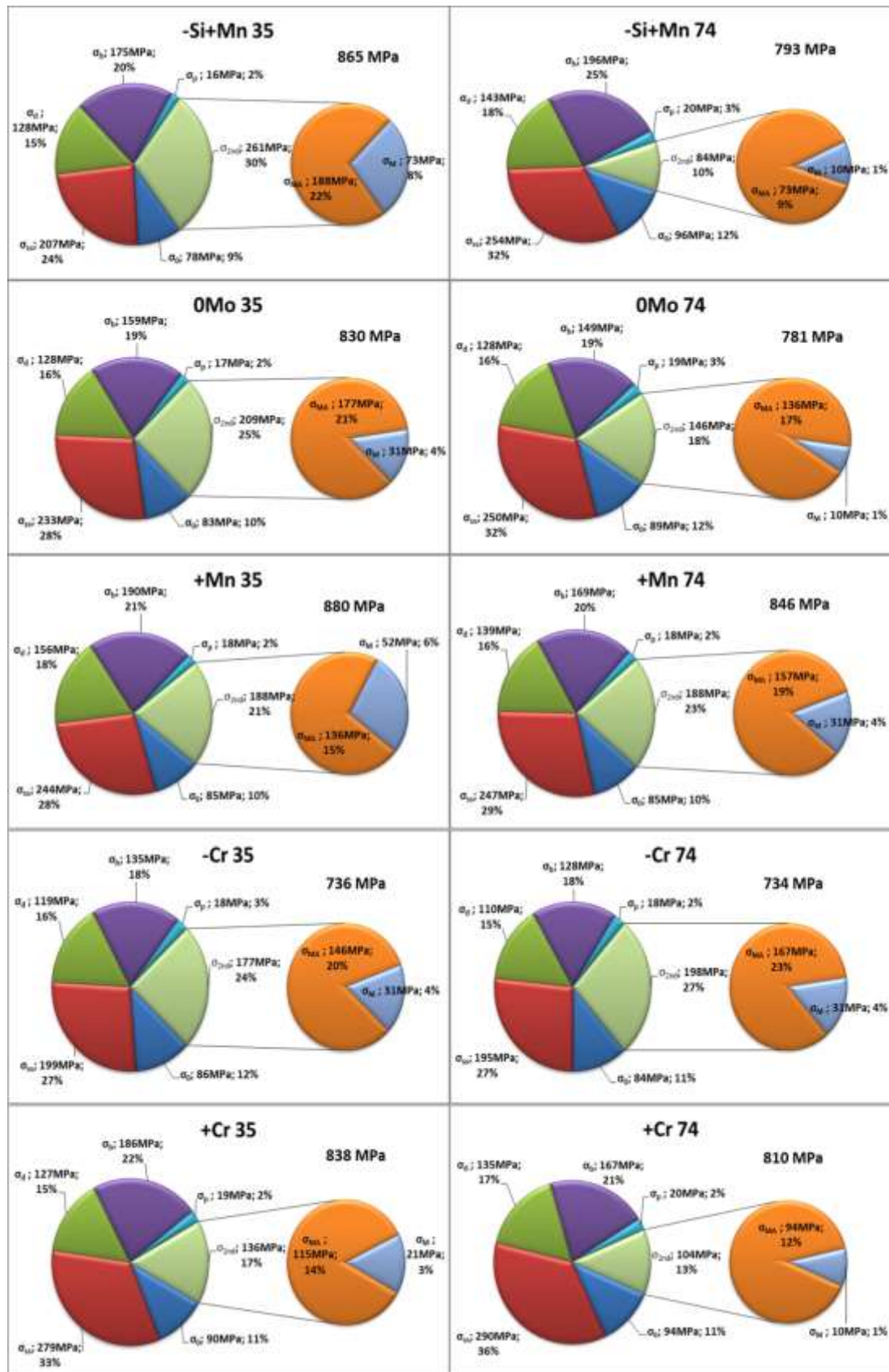


Figure 111: Diagrams showing the part of each strengthening effect in the total yield strength. σ_0 : base strength and interstitial solid solution strengthening, σ_{ss} : substitutional solid solution strengthening, σ_p : precipitation strengthening, σ_b : strengthening from boundaries, σ_d : dislocation strengthening, σ_{2nd} : strength income of secondary microstructural constituent, σ_{MA} : strength income of MA constituent, σ_M : strength income of martensite, σ_F : strength income of ferrite.

	σ_0	σ_{ss}	σ_d	σ_b	σ_p	σ_{BA}	σ_{2nd}	σ_{MA}	σ_M	σ_F
Base 35	78	214	116	161	16	586	261	209	52	0
+Ni 35	86	247	145	191	18	687	177	125	52	0
ONb 35	85	232	125	180	12	634	188	167	21	0
-Si 35	81	209	127	172	17	606	230	198	31	0
-Si+Mn 35	78	207	128	175	16	604	261	188	73	0
OMo 35	83	233	128	159	17	621	209	177	31	0
+Mn 35	85	244	156	190	18	693	188	136	52	0
-Cr 35	86	199	119	135	18	558	177	146	31	0
+Cr 35	90	279	127	186	19	702	136	115	21	0
average	84	229	130	172	17	632	203	162	41	0
minimum	78	199	116	135	12	558	136	115	21	0
maximum	90	279	156	191	19	702	261	209	73	0
max-min	0	80	39	56	7	144	125	94	52	0

	σ_0	σ_{ss}	σ_d	σ_b	σ_p	σ_{BA}	σ_{2nd}	σ_{MA}	σ_M	σ_F
Base 74	83	225	120	165	17	611	209	188	21	0
+Ni 74	82	233	119	180	17	631	219	167	52	0
ONb 74	87	236	123	179	12	637	152	136	10	6
-Si 74	93	240	127	160	19	639	115	104	10	0
-Si+Mn 74	96	254	143	196	20	709	84	73	10	0
OMo 74	89	250	128	149	19	635	146	136	10	0
+Mn 74	85	247	139	169	18	658	188	157	31	0
-Cr 74	84	195	110	128	18	535	198	167	31	0
+Cr 74	94	290	135	167	20	706	104	94	10	0
average	88	241	127	166	18	640	157	136	21	1
minimum	82	195	110	128	12	535	84	73	10	0
maximum	96	290	143	196	20	709	219	188	52	6
max-min	0	94	34	67	8	174	136	115	42	6

all	σ_0	σ_{ss}	σ_d	σ_b	σ_p	σ_{BA}	σ_{2nd}	σ_{MA}	σ_M	σ_F
average	86	235	129	169	17	636	180	149	31	0
minimum	78	195	110	128	12	535	84	73	10	0
maximum	96	290	156	196	20	709	261	209	73	6
max-min	0	94	46	67	8	174	177	136	63	6

Table 29: Value of different estimated contributions to yield strength. Light blue background corresponds to contributions coming from the bainite, light red background correspond to contributions coming from the secondary microstructural constituents.

despite more granular bainite was expected in the final microstructure according to CCT diagrams. This slight decrease in the contribution played by secondary microstructural constituents is redistributed between constant strengthening mechanisms, un-sensitive to such variation of cooling rate, as solid—solution strengthening, base strength and precipitation strengthening. Dislocation hardening and strengthening from boundaries show a decrease of 3 and 7MPa respectively, but stay at the same level of involvement in the total yield strength. This decrease was expected as both strengthening effects are dependent on transformation temperatures, and thus, on the cooling rate.

Substitutional solid solution is the first main source of strengthening in such bainitic steels. These high values of strengthening are provided by chemical composition having a significant variety of alloying elements in noticeable amount. Indeed alloying elements are between 3.72 to 4.35wt% of the nominal composition from which 3.37 to 4.03wt% are believed to play a role in solid solution strengthening. As shown in Table 29, this contribution allows creating some significant distinctions between the different combinations. Indeed, the difference between the lowest and the highest solid solution strengthening is 94MPa.

This is not surprising, in view of the strengthening coefficient that has been found for chromium in solid solution, that $-Cr$ and $+Cr$ chemical compositions exhibit, for both geometries of forged parts, the minimum and maximum nominal values in solid solution strengthening, respectively. Despite this, the contribution of solid solution strengthening to the total yield strength for $-Cr$ and $+Cr$ forged parts does not show obvious variation compared to the average ones noticed for both forged parts. Nevertheless, in the case of $+Cr$, this contribution to the total YS increases by 6% (36% instead of 30% in average for 74x74mm² forged parts and 33% instead of 27% in average for 35x35mm² forged parts).

In most cases, the second highest contribution to yield strength comes from the secondary microstructural constituents. This strengthening mechanism accounts from 84 to 261 MPa of the total yield strength, showing a variation by 177MPa between combinations. The minimum and maximum values come from $-Si+Mn$ 74 and $-Si+Mn$ 35, respectively. It is interesting to notice that the second highest variation of this strengthening contribution for a given chemical composition is found for $-Si$ (+115MPa between $-Si$ 74 and $-Si$ 35). As shown in Chapter 2, these two combinations have been found very sensitive to undercooling, with a fraction of MA constituent in 35x35mm² forged parts well over the expected one in regards of CCT diagrams (for a cooling rate of 0.2°C/s). This sensitivity might be linked with the highest extent of bainite transformation for chemical composition with a reduced content of silicon. For an equivalent undercooling to other chemical compositions, $-Si$ and $-Si+Mn$ chemical compositions might exhibit a higher loss in bainite fraction.

As a result, the contribution of σ_{2nd} to the total yield strength for $-Si+Mn$ 74 and $-Si$ 74 falls down to 10% (minimum among all combinations) and 15% instead of the average 20% for 74x74mm² forged parts. On the contrary, the contribution of σ_{2nd} to total yield strength for $-Si+Mn$ 35 and $-Si$ 35 rises up to 30% (maximum among all combinations) and 28% instead of the average 24% for 35x35mm² forged parts.

For most of the combinations, the third highest contribution to total yield strength comes from high angle boundaries ($>15^\circ$). Boundaries provide between 128 and 196MPa of the total yield strength. As σ_b is dependent of the bainitic ferrite packet size, $-Cr$ forged parts, which exhibit the highest bainitic ferrite packet sizes, have the lowest nominal values of σ_b . $+Ni$ forged parts, which exhibit some of the lowest bainitic ferrite packet sizes, have high nominal values of σ_b . The contribution of σ_b to the yield strength varies between 18 and 25% according to the combination for an average of 21%. 25% is reached for $-Si+Mn$ 74 combination, due to a very low fraction of secondary microstructural constituents (0.08) as well as a slightly lower average bainitic ferrite packet size. Both $+Cr$ forged parts have a

contribution of σ_b to yield strength higher than that of σ_{2nd} , as they also have very low fraction of secondary microstructural constituents like –Si+Mn 74.

Dislocation hardening is the last main strengthening mechanism for the considered steel grade. –Cr chemical composition has the highest B_S and B_{50} temperatures, and thus low nominal values of σ_d (119 and 110MPa for –Cr 35 and –Cr 74, respectively). On the contrary, +Mn forged parts, which have the lowest B_S and B_{50} temperatures, have high nominal values of σ_d (156 and 139MPa for +Mn 35 and +Mn 74, respectively). However, the contribution of σ_d to the total yield strength of all combinations does not show significant variations compared to the average one noticed for both forged parts (16%).

As both nominal values of σ_b and σ_d are small in –Cr forged parts, secondary microstructural constituents becomes the first source of strengthening despite that their fractions are not the highest ones that have been measured in the considered materials.

5.2.8.b Calculation of yield strength for reference steels

From our data, σ_{ss} , σ_b and σ_{2nd} can be estimated for both as-forged and as-rolled reference steels. Considering that additional nickel content does not affect transformation temperatures and transformation kinetics at low cooling rates (as shown in Chapter 2), B_{50} temperatures have been set to 480°C (=B₅₀ of +Ni 74) allowing the calculation of σ_d . If σ_0 and σ_p are the same as for 74x74mm² forged parts, differences between experimental yield strength and calculation are -12MPa and +37MPa for as-rolled and as-forged parts respectively (0MPa and 29MPa when taking experimental uncertainties into account).

5.2.8.c Comparison between as-rolled and as-forged reference steel

As-forged reference steel shows a noticeable decrease by 85MPa in $YS_{0.2}$ compared to the as-rolled one. The fraction of secondary microstructural constituents is also slightly higher in the as-rolled steel (+ 0.02). Such difference may lead to an improvement in yield strength by only 20MPa. However, as seen earlier in this chapter, MA constituent seems more brittle, thus stronger, in the case of as-forged steel, so the final improvement in yield strength might be lower.

Most of the yield strength improvement comes from the difference in effective packet size between both states. Effective packet sizes are 21 μ m and 24 μ m for as-rolled and as-forged reference steel, respectively. Such slight difference in size corresponds to an increase in strengthening from boundaries by 44MPa according to their respective bainite fraction. As both states share the same chemical composition, the smaller effective packet size comes from lower PAGS and perhaps, higher cooling rate for the as-rolled steel. As primary austenite grains were found equiaxed in the as-rolled steel, the finish rolling temperature might be higher than the T_{nr} , which would not increase the dislocation density.

Cooling rates before the bainitic transformation and at the beginning of this one are not available for both states of the reference steel but they might be higher for as-rolled than for as-forged due to their respective geometry (as-rolled section=5026mm², as-forged section~5440mm²). As B_S and B_{50} temperatures might be lowered, the dislocation density, and thus the dislocation strengthening might be higher in the as-rolled reference steel. Considering the volume fraction of bainite in the as-rolled reference steel, a decrease by 10°C in B_{50} would lead to an increase by 16MPa in yield strength. However, there is a noticeable difference in PAGS between the two states: as-rolled steel exhibits a PAGS of 31 μ m, compared to 52 μ m for the as-forged steel. As a consequence, the lowering of B_{50} might not be important and resulting difference in dislocation strengthening too.

Finally, the volume fraction of precipitates might be higher in the as-rolled steel, as the range of deformation temperatures in rolling (>900°C) is believed to be below the one of forging (>1050°C), leading to more strain-induced precipitation.

5.2.8.d Comparison between as-forged reference steel and as-forged laboratory heats

As-forged reference steel has better strength properties than most of the 74x74mm² forged parts (in fact all of them with the exceptions of 74x74mm² 0Ti/base/+Ni that are suspected to have encountered forging issues). This is not surprising as:

- Cooling rates are believed to be equivalent between the two different products due to similar section area in the vicinity of the tensile specimens (5476mm² versus 5440mm²).
- But with a nickel content two times superior than +Ni chemical composition for the reference forged part.

CCT diagram analysis of +Ni chemical composition showed that for low cooling rates (0.1°C/s and 0.08°C/s), MA constituent fraction reaches nearly 0.2, which is one of the highest levels measured at these cooling rates (with +Mn) without prior formation of allotriomorphic ferrite. With even higher nickel content, the fraction of MA constituent in the as-forged reference steel reaches 0.24. Where all other 74x74mm² forged parts exhibit an average σ_{2nd} of 155MPa, the value of σ_{2nd} of the reference as-forged part is 269MPa.

Even if nickel was not found to affect transformation temperatures at low cooling rates, nickel has a noticeable effect on solid solution strengthening of bainitic ferrite. However, σ_{ss} value is weighted by the fraction of bainite in the calculation. Then, an average value of σ_{ss} of 235 MPa (240MPa for bainite fraction equal to 1) is found for 74x74mm² forged parts, which is barely equal to 230MPa, the value of σ_{ss} found for as-forged reference steel (312MPa for bainite fraction equal to 1).

5.2.8.e Ways for simplifications of the calculation

No SEM in Gandrange R&D centre is equipped with EBSD. This equipment cannot be used on a routine base. However it is the only equipment available to obtain the effective packet or effective lath sizes that are necessary to estimate the strengthening contribution from boundaries. Nevertheless, empirical equations to estimate them from transformation temperatures have been found in the European commission report of Parker et al. [174]. Parker et al. worked on property model for mixed microstructures. These equations (eq.5.33 to eq.5.37) are the following:

- Chang [194]: $d_{Sub-Unit} [\mu m] = -0.2681 + 1077 \times 10^{-3}T$ eq.5.33
- Parker et al: $d_L [\mu m] = -0.90 + 6.70 \times 10^{-3}T$ eq.5.34
- Parker et al.: $d_l [\mu m] = -1.78 + 7.56 \times 10^{-3}T$ eq.5.35
- Parker et al.: $d_l [\mu m] = -1.187 + 7.00 \times 10^{-3}T$ eq.5.36
- Parker et al.: $d_p [\mu m] = -6.76 + 0.22 \times 10^{-3}T$ eq.5.37

Where T is the transformation temperature in °C, taken as B₅₀ in our case (hypothesis 1). A calculation of the yield strength has been realized by considering only the strengthening from boundaries as a variable, using eq.5.17 with the packet or lath sizes obtained with eq.5.29 to eq.5.33. Table 30 shows the results of such calculations. It can be seen that they all give barely the same average difference between the calculated yield stress and the experimental proof stress. However, the only one that gives acceptable σ_0^b to reflect the influence of other strengthening effects is the last one, using a cut-off angle of 15° (eq.5.33). So once again, yield strength seems to be more relative to an effective packet size rather than to an effective lath size.

	Chang TEM in-situ measurement	Pickering & McIvor EBSD cut-off angle >2°	Parker et al. EBSD cut-off angle >2°	Parker et al. EBSD cut-off angle >3°	Parker et al. EBSD cut-off angle >15°
σ_0^b [MPa]	377	136	351	201	501
k_y [MPa.mm]	0.104	1.533	0.825	1.276	1.126
Avg. difference [MPa]	29	28	28	28	29
Min. difference [MPa]	1	0	0	0	0
Max. difference [MPa]	70	65	68	66	64

Table 30: Fitting coefficient and associated lowest average difference reached between calculated YS (using eq.5.17 with eq.5.29 to eq.5.33) and experimental YS. $n=1$.

However, effective packet sizes (from 1.7 to 4.3 μm) found using Parker et al. equation are far from the values measured using EBSD in the present study (from 21 to 30 μm). This equation has been built on bainite isothermally transformed between 375 and 500°C from C-Mn steels. These temperatures are not so far from the calculated B_{50} in this study (from 426 to 504°C), which is not the case for the PAGS, not given directly by the authors, but that can be perceived on EBSD maps shown in their report. The PAGS seems to range from 10 to 20 μm , so 20-40 μm lower than the one measured on the forged parts, leading to such a significant difference in packet size.

Figure 112a to Figure 112c show the dependence of the effective packet size on transformation temperatures, transformation kinetics and PAGS. The effective packet size does not exhibit significant variation (from 22 to 25 μm) for PAGS lower than 45 μm and/or B_{50} lower than 480°C. At least, only a slight tendency of decrease with decreasing B_s or B_{50} temperature can be perceived below these limits. Beyond these limits, the effective packet size increases fast and reaches 30 μm (an increase by 5 μm) with an increase by less than 20°C in B_{50} or an increase by less than 6 μm on PAGS. The occurrence of such limitation might be due to a change in ratio between the nucleation and the growth rate of bainitic laths. For PAGS grain size higher than 45 μm , growth might be dominant, so the first packet penetrates the parent grain rapidly with only few obstacles, being able to go from one side to another side of the primary austenite grain. For PAGS grain size lower than 45 μm , nucleation might be dominant so several packets can grow simultaneously, restricting their maximum reachable size.

Considering both PAGS and B_{50} parameters, an empirical equation has been built to estimate the effective packet size on the model of the equations used by Parker et al. The influence of PAGS (d) is introduced as follows:

$$d_p[\mu\text{m}] = (a + bd) + (a' + b'd)B_{50} \quad \text{eq. 5.38}$$

Where a , b , a' , b' are fitting coefficients. Best agreement between calculation and experimental measurements is reached with:

$$d_p[\mu\text{m}] = (0.0115 + 0.009d)B_{50} \quad \text{eq. 5.39}$$

Results of such calculation, when plotted against experimental measurements, allow to more easily discerning some chemical compositions out of the tendency than by considering only one parameter. These ones are -Cr, +Mn and 0Nb. Effective packet sizes of -Cr and +Mn steels are under-evaluated by eq.5.35. These two combinations have two of the lowest ratio between the average number of packets per primary austenite grain (2.4 and 2.6 for -Cr and +Mn, respectively). The lowest ratio is obtained for as-rolled reference steel (2.3). On the

contrary, 0Nb chemical composition, which is over-evaluated by the calculation, has the second highest ratio (3.8). The highest ratio, which does not appear in Figure 112d, is 0Ti 35 with a 8.8 ratio due to smaller measurement area for the determination of the effective packet size than for the PAGS, which can introduce errors especially for very heterogeneous PAGS (the effective packet size becomes very dependent on the EBSD map location). 0Ti 35 does not display the highest average effective packet size despite its highest measured PAGS.

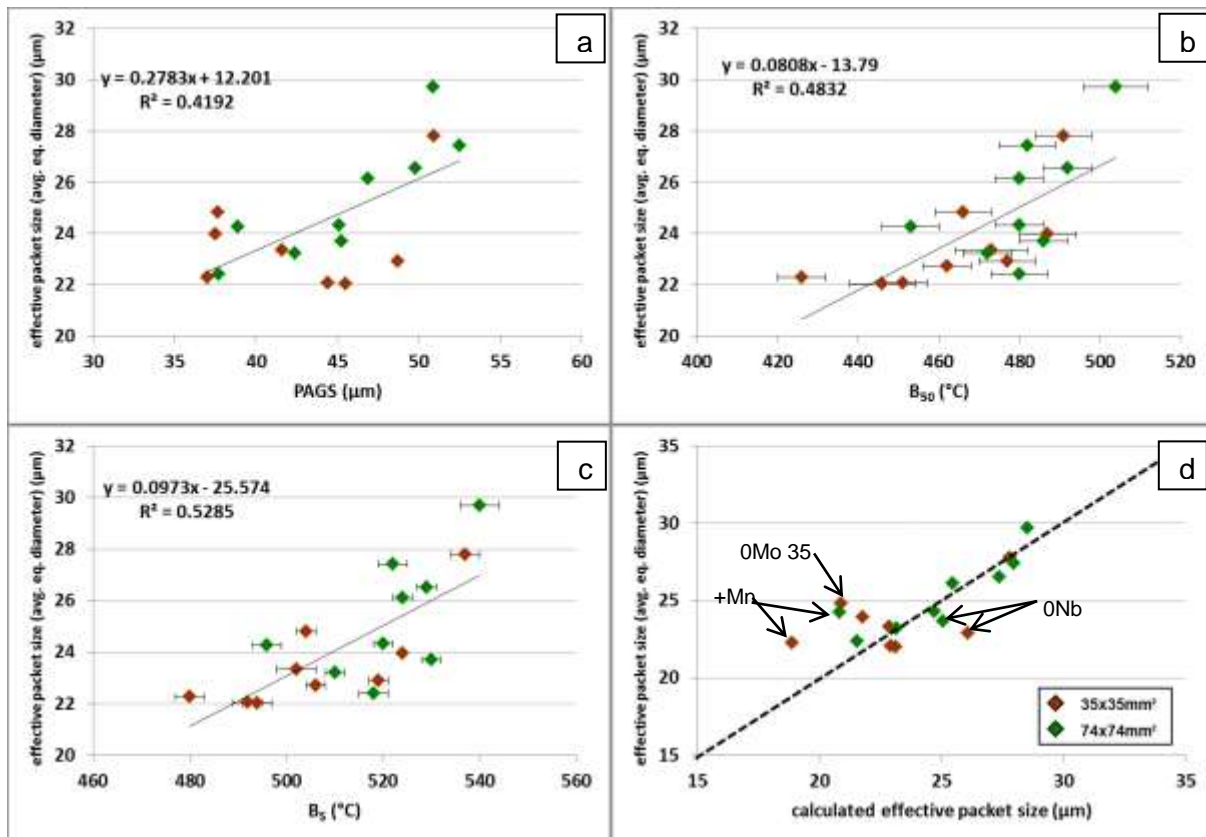


Figure 112: Effective bainitic ferrite packet size (average equivalent diameter) measured from EBSD using a cut-off angle of 15° versus (a) B_{50} temperature calculated from hypothesis 1, (b) primary austenite grain size measured by LM and image analysis, (c) B_s from corresponding cooling rates (0.8°C/s and 0.4°C/s for 35x35mm² and 74x74mm² forged parts respectively) and (d) calculated effective packet size from eq.5.39.

The average difference between the packet size estimated using eq.5.35 and the experimental one is 1.4μm with a maximum difference of 3.9μm. Considering the average fraction of bainite is 0.83 on the set of 18 data used for the global calculation, an error of 1.4μm on the average packet size might lead to an error of 12MPa, and an error of 3.9μm on the average packet size might lead to an error of 33MPa, which may decrease significantly the accuracy of the calculation.

5.3 Conclusion & Outlooks

The different combinations of chemical composition and forged part geometry, in addition to the two reference steels exhibit a wide range of 0.2% proof stress (from 697MPa to 908MPa), ultimate tensile strength (from 963MPa to 1184MPa), HV30 (from 303 to 360), $YS_{0.2}$ over UTS ratio (from 0.71 to 0.81), total elongation (from 10.2% to 12.5%), uniform elongation (from 4.8% to 6.6%), elongation after the onset of necking (from 4.6% to 7.2%) and reduction of area at fracture or necking ratio (from 39% to 61%) together with a variety of bainitic microstructures.

All observed fracture surfaces present four regions. The central region is ductile (dimples), surrounded by a brittle region (made of cleavage facets and some traces of ductility as

porosity, isolated dimples and veins). Between these two regions, there is a relatively broad ductile-to-brittle transition region. The last observed region is made of shear lips surrounding the entire fracture surface.

Different cavities and dimples with different sizes were observed on fracture surfaces depending on which kind of sources they originated from. The void nucleation sites were determined by damage study. They are the following:

- Inclusions and precipitates from 5 to 20 μm in size create cavities between 8 and 20 μm on fracture surfaces. Both cleavage cracking of particles and decohesion at interfaces between matrix and particle are responsible for the occurrence of such voids.
- Inclusions and precipitates lower than 5 μm in size create voids that grow into dimples between 2 and 8 μm in size. These voids nucleate at the interface between the particle and the matrix.
- Interfaces between harder and softer phases such as MA constituent and bainitic ferrite respectively, and especially multiple-interface regions normal to the loading direction, are responsible for the most part of dimples observed in fracture surfaces. Such dimples are generally lower than 3 μm in size.

It seems that MA constituents of as-forged reference steel are more brittle than those in the as-rolled one. It is probable that the fast growth of voids into MA constituents could initiate a brittle crack that would extend into the adjacent bainitic ferrite packets, which may be responsible for a faster formation of brittle micro-cracking and the reduction of the size of both ductile and ductile-to-brittle transition regions.

A hardness vs. tensile strength relationship similar to that proposed by Zajac et al. [7] has been found. Both –Cr combinations have a high bainite transformation temperature, leading to a bainitic ferrite with a lower density of dislocations that keeps good work hardening ability. On the contrary, 0Ti 35, base 35, and +Ni 35 combinations seem to have a higher dislocation density in their bainitic ferrite that may come from unknown forging issues, such as higher than expected cooling rates.

As both tensile and Charpy impact specimens exhibit ductile-to-brittle transition fracture surfaces, impact toughness has been tentatively compared to the reduction of area at fracture. It seems that impact toughness is more sensitive than tensile ductility to the bainitic packet size, to the presence of coarse inclusions and to the banded structure.

The contribution of each different strengthening mechanism to the total yield strength has been determined for all combinations except those coming from 0Ti chemical composition. Their determination has been realized using an empirical equation built by extending of existing relationships between microstructure and yield strength from ferrite-pearlite to bainitic steels. In addition, the secondary microstructural constituents have been taken into consideration as they represent a significant fraction of the steel microstructure (from 8 to 28%). Firstly, each contribution has been considered individually as variable, all the others being set constant. Then, all contributions have been considered as variable at the same time (with the exception of the base strength). Fitting coefficients have been set mathematically or according to their value in the literature in order to find the lowest sum of absolute difference between the calculated yield strength and the experimental yield strength. “Best fit result” in the following means the lowest difference between calculation and experiment with physically meaningful coefficients.

Taken all together rather than individually, the solid solution strengthening, the strengthening from boundaries and the contribution of the secondary microstructural constituents have a tendency to decrease. It points out that strengthening mechanisms might be over-evaluated when viewed individually, as they are not independent of each other. Only eight calculation parameters have been fitted in order to obtain the lowest difference between calculated and experimental yield strength. Other parameters have not been considered for the fitting as their values are consistent with those in the literature, or fixed by combining existing empirical equations in literature.

The “best fit result” exhibits an accuracy on YS calculation of $\pm 14\text{MPa}$. If experimental measurement uncertainties are taken into account, the average difference decreases down to $\pm 7\text{MPa}$. The YS of the reference steels are also well estimated, with differences of -12MPa and $+37\text{MPa}$ for as-rolled and as-forged parts respectively (0MPa and 29MPa when taking experimental uncertainties into account).

The yield strength of the studied steel family is mainly based on four strengthening mechanisms. Substitutional solid solution is the first source of strengthening in such bainitic steels (27% and 30% of the total yield strength for $35\times 35\text{mm}^2$ and $74\times 74\text{mm}^2$ forged parts, respectively). The second highest contribution to yield strength comes from secondary microstructural constituents (24% and 20% of the total yield strength for $35\times 35\text{mm}^2$ and $74\times 74\text{mm}^2$ forged parts, respectively). Noticeable variations of the nominal value of this strengthening mechanism have been observed among the considered materials (177MPa). The third highest contribution in total yield strength comes from high angle boundaries ($>15^\circ$) (21% of the total yield strength for both forged part geometries). Dislocation hardening is the last main strengthening mechanism (16% of the total yield strength for both forged part geometries).

There is a slight decrease by 4% in the role played by secondary microstructural constituents between $35\times 35\text{mm}^2$ and $74\times 74\text{mm}^2$ forged parts (contribution the most strongly impacted by the cooling rate). This is due to the decrease in MA constituent fraction and martensite fraction in the final microstructure of the $74\times 74\text{mm}^2$ forged parts. Indeed, the fraction of MA constituent decreases as undercooling becomes negligible, leading to more complete bainitic transformation. This decrease happens despite more granular bainite was expected in the final microstructure according to CCT diagrams. This slight decrease in the contribution played by secondary microstructural constituents is redistributed between constant strengthening mechanisms, un-sensitive to such variation of cooling rate, such as solid—solution strengthening, base strength and precipitation strengthening. Dislocation hardening and strengthening from boundaries show a decrease by 3 and 7MPa respectively, but stay at the same level of involvement in the total yield strength. This decrease was expected as both strengthening effects are dependent on transformation temperature, and thus, on the cooling rate.

The following tables summarize the equations and fitting coefficients that have been used for the different calculations to estimate the YS in this chapter.

CHAPTER 5 – MICROSTRUCTURAL PARAMETERS THAT CONTROL STRENGTH

Yield strength:

$$\sigma_y [MPa] = (\sigma_0 + \sigma_{SS} + \sigma_p + \sigma_b + \sigma_d)x_{BA} + \sigma_{MA}x_{MA} + \sigma_Mx_M + \sigma_Fx_F \quad eq.5.8$$

With σ_0 being the base strength, σ_{ss} being the substitutional solid solution strengthening, σ_p being the strength contribution of precipitation, σ_b being the contribution of boundaries, σ_d being the contribution of dislocations, x_i being the fraction of microstructural constituent i and σ_i being the strength income in MPa of microstructural constituent i (when $x_i = 1$). BA = bainite, MA = MA constituent, M = martensite, F = allotriomorphic ferrite and 2nd = M + MA

σ_{BA} (MPa)	σ_{MA} (MPa)	σ_M (MPa)	σ_F (MPa)
variable	1044	1044	300

direct calculation of the yield strength is possible
using only the fraction of microstructural constituent

$$\sigma_y [MPa] = 743x_{BA} + 1165(x_{MA} + x_M) + 300x_F \quad eq.5.32$$

Base strength:

$$\sigma_0 [MPa] = 104 \text{ MPa}$$

intrinsic strength of bcc iron + interstitial C and N, which are expected to be near their respective limit of solubility in bainitic ferrite (all the remaining C and N is expected to be in residual phases and in precipitates)

Solid-solution strengthening:

$$\sigma_{SS} [MPa] = \sum (s_i \cdot c_i) \quad eq.5.10$$

Where s_i the strengthening in MPa resulting from a 1%wt addition, and c is the solute concentration in wt%

s_{Mn}	s_{Si}	s_{Cr}	s_{Ni}	s_{Mo}	s_{Nb}	s_{Cu}	s_P	range of wt%
32	83	144	53	11	11	39	678	3.37-4.03

direct calculation of the yield strength is possible using only the nominal composition of the steel:

$$\sigma_y [MPa] = 473 + 185(c_{Cr} + c_{Ni}) + 83c_{Si} + 32c_{Mn} + 11(c_{Mo} + c_{Nb}) + 678c_P + 39c_{Cu} \quad eq.5.18$$

Strengthening from boundaries:

$$\sigma_b [MPa] = k_y d^{-n} \quad eq.5.19$$

with k_y being a constant in MPa.mmm, n being a dimensionless constant and d being the effective grain size (in mm)
Caution: statistical correction due to non-optimized condition of effective grain size acquisition with:

$d [\mu m] = \sqrt{A_{>15^\circ}}$
 $A_{>15^\circ}$: effective packet size
determined using EBSD with a cut-off angle of 15°

eq	K_y [MPa.mmm ⁿ]	n	cut-off angle [°]	range of effective packet size $d [\mu m]$
eq.5.8	5	1	15	21-30
eq.5.21	8.9			

direct calculation of the yield strength is possible
using eq.5.21 with $\sigma_0^b = 455 \text{ MPa}$

$$\sigma_y [MPa] = \sigma_0^b + k_y (\sqrt{A_{>15^\circ}})^{-n} \quad eq.5.21$$

Strengthening from dislocations:

$$\sigma_d [MPa] = \alpha \mu b \rho^{0.5} \quad eq.5.22$$

$$\text{or} \quad \sigma_d [MPa] = 1.3(600 - T) \quad eq.5.24$$

with μ being the shear modulus (81GPa for iron), b being the Burgers vector ($2.5 \times 10^{-10} \text{ m}$), α being dimensionless coefficient, ρ being the dislocation density (m^{-2}) and T the transformation temperature in °C for isothermal transformation or T_{50} for continuous cooling

to calculate ρ with K or K50 the transformation temperature in Kelvin

$$\log_{10}(\rho) = 9.3 + \left(\frac{6880}{T} \right) - \left(\frac{1780360}{T^2} \right) \quad eq.5.23$$

α	range of B_{50} [°C]
0.17	426-504

direct calculation of the yield strength is possible using
eq.5.27 with $\sigma_0^d = 666 \text{ MPa}$ using eq.5.22 or eq.5.24

$$\sigma_y [MPa] = \sigma_0^d + \sigma_d \quad eq.5.27$$

Strengthening from precipitation:

$$\sigma_p [MPa] = \frac{\beta \mu b f^{0.5}}{r} \ln \left(\frac{r}{b} \right) \quad eq.5.30$$

$$\text{Or} \quad \sigma_p [MPa] = \frac{5.9 f^{0.5}}{\emptyset} \ln(2000 \emptyset) \quad eq.5.31$$

with f being the volume fraction of precipitates, r being the average radius (m), \emptyset is the average particle size in μm , μ being the shear modulus (81GPa for iron), b being the Burgers vector ($2.5 \times 10^{-10} \text{ m}$) and β being dimensionless coefficient.

β	range of f [%]	range of $\emptyset [\mu m]$
72000	0.08-0.21	0.53-0.59

CONCLUSIONS & OUTLOOKS

In the following, the achievement of the objectives of the study is discussed first. To further comment links between chemical composition and microstructure, remarks about microstructural robustness of this steel family are made. Finally, key microstructural parameters controlling mechanical properties are discussed. Possible outlooks are indicated in italics throughout this part.

Achievement of the general objectives of the study

The objective of this PhD project was to improve the understanding and quantitative physically-based modelling of the relationships between chemical composition, microstructure and mechanical properties of high strength bainitic steels after forging and air-cooling. **The main results can be summarized as follows:**

- **The influence of several alloying elements on the microstructure**, as well as some synergies between these elements on phase transformation, **have been established** using CCT diagrams relevant to the targeted forging process and a comprehensive quantification of resulting microstructures. *Determination of TTT diagrams, for selected chemical compositions, would improve understanding of matrix decomposition although final microstructures would differ from those of industrial interest.*
- **Physical phenomena and microstructural parameters that control impact toughness have been identified** thanks to comprehensive observations of fracture surface and damage on as-forged laboratory heats. A mathematical description of their contribution to impact toughness has been established. Using this equation, the average accuracy on calculation of impact toughness is $\pm 3J$. However, this calculation is not predictive, as the measurement of the ductile crack extension is necessary. The validity of this equation only stands when the fracture surface can be considered as flat, without considerable amount of ductility. The extent of the ductile crack propagation depends on the critical defect density and the minimum critical stress to initiate and propagate cleavage. The next step of this study is *to find a way to predict these two parameters, starting from proper inclusion quantifications*. This work has not been realized in the present study as the brittle fracture initiation sites in the laboratory heats were not considered to be representative of the reference steel. *Determination of ductile-to-brittle transition curves, for selected chemical compositions with a tightly controlled population of oxide inclusions, would shed light on the links between microstructure, fracture mechanisms and impact toughness.*
- **The contribution of each different strengthening mechanism to the total yield strength has been determined.** The model has been built through the extension of existing relationships between microstructure and yield strength for ferrite-pearlite to bainitic steels. In addition, secondary microstructural constituents have been taken into consideration as they represent a significant fraction in the steel microstructure. The lowest average difference between calculated and experimental yield strength with meaningful fitting coefficients is $\pm 14\text{MPa}$ for yield strength ranging from 700 to 900MPa.

Evaluation of the microstructural robustness of this steel family

The **complex chemical composition of this steel family is its first strength**. Indeed, this chemical composition provides a **high value of solid solution strengthening**, as alloying elements are between 3.72 to 4.35wt% of the nominal composition from which 3.37 to 4.03wt% are believed to play a role in solid solution strengthening. This strengthening mechanism is believed to bring the first contribution to yield strength, providing one third of the total yield strength value.

This chemical composition leads to a **noticeable microstructural robustness**. No disruption on CCT diagrams has been observed for any investigated chemical composition, especially on the top of the bainitic domain. The bainitic transformation temperatures B_S and B_F show only little variations in the targeted range of cooling rates ($<0.8^\circ\text{C/s}$). The same microstructural domains (defined from the variations of microstructural constituent, hardness and austenite fraction evolution) were present in all chemical compositions but for different cooling rates. All chemical compositions were in microstructural domain A (coarse upper/granular bainite microstructure) or at the very beginning of domain B (upper bainite) for the cooling rates measured during forging once the bainitic transformation starts ($<0.2^\circ\text{C/s}$).

Some chemical compositions exhibit noticeable fraction of allotriomorphic ferrite in their microstructure after pure continuous cooling from 800°C (CCT diagram conditions). However, no significant amount of allotriomorphic ferrite has been observed in the as-forged state due to the relatively high cooling rate ($>0.4^\circ\text{C/s}$) before the onset of the bainitic transformation.

However, the B_S of this robust chemical composition seems **very sensitive to a decrease in chromium content**. Indeed, the maximum increase in B_S by 40°C was found in the chemical composition with a drop in chromium content by 30%. Such a drop obviously affects both microstructure and mechanical properties. The microstructure that forms from such high B_S temperature (540°C) exhibits bainite packets with an apparent lath width of several micrometres and other packets for which the lath-like structure is only barely observable. Microstructural coarsening and loss in Cr content in solid solution (Cr has been found to have the strongest strengthening effect in solid solution) significantly decreases the yield strength and the capacity of the microstructure to absorb energy during cleavage crack propagation.

An increase in chromium content does not lead to further decrease in B_S as compared to the base chemistry. Chromium was not found to have the same saturation effect on the solid solution strengthening as on B_S . Beyond a critical concentration, the excess chromium content may start to precipitate in austenite at temperatures higher than B_S , which would decrease B_S by trapping Cr, C and/or N atoms into precipitates. The resulting precipitation would strengthen the matrix despite the decrease in chromium concentration in solid solution. In such a situation, the high strengthening coefficient found here for chromium would also integrate a part of precipitation strengthening. Concluding on this point requires *investigation of the precipitation state of the +Cr forged parts using carbon replicas*.

Key microstructural parameters controlling mechanical properties

This PhD study has identified two microstructural parameters that play an important role in yield strength and, to a lower extent, in impact toughness: the bainitic ferrite packet size and the fraction of hard secondary microstructural constituent (Figure 113). A third microstructural parameter, i.e. the retained austenite content, plays a significant role in impact toughness. All of them are discussed below, pointing out their role on mechanical properties as well as metallurgical tools to control them.

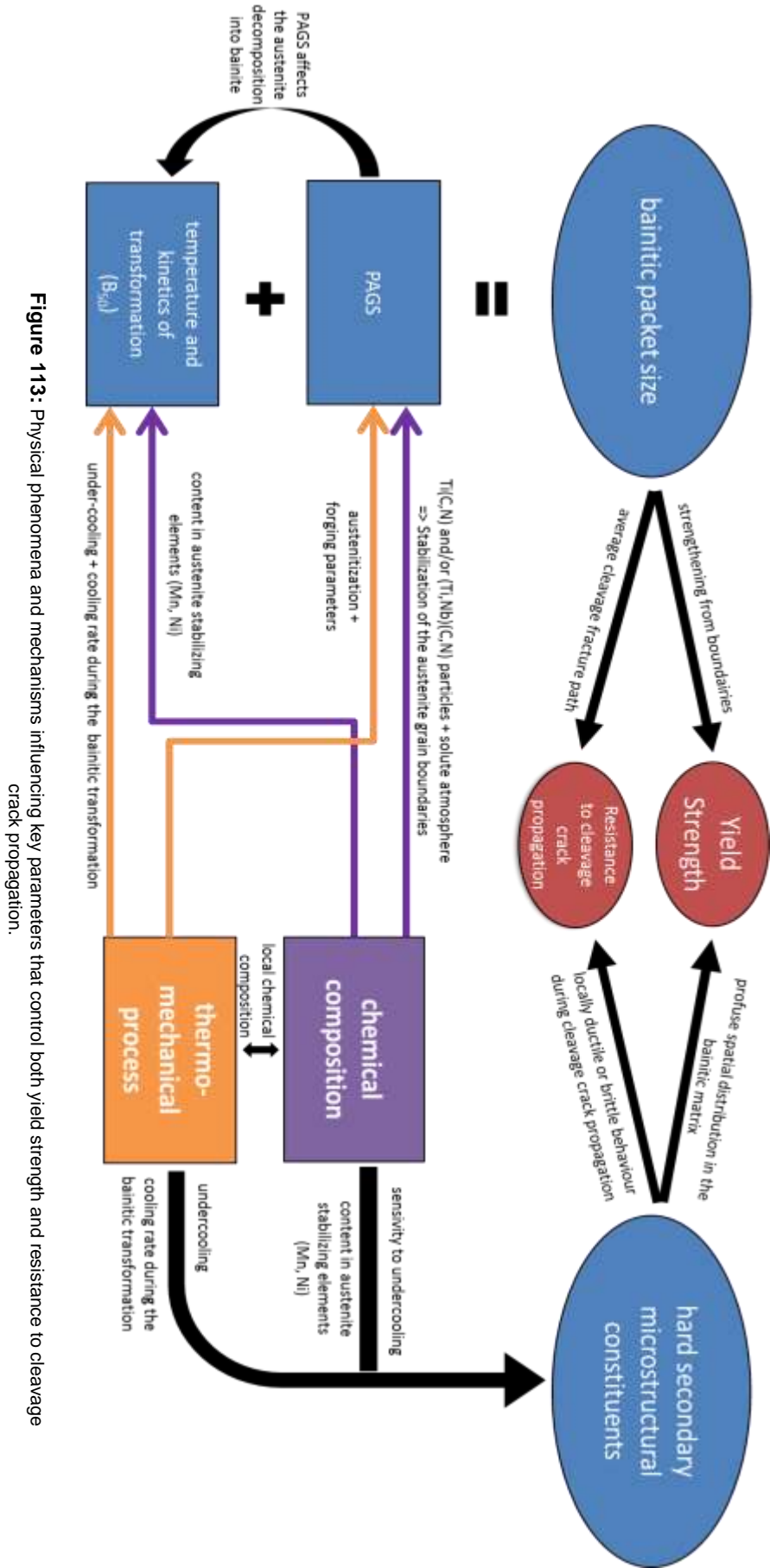


Figure 113: Physical phenomena and mechanisms influencing key parameters that control both yield strength and resistance to cleavage crack propagation.

1. The bainitic ferrite packet size

A decrease in bainitic ferrite packet size from 30µm down to 21µm leads to a significant increase in the contribution of boundaries to strengthening (by 92MPa). This strengthening mechanism is the third highest contribution to the total yield strength. Such a decrease in bainitic ferrite packet size also increases the energy absorbed during cleavage propagation from 6.4J to 8.1J, representing 10.6% to 72.6% of the total impact toughness value.

For a given chemical composition, **the bainitic packet size depends on the primary austenite grain size, transformation temperature and transformation kinetics** (described using B_{50} in this study). This dependency does not appear to be linear as there is a limit on the PAGS (45µm) below which the bainitic packet size seems less sensitive to it. This limitation might be due to a change in ratio between nucleation and growth rates of bainitic laths. For PAGS higher than 45µm, growth might dominate the transformation kinetics, so the first packets penetrate the parent grain rapidly with only few obstacles. For PAGS grain size lower than 45µm, nucleation might dominate the transformation kinetics so packets can grow simultaneously, restricting their maximum reachable size.

1.1 Control of the PAGS

The PAGS is affected by the soaking temperature and forging parameters such as the reduction ratio, the temperature at the end of forging and the cooling rate in the temperature range in which grain coarsening is possible. In order to ensure a satisfactory robustness of the steel grade regarding austenite grain coarsening, the **primary austenite grain boundaries have to be pinned using fine Ti(C,N) and/or (Ti,Nb)(C,N) precipitation** that can remain stable even for high soaking temperatures. However, relatively coarse (Ti,Nb)(N,C) and (Nb,Ti)(C,N) particles have been observed in the reference steel grade. A noticeable amount of Ti and Nb has been trapped in such particles during solidification; it is therefore no longer available to form fine precipitates later in austenite. Moreover, these particles might decrease the amount of absorbed energy during Charpy impact test as they may act as initiation sites for cleavage cracking. *These relatively coarse primary carbides have to be limited by adapting the solidification process.*

In addition, **austenite grain coarsening can be limited by the solute atmosphere** provided by alloying elements. Niobium, when high enough content remains in solid solution, is well known to decrease the motion of austenite grain boundaries at high temperature. The opposite effect is attributed to Mo. Both are added to avoid boron precipitation as iron borocarbides ($\text{Fe}_{23}(\text{B,C})_6$). It has been shown in this study that around 81% of the niobium but only 6% of molybdenum precipitated in the as-forged laboratory heats. *In this case, it is reasonable to think that the molybdenum content could be replaced by an extra niobium addition. This further addition of niobium might e.g. enhance precipitation strengthening and further limit the motion of austenite grain boundaries at high temperature.*

However, no comprehensive study of the secondary precipitation has been realized on the reference steel grade *to ensure that the precipitation behaviours of niobium and molybdenum in the as-forged reference steel are the same as in as-forged laboratory heat.* This point has to be investigated in order to rationalize the optimization of the micro-alloying content of this steel grade.

1.2 Control of the austenite decomposition into bainite

Transformation temperatures and transformation kinetics are influenced by the primary austenite grain size. This last dependency, which suffers from a lot of controversies in the literature regarding the bainitic transformation [61;130-135], has not been properly evaluated for this steel grade. The study of the influence of the primary austenite grain size on the bainitic transformation would be interesting in order *to determine*

the robustness of the steel grade regarding the soaking and forging parameters. A first approach can be made using dilatometry cycles designed for that purpose. In the present steel family, a non-linear effect of the PAGS on the bainitic transformation might be observed as it is closely related to the boron segregation behavior. Indeed, from a given PAGS, $\text{Fe}_{23}(\text{B,C})_6$ might start to precipitate extensively as the boron concentration along the grain boundaries reaches a critical value, leading to a fast increase in the bainitic transformation temperatures and in the allotriomorphic ferrite fraction.

Another lever to control the transformation temperatures and the transformation kinetics is the chemical composition. Further addition of austenite stabilizers might decrease the transformation temperatures and thus decrease the bainitic packet size. According to the CCT diagrams, Ni does not lead to a noticeable decrease in transformation temperatures in the targeted range of cooling rates. However, the as-forged part realized with +Ni chemical composition seems to indicate that a further increase in nickel might decrease the bainitic packet size. The addition of manganese, on the other hand, can decrease the transformation temperatures by 10 to 30°C even for these relatively slow cooling rates. In both cases, it would be interesting *to assess the decrease in average bainitic ferrite packet size directly on the samples that have been heat-treated for the CCT diagrams of chapter 3.*

At last, for a given chemical composition, **the transformation temperatures and the transformation kinetics are influenced by the cooling rate.** A lower bainitic packet size might be obtained by accelerating the cooling rate (using pulsed air) to limit the effect of latent heat release due to bainite transformation. The transformation kinetics would be thus accelerated, decreasing the resulting bainitic packet size (as the nucleation rate might be prevalent over the growth rate).

2. The fraction of hard secondary microstructural constituent

The amount of secondary microstructural constituents in the studied materials is rather high (from 8% of 28% of the microstructure). **This profuse distribution of hard microstructural constituents, which are mainly MA constituent, in a relatively soft matrix leads to the second highest contribution to yield strength.** This strengthening mechanism accounts for 84 up to 261 MPa in the investigated conditions. It represents, in average, 20% and 24% of the total yield strength for 74x74mm² and 35x35mm² forged parts respectively.

Depending on their chemical composition, shape and size, a certain part of secondary phases brings some ductility during the cleavage crack propagation. These secondary microstructural constituents would absorb energy by creating local crack deviations compensated by ductile failure. This is translated on brittle fracture surfaces by the occurrence of numerous ductile bridges of several micrometres in width between packets, and ductile veins of some tens of nanometres between two laths sharing close orientations. However, a certain part of secondary microstructural constituents might also have a strong tendency to split by cleavage. This could affect cleavage crack propagation into the bulk, in particular at high-angle boundaries.

For a given chemical composition, as the MA constituent fraction increases, the average carbon concentration in these MA constituents decreases. Assuming that brittle behaviour is associated with high carbon content, MA constituent may be less harmful to impact toughness at sufficiently large fractions. *The average carbon content of MA constituents might also be considered in the calculation of their contribution to strengthening.* This has to be the next step in the calculation of the yield strength but requires quantitative data about the MA chemistry and mechanical behaviour.

Statistical analysis of their shape and size might help differentiate hard and brittle MA constituents from soft and ductile ones. To realize such statistical analysis, spatial resolution of the quantification has to be better than the one used in the present study (light microscopy after LePera etching). Indeed, a significant amount of the secondary phases (around 10% of the microstructure) are lower than 650nm in size. This amount tends to increase with the cooling rate as the microstructure becomes finer while keeping the colour etching to realize a fast and reproducible numerical quantification.

The fraction of MA constituent in the microstructure depends on the chemical composition and thermo-mechanical processing. An increase in Mn or Ni content in the chemical composition has shown noticeable increase in MA constituent fraction for cooling rates lower than 0.2°C/s (in CCT diagram samples). For all chemical compositions, the fraction of MA constituents larger than 650nm decreases with the increase in cooling rate.

The undercooling phenomenon noticed in some 35x35mm² forged parts **is believed to be responsible for an increase in the fraction of MA constituent.** This undercooling comes from the difference in the cooling rate before and during the bainitic transformation, affecting both the temperature range and the kinetics of the bainitic transformation. From dilatometry measurements, the transformation kinetics is very high in the first 40-50°C of the bainitic transformation (50% of the bainitic transformation occurs in this temperature range), so starting the bainitic transformation 15-30°C lower than expected might decrease significantly its extent. -Si and -Si+Mn have been found very sensitive to undercooling. This sensitivity might be linked with the highest extent of bainite transformation for chemical composition with a reduced content of silicon.

3. Retained austenite

The retained austenite content is also an important microstructural parameter. **The amount of energy absorbed during ductile cracking before cleavage initiation in Charpy impact test increases with the retained austenite content** for forged parts made of laboratory heats. Retained austenite is believed to reduce the stress concentration field in the material by phase transformation under mechanical loading, delaying void initiation and growth, and thus the development of damage and cracking. This is the so-called TRIP effect. The retained austenite that is available for this TRIP effect (denoted as TRIP-available) is believed to be the film-like austenite between bainitic laths, but its stability under mechanical solicitation also depends on its chemical composition [161-164].

Reasons why the reference steel is out of this tendency are not well understood at this point. Perhaps the stability of austenite or the ratio between TRIP-available austenite and total austenite content of as-forged and as-rolled reference steels are very different from that of the as-forged laboratory heats due to the different thermo-mechanical processing and higher nickel content. Unfortunately, it is not possible to determine the absolute amount of TRIP-available austenite from XRD measurements. Indeed, the total austenite content determined by XRD is shared between MA constituents, martensite and bainite.

APPENDIX A - MICROSTRUCTURAL CHARACTERIZATION METHODS

Appendix A is dedicated to the work that has been realized to establish comprehensive methods of microstructural quantification applied on the steel grades considered in this PhD project.

A.I Quantification of the fraction of microstructural constituents

A.I.1 Quantification using light microscopy

This quantification has been built on the reference as-forged reference steel. It has been first validated by crossing results with two other methods of quantification. Then, the LM quantification has been applied on every combination of chemical composition and thermo-mechanical treatment that has been considered in the present study.

A.I.1.a Etching tests

The etching tests have been realized on samples coming from the as forged reference steel. Samples have encountered a typical mirror polishing until 1µm diamond paste. Two cycles of very slight Nital2% etching (less than 3s) and 1µm diamond paste polishing have been realized to remove all the cold working generated earlier during mechanical polishing. Then final polishing has consisted in 0.25µm diamond paste polishing and a 80s polishing with colloidal silica. The material is characterized in a plane parallel to its rolling direction, at mid-radius of a reference forged part. Only microstructures out of segregated regions have been observed. LM pictures have been taken on a Zeiss Axiovert 405M equipped with ProgRes CF scan camera from Jenoptik.

Several etching procedures have been tested in order to find the one that gives the best colour/microstructural constituent combination. The final objective was to realize a fast and reproducible numerical quantification of the microstructural constituent as accurate as possible. The different etching procedures that have been tried as well as the obtained colour/microstructural constituent combinations are shown in Table 31.

Etching	Immersion time in etchant 1 + immediate washing + immersion time in etchant 2 (s)	Observed colour/microstructural constituent combination
1: Nital2% 2: aqueous solution of 10% sodium metabisulfite	6 + 0	Bainite: light brown to dark brown MA: white to light grey Martensite: dark grey
	6 + 6	
	6 + 10	
	6 + 20	
1: Nital4% 2: aqueous solution of 10% sodium metabisulfite	6 + 0	Bainite: light brown to dark brown MA: white to light grey Martensite: dark grey to light brown
	6 + 6	
	6 + 10	
	6 + 20	
1: Picral4% 2: aqueous solution of 10% sodium metabisulfite	6 + 0	Bainite: white MA: grey to light blue Martensite: dark brown
	6 + 6	
	6 + 10	
	6 + 20	
LePera = Picral4% + aqueous solution of 1% sodium metabisulfite	6	Bainite: dark blue to light blue MA: white Martensite: yellow to brown
	12	

Table 31: Etching results. Best rendering procedures are in bold characters. The observed colour/microstructural constituent combination corresponds to the one obtained in the case of the best rendering.

APPENDIX A – METHODS OF MICROSTRUCTURAL CHARACTERIZATION

All etchings are based on the coloration power produced by sodium metabisulfite ($\text{Na}_2\text{S}_2\text{O}_3$). In aqueous solution, the metabisulfite decomposes in SO_2 , H_2S and H_2 at the surface of the metal. SO_2 depassivates the steel surface while sulphur ions from H_2S will combine with metallic ions from the sample to produce a sulphide staining film, which will interfere with light and create coloration [195]. This coloration mainly depends on the local chemical composition, which has an influence on thickness of the sulphide staining film, and on the surface relief of the sample that has been created by the acid reagent or the polishing step with colloidal silica.

The first three etchings have to be realized in two steps. These ones have been found in the publication of Amar De et al. [196] and are related to the books of George Vander Voort [195], Bruce Bramfitt and Arlan Benschoter [197]. The first step consists in immersing briefly the sample inside the acid etchant. Then the sample is immediately washed using water plus ethanol and dried in hot air. The second step is a longer time of immersion in aqueous solution of sodium metabisulfite. The last etching is a mixture of Picral4% and aqueous sodium metabisulfite. Its name comes from Frank LePera [198]. LePera etching has a poor stability so the mixture has to be prepared just before immersion of the samples. Indeed, the lifetime of LePera etching is no longer than a few minutes, the colour/microstructural constituent combination changing very fast.

Whatever the etching used, the sample has to be gently oscillated during any immersion step. Once etched, the sample surface becomes very sensitive to local pitting so observations have to be realized in the very next days.

LePera etching has been eventually chosen to realize the quantification using numerical image processing. This etching procedure avoids in most cases the occurrence of grey shades that are not suitable to realize a threshold based on hue, saturation and brightness (**HSB**) spectra. In addition, once the proper time of immersion is found, each microstructural constituent can have very distinct limits of domain on HSB spectra.

Figure 114 shows the full range of colours that can be found using LePera etching with the microstructures encountered in this study. Ideal ranges of colour for each microstructural constituent encountered in upper bainite microstructure are exhibited with dashed lines. It seems that prolonged time on the final polishing step leads to move colour ranges toward the right side of Figure 114, as well as reduced time of immersion will move them toward the left side.



Figure 114: Full range of coloration that has been encountered using LePera etching on carbide free upper bainite for the present study.

Figure 115 shows some colour range variations that can be found on microstructures coming from dilatometric samples of different laboratory heats. Figure 15c to Figure 15e present exploitable colour contrast, others have been done again to realize the image analysis. The most difficulties to obtain proper colour ranges have been encountered on chemical composition with less silicon.

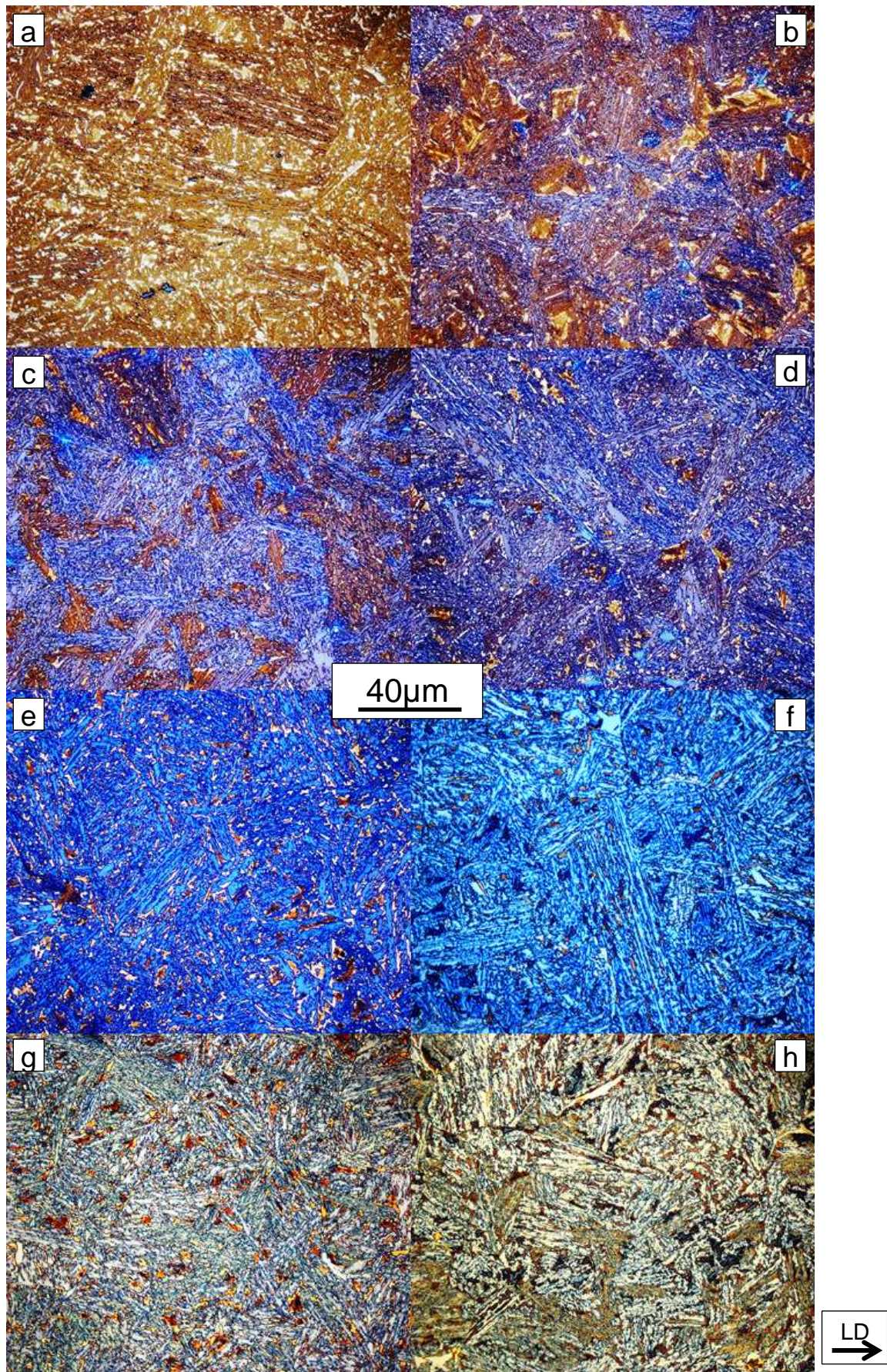


Figure 115: LM picture, x500, LePera etching. (a) –Si 0.4, (b) base 0.6, (c) –Cr 0.6, (d) –Cr 0.6, (e) base 0.2, (f) 0Nb 0.6, (g) 0Nb 0.4, (h) 0Mo 0.2. With this exception of (h), all these microstructures belong to microstructural domain B; (h) belongs to domain A.

A.I.1.b Pre-processing

The objective of the pre-processing is to facilitate the determination of thresholding parameters of each set of pictures in the processing step and to ensure the validity of these thresholding parameters on the whole surface of each picture of the set.

12 pictures in high resolution (1360x1024 pixels, 16-bit, hyperstacks RGB, uncompressed .TIF format) with a magnification of x500 have been taken in white beam after LePera etching for each analysed sample.

Pre-processing has been made using ImageJ software (version 1.47t). The following text in italics is the macro that has been built to be used in ImageJ software in order to apply the post processing on a huge amount of pictures efficiently using the “batch macro” function. This macro has been divided in 4 steps (A to D) to facilitate understanding by the reader. Figure 116 shows an example on one picture following several post-processing paths.

(A)

```
a=getTitle();
rename("x.TIF");
run("Stack to RGB");
selectWindow("x.TIF");
close();
rename(a);
```

This first step transforms the hyperstacks RGB image (3 superimposed 16bit stacks: red, green and blue) into a RGB composite image (one stack in RGB colour space).

(B)

```
//setTool("rectangle");
makeRectangle(124, 37, 1112, 950);
run("Crop");
```

The second step that is realized is a trimming that excludes the edges which are of lesser quality than the centre of the image due to noticeable decrease in brightness and in sharpness. The first two coordinates in the function “*make rectangle*” correspond to the location of the pixel located at the upper left corner of the trimming rectangle, the two last ones are the x and y dimensions of the trimming rectangle. In this example, the rectangle is centered in the original picture but it has to be adjusted according to the location of the centre brightness halo with respect to the centre of the picture.

(C)

```
run("Enhance Contrast...", "saturated=0.4 equalize");
run("Sharpen");
```

These two steps increase contrast (using histogram equalization) and accentuate details in the image. The saturated value determines the number of pixels in the image that are allowed to become saturated. Increasing this value will increase contrast. This value should be greater than zero to prevent a few outlying pixels from causing the histogram stretch to not work as intended [199]. This step guarantees that the fraction of MA constituent will not be underestimated.

(D)

```
run("Set Scale...", "distance=100 known=20 pixel=1 unit=μm");
```

This is the final post-processing step that attributes a length scale to the picture.

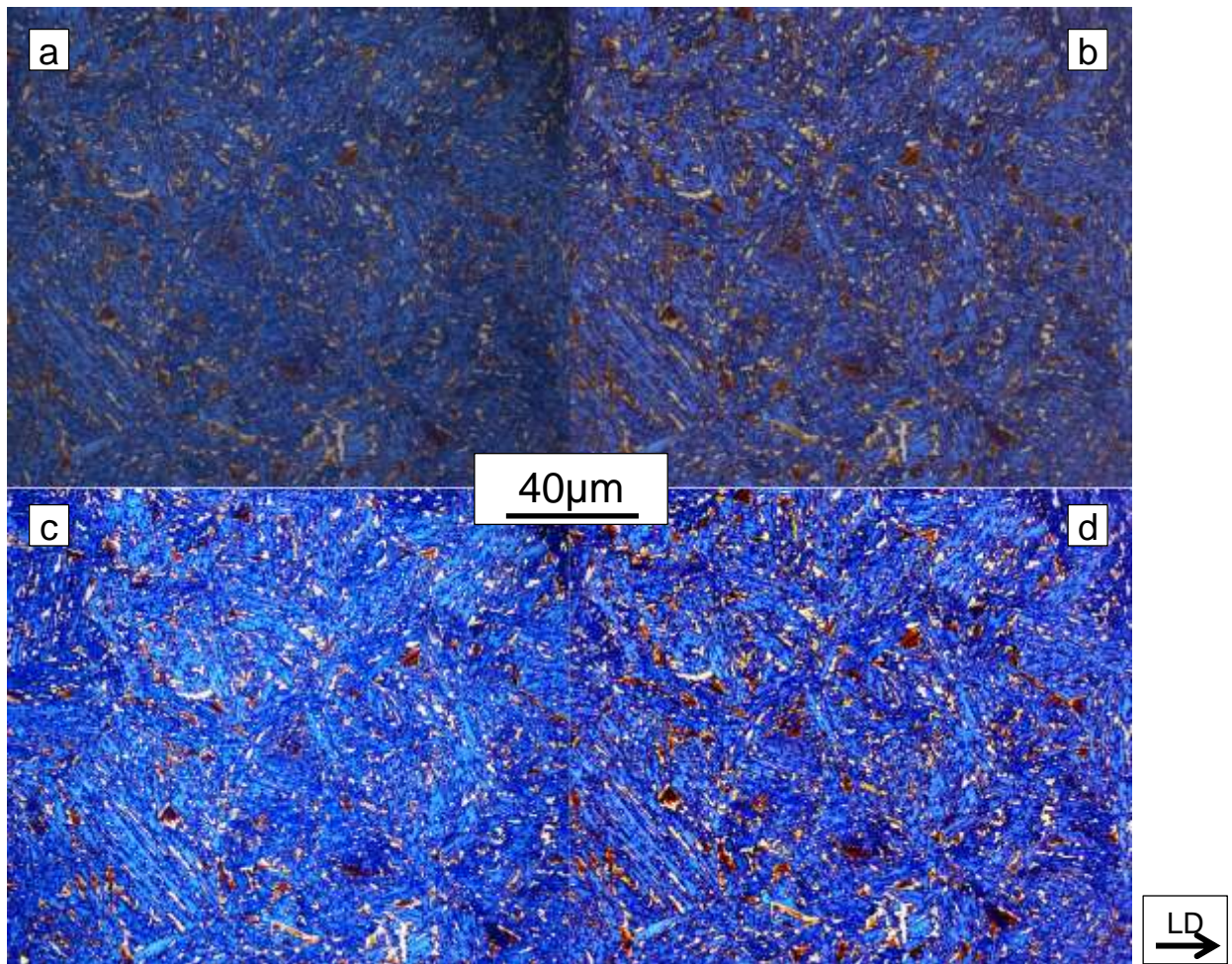


Figure 116: LM picture, x500, LePera etching, base 0.2. Initial picture after, (a) step B, (b) steps A'+B, (c) steps A+B+C, (d) steps A'+B+C.

To limit the extent of the trimming that is realized in the second step of the post-processing, one can use Gaussian blur to realize a brightness homogenization. In this case step A is replaced by step A' as follows.

(A')

```

a=getTitle();
rename("x.TIF");
run("Split Channels");
selectWindow("C1-x.TIF");
run("Duplicate...", "title=C1-x-1.TIF");
run("Gaussian Blur...", "sigma=80");
imageCalculator("Subtract create 32-bit", "C1-x.TIF", "C1-x-1.TIF");
run("16-bit");
selectWindow("C1-x.TIF");
close();
selectWindow("C1-x-1.TIF");
close();
selectWindow("C2-x.TIF");
run("Duplicate...", "title=C2-x-1.TIF");
run("Gaussian Blur...", "sigma=80");
imageCalculator("Subtract create 32-bit", "C2-x.TIF", "C2-x-1.TIF");
run("16-bit");
selectWindow("C2-x.TIF");
close();
  
```

```

selectWindow("C2-x-1.TIF");
close();
selectWindow("C3-x.TIF");
run("Duplicate...", "title=C3-x-1.TIF");
run("Gaussian Blur...", "sigma=80");
imageCalculator("Subtract create 32-bit", "C3-x.TIF", "C3-x-1.TIF");
run("16-bit");
selectWindow("C3-x.TIF");
close();
selectWindow("C3-x-1.TIF");
close();
run("Merge Channels...", "c1=[Result of C1-x.TIF] c2=[Result of C2-x.TIF] c3=[Result of C3-x.TIF] create");
run("Stack to RGB");
selectWindow("Composite");
close();
rename(a);

```

Here the three different stacks that composes a colour image (red=C1, green=C2, blue=C3) are separated and duplicated. The duplicates are blurred using a Gaussian filter in a way that only the background stays visible. Each blurred duplicate is subtracted to its original using the “image calculator” function. Then, images that have been created using the “image calculator” function are merged together in order to obtain a background-corrected hyperstack RGB picture.

The use of this last stage has to be avoided if one intends to use the same thresholding parameters for all 12 pictures of a set because it generates some variations on the global colour shade that is dependent on each picture.

At the beginning of the project, some parts of the post-processing were realized using GIMP2.0 software because colour thresholding option was missing on anterior version of imageJ software used initially (v 1.41a). The trimmed images were converted into 8-bit images (256 grey levels) by using brightness and saturation parameters of each basic colour (red, yellow, green, cyan, blue and mauve). The objective of this step was to darken the bainite and to lighten MA constituents as much as possible before decreasing the saturation level of every colour to obtain a 8-bit image. These images (256 grey levels) were afterward converted into binary images (black and white) using an adapted thresholding to separate each microstructural constituent.

Nevertheless, this method led to an under-evaluation of 0.03 in average of the MA constituent fraction for the benefit of the bainite fraction. Indeed, the white balance and the brightness spectrum of each image were affected by this post-processing step. The fraction of MA constituent is directly linked to the amount of bright white pixels.

A.1.1.c Processing

As the pre-processing, the processing is also realized on ImageJ software using the “colour thresholding” function on the hue, saturation and brightness spectra. The most critical step of this phase quantification is realized here as the thresholding parameters (range on each spectrum) have to be set, allowing the separation of the different microstructural constituents.

Figure 117 shows how the “colour thresholding” function appears on ImageJ. If the picture allows it, each microstructural constituent can be isolated by defining on each spectrum a range of inclusion (pass) or exclusion (stop). It is preferable to set the ranges while using the red colour thresholding (afterward the red will become the black in the B&W picture).

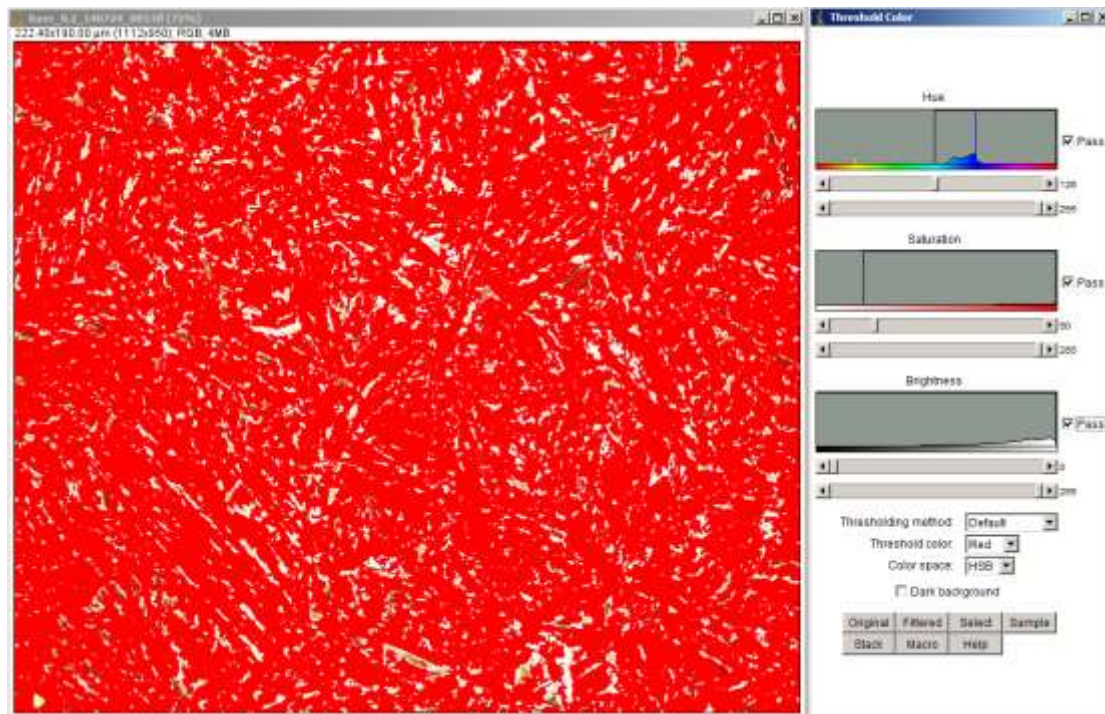


Figure 117: Screenshot showing an example of colour thresholding using ImageJ software.

In the following, the limits of these ranges are named the thresholding parameters and are specific for each set of images (or, if the A' post-processing has been realized, they are specific to each image of a set).

As there are three different microstructural constituents investigated in this quantification, only two of them need to be separated, so two sets of thresholding parameters are required for each set of images.

The thresholding parameters are operator dependant, so it is important that this step is realized by someone that has some knowledge on the different kinds of microstructures that can be obtained on the studied steel grade and their possible appearance after LePera etching. As an example, the study of martensitic and lower bainite microstructures on our steel family shows us that we initially had a tendency to over-evaluate the fraction of martensite in upper bainite microstructure by 0.03 in average.

The following macro (that can be auto-generated in the "color thresholding" function) has been used with the "batch macro" function using the specific thresholding parameters that have been found for each set of 12 images in order to generate B&W pictures (with the selected microstructural constituent in black and, in white, the other two).

```
// Color Thresholder 1.47t
min=newArray(3);
max=newArray(3);
filter=newArray(3);
a=getTitle();
run("HSB Stack");
run("Convert Stack to Images");
selectWindow("Hue");
rename("0");
selectWindow("Saturation");
rename("1");
selectWindow("Brightness");
rename("2");
```

```

min[0]=n1;
max[0]=n2;
filter[0]="a";
min[1]=n3;
max[1]=n4;
filter[1]="b";
min[2]=n5;
max[2]=n6;
filter[2]="c";
for (i=0;i<3;i++){
    selectWindow(""+i);
    setThreshold(min[i], max[i]);
    run("Convert to Mask");
    if (filter[i]=="stop") run("Invert");
}
imageCalculator("AND create", "0","1");
imageCalculator("AND create", "Result of 0","2");
for (i=0;i<3;i++){
    selectWindow(""+i);
    close();
}
selectWindow("Result of 0");
close();
selectWindow("Result of Result of 0");
rename(a);
// Colour Thresholding-----
run("Make Binary");

```

In this macro n_1 , n_2 , n_3 , n_4 , n_5 and n_6 are the thresholding parameters, integers set between 0 and 255 included, with $n_1 < n_2$, $n_3 < n_4$ and $n_5 < n_6$. a, b and c have to be set to pass or stop.

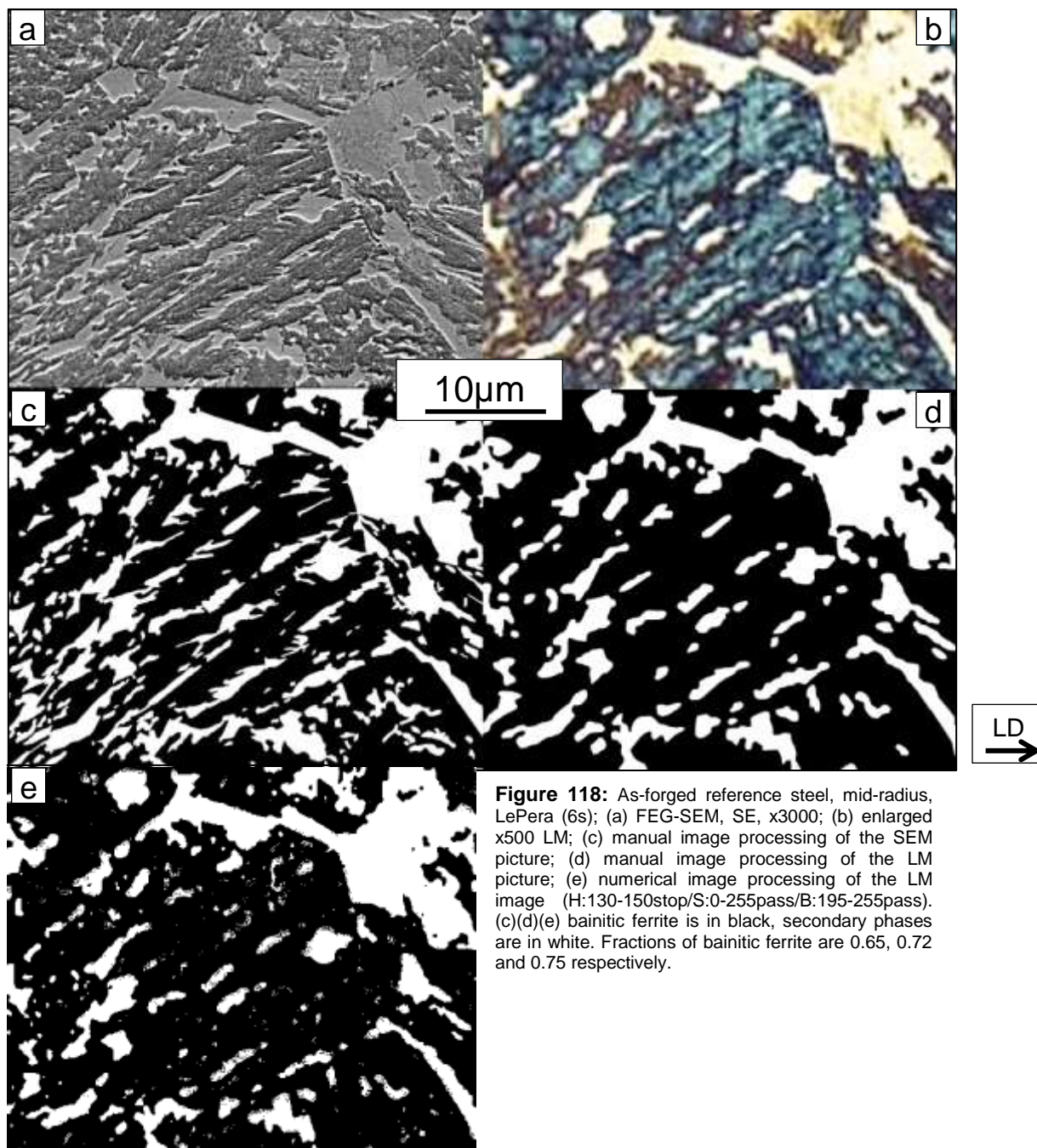
Once the B&W images have been created, the fraction of each microstructural constituent can be obtained using the “batch measure” function in ImageJ software. Several other parameters can be measured such as some shape descriptors (solidity, roundness, aspect ratio ...) or dimensions (fit ellipse, perimeter ...). They can be used for the comparison of the spatial distribution and shapes of secondary phases in the bainitic matrix from one microstructure to another.

Errors associated to this quantification, that are shown in Figure and Tables of this present manuscript are the standard deviation calculated from the individual results of each picture from a given set.

A.1.1.d Limit of this quantification

As shown in Figure 118, some regions of a same sample from as-forged reference steel have been observed with LM and FEG-SEM in order to point out the resolution limit of the light microscopy under these conditions of observations (x500, LePera etching), but also, to evaluate the error introduced by the numerical processing step. FEG-SEM observations have been performed on a Zeiss DSM 982 Gemini.

By comparing Figure 118a and Figure 118b, all microstructural constituents, which have one spatial dimension lower than 420nm in the observation plane, are not detected under light microscopy in these conditions of observation. This spatial and physical limit leads to a consequent loss in the fraction of secondary phases to the benefit of the fraction of bainitic ferrite. As an example, this loss has been evaluated to 0.07 (about 20% of the fraction of secondary phases) using Figure 118c and Figure 118d.



Comparison between Figure 118d and Figure 118e shows the difference between the manual and the numerical processing of the LM picture. An additional error comes from the numerical processing with a loss of 0.03 (11% in relative values) on the fraction of the secondary phases, which corresponds to a loss of 0.10 (29% in relative values) compared to manual processing of the SEM picture. In fact, this is due to light interference between neighbouring phases, edges of MA constituent are not well defined and are often blue tinted (or brown tinted according to the colour of neighbouring bainite), especially for the smallest element visible using LM. By comparing with reference measurements on the SEM picture (Figure 118a), interference problems affect all microstructural elements that have a dimension lower than 650nm.

Most of the loss is attributed to the secondary phases being very rich in austenite or even purely austenitic. Indeed, as seen in chapter 2, there is a gradient in carbon concentration in the microstructural elements of secondary phases, the edge being very rich in carbon and stays always untransformed. So, thin elements of secondary phases are mainly composed of

austenite. In addition, as shown in Figure 119, TEM observations of samples coming from laboratory heats, have pointed out pure austenite films with a width around 200nm between the laths of bainitic ferrite (maximum observed width for austenite film is 270nm).

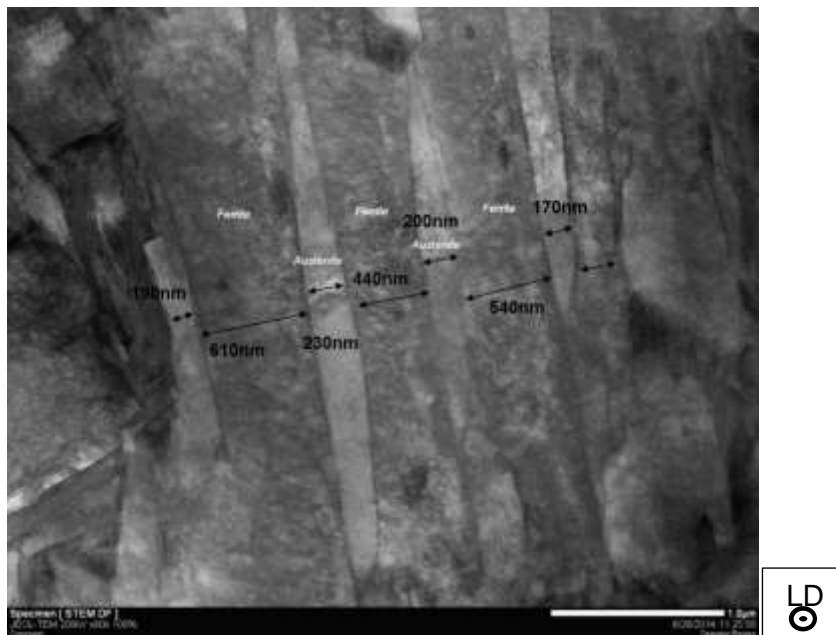


Figure 119: STEM picture of a thin foil extracted from a Charpy impact test specimen of +Mn 35 combination, observation plane = transversal plane. Austenite and bainitic ferrite have been identified using in-situ EBSD. Observations were realized by P. Barges at Maizières R&D centre.

Due to the same problem of spatial resolution, a little fraction of martensite is artificially transferred in the fraction of MA constituent, which corresponds to the isolated and fine laths of martensite in the middle of the residual blocks of MA constituent. The fraction in concern is very low (<0.02). Moreover, the contributions of MA constituent and martensite to the strength of this steel have been found close to each other.

Using a higher magnification would have limited these two issues but x500 magnification has been preferred because it avoids any use of multi-focus to obtain good sharpness. The realization of multi-focus pictures substantially increases the acquisition time per picture. In addition, with higher magnification, more pictures are necessary to obtain the same acquisition area. Both will lead to an obvious increase of the time spent per set of pictures on one sample.

During the course of the project, this quantification has been realized on about 110 different combinations of chemical composition and thermo-mechanical treatment and, as the suitable colour/microstructural constituent combination is not always obtained on the first attempt, we believe that the choice to stay with this magnification was the most acceptable one.

Further numerical processing to avoid the artefact that can be seen in Figure 118e have been developed using several functions in ImageJ software such as “Fill Holes” and “Remove Outliers”. However, it only works on upper bainite microstructures and not for lower bainite and martensite-rich microstructures. In consequence, these error corrections have not been used in order to homogenize the numerical processing through the entire study.

A.1.1.e Special case of allotriomorphic ferrite

The fraction of allotriomorphic ferrite has been measured using a different method compared to the other microstructural constituents. Indeed, ferrite is not discernible from bainite considering only the colour/microstructural combination. However, surface aspect and shape

of the ferrite grains are completely different from the ones of bainite. Allotriomorphic ferrite appears completely smooth with barely no internal secondary microstructural element (with the exception of some precipitation which is believed to be $\text{Fe}_{23}(\text{BC}_6)$). Ferrite nucleates at the primary austenite grain boundaries. Ferrite grains have regular edges and present no specific shape in contrast to bainitic packets.

Edges of ferrite grains have been highlighted manually on numerical stack using GIMP 2.0 software. These stacks are afterward transformed into B&W pictures in which only ferrite appears in black. B&W pictures have then been processed using ImageJ software in order to obtain the fraction of allotriomorphic ferrite. The fraction of bainite has to be subtracted by the obtained fraction of ferrite in the final result.

A.1.1.f Special case of martensite-rich microstructures

During the realization of the CCT diagrams, microstructures coming from relatively high cooling rates have been analysed. These microstructures contained a high fraction of martensite with a certain amount of auto-tempered martensite that has been identified thanks to its typical multi-variant carbide precipitation [200]. As shown in Figure 120, by comparing SEM pictures after Nital2% etching and with LM pictures after LePera etching, it appears that auto-tempered martensite appears blue using LePera etching. In these cases, it has been impossible to separate auto-tempered martensite from bainite (lower bainite, more precisely) using the procedure described above. In addition, even without auto-tempered martensite addition, measurement errors increases due to a slight overlapping of the colour range exhibited by each microstructural constituent. In these cases, the area fraction of each microstructural constituent is still given, but has to be used with caution.

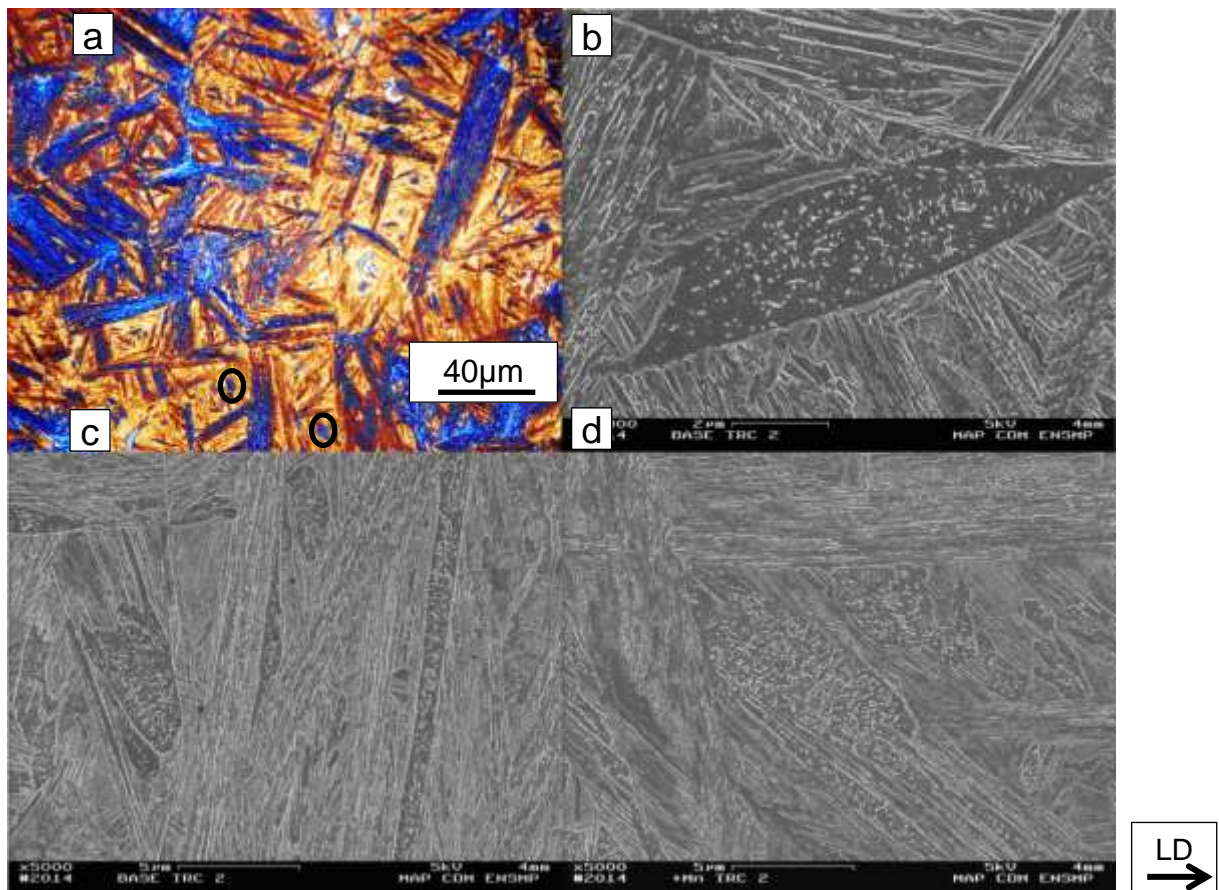


Figure 120: (a) LM picture of base 2°C/s after LePera etching, (b)(c) SEM pictures of base 2°C/s after Nital2% etching and (d) SEM picture of +Mn 2°C/s after Nital2% etching. Using SEM, auto-tempered martensite appears as smooth dark regions containing small white particles. Some identified auto-tempered martensite has been highlighted in black on (a).

A.1.2 Quantification using electron backscatter diffraction

A.1.2.a Sample preparation and EBSD data acquisition

This quantification has been realized on the sample coming from the as forged reference steel, over the same region as for the LM. As this sample has already been used for the LM quantification, and in order to analyse the closest region as possible as the previous quantification, only a smooth 3 μm and 1 μm diamond paste polishing has been realized to remove etching. The final polishing consisted in a 0.25 μm diamond paste polish and a 40s polish with colloidal silica. The time spent with colloidal silica was as short as possible to avoid the creation of a too sharp surface relief that can induce diffraction problems.

The EBSD map was first realized using an acquisition step size of 250nm. The objectives were to obtain at the same time, information on fraction of microstructural constituents and bainitic ferrite packet size. The map area was 57720 μm^2 (160x361 μm^2 , i.e. 0.05772mm 2) which is equal to the area of a picture taken with light microscopy using a magnification of x500. The obtained results were unsatisfactory for both objectives, which led us to realize two separate maps, one for each objective, using two different sets of acquisition parameters (acquisition step size and mapping area).

The main concern for the objective of microstructural quantification was the acquisition step size. The smaller the step size, the lower the spatial resolution limit and the better the phase or boundary definition. We realized a new map using an acquisition step size of 70nm. The mapping area was reduced to a square of 100x100 μm^2 (10000 μm^2 = 0,010 mm 2) to avoid long time data processing, which, on the other hand, reduced the statistical significance of the results. An IPF map resulting from the new mapping is shown in Figure 121a.

A.1.2.b Processing of EBSD data

Once the mapping has been realized, we can start a specific processing in order to obtain the most comprehensive phase quantification using both OIM Analysis and ImageJ softwares:

Step 1 (Figure 121b): First we used the map that shows body centred cubic (BCC) and face centred cubic (FCC) microstructures. We assume that the area fraction of bainitic ferrite, martensite and MA constituent is equal to the BCC area fraction and that the FCC area fraction corresponds to pure austenite only. However the area fraction of retained austenite is underestimated using EBSD in the case of complex microstructures as explained in A.II.1. The main reason lies in two points: high dislocation density and the fineness of austenite (especially for the austenite mixed in the martensite inside MA constituents). In fact, the austenite content of the reference steel has been measured using XRD to be 0.129 whereas a value of only 0.044 is found using EBSD.

Step 2 (Figure 121c to Figure 121f): For the same reasons, the confidence index (**CI**) and the image quality (**IQ**) can be used as parameters to separate secondary phases from bainitic ferrite. The IQ seems to provide better contrast between bainitic ferrite and secondary phases than does the CI. The resulting image after thresholding provides a better representation of the microstructure with detection of smaller islands or films and better edge definition. Moreover, CI thresholding requires an additional processing step under image J (despeckle function) to remove bad CI isolated pixels.

At this point we got measurements of the area fraction of MA constituents, which can be deduced by subtracting the austenite fraction obtained in step 1 from the fraction of MA constituent and austenite obtained with step 2. The fraction of MA constituent is 0.23 and 0.27 for the CI (set to 0.3) and IQ (set to 0.5 times of the maximal value) thresholding, respectively. Comparing both results with other quantification methods, especially the SEM-based method, will allow determining the best suited thresholding method.

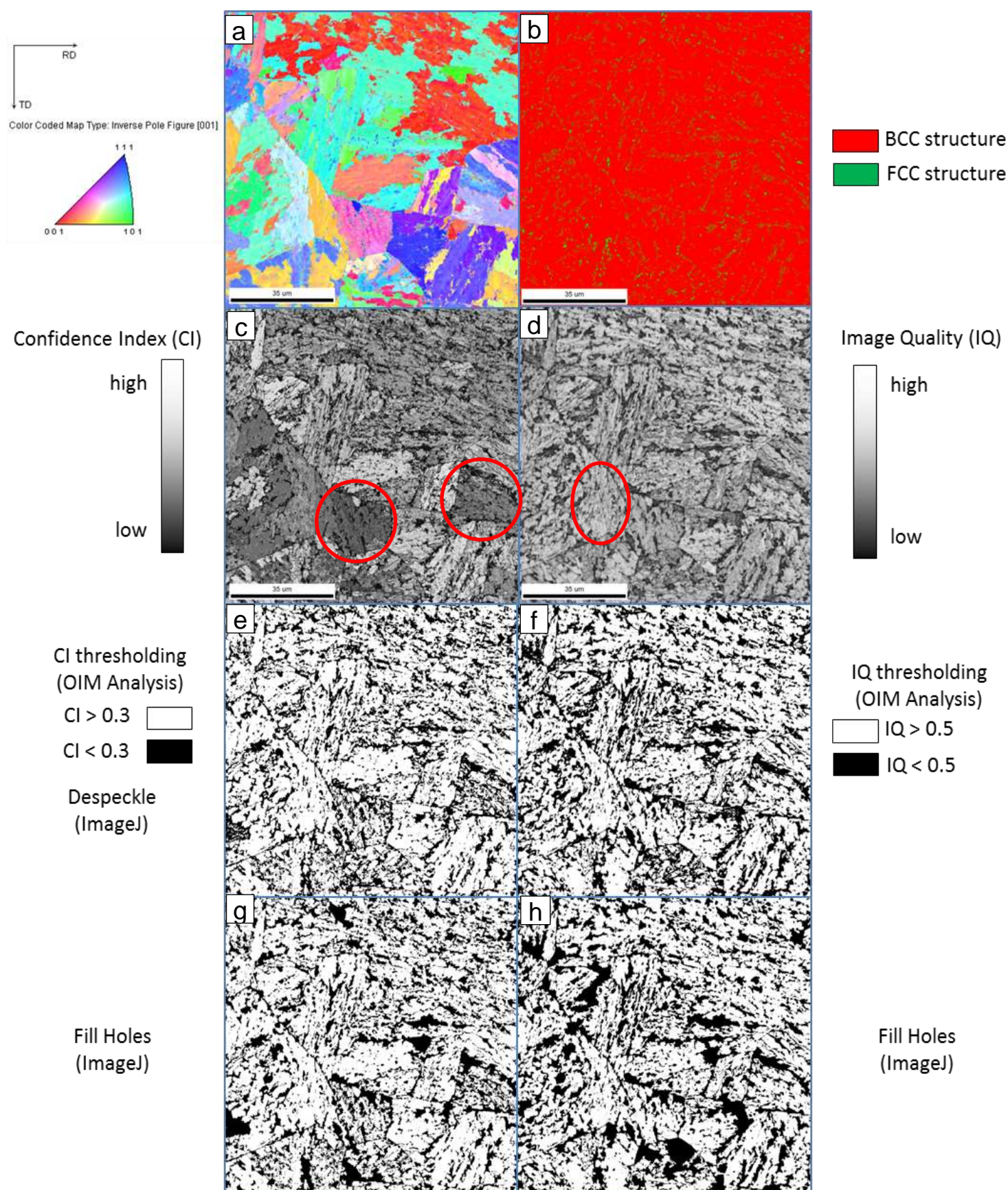


Figure 121: As-forged reference steel, mid-radius, EBSD, 70nm of acquisition step size. (a) Inverse Pole Figure map. (b) BCC (ferrite) and FCC (austenite) map. (c) CI map. (d) IQ map. (e)(f) EBSD maps with in black, pixels that have a CI < 0.30 (e) or IQ

APPENDIX A – METHODS OF MICROSTRUCTURAL CHARACTERIZATION

< 0.50 (f), and in white, pixels that have a CI > 0.30 (e) or IQ > 0.5 (f). (g)(h) Upper image with in black, martensite, MA constituents and austenite, and in white, bainitic ferrite.

Increasing the CI thresholding leads to completely fill some bainitic ferrite packets (those highlighted in red in Figure 121c) whereas decreasing the IQ thresholding will lead to a loss in the definition of the smallest microstructural elements (for example, in the region highlighted in red in Figure 121d).

Step 3 (Figure 121g to Figure 121h): Using ImageJ, martensite has been separated from bainitic ferrite. Martensite is found in the middle of the large residual blocks. It is thus surrounded by MA constituents. So we assume that all the BCC phase that is trapped into MA constituent is martensite. Using "Fill Holes" functions, these spans of martensite will be filled in black, as a result, only the bainitic ferrite will appear in white.

The martensite fraction can be obtained by subtracting the fraction of MA constituent and austenite obtained in step 2 by the fraction of all residual phases (i.e. all phases with the exception of bainitic ferrite) obtained with step 3. Once again, there is a difference depending on the use of either IC or IQ thresholding. The fraction of martensite is 0.02 and 0.04 for the CI and IQ thresholding respectively.

Step 4: This step is realized in order to estimate the error generated by missing artificially every microstructural constituent that are narrower than 650nm by using a shape criterion. This step will help to compare the results of the EBSD quantification method with that of LM quantification method. This size criterion is the minimum Feret diameter. The fraction of microstructural constituent that has a minimum Feret diameter lower than 650nm is 0.03 and 0.02 for the CI and IQ thresholding respectively.

A.1.2.c Results

The detailed results of this quantification are discussed in part A.1.4 where they are compared to the results obtained with the other two quantification methods (A.1.1 and A.1.3) used on the same sample.

A.1.3 Quantification using scanning electron microscopy

This very long processing but very accurate quantification has been performed as a reference in order to assess the validity of the EBSD and LM quantifications.

A.1.3.a Protocol

This quantification has been realized on the same region from the same sample as for the LM and EBSD quantifications. So the material is once again characterized in a plane parallel to its rolling direction, at mid-radius of the forged part. As previously, only microstructures out of segregated regions have been observed. After the EBSD quantification, the sample has only encountered the two final polishing steps (0.25 μ m diamond paste and colloidal silica, 80s) to remove any amorphous carbon contamination after EBSD mapping. Then, the polished surface has been etched with Nital2% reagent for 3s.

This quantification is realized from a map made by stitching 63 SEM images taken at a magnification of x3000. This map is shown in Figure 122. Each SEM image is a mixed combination of secondary electron and back-scattered electron imaging modes. The area of acquisition is 0.058 mm², but as the manual processing took several days (30 hours of work), the analysed area has been reduced to 0.018mm² (267.3 x 67.25 μ m²).

A computer assisted manual processing of the map has been realized using GIMP2.0 and ImageJ softwares. The use of a fully numerical processing is not possible in this case because there are no specific contrast/phase relationships and no specific shape/phase

relationships that can be used to set up a convenient and reliable data processing procedure. Spatial resolution has been estimated to be around 60nm.

A.1.3.b Processing

Image processing has been realized in several steps:

Step 1 (Figure 122): using Gimp2.0, two overlays have been made, one containing the highlights of the structure in red, the other containing the highlights of the sub-structure in purple. The overlay showing the first level of microstructure has been realized by highlighting the limits of every microstructural element that emerges from the bainitic ferrite matrix, so, in other words, every secondary phase. The overlay showing the sub-structure (second level of microstructure), on the other hand, has been realized by highlighting the limits of every microstructural element that emerges from the secondary phases which is mainly the martensite present at the centre of the large blocks of residual phases.

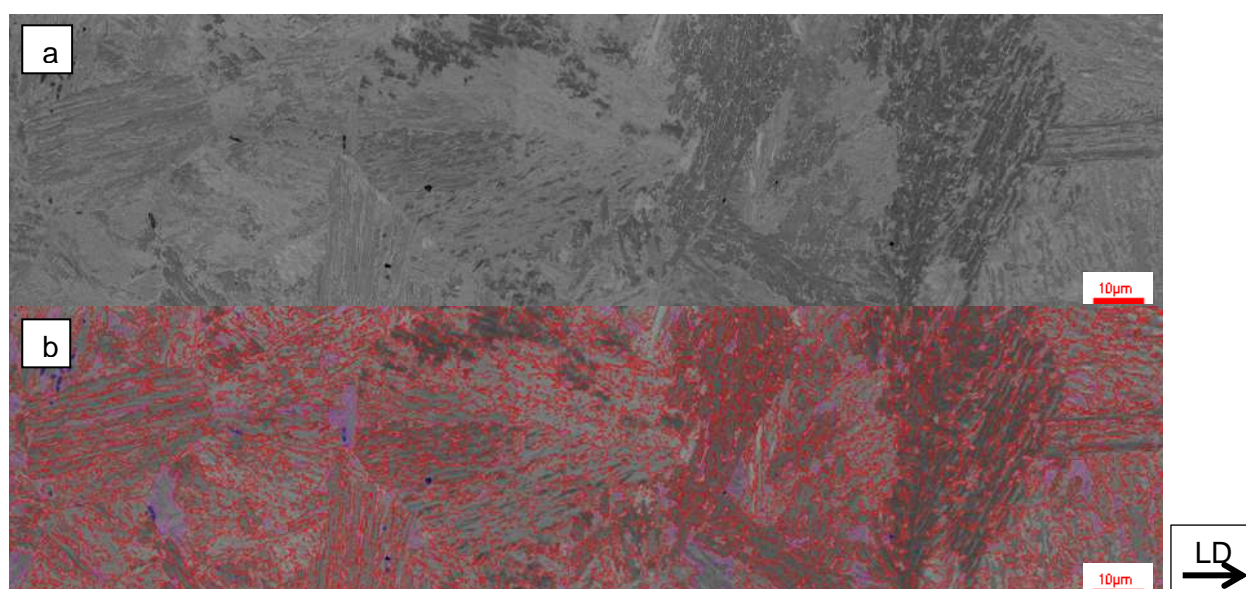


Figure 122: As-forged reference steel, mid-radius, Nital2% etching (a) SEM picture, SE mixed with BSE mode, (b) the same image with the two overlays (structure overlay is in red, sub-structure overlay is in purple).

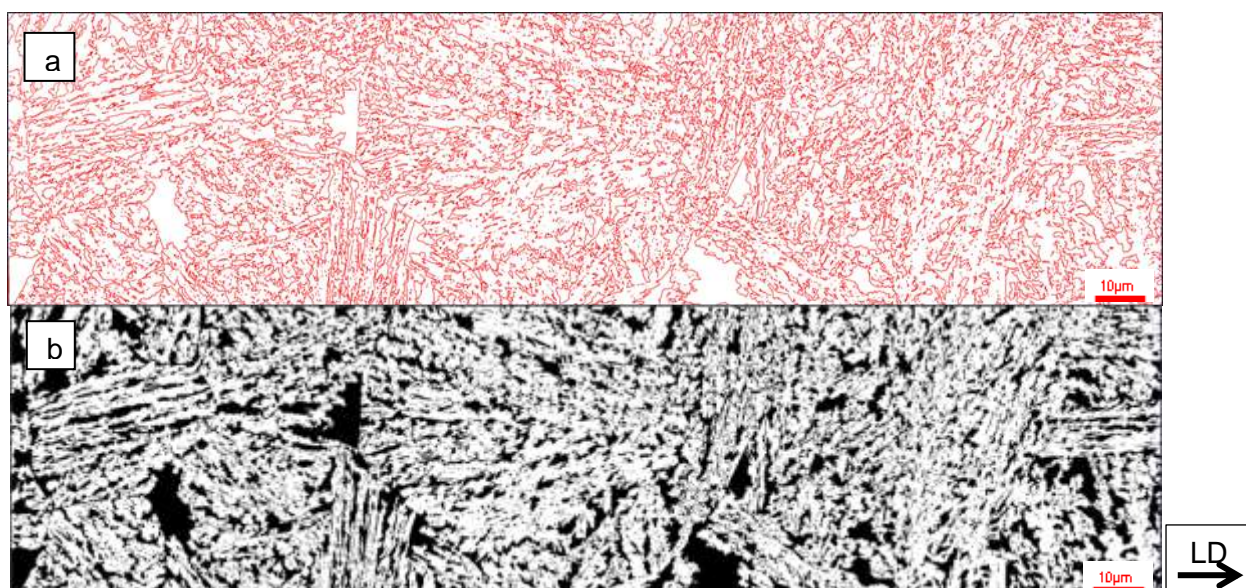


Figure 123: Same region as in Figure 122. (a) Picture from the overlay containing the highlights of the structure, (b) the same picture in black and white after using "Make Binary" and "Fill Holes" functions in ImageJ.

Step 2 (Figure 123): the overlay containing the highlights of the structure is extracted and transformed into a .TIF picture (Figure 123a). With ImageJ, the picture is converted into a black and white picture using "Make Binary" and "Fill Holes" functions (Figure 123b). Bainitic ferrite now appears in white and all secondary phases appear in black. Then, this picture is used to measure the area fraction of secondary phases.

Step 3 (Figure 124): the overlay containing the highlights of the sub-structure is extracted and transformed into a .TIF picture (Figure 124a). With ImageJ, the picture is then converted into a black and white picture using "Make Binary" and "Fill Holes" functions (Figure 124b). Then, this picture is used to measure the fraction of martensite. At this stage, by subtraction of the area fraction from the previous one measured in step 2, we are able to separate, within secondary phases, martensite from MA constituent and austenite.

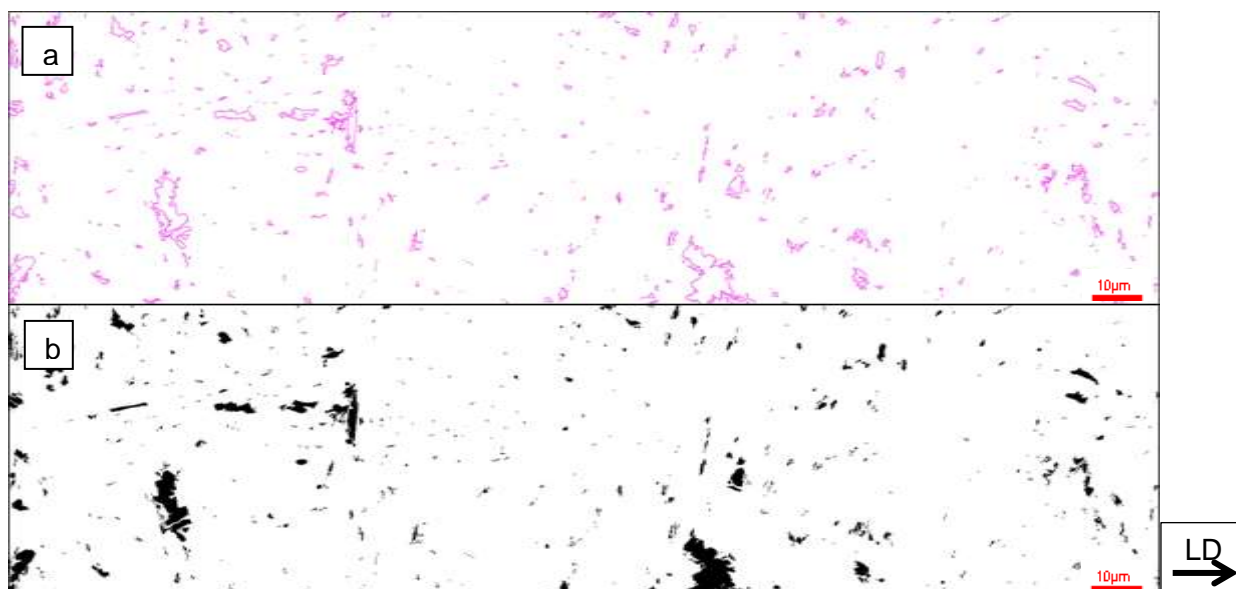


Figure 124: Same region as in Figure 122. (a) Picture from the overlay containing the highlights of the sub-structure, (b) the same picture in black and white after using "Make Binary" and "Fill Holes" functions in ImageJ.

Step 5: This step is not an image processing but a data processing that is realized in order to estimate the error generated by missing artificially every microstructural constituent that have dimension lower than 650nm in width using a size criterion. This step will help to compare the result of the SEM quantification method with the one of the LM quantification method. This size criterion is the minimum Feret diameter. The fraction of microstructural constituent that has a minimum Feret diameter lower than 650nm is 0.03.

A.I.3.c Results

The detailed results of this quantification are discussed in part A.I.4, where we compare them to the results obtained with the two other quantification methods (A.I.1 and A.I.2) obtained on the same sample.

A.I.4 Comparison of the results obtained from different quantification methods

Table 5 shows the results of all quantification methods used on the same region of a sample from the reference as-forged steel. These results pointed out that only the EBSD quantification can allow separating a part of the austenite from others. However, as shown earlier in section A.I.2.b, we know that this austenite level is underestimated.

APPENDIX A – METHODS OF MICROSTRUCTURAL CHARACTERIZATION

So whatever the method used, due to the very fine distribution of austenite, it is not possible to separate all the phases to realize proper phase quantification. However, it is still possible to find a way to compare, with a recurrent and known error, the different microstructures obtained in this study. If we consider that pure austenite films do not exceed 650nm in width (which is highly probable as no austenite films exceeding 270nm have been detected during TEM observations), we can build a quantification of microstructural constituents as follows:

- The microstructural constituent named ferrite would correspond to allotriomorphic ferrite.
- The microstructural constituent named bainite would correspond to bainitic ferrite (granular, upper or lower) and all the microstructural elements with a dimension lower than 650nm, i.e. all retained austenite films plus a certain amount of MA constituent, which is the recurrent error.
- The microstructural constituent named martensite would correspond to the isolated spans of secondary phases such as martensite, auto-tempered martensite and lower bainite (as they cannot be differentiated in this stage) that are present in the middle of secondary blocks in mixed upper/granular bainite microstructures. It also refers to pure martensitic regions that can be encountered with higher cooling rates (only seen in CCT diagrams, see Chapter 3).
- The microstructural constituent named MA would exclude the austenite films and corresponds to MA islands (very fine mixture of austenite and martensite). In other words, all microstructural constituents that are not bainite or martensite or ferrite.

Following these rules, the results of this quantification are reported in Table 33.

The quantification method using SEM necessitates, in this configuration (magnification 3000, Nital2% etching), a manual processing of the map for phase recognition. Fully numerical processing is not possible in this case because there are no specific contrast/phase relationships, which leads to long processing time (30h) even over a very restricted area. This processing time makes the realization of this quantification only exceptional.

On the other hand, this method allows the use of suitable magnification for the observation of the finest elements of the microstructure. With the exception of the austenite content that can be obtained by other ways (XRD, sigmametry), we believe that the SEM quantification method is the most accurate and comprehensive one among the three tested quantification methods.

phase	LM + LePera etching		EBSD (CI thresholding)		EBSD (IQ thresholding)		SEM + Nital 2% etching
bainitic ferrite	0.74		0.70	0.74	0.67	0.71	0.66
austenite			0.04		0.04		0.31
MA	0.24	0.26	0.23	0.26	0.27	0.29	0.03
martensite	0.02		0.03		0.02		

Table 32: Results of the quantification of phases

microstructural constituent	LM + LePera etching		EBSD (CI thresholding)	EBSD (IQ thresholding)	SEM + Nital 2% etching
bainite	0.74		0.73	0.69	0.69
MA	0.24		0.24	0.29	0.28
martensite	0.02		0.03	0.02	0.03

Table 33: Results of the quantification of microstructural constituents.

The use of electron backscatter diffraction to realize quantification needs to make two assumptions to obtain a complete quantification. Bad CI or IQ is attributed to austenite and

APPENDIX A – METHODS OF MICROSTRUCTURAL CHARACTERIZATION

MA constituents due to their high dislocation density and their fineness. The second assumption is that all the BCC phase that is trapped into MA constituent is martensite.

However, the results of the EBSD quantification stay very close to those of the SEM quantification when the IQ is used as thresholding parameters. In order to avoid equipment over-exploitation, EBSD has only been used for determination of the bainitic ferrite packet size using a larger acquisition step rather than for phase quantification. This technique is well adapted to packet size quantification in an automated and reliable way.

In regard to other results, LM quantification over-evaluates the amount of bainite in the microstructure due to its spatial resolution limit, which is at least 9 times coarser than the one of EBSD and FEG-SEM quantifications. The artificial error applied to other quantification results in order to compare results obtained with similar definitions of microstructural constituent and resolution limits do not bridge the gap between results from this quantification and from the other ones (with the exception of EBSD with CI thresholding).

This is due to the underestimation of the error, the shape criterion does not exclude parts of microstructural elements that present very irregular shapes as in the example shown in Figure 125. In this example, the minimum Feret diameter is higher than the minimum dimension that exists on this microstructural constituent.

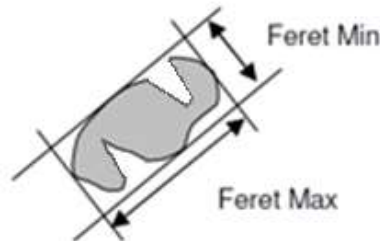


Figure 125: Example showing how the minimum Feret diameter can be higher than the smallest dimension in the case of a very irregularly shaped of microstructural constituent.

However, LM quantification ensures the highest statistical significance of results due to an area of quantification that is 21 times and 37 times larger than the quantification method used with SEM and EBSD respectively. Moreover, numerical processing is fully automated, fast and obtained results are reproducible (very low scatter is obtained between images coming from a given sample).

Light microscopy with LePera etching seems to be the best suited method to realize the quantification of the microstructural constituents defined as earlier in this part, with respect to the addressed microstructural scale and the number of microstructures that have to be investigated. It will nevertheless be necessary to use XRD or sigmometry to realize proper measurement of the total austenite content and to take the over-evaluation of the bainite microstructural constituent into account.

Key numbers:

Total area analysed with:

light microscopy = $13 \times (209 \times 139 \mu\text{m}^2) = 377663 \mu\text{m}^2 \sim 0.378 \text{mm}^2$

scanning electron microscopy = $267.3 \times 67.25 \mu\text{m}^2 = 17976 \mu\text{m}^2 \sim 0.018 \text{mm}^2$

electron backscatter diffraction = $100 \times 100 \mu\text{m}^2 = 10000 \mu\text{m}^2 = 0.010 \text{mm}^2$

Measured resolution limit of:

light microscopy (x500) = 420nm

light microscopy (x500) + processing = 650nm

scanning electron microscopy (x3000) = 60nm

electron backscatter diffraction = 70nm

A.II Quantification of the austenite content

A.II.1 Literature survey

Nemecek et al. [201] compared the austenite content that they obtained for two types of low alloyed high strength steels using several characterization methods (LM, confocal microscopy, XRD, EBSD, TEM and sigmametry). The first steel was described as a TRIP-aided steel with a bainite microstructure and granular retained austenite (0.19C, 1.45Mn, 1.9Si, 1.34Cr in wt%). The second steel is a high strength steel with a martensite microstructure with inter-lath austenite.

The results of this study are shown in Table 34. For both steels, the lower amount of austenite is found using EBSD. A noticeable amount of austenite is missed due to indexing issues and data cleaning operations. Indeed, in critical locations such as boundaries (grains or laths), diffraction might not provide accurate results. The main reason lies in two points: high dislocation density and the fineness of such regions which contain a great amount of austenite.

method / sample	martensitic steel (lath-like austenite)	bainitic steel (granular austenite)
XRD	0.07	0.03
EBSD	0.05	0.01
TEM	0.07	un-evaluated
sigmametry	0.07	0.06
Metallography	Un-observable	0.08

Table 34: Quantification of austenite. After [201].

In the case of the martensitic steel, the other three volume methods (XRD, TEM and sigmametry) give similar results which can be surprising concerning the TEM analysis. TEM is a strongly local method and does not capture the specimen heterogeneity, unless a great number of foils are examined but no indication of the measurement area was given in this paper. No TEM measurements were realized for the bainitic steel as the finest austenite elements of the microstructure were clearly observable with SEM (EBSD) or confocal metallography.

Comparison between XRD and sigmametry results pointed out the difference that can be found between a surface and a volume analysis. In case of a homogenous material, which seems to be the case for the martensitic steel in view of TEM results, XRD and sigmametry give close results, otherwise larger scatter is expected. Indeed, the bainitic steel seems to present some heterogeneity as no experimental methods has given similar result. However, XRD is a well-mastered method in concern of austenite level measurement, relatively quick and with an area analysed in most cases higher than 10mm². The XRD method makes thus a good start for every study of the austenite content in steels.

Inter-lath austenite in the martensitic steel could not be well enough recognized with either light or confocal microscopy (no more details were given by the authors). Regarding the bainitic steel, image analysis of retained austenite was found more accurate at larger magnifications. Quantification was realized with confocal microscopy, using standard planimetric processes. The sample was mirror polished and then etched with Nital and sodium metabisulfite Na₂S₂O₅ (no indication of concentration in solution). Image analysis software NIS-elements was used for quantitative assessment of microstructure. No indication of the area, magnification, or thresholding method is given, which makes it difficult to conclude on the origin of the over-evaluation of the austenite content with this method (perhaps only due to microstructure heterogeneities). However, even if the relative error between sigmametry and confocal microscopy is high, the absolute error is acceptable, especially regarding austenite.

Jacques et al. [202] have presented the results of a blind round robin test on the retained austenite content involving 9 samples, 6 different techniques and 13 partners. The round robin has been realized on four different TRIP steel grades. The chemical composition of these steel grades is shown in Table 35. For each of the four steels, one sample was kept in the as-received condition (samples 1 to 4), while one sample was quenched to liquid nitrogen and held there for 30 min in order to reduce their austenite content (samples LN1 to LN4). Indeed Van der Zwaag et al. [203] showed that the retained austenite fraction dropped from 0.10 to 0.08-0.07 by slow cooling to the liquid nitrogen temperature. The ninth sample was a duplicate of the first one (sample 5). They were coded in an anonymous way and sent without background information to the partners. Each partner tested the experimental methods that they mastered the most. The resulting methods involved in the round robin tests were LM, XRD and EBSD for the surface analyses and magnetic saturation, thermal diffusivity and laser ultrasonics for the bulk analyses.

Steel code	Manufacturer	C	Mn	Si	Samples
A	Industry	0.198	1.48	1.46	1, 1LN, 5
B	Industry	0.167	1.74	1.52	2, 2LN
C	University	0.268	1.53	1.54	3, 3LN
D	Industry	0.1	1.54	1.22	4, 4LN

Table 35: Chemical composition of the investigated steel in [202].

The different partners were completely free to prepare and measure the samples following their own procedures. Large variability in the preparation of the samples and in operation of the equipment was observed, even for a well-established technique. For example, from the 6 partners that made XRD measurements, 4 different sources of radiation (Cu, Cr, Co and Mo) have been used and none of them used the same set of austenite and ferrite peaks to realize their calculations.

Analysis of the results of the duplicated samples 1 and 5 allowed the authors to notice the robustness of each experimental method. Best agreement was found for thermal diffusivity and laser ultrasonics, with an average difference between the two samples of 0.2% and 0.4%. Light microscopy is just behind with a difference of 0.6%. The chosen magnification seems to allow a reasonable statistical significance even with only 5 pictures. Classical methods such as XRD and sigmoidometry present quite good reproducibility, 1.5 and 1.2% respectively. EBSD gives rather different results, 5 or 6% of difference according whether a data clean-up has been realized or not. Authors give the too small probed area as a reason for the discrepancy of EBSD results.

Figure 126 exhibits all the results obtained during that study. The variability on austenite content holds between results from different methods but also within results from each different method. The standard deviation has been found always larger than 3–4%. The authors conclude that no best method seems to exist in order to found the true value of austenite volume fraction but some of them are more reproducible than others in order to compare several steels. Their study pointed out also some strong tendencies: light microscopy, in this configuration, always gives large values and on the other hand, EBSD and laser ultrasonics provide small values. Authors think that could result from resolution and calibration issues respectively.

The over-evaluating of austenite content by light microscopy is once again surprising. A resolution issue may automatically lead to an under-estimation of the austenite content. However, in view of the metallography given in the publication, austenite microstructural elements (islands) are sufficiently large for all of them to be observed with microscopy with the exception of lath-like austenite within bainite and martensite; martensite content was found lower than 1% in most cases (bainite content does not seem higher either). The

reason for the over-evaluation may come from the method that has been chosen to establish the fraction. Indeed, the partner who realized this LM quantification has used a counting method based on which phase is situated under every crossing of a 23x17 grid. For an equivalent surface area, different spatial distribution and size of austenitic elements will give different results. In fact, this method strongly depends on the dimension of the grid [204].

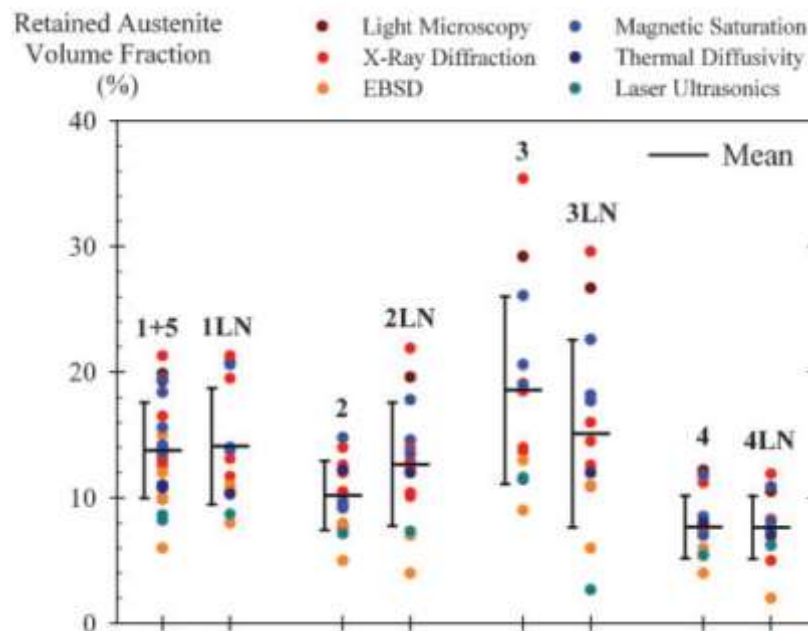


Figure 126: Retained austenite contents estimated by the different methods for each sample in [202]. Surface and bulk methods are represented with reddish or bluish tones respectively. Results of duplicated samples 1 and 5 have been merged.

None of the thesis partners have free access to techniques such as thermal conductivity and laser ultrasonic. In the two previously quoted studies, LM microscopy and EBSD have been found not suitable enough for determining the austenite content for different reasons. Thus, XRD combined with sigmametry measurements have been chosen to reach this objective.

A.II.2 Quantification using X-ray diffraction

X-ray Diffraction only gives a local analysis of a small volume under the surface but does not need any reference sample with no austenite in order to calculate the fraction of austenite.

A.II.2.a Protocol

The XRD spectrum has been realized on a Diffraktometer D500 from Siemens. The equipment was configured in θ -2 θ . The X-ray source is an anti-cathode of cobalt (40kV, 20mA). The K-radiation of cobalt (0.1789nm) is selected using an iron filter. Acquisition lasts for 1s every 0.032° from 48° to 130° and is realized with a linear localization detector from Elphyse. The analysed area is a section of 20x10 mm².

Analysed samples have been prepared with a typical mirror polishing down to 1 μ m diamond paste. Two cycles of very slight Nital2% etching (less than 3s) and 1 μ m diamond paste polishing have been realized to remove all cold working generated earlier during the mechanical polishing.

For every peak identified from the background on the X-ray spectrum, the inter-reticular distance (\AA), the 2 θ angle (°), the net intensity height (counts) and the net area have been determined using DiffracPlus XRD Commander software.

A.II.2.b Data processing

The following relationships have been used to calculate the austenite fraction (f_γ):

$$\frac{f_{\gamma}}{f_{\alpha}} = \frac{\sum R_{\alpha}}{\sum R_{\gamma}} \times \frac{\sum A_{\gamma}}{\sum A_{\alpha}} \quad eq. A. 1$$

$$f_{\gamma} + f_{\alpha} = 1 \quad eq. A. 2$$

This gives:

$$f_{\gamma} = \frac{1}{1 + \frac{\sum R_{\gamma}}{\sum R_{\alpha}} \times \frac{\sum A_{\alpha}}{\sum A_{\gamma}}} \quad eq. A. 3$$

with f_{α} and f_{γ} being fraction of ferrite and austenite respectively, A_{α} and A_{γ} being the net area of ferrite peak and austenite peak respectively, R_{α} and R_{γ} being specific coefficients of ferrite peak and austenite peak respectively.

Specific coefficient of ferrite peak and austenite peak can be found in Table 36. They have been taken from a work of Bach et al. [205]. $\{110\}_{\text{ferrite}}$ and $\{111\}_{\text{austenite}}$ peaks have not been used for the calculation of f_{γ} due to the overlap of these two peaks.

austenite			
h k l	d(hkl) [Å ^o]	2θ (CoKα) [°]	R _γ
111	2.070	51.21	104.0
200	1.793	59.87	46.5
220	1.267	89.78	25.8
311	1.081	111.69	42.3
222	1.035	119.61	14.4

ferrite			
h k l	d(hkl) [Å ^o]	2θ (CoKα) [°]	R _α
110	2.0268	52.38	142.0
200	1.4332	77.24	19.9
211	1.1702	99.71	45.3
220	1.0134	123.93	23.3
310	0.9064	161.38	169.0

Table 36: Miller indices, interplanar spacing, 2θ angle with a Co X-ray source, and specific coefficient for austenite (FCC) and ferrite (BCC). After [205].

In the case of low austenite content ($f_{\gamma} < 0.05$), it happens that the (220) austenite peak is not enough distinguishable from the background to be properly used in eq.A.4. In this case, f_{γ} is defined as the average of fractions of austenite calculated using the following equation using only the two other austenite peaks:

$$\frac{(hkl)_{\alpha} f_{\gamma}}{(hkl)_{\gamma} f_{\gamma}} = \frac{1}{1 + \frac{R_{(hkl)_{\gamma}} \times A_{(hkl)_{\alpha}}}{R_{(hkl)_{\alpha}} \times A_{(hkl)_{\gamma}}}} \quad eq. A. 4$$

with $\frac{(hkl)_{\alpha} f_{\gamma}}{(hkl)_{\gamma} f_{\gamma}}$ being fraction of austenite calculated using ferrite peak $(hkl)_{\alpha}$ and austenite peak $(hkl)_{\gamma}$, $A_{(hkl)_{\alpha}}$ and $A_{(hkl)_{\gamma}}$ being the net area of the ferrite peak and austenite peak respectively, $R_{(hkl)_{\alpha}}$ and $R_{(hkl)_{\gamma}}$ being specific coefficients of ferrite peak and austenite peak respectively.

This method of calculation also allows pointing out texture effect in the case of significant variations being noticed between austenite fractions calculated from the different combination of austenite and ferrite peaks. For example, a texture effect has been noticed for both samples of the reference steel (due to the banded structure) and for 0Ti (abnormal grain growth). In these cases, additional X-ray measurements have been realized on the same

equipment but using a rotating sample holder in order to increase the spread in crystal orientation and to improve counting statistics.

Errors related to XRD measurements that are shown in Figures and Tables of this present project are the difference between the austenite fraction calculated from eq.A.4 and the averaged austenite fractions that have been calculated using eq.A.5. In the case of a missing austenite peak, the error is the standard deviation calculated from austenite fractions that have been calculated using eq.A.5.

A.II.3 Quantification using sigmametry

Austenite quantification by magnetisation consists in measuring the specific magnetization at saturation (σ_s) of the analysed sample. This quantification gives relative values and needs the use of a reference sample from the same chemistry with no austenite. Moreover the measurement accuracy strongly depends on the microstructure of this reference [206].

It is a bulk quantification method, which is reliable and fast. In addition, as the available sigmameter shares the same sample dimension as the dilatometer (diameter: 4mm, length: 10mm), direct measurement of the austenite level can be obtained only a few seconds after the end of the dilatometric cycle.

A.II.3.a Commissioning

ArcelorMittal Gandrange R&D centre is equipped with an old Sigmameter B3513A from Aimants Ugimac. No technical notice, no proper experiment procedure and no calibration samples were ready-to-use for this equipment.

The main work that has been done in order to commission this equipment was the following:

- New sample holders have been designed in order to guarantee the location of the sample at the centre of the magnetic field.
- Calibration samples have been given by Maizières R&D centre and machined in order to fit with the sample holders. The calibration sample for 100% austenite is pure nickel ($\sigma_s=54.5 \text{ Gauss.cm}^3.\text{g}^{-1}$) and the calibration sample for 100% ferrite is pure iron ($\sigma_s=217 \text{ Gauss.cm}^3.\text{g}^{-1}$).
- The calibration procedure of the equipment has been written following a procedure from Maizières R&D centre, which has a sigmameter different from the one at Gandrange but coming from the same manufacturer. Some internal switches and potentiometers that are necessary to calibrate the equipment were identified during this project allowing us to better use this tool than in the past years.

A.II.3.b Protocol

The sigmameter has to be calibrated following the calibration procedure before the realization of any measurement. With our equipment, and because some potentiometers are not easily accessible, we were not able to obtain both awaited σ_s for pure nickel and σ_s for pure iron. When one of them has been correctly set, the second one exhibits a difference between 0.5 and 2 $\text{G.cm}^3.\text{g}^{-1}$ with respect to the expected σ_s value. As only materials with low level of austenite will be analysed through the thesis, calibration in the present study is focused on high specific magnetization at saturation.

The sample has to be weighed on milligram accurate weighing scale. The weight of the sample is then entered on the control panel of the sigmameter. The sample is driven in and out of the magnet box of the sigmameter within a few seconds (less than 3s). σ_s appears on the digital screens present at the front of the control panel.

APPENDIX A – METHODS OF MICROSTRUCTURAL CHARACTERIZATION

For samples with a weight below 1g, it is preferable to realize a correction on σ_s given by the sigmameter. Indeed, it is not possible to enter the milligrams on the control panel. This one stops on centigrams. A variation of 1mg leads to a change by $0.2 \text{ G.cm}^3.\text{g}^{-1}$ for an initial σ_s of $190 \text{ G.cm}^3.\text{g}^{-1}$. So for a round up from 0.985g to 0.99g, the variation is of $1 \text{ G.cm}^3.\text{g}^{-1}$ which is not negligible. The correction is a simple cross multiplication:

$$\sigma_{Sc} = \frac{\sigma_{Si} \times m_e}{m_r} \quad \text{eq. A. 5}$$

with σ_{Sc} being the corrected specific magnetization at saturation in $\text{G.cm}^3.\text{g}^{-1}$, σ_{Si} being the initial specific magnetization at saturation given by the sigmameter in $\text{G.cm}^3.\text{g}^{-1}$, m_e is the entered weight in g, m_r is the real weight of the sample in g.

Every measurement has been realized at least five times (on a same sample) to calculate an average value of σ_{Sc} . Confidence intervals relied to σ_{Sc} that are shown in Figure and Tables of this present thesis are the standard deviation of σ_{Sc} measurements realized on a same sample.

A.II.3.c Creation of a reference sample for the project's steel grade

Several tempers at 500°C for 180min, 210min, 240min and 270min have been performed on four different samples from the as-rolled reference steel to destabilize retained austenite into ferrite and cementite without any other extended microstructural variation. Heat treatments have been made under protective atmosphere to avoid excessive oxidation. Samples have been quenched into water following the heat treatments. As-rolled reference steel has been preferred to all other materials due to the largest amount of available material.

Benchmarking measurements of the austenite fractions have been realized using XRD following the procedure and processing written in part A.II.1. Results of these measurements are shown in Table 37. It seems that no further austenite decomposition happens after 210min.

t(min) at 500°C	f_γ
180	0.019 \pm 0.004
210	0.014 \pm 0.002
240	0.014 \pm 0.004
270	0.014 \pm 0.003

Table 37: f_γ measured using XRD for every heat treated sample.

The microstructure of the heat-treated samples has been observed using FEG-SEM after Nital2% etching in order to examine the effect of the heat treatment, especially on MA constituent and martensite. Figure 127 exhibits some pictures of the as-rolled reference steel before and after the longest heat treatment. The microstructure has the same global aspect at low magnification (apparent size of the bainitic packet, location of the secondary phases) but, as the magnification increases, it becomes obvious that massive cementite precipitation has occurred and that martensite and most of MA islands have decomposed into ferrite and cementite.

However, the finest austenite films and MA islands (rich in austenite) stayed untransformed, which explains the residual amount of austenite measured with XRD. So, the attempt to create a reference sample without any austenite has failed but there is still the possibility to use one of these tempered samples as shown in the very next part.

APPENDIX A – METHODS OF MICROSTRUCTURAL CHARACTERIZATION

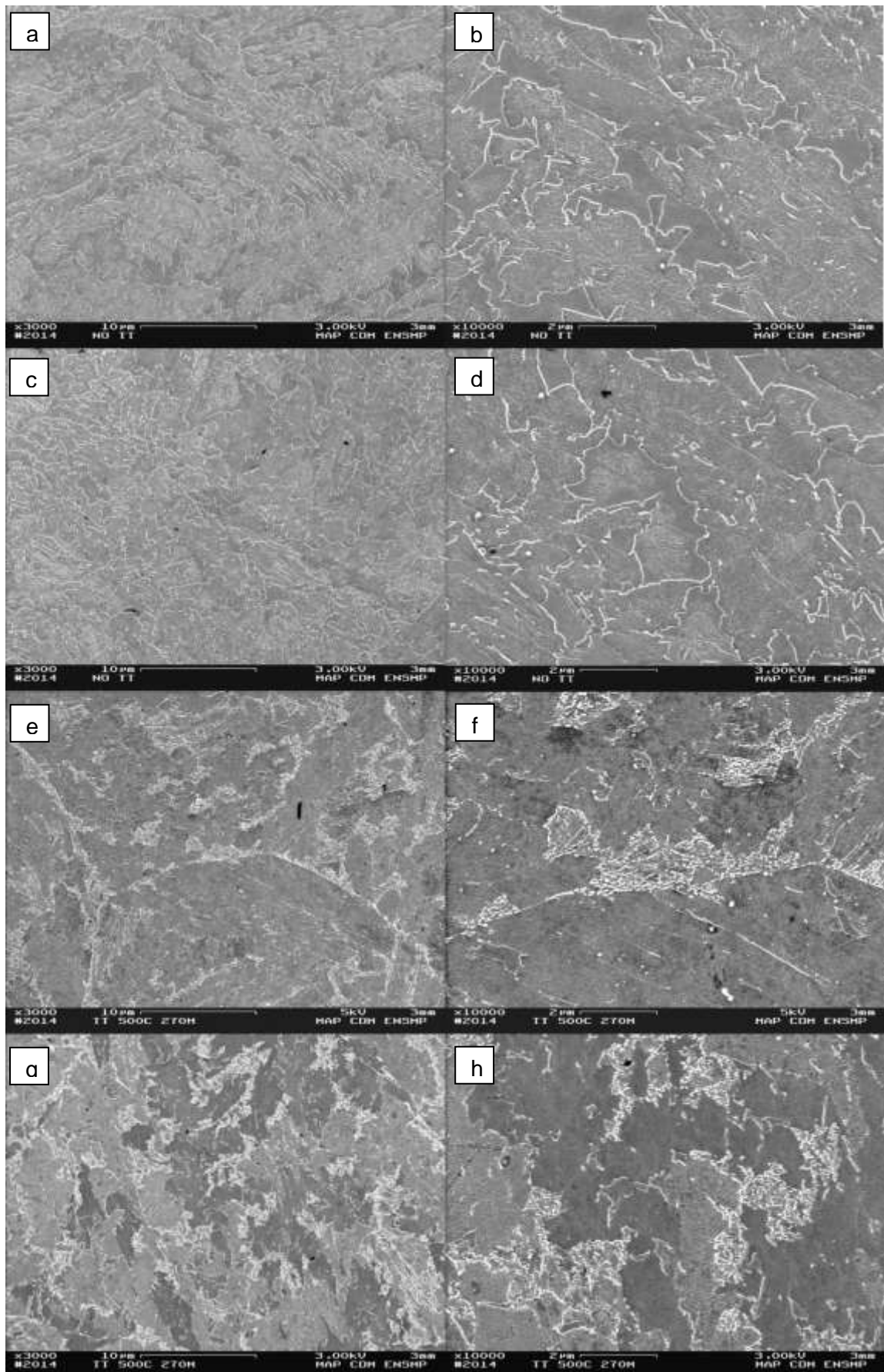


Figure 127: FEG-SEM, as-rolled reference steel, mid-radius, Nital2% etching, (a)(b)(c)(d) before heat treatment, (e)(f)(g)(h) after heat treatment (500°C, 270min).

A mechanical destabilization under tensile test may have been a better choice but time was missing to realize XRD analysis along the axis of broken tensile specimens and the following machining of sigmametry samples.

A.II.3.d Processing

Even if the attempt to create a reference sample without austenite did not fully succeed, samples from heat treatment can still be used in order to calculate the specific magnetization at saturation of a reference sample without austenite (same chemistry and microstructure, very close austenite content).

One sigmametry specimen has been extracted from the sample with the longer heat treatment. Its specific magnetization at saturation has been measured in sigmametry following the protocol in part A.II.2.b. After correction, σ_{Sc} is $203.7 \text{ G.cm}^3.\text{g}^{-1}$.

The specific magnetization at saturation is proportional to the volume fraction of ferromagnetic phases (ferrite, bainitic ferrite, and martensite). The volume fraction of austenite can be calculated using the following equation [207]:

$$V_{\gamma} = \frac{\sigma_{S0} - \sigma_{Sc}}{\sigma_{S0}} \quad \text{eq. A. 6}$$

with V_{γ} being the volume fraction of austenite, σ_{S0} being the specific magnetization at saturation in $\text{G.cm}^3.\text{g}^{-1}$ of a reference sample of the same chemistry and σ_{Sc} being the specific magnetization at saturation after weight correction of the analysed sample in $\text{G.cm}^3.\text{g}^{-1}$.

The value of σ_{S0} in the case of the reference steel can be calculated with making the assumption that f_{γ} is equal to V_{γ} . Using the results of the sample that has encountered the longer heat treatment, eq.A.7 can be transformed into:

$$\sigma_{S0} = \frac{\sigma_{Sc}[TT \ 500^{\circ}\text{C}, 270\text{min}]}{1 - f_{\gamma}[T \ 500^{\circ}\text{C}, 270\text{min}]} = \frac{203.7}{0.986} = 206.6 \text{ G.cm}^3 \text{ g}^{-1} \quad \text{eq. A. 7}$$

If we consider that the value of σ_{S0} found with eq.A.8 does not change obviously with a slight variation in chemical composition, the volume fraction of austenite can be now calculated using eq.A.7 for every chemical composition that has been studied in this thesis. However, this last assumption seems to be risky, as the as-rolled reference steel presents a difference in nickel content plus another slight variation of another substitutional alloying element.

A.II.4 Benchmark measurements between sigmametry and X-Ray diffraction

This round-robin has been realized in order to test the influence of microstructure and chemical composition on the specific magnetization at saturation. If both sensitivities are not so marked for the considered range of materials, a relationship is to be found between the specific magnetization at saturation and the austenite fraction as measured with XRD.

A.II.4.a Experimental methods

36 dilatometry samples per $74 \times 74 \text{ mm}^2$ forged parts have been machined from XD 74 section (see the extraction scheme in Appendix B). σ_s has been measured three times on five different samples taken randomly among the 36 available samples for each chemical composition. Then, σ_{Sf} has been corrected following eq.A.6. These results will be compared to the f_{γ} measurements that have been made on impact toughness specimens in chapter 4.

In order to also investigate significant microstructural variations, measurements of f_{γ} have been realized on samples with a cooling rate of 2°C/s between 800°C and 20°C that have been used for the realization of the CCT diagrams. The X-ray measurements have been

realized following the procedure and data processing described in part A.II.1. The resulting values of f_γ are to be compared to the values of σ_s coming from chapter 2.

A.II.4.b Results and discussion

Figure 128 shows the fraction of austenite as a function of the specific magnetization at saturation. With the exception of 0Nb 74 and 0Mo 74 combinations, it is possible to find a linear relationship between σ_s and f_γ , which is available for every studied sample:

$$f_\gamma = -0.0061 \times \sigma_{sc} + 1.24 \quad \text{eq. A. 8}$$

By taking experimental errors into account, a confidence interval of 0.015 on f_γ around this linear relationship allows to integrate all the considered experimental points.

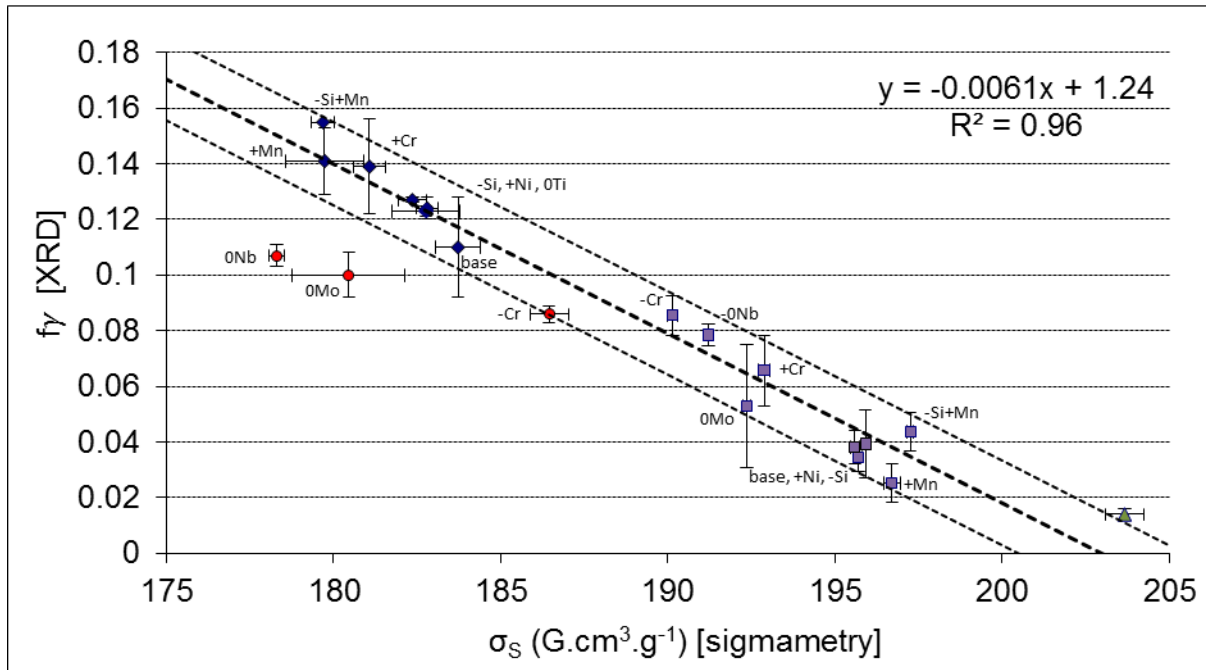


Figure 128: Fraction of austenite versus specific magnetization at saturation. Blue diamonds are the samples from 74x74mm² forged parts, red circles are combinations that present allotriomorphic ferrite (0Nb 74, 0Mo 74 and -Cr 74), purple squares are CCT diagram samples (2°C/s between 800°C and 20°C) and the green triangle is the heat treated as-rolled reference steel (500°C for 270min).

Small amounts of allotriomorphic ferrite have been observed on 0Nb 74, 0Mo 74 and -Cr 74 combinations. The ferrite fraction found with the LM quantification was 0.02, 0.01 and less than 0.01 for 0Nb 74, -Cr 74 and 0Mo 74 combinations respectively. It is surprising that these few amounts of ferrite lead to a decrease in the σ_{sc}/f_γ ratio to this extent. Before the bainitic transformation, the average cooling rate between 750°C and 550°C is between 0.4°C/s and 0.6°C/s according to the location in the 74x74mm² forged parts. The cooling rate gradient can be the source of microstructure heterogeneities for chemical composition sensitive to allotriomorphic ferrite. Locations that have encountered a cooling rate at 0.6°C/s may not present any ferrite at all, whereas locations that have encountered a cooling rate at 0.4°C/s may present small quantities of it. This is thus probable that the regions in which the dilatometric samples have been extracted to measure σ_{sc} , present slightly more ferrite than in the region in which f_γ has been measured (impact toughness specimen). Anyway, the influence of allotriomorphic ferrite on the σ_{sc}/f_γ ratio is obvious.

Samples coming from the CCT diagrams with a cooling rate of 2°C/s between 800°C and 20°C have a martensite fraction between 0.10 and 0.87. In view of Figure 128, the σ_s/f_γ ratio seems to be barely un-affected by the martensite/bainite ratio, which may be due to the absence of cementite precipitation for both martensite and bainite. In the same way, the

massive precipitation of cementite for the as-rolled reference steel that has been heat treated does not lead to obvious variation of the σ_{Sc}/f_{γ} ratio. The variation of chemical composition does not seem to create strong variations of the σ_{Sc}/f_{γ} ratio either.

Experimental errors on σ_{Sc} exhibited by the samples extracted from 74x74mm² forged parts are larger than those from the CCT diagrams because in the first case, each experimental point represents 5 different samples whereas in the second case, it only represents one. This experimental error pointed out the degree of heterogeneities on austenite content that can be found on forged parts. This is not linked to cooling rate gradient in the bulk, which has been found negligible once bainite transformation occurs, but more likely to limited and local chemical composition heterogeneities.

A.II.4.c Conclusions

This benchmark has given a linear relationship with an accuracy of ± 0.015 on f_{γ} . This equation is considered valid for all chemical variations around the reference steel grade studied in the present manuscript with the exception of microstructures presenting any allotriomorphic ferrite. In this last case, the linear relationship tends to over-evaluate the austenite content.

A.III Measurement of grain and packet size

A.III.1 Measurement of the primary austenite grain size

A.III.1.a Literature survey

Garcia de Andrés et al. focused on the best way to measure the PAGS in medium-carbon micro-alloyed steels [208;209]. Chemical etchants may be able to reveal the prior-austenite grain boundaries because the chemical potential of grain boundaries is slightly higher than that of the crystal grains. An appropriate chemical etchant can reveal that small difference in potential. Among all the investigated chemical reagents shown in Table 38, only three (E1, E2 and E3) give positive results on samples tested by Garcia de Andrés et al.

Tag	Description
E1	Saturated aqueous picric acid + sodium tridecylbenzene sulfonate (40% by weight) as a wetting agent
E2	100mL of distilled H ₂ O + 2g of picric acid (C ₆ H ₃ N ₃ O ₇) + 50 mL of sodium alkylsulfonate ("Teepol") + drops of HCl. The number of HCl drops varies between 6 and 12
E3	2% Nital solution (2mL HNO ₃ + 98 mL of ethanol C ₂ H ₅ OH)
E4	Villela's reagent: 1g of picric acid + 5mL of HCl + 100mL of ethyl alcohol
E5	2mL of Br + 100mL of methyl alcohol + drops of HCl
E6	Werner's etchant: 3g of picric acid + 100mL of xylene + 10mL of ethyl alcohol
E7	Picral: 1g of picric acid + 100mL of ethyl alcohol + drops of HCl
E8	Picral + Nital

Table 38: Chemical etchants investigated by Garcia de Andrés et al. [208].

However, they reported that thermal etching provided better results compared to chemical etching. The method of thermal etching consists in directly revealing the austenite grain boundaries during the austenitization stage using a prepolished sample. Grooves, resulting from the equilibration of the triple junction between the grain boundary and the free surface, appear at the intersections of austenite grain boundaries with the polished surface when the sample is exposed to a high temperature in an inert atmosphere. These grooves decorate the austenite grain boundaries and make them visible at room temperature in the light optical microscope. This equilibrium is set up almost instantaneously at high temperatures and so the free surface, adjacent to the line where the grain boundary emerges, becomes tightly curved as in Figure 129.

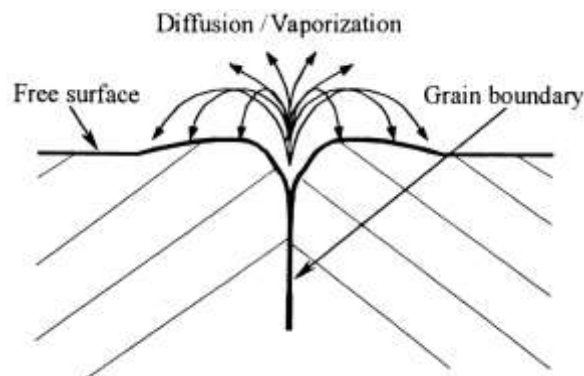


Figure 129: Groove formed at the intersection of a free surface with a grain boundary. After [209].

This method is quick and practical because no metallographic preparation is required after the heat treatment and it is not necessary to have a martensitic final microstructure, as in conventional methods. However, at very high austenitization temperatures, the grooves that reveal the austenite grain boundaries can interfere with the migration of austenite grain boundary, producing serrated migration of the grain boundaries on the polished surface and the presence of ghost traces. Nevertheless, measurements of the AGS on the surface proved to be similar to measurements in the bulk of the sample using chemical etching and the difficulties of AGS measurement caused by the presence of these traces can be avoided by quenching the sample after austenitization. However this method is not applicable for samples which need a specific geometry and/or which are deformed during heat treatment (hot torsion or dilatometric samples).

An electron back-scatter diffraction-based technique has been developed to measure the PAGS prior to transformation by post processing of the EBSD data. This technique is based on the neighbour-to-neighbour method developed for instance by Humbert et al. [210;211]. However, even if this technique works satisfactorily for Ti and Zr alloys, it is not necessarily the case for bainitic or martensitic steels in which the final products are highly deformed and the relationship between parent and product phases is generally not accurately known. Indeed, in this case, the prior austenite grain size may be largely overestimated: the reconstructive map is completely uniformly coloured, colours depending on the orientation of the parent crystal, as illustrated in Figure 130(b).

To overcome the limits of the neighbour-to-neighbour method, Cayron et al. [16] developed a new method based on the theoretical groupoid structure formed by the variants and their operators. Reconstructed maps obtained with this method are very realistic as shown in Figure 130(c): only a few small martensitic grains remain isolated, and one may observe convex and straight boundaries between the prior reconstructed austenitic grains as well as many triple grain junctions, which is usual in classical metallography. In this case, the colour chosen for each parent grain only corresponds to the colour of one of its daughter grains. However, no comparisons with PAGS obtained by chemical or thermal etching have been performed on the studied steel (16MND5-R).

The two methods overviewed previously assume a rational orientation relationship (OR) between the parent and product phases, such as Kurdjumov-Sachs or Nishiyama-Wasserman relationships for fcc to bcc transformation. The method recently developed by Miyamoto et al. [15] uses an experimentally determined OR between the product and parent phase. Local austenite orientation can be reconstructed from non-austenitized bainite structure with errors of 1.7° and 1.0° at spatial resolutions of 5 and 20 μm respectively. The error about angles is further reduced to be less than 0.5° when an analysis area is extended to a whole austenite grain. Application of this reconstruction method to the bainite structure transformed from deformed austenite has clarified that the variation in grain shape and deformation texture of parent austenite can be well reconstructed.

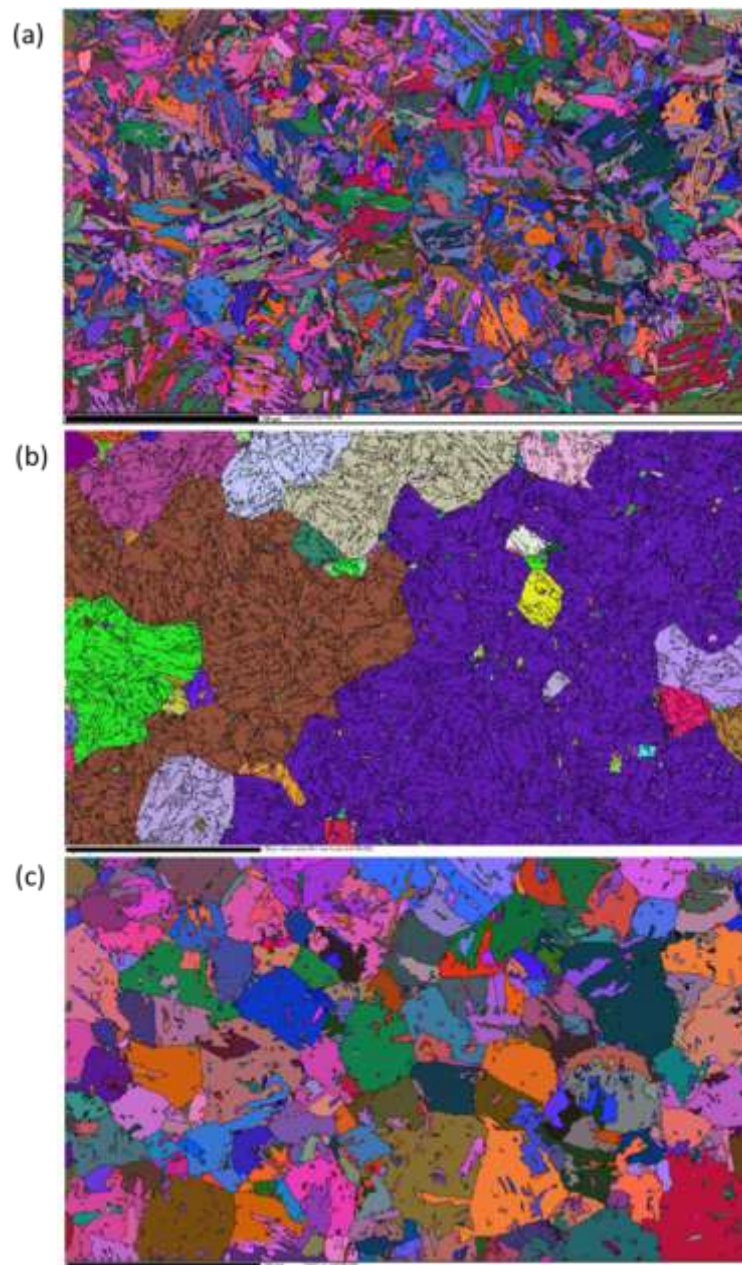


Figure 130: Automatic parent grain reconstruction for the 16 MND5-R martensitic steel assuming a Nishiyama-Wasserman orientation relationship between austenite and martensite. (a) Original EBSD map of the martensitic grains. (b) Reconstruction of the parent grains from the neighbour-to-neighbour method with a tolerance of 3° . (c) Reconstruction of the parent grains from the theoretical groupoid structure method. After [16]. The scale-bar represents 100 μm .

Scientists from the LEM3 have also improved their calculation of PAGES using EBSD since 2002. Their new approach is described by Germain et al. [17] as a two steps calculation. In the first step, different sets of neighbouring crystallographic domains of the product map are identified; each set must contain at least four variants that unambiguously determine a parent orientation with a low tolerance angle. The second step uses the previously identified set to collect other compatible variants in their surrounding but with a higher tolerance angle. This method was proved to give satisfactory results when applied to steels, especially when additional semi-automated correction and completion are proposed to improve the reconstruction at ambiguous locations (locations where product phase shares orientation relationships with more than one possible parent, each consistent with its close neighbourhood). They list the main reasons of the occurrence of ambiguous locations as: the specificity of the OR and the high symmetry of the phases; the high fraction of annealing twins in austenite; and, finally, well-known variant selection mechanisms.

However, we do not have a free and as wanted access to this kind of EBSD data processing. We believe that the low number of bainitic ferrite packets per prior austenite grain, due to the coarse microstructure inheritance after slow still air cooling, will not allow to find enough variants to assure a reliable result. Moreover the non-negligible amount of MA constituent and martensite may generate additional errors (poor confidence index).

In view of this short bibliographic survey, chemical etching has been chosen to reveal the PAGS. Chemical reagents E1 and E2 in Table 38 are really close in composition to the well-known Béchet & Beaujard etching. The protocol has thus been built around the Béchet & Beaujard etching.

A.III.1.b Protocol

The sample has been polished down to 3 μ m diamond paste. Then, 2 cycles of polishing using 1 μ m diamond paste, colloidal silica (30-45s) and etching with Picral 4% (6-8s) have been realized. Finally, the sample has been polished using 1 μ m diamond paste, colloidal silica (30-45s) and etched with Béchet & Beaujard reagent. Béchet & Beaujard reagent is a saturated aqueous solution of picric acid. In order to improve the efficiency of the reagent, 2-3 drops of HCl and 5ml of a wetting agent are added for every 100ml of solution. The sample has to be fully immersed during 4-5min, polished face placed vertically. The use of a magnetic agitator or of an ultrasonic bath is required.

After checking with light microscopy, if the bainitic (or martensite) microstructure is more revealed than the primary austenite grain boundaries, the sample has to be polished very slightly using 1 μ m diamond paste and re-immersed into the Béchet & Beaujard solution for 4-5min. This last step has to be repeated until the primary austenite grain boundaries are sufficiently visible.

Using light microscopy, an adapted magnification has to be chosen in order to observe the smallest grains and to include the biggest grains within a picture. In our case, a x200 magnification was the best suited as shown in the example of Figure 131a from the 0Ti laboratory heat after forging into a bar of 35x35mm² in section. However, in some cases, a x500 magnification has been used because no exploitable picture could be taken using a x200 magnification.

Then, several pictures have been taken in order to ensure statistical significance of the results (an average of 176 primary austenite grains were quantified for each material and processing condition).

A.III.1.c Image processing

Using GIMP software, grain boundaries are manually identified and drawn on a numerical stack for each light microscopy picture (Figure 131b). Even with a proper realization of polishing and etching, it is still difficult to obtain the totality of the grain boundaries and it is sometimes necessary to close some grains more or less arbitrarily. These stacks are transformed into black and white pictures (Figure 131c) without any change in total number of pixels.

The obtained pictures are then used in Neosis image analysis software. Area and some other shape parameters of each grain are measured according to the existing procedure available in Gandrange R&D centre. Attention should be paid to the selection of the scale corresponding to current magnification. Incomplete primary austenite grains at the edge of the picture are excluded from measurements. This is why it is so important to choose a magnification in which the biggest grain can be contained within the picture.

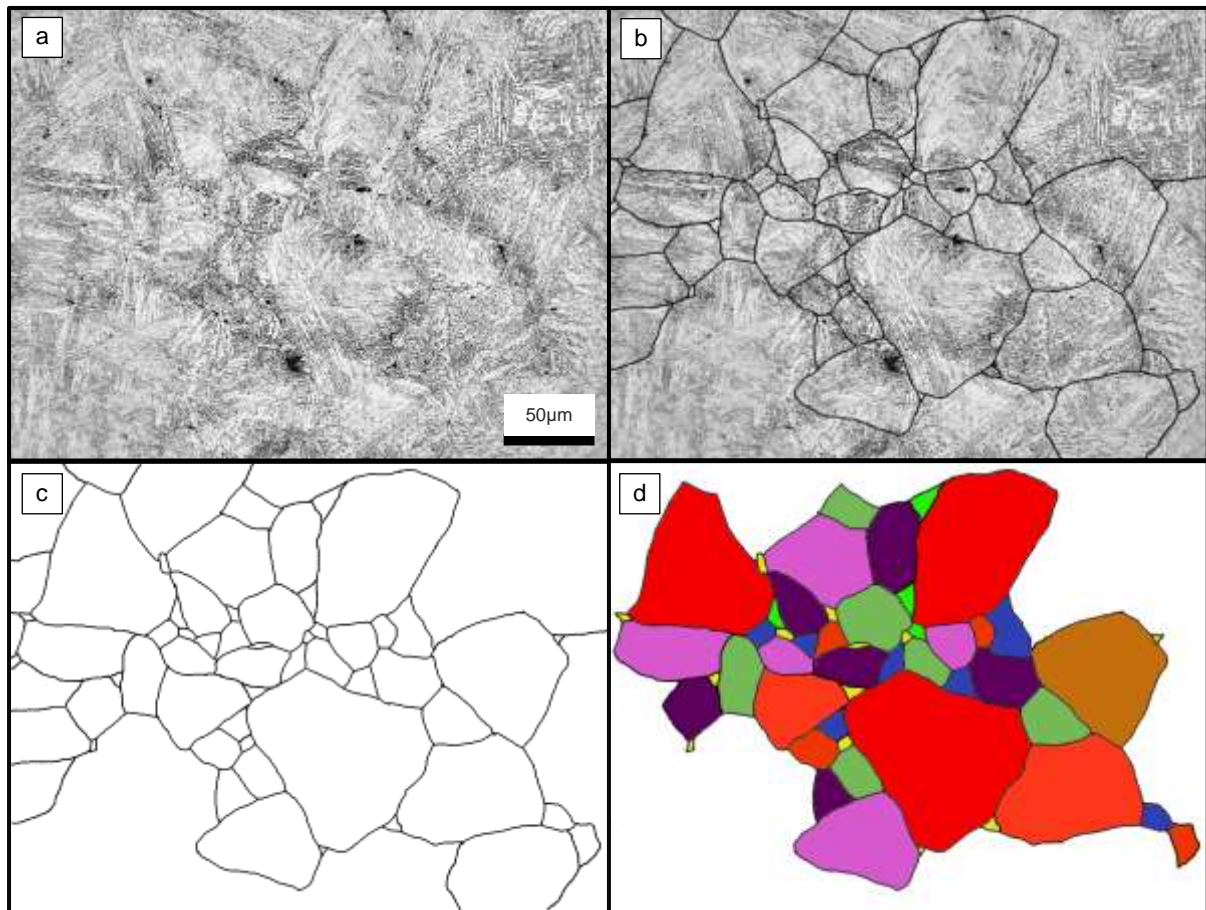


Figure 131: (a) Picture from 35x35mm² 0Ti after etching following the procedure described in text. (b) Same picture with a numerical stack in which primary austenite grain boundaries have been highlighted in black. Uncertain grain boundaries are not highlighted. (c) Numerical stack only. (d) Picture showing in colour grains that have been taken into account for calculation.

Measurements can be further processed directly on Neosis software or exported on Excel. A cleaning step is realized in order to remove all grains below 120µm² that are originated from drawing defects or not well-defined interspace between grains (in yellow in Figure 131d). This size criterion is the same as the one used in the measurement of the effective bainitic packet size to eliminate blocks of residual phases that are encountered between bainitic packets (see in the following part).

The main results of this characterization are the distribution in size and number, as well as the average grain area. The equivalent diameter has been chosen to reflect the grain size. Errors related to the average grain size that are shown in Tables of the present thesis are the standard deviations calculated on distribution of the equivalent diameter in size.

A.III.2 Measurement of the effective bainite packet size

A.III.2.a Protocol

Analysed samples have been prepared with a conventional mirror polishing down to 1µm diamond paste. Two cycles of very slight Nital2% etching (less than 3s) and 1µm diamond paste polishing have been realized to remove all cold working generated earlier during the mechanical polishing. Final step of the preparation is a polish using colloidal silica (30-45s).

As discussed earlier in this appendix, we initially realized EBSD mapping using an acquisition step size of 250 nm that was found not suitable for phase quantification and bainitic ferrite packet size measurement. The main concern for achieving the objective of bainitic ferrite packet size measurement was the number of investigated bainitic ferrite packets which depends on the total acquisition area. The effective bainite packet size

measurement has been realized on 2 different maps of $500 \times 500 \mu\text{m}^2$ each from close regions. The resulting area is of $500,000 \mu\text{m}^2$ which is about 9 times the area used on the first trial realized on reference steel ($57,720 \mu\text{m}^2$). We used an acquisition step size of $1 \mu\text{m}$, as bainitic ferrite packet size was estimated using SEM to several dozens of micrometres. Moreover, indexation is only realized on BCC pattern as austenite films between laths will not be considered.

A.III.2.b Pre-processing

Maps are post-processed using OIM Analysis software. A first clean-up of data is realized in order to erase all small microstructural elements of secondary phase that are present in bainitic ferrite packet (clean-up by grain dilation, tolerance angle 5° , min size $20 \mu\text{m}^2$, multirow 0, single iteration). These elements, as thin austenite films or MA islands, are represented in the maps by small groups of pixels with scattered orientation and bad confidence index.

No acceptable size distribution or average size of bainitic packet can be obtained from the resulting mapping without an additional step of post-processing. Indeed large residual islands, called here blocks, which are mainly composed of martensite-rich MA constituent and martensite, have first to be excluded from the calculation of average bainite packet size. These blocks are generally represented by groups of pixels with no-scattered orientation but still with bad confidence index. As each sample present different confidence index or image quality levels, the use of a unique thresholding value for all of them is not possible. In order to produce the most comparable results between two samples, a size criterion has been used to separate blocks of secondary phases from bainitic ferrite packets.

Two combined approaches have been used to establish the size criterion:

1. Some direct area measurements of identified secondary phases using SEM and Nital2% etching realized on several variants of chemical composition (to increase the variety of secondary phases observed).
2. A statistical study of secondary constituent data obtained from quantification using light microscopy with LePera etching realized on as-forged reference steel.

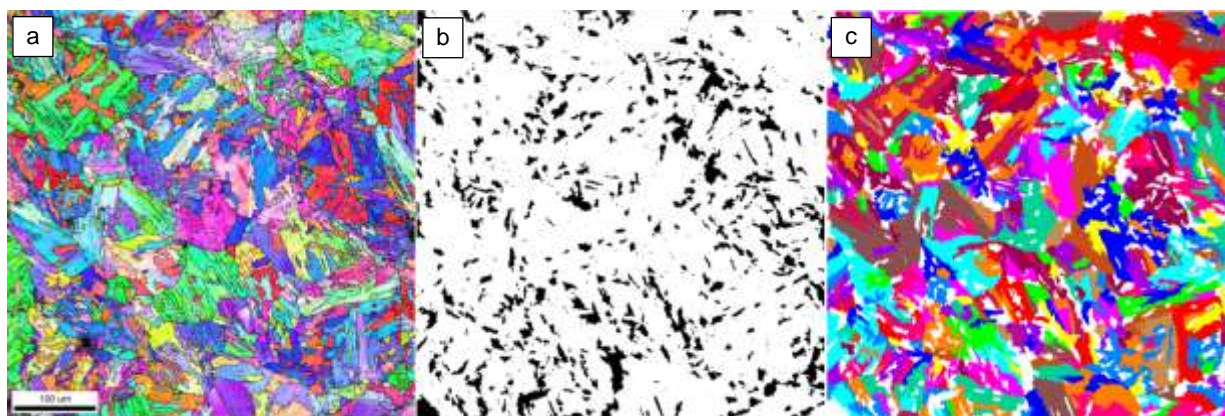


Figure 132: (a) Inverse Pole Figure map, (b) picture used to calculate the area fraction removed from initial EBSD mapping, tolerance angle of 15° , (c) resulting EBSD mapping that will be used for packet size distribution and calculation of the average packet size.

From SEM observations, the smallest blocks of secondary phases (which contain some martensite at their centre) localized in between apparently adjacent bainitic ferrite packets, have an area around $5 \mu\text{m}^2$ but a noticeable part of these elements exceed $20 \mu\text{m}^2$ in area. The average area of these blocks is about $21 \mu\text{m}^2$ but some blocks can be bigger than $100 \mu\text{m}^2$. So, we used a size criterion of $120 \mu\text{m}^2$ to eliminate those blocks from the EBSD maps. As shown in the example (Figure 132), most of these blocks are located along the primary austenite grain boundaries. The resulting area fraction removed from the mapping in

this case is 0.14 for a tolerance angle of 15°. As expected, this fraction is lower than the total fraction of MA constituent, martensite and austenite (0.30) as it mainly represents only the biggest microstructural elements that are trapped between the bainitic ferrite packets and it misses all smaller ones that are present inside these packets.

A.III.2.c Processing

The grain data file is created using OIM Analysis software and exported in Excel. Data that have been collected for each packet are the location of the packet (on edge or not), area in μm^2 , diameter in μm , ASTM, aspect ratio, major axis in μm , minor axis in μm , orientation in ° and average internal misorientation °. Packets located on edges are excluded from the calculation. Errors regarding the bainitic packet size that are exhibited in the Figures and Tables of the present manuscript are the standard deviation of the distribution.

A.IV Precipitation characterization

Two different characterizations of precipitation have been realized in the present work. The first one is a selective dissolution, followed by a mass-spectrometry analysis of the obtained residues. The second one is a FEG-SEM observation of carbon replicas, followed by image analysis of the obtained pictures. The first characterization has been totally realized in Maizières R&D centre, using procedure well-mastered for such kind of precipitates. Only the second one is described here.

A.IV.1 Carbon replica analysis

A.IV.1.a Protocol

Sample preparation is the following:

- Sample has encountered a typical mirror polishing down to 0.25 μm diamond paste.
- Sample is etched with Villela etching (2g of picric acid in 95ml of ethanol and 5ml of hydrochloric acid). Immersion time is only about a few seconds (3-4s). This step allows making the particle apparent on the prepared surface.
- Then the sample is immediately washed using water plus ethanol and blown dried in hot air.
- Un-prepared surfaces are hidden using technical adhesive rubber.
- Several layers of carbon are deposited on the prepared surface until the surface seems homogenously covered with a dark-blue tinted layer. The final thickness of the carbon layer is not known. Particles are then trapped between the steel and the carbon layer.
- The layer is then scratched with a cutting device in order to generate a matrix with squares from 1 to 2mm in size.
- Adhesive rubber is removed.
- The sample is immersed in Villela etchant for 10-15min. The reagent seals the scratches and then starts to etch the steel under the carbon layer but not the carbon layer. Thus, the carbon layer tends to become free, with particles still being trapped on its surface.
- Once this tendency is observed, the whole sample is immersed in an ethanol bath and is shaken softly. Several carbon replicas are now completely removed from the steel and are floating in the ethanol bath. If there is still carbon deposit at the surface of the sample, this one can be immersed again in the Villela etchant for some minutes.
- Carbon replicas have a tendency to retract on themselves once free. Some water teardrops in the ethanol solution can help to avoid this problem.

- Carbon replicas are then put on copper grids using a plier. Copper grids and associated carbon replica being afterward stocked on absorbent paper in separate box.

Observation of the obtained carbon replicas has been realized on FEG-SEM equipped with EDX analyser. Carbon replicas were mounted on a specific sample holder four by four. After manual recognition of the carbon replica surface, an automatic mapping of this one is performed. The manual recognition is performed first to verify that the carbon replica is not on the wrong side, secondly to find a suitable area to realize the mapping, and finally to identify the different kinds of particles that are present on the surface. After this recognition, it seems that an important part of small particles from 40 to 80 μm in size have been snatched from the surface.

The automatic mapping has been realized with a magnification of 10000. This magnification allows the observation of all details with a size higher than 12nm (1 pixel, 144nm²) while keeping a relatively significant area of analysis in concern of particles characterization (12.6x10.9 μm^2). 25 pictures have been taken for each sample and at least 23 pictures have been analysed (i.e. at least 3159 μm^2). Indeed, some pictures have to be removed due to macro-cracks on their surface.

A.IV.1.b Pre-processing

Pre-processing has been realized using ImageJ software, using the following macro in italics (x being the name of the picture):

- Step 1: brightness homogenization using Gaussian Blur.

```
a=getTitle();
rename("x.tif");
run("Duplicate...", "title=x-1.tif");
run("Gaussian Blur...", "sigma=60");
image Calculator("Subtract create 32-bit", "x.tif", "x-1.tif");
close("x.tif")
close("x-1.tif")
```

- Step 2: contrast enhancement in 32bit (only necessary if small holes are taken into account), then picture conversion in 8bit.

```
run("Enhance Contrast...", "saturated=0.4");
run("8-bit");
```

- Step 3: thresholding. If the small holes are not considered as missed particles (see chapter 5), the thresholding windows must to be narrower than in this example (220-255 for instance). In both cases, element coming from the bright relief edges present on the surface of carbon replicas are still present on the obtained pictures as well as some noises and artefacts.

```
setAutoThreshold ("Default dark");
//run("Threshold...");
setThreshold(160, 255);
setOption("BlackBackground", false);
run("Convert to Mask");
close("result of x.tif")
```

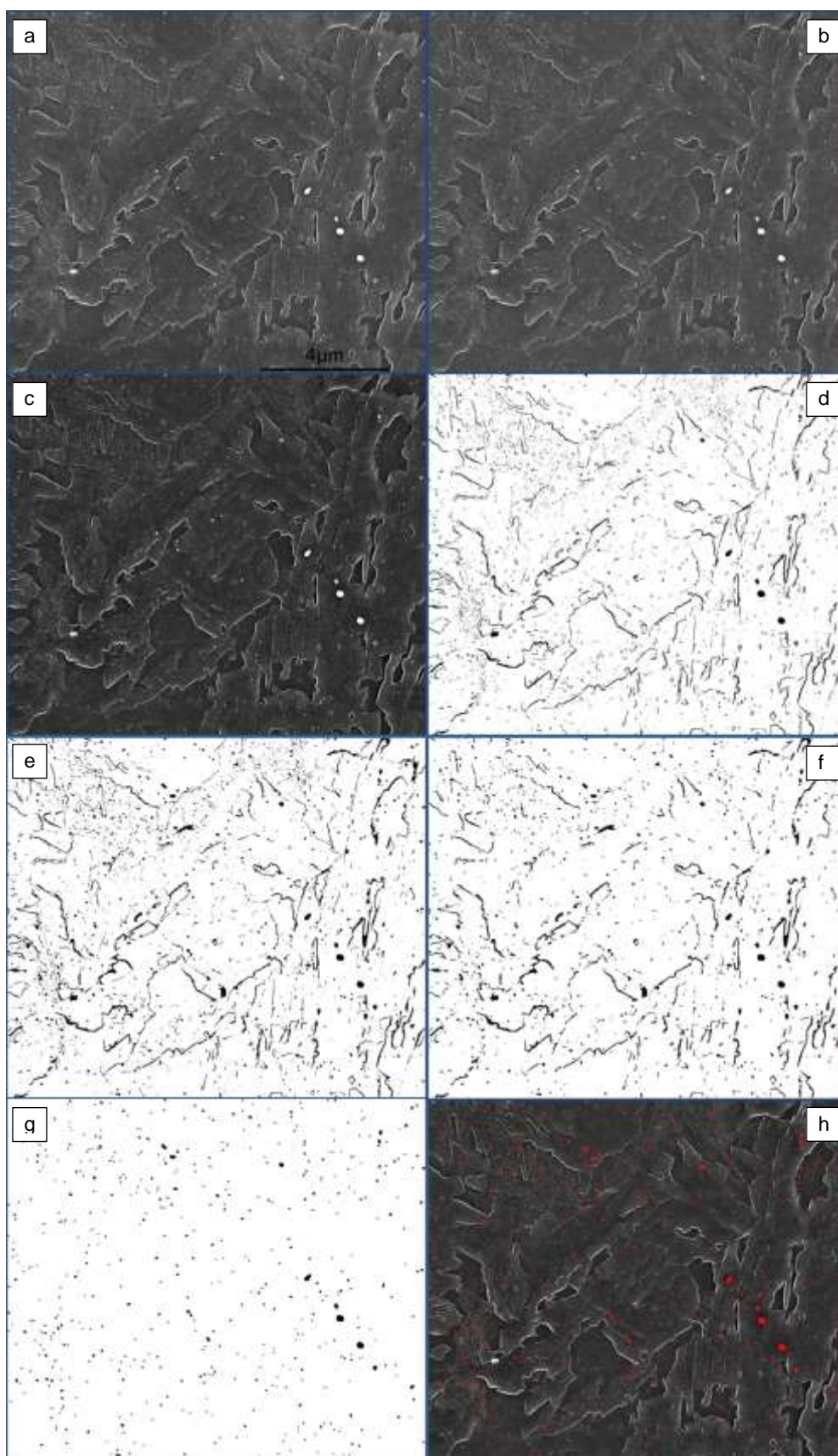



Figure 133: Example of image pre-processing and processing on carbon replica. Small holes between 40nm and 80nm have been considered as particles. (a) initial picture / (b) after step 1, brightness homogenization / (c) after step 2, contrast enhancement / (d) after step 3, thresholding / (e) after step 4, holes closing and filling / (f) after step 5, noise removal / step 6, length scale attribution / (g) after step 7, final picture for image analysis, effect of size and shape criteria / (h) reconstructed image with precipitates in red.

APPENDIX A – METHODS OF MICROSTRUCTURAL CHARACTERIZATION

- Step 4: only realized if small holes have been taken into consideration. This step simply closes and fills these holes (that will be considered as particles by the software afterward).

```
run("Close-");  
run("Fill Holes");
```

- Step 5: remove background noise (=isolated pixels).

```
run("Despeckle");
```

- Step 6: attributes a length scale to the picture

```
run("Set Scale...", "distance=325 known=4000 pixel=1 unit=nm");  
rename(a);
```

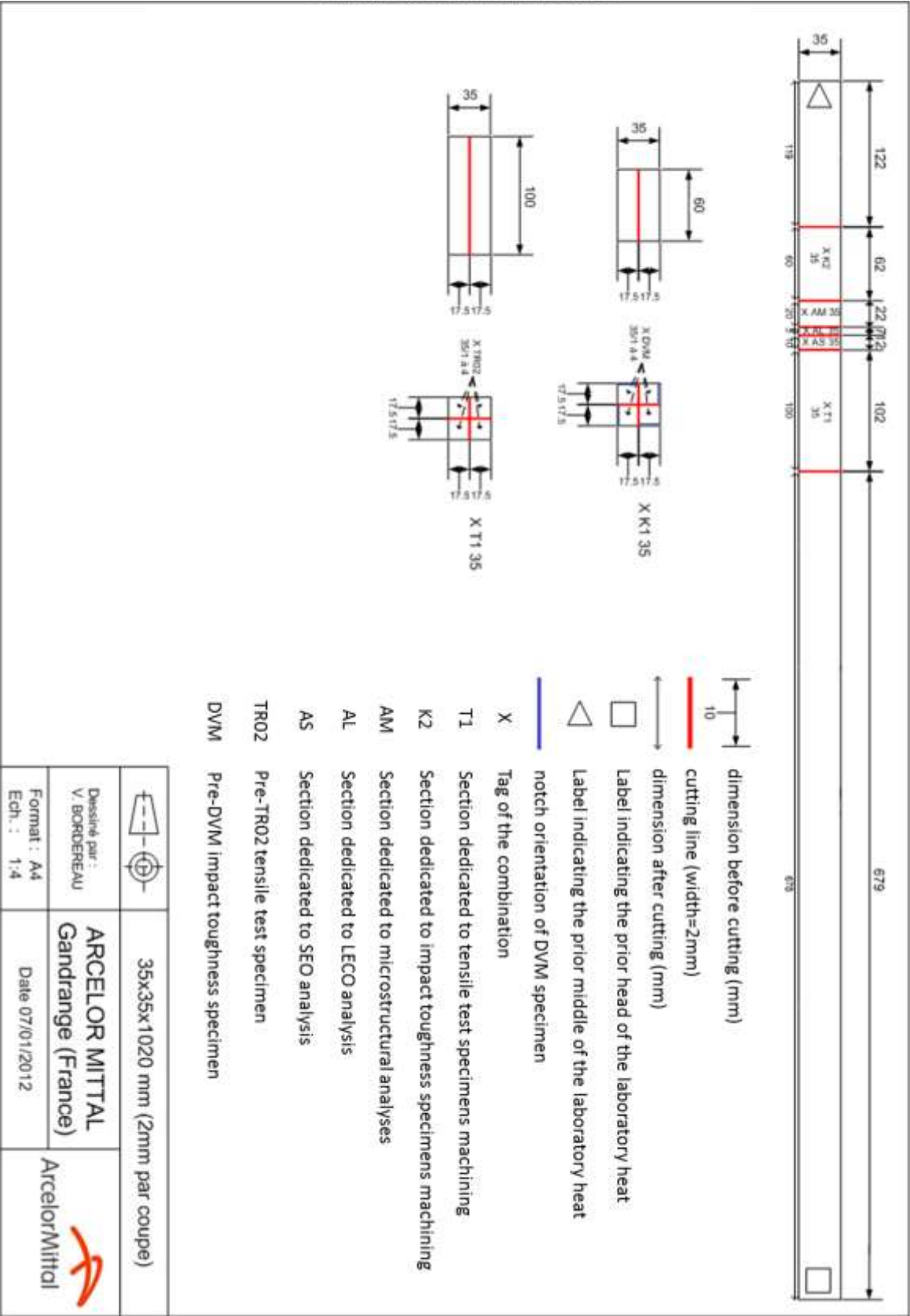
A.IV.1.c Processing

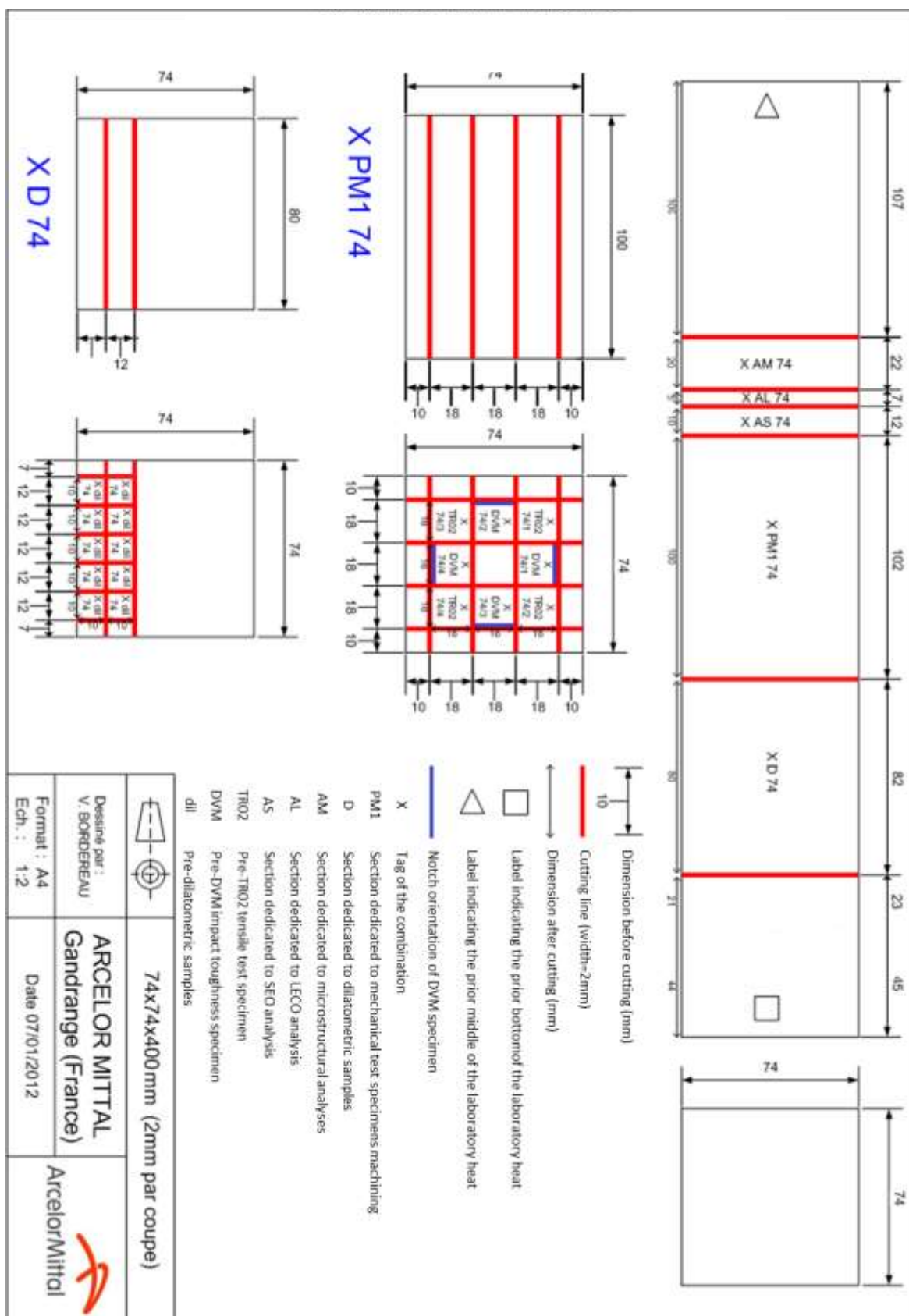
Step7: the data acquisition is realized meanwhile the reference picture in black and white is created. Most of artefacts and the element coming from the bright relief edge are removed using a size and a shape criterion respectively. Only the particles with an area higher than 1200nm² (size of 35nm or a radius of 20nm) and a circularity higher than 0.7, are taken into account. The size criterion has been chosen according to the recognition observation, as the smallest particles that have been identified were about 40nm in size.

```
run("Analyze Particles...", "size=1200-Infinity circularity=0.70-1.00 show=Masks");
```

Two parameters are obtained from image analysis: the area of each particle and the area fraction.

APPENDIX B – MACHINING PLAN





REFERENCES

- [1] C. Keul, V. Wirths and W. Bleck, "New bainitic steels for forgings", Archives of Civil and Mechanical Engineering, vol. 12, pp. 119-125, 2012.
- [2] H. Bhadeshia, Bainite in steels : transformations, microstructure and properties, London: The institute of Materials, 2000.
- [3] Y. Ohmori and T. Maki, "Bainitic Transformation in View of Displacive Mechanism", Materials Transactions JIM, vol 32, pp. 631-641, 1991.
- [4] M. Hillert, "The Nature of Bainite", ISIJ International, vol. 35, pp. 1134-1140, 1995.
- [5] H. Aaronson, W. Reynolds, G. Shiflet and G. Spanos, "Bainite Viewed Three Different Way", Metallurgical Transactions A, vol. 21, pp. 1343-1380, 1990.
- [6] B. Bramfitt and J. Speer, "A perspective on the morphology of bainite", Metallurgical Transactions A, vol. 21, pp. 817-829, 1990.
- [7] S. Zajac, J. Komenda, P. Morris, P. Dierickx, S. Matera and F. Penalba Diaz, "Quantitative structure-property relationships fo complex bainitic microstructures", Rapport EUR 21245, Commision européenne, 157 p., 2005.
- [8] G. Thewlis, "Classification and quantification of microstructures in steels", Materials Science and Technology, vol. 20, pp. 143-160, 2004.
- [9] M. Takahashi and H. Bhadeshia, "Model for Transition from upper to lower bainite", Materials Science and Technology, vol. 6, pp. 592-603, 1990.
- [10] S. Zajac, V. Schwinn and K.-H. Tacke, "Characterization and quantification of complex bainitic microstructure in high and ultra-high strength linepipe steels", Materials Science Forum, vol. 500-501, pp. 387-394, 2005.
- [11] E. Kozeschnik and H. Bhadeshia, "Influence of silicon on cementite precipitation in steels", Materials Science and Technology, vol. 24, pp. 343-347, 2008.
- [12] F. Caballero, C. Capdevila, J. Chao, J. Cornide, C. Garcia-Mateo, H. Roelofs, S. Hasler and G. Mastrogiacomo, "Influence of bainite morphology on impact toughness of continuously cooled cementite-free bainitic steels", Materials Science and Technology, vol. 28, pp. 95-102, 2012.
- [13] L. Habraken, "Sur la transformation bainitique dans les aciers", Revue de Métallurgie, vol. 53, pp. 930-944, 1956.
- [14] L. Habraken and M. Economopolus, Transformation and Hardenability in Steels, Climax Molybdenum, 1967.

BIBLIOGRAPHY

- [15] G. Miyamoto, N. Iwata, N. Takayama and T. Furuhashi, "Reconstruction of parent austenite grain structure based on crystal orientation map of bainite with and without ausforming", ISIJ International, vol. 7, pp. 1174-1178, 2011.
- [16] C. Cayron, B. Artaud and L. Briottet, "Reconstruction of parent grains from EBSD data", Materials Characterization, vol. 57, pp. 386-401, 2006.
- [17] L. Germain, N. Gey, R. Mercier, P. Blaineau and M. Humbert, "An advanced approach to reconstructing parent orientation maps in the case of approximate orientation relations: Application to steels", Acta Materialia, vol. 60, pp. 4551-4562, 2012.
- [18] Q. Wang, C. Zhang, W. Xu, S. Zhao, X. Zhao and Z. Yan, "Refinement of Steel Austenite Grain Under an Extremely High Degree of Superheating", Journal of Iron and Steel Research, International, vol. 14, pp. 161-166, 2007.
- [19] T. Wada and G. Eldis, "Transformation Characteristic of 2.25Cr-1Mo Steel, Application of 2.25Cr-1Mo Steel for Thick-wall Pressure Vessels", in : Application of 2 ¼ Cr-1 Mo steel for thick wall pressure vessels, ASTM STP 755, ed. G.S. Sangdahl, M. Semchyshen, ASTM, pp. 343-362, 1982.
- [20] S. Kimmins and D. Gooch, "Austenite memory effect in 1Cr-1 Mo-O-75V(Ti, B) steel", Metal Science, vol. 17, pp. 519-532, 1983.
- [21] E. Bain, Alloying element in steels, ASM, 1939.
- [22] G. Totten and M. Howes, Steel Heat Treatment Handbook, M. Dekker, 1997.
- [23] R. Hehemann, K. Kinsman and H. Aaronson, "A Debate on the Bainite Reaction", Metallurgical Transactions, vol. 3, pp. 1077-1093, 1972.
- [24] C. Zener, "Kinetics of the decomposition of Austenite", Transactions of the AIME, vol. 167, pp. 550-583., 1946.
- [25] R. le Houillier, G. Bégin and A. Dubé, "A study of the peculiarities of austenite during the formation of bainite", Metallurgical Transactions, vol. 2, pp. 2645-2653, 1971.
- [26] H. Bhadeshia and D. Edmonds, "Tempered martensite embrittlement: role of retained austenite and cementite", Metal Science, vol. 13, pp. 325-334, 1979.
- [27] M. Hillert, L. Höglund and J. Agren, "Role of carbon and alloying elements in the formation of bainitic ferrite", Metallurgical and Materials Transactions A, vol. 35A, pp. 3693-3700, 2004.
- [28] ASM Handbook, Casting, vol. 15, ASM International, 1991.
- [29] J. Duy, M. Strangwood and C. Davis, "Effect of TiN Particles and Grain Size on the Charpy Impact Transition Temperature in Steels", Journal of Materials Science and Technology, vol. 28, pp. 878-888, 2012.

BIBLIOGRAPHY

- [30] A. Ghosh, A. Ray, D. Chakrabarti and C. Davis, "Cleavage initiation in steel : Competition between large grains and large particles", Materials Science and Engineering A, vol. A561, pp. 126-135, 2013.
- [31] A. Ghosh, A. Sahoo, M. Ghosh, R. Ghosh and D. Chakrabarti, "Effect of microstructural parameters, microtexture and matrix strain on the Charpy impact properties of low carbon HSLA steel containing MnS inclusions", Materials Science and Engineering, vol. A 613, pp. 37-47, 2014.
- [32] J. Gregg and H. Bhadeshia, "Ti-rich mineral phases and the nucleation of bainite", Metallurgical and Materials Transactions A, vol. 25A, pp. 1603-1611, 1994.
- [33] I. Madariaga and I. Gutierrez, "Nucleation of acicular ferrite enhanced by the precipitation of CuS on MnS particles", Scripta Materialia, vol. 37, pp. 1185-1192, 1997.
- [34] C. Ouchi, T. Sampei and I. Kozasu, "The effect of hot rolling condition and chemical composition on the onset temperature of γ - α transformation after hot rolling", Transactions ISIJ, vol. 22, pp. 214-222, 1982.
- [35] M. Cohen and S. Hansen, "On the fundamentals of HSLA steels", in : HSLA Steels : Metallurgy and Applications, Beijing, ed. J.M. Gray, T. Ko et al., ASM, pp. 61-72, 1985.
- [36] L. Meyer, F. Heisterkamp and W. Mueschenborn, "Columbium, titanium and vanadium in normalized thermo-mechanically treated and cold rolled steels", in : Microalloying '75, Union carbide corporation, pp. 153-167, 1977.
- [37] R. Priestner and M. S. Biring, "Transformation of low-carbon austenite after small plastic strains", Metal Science Journal, vol. 7, pp. 60-64, 1973.
- [38] S. Liu and G. Zhang, "The Effect of Mn and Si on the Morphology and Kinetics of the Bainite Transformation in Fe-C-Ti Alloys", Metallurgical Transactions A, vol. 21A, pp. 1509-1515, 1990.
- [39] H. Grabke, K. Hennesen, R. Moller and W. Wei, "Effects of manganese on the grain boundary segregation, bulk and grain boundary diffusivity of P in ferrite", Scripta Metallurgica, vol. 21, pp. 1329-1324, 1987.
- [40] N. Usui, K. Sugimoto, E. Nishida, M. Kobayashi and S. Hashimoto, CAMP-ISIJ, vol. 3, pp. 2013-2014, 1990.
- [41] K. Sugimoto, K. Nakano, S. Song and T. Kashima, "Retained austenite characteristics and stretch-flangeability of high-strength low-alloy TRIP type bainitic sheet steels", ISIJ International, vol. 42, pp. 450-455, 2002.
- [42] P. Manohar and T. Chandra, "Continuous cooling transformation behaviour of high strength microalloyed steels for linepipe applications", ISIJ International, vol. 38, pp. 766-774, 1998.

BIBLIOGRAPHY

- [43] A. Salak, M. Selecka and H. Danninger, Machinability of powder metallurgy steels, Cambridge International Science Publishing, 2005.
- [44] C. Sims and F. Dahle, "Effect of aluminium on the properties of medium carbon cast steel", Transactions of the American Foundrymen's Ass., vol. 46, pp. 65-132, 1938.
- [45] K. Oikawa, H. Ohtani, K. Ishida and T. Nishizawa, "The control of the morphology of MnS inclusions in steel during solidification", ISIJ International, vol. 35, pp. 402-408, 1995.
- [46] D. Hilty and J. Farrel, "Modification of inclusions by Ca", Iron Steelmaker, vol. 2, pp. 17-22, 1975.
- [47] G. Shiflet, H. Aaronson and J. Bradley, "On the influence of carbide formation upon the growth kinetics of proeutectoid ferrite in Fe-C-X alloys", Metallurgical Transactions A, vol. 12A, pp. 1743-1750, 1981.
- [48] V. Ollilainen, W. Kasprzak and L. Holappa, "The effect of silicon, vanadium and nitrogen on the microstructure and hardness of air-cooled medium carbon low alloy steels", Journal of Materials Processing Technology, vol. 134, pp. 405-412, 2003.
- [49] M. Cai, H. Ding, J. Zhang, L. Li, X. Li and L. Du, "Transformation behavior of low carbon steels containing two different Si contents", Journal of Iron and Steel Research, International, vol. 16, pp. 55-60, 2009.
- [50] R. Larn and J. Yang, "The Effect of Compressive of Austenite on the Bainitic Ferrite Transformation in Fe-Mn-Si-C Steels", Materials Science and Engineering A, vol. 278, pp. 278-291, 2000.
- [51] J. Wang, P. Van der Wolk and S. Van der Zwaag, "On the influence of alloying elements on the bainite reaction in low alloy steels during continuous cooling", Journal of Materials Science, vol. 35, pp. 4393-4404, 2000.
- [52] H. Bhadeshia and D. Edmonds, "The Bainite Transformation in a Silicon Steel", Metallurgical Transactions A, vol. 10A, pp. 895-907, 1979.
- [53] K. Tsuzaki, C. Nakao and T. Maki, "Formation Temperature of Bainitic Ferrite in Si-Containing Steels", Materials Transactions JIM, vol. 32, pp. 658-666, 1991.
- [54] V. Miihkinen and D. Edmonds, "Microstructural examination of two experimental high-strength bainitic low-alloy steels containing silicon", Materials Science and Technology, vol. 3, pp. 422-431, 1987.
- [55] A. Zarei-Hanzaki, P. Hodgson and S. Yue, "Retained Austenite Characteristics in Thermomechanically Processed Si-Mn Transformation-Induced Plasticity Steels" Metallurgical and Materials Transactions A, vol. 28, pp. 2405-2414, 1997.
- [56] P. Jacques, E. Girault, T. Catlin, N. Geerlofs, T. Kop, S. Van der Zwaag and F. Delannay, "Bainite transformation of low carbon Mn-Si TRIP-assisted multiphase

BIBLIOGRAPHY

- steels : influence of silicon content on cementite precipitation and austenite retention”, Materials Science and Engineering A, vol. 273-275, pp. 475-479, 1999.
- [57] Z. Tan, B. Bingzhe, H. Fang and F. Yang, “Effect of Si on the toughness of High Strength Mn-Si-Cr Series Bainitic Steels”, Materials Science Forum, vol. 475-479, pp. 213-216, 2005.
- [58] T. Suzuki, Y. Ono, G. Miyamoto and T. Furuhashi, “Effects of Si and Cr on bainite microstructure of medium carbon steels”, ISIJ International, vol 50, pp. 1476-1482, 2010.
- [59] S. Han, S. Shin, C. Seo, H. Lee, J. Bae, K. Kim, S. Lee and N. Kim, “Effect of Mo, Cr, and V additions on tensile and charpy impact properties of API X80 pipeline steels”, Metallurgical and Materials Transactions A, vol. 40, pp. 1851-1862, 2009.
- [60] S. Honjo and Y. Saito, “Numerical simulation of phase separation in Fe-Cr binary and Fe-Cr-Mo ternary alloys with use of the Cahn-Hilliard equation”, ISIJ International, vol. 40, pp. 914-919, 2000.
- [61] M. Umemoto, T. Furuhashi and I. Tamura, “Effect of austenitizing temperature on the kinetics of bainite reaction at constant austenite grains size in Fe-C and Fe-Ni-C alloys”, Acta Metallurgica, vol. 34, pp. 2235-2245, 1986.
- [62] A. Joarder and D. Sarma, “Bainite structure in 0.2C-3.6Ni steel”, Materials Transactions JIM, vol. 32, pp. 705-714, 1991.
- [63] Y. Im, Y. Oh, B. Lee, J. Hong and H. Lee, “Effect of carbide precipitation on the strength and Charpy impact properties of low carbon Mn-Ni-Mo bainitic steels.”, Journal of Nuclear Materials, vol. 297, pp. 138-148, 2001.
- [64] T. Nelson, R. Bodnar and J. Fielding, “A critical assessment of ASTM A 508 class 2 steel for pressure vessel applications”, in : Proceedings of the 32nd Mechanical Working and Steel Processing, Warrendale, pp. 323-341, 1991.
- [65] L. Norstrom and O. Vingsbo, “Influence of nickel on toughness and ductile brittle transition in low carbon martensite steels”, Metal Science, vol. 13, pp. 677-684, 1979.
- [66] W. Leslie, The physical metallurgy of steels, Mc Graw Hill, 1981, p. 302.
- [67] U. Hildebrandt and W. Dickenschied, “Plasticity and alloy softening in iron-nickel-alloys”, Acta. Metallurgica, vol. 19, pp. 49-55, 1971.
- [68] V. Sorokin, E. Vorob'eva, M. Gervas'ev and N. Adamova, “Effect of chromium and nickel content on the structure formation over the section of large forgings of Cr-Ni-Mo steels”, Metal science and heat treatment, vol. 30, pp. 661-665, 1988.
- [69] H. Jun, J. Kang, D. Seo, K. Kang and C. Park, “Effects of deformation and boron on microstructure and continuous cooling transformation in low carbon HSLA steels”

BIBLIOGRAPHY

- Materials Science and Engineering A, vol. 422, pp. 157-162, 2006.
- [70] M. Djahazi, Influence of boron distribution on precipitation and recrystallization in hot worked austenite, Thesis, McGill University: Department of Mining and Metallurgical Engineering, Montreal, Canada, 1989.
- [71] M. Ueno and T. Inoue, "Distribution of boron at austenite grain boundaries and bainitic transformation in low carbon steels", Transactions of the Iron and Steel Institute of Japan, vol. 13, pp. 210-217, 1973.
- [72] Y. Ohmori and R. Honeycombe, "The isothermal transformation of plain carbon austenite", in : Proceedings of international Conference on the Science and Technology of Iron and Steel, Tokyo, The iron and Steel Institute of Japan, Supplement of Transactions ISIJ, vol. 11, pp.1160-1165
- [73] J. Fisher, "Influence of boron on hardenability of steel", Transactions of the AIME, vol. 200, pp. 1146-1147, 1954.
- [74] P. Maitrepierre, D. Thivellier and R. Tricot, "Influence of boron on the decomposition of austenite in low carbon alloyed steels", Metallurgical Transactions A, vol. 6A, pp. 287-301, 1975.
- [75] T. Koseki, K. Amano, M. Imanaka, C. Shiga and S. Ueda, "Four transitional stages in hardenability of boron-bearing HSLA steel in direct-quenching process", in : Physical metallurgy of direct-quenched steels, ed. K.A. Taylor, S.W. Thompson et al., 1993, Minerals, Metals & Materials Society, pp. 297-310
- [76] D. Llewellyn and W. Cook, "Metallurgy of boron-treated low-alloy steels", Metals Technology, pp. 517-529, 1974.
- [77] K. Taylor, "Grain-Boundary segregation and precipitation of boron in 0.2 percent carbon steels" Metallurgical transactions A, vol. 23A, pp. 107-119, 1992.
- [78] K. Zhu, J. Drillet and M. Gouné, "Mechanisms of boron hardenability in low carbon steels", report, ArcelorMittal R&D Maizières Research SA, 2007.
- [79] B. Serin, Y. Desalos, P. Maitrepierre and J. Rofes-Vernis, "Characteristics of transformation and properties of low-carbon steels with Nb-Bs", Mémoires Scientifiques de la Revue de Métallurgie, vol. 75, pp. 365-369, 1978.
- [80] Y. Jung, H. Ueno, H. Ohtsubo, K. Nakai and Y. Ohmori, "Effect of small amounts of B, Nb and Ti additions on nucleation and growth processes of intermediates transformation products in low carbon 3% Mn steels", ISIJ international, vol. 35, pp. 1001-1005, 1995.
- [81] K. Zhu, C. Oberbillig, C. Musik, D. Loison and T. Jung, "Effect of B and B+Nb on the bainitic transformation in low carbon steels", Materials Science and Engineering A, vol. 528, pp. 4222-4231, 2011.

BIBLIOGRAPHY

- [82] T. Hara, H. Asahi, R. Uemori and H. Tamehiro, "Role of Combined Addition of Niobium and Boron and of Molybdenum and Boron on Hardenability in Low Carbon Steels" ISIJ International, vol. 44, pp. 1431-1440, 2004.
- [83] S. Watanabe and H. Ohtani, "Precipitation behavior of boron in high strength steel", Transactions of the Iron and Steel Institute of Japan, vol. 23, pp. 38-42, 1983.
- [84] H.-R. Lin and G.-H. Cheng, "Analysis of hardenability effect of boron", Materials Science and Technology, vol. 6, pp. 724-730, 1990.
- [85] T. Baker, "The role of zirconium in microalloyed steels", Materials Science and Technology, vol. 31, pp. 265-294, 2015
- [86] S.-C. Wang, "The effect of titanium and nitrogen contents on the austenite grain coarsening temperature", Journal of Materials Science, vol. 24, pp. 105-109, 1989.
- [87] C. Feng, H. Fang, Y. Zheng and B. Bai, "Mn-series low-carbon air-cooled bainitic steel containing niobium of 0.02%", Journal of Iron Steel Research, International, vol. 17, pp. 53-59, 2010.
- [88] M. Thomas and G. Michal, "The influence of niobium and Nb(C,N) precipitation on the formation of proeutectoid ferrite in low alloy steels", in : Solid-Solid Phase Transformations, ed. H.I. Aaronson et al., AIME, 1981, pp. 469-473.
- [89] X. Yuan, Z. Liu, S. Jiao, L. Ma and G. Wang, "The Onset Temperatures of γ to α -Phase Transformation in Hot Deformed and Non-deformed Nb Micro-alloyed Steels", ISIJ International, vol. 46, pp. 579-585, 2006.
- [90] T. Abe, K. Tsukada and I. Kozasu, in : "Role of interrupted accelerated cooling and microalloying on weldable HSLA steels", in : HSLA Steels : Metallurgy and Applications, Beijing, ed. J.M. Gray, T. Ko et al., ASM, pp. 103-112, 1985.
- [91] S. Hong, S. Lim, H. Hong, K. Lee, D. Shin and K. Lee, "Effect of Nb on strain induced ferrite transformation in C-Mn steel", Materials Science and Engineering A, vol. 355, pp. 241-248, 2003.
- [92] P. Manohar, T. Chandra and C. Killmore, "Continuous cooling transformation behaviour of microalloyed steels containing Ti, Nb, Mn and Mo", ISIJ International, vol. 36, pp. 1486-1493, 1996.
- [93] G. Rees, J. Perdrix, T. Maurickx and H. Bhadeshia, "The effect of niobium in solid solution on the transformation kinetics of bainite", Materials Science and Engineering A, vol. 194, pp. 179-186, 1995.
- [94] L.J. Cuddy, "The Effect of Microalloy Concentration on the Recrystallization of Austenite during Hot Deformation", in : Proc. Conf. Thermomechanical Processing of Microalloyed Austenite, Pittsburgh, pp. 129-140, 1981.

BIBLIOGRAPHY

- [95] R. Barbosa and al., in : Conf. Proc. Processing, Microstructure and Properties of HSLA Steels, Ed. A.J.DeArdo, AIME, pp. 51-61, 1988.
- [96] Y. Cao, F. Xiao, G. Qiao, X. Zhang and B. Liao, "Quantitative research on effects of Nb on hot deformation behaviors of high-Nb microalloyed steels", Materials Science and Engineering A, vol. 530, pp. 277-284, 2011.
- [97] Z.-h. Zhang, Y.-n. Liu, X.-k. Liang and Y. She, "The effect of Nb on recrystallization behavior of Nb micro-alloyed steel", Materials Science and Engineering A, vol. 474, pp. 254-260, 2008.
- [98] C. Miao, G. Zhang and C. Shang, "Effect of Nb content on hot flow stress, dynamic recrystallization and strain accumulation behaviors in low carbon bainitic steel", Materials Science Forum, vol. 654-656, pp. 62-65, 2010.
- [99] A. Guo, R. Misra, J. Xu, B. Guo and S. Jansto, "Ultrahigh strength and low yield ratio of niobium-microalloyed 900MPa pipeline steel with nano/ultrafine bainitic lath", Materials Science and Engineering A, vol. 527, pp. 3886-3892, 2010.
- [100] T. Gladman, "The effect of inclusions on recrystallisation and grain growth", in : Inclusions, ed. F.B. Pickering, The Institution of Metallurgist, 1979, p. 172.
- [101] S. Yuan and G. Liang, "Dissolving behaviour of second phase particles in Nb-Ti microalloyed steel", Materials Letters, vol. 63, pp. 2324-2326, 2009.
- [102] J. Cao, Q. Yong, Q. Liu and X. Sun, "Precipitation of MC phase and precipitation strengthening in hot rolled Nb-Mo and Nb-Ti steels", Journal of Materials Science, vol. 42, pp. 10080-10084, 2007.
- [103] H. Yi, L. Du, G. Wang and X. Liu, "Influence of holding time after deformation on bainite transformation in niobium microalloyed steel", Journal of Iron and Steel Research International, vol. 14, pp. 62-65, 2007.
- [104] C. Sellars, "Modelling microstructural development during hot rolling", Materials Science and Technology, vol. 6, pp. 1072-1081, 1990.
- [105] H. Zurob, G. Zhu, S. Subramanian, G. Purdy, C. Hutchinson and Y. Bréchet, "Analysis of Mn Effect on Recrystallization Kinetics in High Nb Steels", Materials Science Forum, vols. 500-501, pp. 123-130, 2005.
- [106] C. Hutchinson, H. Zurob, C. Sinclair and Y. Brechet, "The comparative effectiveness of Nb solute and NbC precipitates at impeding grain-boundary motion in Nb steels", Scripta Materialia, vol. 59, pp. 635-637, 2008.
- [107] M. Akben, B. Bacroix and J. Jonas, "Effect of vanadium and molybdenum addition on high temperature recovery, recrystallization and precipitation behavior of niobium based steel", Acta metallurgica, vol. 31, pp. 161-174, 1983.

BIBLIOGRAPHY

- [108] M. Akben, I. Weiss and J. Jonas, "Dynamic precipitation and solute hardening in AV microalloyed steel and two Nb steels containing high levels of Mn", Acta Metallurgica, vol. 29, pp. 111-121, 1981.
- [109] S. Kurokawa, J. Ruzzante, A. Hey and F. Dymont, "Diffusion of Nb in Fe and Fe alloys", Metal Science, vol. 17, pp. 433-438, 1983.
- [110] H. Mohrbacher, "Combined effects of Nb and B microalloying in molybdenum based ultra low carbon bainitic (ULCB) steels", in : 6th International Conference on High Strength Low Alloy Steels (HSLA Steels 2011), Beijing, 2011, pp. 785-791.
- [111] R. Fostini and F. Schoen, "Effects of carbon and austenitic grain size on the hardenability of Mo steels" in : Transformation and Hardenability of Steels, Climax Molybdenum 1967, pp. 195-209.
- [112] S. Wang and P. Kao, "The effect of alloying elements on the structure and mechanical properties of ultra low carbon bainitic steels", Journal of Materials Science, vol. 28, pp. 5169-5175, 1993.
- [113] C. Garcia de Andrés, C. Capdevila, F. Caballero and D. San Martin, "Effect of Mo on continuous cooling transformations in two medium carbon forging steels", Journal of Materials Science, vol. 36, pp. 565-571, 2001.
- [114] M. Masimov and N. Kwiaton, "A study of Mo-induced bainitic transformation in continuously cooled steels by X-ray and electron diffraction", in : Euromat, Glasgow, 2009.
- [115] Z. Tang and W. Stumpf, "The role of molybdenum additions and prior deformation on acicular ferrite formation in microalloyed Nb–Ti low-carbon line-pipe steels", Materials Characterization, vol. 59, pp. 717-728, 2008.
- [116] W. Liu and M. Akben, "Softening behavior of two Ti bearing steels during torsional simulation of rolling", Canadian Metallurgical Quarterly, vol. 26, pp. 145-153, 1987.
- [117] C. Chen, H. Yen, F. Kao, W. Li, C. Huang, J. Yang and S. Wang, "Precipitation hardening of high-strength low-alloy steels by nanometer-sized carbides", Materials Science and Engineering, vol. 499, pp. 162-166, 2009.
- [118] Y. Funakawa, T. Shiozaki, K. Tomita, T. Yamamoto and E. Maeda, "Development of High Strength Hot-rolled Sheet Steel Consisting of Ferrite and Nanometer-sized Carbides", ISIJ International, vol. 44, pp. 1945-1951, 2004.
- [119] J. Jang, Y. Heo, C. Lee, H. Bhadeshia and D. Suh, "Interphase precipitation in Ti–Nb and Ti–Nb–Mo bearing steel", Materials Science and Technology, vol. 29, pp. 309-313, 2013.
- [120] J. Jang, C. Lee, Y. Heo and D. Suh, "Stability of (Ti,M)C (M = Nb, V, Mo and W) carbide in steels using first-principles calculations", Acta Materialia, vol. 60, pp. 208-

BIBLIOGRAPHY

- 217, 2012.
- [121] C. Garcia de Andrés, C. Capdevila, D. San Martin and F. Caballero, "Effect of the microalloying elements on nucleation of allotriomorphic ferrite in medium C-Mn steels", Journal of Materials Science Letters, vol. 20, pp. 1135-1137, 2001.
- [122] C. Garcia de Andrés, C. Capdevila, D. San Martin and F. Caballero, "Effect of titanium on the allotriomorphic ferrite transformation kinetics in medium carbon–manganese steels" Materials Science and Engineering A, vol. 328, pp. 156-160, 2002.
- [123] M. Korchynsky, in : Proceedings of the International Conference "Microalloying'95", edited by M. Korchynsky, A.J. Ardo, P. Regas and G. Tither, held under the auspices of the Iron and steel society, Inc., Pittsburgh, PA, USA, June11-14, 1995.
- [124] S. Wang, "The effect of titanium and nitrogen contents on the austenite grain coarsening temperature", Journal of Materials Science, vol. 24, pp. 105-109, 1989.
- [125] H. Adrian and F. Pickering, "Effect of titanium additions on austenite grain growth kinetics of medium carbon V-Nb steels containing 0,008%-0,018%", Materials Science and Technology, vol. 7, pp. 176-182, 1991.
- [126] B. Mintz, J. Banerjee and K. Banks, "A regression equation for the Ar3 temperature for coarse grained as-cast steels", Ironmaking and Steelmaking, vol. 38, pp. 197-203, 2011.
- [127] B. Garbarz and F. Pickering, "Effect of austenite grain boundary mobility on hardenability of steel containing vanadium", Materials Science and Technology, vol. 4, pp. 967-975, 1988.
- [128] S. Lee, J. Park and Y. Lee, "Effect of austenite grain size on the transformation kinetics of upper bainite in a low alloy steel", Scripta Materialia, vol. 59, pp. 87-90, 2008.
- [129] S. Yamamoto, H. Yokoyama, K. Yamada and N. Niikura, "Effects of the austenite grain size and deformation in the unrecrystallized austenite region on bainite transformation behavior and microstructure", ISIJ International, vol. 35, pp. 1020-1026, 1995.
- [130] E. Davenport, R. Grange and R. Hafsten, "Influence of austenite grain size upon isothermal transformation behavior of SAE 4140 steel", Transactions of the AIME, vol. 145, pp. 301-314, 1941.
- [131] K. Winterton, "The effect of overheating on the transformation characteristics of a nickel-chromium-molybdenum steel", Journal of the iron and steel institute, vol. 151, pp. 79-85, 1945.
- [132] S. Cottrell and T. Ko, "Effect of high temperature heating on the isothermal transformation of bainite", Journal of the iron and steel institute, vol. 173, pp. 224-228, 1953.

BIBLIOGRAPHY

- [133] L. Graham and H. Axon, "The effect of austenitizing treatment on formation of lower bainite in a plain carbon steels", Journal of the iron and steel institute, vol. 191, pp. 361-365, 1959.
- [134] J. Barford and W. Owen, "Effect of the austenite grain size and temperature and the bainite formation", Journal of the iron and steel institute, vol. 197, pp. 146-151, 1961.
- [135] M. Umemoto, K. Horiuchi and I. Tamura, "Transformation kinetics of bainite during isothermal holding and continuous cooling", Transactions of the Iron and Steel Institute of Japan, vol. 22, pp. 854-861, 1982.
- [136] A. Matsuzaki and H. Bhadeshia, "Effect of austenite grain size and bainite morphology on overall kinetics of bainite transformation in steels", Materials science and technology, vol. 15, pp. 518-522, 1999.
- [137] H. Yang and H. Bhadeshia, "Austenite grain size and the martensite-start temperature" Scripta Materialia, vol. 60, pp. 493-495, 2009.
- [138] M. Zhao, K. Yang, F. Xiao and Y. Shan, "Continuous cooling transformation of undeformed and deformed low carbon pipeline steels", Materials Science and Engineering A, vol. 355, pp. 126-136, 2003.
- [139] X. Liu, J. Solberg and R. Gjengedal, "Measurement of austenite-to-ferrite transformation temperature after multi-pass deformation of steels", Materials Science and Engineering A, vol. 194, pp. L15-L18, 1995.
- [140] J. Yang, Q. Liu, D. Sun and X. Li, "Microstructure and transformation characteristics of acicular ferrite in high niobium-bearing microalloyed steel", Journal of Iron and Steel Research International, vol. 17, pp. 53-59, 2010.
- [141] F. Xiao, B. Liao, Y. Shan, G. Qiao, Y. Zhong, C. Zhang and K. Yang, "Challenge of mechanical properties of an acicular ferrite pipeline steel", Materials Science and Engineering A, vol. 431, pp. 41-52, 2006.
- [142] C. Capdevila, J. Ferrer, C. Garcia-Mateo, F. Caballero, V. Lopez and C. Garcia de Andr s, "Influence of Deformation and Molybdenum Content on Acicular Ferrite Formation in Medium Carbon Steels", ISIJ international, vol. 46, pp. 1093-1100, 2006.
- [143] K. Fujiwara, S. Okaguchi and H. Ohtani, "Effect of hot deformation on bainite structure in low carbon steels", ISIJ International, vol. 35, pp. 1006-1012, 1995.
- [144] C. Chiou, J. Yang and C. Huang, "The effect of prior compressive deformation of austenite on toughness property in an ultra-low carbon bainitic steel", Materials Chemistry and Physics, vol. 69, pp. 113-124, 2001.
- [145] X. Jin, N. Min, K. Zheng and T. Hsu, "The effect of austenite deformation on bainite formation in alloyed eutectoid steel", Materials Science and Engineering A, vols. 438-440, pp. 170-172, 2006.

BIBLIOGRAPHY

- [146] R. Zhang and J. Boyd, "Bainite transformation in deformed austenite", Metallurgical and Materials Transactions A, vol. 41, pp. 1448-1459, 2010.
- [147] H. Bhadeshia, "Effect of stress and strain on formation of bainite in steels", in : Hot workability of steels and light alloys-composites, ed. H.J. McQueen et al., Montreal, Canadian Institute of Mining, Minerals and Petroleum, 1996, pp. 543-556.
- [148] I. Yakubtsov and J. Boyd, "Bainite transformation during continuous cooling of low carbon microalloyed steel", Materials Science and Technology, vol. 17, pp. 296-302, 2001.
- [149] J. Philibert, A. Vignes, Y. Bréchet and P. Combrade, Métallurgie, du minerai au matériau, 2eme éd., Dunod, 2002.
- [150] J. Adamczyk and M. Opiela, "Influence of the thermo-mechanical treatment parameters on the inhomogeneity of the austenite structure and mechanical properties of the Cr-Mo steel with Nb, Ti, and B microadditions", Journal of Materials Processing and Technology, vol. 157-158, pp. 456-461, 2004.
- [151] S. Khan and H. Bhadeshia, "The bainite transformation in chemically heterogeneous 300M high strength steel", Metallurgical Transactions A, vol. 21A, pp. 859-875, 1990.
- [152] J. Gautam, A. Miroux, J. Moerman, C. Barbatti, P. Van liempt and L. Kestens, "Determination of the Non-Recrystallisation Temperature (T_{nr}) of Austenite in High Strength C-Mn steels", Materials Science Forum, vol. 706-709, pp. 2722-2727, 2012.
- [153] F. Siciliano and J. Jonas, "Mathematical modeling of the hot strip rolling of microalloyed Nb, multiply-alloyed Cr-Mo, and plain C-Mn steels", Metallurgical and Materials Transactions A, vol. 31A, pp. 511-530, 2000.
- [154] J. Dong and F. Siciliano, and J. Jonas et al., "Effect of Silicon on the Kinetics of Nb(C,N) Precipitation during the Hot Working of Nb-bearing steels", ISIJ International, vol. 40, pp. 613-618, 2000.
- [155] K. Irvine, F. Pickering, T. Gladman, "Grain-Refined C-Mn Steels", Journal of the Iron and Steel Institute, vol. 205, pp. 161-182, 1967.
- [156] A. Gorni, Steel forming and heat treating handbook, 2013.
- [157] W. Steven and A. Haynes, "The Temperature of Formation of Martensite and Bainite in Low Alloy Steels", Journal of the Iron and Steel Institute, vol. pp. 349-359, 1956.
- [158] A. Di Schino, I. Gutierrez, B. López, E. Alonso, D. Jorge, S. Medina, L. Rancel, S. Cobo, J. Eliasson, S. Zajac, H. Pettersson, G. Östberg, M. Klein and M. Sonnleitner, "Toughness and ductility improvement in complex microstructure HSS by means of microstructural parameters optimisation", Rapport final European Commission, n° EUR 24185, 2010.

BIBLIOGRAPHY

- [159] D. Das and P. Chattopadhyay, "Influence of martensite morphology on the work-hardening behavior of high strength ferrite–martensite dual-phase steel", Journal of Materials Science, vol. 44, pp. 2957-2965, 2009.
- [160] F. Caballero, J. Chao, J. Cornide, C. Garcia-Mateo, M. Santofimia and C. Capdevila, "Toughness deterioration in advanced high strength bainitic steels", Materials Science and Engineering, vol. A 525, pp. 87-95, 2009.
- [161] C. Garcia-Mateo and F. Caballero, "The Role of Retained Austenite on Tensile Properties of Steels with Bainitic Microstructures", Materials Transactions, vol. 46, pp. 1839-1846, 2005.
- [162] S. Lee, S. Lee and B. De Cooman, "Austenite stability of ultrafine-grained transformation-induced plasticity steel with Mn partitioning", Scripta Materialia, vol. 65, pp. 225-228, 2011.
- [163] X. Xiong, B. Chen, M. Huang, J. Wang and L. Wang, "The effect of morphology on the stability of retained austenite in a quenched and partitioned steel", Scripta Materialia, vol. 68, pp. 321-324, 2013.
- [164] S. Zhang and K. Findley, "Quantitative assessment of the effects of microstructure on the stability of retained austenite in TRIP steels", Acta Materialia, vol. 61, pp. 1895-1903, 2013.
- [165] F. Ghaith and F. Khan, "Three dimensional non-linear finite element modeling of charpy impact test", International Journal of Mechanical Engineering and Technology, vol. 4, pp. 337-386, August 2013.
- [166] A. Di Schino and C. Guarnaschelli, "Effect of microstructure on cleavage resistance of high strength quenched and tempered steels", Materials Letters, vol. 63, pp. 1968-1972, 2009.
- [167] L. Rancel, M. Gomez, S. Medina and I. Gutierrez, "Measurement of bainite packet size and its influence on cleavage fracture in medium carbon bainitic steel", Materials Science and Engineering A, vol. 530, pp. 21-27, 2011.
- [168] H. Bhadeshia, "About calculating the characteristic of the martensite-austenite constituent", in : Proceedings of the International Seminar on welding of high strength pipeline steels, pp. 99-106, 2013.
- [169] F. Pickering, Transformations and hardenability in steels, *Climax Molybdenum*, 1967.
- [170] R. S. Chandel, R. F. Orr, J. A. Gianetto, J. T. McGrath, B. M. Patchett and A. Bicknell, "The Microstructure-Mechanical Properties of Narrow Gap Welds in 2.25Cr±1Mo", Int. Institute of welding doc IX-1377-85, Ottawa, 1985.
- [171] J. P. Naylor and P. R. Krahe, "Effet of bainite packet size on toughness", Metallurgical Transactions, vol. 5, pp. 1699-1701, 1974.

BIBLIOGRAPHY

- [172] P. Brozzo, G. Buzzichelli, A. Mascanzoni and M. Mirabile, "Microstructure and cleavage resistance of low-carbon bainitic steels", Metal Science, vol. 11, pp. 123-129, April 1977.
- [173] Y. Ohmori, H. Ohtani and T. Kunitake, "Tempering of the bainite and the bainite/martensite duplex structure in a low carbon low alloy steel", Metal Science, vol. 8, pp. 357-366, 1974.
- [174] S. Parker, W. J.E.J., I. Gutiérrez, R. Rodriguez, L. Vanderberghe and U. Lotter, "Property models for mixed microstructures" European Commission, 2003.
- [175] T. Gladman, D. Dulieu and I. Mc Ivor, "Structure/property relationships in high-strength micro-alloyed steels", in : Microalloying '75, Union carbide corporation, pp. 32-54, 1977.
- [176] F. Pickering, Physical Metallurgy and the Design of Steels, Applied Science Pub., 1978.
- [177] A. Iza-Mendia and I. Gutierrez, "Generalization of the existing relations between microstructure and yield stress from ferrite-pearlite to high strength steels", Materials Science and Engineering, vol. A561, pp. 40-51, 2013.
- [178] I. Gutierrez, A. Altuna, G. Paul, S. Parker, J. Bianchi, P. Vescovo, C. Mesplont, M. Wojcicki and R. Kawalla, "Mechanical property models for high-strength complex microstructures", Rapport final European Commission EUR 23181, 2008.
- [179] T. Barry and J. Schmitt, "Durcissement des aciers - Mécanismes", Techniques de l'ingenieur, M4340, 2002.
- [180] T. Yokoi, M. Takahashi, N. Maruyama and M. Sugiyama, "Application of controlled Cu nano-precipitation for improvement in fatigue properties of steels", Nippon steel technical report, n°91, pp. 49-55, January 2005.
- [181] I. Madariaga, I. Gutierrez, B. Lopez, "Acicular ferrite microstructure and mechanical properties in a medium carbon forging steel", Materials Science Forum, vols. 284-286, pp. 419-426, 1998.
- [182] S. Song, J. Wu, D. Wang, L. Weng and L. Zheng, "Stress-induced non-equilibrium grain boundary segregation of phosphorus in a Cr-Mo alloy steel", Materials Science and Engineering A, vol. 430, pp. 320-325, 2006.
- [183] B. Chen, P. Flewitt and D. Smith, "Microstructural sensivity of 316H austenitic stainless steel: Residual stress relaxation and grain boundary fracture", Materials Science and Engineering A, vol. 527, pp. 7387-7399, 2010.
- [184] M. Paju and R. Möller, "The effect of boron on phosphorus segregation in austenite" Scripta Metallurgica, vol. 18, pp. 813-815, 1984.
- [185] K. Zhu, O. Bouaziz, C. Oberbillig and M. Huang, "An approach to define the effective lath size controlling yield strength of bainite", Materials Science and Engineering, vol.

BIBLIOGRAPHY

- A527, p. 6614–6619, 2010.
- [186] J. Morris, “Dislocation Plasticity: an overview”, in: Encyclopedia of Materials Science and Technology, Elsevier Science, Amsterdam (2001).
- [187] M. Bush and P. Kelly, “Strengthening mechanisms in bainitic steels”, Acta Metallurgica, vol. 19, pp. 1363-1371, 1971.
- [188] G. Speich and R. Miller, in : Structure and properties of dual-phase steels, ed. R.A Kot, J.W. Morris, TMS-AIME, 1979, pp. 145-182.
- [189] A. Kumar, S. Singh and K. Ray, “Influence of bainite/martensite-content on the tensile properties of low carbon dual-phase steels”, Materials Science and Engineering, vol. A474, pp. 270-282, 2008.
- [190] A. Bag, K. Ray and E. Dwarakadasa, “Influence of Martensite Content and Morphology on Tensile and Impact Properties of High-Martensite Dual-Phase Steels”, Metallurgical and Materials Transactions, vol. 30A, pp. 1193-1202, May 1999.
- [191] C. Lanzillo to and F.B. Pickering, “Structure-property relationships in dual-phase steels”, Metal Science, vol. 16, pp. 371-382, August 1982.
- [192] M. Mazinani, “Deformation and fracture behaviour of low-carbon dual-phase steel”, Thèse, The university of British Columbia, 2006.
- [193] U. Liedl, S. Taint and E. Werner, “An unexpected feature of the stress–strain diagram of dual-phase steel”, Computational Materials Science, vol. 25, pp. 122-128, 2002.
- [194] L. Chang, Bainite Transformations and Novel Bainitic Rail Steels, Thèse, University of Cambridge, 1995.
- [195] G.F. Vander Voort, Metallography: Principles and Practice, ASM International, 1999.
- [196] A.K. De, J.G. Speer and D.K. Matlock, “Color Tint-Etching for Multiphase Steels” Advanced Materials & Processes, pp. 27-30, February 2003.
- [197] B.L. Bramfitt and A.O. Benscoter, Metallographer's Guide: Practices and Procedures for Iron and Steels, ASM International, 2002.
- [198] F.S. LePera, “Improved Etching Technique to Emphasize Martensite and Bainite in High-Strength Dual-Phase Steel”, Journal of Metals, vol. 32, pp. 38-39, March 1980.
- [199] T. Ferreira and W. Rasband, ImageJ User Guide, 2012.
- [200] H. Bhadeshia, “The lower bainite transformation and the significance of carbide precipitation”, Acta Metallurgica, vol. 28, pp. 1103-1114, 1980.
- [201] S. Nemecek, Z. Novy, J. Uhlir, J. Janovec et M. Kusy, “Evaluation of retained austenite in high strength steels”, in : New developments on metallurgy and applications of high

BIBLIOGRAPHY

- strength steels, Buenos Aires, TMS, pp. 1159-1166, 2008.
- [202] P. Jacques, S. Allain, O. Bouaziz, A. De, A. Gourgues, B. Hance, Y. Houbaert, J. Huang, A. Iza-Mendia, S. Kruger, M. Radu, L. Samek, J. Speer, L. Zhao and S. van der Zwaag, "On measurement of retained austenite in multiphase TRIP steels — results of blind round robin test involving six different techniques", Materials Science and Technology, vol. 25, pp. 567-574, 2009.
- [203] S. Van der Zwaag, L. Zhao, S. Kruijver and J. Sietsma, "Thermal and mechanical stability of retained austenite in aluminum-containing multiphase TRIP steels", ISIJ international, vol. 42, pp. 1565-1570, 2002.
- [204] M. Neilson and G. Brockman, "The error associated with point counting", American Mineralogist, vol 62, pp. 1238-1244, 1977.
- [205] M. Bach, N. Broll, A. Cornet and L. Gaide, "Diffraction X en traitements thermiques : dosage de l'austénite résiduelle par diffraction des rayons X", Journal de Physique III, vol. 6, pp. 887-895, juillet 1996.
- [206] J. Drillet and L. Jantzen, "Study of the influence of microstructural heroteneities on austenite stability by magnetism and X-ray diffraction" 2005.
- [207] L. Jantzen, "Mesure de l'austénite résiduelle par sigmamétrie. Application à la détermination de la stabilité de l'austénite", report, ArcelorMittal R&D Maizières Research SA, 2000.
- [208] C. Garcia de Andrés, M. Bartolomé, C. Capdevila, D. San Martin, F. Caballero and V. Lopez, "Metallographic techniques for the determination of the austenite grain size in medium-carbon microalloyed steels", Materials Characterization, vol. 46, pp. 389-398, 2001.
- [209] C. Garcia de Andrés, F. Caballero, C. Capdevila and D. San Martin, "Reaveling austenite grain boundaries by thermal etching : advantages and disadvantages", Materials Characterization, vol. 49, pp. 121-127, 2003.
- [210] M. Humbert, F. Wagner, H. Moustahfid and C. Esling, "Determination of the orientation of the parent beta grain from the orientations of the inherited alpha plates in the phase transformation from bcc to hcp", Journal of Applied Crystallography, vol. 28, pp. 571-576, 1995.
- [211] M. Humbert and N. Gey, "The calculation of the parent grain orientation from inherited variants for approximate (bcc-hcp) orientation relations", Journal of Applied Crystallography, vol. 35, pp. 401-405, 2002.

BIBLIOGRAPHY

Relations quantitatives entre composition chimique, microstructure et propriétés mécaniques d'aciers bainitiques.

RESUME : Les aciers bainitiques refroidis à l'air libre sont de plus en plus utilisés à la place des aciers martensitiques trempés et revenus pour la réalisation de pièces forgées dans le secteur automobile. Ces aciers permettent la réalisation d'économies significatives de temps et d'argent lors de leur fabrication. Leur résistance mécanique élevée est obtenue grâce à une composition chimique complexe, générant une microstructure multi-échelle et multiphasée lors du refroidissement à l'air libre. Dans un souci d'amélioration continue de cet acier, il devient nécessaire de comprendre plus en profondeur les mécanismes physiques mis en jeu lors de la décomposition de l'austénite. L'objectif principal de cette thèse est de contribuer à cette compréhension en établissant des liens quantitatifs entre la composition chimique, la microstructure et les propriétés mécaniques pour cette gamme d'aciers dans des conditions représentatives du forgeage. L'influence de plusieurs éléments d'alliage sur la microstructure brute de forge, ainsi que quelques synergies entre ces éléments, a été établie grâce à l'étude de diagrammes TRC spécifiques à l'application visée. Les mécanismes de rupture dominants et les paramètres microstructuraux contrôlant la résilience ont été identifiés par l'étude des faciès de rupture, de l'endommagement dans le volume et par des caractérisations microstructurales ciblées. Les contributions respectives de chaque mécanisme classique de durcissement structural ont été déterminées de manière quantitative, sur la base de plusieurs hypothèses et de paramètres microstructuraux. Au passage, des informations précieuses sur le comportement global en traction de ces aciers ont été récoltées grâce à l'étude des mécanismes d'endommagement et de rupture en traction. Tous ces résultats ont permis l'identification des paramètres microstructuraux, comme la taille de paquet bainitique et la fraction de constituants microstructuraux secondaires, qui doivent être pris en considération lors de l'optimisation de la composition chimique.

Mots clés : bainite – éléments d'alliage – microstructure – résistance mécanique – résilience – forge - refroidissement air

Quantitative relationships between chemical composition, microstructure and mechanical properties for bainitic steels

ABSTRACT: Air-cooled bainitic steel grades are increasingly being considered as substitutes to quenched & tempered martensitic steels in the realization of automotive forged parts. They allow significant manufacturing cost and time reductions. To compete with martensitic steels, high mechanical strength is provided by a complex chemical composition, leading to a multi-scale and multi-constituent microstructure after air-cooling. In order to optimize such chemical composition, need in rationalization of the steel grade development has emerged. The main aim of this Ph.D project was to build a physically based knowledge of the steel grade by making quantitative links between chemical composition, microstructure and mechanical properties in as-forged condition. The influence of several alloying elements on the as-forged microstructure, as well as some synergies, has been established using relevant CCT diagrams. Dominant fracture mechanisms and controlling microstructural parameters in concern of impact toughness have been identified with the help of comprehensive fracture surface, cross-section observations and targeted quantitative microstructural characterization. The respective contributions to yield strength of classical strengthening mechanisms have been quantitatively linked to microstructural parameters, based on several hypothesis and microstructural parameters. At the same, precious information on tensile behaviour has also been deduced from the observation of the fractured tensile test specimens. All these results allow identifying the key microstructural parameters, such as bainitic packet size or secondary microstructural constituents content, that have to be targeted in the alloy design.

Keywords : bainite – alloying elements – microstructure – mechanical strength – impact toughness – forging – air-cooling.